Analyse théorique et contrôle des instationnarités dans un écoulement de culot en régime compressible.

Philippe Meliga

Thèse de Doctorat en Mécanique
École Polytechnique, 2008

Philippe MELIGA

A theoretical approach for the onset and control of unsteadiness in compressible afterbody flows

Analyse théorique et contrôle des instationnarités dans un écoulement de culot en régime compressible

Jury

M.	Jean-Paul BONNET	
M.	Jean-Marc CHOMAZ	*Directeur de thèse*
M.	Jeffrey CROUCH	*Rapporteur*
M.	Dan HENNINGSON	
M.	Hadrien LAMBARÉ	
M.	Jacques MAGNAUDET	*Rapporteur*
M.	Pierre SAGAUT	
M.	Denis SIPP	

CONTENTS

PRELUDE

Nice, février 2008

Carla, 4 ans : Tonton, Tonton, regarde, j'ai écrit ta thèse!
Moi : C'est très gentil ma puce, mais tu sais, dans une thèse, il y a plein de pages! Tu veux bien en écrire d'autres pour m'aider?
Carla : Non, le reste, d'abord, tu le fais tout seul!

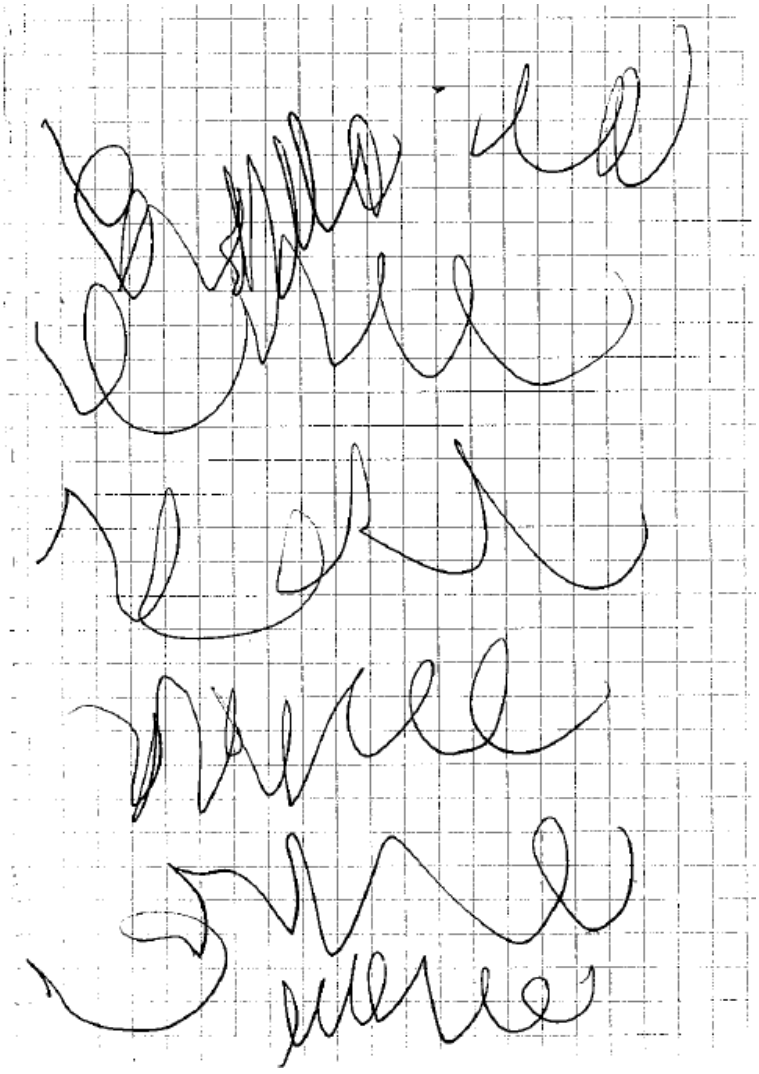

ONCE UPON A TIME...

Comme toutes les thèses, la mienne a commencé près d'une machine à café (c'est une sorte de principe fondamental, l'équivalent pour une thèse de la croissance de l'entropie ou de la chute de la tartine beurrée). Par un froid matin de décembre, donc, Laurent et Denis m'ont proposé de travailler sur ce sujet. A l'époque, mes certitudes étaient encore fragiles : s'en sont donc suivies quelques semaines de réflexion pendant lesquelles j'ai sollicité les avis des uns et des autres. La réponse (unanime) que j'ai obtenue tient en deux mots : *Non. NOOOOOON!* Rien de tel qu'une réponse unanime pour piquer la curiosité... alors j'ai dit oui.

Dans le même temps, un peu par hasard, j'ai découvert l'escalade. Pour bien débuter en escalade, il faut avoir de bons guides. La première fois que l'on doit passer sa corde dans la dégaine, on se débrouille comme on peut. Ensuite, on apprend à être patient et à réfléchier, à sentir le relief, à choisir entre la fluidité et la force. Parfois, on tombe, et le plus souvent, on repart, sans avoir la certitude d'arriver tout en haut. Pourtant, la sensation qu'on éprouve, suspendu par le bout des doigts au-dessus du vide, est indescriptible. Pour cette ascension un peu particulière qu'a été la thèse, il m'a fallu quatre ans pour accrocher la dernière dégaine. De temps à autre, je suis tombé, et à l'occasion je me suis fait rudement mal (l'avantage, avec l'escalade, c'est qu'on a très peu de chances de croiser la trajectoire d'une porte après avoir franchi un dévers). Mais je garderai le souvenir de quatres années extraordinaires, intenses, passionnantes et pleines de rebondissements.

Tout d'abord, merci à Jean-Marc, l'homme qui aime la science, le jazz, F'Murrr et Franquin. Que demander de plus? Merci pour ta bonne humeur jamais démentie et pour ta confiance sans faille. Je reste admiratif devant ton enthousiasme et ta passion contagieuse. Merci pour tout le temps que tu m'as consacré, j'ai beaucoup appris et j'ai pris beaucoup de plaisir à travailler avec toi.

Merci à Denis pour ta curiosité et ton énergie inépuisable, même au milieu d'une tempête de cris d'enfants. Ce travail doit beaucoup à nos parties de ping-pong scientifique, à tes conseils avisés, qui m'ont sorti de quelques fameuses ornières, et à ton stoïcisme face à l'adversité numérique. Merci à Philippe et Hadrien, qui ont continué à me faire confiance quand ce sujet s'est mis rebondir de manière non linéaire et dans des directions vraisemblablement déroutantes. Merci enfin à Laurent qui m'a d'abord

accueilli à Meudon en tant que stagiaire avant de m'intégrer à son commando de choc.

Merci aux membres du jury qui ont jugé et apprécié ce travail avec exigence et pertinence. A Jeffrey Crouch et Jacques Magnaudet qui ont accepté de s'investir en tant que rapporteurs de ce mémoire. A Jean-Paul Bonnet, qui a présidé ce jury, Dan Henningson et Pierre Sagaut. L'intérêt et la curiosité que vous tous avez manifesté à l'égard de ce travail sont un honneur et un plaisir.

Merci à Sabine, qui m'a confié ses groupes d'élèves en travaux dirigés à l'ENSTA. Je me souviens avoir très peu dormi à la veille de ma première intervention. Depuis, j'y prends beaucoup de plaisir, et enseigner m'apporte énormément, humainement et scientifiquement.

Merci aux collègues étonnants et attachants que j'ai côtoyés au quotidien, beaucoup d'entre vous sont devenus des amis. Dans le désordre, merci à Pascal, Yves & Yves, Serge, Thierry et ses pépites jazzy, Florent, Patrick, Jean-Pierre et tous les autres, pour votre sympathie, vos coups de main, votre bonne humeur et aussi vos coups de gueule. Merci à Benji, P.Q., Bruno, Greg, Caro, Benoît, J.B., Raph, Olivier, qui m'ont accompagné tout au long de l'aventure, qui en ont partagé les moments de grandeur et de décadence. De nombreuses soirées à refaire le monde et quelques coups de folie ont grandement contribué à la réussite de cette thèse. Merci à Adelaïde pour son mot d'encouragement. Merci à Vince, avec qui j'ai partagé les affres du premier amphi. Merci à Seb, *celui dont il ne faut pas écouter la musique*, avec qui j'ai ressuscité les vamps. Et puis j'ai une pensée pour Pierre, je sais que dans d'autres circonstances, nos chemins n'auraient pas fini de se croiser.

Pour terminer, merci à ma soeur Laurence, qui, avec sa petite tribu niçoise, a été mon plus grand soutien. Tu as été d'une patience infinie pour supporter les doutes et les angoisses qui m'ont assailli, bien au-delà du cadre de cette thèse. J'ai toujours trouvé auprès de toi une oreille attentive, même (surtout?) à des heures indues. Merci de t'être obstinée, merci d'avoir cru en moi. J'ai conscience de te devoir davantage que ce que mes mots ne sauraient exprimer.

Philippe

Cette thèse a été réalisée à l'ONERA, au sein du Département d'Aérodyamique Fondamentale et Expérimentale. Elle a été financée par le CNES et l'ONERA pendant trois ans, puis par l'ONERA pendant 9 mois.

INTRODUCTION

Of afterbody flows

The flow around a space launch vehicle (Figure 1.1) exhibits a massive separation that occurs owing to the abrupt change in the geometry of the first stage. The first consequence of this geometry is a dramatic increase in the base drag which may represent up to 70% of the total drag, owing to the low-pressure levels within the recirculation. Furthermore, the unsteadiness of the separated flow triggers a complex dynamics characterized by intense low-frequency wall-pressure fluctuations. As a result, the base region is submitted to high dynamic loads or side-loads, that can be critical during the transonic phase of flight and disturb the launcher stability, as experienced by the Ariane V launcher. Such oscillations can excite structural vibrations that may, amongst other disagreements, cause fatigue failure, resulting in early deterioration of the materials, or affect the integrity of the payload. This unsteady behaviour is also detrimental to the engineering application by limiting the maximum thrust, whereas high-thrust delivering is precisely needed to face the increase in the payload capabilities. The prediction for the occurrence of these undesirable flow conditions is thus needed to guide the future engineering designs, in order to improve the aerodynamic performances and reliability of launch vehicles. To alleviate or control such unsteadiness, a better knowledge of the underlying physical mechanisms is also required. Though, the understanding of the separated dynamics remains by now somehow limited, as several unsteady aerodynamic phenomena are simultaneously at work, including the dynamics of the recirculating bubble, the interaction of the separated free-shear layer with the solid walls of the nozzle and the boosters, or the aeroacoustic field radiated by the supersonic propulsive jets.

Unsteadiness in separated flows has been a subject of great interest in the last decades. Model configurations have been investigated so as to ease the determination of the major features of the mean flow structure and the predominant mechanisms involved in the onset of unsteadiness. In particular, two-dimensional flows featuring separation from a sharp edge, have been extensively studied, both numerically and experimentally (Roshko [68]; Schumm *et al.* [71]; Roussopoulos & Monkewitz [69]). Nevertheless, only a limited amount of data is available on axisymmetric geometries, that model more appropriately the first stage of the launcher. The differences featured by two and three-dimensional wake flows is illustrated well by the study of

(a) *Ariane 5 (EU).*

(b) *Proton-K (Russia).*

(c) *Delta IV (USA).*

(d) *Primitive prototype (Gaul).*

Figure 1.1. *Space launch vehicles.*

Gai & Patil [32], who investigated the effect on a subsonic axisymmetrical blunt base of various control devices, which had been proven fruitful to yield a significant drag reduction in two-dimensional low-speed flows. As a result, the efficiency of these devices was found to be questionable.

The base pressure properties of blunt axisymmetric bodies have been studied in the early 1960's (Eldred [25]; Merz [56]). Experimental results obtained on more complex axisymmetric afterbodies have shown that the wall-pressure is highly dependent on the geometry (Délery & Sirieix [19]). In particular, mainly two different kinds of flow separation are to be considered, depending on whether a downstream reattachment of the separated shear-layer on a solid surface occurs or not. This has been confirmed by an experimental test campaign carried out in 2002 in the ONERA/DAFE S3Ch transonic wind tunnel, presented in Figure 1.2 (Deprés [20], see also Deprés *et al.* [21]). The wall-pressure properties of axisymmetric blunt-based bodies modeling ideal launcher shapes have been investigated in the fully turbulent and transonic regimes, in the framework of the research and technology ATAC program on Afterbody and Nozzle Aerodynamics for Launchers, undertaken by CNES and ONERA, with support of French research laboratories (Laboratoire d'Études Aérodynamiques at Poitiers) and industrials (EADS Astrium, SNECMA). Typical bodies used for these tests are presented in Figure 1.3. Figure 1.3(a) shows a simple axisymmetric blunt base for which no reattachment occurs, a configuration hereafter referred to as Type I. Figure 1.3(b) shows the same base, now equipped with a rear-body extension of length $L = 1.2D$, modeling an ideal nozzle shape. Such configuration, where a reattachment does occur close to the end of the protruding wall, is hereafter referred to as Type II. The spectrum of the wall-pressure fluctuations corresponding to these two bodies are presented in Figures 1.3(c) and 1.3(d). For Type I, the spectrum is clearly dominated by a well-defined energetic peak at the Strouhal number $St = 0.20$ based on the body diameter, corresponding to the low-frequency periodical shedding of large-scale vortices resulting from the self-interaction of the axisymmetric separating shear-layer. Even in the presence of a supersonic propulsive jet, which strongly modifies the flow topology owing to its interaction with the external separated flow region, the latter vortex-shedding phenomenon was found to be persistent. For Type II, the spectrum obtained in the core of the recirculating bubble at a distance $0.72D$ from the base (black line in Figure 1.3(d)) exhibits a similar peak at the Strouhal number $St = 0.19$, meaning that the formation of large-scale vortex structures in the wake is not inhibited. Though, at a distance $1.15D$ located in the vicinity of the reattachment point (grey line in Figure 1.3(d)), the latter peak is barely visible, as the unsteady dynamics is now dominated by broadband high frequencies that have been ascribed to the shear-layer vortices impinging the downstream surface. It can be seen that the associated frequencies are three to five times larger than the typical vortex-shedding frequency. Note that three-dimensional afterbodies have also been investigated in 2004 in the S3Ch wind tunnel. The dynamics of such complex configurations lies out of the scope of this dissertation. Still, all results pertaining to these tests can be found in the dedicated report [54].

Figure 1.2. *View of the S3Ch transonic wind tunnel and of the upstream forebody used as supporting device in the ATAC test campaigns.*

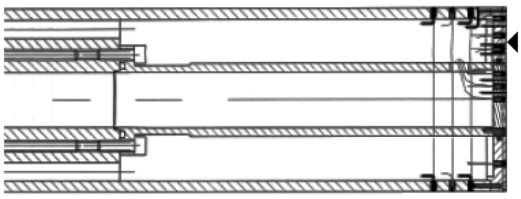

(a) *Type I configuration, made of an axisymmetric blunt base of diameter D.*

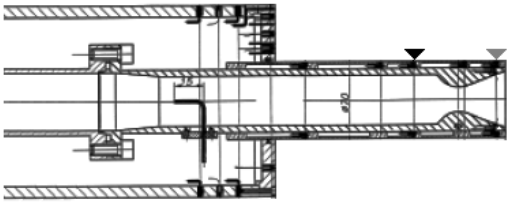

(b) *Type II configuration: an additional rear-body extension of length $L = 1.2\,D$ is now mounted at the rear of the base.*

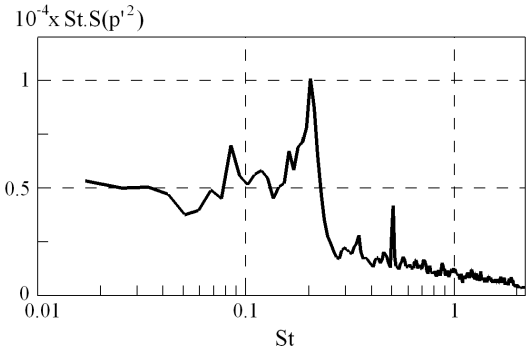

(c) *Type I spectrum of the wall-pressure fluctuations. The location of the experimental measurements is shown as the triangle symbol in* (a).

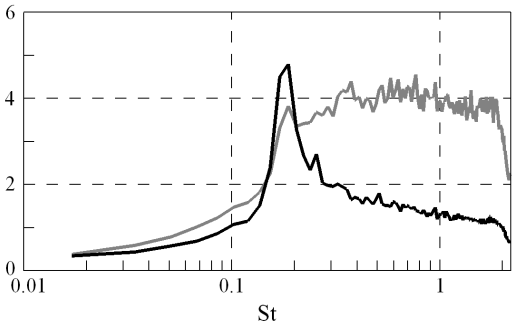

(d) *Same as* (c) *for the Type II configuration shown in (b).*

Figure 1.3. *Typical configurations issuing from the S3Ch wind tunnel tests and associated wall-pressure fluctuations spectra, $Re \simeq 10^6$ - $M = 0.7$. Adapted from Deprés [20].*

From afterbodies to oscillators

The hydrodynamic stability theory provides a theoretical framework to investigate the dynamics of free shear flows, such as wakes and jets. It relies on the existence of an unperturbed solution called base flow, subjected to perturbations, and aims at determining the long-time response of the flow to an initial condition, in order to assess its ability to return to its unperturbed state. All flows are then divided into three categories: in response to perturbations, they may be stable, or otherwise act as amplifiers or oscillators (Huerre & Monkewitz [40]). In stable flows, all external disturbances are damped. An oscillator-type flow displays a self-excited behaviour. Starting from a steady state, such flow develops persisting oscillations in response to any initial perturbation, and never returns to the unperturbed state. It is worthwhile emphasizing that the long-time dynamics of an oscillator is intrinsic to the flow, i.e. it is insensitive to low levels of external excitation for forcing frequencies far enough from the natural one. On the contrary, a flow acts as an amplifier if disturbances are driven by external excitation: perturbations then grow in time as they travel downstream. The control parameter for amplifiers is the level of external noise. In perfectly quiet surroundings, an amplifier-type flow remains unperturbed. In case there is noise in the system, the associated spectra are generally broadband, as all noise components are amplified.

In most experimental set-ups, a flow is inherently subject to noise. In the case of the S3Ch experiments presented above, the flow is subjected to noise owing to the small-scale structures developing in the incoming turbulent boundary-layer. The present study was originally motivated by the fact that the differences featured by both kinds of separations, namely Type I and Type II, can be interpreted in the light of the oscillator/amplifier dichotomy. Indeed, in this fully turbulent regime, although the Type I configuration displays a low-level broad high frequency energy spectrum, meaning that small-scales are indeed excited, it appears to be dominated by the well-defined, intrinsic vortex-shedding frequency. This straightforwardly identifies Type I flows as being of the oscillator kind. The case of the Type II separating-reattaching configuration is more complex. Far from the reattachment point, its spectrum is dominated by the vortex-shedding frequency, which is typical of oscillators. Though, close to the reattachment point, it is dominated by broadband high frequencies, suggesting that the flow rather acts as an amplifier, the small-scale turbulent eddies then acting as external sustained perturbations.

The present study stands as a theoretical investigation of the dynamics of Type I axisymmetric wakes in the high subsonic regime. Neither the reattaching shear-layer, nor the propulsive jets are considered, as we deal with the simplest rear geometry of revolution, whose unsteady dynamics is therefore fully dominated by the vortex-shedding phenomenon. We have chosen not to study the flow at the Reynolds numbers prevailing in the 'industrial' application, which would require high resolution numerical simulations of the turbulent flow. As a step towards the understanding of more complex flow configurations, we study instead the flow dynamics at significantly lower Reynolds numbers, but still in the high subsonic regime. We aim here at improving the knowledge of the physical mechanisms responsible for the transition from steady to unsteady flow conditions, as well as the specific compressible effects that may arise at flight conditions. Of course, such an approach is questionable, as one may expect the effects owing to the high-Reynolds-number shear-layer turbulence to be larger than that owing to compressibility. It is worth mentioning here that the complex theoretical approaches that will be presented

throughout this dissertation could not have been developed along with the turbulent solvers at our disposal. Still, high-Reynolds-number effects will be discussed in conclusion of this dissertation.

Figure 1.4. *Bénard–Kármán alley in the wake of a cylinder.*

The best-known archetype of oscillator is the wake of a circular cylinder, which models water flowing past a submarine cable, or wind blowing past a high-rise building. At sufficiently low Reynolds numbers, the cylinder wake exhibits a steady recirculating bubble. At Reynolds numbers between 47 and 180, it is unstable to small-amplitude disturbances, thus giving rise to the periodic shedding of counter-rotating vortices under the form of the Bénard-Kármán vortex street pictured in Figure 1.4. In this range of Reynolds numbers, the steady wake flow prevailing for $Re < 47$ is unstable to any arbitrary perturbation and can never be observed, although it is still a solution to the Navier-Stokes equations. Note that as long as the amplitude of disturbances remains small, their growth can be investigated in the framework of linear stability theory. The vortex-shedding state depicted in Figure 1.4 is reached under the action of nonlinear effects occurring as the disturbances of largest growth rates reach typically the same order of magnitude as the base flow, thus causing the fluctuation amplitudes to saturate at finite levels. These intrinsic oscillations in the cylinder wake were first observed and described by Bénard [6]. The main idea underlying this dissertation is that in the absence of a downstream reattachment, axisymmetric wakes may display a similar behaviour.

The large-scale structures developing in the lee of axisymmetric bodies have been investigated for different model geometries, including spheres (Achenbach [2]; Thompson *et al.* [80]; Gumowski *et al.* [36]), circular disks (Fuchs *et al.* [31]; Berger *et al.* [7]; Fabre *et al.* [28]) or axisymmetrical blunt bases (Schwarz & Bestek [72]; Siegel & Fasel [74]). It was found that the dynamics of these bodies bears similarities, as a self-excited vortex-shedding regime appears at low and moderate Reynolds numbers. It has been generally acknowledged that this class of flows is dominated by an instability of the helical mode, resulting in the low frequency shedding of large-scale coherent structures in the form of two superimposed modes of azimuthal wavenumbers $m = \pm 1$. The periodic regime is illustrated in Figure 1.5 by flow visualizations for an axisymmetric blunt-based body at $Re = 1500$ and a sphere at $Re = 300$. The flow organization is strikingly similar, taking the form of kinks developing into strongly

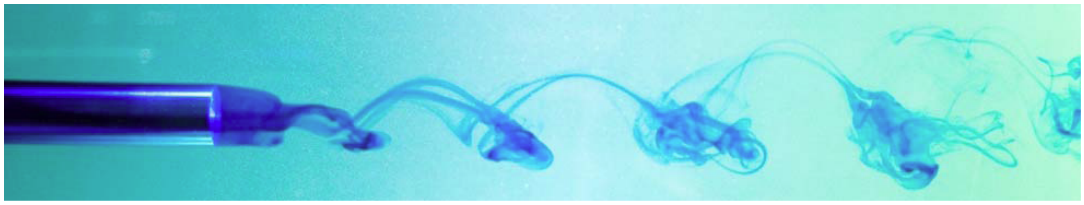

(a) *Blunt-based body at* $Re = 1500$*, taken from Siegel et al. [73].*

(b) *Sphere at* $Re = 300$*, taken from Johnson & Patel [45].*

Figure 1.5. *Dye visualizations of the periodic vortex-shedding regime in the wake of axisymmetric bodies.*

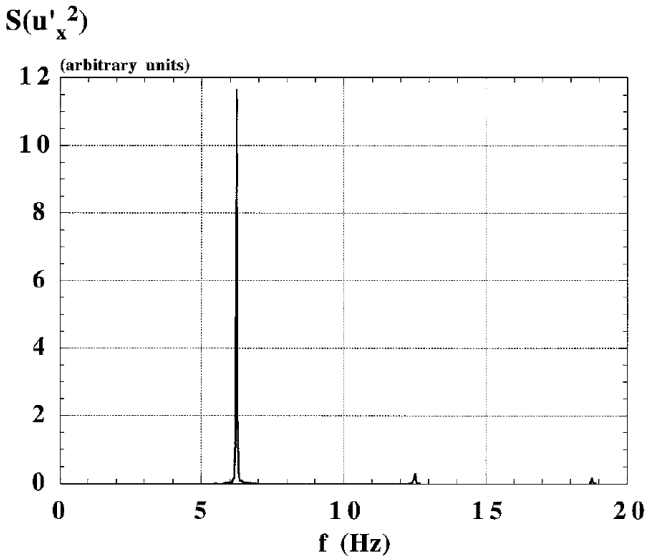

Figure 1.6. *Spectrum of the streamwise velocity fluctuations measured by LDV in the wake of a sphere at* $Re = 329$*, taken from Ormières & Provansal [62].*

skewed loops that move away downstream. A typical spectrum corresponding to streamwise velocity fluctuations measured in the periodic regime of the sphere is shown in Figure 1.6. It exhibits a fundamental frequency 6.24 Hz, corresponding to a low Strouhal number of 0.13 based on the body diameter, characteristic of vortex-shedding phenomena. Comparing the Type I spectrum in Figure 1.3(c) with the present spectrum, one notes that the low Reynolds number prevailing in the sphere flow results in a very sharp frequency selection, the magnitude of fluctuations at all other frequencies being almost nil.

Interestingly, the vortex-shedding phenomenon is not restricted to this range of Reynolds numbers, as it was shown to persist also at high Reynolds numbers. For instance, Achenbach [1] and Taneda [77] investigated the turbulent wake past a sphere. The flow visualization in Figure 1.7, reproduced from the latter study, evidences vortex-shedding as a coherent phenomenon superimposed on the turbulent flow field. It is worthwhile emphasizing that Kim & Durbin [46] have shown that the turbulent self-excited regime arising in the wake of a sphere is intrinsic, a feature typical of oscillators. Another study by Flodrops & Desse [29] considered the turbulent flow past an axisymmetric base at high subsonic Mach numbers, and clearly evidenced the vortex-shedding frequency $St = 0.2$, based on the body diameter. These results suggest that the present low-Reynolds number approach can still be pertinent to improve the understanding of the large-scale dynamics of the fully turbulent flow.

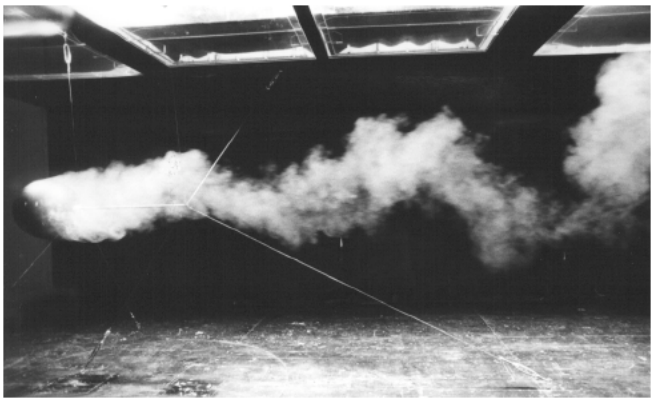

Figure 1.7. *Vortex-shedding at high Reynolds numbers: smoke visualization of the wake past a sphere at* $Re = 23000$*, taken from Taneda [77].*

Means & Objectives

This section is devoted to a review of the main theoretical concepts underlying the present study, namely stability analyses, adjoint methods and their application to flow control. The objectives of this dissertation are then presented in the light of this review. Particular attention is paid to the connection between these concepts and the previously introduced oscillator/amplifier dichotomy.

Stability analyses

Open shear flows have first been studied in the framework of the local stability theory, for which only the cross-stream flow direction is an eigendirection. The fate of perturbations at each streamwise station is analysed by studying the stability of the fictitious parallel flow obtained by extending to infinity the base flow profiles prevailing at each streamwise station. In the local approach, the instability can be either convective or absolute (Briggs [10], Bers [8]). The amplifier dynamics is associated with the existence of convectively unstable regions, where advection overwhelms the upstream propagation of the small-amplitude wave packet generated by an arbitrary perturbation, the latter being swept downstream with the flow while growing, as illustrated in Figure 1.8(a). As a consequence, a base flow which is convectively unstable at all streamwise locations may amplify external perturbations, but in the absence of continuous forcing, the flow eventually returns to its initial state, i.e. it behaves as an amplifier. On the contrary, the oscillator dynamics is associated with the existence of absolutely unstable regions, where the spreading of the wave packet withstands the downstream advection, so that the latter propagates both upstream and downstream and ultimately grows in time at any fixed location. Such situation is depicted in Figure 1.8(b). For synchronized oscillations to be observed, the size of the absolutely unstable region must reach a critical size (Chomaz *et al.*. [14]; Monkewitz *et al.* [58]; Le Dizès *et al.* [47]). In the long-time limit, energy is continuously extracted from the base flow within this region and transferred to perturbations, making the oscillations self-sustained. Consistently with experimental observations, the inviscid analysis of Monkewitz [59] has shown that in the incompressible homogeneous limit, axisymmetric wakes can sustain a helical absolute instability of azimuthal wavenumber $m = 1$, thus supporting the idea that this class of flows is of the oscillator kind.

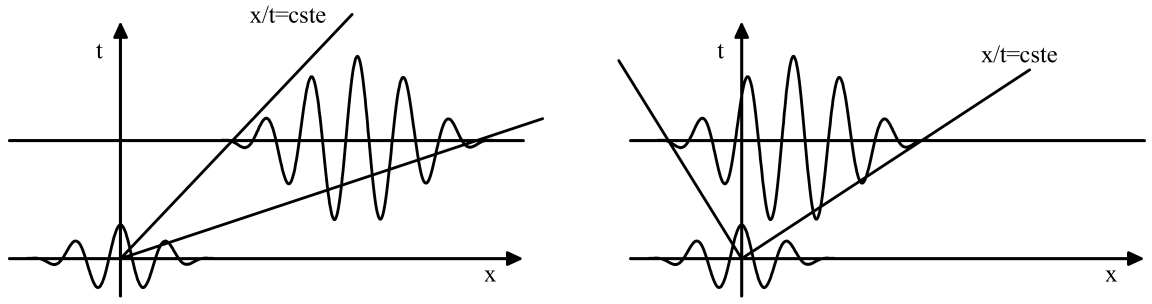

(a) *Convective instability.* (b) *Absolute instability.*

Figure 1.8. *Amplification of a wave packet.*

The use of local stability analysis has the advantage of requiring very little computational cost. Though, in the case of oscillators, where the flow exhibits a sharp spatial pattern and frequency selection, it has the disadvantage of needing additional criteria to connect the local instability properties to the global dynamics, where the term global emphasizes here that the oscillating solution encompasses the entire flow field. This is done via a slowly varying or WKBJ approach, where one assumes that the streamwise variations of the base flow are slow over an instability wavelength, so that perturbations at any streamwise station develop as if the base flow was locally parallel. A theoretical criterion for the onset and frequency of

global oscillations has been derived from the analyses of Ginzburg-Landau model equations in the fully nonlinear regime (Chomaz [12]; Couairon & Chomaz [16]; Pier & Huerre [64]), thus giving rise to the so-called theory of nonlinear global modes. The main idea conveyed by these studies is that the flow is dominated by a stationary front acting like a *wavemaker*, and that its frequency and spatial structure are determined by the local linear stability properties at the upstream boundary of the region of absolute instability. Many of the results pertaining to the model equations have been shown to hold in real flows, despite the fact that the slow streamwise variation assumption is not respected. In the case of the cylinder wake, the frequency of the Bénard-Kármán alley, as observed in direct numerical simulations, matches the theoretically predicted frequency within $10\,\%$ accuracy over the range of Reynolds numbers $100 \leq Re \leq 180$ (Pier [63]). Since then, several successful analyses have been carried out in the context of swirling jets (Gallaire & Chomaz [33]; Gallaire *et al.* [34]), hot round jets (Lesshafft *et al.* [49]), or inter-disk flow (Viaud *et al.* [82]).

However, real wakes are strongly non-parallel and the assumption inherent to the local approach is thus not valid. In the last decades, a global approach of linear stability theory has been developed, for which both the streamwise and cross-stream flow directions are eigendirections. The term global now refers to the specific streamwise structure of the base flow and disturbances. This approach has first been introduced by Jackson [42] and Zebib [85]. Increased computer capacities together with iterative Krylov-subspace methods, such as the Arnoldi method, has made it possible to generalize this method, which has received much attention and has been applied to a large variety of flows, including the cylinder wake (Ding & Kawahara [23]; Giannetti & Luchini [35] among others), backward-facing steps (Barkley *et al.* [4]), open cavities (Sipp & Lebedev [75]) or boundary-layer flows (Ehrenstein & Gallaire [24]). The review by Theofilis [78] provides a view of the recent achievements in the field. It is worthwhile emphasizing that the global stability of axisymmetric configurations has received less attention, although Narajan & Acrivos [61] have studied the wake past a disk and a sphere. In the global approach, the oscillator dynamics is studied by examining the spectrum of perturbations. To that end, a global stability analysis is performed assuming disturbances in the form of structures growing exponentially in time. If the growth rate of the leading global mode is positive, the base flow is said globally unstable and the flow may act as an oscillator, the frequency of the synchronized oscillations being that of the unstable global mode. The amplifier dynamics, characterized by the ability of the flow to exhibit large transient amplifications of initial perturbations, is rather viewed as a superposition of damped global modes (Ehrenstein & Gallaire [24]; Schmid [70]).

Nevertheless, these analyses have so far been applied almost exclusively to incompressible flows, whereas its application to transonic afterbody flows requires to consider the effect of compressibility. This means higher computer capacities and introduces a number of specific issues associated with the computation of the steady base flow and the resolution of the eigenvalue problem for the unsteady disturbances. A first attempt of compressible global stability analysis is that of Theofilis [79], who considered the flow *within* a cavity as a crude approximation for the real and complex problem of open cavity flows. Since then, only a very limited number of studies have been carried out in the compressible regime, including that of Crouch *et al.* [18] on the shock-induced buffet over a two-dimensional airfoil and of Robinet [67] on a shock wave/boundary-layer interaction.

Nonnormality and adjoint methods

Adjoint equations have recently attracted the increased attention of fluid dynamicists, for a number of applications ranging from atmospheric sciences (Hall [37]) to shape optimization (Pironneau [65]). They are widely used in the context of sensitivity analyses which can be formulated as input/output problems aiming at evaluating the gradient of an output variable with respect to an input variable. For instance, it is of practical interest for the fluttering of wings to estimate the sensitivity of the position of a shock with respect to the flow parameters, such as the Reynolds and Mach numbers or the incidence of the wing (Di Cesare & Pironneau [22]). In this example, the input variable is for instance the angle of attack, and the output variable is the position of the shock. Such gradients can be obtained from forward calculations. Namely for the previous example, one must solve the state equations once to obtain the nominal shock position, and once more to find the shock position resulting from each change in the flow parameters. Consequently, this approach can be extremely time-consuming if the number of degrees of freedom is large. The main advantage of adjoint methods is that the same gradient can be obtained by solving only once the state equations and adjoint problem, with a relatively 'low' computational cost. In optimal shape design, typical input and output are the shape of a given body and its relative drag or lift coefficient. In this context, the adjoint-based optimal design of transonic wings at realistic cruise conditions has been widely investigated (Jameson [43]; Jameson *et al.* [44]). Such studies now allow to optimize entire airplanes for a criterion such as drag under geometric and aerodynamic constraints such as volume and lift (see Mohammadi & Pironneau [57] for a review).

Adjoint methods are also widely used in the context of stability analysis, which aims at understanding the mechanisms responsible for the growth of disturbances. Indeed, such growth may be altered by some modifications encountered in the flow. The flow region where the instability mechanisms are active can thus be identified as the region where the sensitivity of the disturbance to modifications of the stability problem is the highest, as discussed in Giannetti & Luchini [35]. If such modifications are due to surface inhomogeneities and forcing, sensitivity analyses are rather termed receptivity. For instance, Crouch [17] studied the receptivity to acoustic forcing of two-dimensional disturbances in a Blasius boundary-layer. The input is now some forcing on the wall or in the flow, and the output is a measure of the disturbance in the domain, for instance the disturbance growth rate or its energy at some downstream position or in the whole domain. The estimation of the corresponding gradient therefore allows a straightforward identification of the flow regions which are most receptive to a given forcing mechanism. Adjoint methods have naturally arisen in the study of boundary-layer flows. Hill [39] studied the receptivity of Tollmien-Schlichting waves in the local approach, whereas Pralits *et al.* [66] investigated in the WKBJ approach the receptivity of two and three-dimensional disturbances to periodic wall conditions and momentum forcing in the compressible regime.

Another interesting example is that of arbitrary modifications of the base flow, the input variable being now the base flow itself. This point is of practical interest for those aiming at turning theoretical predictions into practice. Indeed, they often investigate the stability of imperfect experimentally measured base flow profiles, meaning that the real flow generally departs from its ideal, theoretical counterpart. Adjoint-based formalisms have thus been used to appraise the variations of a disturbance growth rate owing to an arbitrary base flow modification, thus defining

the so-called sensitivity analysis to base flow modifications (Bottaro *et al.* [9]; Marquet *et al.* [53]).

It is worthwhile noting that some physical mechanisms cannot be straightforwardly identified from the knowledge of the disturbances growth rates and eigenfunctions only. For instance, stability analyses, as governed in the local approach by the Orr-Sommerfeld equation, fail to predict the experimentally observed bifurcations in the plane Couette and Poiseuille flows. Such transition in parallel shear flows, even though the flow is stable, has been ascribed to the fact that the linearized Navier-Stokes operator may be highly nonnormal (Trefethen *et al.* [81]). The transition can then be explained by considering a superposition of cooperating modes, as introduced by Butler & Farrell [11] (see also Ehrenstein & Gallaire [24]; Schmid [70]). The main idea underlying these studies is that because the eigenmodes issuing from the stability analysis (also referred to as the direct modes) are not orthogonal one to the other, linear transient amplification of some disturbances may trigger strong nonlinear effects and prevent the eventual decay of those disturbances predicted by the only stability theory, thus inducing the observed flow transition. The nonnormalilty of the evolution operator is also responsible for the ability of the flow to respond to external noise, a specificity of the amplifier dynamics. In this context, the computation of adjoint eigenmodes has proven fruitful to provide additional insight into the flow physics. It allows to establish a natural distinction between the *lift-up* and the *convective* nonnormalities (Chomaz [13]; Marquet *et al.* [51]). The lift-up nonnormality is associated with direct and adjoint eigenmodes that tend to be orthogonal one to the other because concentrated on different components of the state vector. In simple parallel shear flows, it gives rise to the so-called lift-up effect, linked to the generation of strong streamwise velocity perturbations by small displacements along the direction of the base flow gradient. The convective nonnormality is associated with direct and adjoint modes that tend to be orthogonal one to the other because localized in different regions of the flow. Of course, for real non-parallel flows, both mechanisms act and the spatial structures of the direct and adjoint modes result from their interactions.

Flow control

Flow control has been a subject of great interest in the last decade. While the subject of hydrodynamic stability is to understand the mechanisms responsible for the growth of disturbances, control aims at using this knowledge to appropriately alter their dynamics. It can be performed in two ways, either open-loop for methods involving actuators only, or closed-loop for methods involving actuators and sensors, the control input being then real-time modified according to the response of the flow as monitored by the sensors.

Closed-loop/feedback methods seem a priori an attractive choice over open-loop controls, and many studies have been devoted to their numerical implementation, with quite promising results. Practically, though, sensing and actuation rely on devices whose time response has to be very short compared to the time scale of the unsteady phenomenon to be controlled. Consequently, experimental implementation of feedback control often remains a challenge. On the contrary, open-loop strategies are much easier to implement, and have been successfully applied to many flow configurations. For instance, a small control cylinder has been shown to suppress un-

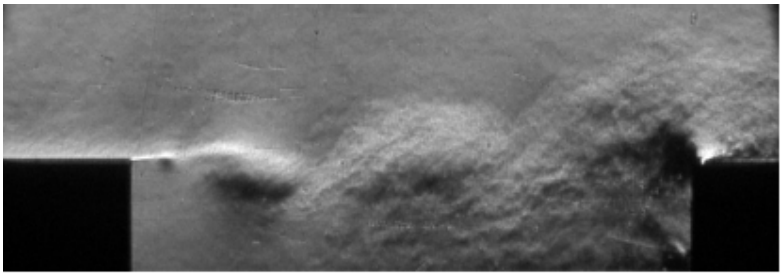

(a) *Natural flow.*

(b) *Open-loop control by means of a small cylinder above the upstream separation point.*

Figure 1.9. *Strioscopy visualizations of a transonic cavity flow,* $Re \simeq 8 \times 10^5$ - $M = 0.755$. *Taken from Illy [41].*

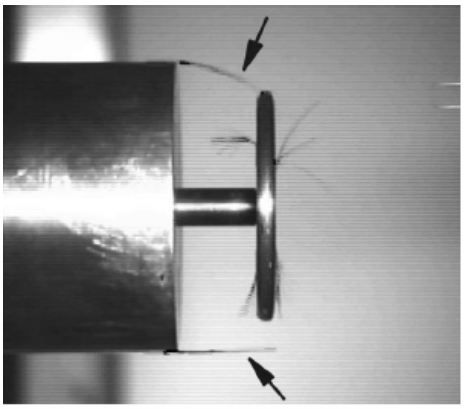

(a) *Control disk mounted ar the rear of an axisymmetric blunt base, taken from Weickgenannt & Monkewitz [83].*

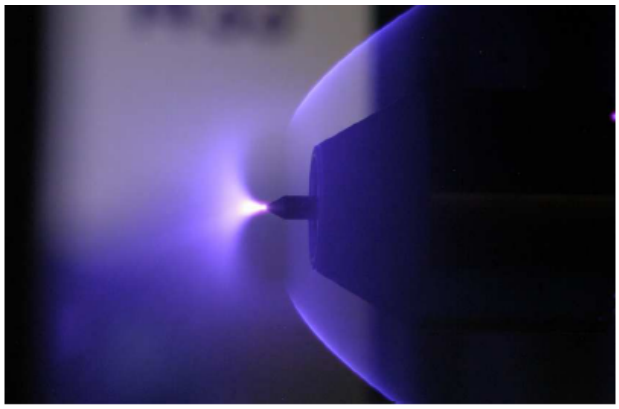

(b) *Gas discharge upstream of a conical body equipped with a central pike, in the ONERA/DAFE R1Ch wind tunnel. Taken from Elias [26].*

Figure 1.10. *A selection of open-loop controls used to alleviate flow unsteadiness.*

steadiness if suitably placed in the cylinder wake (Strykowski & Sreenivasan [76]) and in a transonic cavity flow (Illy [41]). The latter case is illustrated in Figure 1.9, which shows strioscopy visualizations of the cavity flow in the ONERA/DAFE S8Ch wind tunnel. The unforced flow is presented in Figure 1.9(a): it exhibits large-scale vortical structures impinging the downstream edge of the cavity, which causes the radiation of high acoustic levels. Figure 1.9(b) shows to the same flow in the presence of the control cylinder: strikingly, the previous flow pattern has disappeared, as one now observes only the Bénard-Kármán alley in the wake of the control cylinder.

Similar techniques have been used in the context of afterbody flows. Revisiting a problem originally studied in the mid-1960s by Mair [50], Weickgenannt & Monkewitz [83] identified different regions of the flow where a control disk mounted at the rear of the main body, as illustrated in Figure 1.10(a), triggers either a reduction or a sharp increase of the vortex-shedding activity. Localized gas discharges acting as volumetric heat sources have also been proven fruitful to significantly alter supersonic airflows (Fomin *et al.* [30]). Elias [26] has studied the unsteady flow past a truncated conical body with a central spike, characterized by a pulsating shock wave, and has shown that the use of a discharge, such as that presented in Figure 1.10(b), allows to inhibit the unsteadiness of the shock wave (see also Elias *et al.* [27]). Wall forcing has also been considered since the early 1960s and the use of mass injection into the wake of bluff bodies, also termed base bleed (Bearman [5]; Leal & Acrivos [48]; Motallebi & Norbury [60], among others). Though, it is worthwhile noting that such approaches are often empirical and may be extremely time-consuming, as they require exhaustive investigations over wide ranges of control parameters. For the small cylinder device used in the cavity flow, this means to test different sizes and locations of the device, and for each case, evaluate the effect on the disturbances growth by carrying out either experimental measurements or numerical simulations.

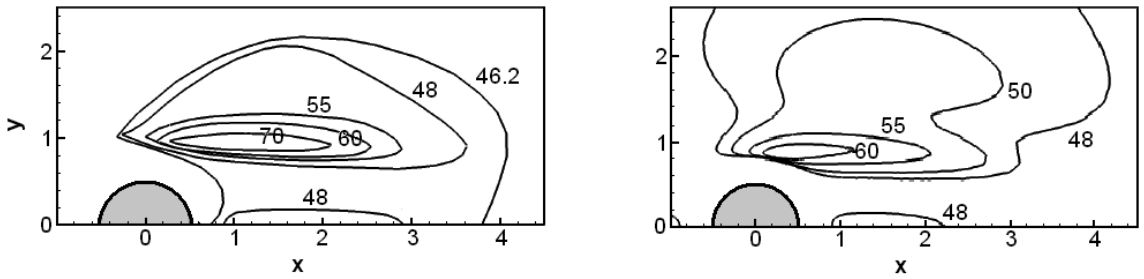

(a) *Experimental results from Strykowski & Sreenivasan [76].*

(b) *Theoretical results from Marquet et al. [53].*

Figure 1.11. *Open-loop control of the cylinder wake. A control cylinder* 10 *times smaller than the main cylinder is placed at various locations in the flow. For each location of the control cylinder and for various Reynolds numbers, the growth rate of the perturbations is measured. Contours where the growth rate is nil are represented, along with the corresponding value of the Reynolds number.*

A systematic adjoint-based approach for the open-loop control of globally unstable flows has been developed by Hill [38] and Marquet *et al.* [53]. In case undesirable flow conditions arise owing to a global instability, for instance unsteadiness in the cylinder wake, their control is indeed closely connected to the damping of the instability. These authors revisited the experimental study of Strykowski & Sreenivasan [76] by investigating theoretically the effect of a small control cylinder on the incompressible

cylinder wake. The main idea conveyed by their studies is that adjoint methods can be used to predict beforehand the effect of a small-amplitude forcing on the growth of the unstable global mode. The presence of the control cylinder being modeled by the body force it exerts on the base flow, it becomes possible to identify specific flow regions where the control cylinder, if suitably placed, alleviates or suppresses unsteadiness. As seen in Figure 1.11, the theoretical predictions exhibit a striking agreement with the experimental results. The main advantage of such adjoint-based formalisms is that they can easily be extended to provide optimal control strategies with a relatively low computational cost, using gradient-based optimization techniques as described in Collis *et al.* [15].

Objectives

The main objective of this dissertation is to establish whether the intrinsic dynamics observed in high-Reynolds number compressible axisymmetric wakes may be ascribed to a hydrodynamic instability occurring at low Reynolds numbers. A particular attention is paid to the question of the frequency and spatial pattern selected by local and global stability analyses. Since it has been said that the effects of compressibility are particularly interesting in the perspective of the engineering application, the originality of this study lies in the use of a fully compressible approach of global stability. The second objective is to use adjoint methods to identify the flow regions that are of particular interest in the perspective of control. We aim at eventually extending the global formalism of Hill [38] and Marquet *et al.* [53] to the compressible regime, so as evaluate the effect of realistic control methods on an afterbody configuration.

Outline

The body of this dissertation is composed of five chapters, mainly dealing with the question of flow dynamics (chapter 2 to 5), the question of flow control being ultimately addressed in chapter 6.

The **local stability** of **parallel axisymmetric wakes** up to the **high subsonic regime** is investigated in chapter 2 under the form of two publications. The first article presents a characterization of the convective/absolute transition of axisymmetric wake models, thus generalizing to variable density and compressible wakes the results of Monkewitz [59]. A complete parametric study allows to identify the modes of interest. We discuss the effect of varying the base flow and free-stream Mach number on the stability of the latter modes, and a physical interpretation is proposed, based on the competition between the production of disturbances and their advection by the base flow. The azimuthal wavenumber and frequency of the dominant mode, i.e. the mode that leads the convective-absolute transition, are also compared to experimental observations. The second article investigates to what extent these local instability properties can be used to reconstruct the dynamics of a realistic spatially developing afterbody flow, computed via a high resolution Large Eddy Simulation in the turbulent and compressible regimes. In particular, the global frequency of the flow is compared to that predicted by the theory of nonlinear global

modes.

The following chapters are devoted to the **global stability** of **non-parallel axisymmetric wakes**. In chapters 3 and 4, the linear and nonlinear dynamics of model geometries are studied in the **incompressible regime**. This part of the dissertation takes the form of two self-contained articles. The global modes of largest growth rates are first identified by investigating the stability of small disturbances superimposed on the steady axisymmetric base flow developing past a disk and a sphere (chapter 3). This analysis is completed by a discussion on the nonnormality of the evolution operator. The receptivity of each bifurcating mode to particular initial conditions or forcing is also estimated by the computation of its adjoint global mode. The dynamics arising from the nonlinear interaction between these bifurcating modes is then further investigated using the slow manifold theory and normal forms (chapter 4). The resulting spatial pattern and frequency selection is discussed and compared to numerical results existing in the literature.

Chapters 5 and 6 are structured under the form of two complementary articles in preparation, presenting a theoretical framework for the study of **global modes** in **compressible flows**, up to the high subsonic regime. In chapter 5, the equations for the global modes and adjoint global modes are derived in a consistent way. This formalism is then applied to an afterbody flow. The growth rates of the leading global modes are investigated as functions of the base flow and of the free-stream Mach number by means of a sensitivity analysis. We discuss the effect of compressibility on the flow dynamics, and a physical interpretation is proposed by generalizing the advection/production dichotomy introduced for parallel wakes in chapter 2 to the global framework. Chapter 6 presents a systematical approach for the **open-loop control of compressible flows**. The incompressible framework of Hill [38] and Marquet *et al.* [53] is extended and applied to the control of the same afterbody. The effect of small-amplitude forcing on the growth rate of the unstable global modes is discussed. Various control techniques are considered, including body forces, heat sources and mass injection. A physical interpretation for the stabilizing effect of base bleed is proposed.

CHAPTER
TWO

ABSOLUTE INSTABILITY IN COMPRESSIBLE AXISYMMETRIC WAKES

This chapter is presented under the form of two independent articles investigating the local stability of axisymmetric wakes. In the first paper, published in the *Journal of Fluid Mechanics* in 2008, it is demonstrated that model axisymmetric wake profiles can sustain absolute instability up to the high subsonic regime. The effect of compressibility on the unstable modes is investigated, and the resulting frequency and azimuthal wavenumber selection is discussed in the light of experimental observations.

The second article, currently submitted to *Physics of Fluids* analyzes the stability of realistic profiles issuing from a high resolution Large Eddy Simulation, and evidences the simultaneous occurrence of large-scale oscillations and absolute instability in the fully turbulent and compressible regimes. The main objective is to examine whether the frequency of the intrinsic oscillations measured in the numerical simulation can be accurately estimated from theoretical predictions.

keywords: compressible flows, local stability, convective/absolute transition, frequency selection.

J. Fluid Mech. (2008), *vol.* 600, *pp.* 373–401.
DOI: 10.1017/S0022112008000499 Printed in the United Kingdom

Absolute instability in axisymmetric wakes: compressible and density variation effects

By PHILIPPE MELIGA[1], DENIS SIPP[1] AND JEAN-MARC CHOMAZ[1,2]

[1]ONERA/DAFE, 8 rue des Vertugadins, 92190 Meudon, France
[2]LadHyX, CNRS-Ecole Polytechnique, 91128 Palaiseau, France

(Received 27 April 2007 and in revised form 8 January 2008)

Lesshafft & Huerre (*Phys. Fluids*, 2007; vol. 19, 024102) have recently studied the transition from convective to absolute instability in hot round jets, for which absolute instability is led by axisymmetric perturbations and enhanced when lowering the jet density. The present paper analyses similarly the counterpart problem of wake flows, and establishes that absolute instability is then led by a large-scale helical wake mode favoured when the wake is denser than the surrounding fluid. This generalizes to variable density and compressible wakes the results of Monkewitz (*J. Fluid Mech.* vol 192, 1988, p.561). Furthermore, we show that in a particular range of density ratios, the large-scale helical wake mode can become absolutely unstable by increasing only the Mach number up to high subsonic values. This possibility of an absolute instability triggered by an increase of the Mach number is opposite to the behaviour previously described in shear flows such as plane mixing layers and axisymmetric jets. A physical interpretation based on the action of the baroclinic torque is proposed. An axisymmetric short-scale mode, similar to that observed in plane mixing layers, leads the transition in light wakes, but the corresponding configurations require large counterflow for the instability to be absolute.

These results suggest that the low-frequency oscillation present in afterbody wakes may be due to a non-linear global mode triggered by a local absolute instability, since the azimuthal wavenumber and absolute frequency of the helical wake mode agree qualitatively with observations.

1. Introduction

Wake flows past axisymmetric bodies have been studied both experimentally and numerically in the last decades - see for instance the studies of Achenbach (1974) on spheres, of Fuchs *et al.* (1979) and Berger *et al.* (1990) on circular disks. It has been generally acknowledged that this class of flow is dominated by an instability of the helical mode, resulting in the low-frequency shedding of large-scale coherent structures in the form of two superimposed modes of azimuthal wavenumbers $m = \pm 1$. Low Strouhal numbers of 0.2 and 0.135, characteristic of vortex-shedding phenomena, have been reported for the sphere and the disk, respectively, based on the body diameter. Kim & Durbin (1988) showed that the periodic shedding regime was intrinsic, i.e. insensitive to low levels of external acoustic excitation for forcing frequencies far enough from the natural one.

The onset of this type of self-sustained synchronized oscillations in free shear flows, such as wakes and jets, has been analyzed using the local stability theory, that computes

the instability properties of a fictitious parallel flow obtained by extending to infinity the velocity profiles measured at each streamwise station. Numerous theoretical approaches have provided strong evidence that the transition from convective to local absolute instability (Briggs 1964; Bers 1975) plays a crucial role in the existence of such oscillations. The works of Koch (1985) and Monkewitz & Nguyen (1987), among others, have shown that synchronized oscillations for the two-dimensional wake are linked to the existence of a region of local absolute instability in the near wake, where the small-amplitude wave packet generated by an arbitrary perturbation propagates both in the upstream and downstream directions, and grows in time at any fixed location. Similar results have been established for sufficiently light or heated jets in the theoretical and experimental studies of Monkewitz & Sohn (1988) and Monkewitz *et al.* (1990). Striking results have also been obtained in the context of flow control. The experimental and theoretical work of Sevilla & Martínez-Bazàn (2004) shows in particular that it is possible to suppress the vortex shedding past an axisymmetric blunt-based body using a base bleed control strategy aiming at promoting the convective nature of the instability.

Recent studies have extended these analyses to the fully non-linear regime, and have provided theoretical predictions for the onset and frequency of such synchronized oscillations in spatially developing flows. The analyses of Chomaz (1992), Couairon & Chomaz (1997); Tobias *et al.* (1997, 1998); Pier *et al.* (2001) on model equations in semi-infinite and infinite domains have highlighted the connection between non-linear global modes and front dynamics that characterize the propagation of a saturated instability wave into a quiescent region (Dee & Langer 1983; van Saarloos 1987, 2003), provided the streamwise variations of the baseflow are sufficiently slow (see Chomaz (2005) for a review). The main idea developed in these studies is that the non-linear global mode is dominated by a stationary front acting like a *wave-maker*, and that its frequency and spatial structure are determined by the local linear stability properties at the upstream boundary of the region of absolute instability. These conclusions apply under the assumption that the front velocity is linearly selected, i.e. the front is pulled under the action of linear mechanisms at work in the upstream tail (van Saarloos 2003). In that case, if the flow displays convectively unstable inlet conditions, so that absolute instability arises only beyond a specific downstream station x^{ca}, then the associated spatial structure consists of a steep front pinned at this position of marginal absolute instability. The front then separates an upstream region of vanishing amplitude, where perturbations decay exponentially, from the finite-amplitude downstream tail, made of a saturated wavetrain. The global frequency is then given by the linear absolute frequency ω_r^{0ca} at this transition station x^{ca}, and the spatial growth rate upstream of the front is given by the absolute wavenumber $-k_i^{0ca}$. In the case where the flow displays an absolutely unstable inlet conditions, the front is pinned against the body, where the perturbation amplitude is forced to be zero. The same global frequency selection criterion applies at the threshold of global instability, i.e. the global frequency is given by ω_r^{0inlet}. Above the global instability threshold, the criterion provides only a leading-order prediction of the global frequency (Couairon & Chomaz 1999).

These theoretical predictions, rigorously derived only for these model equations, have been shown to apply also to real flow configurations. In the case of a two-dimensional *synthetic* wake - i.e. with no solid boundaries and no recirculation, Pier & Huerre (2001) demonstrated that absolute instability arises beyond a specific downstream position x^{ca}. They also found that the upstream front of the vortex street was located at x^{ca} and that the frequency of the von Karman vortex street, as observed in direct numerical simulations, matches the absolute frequency ω_0^{ca} within 2 %. In the naturally developing wake behind a circular cylinder, despite the fact that the slow streamwise variation

hypothesis is not valid in the separated region, Pier (2002) has shown that the same frequency criterion provides a 10 % accurate prediction over the range of Reynolds numbers $100 \leqslant Re \leqslant 180$. Similar work has been carried out by Gallaire & Chomaz (2003) in the case of the double helix mode arising in swirling jets, by Lesshafft *et al.* (2006) in the case of hot round jets and by Gallaire *et al.* (2006) in the case of spiral vortex breakdown. Lesshafft *et al.* (2006) also considered the case of an absolutely unstable inlet condition, where the frequency selection criterion is valid in the vicinity of the global instability threshold. These studies show that, as for model equations, the global oscillations observed in these flows may be interpreted as a non-linear global mode driven by a pulled front located at the upstream station of marginal absolute instability x^{ca} or at the inlet when the flow is absolutely unstable there, the global frequency being approximated well by the absolute frequency at the front location, at least close to the global instability threshold.

Following this line of thought, we view unsteadiness in the wake of axisymmetric bodies as the manifestation of such a non-linear global mode induced by a region of absolute instability. Therefore, only critical parameters at the transition between convective and absolute instability matter in predicting the existence and the frequency of such unstable modes. Consistently with experimental observations, the inviscid analysis of Monkewitz (1988) has already shown that in the incompressible homogeneous limit, such axisymmetric wakes can sustain a helical absolute instability of azimuthal wavenumber $m = 1$. However, many applications, such as afterbody flows, require us to consider the effect of compressibility and density variations, as in the experimental studies of Flodrops & Desse (1985) and Deprés *et al.* (2004). The present study aims at generalizing the study of Monkewitz to non-homogeneous compressible wakes, and at providing a complete characterization of the convective/absolute transition of axisymmetric wake models and eventually to predict the onset and frequency of self-sustained oscillations in more complex flow configurations. In particular, physical interpretations are given in terms of a baroclinic factor, that extends to non-axisymmetric perturbations and compressible flow the effect of the baroclinic torque on the instability, discussed by Lesshafft *et al.* (2006) and Nichols & Schmid (2007) in the case of jets. The paper is organized as follows: the problem formulation for the base flow and its disturbances is given in § 2.1. Section 2.2 presents the numerical procedure used to determine the linear instability properties of the base flow. In § 3, the different instability modes of interest are identified through an investigation of the linear impulse response that highlights the wake/jet dichotomy and the azimuthal wavenumber selection. In §§ 4.1 to 4.3, we provide a characterization of the convective/absolute transition in terms of control parameter ranges (Mach number, steepness parameter, velocity and density ratios), frequency and wavenumber.

2. Theoretical framework

2.1. *Parallel base flow and disturbances*

We consider a non-homogeneous compressible ideal gas with constant specific heat c_p, thermal conductivity κ, and dynamic viscosity μ, related by a unit Prandtl number. All equations are formulated in cylindrical coordinates (r, θ, z). We use the upstream quantities ρ_∞, T_∞ and P_∞ as density, temperature and pressure scales respectively. The fluid motion is governed by the compressible Navier-Stokes equations, written as

$$D_t \rho + \rho \boldsymbol{\nabla}.\boldsymbol{u} = 0 \tag{2.1}$$

$$\rho D_t \boldsymbol{u} = -\frac{1}{\gamma M_\infty^2}\boldsymbol{\nabla} p + \frac{1}{Re_\infty}\boldsymbol{\Delta u} \tag{2.2}$$

$$\rho D_t T = -p\boldsymbol{\nabla}.\boldsymbol{u} + \gamma(\gamma-1)\frac{M_\infty^2}{Re_\infty}\left(-\frac{2}{3}\boldsymbol{\nabla}.\boldsymbol{u}^2 + 2\boldsymbol{d}:\boldsymbol{d}\right) + \frac{\gamma}{PrRe}\boldsymbol{\Delta} T \tag{2.3}$$

where D_t is the material derivative, $\boldsymbol{d}$ is the strain tensor given by

$$\boldsymbol{d} = \frac{1}{2}\left(\boldsymbol{\nabla u} + \boldsymbol{\nabla u}^T\right) \tag{2.4}$$

and the Reynolds, Mach and Prandtl numbers are defined as

$$Re_\infty = \frac{\rho_\infty R W_\infty}{\mu}, \qquad M_\infty = \frac{W_\infty}{\sqrt{\gamma R_g T_\infty}}, \qquad Pr = \frac{\mu c_p}{\kappa}\,, \tag{2.5}$$

with R_g and γ the ideal gas constant and the ratio of specific heats.

The unperturbed wake is assumed to be steady, axisymmetric and uniform in the axial direction. This holds under the assumption that the instability wavelength is short compared to the viscous diffusion spatial scale. The base flow is therefore chosen as an inviscid solution of $(2.1)-(2.3)$. An analytical expression of the velocity profile is taken from the studies of Monkewitz & Sohn (1988) and Monkewitz (1988). In dimensional variables, indicated by an asterisk, the base flow under consideration reads:

$$W_b^*(r^*) = W_\infty + (W_c - W_\infty)F(r^*)\,, \tag{2.6}$$

where $F(r^*)$ is the distribution

$$F(r^*) = \frac{1}{1+\left(2^{(r^*/R)^2}-1\right)^N}\,. \tag{2.7}$$

In (2.6), subscripts c and ∞ refer, respectively, to the centreline and free-stream velocities. In (2.7), R is the wake radius R defined as $W_b^*(R) = W_m$ where W_m is the mean velocity $W_m = (W_c + W_\infty)/2$. Using the mean velocity W_m as velocity scale and the wake radius R as length scale, we introduce the velocity ratio $\Lambda = (W_c - W_\infty)/(W_c + W_\infty)$. In non-dimensional variables, the base flow reads

$$W_b(r) = 1 - \Lambda + \frac{2\Lambda}{1+\left(2^{r^2}-1\right)^N}\,. \tag{2.8}$$

In the context of wakes, Λ varies in the range $-\infty < \Lambda < 0$, with $\Lambda = -1$ in the particular case of a wake with zero centerline velocity. The centerline and free streams are coflowing for $-1 < \Lambda < 0$ and counterflowing for $\Lambda < -1$. Positive values of Λ correspond to jet velocity profiles. Figure 1 shows typical wake and jet profiles that are symmetric with respect to the unity velocity, i.e. $W_b(\Lambda, r) = 2 - W_b(-\Lambda, r)$. The thickness of the shear layer is characterized by the steepness parameter D/θ, where D is the wake diameter $D = 2R$ and θ is the momentum thickness defined in the homogeneous limit as

$$(W_\infty - W_c)^2\theta = \int_0^\infty (W_b(r) - W_c)(W_\infty - W_b(r))\mathrm{d}r\,. \tag{2.9}$$

Considering variations of θ relative to a fixed diameter D, this parameter allows for continuous variation between the top-hat wake bounded by a cylindrical vortex sheet obtained for $N \to \infty$ ($D/\theta \to \infty$), and the Gaussian profile obtained for $N = 1$ ($D/\theta = 6.5$). For $N < 1$, this family of profiles is not appropriate, as the second-order derivative of the velocity profile is singular at $r = 0$. The corresponding range of steepness parameters accessible through $(2.6)-(2.7)$ is therefore $6.5 \leqslant D/\theta < \infty$.

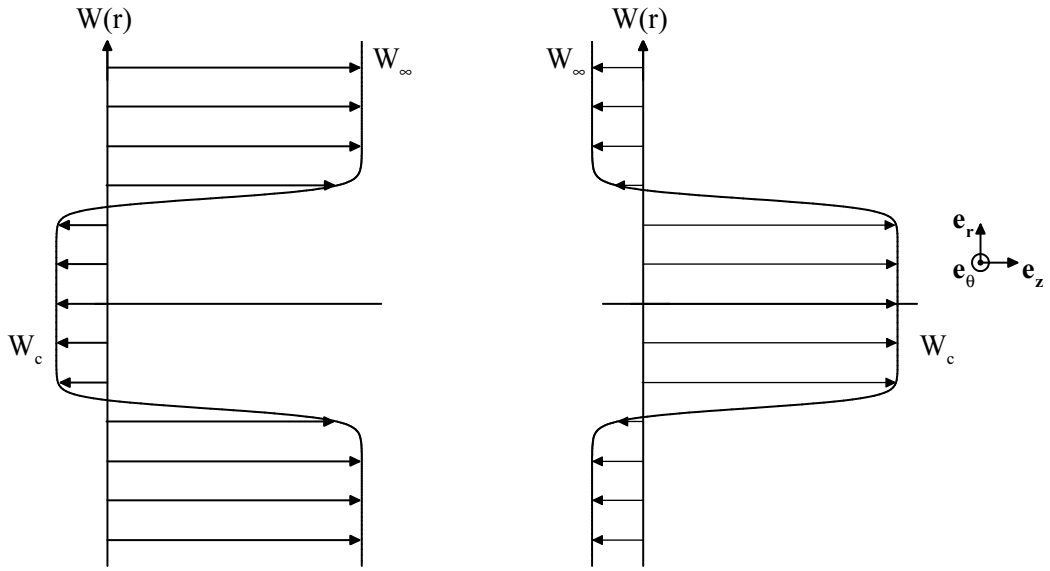

FIGURE 1. Typical velocity wake profile, and corresponding jet profile symmetric with respect to the unity velocity.

In the absence of body forces, the pressure P_b is uniform throughout the flow. For a fixed ratio of centerline to free-stream density $S = \rho_c/\rho_\infty$ ($S > 1$ for cold heavy wakes and $S < 1$ for hot light wakes), the energy equation for the base flow is replaced by the Crocco−Busemann relation (Schlichting 1978), obtained from the three-dimensional steady boundary-layer equations, and modelling a heat transport across the shear layer similar to the momentum transport. The temperature field is given by

$$T_b(r) = 1 + \left(\frac{1}{S} - 1\right) F(r) - \frac{(\gamma-1)M_\infty^2}{2}\left(\frac{2\Lambda}{1-\Lambda}\right)^2 F(r)(F(r)-1) \tag{2.10}$$

and the density is obtained from the ideal gas relation as

$$\rho_b(r) = T_b(r)^{-1}\,. \tag{2.11}$$

In the framework of the linear stability theory, all flow field quantities are decomposed into base flow and infinitesimal disturbances (ρ', u', v', w', t', p') where u', v', w' are the radial, azimuthal and axial components of the velocity perturbation. Disturbances are chosen in the usual normal mode form

$$\phi(r,\theta,z,t) = \phi_b(r) + \epsilon\left(\phi'(r)e^{\mathrm{i}(kz+m\theta-\omega t)} + \text{ c.c.}\right) \tag{2.12}$$

where c.c. denotes the complex conjugate and ϕ' stands for any disturbance quantity. $k = k_r + \mathrm{i}k_i$ is the complex axial wave number, $\omega = \omega_r + \mathrm{i}\omega_i$ is the complex pulsation, ω_i and $-k_i$ being, respectively, the temporal and spatial growth rates, and m is the integer azimuthal wavenumber. Substitution of (2.12) into the governing equations (2.1) − (2.3) linearized about the base flow and elimination of the pressure disturbances p' lead to a generalized eigenvalue problem for either k or ω, whose equations are given in Appendix A. For all calculations, a complete set of eigenvalues and associated eigenfunctions is obtained for a Reynolds number $Re_\infty = 2000$, using a spectral Chebyshev−Gauss collocation method.

2.2. *Numerical method*

A mode of zero group velocity $\partial\omega/\partial k = 0$ is associated with a saddle point k^0 and a branch point $\omega^0 = \omega(k^0)$ for the complex pulsation $\omega(k)$. The saddle point k^0 must be *causal* and be formed by the pinching of an upstream and a downstream propagating branch, i.e. the spatial branches issuing from the saddle point must separate into the upper and lower half of the complex k-plane when $\omega_i \geqslant \omega_{i,max}$, where $\omega_{i,max}$ is the maximum temporal growth rate, the largest ω_i over all temporal waves with $k \in \mathbb{R}$. A mode of non-zero group velocity $\partial\omega/\partial k = v_g$ is associated with a wavenumber k^v and a pulsation $\omega^v = \omega(k^v)$, corresponding to a saddle point $\tilde{k}^0$ and a branch point $\tilde{\omega}^0 = \tilde{\omega}(\tilde{k}^0)$ in the Galilean frame travelling at the velocity v_g for the accordingly modified velocity scale and resulting dimensionless parameters, obtained as

$$\tilde{\omega}^0 = \omega^v - v_g k^v \,, \tag{2.13a}$$

$$\tilde{k}^0 = k^v \,. \tag{2.13b}$$

In the present study, modes of zero group velocity are searched by an iterative procedure: owing to the saddle point singularity in the complex k-plane, $\omega(k)$ admits a quadratic Taylor expansion around k^0. The numerical procedure used follows that of Deissler (1987): saddle points k^0 are computed by fitting a generic quadratic expression of the form

$$\omega(k) = \omega^0 + l(k - k^0)^2 \tag{2.14}$$

on the eigenvalues $\omega(k^{(i)})$ obtained for three wave numbers $k^{(i)}$ close to an initial guess value of k^0. All constants k^0, ω^0 and l are computed and three new wavenumbers are chosen closer to the extrapolated value of k^0. The procedure is repeated until both k^0 and ω^0 become stationary within the desired tolerance (four significant digits in the present study). Note that the discrimination between pinching points and physically impermissible k^-/k^- saddle points requires the computation of the spatial branches. For modes of group velocity v_g, k^v and ω^v are obtained similarly by using a quadratic expression of the form

$$\omega(k) = \omega^v + v_g(k - k^v) + l(k - k^v)^2 \,. \tag{2.15}$$

This method was found to provide results matching the associated saddle point in the co-moving frame $(\tilde{r}^*, \tilde{z}^*) = (r^*, z^* - v_g^* t^*)$.

In the laboratory frame, the asymptotic impulse response of the flow at large times is proportional to the quantity $e^{\mathrm{i}(k^0 z + m\theta - \omega^0 t)}$ - see Huerre & Monkewitz (1985). Therefore, only the k^+/k^- pinching point of highest absolute growth rate is taken into account in this study, as this mode will dominate in the long time limit. The base flow is then classified as absolutely unstable if a mode of zero group velocity has a positive absolute growth rate ω_i^0 and fulfils the pinching requirements. In the following, we use the Strouhal number St built up from ω_r^0, W_∞ and D, and the absolute wavelength λ^0 built up from k_r^0 and D, defined by

$$St = \frac{\omega_r^0 D}{2\pi W_\infty}, \qquad \lambda^0 = \frac{2\pi}{k_r^0 D} \,. \tag{2.16}$$

Similarly, for a non-zero group velocity, we use the wavelength λ^v built up from k_r^v and D.

3. Linear impulse response of an incompressible wake

In the linear stability theory, an arbitrary perturbation generates a small-amplitude wave packet composed, for any particular azimuthal wavenumber, of a continuous set of spatio-temporal modes, each mode propagating with its own specific group velocity. In this section, the linear impulse response of an axisymmetric wake is investigated in the zero-Mach-number limit as a convenient way to identify the spatio-temporal modes of interest. All results are provided in terms of the spatio-temporal growth rate $\sigma = \omega_i^v - v_g k_i^v$. Note that the linear impulse response for a wake flow represents also the impulse response of the jet flow with $\Lambda^{jet} = -\Lambda^{wake}$ (see figure 1), if a symmetry with respect to $v_g = 1$ is applied, i.e. $\sigma(v_g^{jet}) = \sigma(2 - v_g^{wake})$. This symmetry is of particular importance when the absolute−convective transition is of interest, as the trailing edge and the leading edge of the wave packet exchange roles. For clarity, the properties of the trailing and leading edges are always discussed for a wake wave packet propagating in a wake flow, i.e. the trailing edge is located at the 'wake side' of the wave packet, and the leading edge at 'the jet side' of the wave packet. A wake of particular Λ will then be absolutely unstable if the *trailing* edge of the impulse response travels with a velocity $v_g < 0$, whereas the jet counterpart will be absolutely unstable if the *leading* edge travels with a velocity $v_g > 2$. This section extends to the 'wake side' of the wave packet the study of Lesshafft & Huerre (2007), where the impulse response is computed and discussed only for the 'jet side'.

3.1. *Helical wave packet,* $m = 1$

We choose a profile characterized by a velocity ratio $\Lambda = -1.2$ (corresponding to a centerline counterflow of 9% of the free-stream velocity) and a steepness parameter $D/\theta = 60$ to illustrate the physics of the impulse response. Figure 2(a) shows the spatio-temporal growth rate σ of the helical modes ($m = 1$) as a function of the group velocity v_g (thick line).

At the trailing edge of the wave packet, the spatio-temporal growth rate distribution exhibits an angular point for $v_g = 0.080$ that divides the wave packet into two domains, corresponding to two distinct modes. Modes dominating at low group velocities $v_g \leqslant 0.080$ correspond to absolute instability modes which trigger the vortex-shedding phenomenon in homogeneous wakes (Monkewitz 1988). These modes will be referred to as *wake* modes. Modes dominating at higher group velocities $v_g \geqslant 0.080$ continually extend to the other side of the wave packet. These modes, that will be referred to as *shear-layer* modes, are the equivalent for $m = 1$ of the short scale modes that have been identified in hot jets by Jendoubi & Strykowski (1994) for axisymmetric disturbances ($m = 0$).

This distinction between wake and shear-layer modes is confirmed by figure 3(a), where the radial velocity eigenfunctions u' of each mode are presented, respectively, for $v_g = 0$ (wake mode) and $v_g = 0.15$ (shear-layer mode). All velocity magnitudes have been normalized with respect to the maximum radial velocity perturbation. For both modes, a non-zero radial velocity component of the disturbance energy is allowed in the centerline region by the boundary conditions that apply at $r = 0$ for $m = 1$. As expected for the shear-layer mode, the perturbation is concentrated in the shear-layer region, decays rapidly at large cross-stream distances and when approaching the centerline. For the wake mode, the perturbation also peaks in the shear region, but maintains a significant level at larger cross-stream distances. The large value of the perturbations at $r = 0$ indicates that the shear layer can no longer be considered as isolated, but interacts strongly with the boundary condition at the centerline. The wavelength λ^v at the angular point close to the trailing edge of the $m = 1$ wave packet is also plotted in figure 3(b), all other

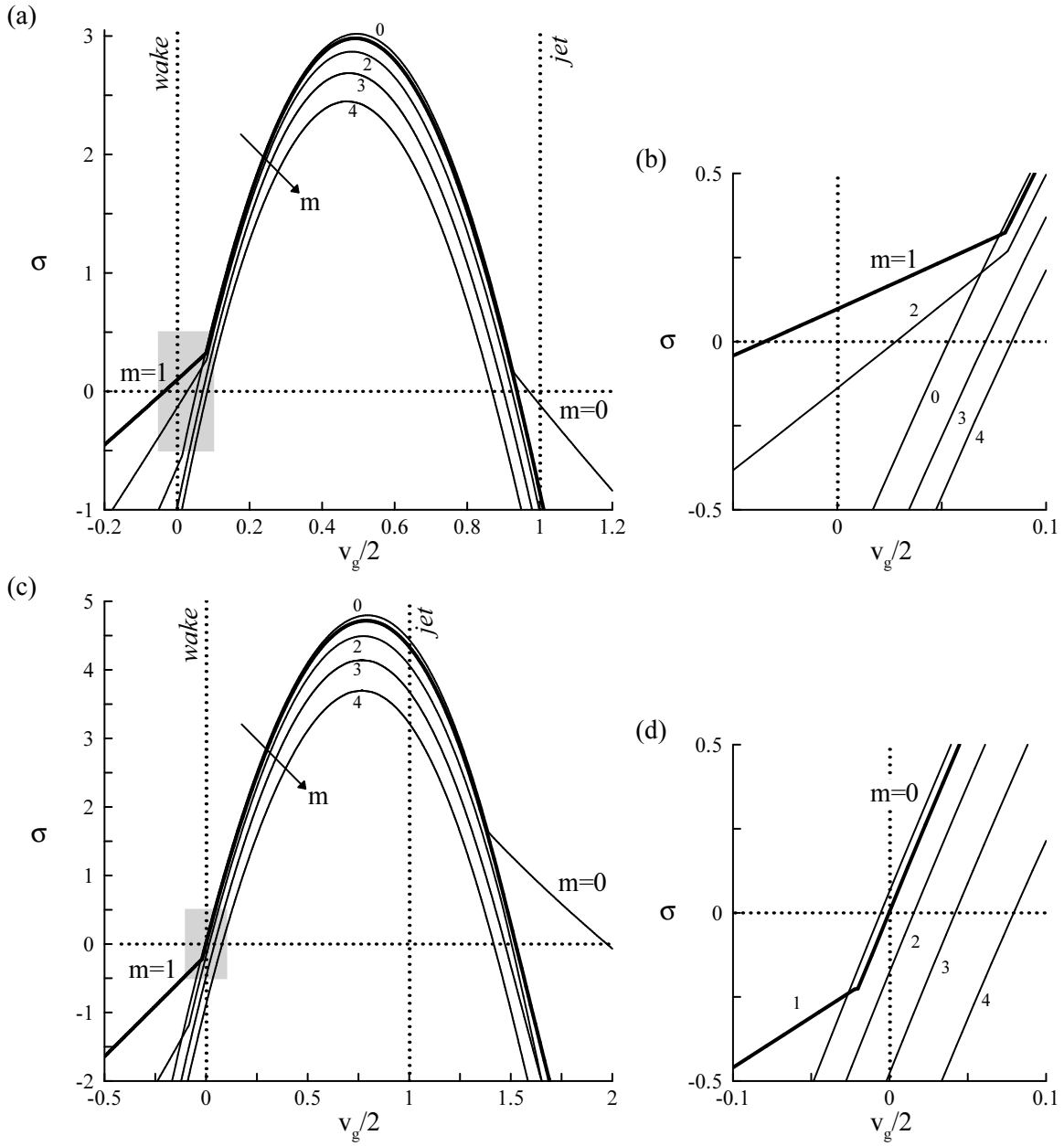

FIGURE 2. Spatio-temporal growth rates σ of the helical mode $m = 1$ (thick line), and of the modes of azimuthal wavenumbers $m = 0, 2, 3, 4$ (thin lines), for $D/\theta = 60$, $M_\infty = 0$ and $Re_\infty = 2000$. When the trailing edge of a wave packet ($\sigma = 0$) extends over the $v_g = 0$ dotted line, the corresponding wake is absolutely unstable. Symmetrically, when the leading edge of the wave packet extends beyond the dotted line $v_g/2 = 1$, the jet profile associated to $\Lambda^{jet} = -\Lambda^{wake}$ is absolutely unstable. (a) Homogeneous wake ($S = 1$) for $\Lambda = -1.2$. (b) Enlargement of the $v_g = 0$ shaded area of (a). (c) Light wake ($S = 0.3$) for $\Lambda = -2.25$. (d) Enlargement of the $v_g = 0$ shaded area of (c).

parameters being identical to that used in figure 3(a). For these parameter settings, the angular point corresponds always to a group velocity $v_g > 0$. The wake mode wavelength is almost independent of D/θ, so that λ^v rescaled by D/θ varies proportionally to D/θ in figure 3(b). The shear-layer mode rescaled wavelength is almost independent of D/θ, confirming that λ^v scales on the momentum thickness θ and is insensitive to curvature

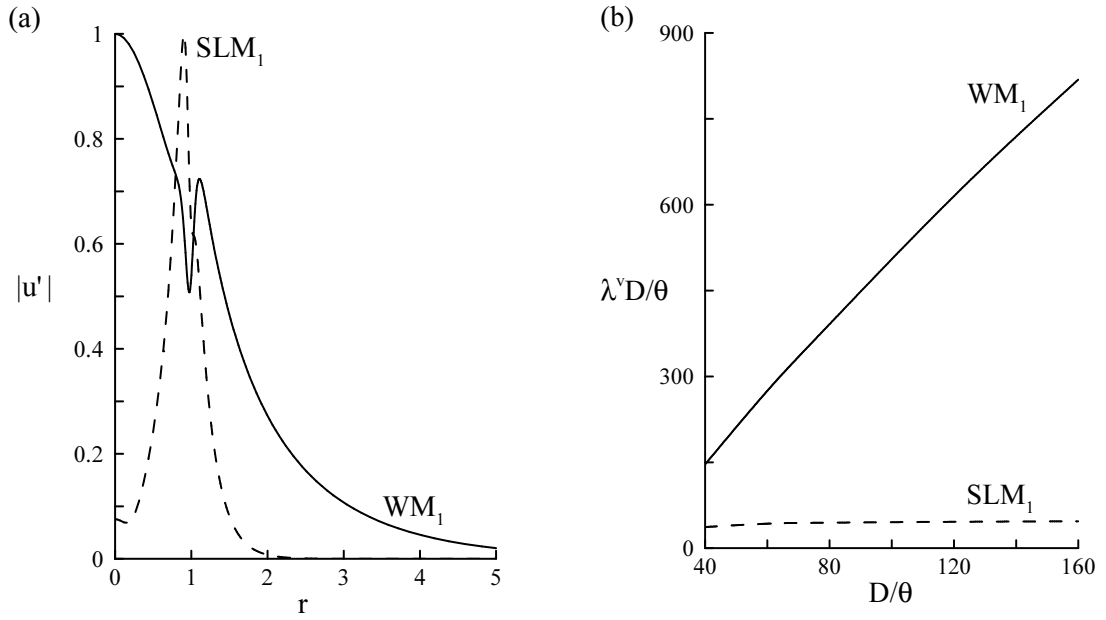

FIGURE 3. $\Lambda = -1.2, S = 1, M_\infty = 0$ and $Re_\infty = 2000$ and azimuthal wavenumber $m = 1$. (a) Normalized radial velocity eigenfunctions for $D/\theta = 60$. Wake mode at $v_g = 0$ (———, WM_1) and shear-layer mode at $v_g = 0.15$ (− − −, SLM_1). (b) Wavelength λ^v renormalized by the momentum thickness θ as a function of D/θ at the group velocity corresponding to the angular point close to the trailing edge of the $m = 1$ wave packet.

effects, a result supporting the idea that this mode is analogous to the disturbances in plane mixing layers, as D/θ goes to infinity.

Complete maps $k(\omega)$ obtained for contours parallel to the real axis of the ω-plane (i.e. for different fixed values of ω_i), are presented in figures 4(a) and 4(b) for $v_g = 0$ and in figure 4(c) for $v_g = 0.15$. The saddle points corresponding to the pinching events producing the different instability modes documented in figure 3(a) are represented. k_1^- denotes the spatial branch which, by pinching with the k^+ branch, gives rise to a wake mode, and k_2^- its counterpart for the shear-layer mode. The saddle point associated with the k_3^- branch (open diamond symbol) is not considered here, as extensive computations, carried out for different control parameters, show that this point displays the highest absolute growth rate only in cases where it is a non-physical k_2^-/k_3^- point. For $v_g = 0$, the k^+/k^- pinching point of highest absolute growth rate is the wake mode, owing to the pinching of the k^+ and k_1^- branches at $k^0 = 0.625 - 1.401\,\mathrm{i}$, for $\omega^0 = 1.484 + 0.097\,\mathrm{i}$. Note that the k_1^- branch issues from the $k_r < 0$ domain, more clearly visible on the close-up in 4(b). Studies by Healey (2005, 2006) have warned against the specific dynamics that may be associated with such pinching with branches issuing from the $k_r < 0$ half domain, i.e. the other side of the branch cut, the other side of the looking-glass (Carroll 1872), where eigenmodes grow in the cross-stream direction. Fortunately, in the present case, we observe that the wake mode saddle point remains at a distance $k_r \sim 0.5$ from the $k_r = 0$ axis, which is consistent with the idea that k_r scales on the wake diameter. Therefore, standard results remain valid. If ω_i is decreased further below $\omega_i^0 = 0.097$, the shear-layer mode arises owing to the coalescence of the merged k^+/k_1^- branch with the k_2^- branch. Similar maps $\tilde{k}(\tilde{\omega})$ are presented in figure 4(c) for $v_g = 0.15$. In this case, the pinching point of highest absolute growth rate is the shear-layer mode, formed by the pinching of the k^+ and the k_2^- branch at $\tilde{k}^0 = 5.269 - 4.896\,\mathrm{i}$, for $\tilde{\omega}^0 = 5.016 + 2.262\,\mathrm{i}$. If $\tilde{\omega}_i$ is decreased further, the wake mode arises owing to the coalescence of the merged k^+/k_2^- branch with the k_1^- branch. This existence of two distinct helical instability modes

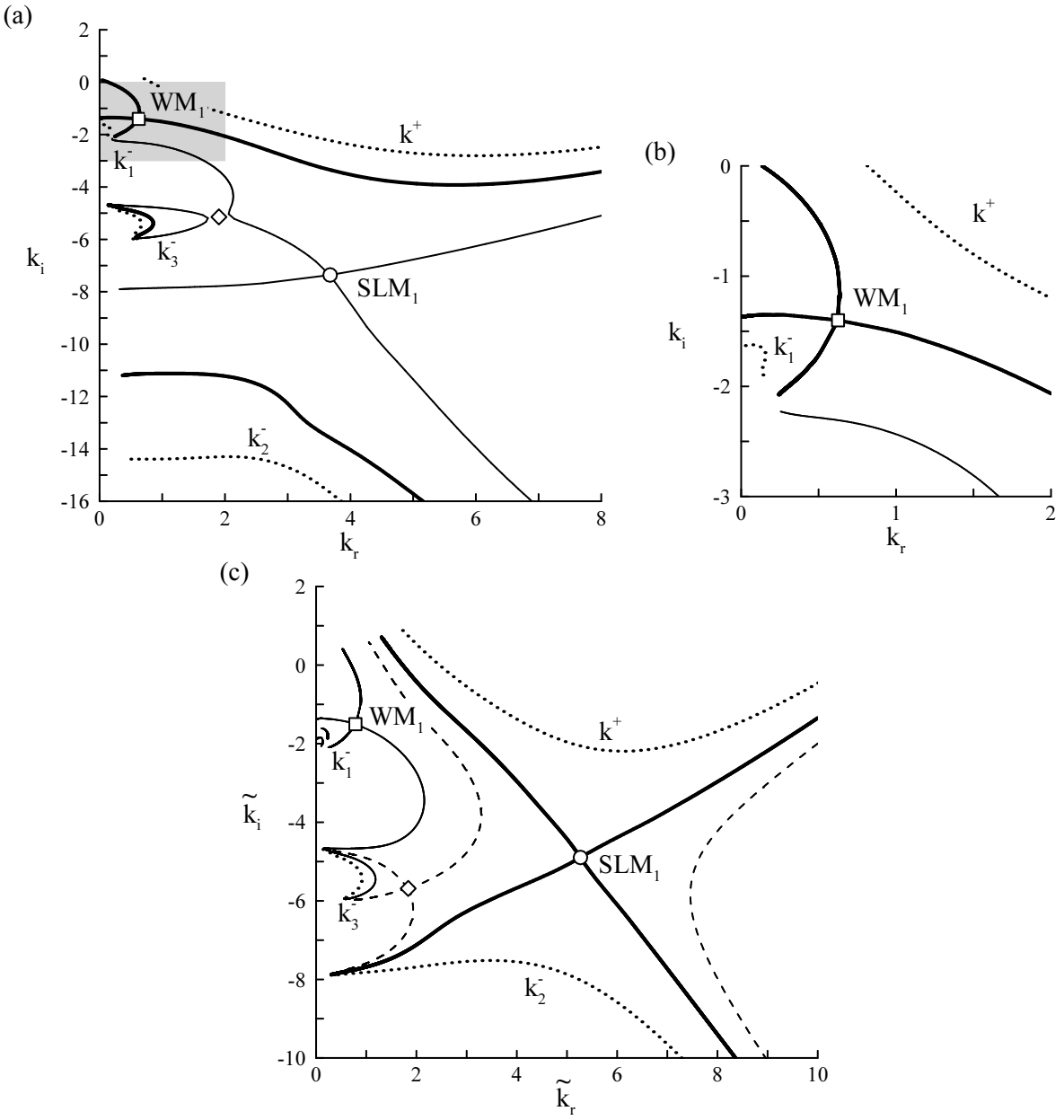

FIGURE 4. Spatio-temporal branches $k(\omega)$ in the complex k-plane for various values of ω_i. $\Lambda = -1.2$, $D/\theta = 60$, $S = 1$, $M_\infty = 0$ and $Re_\infty = 2000$. The WM_1 and SLM_1 labels mark the saddle points associated, respectively, to the wake mode and the shear-layer mode. (a) $v_g = 0$. (b) Enlargement of the shaded pinching area of (a). (c) $v_g = 0.15$.

resulting from the pinching of a single unstable k^+ branch with two distinct k^- branches is somehow reminiscent of that resulting in the competition between axisymmetric jet column and shear-layer modes in heated jets, documented by Jendoubi & Strykowski (1994), although there is no connection between the leading edge modes of the $m = 0$ wave packet and the trailing edge modes of the $m = 1$ wave packet. Similar results are also discussed in the study of Juniper (2006) on confined two-dimensional jets (see figure 3 for instance).

3.2. *Overall wave packet : azimuthal wavenumber selection*

The spatio-temporal growth rate for axisymmetric disturbances ($m = 0$) is also plotted in figures 2(a) and 2(b). The angular point close to the leading edge corresponds to the existence of the jet-column modes alluded to above, that lead the convective-absolute transition for isothermal or hot jets, as discussed in Jendoubi & Strykowski (1994) and Lesshafft & Huerre (2007). At the trailing edge, the $m = 0$ spatio-temporal growth rate exhibits a second angular point (barely noticeable in figure 2b) corresponding to the existence of axisymmetric wake modes at low group velocities.

The structure of the $m = 2$ wave packet is similar to that of the $m = 1$ modes, with the possibility of the trailing edge being dominated by a large-scale wake mode (see the close-up of figure 2a), but its growth rate is smaller at all group velocities than its $m = 1$ counterpart.

For higher azimuthal modes $m > 2$, the growth rate for each group velocity decreases as m increases. If the curvature effect is neglected at leading order for this large steepness parameter ($D/\theta = 60$), the stabilization of the shear-layer mode for increasing azimuthal wavenumbers may be interpreted as an effect of the Squire theorem, since the misalignment of the local wave vector $m/r\boldsymbol{e_\theta} + k_r\boldsymbol{e_z}$ with the direction of the axisymmetric wave vector $\boldsymbol{e_z}$ increases with m. For the parameter settings of figure 2(a), the overall azimuthal wavenumber trailing edge is dominated by the absolutely unstable helical wake mode ($m = 1$), whereas the overall leading edge is dominated by the axisymmetric jet column mode ($m = 0$). To our knowledge, these results on three-dimensional jets and wakes have never been shown since emphasis was put on jets, and even publications that have shown the entire jet wave packet for both $m = 0$ and $m = 1$ (Lesshafft & Huerre 2007) have overlooked the possibility of a different mode at the 'wake side' of the wave packet, corresponding to the existence of the wake modes described above. Extensive calculations in the wide range of parameters investigated here suggest that the overall trailing edge can be dominated by the axisymmetric shear-layer mode for sufficiently light wakes. Figure 2(c) presents the modification of the wave packet when the density is decreased down to $S = 0.3$. The trailing edge of the $m = 1$ wave packet is now led by the shear-layer mode, and the overall wave packet is dominated by the $m = 0$ shear-layer mode (see the close-up in figure 2d). Comparing figures 2(a) and 2(c), we see at the trailing edge that the angular point of the $m = 1$ wave packet has moved to negative growth rates, meaning that lightening the wake stabilizes the helical wake mode. The strong negative value of the velocity ratio Λ used in figure 2(c) in order to show the wave packet at the threshold of absolute instability demonstrates that, as in the two-dimensional case (Yu & Monkewitz 1990), the lighter the wake, the stronger the backflow required for the instability to be absolute. The effect is opposite at the leading edge, where the angular point of the $m = 0$ wave packet has moved to large growth rates. This is in agreement with the promotion of absolute instability in axisymmetric low-density jets (Jendoubi & Strykowski 1994).

3.3. *Evolution of the largest spatio-temporal growth rate*

The top of the wave packet in figure 2, i.e. the mode of maximum spatio-temporal growth rate σ_{max} is of particular interest since it is identical to the mode of maximum temporal growth rate $\omega_{i,max}$ (Huerre & Rossi 1998). It defines the largest growth rate that may be observed while moving with the perturbation at the velocity v_{gmax} for which $\sigma(v_g) = \sigma_{max}$. Values of σ_{max} have been computed for different values of the steepness parameter D/θ. The results are presented in figure 5, where the smallest physical value of D/θ is 6.5, corresponding to the standard Gaussian velocity profile considered by Batchelor & Gill (1962), which is here recovered for $D/\theta = 6.5$ ($N = 1$). σ_{max} is asymptotically

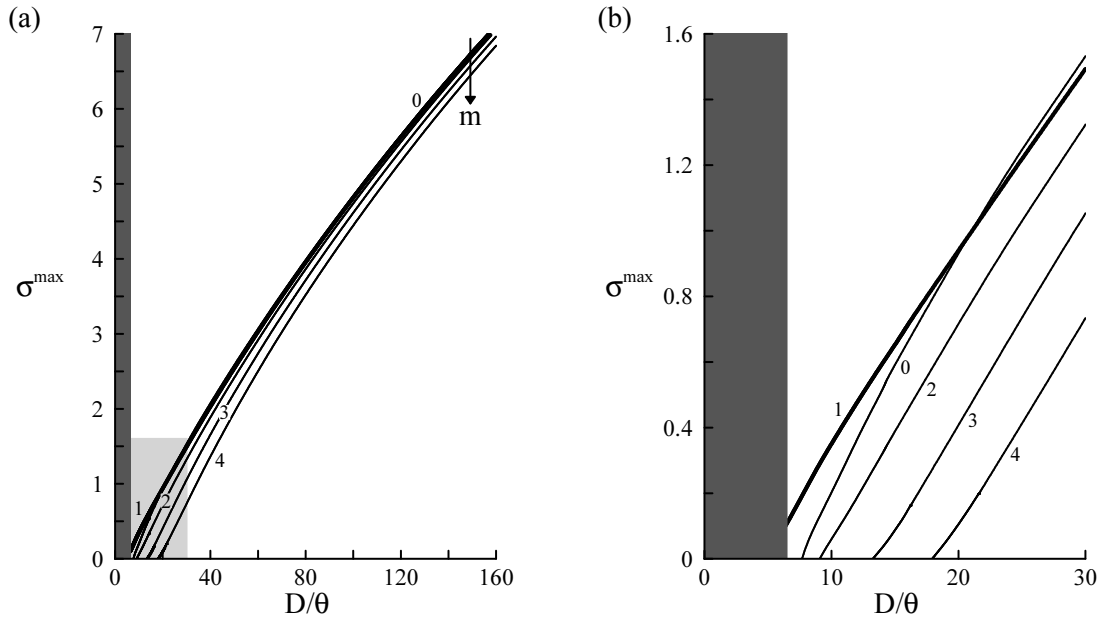

FIGURE 5. (a) Maximum spatio-temporal growth rate σ_{max} as a function of D/θ, for the helical mode $m = 1$ (thick solid line), and the modes of azimuthal wavenumbers $m = 0, 2, 3, 4$. $\Lambda = -1.2$, $S = 1$, $M_\infty = 0$ and $Re_\infty = 2000$. The dark shaded area corresponds to $D/\theta < 6.5$, these values not being allowed for profiles defined by (2.6) − (2.7). (b) Enlargement of the light shaded area of (a).

proportional to D/θ, confirming that the shear-layer mode is closely related to the Kelvin-Helmholtz instability. Consistently with the results previously discussed from figure 2, the $m = 0$ and the $m = 1$ maximum spatio-temporal growth rates are remarkably similar, although the axisymmetric mode is slightly more unstable for $D/\theta \gtrsim 23$. The maximum spatio-temporal growth rate then slowly decreases as m is increased, in agreement with the prediction of the Squire theorem that applies for large steepness parameters. Figure 5(b) shows that helical disturbances ($m = 1$) are the most amplified for sufficiently small values of D/θ, namely $D/\theta \lesssim 23$, and that only helical disturbances are amplified for $D/\theta \leqslant 8$. Identical results can be found in the analysis of axisymmetric jets by Batchelor & Gill (1962), showing that only helical disturbances are amplified when the shear region of the jet is sufficiently thick. Figure 6 presents the variation of σ_{max} as a function of S and M_∞, for $D/\theta = 60$. All azimuthal wavenumbers display a maximum amplification for $M_\infty = 0$ and $S \sim 1$. These results are typical of shear instability and have already been documented in the context of plane vortex sheets, see for instance Miles (1958) for the effect of the Mach number and Drazin & Reid (1981) for the effect of the density ratio. Note that the effect of the density ratio on the most amplified spatio-temporal mode contrasts with that described for the edges of the wave packet. Decreasing the density ratio below $S = 1$ reduces the maximum spatio-temporal growth rate but accelerates the wave packet, promoting convective instability at the trailing edge ('wake side') and absolute instability at the leading edge ('jet side'). Increasing the density ratio above $S = 1$ also reduces the maximum spatio-temporal growth rate, but it slows down the wave packet, promoting absolute instability at the trailing edge and convective instability at the leading edge.

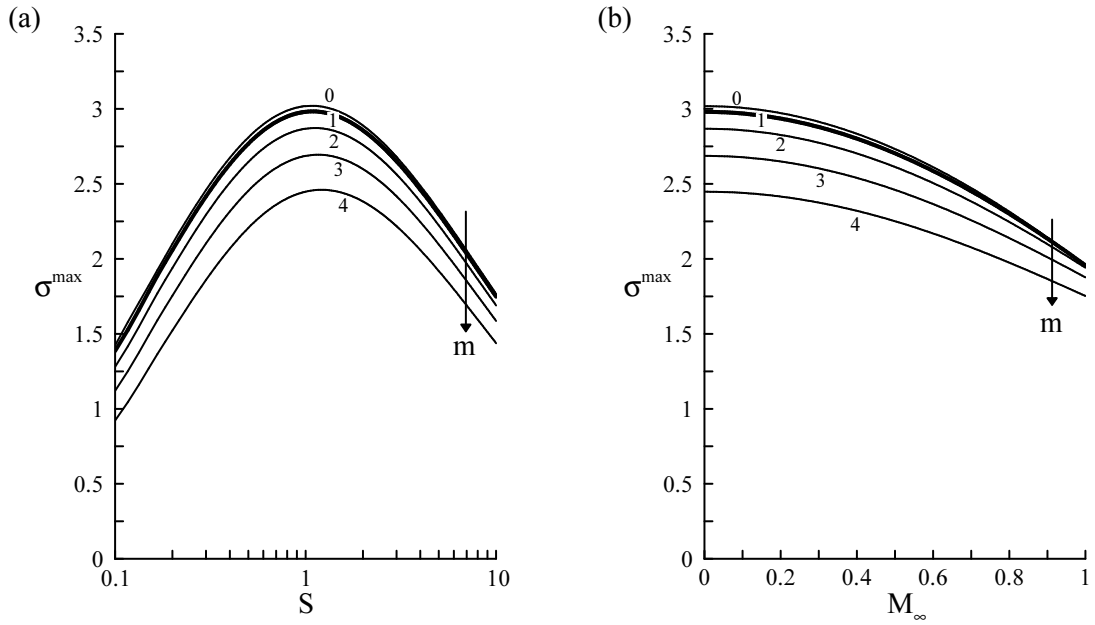

FIGURE 6. Maximum spatio-temporal growth rate σ_{max} of the helical mode $m = 1$ (thick solid line), and of the modes of azimuthal wavenumbers $m = 0, 2, 3, 4$. $\Lambda = -1.2$, $S = 1$, $M_\infty = 0$ and $Re_\infty = 2000$, (a) as a function of the density ratio, at $M_\infty = 0$. (b) as a function of the Mach number, at $S = 1$.

4. Convective–absolute transition

A wake is absolutely unstable if the trailing edge of the linear impulse response propagates at a negative group velocity. Therefore, it is deduced from the previous discussion that the convective-absolute transition is led either by the axisymmetric shear-layer mode $m = 0$ (SLM_0) or the helical wake mode $m = 1$ (WM_1). In this section, we investigate the convective/absolute transition of axisymmetric wakes, and identify the selected dominant mode that leads the transition in the laboratory frame ($v_g = 0$), in a parameter space including the velocity ratio Λ, the steepness parameter D/θ, the density ratio S, and the Mach number M_∞. For simplicity, a control parameter is said to be destabilizing (resp. stabilizing) when its variation results in an extension (resp. reduction) of the domain of absolute instability.

4.1. *Effect of the density ratio*

We study the effect of the density ratio and the velocity ratio on the stability properties of the base flow, for a wake of steepness parameter $D/\theta = 60$ at zero Mach number. The boundary of the domain of absolute instability in the (S, Λ)-plane is presented in figure 7. We use a dashed curve when the transition is led by the axisymmetric shear-layer mode and a plain curve when it is led by the helical wake mode. The instability is absolute for combinations of parameters located in the shaded region, labeled AU, and convective for all other combinations of parameters (CU-labeled region).

The absolute instability boundary is reminiscent of that documented by Yu & Monkewitz (1990) in the case of two-dimensional wakes, namely large high (resp. low) density ratios are destabilizing (resp. stabilizing) and promote absolute (resp. convective) instability. A discontinuity in the boundary occurs at $S = 0.396$, a point marked by an open circle in figure 7, where the dominant mode switches from the axisymmetric shear-layer mode ($S \leqslant 0.396$) to the helical wake mode ($S \geqslant 0.396$). In the following, this particular point where both modes are simultaneously marginally absolutely unstable is referred to as the crossover point. Note also that the marginal curve crosses the $\Lambda = -1$ line at

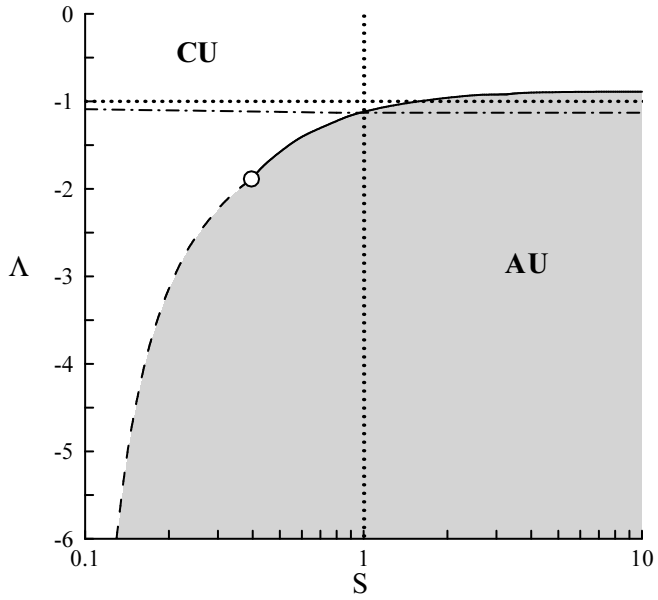

FIGURE 7. Boundary separating the regions of absolute (shaded domain labeled AU) and convective (domain labeled CU) instability in the (S, Λ)-plane, for $D/\theta = 60$, $M_\infty = 0$ and $Re_\infty = 2000$. The transition to absolute instability is led either by the axisymmetric shear-layer mode (dashed line) or the helical wake mode (solid line). The open circle marks the crossover point corresponding to the change in the selection of the dominant mode. The dash-dotted line is the curve of marginal absolute instability in the absence of baroclinic effects.

$S = 1.551$. Therefore, wakes with sufficiently high density ratios can be absolutely unstable to $m = 1$ perturbations (wake mode), even with a coflow on the axis. The threshold is found to be asymptotic to $\Lambda = -0.9$ as S increases, indicating that the critical velocity ratio depends weakly on the density ratio: for instance, absolute instability occurs in presence of a coflow rate of 5.3% at $S = 10$ and of 5.8% at $S = 4$. On the contrary, for low density ratios, the critical velocity ratio required to reach absolute instability is dramatically affected by small variations of S: for instance, absolute instability occurs in presence of a counterflow rate of 22.5% at $S = 0.5$ and of 51.7% at $S = 0.2$.

This striking behaviour may be understood by considering the effect of the baroclinic torque, as first suggested by Soteriou & Ghoniem (1995) for the stability of homogeneous and non-homogeneous shear layers. The main idea is that a baroclinic torque arising from base flow density gradients and from the pressure perturbations $\mathbf{\Gamma} = (\boldsymbol{\nabla}\rho_0 \times \boldsymbol{\nabla}p')/\rho_0^2$ can act as a source for the vorticity perturbations, as discussed by Nichols & Schmid (2007) in the case of non-homogeneous round jets, for instance. On similar jet configurations, Lesshafft & Huerre (2007) have shown that the impact of baroclinic effects can be assessed by solving a modified dispersion relation, in which the linearized momentum equations are artificially forced in order to cancel the baroclinic torque, which has only one non-trivial component $\Gamma_\theta \mathbf{e}_\theta$ due to the axisymmetry. This method is generalized here to the case of non-axisymmetric disturbances, leading to a two-component baroclinic torque $\Gamma_\theta \boldsymbol{e_\theta} + \Gamma_z \boldsymbol{e_z}$, where

$$\Gamma_\theta = \quad \mathrm{i}k^0 \frac{\partial_r \rho_0}{\rho_0^2} p'(r) e^{(\mathrm{i}k^0 z + m\theta - \omega^0 t)}\,, \tag{4.1a}$$

$$\Gamma_z = -\mathrm{i}\frac{m}{r} \frac{\partial_r \rho_0}{\rho_0^2} p'(r) e^{(\mathrm{i}k^0 z + m\theta - \omega^0 t)}\,, \tag{4.1b}$$

Γ_z being non-zero for $m \neq 0$. More details on the vorticity equations can be found in

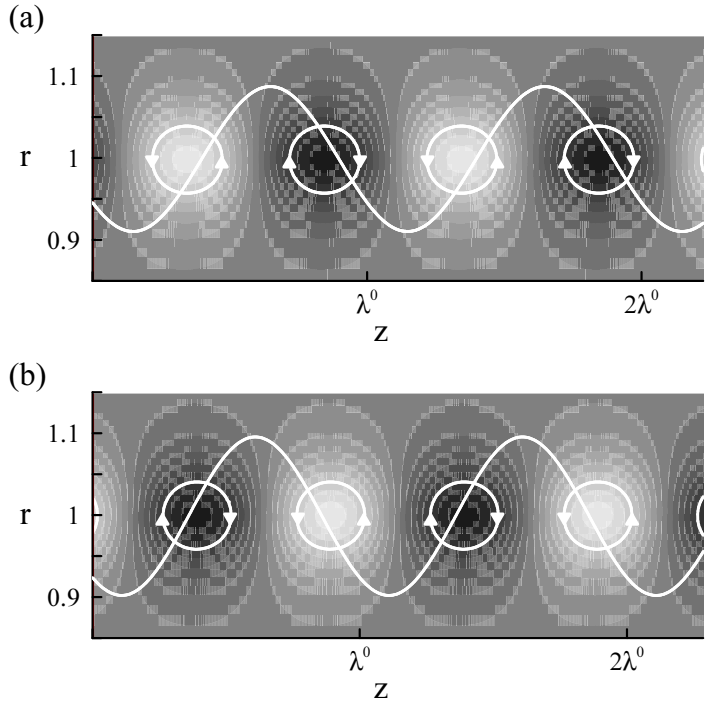

FIGURE 8. (*a*) Displacement $\eta(r=1,\theta=0,z)$ (drawn with an arbitrary finite amplitude) and baroclinic torque Γ_t associated to the marginally absolutely unstable eigenmode, projected along the vector $\boldsymbol{t}(r=1)$ tangent to the phase lines of η, for $S=2.5$. The rotation induced by the torque is visualized by the white circles with arrows. ($D/\theta=60$, $M_\infty=0$ and $Re_\infty=2000$). (*b*) Same as (*a*) but for $S=0.45$. This figure extends to non-axisymmetric perturbations the arguments of Lesshafft & Huerre (2007) and Nichols & Schmid (2007) (see their figures 5 and 8, respectively).

Appendix B. The absolute instability boundary associated to the modified dispersion relation, where the two-component baroclinic torque has been cancelled, is shown in figure 7 (dash-dotted line). When the baroclinic effects are removed, the transition from convective to absolute instability is led by the helical wake mode ($m=1$) whatever the value of the density ratio. For $S=1$, forced and unforced marginal absolute instability curves cross since the baroclinic torque vanishes in the homogeneous case. Surprisingly, the convective-absolute transition is nearly independent of S when the baroclinic torque is cancelled, even though the density ratio still enters the dispersion relation, the relative difference not being measurable for $S>1$, and being negligible for $S<1$ (0.9% at $S=0.5$ and 3.5% at $S=0.1$). It may therefore be concluded that the baroclinic torque $\boldsymbol{\Gamma}$ promotes the onset of absolute instability in heavy wakes and delays it in light wakes. The physical mechanism proposed by Lesshafft & Huerre (2007) to explain the stability of axisymmetric disturbances in hot jets may be extended to non-axisymmetric perturbations by examining how the baroclinic torque associated with the spatio-temporal absolute eigenmode interacts with the associated displacement η of the shear layer at $r=1$, computed from the radial velocity perturbation as $\partial_t\eta + W\partial_z\eta = u'$, so that

$$\eta = \frac{-\mathrm{i}u'}{k^0 W_b - \omega^0}\,. \tag{4.2}$$

Considering the vector tangent to the phase lines of η, defined as $\boldsymbol{t} = k_r^0\boldsymbol{e_\theta} - m/r\boldsymbol{e_z}$, only the component of the baroclinic torque along $\boldsymbol{t}$

$$\Gamma_t = \boldsymbol{\Gamma}.\frac{\boldsymbol{t}}{\|\boldsymbol{t}\|} \tag{4.3}$$

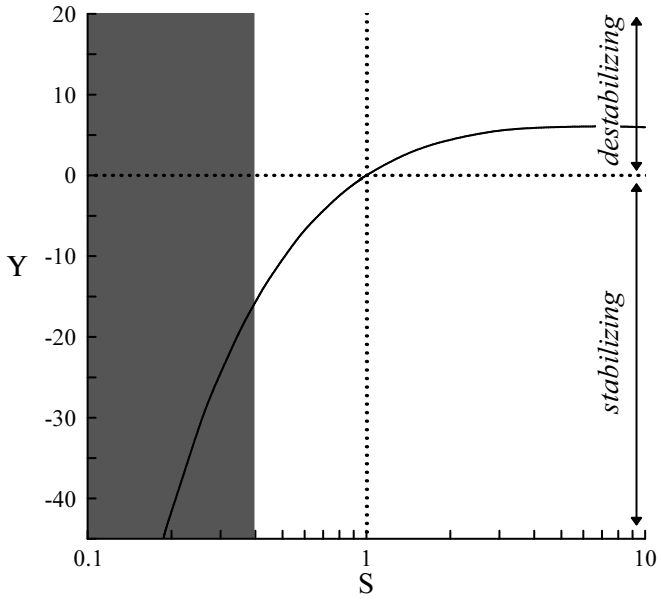

FIGURE 9. Baroclinic factor Υ at the absolute instability threshold, i.e. along the curve $\Lambda(S)$ plotted in figure 7, valid only in the non-shaded area where the wake mode leads the absolute transition ($D/\theta = 60$, $M_\infty = 0$ and $Re_\infty = 2000$). In the shaded area are reported the values of Υ of the mode associated with the wake mode saddle point, followed by continuity.

plays a role in the displacement of the shear-layer. Figure 8(a) shows the shear-layer displacement and the spatial distribution of Γ_t in a meridional plane, computed for the helical wake mode at the absolute instability threshold, for a heavy wake of ratio $S = 2.5$. All spatial amplifications are neglected for clarity by setting the spatial growth rate $-k_i^0$ to zero. Results are reminiscent of that documented in Lesshafft & Huerre (2007) and Nichols & Schmid (2007): the baroclinic torque is concentrated within the shear layer, in regions of alternating sign. The baroclinic torque is destabilizing since it induces a clockwise rotation when η decreases with z, and a counterclockwise rotation when η increases with z. This effect of the baroclinic torque is thus determined by the relative phase ϕ of the projected torque Γ_t, evaluated in the shear layer ($r = 1$), with respect to the displacement η

$$\phi = \arg\{\Gamma_t|_{r=1}\} - \arg\{\eta|_{r=1}\}\,. \tag{4.4}$$

Because there is almost a quadrature advance between Γ_t and η ($\phi = 1.90$), the baroclinic torque tends to enhance the deformation of the shear layer, and is therefore destabilizing, as indeed is predicted by the direct stability analysis. Figure 8(b) shows similar results for a light wake of density ratio $S = 0.45$, but owing to the change of sign of the base flow density gradient, we find in that case a quadrature delay between Γ_t and η ($\phi = -1.77$), so that Γ_t now induces stabilizing deformations that oppose the shear-layer deformation. These results, generalizing the argument of Lesshafft & Huerre (2007) to the case of non-axisymmetric disturbances, show that the action of the baroclinic torque may result in an increase or in a decrease of the instability growth rate. This baroclinic effect depends on the magnitudes of Γ_t and on its relative phase ϕ with the displacement η: the stabilizing (resp. destabilizing) effect is maximum when ϕ is $-\pi/2$ (resp. $\phi = \pi/2$). When ϕ is close to 0 or π, the leading-order effect of the torque is neutral, as it then displaces upstream or downstream the shear-layer undulation. Therefore, we propose to cast the effect of the

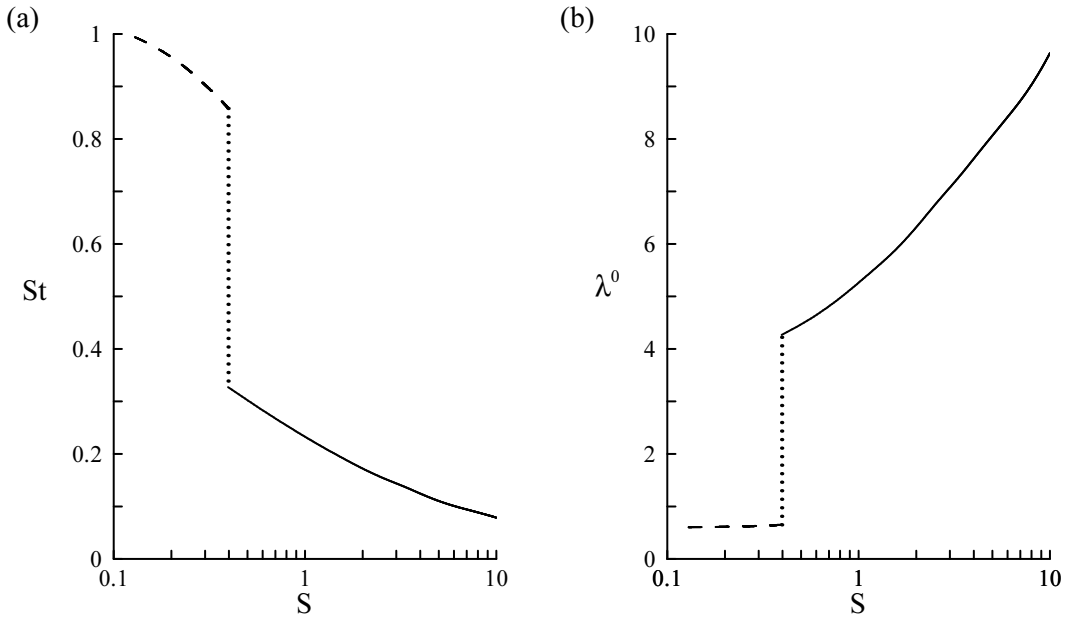

FIGURE 10. (*a*) Strouhal number St and (*b*) absolute wavelength λ^0 as a function of the density ratio at the absolute instability threshold. $D/\theta = 60$, $M_\infty = 0$ and $Re_\infty = 2000$. The curve is dashed when the transition is led by the axisymmetric shear-layer mode, and solid when it is led by the helical wake mode.

baroclinic torque in the single baroclinic factor

$$\Upsilon = \sin\phi \left| \frac{\Gamma_t}{\eta} \right|_{r=1}, \tag{4.5}$$

i.e. we consider baroclinic effects for a fixed amplitude of the displacement. Figure 9 shows the calculated value of Υ at the absolute instability threshold of the helical wake mode. In agreement with the results discussed from figure 7, values of Υ indicate a destabilizing effect of the baroclinic torque for $S > 1$ (positive values), and a strong baroclinic stabilization as S decreases to zero (low negative values).

Figure 10 presents the Strouhal number St and wavelength λ^0 as a function of the density ratio at the absolute instability threshold, i.e. for parameter couples (S, Λ) varying along the boundary of the absolutely unstable domain shaded in figure 7. At the crossover ratio $S = 0.396$, both curves undergo a brutal discontinuity, owing to the change in the selection of the dominant mode, from the axisymmetric shear-layer mode to the helical wake mode. When the density ratio increases in the range $0.1 \leqslant S \leqslant 0.396$, the axisymmetric shear-layer mode dominates: the absolute wavelength remains constant, of order 0.5 wake diameter, and the absolute frequency is high and decreases from 1 to 0.9. When S is increased above 0.396, the helical wake mode dominates: the absolute wavelength jumps to 4 wake diameters and grows up to 10 diameters. At the same time, the absolute frequency drops to 0.3 and keeps decreasing to 0.1 at $S = 10$.

4.2. *Effect of the steepness parameter*

We investigate the effect of varying the steepness parameter on the absolute instability threshold of the flow, keeping $M_\infty = 0$.

Figure 11 presents absolute instability boundaries when the steepness parameter varies within the range $40 \leqslant D/\theta \leqslant 160$. The crossover points between the axisymmetric shear-layer mode and the helical wake mode are marked by an open circle. All curves reflect the same trend as for $D/\theta = 60$ (figure 7). The steepness parameter has essentially no

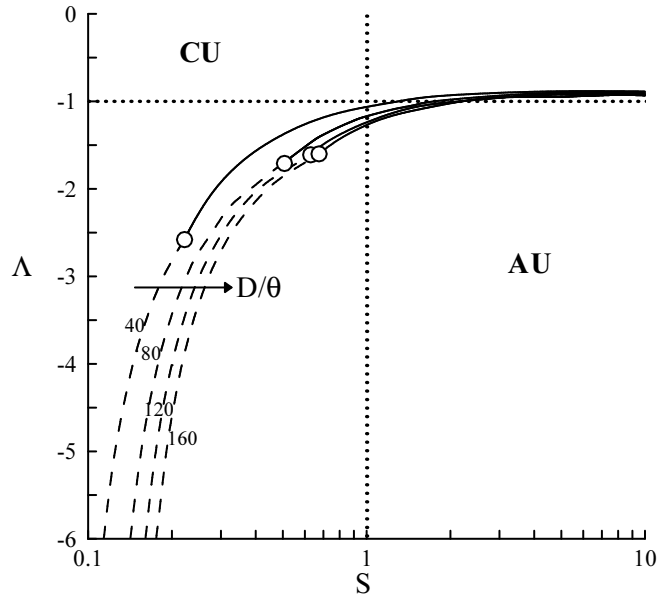

FIGURE 11. Boundary separating the regions of absolute (AU) and convective (CU) instability and crossover points $(\circ)$ in the (S, Λ)-plane for the steepness parameters 40, 80, 120 and 160, at $M_\infty = 0$ and $Re_\infty = 2000$ ($- - -$, SLM_0; ———, WM_1).

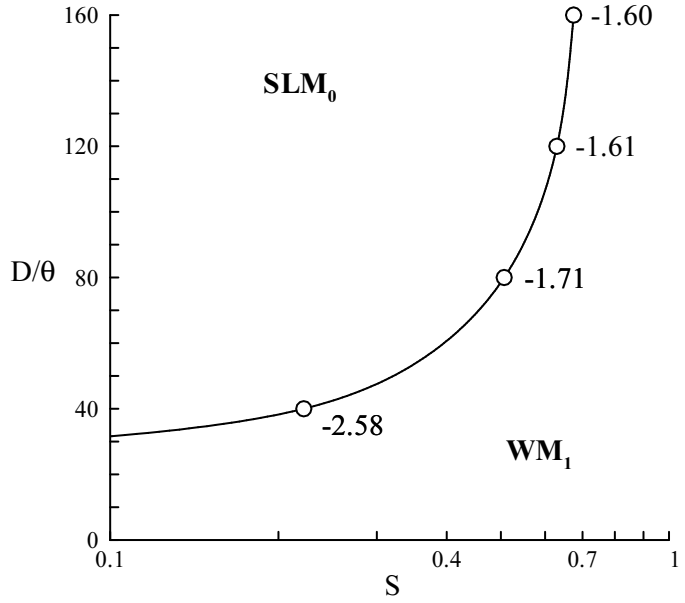

FIGURE 12. Locus of the crossover point in the $(S, D/\theta)$-plane, for $M_\infty = 0$ and $Re_\infty = 2000$. This curve separates domains where the transition to absolute instability is led, respectively, by the axisymmetric shear-layer mode (domain labeled SLM_0) and the helical wake mode (domain labeled WM_1). Open circles correspond to the crossover points for the four values of D/θ plotted in figure 11 and are labeled here with their corresponding velocity ratio Λ.

effect at high density ratios, where the helical wake mode leads the transition. However, at low density ratios, increasing the steepness parameter has a stabilizing effect, and the domain of absolute instability shrinks significantly. The density ratio at the crossover point monotonically increases with D/θ, from 0.202 at $D/\theta = 40$ to $S = 0.673$ at $D/\theta = 160$, whereas at the same time, the rate of counterflow necessary to reach absolute instability decreases from 48.6% ($\Lambda = -2.89$) to 23.4% of the free-stream velocity ($\Lambda = -1.61$). This effect is synthesized in figure 12, which shows the variations of the density

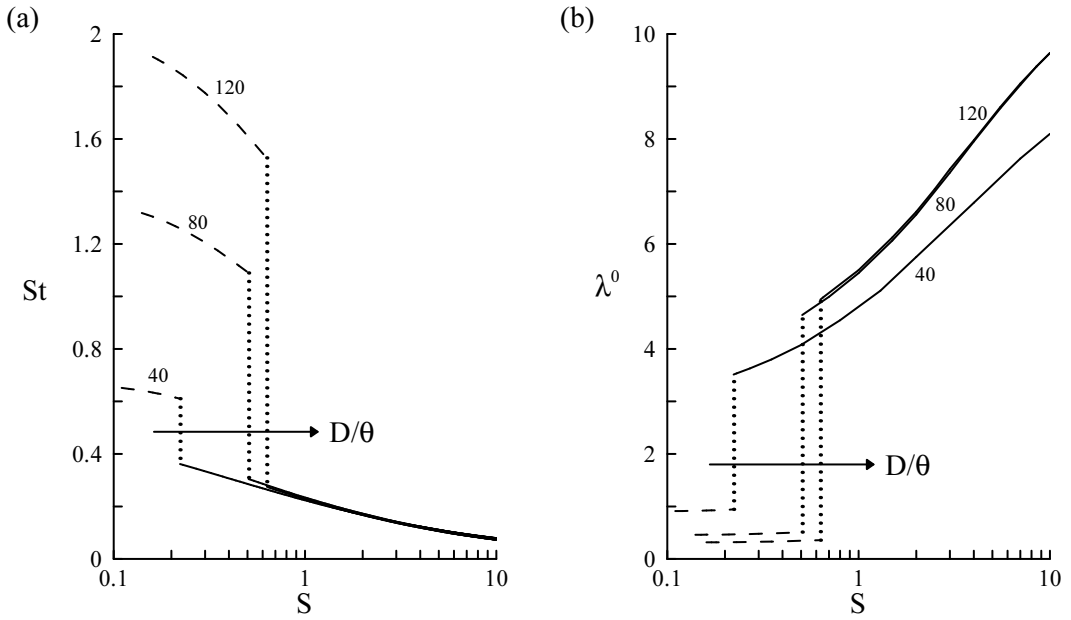

FIGURE 13. (a) Strouhal number St and (b) absolute wavelength λ^0 at the absolute instability threshold for steepness parameters $D/\theta = 40$, 80 and 120. $M_\infty = 0$ and $Re_\infty = 2000$ (– – –, SLM_0; ———, WM_1).

ratio at the crossover point as a function of D/θ. Values of the critical velocity ratios Λ below which the instability becomes absolute are reported along the crossover curve for the four values of D/θ presented in figure 11. The axisymmetric shear-layer mode is dominant for combinations of parameters located above the curve (region labeled SLM_0), and the helical wake mode is dominant for parameters located below the curve (region labeled WM_1). The convective−absolute transition is essentially led by the helical wake mode, the axisymmetric shear-layer mode being dominant only at low density ratios and large steepness parameters. For small values of the steepness parameter $D/\theta \leqslant 32$, the helical wake mode is dominant for all density ratios $0.1 \leqslant S \leqslant 10$ considered in this study. Note that in the homogeneous case ($S = 1$), the absolute instability is led by the helical wake mode for all steepness parameters, as reported in Monkewitz (1988) for incompressible homogeneous wakes. Figure 13 shows the Strouhal number and wavelength at the absolute instability threshold for different values of the steepness parameter D/θ. The curve trends are similar to that presented in figure 10, namely the frequency and the wavelength respectively increases and decreases when the density ratio increases, and all curves are discontinuous at the crossover point characterizing the change in the selection of the dominant mode. For low values of S, the axisymmetric shear-layer mode is dominant and selects high frequencies increasing with D/θ ($St \sim 0.6$ for $D/\theta = 40$ and $1.5 \leqslant St \leqslant 1.9$ for $D/\theta = 120$), and short wavelengths decreasing with D/θ (of order 0.9 wake diameter for $D/\theta = 40$ and 0.3 wake diameter for $D/\theta = 120$, these values being almost independent of S). For higher values of S, the helical wake mode is dominant and is characterized by low frequencies $0.1 \leqslant St \leqslant 0.4$ depending on S, but almost independent of the steepness parameter, and by large wavelengths varying between 4 and 10 wake diameters, the values obtained for $D/\theta = 80$ and 120 being equal.

The behaviour is different for smaller values of the steepness parameter. We present in figure 14 the absolute instability threshold in the range $D/\theta \leqslant 15$. For all values of D/θ in that range and for all density ratios, convective−absolute transition is led by the helical wake mode, a result consistent with that discussed from figure 12. In opposition to the behaviour described in figure 11, lowering D/θ has a stabilizing effect for all density

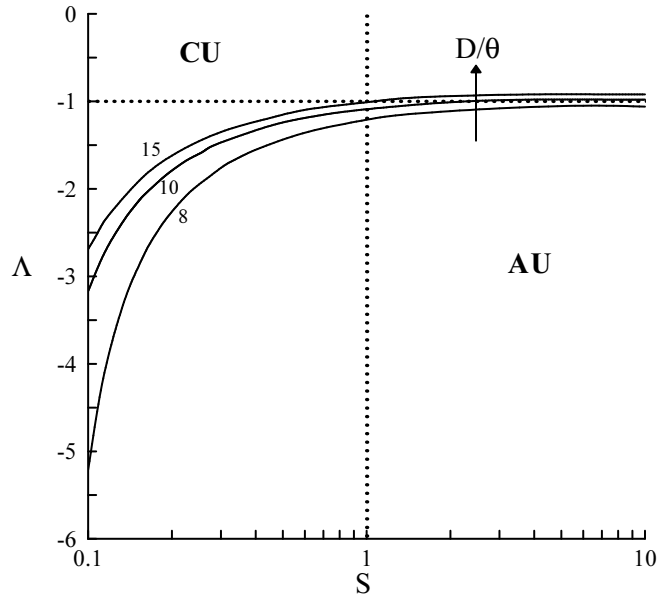

FIGURE 14. Boundary separating the regions of absolute (AU) and convective (CU) instability in the (S, Λ)-plane for $D/\theta = 8$, 10 and 15, at $M_\infty = 0$ and $Re_\infty = 2000$. For these values of the steepness parameter, the transition is led by the helical wake mode only (no crossover point in the domain).

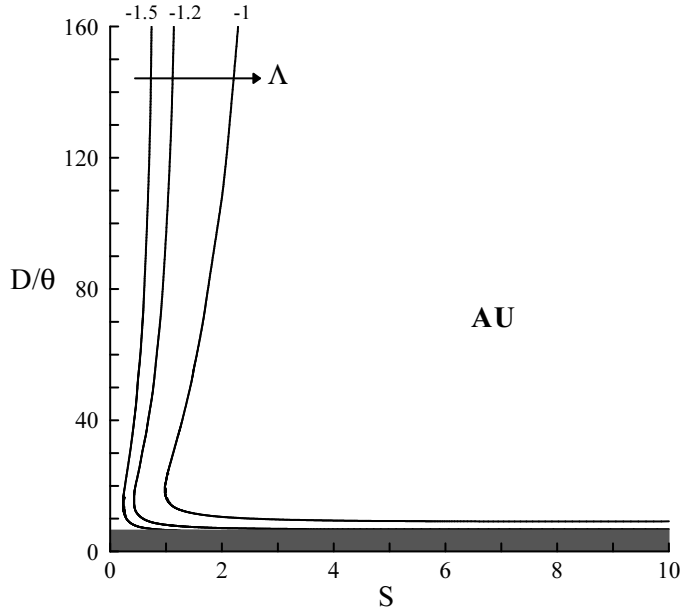

FIGURE 15. Absolutely unstable domains (AU) in the $(S, D/\theta)$-plane for three velocity ratios $\Lambda = -1$, -1.2 and -1.5, at $M_\infty = 0$ and $Re_\infty = 2000$. For these values of Λ, the transition is led by the helical wake mode only (no crossover point in the domain). The shaded area corresponds to $D/\theta < 6.5$, these values not being allowed for profiles defined by (2.6) – (2.7).

ratios S, and it results in a significant reduction of the absolutely unstable region. In particular, absolute instability requires counterflowing streams at $D/\theta = 8$, even for heavy wakes, since the critical velocity ratios are located in this case below $\Lambda = -1$ for all values of S.

The stability properties of the helical wake mode are further investigated by considering regions of absolute and convective instability in the $(S, D/\theta)$-plane for different values of Λ. Figure 15 presents the absolute instability boundaries obtained for $\Lambda = -1.5$, -1.2, and

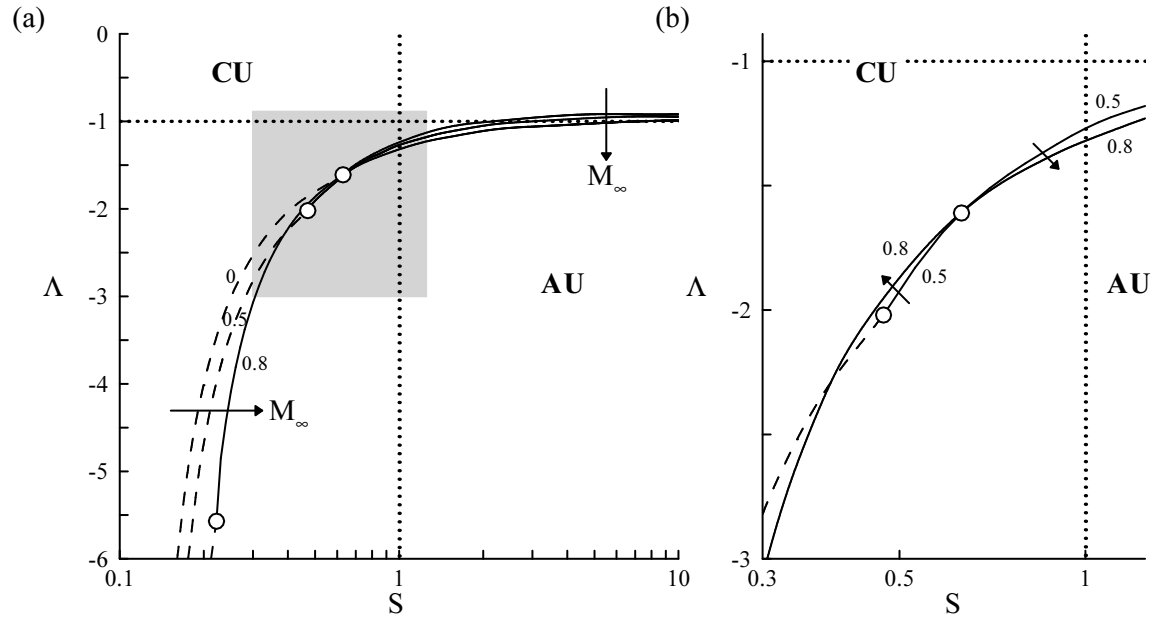

FIGURE 16. (*a*) Boundary separating the regions of absolute (AU) and convective (CU) instability and crossover points $(\circ)$ in the (S, Λ)-plane for the Mach numbers $M_\infty = 0$, 0.5 and 0.8, at $D/\theta = 120$ and $Re_\infty = 2000$ (– – –, SLM_0; ———, WM_1). (*b*) Enlargement of the shaded area of (*a*). The $M_\infty = 0$ curve has been removed for clarity.

-1, corresponding to counterflow rates of 20%, 9.1% and zero. Note that since velocity ratios below -1.61 are required for the axisymmetric shear-layer mode to be dominant (see figure 12), the transition to absolute instability is led by the helical wake mode for all the values of Λ presented in figure 15. In the absence of counterflow ($\Lambda \geqslant -1$), the lowest density ratio at which an absolute instability exists is $S = 0.982$, for $D/\theta = 19$. For each value of Λ, the critical density ratio for the helical wake mode increases slightly when D/θ varies from 30 to 160, a behaviour corresponding to the stabilizing effect discussed from figure 11. The trend is reversed when D/θ is decreased further below 15, as the critical density ratio increases significantly, illustrating the stabilizing effect shown in figure 14. For $\Lambda = -1$ (resp. $\Lambda = -1.2$), wakes with steepness parameters $D/\theta \lesssim 9$ (resp. $D/\theta \lesssim 7$) are found to be convectively unstable for all density ratios (part of the curves parallel to the S-axis in figure 15). For $\Lambda = -1.5$, absolute instability can be reached by increasing sufficiently the density ratio, even for the smallest steepness parameter $D/\theta = 6.5$ accessible through profiles (2.6). This means that for $\Lambda = -1.5$, the gaussian wake (associated to $D/\theta = 6.5$ and $N = 1$) is absolutely unstable for $S \geqslant 1.14$, whereas for $\Lambda = -1.2$ or larger, it is convectively unstable for all values of the density ratios.

4.3. *Effect of the free stream Mach number*

We consider now the effect of the Mach number on the stability properties of the flow. Our calculations show that the effect of compressibility is negligible for free-stream Mach numbers below 0.3, the variations of the critical parameters being less than 10%. Figure 16(*a*) presents the absolute instability boundaries in the (S, Λ)-plane for $D/\theta = 120$ and $M_\infty = 0, 0.5$ and 0.8. In the homogeneous case ($S = 1$), increasing the Mach number to high subsonic values is seen to weakly stabilize the helical wake mode, in agreement with the intuitive idea that compressibility slows down the upstream propagation of disturbances and therefore favors convective instability. A similar stabilizing effect is observed on the helical make mode when $S \gtrsim 0.65$, and for light wakes when the axisymmetric shear-layer mode is dominant. This stabilizing effect of compressibility on the shear-layer

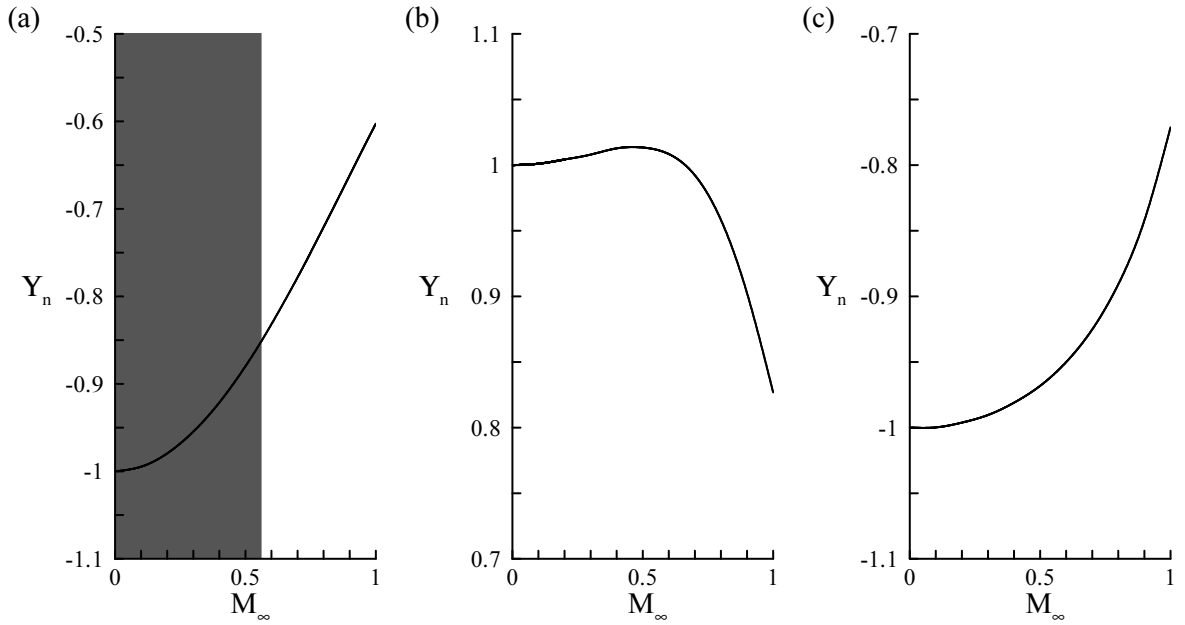

FIGURE 17. Effect of the Mach number on the normalized baroclinic factor Υ_n at the absolute instability threshold, for $D/\theta = 120$ and $Re_\infty = 2000$. (a) Helical wake mode for $S = 0.5$, valid only in the non-shaded area where the wake mode leads the absolute transition for this density ratio. In the shaded area are reported the values of Υ_n of the mode associated with the wake mode saddle point, followed by continuity. (b) Helical wake mode for $S = 2$ (for this value of S, the transition is led by this mode only). (c) Axisymmetric shear-layer mode for $S = 0.2$ (for this value of S, the transition is led by this mode only).

mode is consistent with the analysis of Pavithran & Redekopp (1989) on plane mixing layers. For $S \lesssim 0.65$, the helical wake mode is destabilized by an increase of the Mach number (solid lines in figure 16(b) when this mode is dominant), a behaviour in contrast with that of the axisymmetric jet column modes, for which convective instability is promoted by increasing the Mach number in the high subsonic regime, for all values of S (Monkewitz & Sohn 1988; Jendoubi & Strykowski 1994). We propose to interpret these different compressibility effects for light and heavy wakes as the result of a competition between the classical stabilizing effect due to the decrease in the pressure wave speed, and baroclinic effects discussed in § 4.1. Results are given in terms of the baroclinic factor Υ defined by (4.5), normalized by the magnitude of the baroclinic factor of the incompressible wake

$$\Upsilon_n(M_\infty, S, \Lambda, D/\theta, Re) = \frac{\Upsilon(M_\infty, S, \Lambda, D/\theta, Re)}{|\Upsilon(M_\infty = 0, S, \Lambda, D/\theta, Re)|}\,, \tag{4.6}$$

so that $\Upsilon_n(M_\infty = 0) = \pm 1$. Figure 17 shows the evolution of Υ_n as a function of the Mach number for wakes of different density ratios. The case of a moderately light wake of density ratio $S = 0.5$ is presented in figure 17(a), where the transition is led by the helical wake mode for $M_\infty \geqslant 0.63$. The increase of the negative baroclinic factor corresponds to a decrease of the stabilizing effect at this density ratio, i.e. to a destabilization. This suggests that the absolute instability triggered by an increase of the Mach number arises from a weakening of the stabilizing baroclinic torque. Figure 17(b) shows the case of a heavy wake of ratio $S = 2$, where the transition is led by the helical wake mode for all Mach numbers. The baroclinic torque remains positive and almost constant until $M_\infty \leqslant 0.5$ and then decreases rapidly, inducing a decrease of the destabilizing effect at this density ratio, i.e. a stabilization consistent with the effect observed in figure 16. The case of a very light wake of density ratio $S = 0.2$ is presented in figure 17(c), the

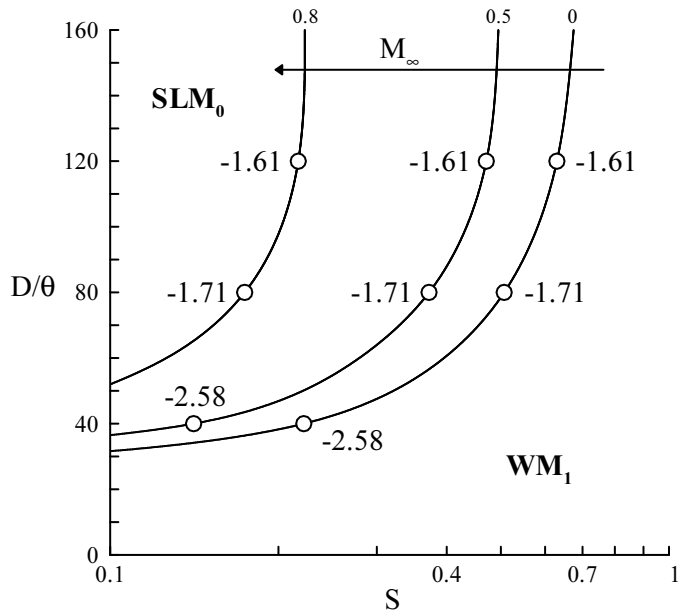

FIGURE 18. Crossover curves in the $(S, D/\theta)$-plane for three values of the Mach number, at $Re_\infty = 2000$. Curves separate domains where the transition to absolute instability is led, respectively, by the axisymmetric shear-layer mode (SLM_0) and the helical wake mode (WM_1). Open circles at $D/\theta = 120$ correspond to the crossover points of figure 16 and are plotted together with their corresponding velocity ratio Λ.

transition being led by the axisymmetric shear-layer mode for all Mach numbers. The results are similar to those obtained for the $S = 0.5$ wake, namely the baroclinic effect is destabilizing. Therefore, the global stabilizing effect observed in figure 16 for the shear-layer mode does not result from a variation of the baroclinic torque and should be blamed on the decrease in the disturbance wave speeds when the Mach number is increased.

As a result of the stabilizing effect of the Mach number on the axisymmetric shear-layer mode, and of its destabilizing effect on the helical wake mode for light wakes, the crossover point is displaced in the region of very low density ratios as M_∞ is increased (figure 16). The corresponding critical velocity ratio drops to very small values, illustrating the necessity of strong counterflows to achieve the transition to absolute instability at large M_∞ and small S. For instance, at $M_\infty = 0$, the crossover density ratio is $S = 0.625$ with a critical counterflow rate of 23.7% of the free-stream velocity ($\Lambda = -1.62$). At $M_\infty = 0.8$, the crossover density ratio is $S = 0.215$ with a critical counterflow rate of 70.1% ($\Lambda = -5.70$).

This tendency is visible in figure 18, which generalizes the results presented in figure 12 to Mach numbers $M_\infty = 0.5$ and 0.8. Values of the velocity ratio at the crossover point are reported for the same values of D/θ as in figure 12. Consistently with the results presented in figure 16, the helical wake mode ($m = 1$) is promoted as the dominant mode for high subsonic Mach numbers, this effect being more pronounced for large values of D/θ. For small values of D/θ, the helical wake mode leads the transition to absolute instability at all density ratios, a trend already documented for $M_\infty = 0$. Figure 19 presents the effect of the Mach number on the critical Strouhal number St and wavelength λ^0 at the absolute instability threshold for different values of the Mach number, at $D/\theta = 120$. The frequency of both modes are lowered at high subsonic Mach numbers, whereas the wavelength increases slightly. For the axisymmetric shear-layer mode, we hence find values of approximately $St \sim 1.8$ for $M_\infty = 0$ and ~ 1.5 for $M_\infty = 0.8$, with

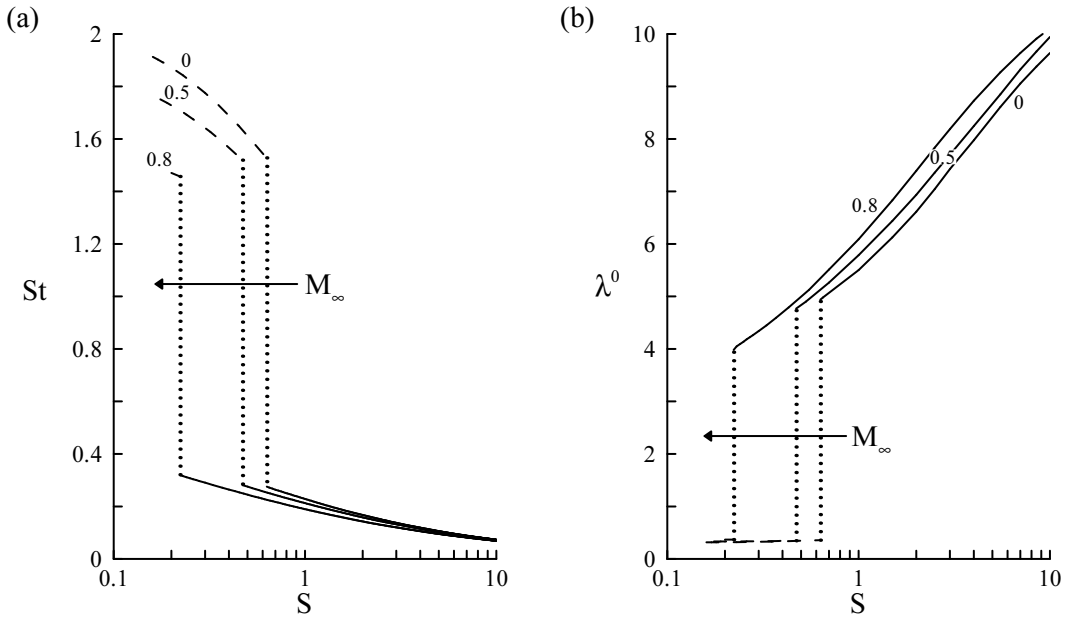

FIGURE 19. (*a*) Strouhal number St and (*b*) absolute wavelength λ^0 at the absolute instability threshold for Mach numbers $M_\infty = 0$, 0.5 and 0.8, *i.e.* along the curves $\Lambda(S)$ plotted in figure 16. $D/\theta = 120$ and $Re_\infty = 2000$ (− − −, SLM_0; ———, WM_1).

wavelengths of order 0.3 wake diameter. For the helical wake mode, we find Strouhal numbers $0.1 \leqslant St \leqslant 0.3$, with wavelengths varying between 4 and 10 wake diameters.

The properties of the helical wake mode are finally investigated by considering the combined effect of M_∞ and S in the particular configuration of zero centerline velocity ($\Lambda = -1$). The absolute instability boundaries in the (S, M_∞)-plane are presented in figure 20 for different values of D/θ. Since the axisymmetric shear-layer mode requires a counterflow to become absolutely unstable, the helical wake mode leads the transition for all the combinations of parameters examined here. For all values of the steepness parameter, the range of absolutely unstable density ratios is significantly reduced by increasing the Mach number. For instance, in the range of density ratios under consideration, the lowest steepness parameter at which an absolute instability exists is $D/\theta = 12$ for $M_\infty = 0.9$, and $D/\theta = 9$ for $M_\infty = 0$. Note that the region of absolute instability, quite limited for $D/\theta = 10$, extends dramatically when D/θ is increased to 20, and then shrinks again when D/θ is further increased from 20 to 160. This behaviour is associated to the non-trivial effect of D/θ described for $M_\infty = 0$ in § 4.2, both destabilizing and stabilizing effects being more pronounced as the Mach number increases. For instance, in the range of density ratios under investigation, no absolute instability occurs for Mach numbers above 0.615 at $D/\theta = 10$, and above 0.773 at $D/\theta = 160$.

5. Conclusion

The convective−absolute transition in axisymmetric wakes has been investigated for a fixed Reynolds number $Re_\infty = 2000$, in a parameter space including the velocity and density ratios, the steepness parameter and the free-stream Mach number. Depending on the parameter settings, i.e. to the flow regime, the transition to absolute instability is led either by a large-scale helical wake mode of azimuthal wavenumber $m = 1$, or by a small-scale axisymmetric shear-layer mode ($m = 0$). An increase of the density ratio or an increase of the velocity ratio promotes absolute instability, no matter which mode leads the transition. Varying the Mach number has a more complex effect. For very light

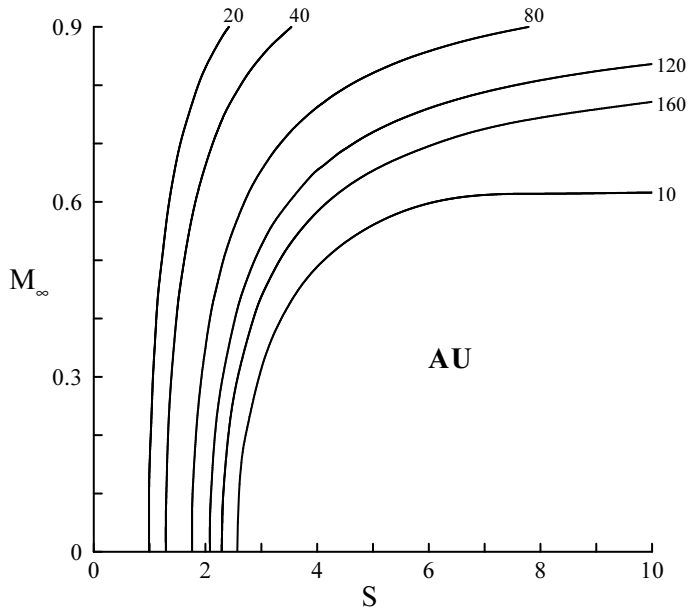

FIGURE 20. Absolutely unstable domains (AU) in the (S, M_∞)-plane as a function of D/θ, at $\Lambda = -1$ and $Re_\infty = 2000$. For this value of Λ, the transition is led by the helical wake mode only (no crossover point in the domain).

or heavy wakes, increasing the Mach number promotes convective instability, but for intermediate values of the density ratio, an increase of the Mach number promotes an absolute instability of the helical wake mode, a behaviour strikingly different from that documented for other shear flows. We show that this behaviour may be attributed to the effect of the baroclinic torque. The axisymmetric shear-layer mode is dominant only for low density ratios and high rates of counterflow on the wake axis (large negative velocity ratios). In all other cases, and in particular for small rates of coflow or counterflow more realistic of a real afterbody wake, the transition to absolute instability is led by the helical wake mode. The frequency of the helical wake mode at the absolute instability threshold is weakly dependent on the parameters, and is characterized by Strouhal numbers varying in the range $0.1 \leqslant St \leqslant 0.3$. These results give credence to the interpretation of the large-scale oscillation observed in the experimental studies of flows past spheres, disks and more complex axisymmetric afterbodies in terms of a non-linear global mode triggered by a local transition to absolute instability. In the whole range of parameters explored here, the azimuthal wavenumber and frequency selection is in qualitative agreement with such a mode made of a front located at the upstream boundary of the absolutely unstable region (separated or not from the body), and followed by a saturated wavetrain (Couairon & Chomaz 1999; Pier 2002). In that case, the front region is the wave-maker and imposes its azimuthal wavenumber and frequency to the entire flow.

Appendix A. Linearized equations of motion

The set of equations is presented for the eigenfunction (ρ', u', v', w', t').

$$(kW_b - \omega)\rho' + \left[d_r\rho_b + \rho_b\left(d_r + \frac{1}{r}\right)\right](-\mathrm{i}u') + m\frac{\rho_b}{r}v' + k\rho_b w' = 0 \qquad (\mathrm{A}\,1a)$$

$$-\frac{1}{\gamma M^2}\left(d_r T_b + T_b d_r\right)\rho' + (kW_b - \omega)\rho_b(-\mathrm{i}u') - \frac{1}{\gamma M^2}\left(d_r\rho_b + \rho_b d_r\right)t' =$$

$$\frac{-\mathrm{i}}{Re}\left[\left(\frac{4}{3}d_{rr}+\frac{4}{3r}d_r-\frac{4+3m^2+3k^2r^2}{3r^2}\right)(-\mathrm{i}u')+\frac{m}{3r}\left(d_r-\frac{7}{r}\right)v'+\frac{k}{3}d_rw'\right] \tag{A 1b}$$

$$\frac{mT_b}{\gamma M^2 r}\rho'+\rho(kW_b-\omega)v'+\frac{m\rho_b}{\gamma M^2 r}t' =$$
$$\frac{-\mathrm{i}}{Re}\left[-\frac{m}{3r}\left(d_r+\frac{7}{r}\right)(-\mathrm{i}u')+\left(d_{rr}+\frac{1}{r}d_r-\frac{3+4m^2+3k^2r^2}{3r^2}\right)v'-\frac{mk}{3r}w'\right] \tag{A 1c}$$

$$\frac{kT_b}{\gamma M^2}\rho'+\rho_b d_rW_b(-\mathrm{i}u')+\rho(kW_b-\omega)w'+\frac{k\rho_b}{\gamma M^2}t' =$$
$$\frac{-\mathrm{i}}{Re}\left[-\frac{k}{3}\left(d_r+\frac{1}{r}\right)(-\mathrm{i}u')-\frac{mk}{3r}v'+\left(d_{rr}+\frac{1}{r}d_r-\frac{3m^2+4k^2r^2}{3r^2}\right)w'\right] \tag{A 1d}$$

$$\rho_b\frac{dT_b}{dr}(-\mathrm{i}u')+(\gamma-1)P_b\left[\left(d_r+\frac{1}{r}\right)(-\mathrm{i}u')+\frac{m}{r}v'+kw'\right]+\rho(kW_b-\omega)t' =$$
$$\frac{-\mathrm{i}}{Re}\left[-2\gamma(\gamma-1)M^2\left(kd_rW_b(-\mathrm{i}u')-d_rW_bd_rw'\right)+\frac{\gamma}{Pr}\left(d_{rr}+\frac{1}{r}d_r-\frac{m^2+k^2r^2}{r^2}\right)t'\right] \tag{A 1e}$$

where d_r and d_{rr} denote the r derivatives of first and second order. The pressure perturbation p' is built from ρ' and t' by the linearized ideal gas relation

$$p'=T\rho'+\rho t'\,. \tag{A 2}$$

Appendix B. Baroclinic effect and forced equations of motion

For clarity, we detail here the formalism only in the case of the compressible inviscid problem. However, the method is identical for the viscous equations, although additional non-homogeneous terms arise due to the presence of dissipation. Note that non-homogenous terms exist in the continuity and energy equations, but our calculations strongly suggest that their effect is negligible compared to that of the baroclinic torque.

In the presence of volumic source terms S_r, S_θ and S_z, the momentum equations can be written as

$$\partial_t u' = -W_b\partial_z u'-\frac{1}{\gamma M_\infty^2}\frac{1}{\rho_b}\partial_r p'+S_r \tag{B 1a}$$

$$\partial_t v' = -W_b\partial_z v'-\frac{1}{\gamma M_\infty^2}\frac{1}{\rho_b}\partial_\theta p'+S_\theta \tag{B 1b}$$

$$\partial_t w' = -W_b\partial_z w'-\frac{1}{\gamma M_\infty^2}\frac{1}{\rho_b}\partial_z p'+S_z\,. \tag{B 1c}$$

The vorticity perturbation $\boldsymbol{\Omega}=\nabla\times\mathbf{u}$ evolves as

$$\partial_t\Omega_r' = -W_b\left(\frac{1}{r}\partial^2_{\theta z}w'-\partial^2_{zz}v'\right)+\frac{1}{r}\partial_\theta S_z-\partial_z S_\theta \tag{B 2a}$$

$$\partial_t\Omega_\theta' = -W_b\left(\partial^2_{zz}u'-\partial^2_{rz}w'\right)+d_rW_b\partial_z w'-\frac{1}{\gamma M_\infty^2}\frac{\partial_r\rho_b}{\rho_b^2}\partial_z p'+\partial_z S_r-\partial_r S_z \tag{B 2b}$$

$$\partial_t\Omega_z' = -W_b\left(\partial^2_{rz}v'-\frac{1}{r}\partial^2_{\theta z}u'\right)-d_rW_b\partial_z v'$$

$$+\frac{1}{\gamma M_\infty^2}\frac{\partial_r \rho_b}{\rho_b^2}\frac{1}{r}\partial_\theta p' + \partial_r S_\theta - \frac{1}{r}\partial_\theta S_r \qquad (\mathrm{B}\,2c)$$

where we recognize the expression of the baroclinic torque $\mathbf{\Gamma} = \boldsymbol{\nabla}\rho_b \times \boldsymbol{\nabla} p'/\rho_b^2$.

In order to eliminate the effect of the baroclinic torque, the source terms are selected so as to satisfy

$$\frac{1}{r}\partial_\theta S_z - \partial_z S_\theta = 0 \qquad (\mathrm{B}\,3a)$$

$$\partial_z S_r - \partial_r S_z = \frac{1}{\gamma M_\infty^2}\frac{\partial_r \rho_b}{\rho_b^2}\partial_z p' = \Gamma_\theta \qquad (\mathrm{B}\,3b)$$

$$\partial_r S_\theta - \frac{1}{r}\partial_\theta S_r = -\frac{1}{\gamma M_\infty^2}\frac{\partial_r \rho_b}{\rho_b^2}\frac{1}{r}\partial_\theta p' = \Gamma_z\,. \qquad (\mathrm{B}\,3c)$$

All source terms are considered as additional variables of the generalized eigenvalue problem. The modified dispersion relation is therefore constructed from the unforced continuity and energy equations, the forced momentum equations (B 1) and the source equations (B 3).

REFERENCES

Achenbach, E. 1974 Vortex shedding from spheres. *J. Fluid Mech.* **62**, 209–221.

Batchelor, G.K. & Gill, A.E. 1962 Analysis of the stability of axisymmetric jets. *J. Fluid Mech.* **14**, 529–551.

Berger, E., Scholz, D. & Schumm, M. 1990 Coherent vortex structures in the wake of a sphere and a circular disk at rest and under forced vibrations. *J. Fluids Struct.* **4**, 231–257.

Bers, A. 1975 *Plasma physics*, chap. Linear waves and instabilities, pp. 117–215. Gordon & Breach, edited by C. De Witt and J. Peyraud.

Briggs, R.J. 1964 *Electron stream interaction with plasmas*. M.I.T. Press.

Carroll, L. 1872 *Through the looking-glass: and what Alice found there*. MacMillan Press.

Chomaz, J.-M. 1992 Absolute and convective instability in non linear systems. *Phys. Rev. Lett.* **69**, 1931–1934.

Chomaz, J.-M. 2005 Global instabilities in spatially developing flows: Non-normality and nonlinearity. *Annu. Rev. Fluid. Mech.* **37**, 357–392.

Couairon, A. & Chomaz, J.-M. 1997 Absolute and convective instabilities, front velocities and global modes in nonlinear systems. *Physica D* **108**, 236–276.

Couairon, A. & Chomaz, J.-M. 1999 Fully nonlinear global modes in slowly varying flows. *Phys. Fluids* **11** (12), 3688–3703.

Dee, G. & Langer, J. 1983 Propagating pattern selection. *Phys. Rev. Lett.* **50**, 383–386.

Deissler, R.J. 1987 The convective nature of instability in plane poiseuille flow. *Phys. Fluids* **30** (8), 2303–2305.

Deprés, D., Reijasse, P. & Dussauge, J.-P. 2004 Analysis of unsteadiness in afterbody transonic flows. *AIAA Journal* **42** (12), 2541–2550.

Drazin, P. & Reid, W. 1981 *Hydrodynamic stability*. Cambridge University Press.

Flodrops, J.-P. & Desse, J.-M. 1985 Sillage d'un culot axisymétrique. *Tech. Rep.* 85/19. Institut de Mécanique des Fluides de Lille, France.

Fuchs, H.V., Mercker, E. & Michel, U. 1979 Large-scale coherent structures in the wake of axisymmetric bodies. *J. Fluid Mech.* **93**, 185–207.

Gallaire, F. & Chomaz, J.-M. 2003 Mode selection in swirling jet experiments: a linear stability analysis. *J. Fluid Mech.* **494**, 223–253.

Gallaire, F., Ruith, M., Meiburg, E., Chomaz, J.-M. & Huerre, P. 2006 Spiral vortex breakdown as a global mode. *J. Fluid Mech.* **549**, 71–80.

Healey, J.J. 2005 Long-wave theory for a new convective instability with exponential growth normal to the wall. *Phil. Trans. R. Soc. Lond. A* **363**, 1119–1130.

Healey, J.J. 2006 A new convective instability of the rotating-disk boundary layer with growth normal to the disk. *J. Fluid Mech.* **560**, 279–310.

Huerre, P. & Monkewitz, P.A. 1985 Absolute and convective instabilies in free shear layers. *J. Fluid Mech.* **159**, 151–168.

Huerre, P. & Rossi, M. 1998 *Hydrodynamics and Nonlinear Instabilities*, chap. Hydrodynamic instabilities in open flows, pp. 81–294. Cambridge University Press, edited by C. Godrèche and P. Manneville.

Jendoubi, S. & Strykowski, P.J. 1994 Absolute and convective instability of axisymmetric jets with external flow. *Phys. Fluids* **6** (9), 3000–3009.

Juniper, M. 2006 The effect of confinement on the stability of two-dimensional shear flows. *J. Fluid Mech.* **565**, 171–195.

Kim, H.J. & Durbin, P.A. 1988 Observations of the frequencies in a sphere wake and of drag increase by acoustic excitation. *Phys. Fluids* **31** (11), 3260–3265.

Koch, W. 1985 Local instability characteristics and frequency determination of self-excited wake flows. *J. Sound Vib.* **99**, 23–83.

Lesshafft, L. & Huerre, P. 2007 Linear impulse response in hot round jets. *Phys. Fluids* **19** (2), 024102 1–11.

Lesshafft, L., Huerre, P., Sagaut, P. & Terracol, M. 2006 Nonlinear global modes in hot jets. *J. Fluid Mech.* **554**, 393–409.

Miles, J.W. 1958 On the disturbed motion of a plane vortex sheet. *J. Fluid Mech.* **4**, 538–552.

Monkewitz, P.A. 1988 A note on vortex shedding from axisymmetric bluff bodies. *J. Fluid Mech.* **192**, 561–575.

Monkewitz, P.A., Bechert, D.W., Barsikow, B. & Lehmann, B. 1990 Self-excited oscillations and mixing in a heated round jet. *J. Fluid Mech.* **213**, 611–639.

Monkewitz, P.A. & Nguyen, L.N. 1987 Absolute instability in the near-wake of two-dimensional bluff-bodies. *J. Fluids Struct.* **1**, 165–184.

Monkewitz, P.A. & Sohn, K.D. 1988 Absolute instability in hot jets. *AIAA Journal* **26** (8), 911–916.

Nichols, J.W. & Schmid, P.J. andRiley, J.J. 2007 Self-sustained oscillations in variable-density round jets. *J. Fluid Mech.* **582**, 341–376.

Pavithran, S. & Redekopp, L.G. 1989 The absolute-convective transition in subsonic mixing layers. *Phys. Fluids A* **1** (10), 1736–1739.

Pier, B. 2002 On the frequency selection of finite-amplitude vortex shedding in the cylinder wake. *J. Fluid Mech.* **458**, 407–417.

Pier, B. & Huerre, P. 2001 Nonlinear self-sustained structures and fronts in spatially developing wake flows. *J. Fluid Mech.* **435**, 145–174.

Pier, B., Huerre, P. & Chomaz, J.-M. 2001 Bifurcation to fully nonlinear synchronized structures in slowly varying media. *Physica D* **148**, 49–96.

van Saarloos, W. 1987 Dynamical velocity selection: marginal stability. *Phys. Rev. Lett.* **58**, 2571–2574.

van Saarloos, W. 2003 Front propagation into unstable states. *Phys. Rep.* **386**, 29–222.

Schlichting, H. 1978 *Boundary layer theory*, 7th edn. McGraw-Hill.

Sevilla, A. & Martínez-Bazàn, C. 2004 Vortex shedding in high reynolds number axisymmetric bluff-body wakes: Local linear instability and global bleed control. *Phys. Fluids* **16** (9), 3460–3469.

Soteriou, M.C. & Ghoniem, A.F. 1995 Effects of the free-stream density ratio on free and forced spatially developing shear layers. *Phys. Fluids* **7** (8), 2036–2051.

Tobias, S.M., Proctor, M.R.E. & Knobloch, E. 1997 The role of absolute instability in the solar dynamo. *Astron. Astrophys.* **318**, 55–58.

Tobias, S.M., Proctor, M.R.E. & Knobloch, E. 1998 Convective and absolute instabilities of fluid flows in finite geometry. *Physica D* **113**, 4–72.

Yu, M.H. & Monkewitz, P.A. 1990 The effect of non uniform density on the absolute instability of two-dimensional inertial jets and wakes. *Phys. Fluids A* **2** (7), 1175–1181.

Elephant modes and low frequency unsteadiness in a high Reynolds number, transonic afterbody wake

Philippe Meliga* and Denis Sipp
ONERA/DAFE, 8 rue des Vertugadins, 92190 Meudon, France

Jean-Marc Chomaz
LadHyX, CNRS-Ecole Polytechnique, 91128 Palaiseau, France

(Dated: June 27, 2008)

Experiments and Large Eddy numerical Simulation (LES) of a fully turbulent afterbody flow in the high subsonic regime, typical of that developing in the wake of a space launcher, exhibit a large-scale low frequency oscillation of the wake. In the present paper, we investigate to what extent the existence of the synchronized oscillations can be predicted, at the high Reynolds numbers prevailing in this class of flows, by a local stability analysis of the mean flow, as measured in experiments or computed in numerical simulations. This analysis shows the presence of a pocket of absolute instability in the near wake, slightly detached from the body. The global frequency is strikingly well predicted by the absolute frequency at the upstream station of marginal absolute instability, this frequency selection being in agreement with the theory of nonlinear global modes. This result strongly suggests that a so-called elephant mode is responsible for the intense oscillations observed in the lee of space launcher configurations.

I. INTRODUCTION

Experimental and numerical studies have shown that wake flows past axisymmetric bodies, such as spheres[1], disks[2,3] or axisymmetric blunt based bodies modeling an ideal rocket shape[4], are dominated by an instability of helical modes of azimuthal wavenumbers $m = \pm 1$, resulting in the low frequency shedding of large-scale coherent structures. The use of local stability to analyze such self-sustained synchronized oscillations in free shear flows[5] at low Reynolds numbers suggests that they are linked to the existence of a region of local absolute instability in the near wake.[6,7]

Recent studies have considered the fully nonlinear regime associated with the existence of a pocket of absolute instability when the streamwise variations of the base flow are slow enough to apply the WKBJ theory of slowly developing flows. Chomaz[8], Couairon and Chomaz[9], Tobias et *al.*[10], Pier et *al.*[11], have analyzed the solutions of model equations in semi-infinite and infinite domains and discussed the connection between nonlinear global modes and front dynamics that characterize the propagation of a saturated instability wave into a quiescent region (see Chomaz[12] for a review). If absolute instability arises beyond a specific downstream position z^{ca}, the nonlinear global mode, the so-called elephant mode, consists of a front pinned at the position z^{ca}. The front acts as the *wavemaker* and separates an upstream region where perturbations are evanescent, from a finite-amplitude wavetrain downstream. The global frequency is then given by the linear absolute frequency at the transition station z^{ca}, i.e. $\omega_G = \omega_r^0(z^{ca})$, and the spatial growth rate at the front location is given by the absolute wavenumber $-k_i^G = -k_i^0(z^{ca})$. In the case of an absolutely unstable inlet condition, the same frequency selection criterion remains valid only in the vicinity of the global instability threshold, whereas above the threshold, the front deforms to accommodate the inlet condition and the global frequency shifts from the absolute value.

Many of the results pertaining to the model equations have been shown to hold also in real flow situations, despite the fact that the slow streamwise variation assumption is not respected. In the case of the wake developing past a circular cylinder, the von Kàrmàn vortex street presents a front located at z^{ca} and its frequency, as observed in direct numerical simulations, matches the absolute frequency $\omega_r^0(z^{ca})$ within 10 % accuracy over the range of Reynolds numbers $100 \leq Re \leq 180$.[13] Since then, several successful analyses have been been carried out in the context of swirling jets[14], hot round jets[15], spiral vortex breakdown[16], or inter-disk flow[17], but all these cases pertain to moderate Reynolds numbers.

Recently, the stability analysis of compressible non-homogeneous model wakes[18] has shown that the transition to absolute instability is led

essentially by a low frequency, large-scale mode of azimuthal wavenumber $m = 1$. These results have given credit to the interpretation of the large-scale oscillation observed in the wake of axisymmetric bodies in terms of a nonlinear global mode triggered by a local transition to absolute instability of this helical *wake* mode, since its azimuthal wavenumber and absolute frequency match the observations. But agreement is only qualitative and can be fortuitous, since at the transition point, the model profiles are far from representing the instantaneous or mean velocity profiles. Therefore, the aim of the present study is to analyze the stability of realistic velocity profiles, and so to investigate to what extent the dynamics of an afterbody flow, computed via a high resolution Large Eddy Simulation (LES), in the fully turbulent and compressible regimes, may be interpreted using the local stability theory. In the context of such 'industrial' applications, the steady axisymmetric base flow, i.e. the flow that would be naturally observed if all perturbations were damped, is not accessible and Arclength continuation associated with Newton methods[19], widely used at low Reynolds numbers to compute the base flow beyond the threshold of instability, cannot be pursued to such large Reynolds numbers. Only the mean flow, obtained by time and azimuth average, can be used to assess the stability properties, keeping in mind that this mean flow is not a solution of the steady axisymmetric Navier-Stokes equations.

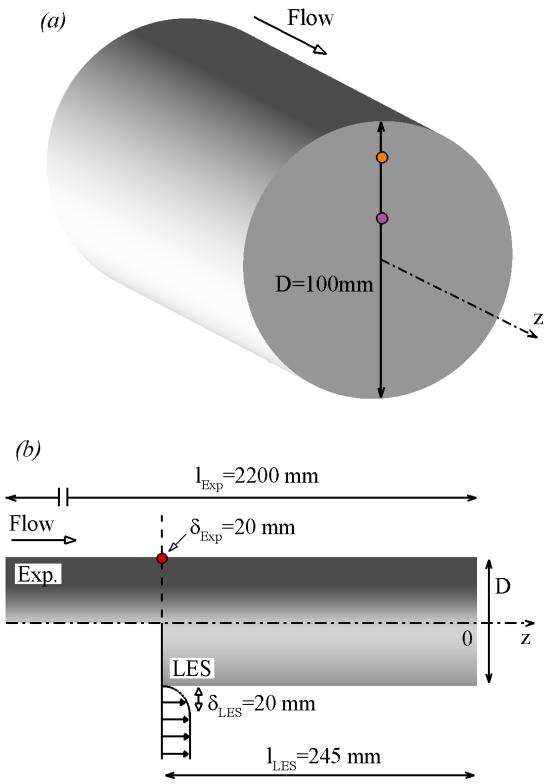

FIG. 1: Schematic of the axisymmetric afterbody model. (a) Three-dimensional view: the orange circle is located 35 mm away from the revolution axis and corresponds to the experimental power spectral density (PSD) shown in Fig. 2(a). The purple circle is located 14 mm away from the revolution axis and corresponds to the numerical PSD shown in Fig. 2(b). (b) Side view: the upper half shows the experimental setup with the upstream forebody of length 2.2 m. The thickness of the turbulent boundary-layer was measured 245 mm upstream from the base (red circle). The lower half shows the numerical modelisation used for the LES simulation.

II. UNSTEADY DYNAMICS AND MEAN FLOW

The afterbody retained for this numerical study is taken from experiments carried out in ONERA's S3Ch wind tunnel[20], and was originally designed to model the first stage of a space launcher vehicle. The general configuration, shown in Fig. 1(a), is a cylindrical body of diameter $D = 100$ mm. The flow is subsonic, turbulent, of free-stream velocity $W_\infty = 235$ m/s, the total pressure and temperature being respectively of $p_i = 1.01 \times 10^5$ Pa and $T_i = 310$ K. In the following, the diameter D and the free-stream quantities are used as reference scales, leading to a Mach number of 0.7 and a Reynolds number of 1.2×10^6. The wind tunnel configuration is detailed in the upper half of Fig. 1(b): a turbulent boundary-layer develops on an upstream forebody of length 2.2 m. Its nondimensional thickness was measured to be $\delta = 0.2$ at the nondimensional upstream position $z = -2.45$, identified by the red circle in Fig. 1(b). Fig. 2(a) shows the power spectral density of wall-pressure fluctuations G, measured experimentally 35 mm away from the axis (orange circle in Fig. 1(a)), plotted as $St.G(St)$ in log/linear axes, where St is the Strouhal number defined as $St = fD/W_\infty$, so that the energy contained in a peak is given by the area below that peak. The spectrum is the average of 64 overlapping subtime intervals, the nondimensional frequency resolution being of 0.0085. In this fully turbulent regime, small-scales are energetic and Fig. 2(a) shows a broad high frequency energy spectrum. We note the well defined energetic peak at $St = 0.20$, corresponding to a low frequency oscillation. Similar results have also been reported in Ref. [21].

A Large Eddy Simulation (LES) of this configuration has been carried out using the FLU3M

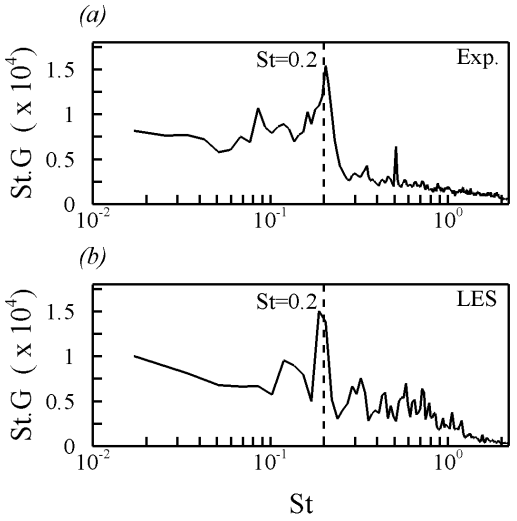

FIG. 2: Power spectral density (PSD) of the wall pressure fluctuations at the base. (a) Experimental measurements. (b) LES simulation.

code developed by ONERA, which solves the governing compressible Navier-Stokes equations on multiblock structured grids. Details, including time and space discretization and turbulence modelling, can be found in Ref. [22], where the agreement between numerical results and experimental data is assessed, validating the use of the LES solver. The retained configuration is shown in the upper half of Fig. 1: an inlet condition directly injects at the nondimensional upstream position $z = -2.45$ a turbulent boundary-layer around the cylinder shaped body, whose nondimensional thickness $\delta = 0.2$ corresponds to that measured in the experiments. Turbulence is forced by superimposing random fluctuations to this leading-order inlet condition. It was found that this inflow condition has little influence on the numerical results. Fig. 2(b) shows the power spectral density of the wall pressure fluctuations obtained from the numerical simulation, 14 mm away from the axis (purple circle in Fig. 1(a)). The total duration of the numerical simulation is about 20 ms, corresponding to $\sim$ 10 low frequency cycles. The spectrum presented in Fig. 2 is obtained by averaging 15 overlapping samples, the frequency resolution being of 0.017. Although the numerical simulation gives access only to short time series, we obtain a good agreement between both spectra, in particular, we retrieve a well defined energetic peak at $St = 0.20$, corresponding to the experimentally observed large-scale oscillation. Note that the high frequencies are more energetic in the LES calculation, this being probably due to the small discrepancy in the location of the experimental and numerical measurements.

In the following, we use cylindrical coordinates (r, θ, z) with origin taken at the center of the base. ρ is the density, p the pressure, T the temperature, and $\boldsymbol{U} = (U, V, W)^T$ the three-dimensional velocity field with U, V and W its radial, azimuthal and streamwise components. The fluctuating non-axisymmetric three-dimensional field has been averaged in time and azimuth on the fly, during the calculation. The resulting mean flow $\overline{\boldsymbol{Q}} = (\overline{\rho}, \overline{U}, \overline{V} = 0, \overline{W}, \overline{T}, \overline{p})^T$ is therefore steady and axisymmetric. Fig. 3(a) shows the mean axial velocity component: the classical topology of wake flows is retrieved, with a recirculation region of length ~ 1.33 developing in the wake of the afterbody, and negative values of axial velocity reaching approximately 30 % of the freestream velocity. Fig. 3(b) depicts the streamwise evolution of the velocity ratio $\Lambda(z) = (\overline{W}_c(z) - \overline{W}_\infty)/(\overline{W}_c(z) + \overline{W}_\infty)$ and of the steepness parameter $D/\theta(z)$, where θ is the momentum thickness defined as

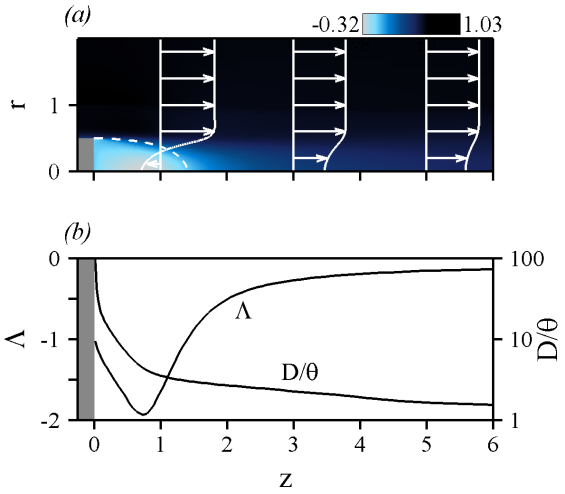

FIG. 3: LES mean flow obtained by time and azimuth average. (a) Axial velocity field. The dashed line stands for the edge of the recirculating bubble, marked by the streamline linking the separation point to the stagnation point on the axis. The axial velocity profiles $\overline{W}(r)$ are superimposed for three streamwise locations ($z = 1$, 3 and 5). (b) Streamwise evolution of the velocity ratio $\Lambda(z)$ and of the steepness parameter $D/\theta(z)$.

$$\theta(z) = \int_0^\infty \frac{\overline{W}(r,z) - \overline{W}_c(z)}{\overline{W}_\infty - \overline{W}_c(z)} \times \frac{\overline{W}_\infty - \overline{W}(r,z)}{\overline{W}_\infty - \overline{W}_c(z)} \mathrm{d}r \tag{1}$$

where subscripts c and ∞ refer to the centerline and to the free-stream quantities, respectively. The velocity ratio gets close to $\Lambda = -2$ in the recirculating bubble, whereas the steepness parameter decays rapidly in the near-wake and more slowly in the far-wake, indicating that

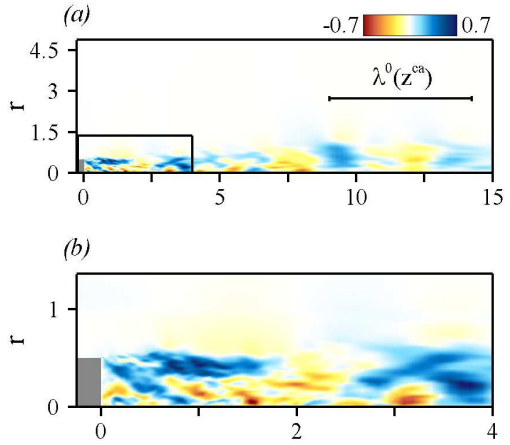

FIG. 4: (a) Instantaneous spatial structure of the $m = 1$ axial velocity coefficient $Re(W_1)$ extracted from the LES calculations. (b) Close-up on the near wake area depicted on Fig. (a)

the shear-layer thickens progressively as the flow develops. Note that the density ratio defined as $S(z) = \overline{\rho}_c(z)/\overline{\rho}_\infty$ departs little from unity (not shown here).

An instantaneous velocity field $\boldsymbol{U}(r, \theta, z)$ is decomposed into the azimuthal Fourier series

$$\boldsymbol{U}(r, \theta, z) = \sum_{m=-\infty}^{\infty} \boldsymbol{U}_m(r, z) e^{im\theta} . \qquad (2)$$

The real part of the axial velocity coefficient $Re(W_1)$ of the $m = 1$ component is presented in Fig. 4(a). The large-scale structure is visible downstream as an alternation of blue and red hues. Though, it is strongly modulated by a sea of small-scale turbulence close to the body, where the colored strips are blurred, as seen in Fig. 4(b).

III. LOCAL STABILITY

The cross-stream and streamwise directions are both inhomogeneous directions for the mean flow, i.e. $\overline{\boldsymbol{Q}}(r, z)$. At this point, we make the classical weakly nonparallel approximation, and consider the stability of the parallel flow, generated by neglecting the cross-stream velocity and extending to infinity the streamwise velocity profiles.[23] Disturbances $\boldsymbol{q}' = (\rho', \boldsymbol{u}', p', t')^T$ to the parallel flow are chosen as normal modes $q'(r)e^{i(kz+m\theta-\omega t)}$ characterized by the complex axial wavenumber $k = k_r + ik_i$, the complex pulsation $\omega = \omega_r + i\omega_i$, ω_i and $-k_i$ being respectively the temporal and spatial growth rates, and m the azimuthal wavenumber. $\boldsymbol{q}'$ is the solution of the classical generalized eigenvalue problem for either k or ω. This eigenvalue problem is solved using a Chebyshev collocation method, as discussed in Ref. [18]. The local mean flow velocity, temperature and density profiles, measured on the mesh of the LES simulation, are first interpolated on the collocation points of the stability solver using cubic spline interpolation. Complex pairs (k^0, ω^0) corresponding to modes of zero group velocity (i.e. $\partial\omega/\partial k = 0$) are then computed by the iterative technique described in Ref. [18]. For all streamwise positions, we find

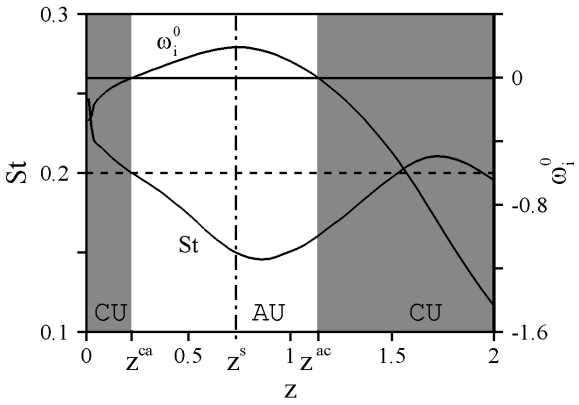

FIG. 5: Streamwise evolution of the Strouhal number St and of the absolute growth rate ω_i^0 obtained from the LES profiles. The solid horizontal lines represents the threshold of marginal absolute instability $\omega_i^0 = 0$. The dashed horizontal line marks the global frequency of the observed large-scale oscillations $St = 0.20$. The shaded areas correspond to convectively unstable domains. The dash-dotted line indicates the locus of the saddle point predicted by the linear global mode theory, that turns out to be nearly real in the present case.

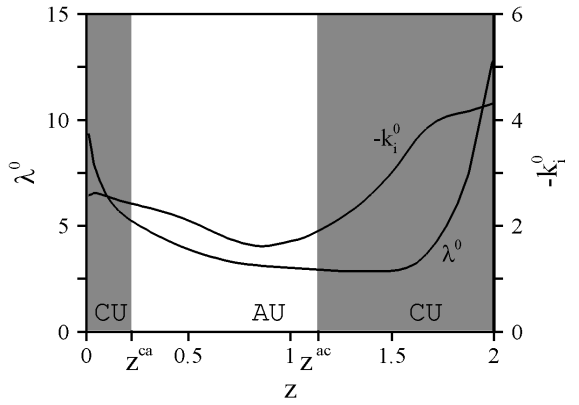

FIG. 6: Streamwise evolution of the absolute wavelength λ^0 and of the absolute spatial growth rate $-k_i^0$. The shaded areas correspond to convectively unstable domains.

that the transition to absolute instability is led by a large-scale $m = 1$ mode. This is consistent with the results presented in Ref. [18], in which the absolute instability has been shown to be led

by the large-scale $m = 1$ *wake* mode for velocity ratios similar to that of the present LES velocity profiles. The streamwise variations of the Strouhal number based on the absolute frequency $St = \omega_r^0/2\pi$ and that of the absolute temporal growth rate ω_i^0 are presented in Fig. 5. The solid and dashed horizontal lines stand for the threshold of marginal absolute instability $\omega_i^0 = 0$ and for the global frequency of the observed large-scale oscillations $St = 0.20$, respectively. The variations of the absolute wavelength $\lambda^0 = 2\pi/k_r^0$ and of the absolute spatial growth rate $-k_i^0$ are shown in Fig. 6. The mean flow is convectively unstable in an upstream region extending from the base to $z^{ca} = 0.23$. Owing to the high rates of reverse flow at the centerline, absolute instability prevails in the domain $z^{ca} < z < z^{ac} = 1.14$. Downstream of z^{ac}, the thickening of the shear-layer and the decrease in magnitude of the counterflow induce a decrease of ω_i^0 to negative values, and thus the mean flow is convectively unstable. The observed global frequency $St = 0.20$ is predicted with excellent accuracy, by the absolute frequency $\omega_r^0(z^{ca}) = 1.25$ corresponding to the same frequency $St = 0.20$ than that evidenced in the experimental and numerical spectra. The absolute wavelength and spatial growth rate at the transition station are $\lambda^0(z^{ca}) = 5.21$ and $k_i^0(z^{ca}) = -2.41$ respectively. The absolute wavelength $\lambda^0(z^{ca})$ is shown in Fig. 4(a), and compares favorably with the spatial distribution of the large-scale $m = 1$ component. A more precise measure of the spatial wavelength associated to the $St = 0.2$ mode is presently not accessible since it would require the storage and processing of a time series of three-dimensional flow fields, that would be far too glutton with the available computer resources. For the same reason, the spatial envelop of the $St = 0.2$ oscillation cannot be retrieved from the numerics and comparison of the front location and slope as in the studies of Gallaire et *al.*[16] or Lesshafft et *al.*[15] is not possible.

IV. DISCUSSION

This study shows the existence of a pocket of absolute instability of the mean flow in the near wake of the afterbody, detached from the base. Although the large-scale contribution is partially overwhelmed by the small-scale turbulence at the high Reynolds number under consideration, the global frequency is well predicted by the absolute frequency at the upstream station of marginal absolute instability, which is located at the origin of the growing part of the $m = 1$ fluctuations. These results agree with the theory of nonlinear global modes, and make probable that a so-called elephant mode develops in the wake of the afterbody and is responsible for the large-scale synchronized oscillations.

In contrast, previous studies on the cylinder wake[13,23,24] have shown that up to the large Reynolds number $Re = 4600$, the global frequency ω_G is well predicted by the linear stability theory of slowly varying flows, also applied to the mean flow. In that case, the frequency ω_G is given by the saddle-point condition

$$\omega_G = \omega^0(z^s)\,, \qquad \frac{\partial \omega^0}{\partial z}(z^s) = 0. \qquad (3)$$

Since derivatives of $\omega^0(z)$ are known only along the real z-axis, the location of the saddle point z^s is found through the use of the Cauchy-Riemann equations and analytic continuation of $\omega^0(z)$ in the complex z-plane.[25] Applying this linear global mode prediction to the present case, we obtain a saddle point at $z^s = 0.735 - 0.022\mathrm{i}$, nearly on the real z axis, close to the position of the maximum absolute growth rate (see Fig. 5), associated with a Strouhal number $St = 0.15$, different from that found in the experimental and numerical spectra. We interpret this result in the following manner: in the weakly nonlinear approximation, Sipp & Lebedev[26] have shown that in the case of the cylinder wake, resonance with the harmonics is weak, i.e. the leading-order nonlinear effects are restricted to base flow modifications. In this particular case, the mean flow is then approximately marginally stable and the global frequency predicted by the linear stability analysis of the mean flow approximates well the observed frequency, which explains the success of the saddle point condition (3). Though, this is no more true if resonance occurs with the harmonics of the global mode. In that far more generic case, the linear stability analysis of the mean flow fails, i.e. the mean flow is no more marginally stable, and its frequency differs from the observed one. Fig. 5 shows that the saddle point z^s is associated with a large growth rate $\omega_i^0(z^s) = 0.19$. This result indicates that the mean flow is presently strongly linearly unstable, and suggests that this configuration exhibits strong resonance with the harmonics of the global mode. The elephant mode theory, which predicts with amazing precision the observed frequency, does not suffer similar restrictions, since harmonics forcing is at work in the saturated wave region downstream of the front, so that departure from criticality can be arbitrary. It has been derived assuming only the flow to be weakly nonparallel, in order to use the WKBJ approximation.

The validity of this slowly varying approximation may be questioned, owing to the streamwise development of the mean flow. This can be done

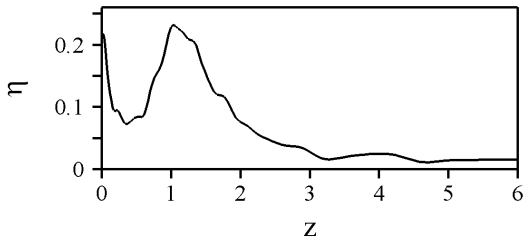

FIG. 7: Streamwise evolution of the parameter η measuring the nonparallelism of the spatially developing LES mean flow.

by considering the parameter η measuring the nonparallism of the mean flow, defined as the ratio

$$\eta = \frac{1}{k_{max}} \frac{1}{\theta} \frac{d\theta}{dz}, \tag{4}$$

where k_{max} is the wavenumber of the most amplified temporal instability mode and θ is the momentum thickness of the velocity profile $\overline{W}(r,z)$, so that the ratio $\theta^{-1}d\theta/dz$ characterizes the streamwise variations of the mean flow.[23] The streamwise evolution of η is shown in Fig. 7. Although η remains smaller than 5 % for $x > 2.5$, we find that the nonparallel effects are quite important close to the stagnation points. As already observed in other configurations[15,17], the elephant mode theory, which is solely an asymptotic theory in η, gives strikingly precise predictions of the frequency and spatial distribution of the nonlinear fluctuations, even in complex situations where high Reynolds numbers prevail, when it is outside its validity domain. It represents a guideline to understand the physical origin and eventually propose control strategies of the large-scale synchronized oscillations developing in the wake of realistic afterbodies.

Such a control may be achieved through base flow modifications, for instance base bleed.[4,27] In this context, the implementation of optimization procedures would be considerably eased if predictions of the absolute frequency as a function of the streamwise position z could be obtained using the known stability properties of analytical profiles. Such an analysis is carried out in Appendix A, using the model wake profiles introduced by Monkewitz & Sohn.[28] We find that the associated predicted Strouhal number $\widetilde{St} = 0.22$ overestimates only by 10 % that issuing from the experimental and numerical spectra. In this context of flow control, the use of fitted profiles hence provides with decent estimates of the global frequency, that may be refined when needed by carrying out the stability analysis on the actual profiles.

APPENDIX A: FITTING OR NOT FITTING, ABOUT THE INFLUENCE OF THE MEAN FLOW PROFILES

Many experimental or numerical identification of absolutely unstable regions rely on the stability properties of analytical model profiles on which the actual mean flow measurements are systematically fitted.[14,24] The aim of the present appendix is to investigate, in the present case, to what extent such a fitting procedure alters the results of the stability analysis. For clarity, all results pertaining to the fitted profiles are noted with a $\widetilde{\ }$ symbol. We have used the two-parameter $(\widetilde{\Lambda}, \widetilde{N})$ model velocity profiles taken from Monkewitz & Sohn[28], where the axial velocity profile reads

$$\widetilde{W}(r,z) = 1 + \frac{2\widetilde{\Lambda}}{1-\widetilde{\Lambda}} F(r,z), \tag{A1}$$

with

$$F(r,z) = \frac{1}{(2^{r^2}-1)^{\widetilde{N}(z)}}. \tag{A2}$$

Since we consider here compressible flows, the temperature field is deduced from the fitted velocity profile through the Crocco-Busemann relation[29] and from the density ratio $S = \overline{\rho}_c/\overline{\rho}_\infty$ computed at each streamwise station from the LES calculations. Finally, the density is obtained from the perfect gas state equation (see Ref. 18 for details).

For each streamwise position, the fitting parameters $\widetilde{\Lambda}(z)$ and $\widetilde{N}(z)$ have been determined using a standard least square method. The momentum thickness $\widetilde{\theta}$ of the fitted profile implicitly depends on $\widetilde{N}(z)$ as

$$\widetilde{\theta}(z) = \int_0^\infty F(r,z)(1-F(r,z))\mathrm{d}r. \tag{A3}$$

Fig. 8 depicts the streamwise evolution of $\widetilde{\Lambda}(z)$ and of the steepness parameter $D/\widetilde{\theta}(z)$ (dashed lines). The values of the LES parameters $\Lambda(z)$ and $D/\theta(z)$ introduced in section II are also reported for comparison (solid lines). We observe a good agreement between the real and fitted velocity ratios, although the fitting procedure slightly underestimates the magnitude of the counterflow. However, the evolution of the shear parameter shows discrepancies, as the fitted momentum thickness of the developing wake systematically underestimates that of the real profiles. Confirmation comes from Fig. 9 that shows a comparison between the LES profile and the corresponding fitted profile at the position $z = 0.05$, within the recirculating bubble. We

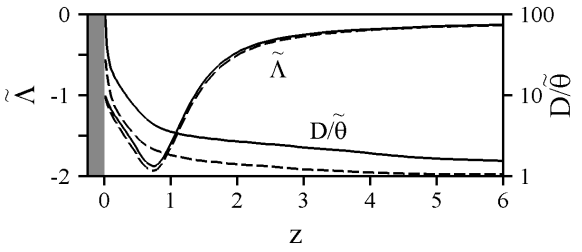

FIG. 8: Streamwise evolution of the fitted parameter $\widetilde{\Lambda}$ and of the fitted steepness parameters $D/\widetilde{\theta}$ (dashed lines). The values already shown in Fig. 3(b) are reported as solid lines for comparison.

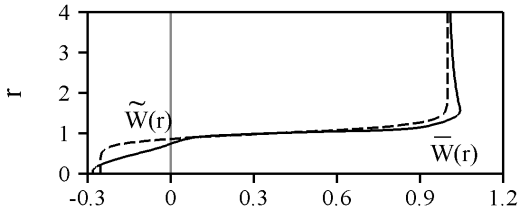

FIG. 9: Comparison between the LES (solid line) and the fitted (dashed line) velocity profiles at the streamwise station $z = 0.05$.

notice that the fitted profiles account neither for the small velocity overshoot existing just outside of the shear-layer region, nor for the deformation of the velocity field close to the axis.

Fig. 10 shows the streamwise variations of the Strouhal number based on the absolute frequency $\widetilde{St} = \widetilde{\omega}_r^0/2\pi$ and that of the absolute growth rate $\widetilde{\omega}_i^0$ obtained using the fitted profiles (dashed lines). The solid lines refer to the Strouhal number St and to the absolute growth rate ω_i^0 shown in Fig. 5 for the exact LES profiles. The frequencies obtained from the fitted profiles match reasonably well with that obtained from the LES profiles. We find that absolute instability prevails in the domain $\widetilde{z}^{ca} = 0.01 < z < \widetilde{z}^{ac} = 1.34$, the amplification rates $\widetilde{\omega}_i^0$ being significantly overestimated in the whole absolute domain. In the range of parameters $(\Lambda, D/\theta, S)$ involved here, this can be explained by the fact that a lower steepness parameter results in a lower absolute growth rate ω_i^0.[18] As a result, using fitted profiles, the position of the upstream transition station, that predicts the location of the front in the elephant mode theory, is strongly shifted downstream. The global frequency selected at $\widetilde{z}^{ca}$, $\widetilde{\omega}_r^0(\widetilde{z}^{ca}) = 1.39$, corresponds to a Strouhal number of $\widetilde{St} = 0.22$ that slightly overestimates the global frequency obtained for the real profiles by 10 %. Thus, the results obtained by fitting the actual LES profiles by model analytical profiles $(A1) - (A2)$ agree reasonably well with the experimental observations and with the results issuing from the stability analysis of the exact LES profiles. In this specific case, this result therefore demonstrates the validity of the use of model profiles to estimate the global frequency with limited discrepancy.

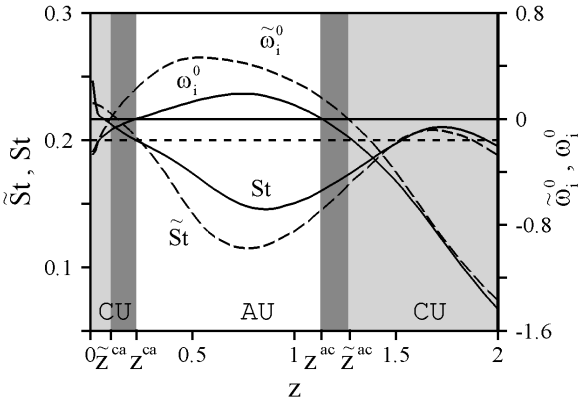

FIG. 10: Streamwise evolution of the Strouhal number $\widetilde{St}$ and of the absolute growth rate $\widetilde{\omega}_i^0$ obtained using fitted velocity profiles (dashed lines). The shaded areas correspond to convectively unstable domains. The solid lines refer to the results $(St,\ \omega_i^0)$ presented in Fig. 5 for the real profiles. The solid horizontal lines represents the threshold of marginal absolute instability $\omega_i^0 = 0$. The dashed horizontal line marks the global frequency of the observed large-scale oscillations $St = 0.20$.

* Electronic address: philippe.meliga@onera.fr

[1] E. Achenbach, "Vortex shedding from spheres," J. Fluid Mech. **62** 209-221 (1974).

[2] H.V. Fuchs, E. Mercker and U. Michel, "Large-scale coherent structures in the wake of axisymmetric bodies," J. Fluid Mech. **93**, 185-207 (1979).

[3] E. Berger, D. Scholz and M. Schumm, "Coherent vortex structures in the wake of a sphere and a circular disk at rest and under forced vibrations," J. Fluids Struct. **4** 231-257 (1990).

[4] A. Sevilla and C. Martínez-Bazàn, "Vortex shedding in high Reynolds number axisymmetric bluff-body wakes: Local linear instability and global bleed control," Phys. Fluids **16**, 3460-3469 (2004).

[5] P.A. Monkewitz and L.N. Nguyen, "Absolute instability in the near-wake of two-dimensional bluff-bodies," J. Fluids Struct. **1**, 165-184 (1987).

[6] R.J. Briggs *Electron stream interaction with plasmas* (M.I.T. Press, Cambridge, 1964).

[7] A. Bers "Linear waves and instabilities," In

Plasma physics (by C. De Witt and J. Peyraud), 117–215 (Gordon and Breach, 1975).

[8] J.-M. Chomaz, "Absolute and convective instability in non linear systems," Phys. Rev. Lett. **69**, 1931-1934 (1992).

[9] A. Couairon and J.-M. Chomaz, "Absolute and convective instabilities, front velocities and global modes in nonlinear systems," Physica D **108**, 236-276 (1997).

[10] S.M. Tobias, M.R.E. Proctor and E. Knobloch, "Convective and absolute instabilities of fluid flows in finite geometry," Physica D **113**, 4-72 (1998).

[11] B. Pier, P. Huerre and J.-M. Chomaz, "Bifurcation to fully nonlinear synchronized structures in slowly varying media," Physica D **148**, 49-96 (2001).

[12] J.-M. Chomaz, "Global instabilities in spatially developing flows: Non-normality and nonlinearity," Annu. Rev. Fluid. Mech. **37**, 357-392 (2005).

[13] B. Pier, "On the frequency selection of finite-amplitude vortex shedding in the cylinder wake," J. Fluid Mech. **458**, 407-417 (2002).

[14] F. Gallaire and J.-M. Chomaz, "Mode selection in swirling jet experiments: a linear stability analysis," J. Fluid Mech. **494**, 223-253 (2003).

[15] L. Lesshafft, P. Huerre, P. Sagaut and M. Terracol, "Nonlinear global modes in hot jets," J. Fluid Mech. **554**, 393-409 (2006).

[16] F. Gallaire, M. Ruith, E. Meiburg, J.-M. Chomaz and P. Huerre, "Spiral vortex breakdown as a global mode," J. Fluid Mech. **549**, 71-80 (2006).

[17] B. Viaud, E. Serre and J.-M. Chomaz, "The elephant mode between two rotating disks," J. Fluid Mech. **598**, 451-464 (2008).

[18] P. Meliga, D. Sipp and J.-M. Chomaz, "Absolute instability in axisymmetric wakes: compressible and density variation effects," J. Fluid Mech. **600**, 373-401 (2008).

[19] D. Barkley, M.G.M. Gomes and R.D. Henderson, "Three-dimensional instability in flow over a backward-facing step," J. Fluid Mech. **473**, 167-190 (2002).

[20] D. Deprés, P. Reijasse and J.-P. Dussauge, "Analysis of unsteadiness in afterbody transonic flows," AIAA Journal **42**, 2541-2550 (2004).

[21] J.-P. Flodrops and J.-M. Desse, "Sillage d'un culot axisymétrique," Report 85/19 from the Institut de Mécanique des Fluides de Lille, France (1985).

[22] S. Deck, E. Garnier and P. Guillen, "Turbulence modelling applied to space launcher configurations," Journal of Turbulence **57**, 1-21 (2002).

[23] D. Hammond and L. Redekopp, "Global dynamics of symmetric and asymmetric wakes," J. Fluid Mech. **331**, 231-260 (1997).

[24] M. Khor, J. Sheridan, M.C. Thompson and K. Hourigan, "Global frequency selection in the observed time-mean wakes of circular cylinders," J. Fluid Mech. **601**, 425-441 (2008).

[25] P. Huerre and P.A. Monkewitz, "Absolute and convective instabilies in free shear layers," J. Fluid Mech. **159**, 151-168 (1985).

[26] D. Sipp, and A. Lebedev, "Global stability of base and mean flows: a general approach and its applications to cylinder and open cavity flows," J. Fluid Mech. **593**, 333-358 (2007).

[27] A. Sevilla and C. Martínez-Bazàn, "A note on the stabilization of bluff-body wakes by low density base bleed," Phys. Fluids **18**, 098102 (2006).

[28] P.A. Monkewitz and K.D. Sohn, "Absolute instability in hot jets," AIAA Journal **26**, 911-916 (1988).

[29] H. Schlichting, *Boundary layer theory* (McGraw-Hill, 7th ed., 1978).

INTERLUDE: A TALE OF WHITE RABBITS AND SADDLE POINTS

En 2007, j'ai soumis au *Journal of Fluid Mechanics* un prototype de l'article qui constitue l'essentiel de ce second chapitre, avec sa référence au roman de Lewis Carroll, *Through the Looking-Glass, and What Alice Found There*, qui fait suite à *Alice's Adventures in Wonderland* . En retour, l'un des rapporteurs s'est inspiré de son *Jabberwocky* pour écrire ce poème.

Twas brillig in the complex plane
Of rolling hyperbolic hills,
With path of integration lain
Through points where group speed stills.

Beware the Saddlewok my son!
Which lurks at negative kay-r.
Its growth rate, hardly e'er outdone,
Runs perpendicular.

So take numeric tool in hand
And bend the branch cut from the axe.
Reveal that tulgey curious land
Where navely Briggs-Bers cracks.

Thou'll findst the Saddlewok spits wrath:
My mode blows up. Thou can'st touch me!
Yet integrate 'long bended path,
I'll wage thou'd disagree.

The Saddlewok, you'd be surprised,
Can be most easily explained:
Its growing mode is localised;
The wavepacket contained.

Twas brillig in the complex plane
Of rolling hyperbolic hills,
With path of integration lain
Through points where group speed stills.

CHAPTER
THREE

GLOBAL MODES IN THE WAKE OF AXISYMMETRIC BODIES

This chapter is devoted to the linear dynamics of incompressible wakes, as predicted by a global stability analysis of the axisymmetric state. Two model geometries of blunt and bluff bodies are considered, namely the disk and the sphere. The global modes of largest growth rates are first identified, and results are compared to that existing in the literature. The receptivity of each mode to particular initial conditions or forcing is also discussed, which allows to identify the flow regions that are of particular interest in the perspective of control. This study takes the form of a paper submitted to the *Journal of Fluids and Structures*.

keywords: incompressible flows, global modes, adjoint-methods, nonnormality, receptivity.

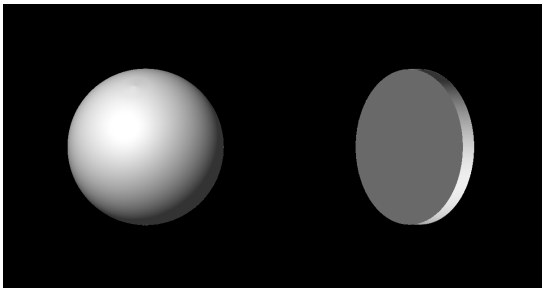

ELSEVIER

Journal of Fluids and Structures 25 (2009) ??–??

JOURNAL OF FLUIDS AND STRUCTURES

www.elsevier.com/locate/jfs

Unsteadiness in the wake of disks and spheres: instability, receptivity and control using direct and adjoint global stability analyses

Philippe Meliga [a] Jean-Marc Chomaz [b] Denis Sipp [a]

[a] *ONERA/DAFE, 92190 Meudon, France*

[b] *LadHyX, CNRS-Ecole Polytechnique, 91128 Palaiseau, France*

Received 20 June 2008

Abstract

We consider the stability of the steady, axisymmetric wake of a disk and a sphere as a function of the Reynolds number. Both the direct and adjoint eigenvalue problems are solved. The threshold Reynolds numbers and characteristics of the destabilizing modes agree with the study of Natarajan & Acrivos [17]: for both configurations, the first destabilization occurs for a stationary mode of azimuthal wavenumber $m = 1$, and the second destabilization for an oscillating mode of same azimuthal wavenumber. For both geometries, the adjoint mode computation allows us to determine the receptivity of each mode to particular initial conditions or forcing and to define control strategies. We show that the adjoint global mode reaches a maximum amplitude close to the separation point for both the disk and the sphere. In the case of the sphere, the optimal forcing corresponds to a displacement of the separation point along the sphere surface with no tilt of the separation line. However, in the case of the disk, its blunt shape does not allow such displacement and the optimal forcing corresponds to a tilt of the separation line with no displacement of the separation point. As a result, the magnitudes of the adjoint global modes are larger for the sphere than for the disk, showing that the wake of the sphere is more receptive to forcing than the disk. In the case of active control at the boundary through blowing and suction at the body wall, the actuator should be placed close to the separation point, where the magnitude of adjoint pressure reaches its maximum in the four cases. In the case of passive control, we show that the region of the wake that is most sensitive to local modifications of the linearized Navier-Stokes operator, including base flow alterations, (Giannetti & Luchini [13]) is limited to the recirculating bubble for both geometries and both instability modes. This region may therefore be identified as the intrinsical wavemaker.

Keywords: axisymmetric wakes; instability; global mode; adjoint; nonnormality; receptivity; control
PACS:

1. Introduction

A large body of works has been devoted to the wake of axisymmetric bodies in the last decades. For different objects, such as spheres, disks or bullet-shaped bodies [1, 4, 12, 21], the dynamics bears similarities: at low Reynolds numbers, the steady separated flow field is axisymmetric and consists of a toroidal recirculation eddy past the body. Increasing the Reynolds number, a stationary bifurcation first occurs and breaks the axisymmetry, the entire wake being shifted in one direction. The series of bifurcation that follows is complex and body's shape dependent [2], but eventually, for large enough Reynolds numbers, the flow is dominated by helical modes of azimuthal wavenumbers $m = \pm 1$, resulting in the low frequency shedding of large-scale coherent structures. These vortex shedding phenomena are characterized by low Strouhal numbers based on the body diameter of order $0.1 - 0.2$.

Natarajan & Acrivos [17] have carried out a global stability analysis of the axisymmetric wake past a circular flat disk set normal to the flow and a sphere. In both cases, they have shown that the axisymmetric base flow presents several successive destabilizations. The first instability is stationary and involves a global eigenmode of azimuthal wavenumber $m = 1$. The associated bifurcation, breaking the axisymmetry but preserving the time invariance, leads to a 3D steady state. Above the threshold of instability, these authors have not studied the stability of this 3D state but that of the axisymmetric wake. They have shown that a second instability occurs at a larger Reynolds number, for $m = \pm 1$ oscillating global eigenmodes that breaks the time invariance. From direct numerical simulations (DNS) and experimental observations, it turns out that this second instability mode dominates the dynamics of the fully 3D flow at large Reynolds numbers, hence explaining the occurrence of a fully 3D periodic state [18]. Such a domination of the periodic instability mode over the stationary mode, despite the fact that the latter is the first to destabilize the axisymmetric base flow has recently been explained using slow manifold theory and normal forms [10]. This nonlinear competition between modes is not the scope of the present study that focuses instead on the respective sensitivity and receptivity properties of these unstable global modes in two model geometries of blunt and bluff bodies, namely the disk and the sphere.

This study extends the work of Natarajan & Acrivos [17] by carrying out an adjoint analysis of the wake past a circular flat disk and a sphere. We compute the direct and adjoint global modes associated to the first two instabilities. We discuss the nonnormality of the flow and point out the role of the so-called *convective* nonnormality [5, 6, 15] associated to the transport of the perturbations by the base flow. The paper is organized as follows. The problems of direct and adjoint global modes are presented in § 2., where we discuss the physical origin of the nonnormality of the linearized Navier-Stokes equations. § 3. presents the numerical method and the results of the direct and adjoint global stability analysis. We finally discuss physical interpretations of the adjoint global mode in terms of receptivity of the global mode to initial perturbations and forcing and, following Giannetti & Luchini[13], we identify the 'wavemaker' region as the region of the flow where the instability is sensitive to local modification of the linearized evolution operator. These properties are crucial when control or, for instance, departure from the ideal axisymmetry owing to imperfect experimental set-ups are concerned.

2. Problem formulation

We investigate the stability of the axisymmetric flow developing past an axisymmetric body, that can be a flat circular disk normal to the incoming flow, or a sphere. Standard

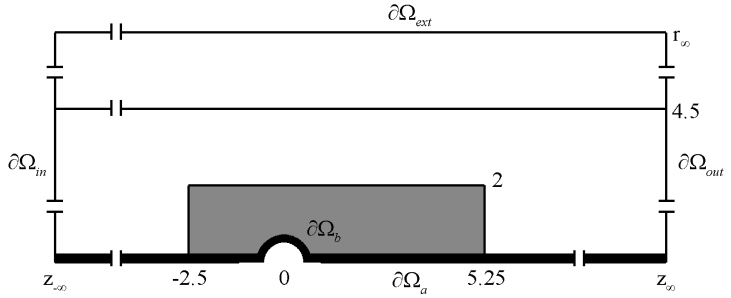

Fig. 1. Schematic of the mesh structure: $z_{-\infty}$, z_{∞} and r_{∞} are, respectively, the location of the inlet, outlet and external boundaries. The inner solid lines delimit regions characterized by different vertex densities. The grey shaded area correspond to the region of highest density.

cylindrical coordinates r, θ and z with origin taken at the center of the body are used. The configuration is shown in Fig. 1 for the flow past a sphere. The body of boundary $\partial\Omega_b$ is located on the axis of an enclosing cylinder of radius $r_{\infty} = 25$ defining the computational domain Ω, with boundaries $\partial\Omega_a$ and $\partial\Omega_{ext}$ representing respectively the revolution axis of the base flow and the boundary of the enclosing cylinder. The inlet $\partial\Omega_{in}$ and outlet $\partial\Omega_{out}$ are located respectively at $z_{-\infty} = -100$ and $z_{\infty} = 200$.

All quantities are made nondimensional using the diameter of the body D and the free-stream velocity U_{∞}. The state vector $\boldsymbol{q}$ stands for the flow field $(\boldsymbol{u}, p)^T$, where ^{T} designates the transpose, $\boldsymbol{u} = (u, v, w)$ is the fluid velocity where u, v and w are the radial, azimuthal and streamwise components, and p is the pressure. The fluid motion is governed by the incompressible Navier-Stokes equations that read

$$\boldsymbol{\nabla} \cdot \boldsymbol{u} = 0\,, \qquad \partial_t \boldsymbol{u} + \boldsymbol{\nabla}\boldsymbol{u} \cdot \boldsymbol{u} + \boldsymbol{\nabla} p - \frac{1}{Re}\boldsymbol{\nabla}^2 \boldsymbol{u} = \boldsymbol{0}\,, \tag{1}$$

where Re is the Reynolds number based on D and U_{∞}. We use the inlet condition $\boldsymbol{u} = (0, 0, 1)^T$ on $\partial\Omega_{in}$, no-slip conditions $\boldsymbol{u} = \boldsymbol{0}$ on the body wall $\partial\Omega_b$ and no-stress conditions $-p\boldsymbol{n} + Re^{-1}\boldsymbol{\nabla}\boldsymbol{u} \cdot \boldsymbol{n} = \boldsymbol{0}$ on the outlet $\partial\Omega_{out}$. On the external boundary $\partial\Omega_{ext}$, we impose a free slip boundary condition $u = v = \partial_r w = 0$, so that the body surface $\partial\Omega_b$ is the only source of vorticity, as it would be the case without this artificial boundary.

Base flow For Reynolds numbers below the threshold of the first instability, the flow can be searched as a steady, axisymmetric solution $\boldsymbol{q^0} = (u^0, 0, w^0, p^0)^T$ satisfying equations

$$\boldsymbol{\nabla} \cdot \boldsymbol{u^0} = 0\,, \qquad \boldsymbol{\nabla}\boldsymbol{u^0} \cdot \boldsymbol{u^0} + \boldsymbol{\nabla} p^0 - \frac{1}{Re}\boldsymbol{\nabla}^2 \boldsymbol{u^0} = \boldsymbol{0}\,. \tag{2}$$

On the axis $\partial\Omega_a$, we impose $u^0 = \partial_r w^0 = 0$, a condition given by mass and momentum conservation as $r \to 0$ for axisymmetric solutions.

Global mode analysis The stability of the steady axisymmetric base flow is examined by considering small-amplitude three-dimensional perturbations $\boldsymbol{q^1} = (u^1, v^1, w^1, p^1)^T$ which satisfy the unsteady equations linearized about $\boldsymbol{q^0}$

$$\boldsymbol{\nabla} \cdot \boldsymbol{u^1} = 0\,, \qquad \partial_t \boldsymbol{u^1} + \mathcal{C}(\boldsymbol{u^1}, \boldsymbol{u^0}) + \boldsymbol{\nabla} p^1 - \frac{1}{Re}\boldsymbol{\nabla}^2 \boldsymbol{u^1} = \boldsymbol{0}\,, \tag{3}$$

where $\mathcal{C}(\boldsymbol{a},\boldsymbol{b}) = \boldsymbol{\nabla a}\cdot\boldsymbol{b} + \boldsymbol{\nabla b}\cdot\boldsymbol{a}$ is the advection operator. Note that $\mathcal{C}$ is symmetrical, i.e. $\mathcal{C}(\boldsymbol{a},\boldsymbol{b}) = \mathcal{C}(\boldsymbol{b},\boldsymbol{a})$. When considering the perturbation and base flow velocity fields $\boldsymbol{u^1}$ and $\boldsymbol{u^0}$, this operator accounts for the advection of the perturbation by the base flow via the term $\boldsymbol{\nabla u^1}\cdot\boldsymbol{u^0}$ and for the advection of the base flow by the perturbation via the term $\boldsymbol{\nabla u^0}\cdot\boldsymbol{u^1}$. Since the base flow is axisymmetric, all perturbations are chosen in the form of normal eigenmodes of azimuthal wavenumber m and complex pulsation $\sigma + \mathrm{i}\omega$, σ and ω being respectively the growth rate and pulsation of the eigenmode ($\sigma > 0$ for an unstable eigenmode):

$$\boldsymbol{q^1} = \hat{\boldsymbol{q}}^{\boldsymbol{1}}(r,z)e^{(\sigma+\mathrm{i}\omega)t+\mathrm{i}m\theta} + \text{ c.c.}\,, \tag{4}$$

where $\hat{\boldsymbol{q}}^{\boldsymbol{1}} = (\hat{u}^1,\hat{v}^1,\hat{w}^1,\hat{p}^1)$ is the so-called global mode, herein referred to as the *direct* global mode, for which both the cross-stream and streamwise directions (r,z) are eigendirections. Substitution of decomposition (4) in equations (3) leads to a generalized eigenvalue problem for $\sigma + \mathrm{i}\omega$ and $\hat{\boldsymbol{q}}^{\boldsymbol{1}}$ that reads

$$(\sigma + \mathrm{i}\omega)\mathcal{B}\hat{\boldsymbol{q}}^{\boldsymbol{1}} + \mathcal{A}_m\hat{\boldsymbol{q}}^{\boldsymbol{1}} = \boldsymbol{0}\,, \tag{5}$$

where $\mathcal{A}_m$ and $\mathcal{B}$ are the linear operators defined by

$$\mathcal{A}_m = \begin{pmatrix} \mathcal{C}_m(\cdot,\boldsymbol{u^0}) - \frac{1}{Re}\boldsymbol{\nabla_m}^2 & \boldsymbol{\nabla_m} \\ \boldsymbol{\nabla_m}^T & 0 \end{pmatrix}, \qquad \mathcal{B} = \begin{pmatrix} \mathcal{I} & 0 \\ 0 & 0 \end{pmatrix}. \tag{6}$$

For a normal mode $\hat{\boldsymbol{a}}$ of azimuthal wavenumber m, the gradient operator and the velocity gradient tensor read

$$\boldsymbol{\nabla_m} = \begin{pmatrix} \partial_r \\ \frac{im}{r} \\ \partial_z \end{pmatrix}, \qquad \boldsymbol{\nabla_m}\hat{\boldsymbol{a}} = \begin{pmatrix} \partial_r\hat{u} & \frac{im}{r}\hat{u} - \frac{1}{r}\hat{v} & \partial_z\hat{u} \\ \partial_r\hat{v} & \frac{im}{r}\hat{v} + \frac{1}{r}\hat{u} & \partial_z\hat{v} \\ \partial_r\hat{w} & \frac{im}{r}\hat{w} & \partial_z\hat{w} \end{pmatrix}. \tag{7}$$

The complex advection operator $\mathcal{C}_m$ in (6) is then defined as $\mathcal{C}_m(\hat{\boldsymbol{u}}^{\boldsymbol{1}},\boldsymbol{u^0}) = \boldsymbol{\nabla_m}\hat{\boldsymbol{u}}^{\boldsymbol{1}}\cdot\boldsymbol{u^0} + \boldsymbol{\nabla_0}\boldsymbol{u^0}\cdot\hat{\boldsymbol{u}}^{\boldsymbol{1}}$ and accounts for the specific azimuthal periodicity of the normal mode. In the following, we restrict to the case of $|m| = 1$ disturbances. The associated global modes satisfy the following boundary conditions

$$\partial_r\hat{u}^1 = \partial_r\hat{v}^1 = \hat{w}^1 = \hat{p}^1 = 0 \quad \text{on} \quad \partial\Omega_a \text{ (axis)}, \tag{8a}$$

$$\hat{\boldsymbol{u}}^{\boldsymbol{1}} = \boldsymbol{0} \quad \text{on} \quad \partial\Omega_{in} \cup \partial\Omega_b \text{ (inlet and body)}, \tag{8b}$$

$$-\hat{p}^1\boldsymbol{n} + Re^{-1}\boldsymbol{\nabla_1}\hat{\boldsymbol{u}}^{\boldsymbol{1}}\cdot\boldsymbol{n} = \boldsymbol{0} \text{ (no-stress)} \quad \text{on} \quad \partial\Omega_{out} \text{ (outlet)}, \tag{8c}$$

$$\hat{u}^1 = \partial_r\hat{v}^1 = \partial_r\hat{w}^1 = 0 \text{ (free slip)} \quad \text{on} \quad \partial\Omega_{ext} \text{ (external boundary)}, \tag{8d}$$

the condition at the axis $\partial\Omega_a$ being specific to the azimuthal wavenumbers $|m| = 1$.

Adjoint global modes The adjoint evolution operator $\mathcal{A}_m^\dagger$ is defined so that for any vectors $\hat{\boldsymbol{q}}^{\boldsymbol{1}}$ fulfilling boundary conditions (8) and $\hat{\boldsymbol{q}}^{\boldsymbol{1}\dagger}$ fulfilling boundary conditions to be determined,

$$\left\langle \hat{\boldsymbol{q}}^{\boldsymbol{1}\dagger}, \mathcal{A}_m\hat{\boldsymbol{q}}^{\boldsymbol{1}} \right\rangle = \left\langle \mathcal{A}_m^\dagger\hat{\boldsymbol{q}}^{\boldsymbol{1}\dagger}, \hat{\boldsymbol{q}}^{\boldsymbol{1}} \right\rangle, \tag{9}$$

with $\langle,\rangle$ the inner product on Ω defined by $\langle\hat{\boldsymbol{a}},\hat{\boldsymbol{b}}\rangle = \int_\Omega \hat{\boldsymbol{a}}^*\cdot\hat{\boldsymbol{b}}\,r\mathrm{d}r\mathrm{d}z$, where $\hat{\boldsymbol{a}}$ and $\hat{\boldsymbol{b}}$ belong to $\mathbb{C}^n$, the superscript $*$ stands for the complex conjugate, and $\cdot$ refers to the canonic

hermitian scalar product in $\mathbb{C}^n$. The adjoint equations are obtained using integration by parts of equations (3) [20]. The boundary conditions to be fulfilled by adjoint perturbations are such that all boundary terms arising during the integration are zero. For $|m| = 1$ disturbances, we obtain:

$$\partial_r \hat{u}^{1\dagger} = \partial_r \hat{v}^{1\dagger} = \hat{w}^{1\dagger} = \hat{p}^{1\dagger} = 0 \quad \text{on} \quad \partial\Omega_a, \tag{10a}$$

$$\hat{\boldsymbol{u}}^{\mathbf{1}\dagger} = \mathbf{0} \quad \text{on} \quad \partial\Omega_{in} \cup \partial\Omega_b, \tag{10b}$$

$$(\boldsymbol{u^0}.\boldsymbol{n})\hat{\boldsymbol{u}}^{\mathbf{1}\dagger} + \hat{p}^{1\dagger}\boldsymbol{n} + Re^{-1}\boldsymbol{\nabla_1}\hat{\boldsymbol{u}}^{\mathbf{1}\dagger} \cdot \boldsymbol{n} = \mathbf{0} \quad \text{on} \quad \partial\Omega_{out}, \tag{10c}$$

$$\hat{u}^{1\dagger} = \partial_r \hat{v}^{1\dagger} = \partial_r \hat{w}^{1\dagger} = 0 \quad \text{on} \quad \partial\Omega_{ext}. \tag{10d}$$

With our notation, $\hat{\boldsymbol{q}}^{\mathbf{1}\dagger}$ is then solution of an eigenvalue problem that reads

$$(\sigma - \mathrm{i}\omega)\mathcal{B}\hat{\boldsymbol{q}}^{\mathbf{1}\dagger} + \mathcal{A}_m^\dagger \hat{\boldsymbol{q}}^{\mathbf{1}\dagger} = \mathbf{0}\,, \tag{11}$$

where $\mathcal{A}_m^\dagger$ is the complex evolution operator defined as

$$\mathcal{A}_m^\dagger = \begin{pmatrix} \mathcal{C}_m^\dagger(\cdot, \boldsymbol{u^0}) - \frac{1}{Re}\boldsymbol{\nabla_m}^2 & -\boldsymbol{\nabla_m} \\ \boldsymbol{\nabla_m}^T & 0 \end{pmatrix}, \tag{12}$$

and $\mathcal{C}_m^\dagger(\hat{\boldsymbol{u}}^{\mathbf{1}\dagger}, \boldsymbol{u^0}) = \boldsymbol{\nabla_0}\boldsymbol{u^0}^T \cdot \hat{\boldsymbol{u}}^{\mathbf{1}\dagger} - \boldsymbol{\nabla_m}\hat{\boldsymbol{u}}^{\mathbf{1}\dagger} \cdot \boldsymbol{u^0}$ is the adjoint advection operator. Comparing $\mathcal{A}_m$ and $\mathcal{A}_m^\dagger$, we note that the nonnormality comes only from the advection operator and can be split in two complementary effects. The *lift-up* type nonnormality is due to the advection of the base flow by the perturbation, given by $\boldsymbol{\nabla_0}\boldsymbol{u^0} \cdot \hat{\boldsymbol{u}}^{\mathbf{1}}$ for the direct operator $\mathcal{A}_m$ and $\boldsymbol{\nabla_0}\boldsymbol{u^0}^T \cdot \hat{\boldsymbol{u}}^{\mathbf{1}\dagger}$ for the adjoint operator $\mathcal{A}_m^\dagger$. When the flow is a simple parallel shear, this term gives rise to the so-called lift-up effect, linked to the generation of strong streamwise velocity perturbations by small displacements along the direction of the base flow gradient. The lift-up nonnormality is then associated to direct and adjoint global modes that tend to be orthogonal one to the other because concentrated on different components of the velocity vector [15]. The convective nonnormality [5, 6, 15] is due to the transport of disturbances by the base flow, given by $\boldsymbol{\nabla_m}\hat{\boldsymbol{u}}^{\mathbf{1}} \cdot \boldsymbol{u^0}$ for the direct operator $\mathcal{A}_m$ and $-\boldsymbol{\nabla_m}\hat{\boldsymbol{u}}^{\mathbf{1}\dagger} \cdot \boldsymbol{u^0}$ for the adjoint operator $\mathcal{A}_m^\dagger$, which have opposite signs. Physically, this indicates that direct perturbations are convected downstream and that adjoint perturbations are convected upstream [5]. As noticed in [6] in the case of the Ginzburg Landau model equation, this nonnormality is specific to open flows and tends to spatially separate the perturbation velocity fields, downstream for the direct perturbations and upstream for the adjoint perturbations. The convective nonnormality is then associated to direct and adjoint global modes that tend to be orthogonal one to the other because localized in different regions of the flow. Of course, for real nonparallel flows, such as those considered here, both mechanisms act and the spatial structures of the direct and adjoint global modes result from their interactions (see § 3.).

As discussed in [5], the adjoint global mode may receive different physical interpretations. For an unstable flow, it defines the most *dangerous* initial perturbation of unit norm, i.e. that maximizes the large-time amplitude of the direct global mode [5, 20]. Presently, we will discuss only the physics of the initial perturbation but not its time evolution, that may lead to possibly energetic transient regimes before the large-time dynamics is reached.

For a marginally stable global mode, of growth rate $\sigma < 0$ ($|\sigma| \ll 1$) and of frequency ω, the adjoint global mode also characterizes the receptivity of the global mode to near-resonance harmonic forcing. This point is crucial in the perspective of active control,

where the idea is to produce a large effect in the flow by introducing a small amount of energy, either by periodic blowing and suction at the wall, or by use of a volumic force. If forcing occurs through a body force $\hat{\boldsymbol{f}} = (\hat{f}_r, \hat{f}_\theta, \hat{f}_z)$ of frequency ω_f close to ω and of same azimuthal wavenumber as the global mode, the receptivity of the global mode, i.e. the amplitude of the forced global mode, is given by

$$\alpha = \frac{1}{\sigma + i(\omega - \omega_f)} \frac{\left\langle \hat{\boldsymbol{q}}^{\boldsymbol{1}\dagger}, (\hat{\boldsymbol{f}}, 0)^T \right\rangle}{\langle \hat{\boldsymbol{q}}^{\boldsymbol{1}\dagger}, \mathcal{B}\hat{\boldsymbol{q}}^{\boldsymbol{1}} \rangle} , \tag{13}$$

In the case of boundary forcing, for instance by periodic blowing and suction at the body wall $\partial\Omega_b$, also with the frequency ω and the same azimuthal wavenumber than that of the global mode, Giannetti & Luchini [13] have computed the global mode amplitude as a function of the velocity $\hat{\boldsymbol{u}}_{\boldsymbol{w}}$ imposed at the wall by modyfing equation (8b) on $\partial\Omega_b$ into $\hat{\boldsymbol{u}}^{\boldsymbol{1}} = \hat{\boldsymbol{u}}_{\boldsymbol{w}}$:

$$\alpha = \frac{1}{i(\omega - \omega_f)} \frac{1}{\langle \hat{\boldsymbol{q}}^{\boldsymbol{1}\dagger}, \mathcal{B}\hat{\boldsymbol{q}}^{\boldsymbol{1}} \rangle} \int_{\partial\Omega_b} \left(\hat{p}^{1\dagger}\boldsymbol{n} + \frac{1}{Re} \boldsymbol{\nabla}_{\boldsymbol{1}} \hat{\boldsymbol{u}}^{\boldsymbol{1}\dagger} \cdot \boldsymbol{n} \right) \cdot \hat{\boldsymbol{u}}_{\boldsymbol{w}} dl \, . \tag{14}$$

Note that for sufficiently large Reynolds numbers, the term arising from the Reynolds stresses can be neglected compared to the wall pressure $\hat{p}^{1\dagger}$ [15], implying that the amplitude of the response to forcing is large, i.e. the forcing is efficient, in regions of the wall where the magnitude of the adjoint wall pressure $|\hat{p}^{1\dagger}|$ is large. Note that the orientation of the forcing velocity with respect to the wall also influences the response of the global mode since, for a given magnitude of the wall velocity, the closer the orientation to the normal vector to the wall, the larger the amplitude of the forced global mode. Note that relations (13) and (14) are valid only for near-resonance forcing, when $\omega - \omega_f$ is small. They can be generalized to the case of off-resonance forcing by solving for the norm of the resolvent operator $(\omega_f \mathcal{B} + i\mathcal{A}_1)^{-1}$ when a body force is added to the momentum equations [19].

The adjoint analysis is also useful to identify the region of the flow which acts as the 'wavemaker'. By considering small modifications of the evolution operator $\mathcal{A}_m$ with the form of a 'force-velocity' coupling, Giannetti & Luchini [13] have argued that the sensitivity of the eigenvalue to such a local feedback is maximum in the region where the product of the modulus of the direct and adjoint global modes is not zero, and that this overlapping region therefore identifies the wavemaker. This concept of sensitivity has been extended recently to assess how imposed steady base flow modifications or addition of a steady volumic force may alter the stability properties of flows, leading to the definition of the so-called sensitivity to base flow modifications or sensitivity to a steady force, respectively [16]. In the present paper, as in the study of Giannetti & Luchini [13], we present only results pertaining to the sensitivity to a 'force-velocity' coupling that represents a straightforward identification of the wavemaker region, and can be also viewed as a feedback induced by an actuator located at the same station as the sensor.

3. Results

The FreeFem++ software (*http://www.freefem.org*) is used to generate the triangulation with the Delaunay-Voronoi algorithm. The mesh refinement is controlled by the vertex densities on both external and internal boundaries. A schematic of the mesh structure is depicted in Fig. 1 in the case of the sphere, the mesh structure being similar in the

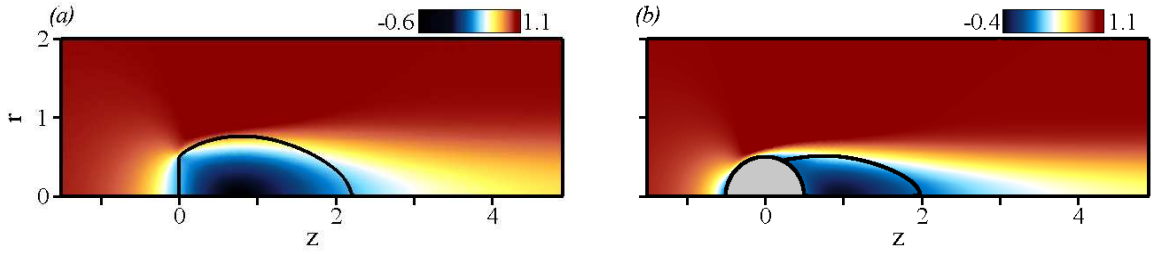

Fig. 2. Base flow at the threshold of the first instability. Iso contours of streamwise velocity w^0. The solid line indicates the separated bubble. (a) Disk at $Re_A = 116.9$. (b) Sphere at $Re_A = 212.6$.

case of the disk, except that for computational reasons, the width of the disk L can not be chosen strictly equal to zero, so that we have used the smallest possible value, corresponding to an aspect ratio $L/D = 10^{-3}$. To avoid any computational difficulty, a zone of width 0.05 and high vertex density (250 vertex per unit length) is defined at the axis $r = 0$ and around the body, corresponding to the shaded area shown in Fig. 1. The base flow equations, as well as the direct (5) and adjoint (11) generalized eigenvalue problems are numerically solved by a finite-element method, using the same mesh. The unknown velocity and pressure fields are spatially discretized using a basis of Taylor-Hood elements, i.e. P2 elements for velocities and P1 elements for pressure. All equations are first multiplied by r to avoid the singularity on the $r = 0$ axis. The associated variational formulation is then derived and spatially discretized on the mesh composed of triangular elements. The sparse matrices resulting from the projection of the variational formulations onto the basis of finite elements are built with the FreeFem++ software. The matrix inverses are then computed using the UMFPACK library, which consists in a sparse direct LU solver [7, 8].

Base flow For all the Reynolds numbers Re considered in this study, the base flow is stable to axisymmetric stationary perturbations, and time-marching a direct numerical simulation of equations (1), with imposed axisymmetry and required boundary conditions provides us with an approximate guess solution of the steady base flow $\boldsymbol{q^0}$. The steady base flow $\boldsymbol{q^0}$ solution of the nonlinear equations (2) is then obtained using an iterative Newton method involving the resolution of simple linear problems. Details of the numerical method may be found in [3] and [22]. In the present study, the iterative process is carried out until the $\mathcal{L}^2$-norm of the residual of the governing equations for $\boldsymbol{q^0}$ becomes smaller than 10^{-12}. Fig. 2(a) shows iso contours of the base flow streamwise velocity w^0 computed for the disk at $Re = 116.9$. The solid line is the streamline linking the separation point to the stagnation point on the $r = 0$ axis, it defines the separatrix delimiting the recirculation bubble behind the disk. The negative values of the streamwise velocity close to the axis reaches 60 % of the free-stream velocity, whereas in the case of the sphere, shown in Fig. 2(b) for $Re = 212.6$, this value does not exceed 40 %. In order to assess the accuracy of the numerical method, the drag coefficient C_d and recirculation length L were computed for the sphere wake. The values obtained at $Re = 100$ ($L = 1.369$, $C_d = 1.087$) and $Re = 200$ ($L = 1.934$, $C_d = 0.770$) show excellent agreement with the calculations obtained by Fornberg [11] using finite-difference methods ($L = 1.373$, $C_d = 1.085$ at $Re = 100$ and $L = 1.934$, $C_d = 0.768$ at $Re = 200$, respectively).

Stability analysis To compute the leading eigenvalues of operators $\mathcal{A}_1$ and $\mathcal{A}_1^\dagger$, which are responsible for the successive instabilities, we use a shift and invert strategy [9].

The generalized eigenvalue problems are solved using the 'Implicitly Restarted Arnoldi method' of the ARPACK library.

Since the adjoint problem (11) has been formulated for continuous operators with associated adjoint boundary conditions, the spatial discretization of operators $\mathcal{A}_1$ and $\mathcal{A}_1^\dagger$ leads to discrete operators that are not hermitian one to the other because the operator $\mathcal{B}$ involved in the right-hand side of problems (5) and (11) does not correspond to the scalar product in cylindrical coordinates. We check a posteriori that the adjoint eigenvalues are complex conjugate with the direct eigenvalues and that a bi-orthogonality relation [5], is satisfied for the 10 leading global modes (i.e. that the scalar product of one of the 10 leading adjoint modes with any of the 10 leading direct global modes associated to a different eigenvalue is less that 10^{-8}) , and conclude that our numerical procedure accurately estimates the direct and adjoint global modes.

Direct global modes are normalized by imposing the phase of the radial velocity to be zero at a particular location, i.e. $\hat{u}^1(0,1)$ must be real positive. The eigenmode energy is then normalized to unity in a fixed domain Ω_{in} defined arbitrarily as $z \in [-2.5, 5.25]$ and $r < 2$ and corresponding to the inner box in Fig. 1: $\langle \hat{\boldsymbol{q}}^{\boldsymbol{1}}, \delta_{in}\mathcal{B}\hat{\boldsymbol{q}}^{\boldsymbol{1}} \rangle = 1$ with δ_{in} the function defined by $\delta_{in}(r,z) = 1$ if $(r,z) \in \Omega_{in}$ and 0 otherwise. The adjoint global modes are then normalized so that $\left\langle \hat{\boldsymbol{q}}^{\boldsymbol{1\dagger}}, \mathcal{B}\hat{\boldsymbol{q}}^{\boldsymbol{1}} \right\rangle = 1$. Note that owing to the symmetries of the problem, equations (5) and (12) remain invariant under the transformation $(\hat{u}^1, \hat{v}^1, \hat{w}^1, \hat{p}^1, m) \rightarrow (\hat{u}^1, -\hat{v}^1, \hat{w}^1, \hat{p}^1, -m)$, so that we need to investigated only the case $m = 1$.

Stationary global mode When the Reynolds number is increased from small values, a first stationary mode ($\omega = 0$) destabilizes the axisymmetric base flow at Re_A, both for the disk and the sphere. In the following, this mode is named mode A and the corresponding eigenvector is referred to $\hat{\boldsymbol{q}}^{\boldsymbol{1}}_{\boldsymbol{A}}$. The critical Reynolds number is $Re_A = 116.9$ for the disk and $Re_A = 212.6$ for the sphere. Fig. 3(a) shows the spatial structure of the streamwise velocity component $\hat{w}^1_A$ for the disk. The global mode is dominated by axially extended streamwise velocity disturbances located downstream of the disk, that induce an off-axis displacement of the wake [14, 23]. The associated adjoint global mode $\hat{\boldsymbol{q}}^{\boldsymbol{1\dagger}}_{\boldsymbol{A}}$ is presented in Fig. 3(b). The adjoint global mode presents high magnitudes of adjoint streamwise velocity $\hat{w}^{1\dagger}_A$ within the recirculating bubble and close to the body, and low magnitude disturbances upstream of the disk. The downstream and upstream localizations of the direct and adjoint global modes resulting from the convective nonnormality of the linearized Navier-Stokes operator are further evidenced on Fig. 3(c) and 3(d). Fig. 3(c) shows the streamwise evolution of the amplitude of the direct global modes, computed as the density energy integrated over a vertical cross-section for each streamwise position, i.e. $E_A(z) = \int_0^{r\infty} |\hat{\boldsymbol{u}}^{\boldsymbol{1}}_{\boldsymbol{A}}(r,z)|^2 r\mathrm{d}r$, as well as the contribution of the streamwise velocity to this amplitude $E_A(z)$, i.e. $S_A(z) = \int_0^{r\infty} |\hat{w}^1_A(r,z)|^2 r\mathrm{d}r$. The direct mode is nil upstream of the body, reaches a maximum in the recirculating bubble, and decreases slowly downstream of the body. The contribution of the streamwise velocity to the direct global mode dominates the entire field. Fig. 3(d) shows similarly the streamwise distribution of energy density for the adjoint global mode, i.e. $E^\dagger_A(z) = \int_0^{r\infty} |\hat{w}^{1\dagger}_A(r,z)|^2 r\mathrm{d}r$, as well as the contribution of the cross-stream velocity components to this amplitude $E^\dagger_A(z)$, i.e. $C^\dagger_A(z) = \int_0^{r\infty} (|\hat{u}^{1\dagger}_A|^2 + |\hat{v}^{1\dagger}_A|^2) r\mathrm{d}r$. The adjoint global mode vanishes downstream of the body, reaches a maximum in the recirculating area. Upstream of the body, its energy density is two orders of magnitude smaller than in the recirculation bubble and decreases exponentially. In regions of the flow where the amplitude of the adjoint global mode is larger than 10^{-1}, in particular in the whole recirculating bubble, the contribution of the cross-stream velocity components to the

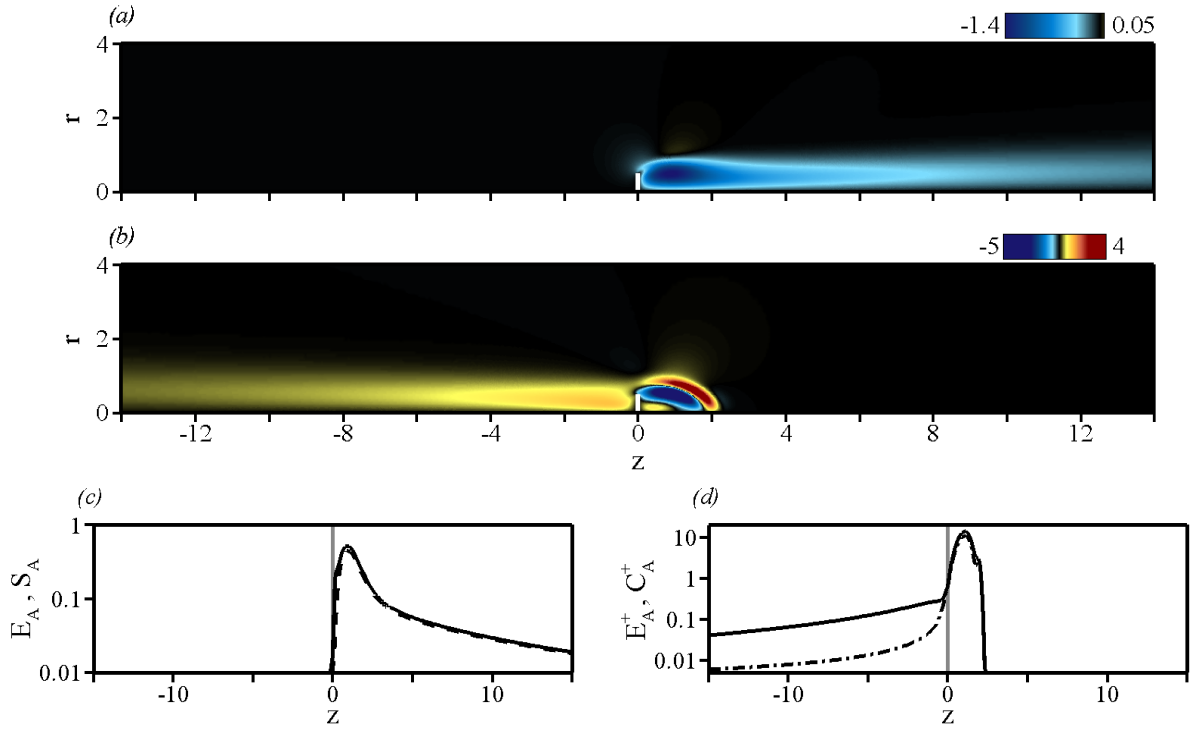

Fig. 3. Steady direct and adjoint global modes A for the disk at threshold - $Re_A = 116.9$. (a) Spatial distribution of streamwise velocity $\hat{w}_A^1$. (b) Spatial distribution of adjoint streamwise velocity $\hat{w}_A^{1\dagger}$. (c) Streamwise distribution of energy density $E_A(z)$ for the direct global mode. The dashed line shows the contribution $S_A(z)$ of the streamwise velocity component to the energy $E_A(z)$. The vertical grey line marks the position of the separation point. (d) Streamwise distribution of energy density $E_A^\dagger(z)$ for the adjoint global mode. The dash-dotted line shows the contribution of the adjoint cross-stream velocity components $C_A^\dagger(z)$ to the energy $E_A^\dagger(z)$. The vertical grey line marks the position of the separation point.

adjoint global mode dominates the adjoint field. For this first unstable mode A, the direct and adjoint global modes are concentrated on different components of the velocity vector, the streamwise and cross-stream velocity components, respectively, suggesting that the lift-up mechanism plays a significant role in the dynamics of the stationary mode. Furthermore, the direct and adjoint global modes are mainly localized in the recirculation, with respectively downstream and upstream tails showing the influence of the convective nonnormality which, for the present flow, is moderate since the amplitude are small away from the recirculation bubble. The nonnormality may be quantified by the angle θ_A defined as

$$\cos\left(\frac{\pi}{2} - \theta_A\right) = \frac{\langle \hat{\boldsymbol{q}}_{\boldsymbol{A}}^{\boldsymbol{1\dagger}}, \mathcal{B}\hat{\boldsymbol{q}}_{\boldsymbol{A}}^{\boldsymbol{1}} \rangle}{\langle \hat{\boldsymbol{q}}_{\boldsymbol{A}}^{\boldsymbol{1\dagger}}, \mathcal{B}\hat{\boldsymbol{q}}_{\boldsymbol{A}}^{\boldsymbol{1\dagger}} \rangle \times \langle \hat{\boldsymbol{q}}_{\boldsymbol{A}}^{\boldsymbol{1}}, \mathcal{B}\hat{\boldsymbol{q}}_{\boldsymbol{A}}^{\boldsymbol{1}} \rangle}, \tag{15}$$

with $\langle \hat{\boldsymbol{q}}_{\boldsymbol{A}}^{\boldsymbol{1\dagger}}, \mathcal{B}\hat{\boldsymbol{q}}_{\boldsymbol{A}}^{\boldsymbol{1}} \rangle = 1$ by convention here. The nonnormality is thus measured by the departure θ_A to $\pi/2$ of the angle between the direct and adjoint global modes, i.e. the larger the nonnormality, the smaller θ_A.

We define the streamwise amplitude of a complex velocity fields $\hat{\boldsymbol{u}}(r,z)$ as the norm $||\hat{\boldsymbol{u}}||_L^2(z) = \int_0^{r_\infty} |\hat{\boldsymbol{u}}|^2 r dr$. We propose to quantify the contribution of the convective non-

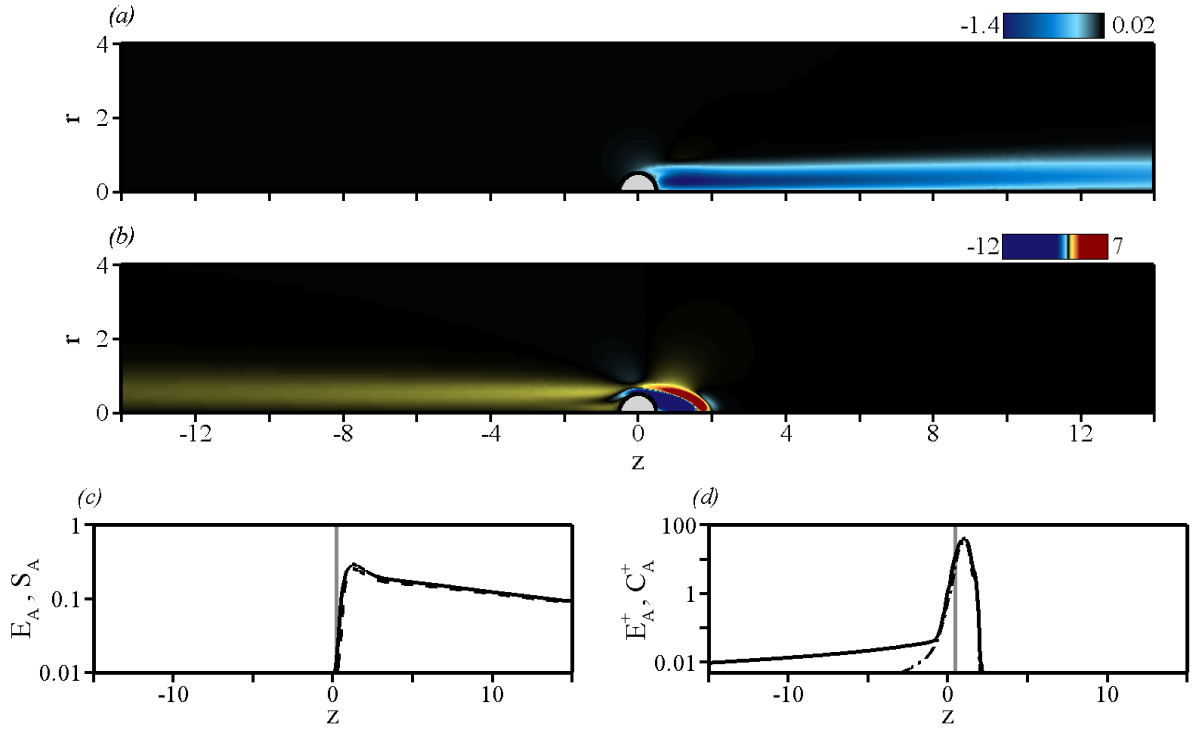

Fig. 4. Same as Fig. 3 for the stationary direct and adjoint global modes A of the sphere - $Re_A = 212.6$.

normality to the overall nonnormality by considering the parameter γ defined by

$$\gamma = 1 - \frac{\int_{z_{-\infty}}^{z_\infty} ||\hat{\boldsymbol{u}}^{\mathbf{1}}||_L \times ||\hat{\boldsymbol{u}}^{\mathbf{1}\dagger}||_L \mathrm{d}z}{\left(\int_{z_{-\infty}}^{z_\infty} ||\hat{\boldsymbol{u}}^{\mathbf{1}}||_L^2 \mathrm{d}z\right)^{1/2} \times \left(\int_{z_{-\infty}}^{z_\infty} ||\hat{\boldsymbol{u}}^{\mathbf{1}\dagger}||_L^2 \mathrm{d}z\right)^{1/2}} = 1 - \frac{\int_{z_{-\infty}}^{z_\infty} ||\hat{\boldsymbol{u}}^{\mathbf{1}}||_L \times ||\hat{\boldsymbol{u}}^{\mathbf{1}}||_L \mathrm{d}z}{\langle \hat{\boldsymbol{q}}_{\boldsymbol{A}}^{\mathbf{1}\dagger}, \mathcal{B}\hat{\boldsymbol{q}}_{\boldsymbol{A}}^{\mathbf{1}\dagger}\rangle^{1/2} \times \langle \hat{\boldsymbol{q}}_{\boldsymbol{A}}^{\mathbf{1}}, \mathcal{B}\hat{\boldsymbol{q}}_{\boldsymbol{A}}^{\mathbf{1}}\rangle^{1/2}}\,. \tag{16}$$

Using a standard Cauchy-Schwartz inequality, it can be shown that $0 \leq \gamma \leq 1$. A value of γ close to 0 is reached if $||\hat{\boldsymbol{u}}_{\boldsymbol{A}}^{\mathbf{1}}||_L = \alpha||\hat{\boldsymbol{u}}_{\boldsymbol{A}}^{\mathbf{1}\dagger}||_L$ meaning that the direct and adjoint global modes have the same spatial distribution of energy. In that case, the convective nonnormality is not active since it would imply a dissymmetry in the distribution of the direct and adjoint modes. On the contrary , a value of γ close to 1 means that the direct and adjoint global modes are spatially separated. For the disk, we find presently that $\theta_A = 0.17$ (10°) and $\gamma_A = 0.40$, meaning that the nonnormality of mode A is moderate and due to the convective nonnormality at most at 40 %, which confirms the importance of the lift-up mechanism.

Fig. 4 shows the marginally stable stationary mode A and its adjoint global mode for the sphere. The general dynamics is identical to that described on Fig. 3 in the case of the disk, indicating that the instability results from similar physical mechanisms in both flows. The direct mode is led by the streamwise velocity component downstream of the sphere and the adjoint global mode is even more concentrated in the recirculation bubble, reaching a maximum just downstream of the separation point marked by the vertical grey line in Fig. 4(c) and 4(d). The cross-stream velocity components dominate in the recirculating area. In the case of the sphere, the energy density of the direct global mode decays downstream slower than in the case of the disk and the adjoint mode presents a weaker upstream energy density. At the separation point, the adjoint global mode exhibits

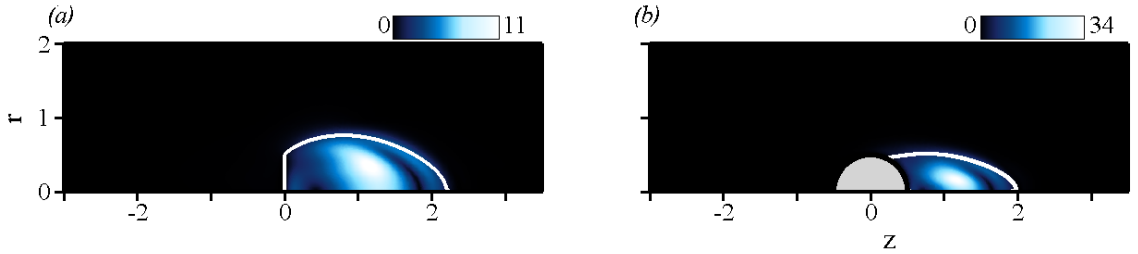

Fig. 5. Receptivity to local modifications of the linearized evolution operator (local 'force-velocity' coupling [13]) for the stationary mode A, quantified by the field $|\hat{\boldsymbol{u}}_{\boldsymbol{A}}^{\boldsymbol{1\dagger}}| \times |\hat{\boldsymbol{u}}_{\boldsymbol{A}}^{\boldsymbol{1}}|(r,z)$. (a) Disk at Re_A=116.9. (b) Sphere at $Re_A = 212.6$.

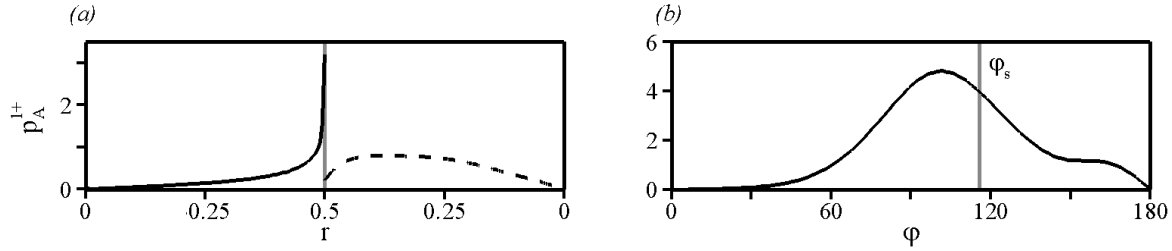

Fig. 6. Receptivity of the global mode A to blowing and suction: adjoint pressure distribution on the wall of the body for the stationary instability - (a) as a function of the radius for the disk at $Re_A = 116.9$. The solid line corresponds to the upstream wall of the disk and the dashed line to the downstream wall. (b) as a function of the angle from the leading stagnation point for the sphere at $Re_A = 212.6$. The vertical grey line marks the position of the separation point.

an energy density larger by one order of magnitude than that found for the disk. The nonnormality of the sphere, as quantified by $\theta_A = 0.07$ (4°), is significantly larger than that of the disk. The contribution of the convective nonnormality evaluated by γ_A is 0.76, and is also more important than in the case of the disk. This shows that the wake of the sphere is more receptive to initial perturbation or forcing (both being $m = 1$ stationary), in particular close to the separation line.

The magnitude of the product between the modulus of the direct and adjoint global modes is shown for the disk and the sphere in Fig. 5(a) and 5(b), where the white solid lines stand for the separation lines. For both bodies, the product is almost nil everywhere in the flow, except close to the body, along the separation line, and in the center of the recirculation bubble where the largest values are reached. This specific spatial localization results from the convective nonnormality that induces the downstream and upstream localizations of the direct and adjoint global modes. The similarity in the results for the disk and the sphere suggests the existence of a single wavemaker for this instability for both shapes of bodies, located in the core of the recirculation. Following the argument of Giannetti & Luchini [13], passive control of the stationary $m = 1$ eigenmode should induce modifications of the base flow close to the core of the recirculation to achieve a maximum stabilizing or destabilizing effect. As already commented, the sensitivity quantified on Fig. 5 is rigorously for a local 'force-velocity' coupling [13], i.e. the effect of a local body force actuation proportional to the signal of a velocity sensor located at the exact same station. By extrapolation, it describes the effect of a steady base flow modification but only qualitatively since the modified advection operator involves also the gradients of the perturbation velocity. Note that in the recirculating bubble, the sphere exhibits a 'force-velocity' sensitivity larger than that of the disk, suggesting that the wake of the sphere

would be more controlable through the use of passive devices.

Fig. 6(a) and 6(b) present the distributions of the magnitude of adjoint pressure $\hat{p}_A^{1\dagger}$ on the body walls, which, following relation (14), quantifies the receptivity to a stationary $m = 1$ blowing and suction. For the disk, results are presented as a function of the radial position r, on the upstream and downstream walls of the body, corresponding to the solid and dashed lines, respectively. The upstream wall exhibits significantly larger receptivity to blowing and suction than the downstream wall. Moreover, the upstream adjoint pressure distribution increases significantly close to the separation point, where the maximum value is reached. Therefore, in the case of active control, an actuator that imposes a stationary $m = 1$ blowing and suction, will achieve maximum efficiency if placed at the edge of the forward facing side of the disk. One may note that a small permanent tilt of the disk corresponds to a small $m = 1$ wall displacement that may be modelled as an equivalent blowing and suction of magnitude proportional to the distance to the axis, and may therefore force efficiently the stationary mode A.

For the sphere, results are presented as a function of the azimuthal position φ, the origin of φ being taken at the leading stagnation point $(-0.5, 0)$. The vertical grey line is located at the separation point, corresponding to $\varphi_s = 116°$. The adjoint pressure $\hat{p}_A^{1\dagger}$ is zero on the axis, owing to the boundary conditions. The magnitude of adjoint pressure reaches a maximum for $\varphi = 102°$, upstream from the separation point. The level then decreases slowly as one moves away from this optimal position, the magnitude of adjoint pressure remaining significant in the range $\varphi \in [80°, 130°]$. The adjoint pressure level decreases upstream and becomes zero at the leading stagnation point. The main difference with the disk is that the region where the $m = 1$ blowing and suction is efficient is extremely extended with large receptivity values everywhere, except close to the stagnation points. Therefore, for the sphere, the actuator would be slightly more efficient if placed just upstream from the separation (and not at the separation) but its precise location is less important. In contrast, controlling the disk wake will be efficient solely if the actuator is precisely positioned.

As mentioned previously, the adjoint global mode also represents the most *dangerous* initial velocity perturbation, since for a fixed initial energy of the perturbation, it maximizes the large-time amplitude of the direct mode A. The effect of the optimal initial perturbation may be physically interpreted by considering the flow reconstructed as the linear superposition of the base flow $\boldsymbol{q^0}$ and the adjoint global mode $\boldsymbol{\hat{q}_A^{1\dagger}}$ with a finite amplitude ϵ. For the disk, ϵ is chosen equal to 1.7×10^{-2} so that the maximum streamwise velocity perturbation represents 10 % of the maximum streamwise velocity w^0_{max}. Fig. 7(a) and 7(b) show the streamlines of the adjoint global mode in the region of the separation point in the azimuthal planes $\theta = 0$ and $\theta = \pi$. The black and grey solid lines stand for the separation line of the base flow and of the total flow $\boldsymbol{q^0} + \epsilon\boldsymbol{\hat{q}_A^{1\dagger}}$, respectively. The levels of adjoint velocity amplitude are indicated by the color shading, where dark regions stand for high perturbation velocities. Close to the separation point, the streamlines are normal to the separation line, and oriented upstream (resp. downstream) for $\theta = 0$ (resp. $\theta = \pi$). Consequently, the separation line is tilted upstream and downstream as we move along in the azimuthal direction, the extremity of the line remaining pinned at the disk rime. The optimal initial perturbation corresponds therefore to a stationary azimuthal modulation of the separation angle with respect to that of the base flow. In the case of the sphere, owing to the larger receptivity of the wake, ϵ is chosen much smaller ($\epsilon = 6.5 \times 10^{-4}$) so that the maximum streamwise velocity perturbation represents 5 % of the maximum streamwise velocity w^0_{max}. Fig. 7(c) and 7(d) show that the streamlines of the optimal initial perturbation are parallel to the sphere surface, and induce a displacement with no tilt of the separation line, in agreement with the physical intuition that the separation

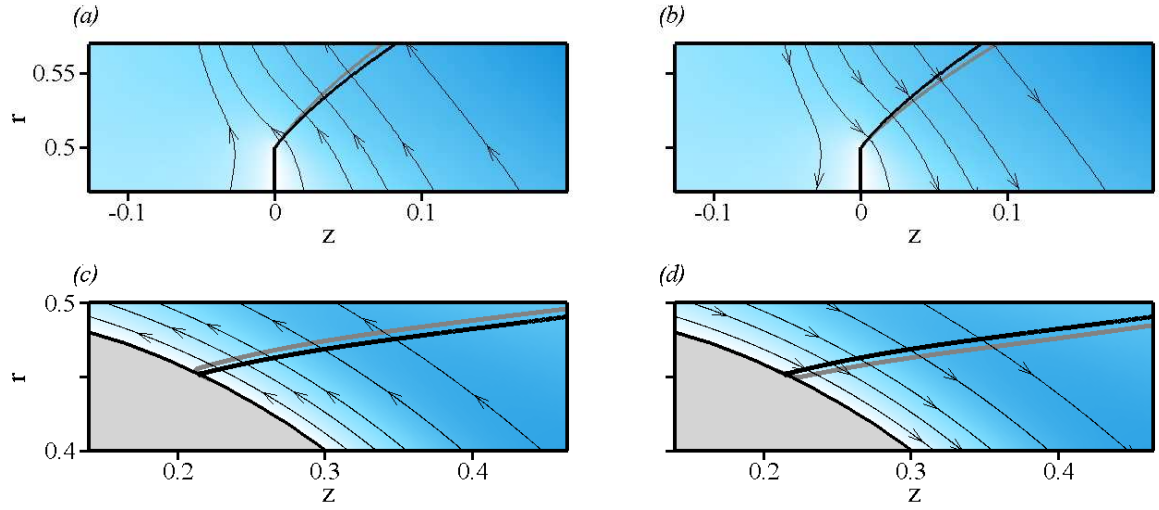

Fig. 7. Optimal initial perturbation for the stationary instability. The black and grey solid lines stand for the separation line of the base flow and of the total flow $\boldsymbol{q^0} + \epsilon \hat{\boldsymbol{q}}_{\boldsymbol{A}}^{\boldsymbol{1\dagger}}$, respectively. (a) Disk at $Re_A = 116.9$: magnified view of the adjoint velocity field $\hat{\boldsymbol{u}}_{\boldsymbol{A}}^{\boldsymbol{1\dagger}}$ close to the separation in the azimuthal plane $\theta = 0$. Blue and white regions correspond respectively to large and low values of the adjoint velocity magnitude, its orientation being shown by the streamlines. (b) Same as (a) but for $\theta = \pi$. $(c) - (d)$ Same as $(a) - (b)$ for the sphere at $Re_A = 212.6$.

line is no more pinned by the bluff geometry of the body. The separation point is hence displaced upstream and downstream, so that the optimal initial perturbation, given by the adjoint global mode, corresponds to a stationary displacement of the separation point in the streamwise direction which ondulates in the azimuthal direction.

Oscillating global mode The second instability occurs at Re_B for an oscillating mode of frequency $\omega = \omega_0$. The associated mode is named mode B and the corresponding eigenvector is referred to as $\hat{\boldsymbol{q}}_{\boldsymbol{B}}^{\boldsymbol{1}}$. The critical Reynolds numbers and frequency are $Re_B = 125.3$, $\omega_0 = 0.760$ for the disk and $Re_B = 280.7$, $\omega_0 = 0.699$ for the sphere, the corresponding Strouhal numbers $St = \omega_0 D/(2\pi U_\infty)$ being 0.121 and 0.111, respectively. Fig. 8(a) and 9(a) show the spatial structure of the streamwise velocity $\hat{w}_B^1$ at the instability threshold for the disk and the sphere. Since the frequency is not zero, the eigenmode $\hat{\boldsymbol{q}}_{\boldsymbol{B}}^{\boldsymbol{1}}$ is complex but we restrict the description to the real part $\hat{\boldsymbol{q}}_{\boldsymbol{Br}}^{\boldsymbol{1}}$ of the eigenvector, as its imaginary part displays a similar structure, but approximately in spatial quadrature, indicating that this global mode B corresponds to a spiralling perturbation behind the body, which rotates in time at the frequency ω_0. Note that because of the symmetries of the problem, the mirror spiral mode rotating in time at the same frequency but in the opposite azimuthal direction also destabilizes the base flow. The general dynamics is identical for the disk and the sphere, the direct modes B exhibiting periodic positive and negative velocity perturbations downstream of the body. The adjoint global modes B are shown in Fig. 8(b) and 9(b). Again, we discuss only the real part of the eigenvector $\hat{\boldsymbol{q}}_{\boldsymbol{Br}}^{\boldsymbol{1\dagger}}$, as its imaginary part displays a similar structure in spatial quadrature. The localization of the adjoint global mode B is similar to that of the adjoint global mode A discussed above. For the disk and the sphere, the oscillating adjoint global modes B exhibit large streamwise velocities $\hat{w}_B^{1\dagger}$ within the recirculating area and close to the body. They also display velocity disturbances upstream of the disk and the sphere under the form of low magnitude periodic

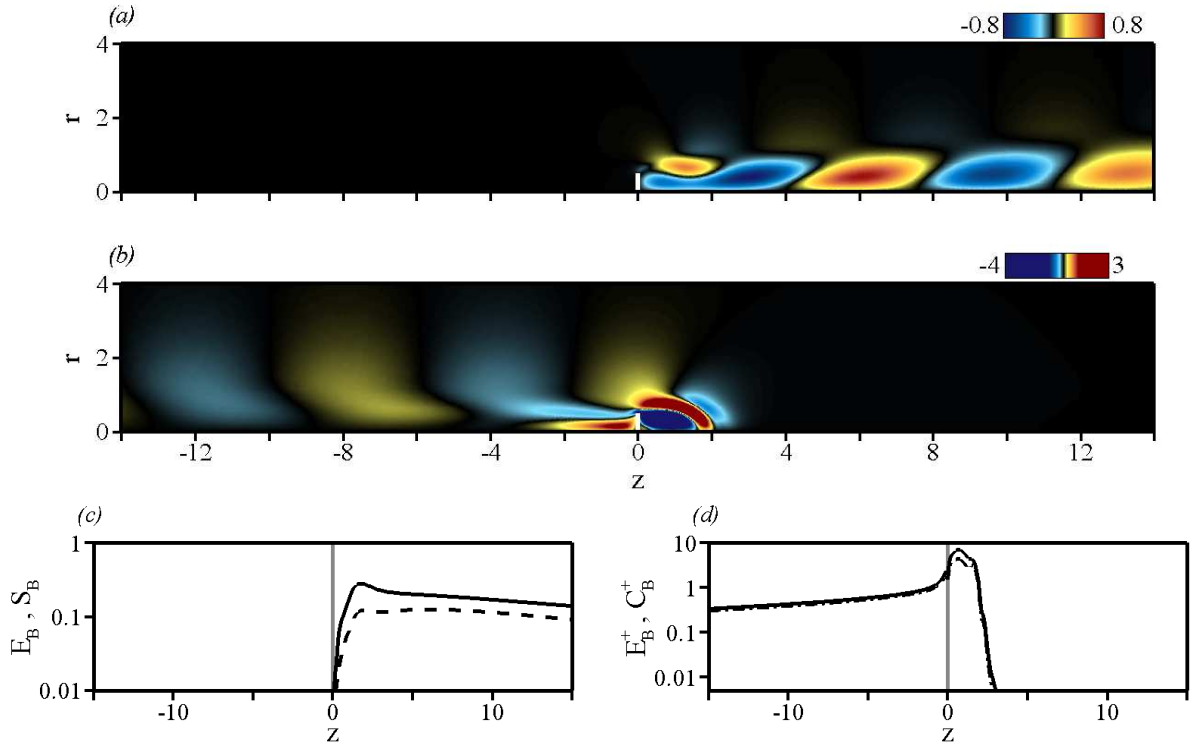

Fig. 8. Same as Fig. 3 for the oscillating instability of the disk - $Re_B = 125.3$.

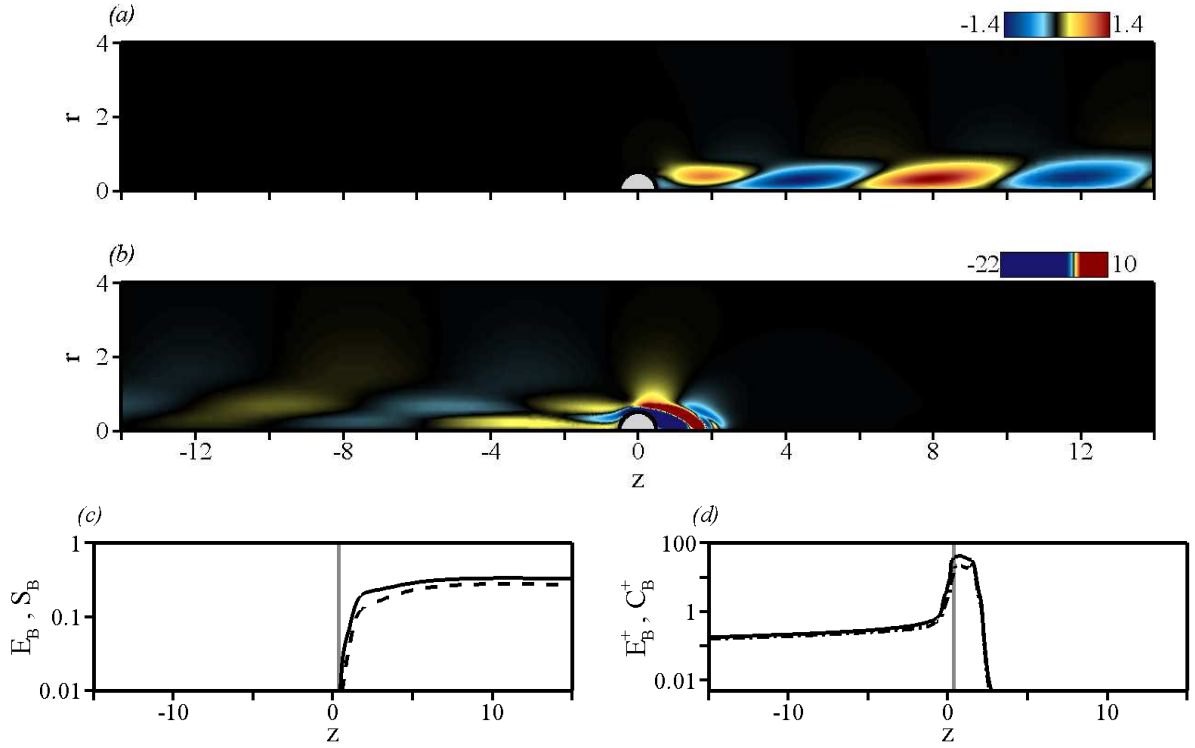

Fig. 9. Same as Fig. 3 for the oscillating instability of the sphere - $Re_B = 280.7$.

structures, visible despite their low amplitude by an appropriate choice of the color look-

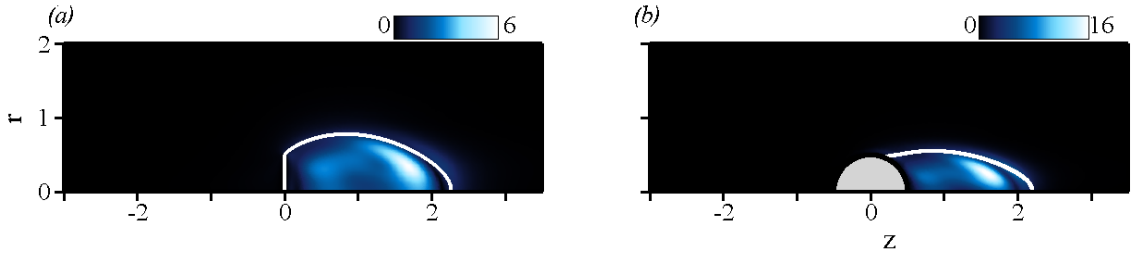

Fig. 10. Same as Fig. 5 for the oscillating mode B. (a) Disk at $Re_{ch} = 125.3$. (b) Sphere at $Re_{ch} = 280.7$.

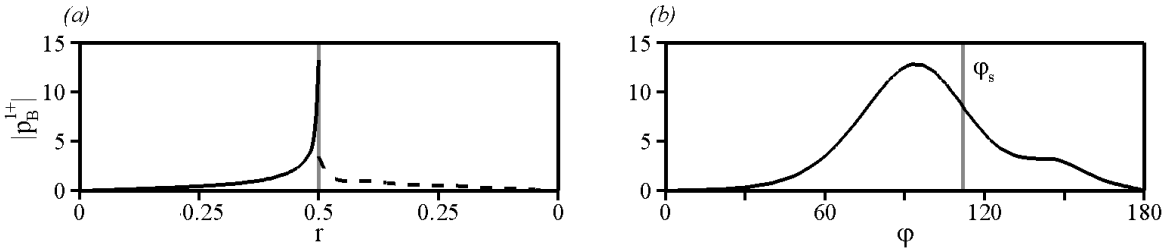

Fig. 11. Same as Fig. 6 for the oscillating mode B. (a) Disk at $Re_B = 125.3$. (b) Sphere at $Re_B = 280.7$.

up table in Fig. 8(b) and Fig. 9(b). Note that the absolute magnitude of these structures is slightly larger in the case of the sphere compared to the disk. The downstream and upstream localizations of the direct and adjoint global modes are further evidenced on Fig. 8(c) and 8(d) for the disk and on Fig. 9(c) and 9(d) for the sphere. Fig. 8(c) and 9(c) show the streamwise distribution of energy density $E_B(z)$ of the direct global modes (solid line), as well as the contribution of the streamwise velocity $S_B(z)$ to this energy (dashed line). We find that the direct mode is evanescent upstream of the body and reaches a maximum in the recirculating area. The downstream evolution differs between the disk, where the energy density decreases slowly, and the sphere, where the fluctuations keep increasing downstream. Fig. 8(d) and 9(d) show similarly the streamwise distribution of energy density $E_B^\dagger(z)$ of the adjoint global mode (solid line), as well as the contribution of the cross-stream velocity components $C_B^\dagger(z)$ to this energy (dash-dotted line). The adjoint global mode vanishes downstream of the body, reaches a maximum in the recirculating area and decreases steadily upstream of the body. In the vicinity of the separation point, the contribution of the cross-stream velocity components to the adjoint global mode dominates. For both geometries, the contribution of streamwise velocity no more dominates the entire direct field, so that the contribution of the lift-up mechanism to the structure of the direct global mode B is less important than for the stationary global mode A. It can be seen comparing Fig. 8(d) and 9(d) that in the case of the sphere, the oscillating adjoint global mode B exhibits an amplitude close to the separation point larger by almost one order of magnitude than that found for the disk. The overall nonnormality is important as we find here that $\theta_B = 0.07$ (4°) for the disk and 0.02 (1°) for the sphere. This indicates that the oscillating global modes B are more receptive to initial perturbation or forcing than the stationary global modes A, the wake of the sphere being more receptive than that of the disk. We find for the convective nonnormality parameter $\gamma_B = 0.88$ for the disk and 0.94 for the sphere. These values are significantly more important than in the case of the stationary global mode A, suggesting that the overall nonnormality is almost entirely due to the convective nonnormality resulting in the streamwise separation of the direct and adjoint global modes.

The magnitude of the product between the modulus of the direct and adjoint global modes is shown for the disk and the sphere in Fig. 10(a) and 10(b). The similarity between both flows suggests, for mode B also, the existence of a single physical mechanism for the oscillating instability, with the recirculating bubble acting as the wavemaker. The results are somehow reminiscent of that discussed for the first stationary instability of mode A, with a product almost nil everywhere in the flow, except within the recirculation. However, comparing to mode A, the largest values are reached along the separation line and no more in the core of the recirculation. This suggests that shear instability is the physical mechanism responsible for the development of spiral modes B. In the case of passive control, the base flow modifications should therefore be induced close to the separation line to achieve maximum efficiency. Note that in the recirculating area, the sphere exhibits an amplitude significantly larger than that of the disk, indicating that the wake of the sphere is more sensitive to local modifications of the evolution operator.

In the case of the boundary control of the oscillating instability, relation (14) indicates that only the magnitude of adjoint pressure $|\hat{p}_B^{1\dagger}|$ determines the receptivity of the global mode, whereas the individual real and imaginary parts $\hat{p}_{Br}^{1\dagger}$ and $\hat{p}_{Bi}^{1\dagger}$ are useful to predict the phase of the response of the forced global mode relative to that of the oscillating wall forcing. Fig. 11(a) and 11(b) present the distributions of the magnitude of adjoint pressure $|\hat{p}_B^{1\dagger}|$ on the body walls. The distributions are amazingly similar to that found for the stationary instability. For the disk, the magnitude is larger on the upstream wall where the adjoint pressure distribution increases significantly at the edge. For the sphere, the magnitude of adjoint pressure is maximum for $\varphi = 86°$, upstream from the separation point located at $\varphi_s = 112°$. It decreases slowly as one moves away from this optimal position, the magnitude of adjoint pressure remaining significant in the range $\varphi \in [75°, 115°]$. Therefore, in the case of active control, an actuator that imposes a periodic $m = 1$ blowing or suction at the frequency ω_0 should be placed at the rime on the forward facing side of the disk, and upstream from the separation in the case of the sphere to be most efficient. Similarly to the results obtained for the stationary instability of mode A, one may achieve good efficiency by moving the actuator position around the separation point of the sphere, as the region of receptivity is quite large. The main difference between both instabilities is that the magnitude of adjoint pressure levels are higher for the oscillating instability of mode B. Therefore, one may expect that the control of the oscillating instability will be less expensive than that of the stationary instability, i.e. that one will obtain the same amplitude of forced global mode by introducing less energy in the flow.

Finally, as for the stationary mode A, we investigate the physical interpretation of the oscillating adjoint global mode interpreted as the optimal initial perturbation. For a time $t = 0$, we reconstruct the linear superposition of the base flow $\boldsymbol{q^0}$ and the adjoint global mode $\hat{\boldsymbol{q}}_{\boldsymbol{B}}^{\boldsymbol{1\dagger}}$ with a finite amplitude ϵ. Similar to the stationary instability, $\epsilon = 2.4 \times 10^{-2}$ for the disk and $\epsilon = 4.9 \times 10^{-4}$ for the sphere, so that the maximum streamwise velocity perturbation represents 10 % of the maximum streamwise velocity w_{max}^0 in the case of the disk, and 5 % in the case of the sphere. Fig. 12 shows the streamlines of the adjoint global mode in the region of the separation point in the azimuthal planes $\theta = 0$ and $\theta = \pi$ at time $t = 0$. The black and grey solid lines stand for the separation line of the base flow and of the total initial flow $\boldsymbol{q^0} + \epsilon \hat{\boldsymbol{q}}_{\boldsymbol{Br}}^{\boldsymbol{1\dagger}}$, respectively. Results are similar to that obtained for mode A. In the case of the disk, the optimal initial perturbation corresponds to a periodic tilting of the separation line around the fixed separation point. In the case of the sphere, it corresponds to a displacement of the separation point along the sphere surface. Finally, it can be seen comparing Fig. 7(a) and 12(a), or Fig. 7(c) and 12(c), for instance, that for the same amount of perturbation, we obtain a larger deformation of the recirculation

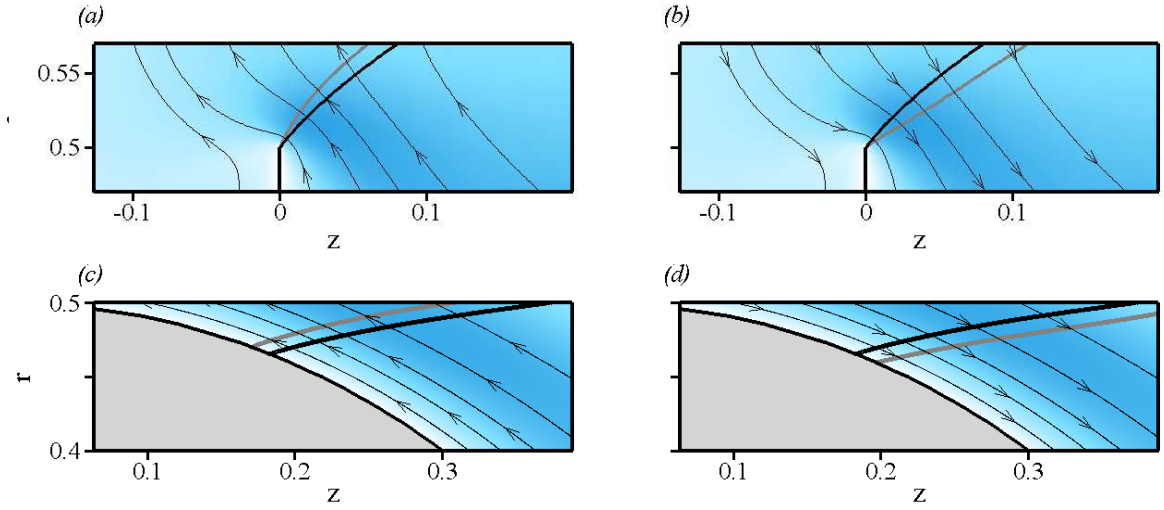

Fig. 12. Same as Fig. 7 for the oscillating mode B. $(a)-(b)$ Disk at $Re_B = 125.3$. $(c)-(d)$ Sphere at $Re_B = 280.7$.

in the case of the oscillating instability, owing to the larger receptivity of the associated global modes.

4. Conclusion

In this study, we have investigated the linear dynamics of the steady axisymmetric flow past an axisymmetric body. Two cases, the disk and the sphere, modelling characteristic geometries of blunt and bluff bodies, have been considered. A linear global stability analysis has been carried out, whose results show good agreement with that of Natarajan & Acrivos [17]. A first instability occurs for a stationary global mode A of azimuthal wavenumber $m = 1$. The adjoint global mode A associated to this direct global mode has been computed and the physical effect of this optimal perturbation on the recirculation area is to modulate the separation angle around the disk edge or to displace the separation point along the sphere surface with no tilting of the separation line. The spatial separation of the direct and adjoint global modes has been interpreted as a result of the convective nonnormality, resulting from the transport of the perturbations by the base flow. Downstream from the body, the direct global mode A is dominated by the streamwise velocity component and in the recirculating bubble, and the adjoint global mode A by the cross-flow components, which suggests that a lift-up mechanism is involved in the energy production of the instability. A second instability occurs for an oscillating global mode B of azimuthal wavenumber $m = 1$. The associated adjoint global mode B has been computed and the physical effect on the recirculation area has been shown to be, as for mode A, a periodic rotation of the separation line at the disk edge or a periodic translation of the separation point along the sphere surface. For both bodies and both instabilities, a detailed analysis of the adjoint global modes has allowed to identify different regions of the flow that are of particular interest in the perspective of control. The recirculation, more specifically the vicinity of the separation point, is where all global modes are most receptive to initial perturbations and forcing of azimuthal wavenumber $m = 1$. As discussed in Giannetti & Luchini [13], considering the overlapping of the direct and adjoint global modes A and B, the wavemakers for the stationary and oscillating

instabilities have been identified as being located in the core of the recirculation, and the vicinity of the separation line, respectively. If control is considered, this analysis suggests different locations of the actuator depending on the control method. In the case of passive control acting through steady, axisymmetric modifications of the base flow, the actuator should be placed so as to modify the base flow in the wavemaker region, presently in the recirculating bubble, to obtain a large impact on the dynamics. In the case of active control by blowing and suction at the body wall, the adjoint pressure distributions show that maximum efficiency is achieved placing the actuator precisely at the rime on the upstream face of the disk, and upstream of the separation point for the sphere. However, in the case of the sphere, the receptivity is one order of magnitude larger and the region of receptivity is broad, so that one may achieve good efficiency by moving the position of the sphere actuator around the separation point. Finally, the magnitude of the adjoint pressure are higher for the oscillating mode B than for the stationary mode A. Therefore, one may expect that the control of the oscillating instability requires less energy to be introduced in the flow to achieve the same efficiency.

References

[1] Achenbach, E., 1974. Vortex shedding from spheres. J. Fluid Mech. 62, 209–221.

[2] Auguste, F., Fabre, D., Magnaudet, J., 2007. XVIII$^{\text{ème}}$ congrès français de mécanique. Grenoble, France.

[3] Barkley, D., Gomes, M., Henderson, R., 2002. Three-dimensional instability in flow over a backward-facing step. J. Fluid Mech. 473, 167–190.

[4] Berger, E., Scholz, D., Schumm, M., 1990. Coherent vortex structures in the wake of a sphere and a circular disk at rest and under forced vibrations. J. Fluids Struct. 4, 231–257.

[5] Chomaz, J.-M., 2005. Global instabilities in spatially developing flows: Non-normality and nonlinearity. Annu. Rev. Fluid. Mech. 37, 357–392.

[6] Chomaz, J.-M., Huerre, P., Redekopp, L., 1990. The effect of nonlinearity and forcing on global modes. In: Proc. Conf. on new trends in nonlinear dynamcs and pattern-forming phenomena: The geometry of nonequilibrium. Vol. 237. NATO ASI Series B, Plenum, edited by P. Coulet & P. Huerre, pp. 259–274.

[7] Davis, T. A., 2004. A column pre-ordering strategy for the unsymmetric-pattern multifrontal method. ACM Transactions on Mathematical Software 30 (2), 165–195.

[8] Davis, T. A., Duff, I., 1997. An unsymmetric-pattern multifrontal method for sparse lu factorization. SIAM Journal on Matrix Analysis and Applications 18 (1), 140–158.

[9] Ehrenstein, U., Gallaire, F., 2005. On two-dimensional spatially evolving open flows: the flat-plate 536, 209–218.

[10] Fabre, D., Auguste, F., Magnaudet, J., 2008. Bifurcations and symmetry breaking in the wake of axisymmetric bodies. Phys. Fluids 20 (5), 051702 1–4.

[11] Fornberg, B., 1988. Steady viscous flow past a sphere at high reynolds number. J. Fluid Mech. 190, 471–489.

[12] Fuchs, H., Mercker, E., Michel, U., 1979. Large-scale coherent structures in the wake of axisymmetric bodies. J. Fluid Mech. 93, 185–207.

[13] Giannetti, F., Luchini, P., 2006. Structural sensitivity of the first instability of the cylinder wake. J. Fluid Mech. 581, 167–197.

[14] Johnson, T., Patel, V., 1999. Flow past a sphere up to a reynolds number of 300. J. Fluid Mech. 378, 19–70.

[15] Marquet, O., Lombardi, M., Chomaz, J.-M., Sipp, D., Jacquin, L., 2008. Direct and adjoint global modes of a recirculation bubble: lift-up and convective nonnormalities. J. Fluid Mech. (in press).

[16] Marquet, O., Sipp, D., Jacquin, L., 2008. Sensitivity analysis and passive control of the cylinder flow. J. Fluid Mech. (in press).

[17] Natarajan, R., Acrivos, A., 1993. The instability of the steady flow past spheres and disks. J. Fluid Mech. 254, 323–344.

[18] Ormières, D., Provansal, M., 1998. Transition to turbulence in the wake of a sphere. Phys. Rev. Lett. 83, 80–83.

[19] Schmid, P., Henningson, D., 2001. Stability and transition in shear flows. Springer Verlag.

[20] Schmid, P., Henningson, D., 2002. On the stability of a falling liquid curtain. J. Fluid Mech. 463, 163–171.
[21] Sevilla, A., Martínez-Bazàn, C., 2004. Vortex shedding in high reynolds number axisymmetric bluff-body wakes: Local linear instability and global bleed control. Phys. Fluids 16 (9), 3460–3469.
[22] Sipp, D., Lebedev, A., 2007. Global stability of base and mean flows: a general approach and its applications to cylinder and open cavity flows. J. Fluid Mech. 593, 333–358.
[23] Thompson, M., Leweke, T., Provansal, M., 2001. Kinematics and dynamics of sphere wake transition. J. Fluid Struct. 15, 575–585.

CHAPTER
FOUR

GLOBAL MODE INTERACTION & PATTERN SELECTION IN THE WAKE OF A DISK

Chapter 3 has shown that axisymmetric wakes can sustain two unstable $m = 1$ global modes, namely a stationary and an oscillating global mode. The present chapter investigates the three-dimensional dynamics of the disk flow resulting from the concomitant instability of the latter modes. It shows in particular that the sharp pattern and frequency selection exhibited by the real flow are accurately predicted by use of a reduced order model describing the leading-order nonlinear interaction of the leading eigenmodes. This chapter is structured as a self-contained article submitted to the *Journal of Fluid Mechanics*.

keywords: incompressible flows, bifurcations, pattern and frequency selection, weakly nonlinear expansion, normal forms.

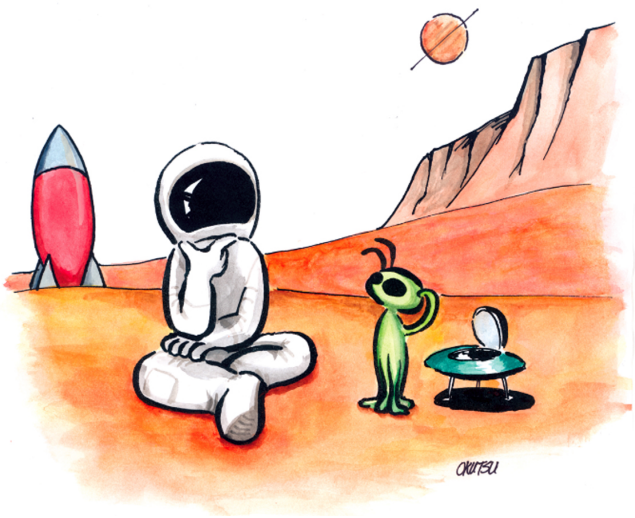

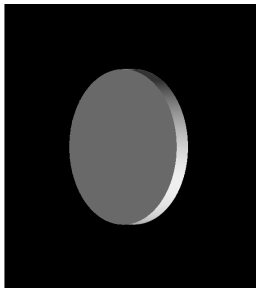

Manuscript in preparation

Global mode interaction and pattern selection in the wake of a disk: a weakly nonlinear expansion

PHILIPPE MELIGA[1],
JEAN-MARC CHOMAZ[2,1] **AND DENIS SIPP**[1]

[1]ONERA/DAFE, 8 rue des Vertugadins, 92190 Meudon, France
[2]LadHyX, CNRS-Ecole Polytechnique, 91128 Palaiseau, France

(Received 17 July 2008 and modified 15 December 2008)

Direct numerical simulations (DNS) of the wake of a circular disk placed normal to a uniform flow show that, as the Reynolds number is increased, the flow undergoes a sequence of successive bifurcations, each state being characterized by specific time and space symmetry breaking or recovering (Fabre *et al.* 2008). To explain this bifurcation scenario, we investigate the stability of the axisymmetric steady wake in the framework of the global stability theory. Both the direct and adjoint eigenvalue problems are solved. The threshold Reynolds numbers Re and characteristics of the destabilizing modes agree with the study of Natarajan & Acrivos (1993): the first destabilization occurs for a stationary mode of azimuthal wavenumber $m = 1$ at $Re_c^A = 116.9$, and the second destabilization of the axisymmetric flow occurs for two oscillating modes of azimuthal wavenumbers $m \pm 1$ at $Re_c^B = 125.3$. Since these critical Reynolds numbers are close to one another, we use a multiple time scale expansion to compute analytically the leading-order equations that describe the nonlinear interaction of these three leading eigenmodes. This set of equations is given by imposing, at third order in the expansion, a Fredholm alternative to avoid any secular term. It turns out to be identical to the normal form predicted by symmetry arguments. Though, all coefficients of the normal form are here analytically computed as the scalar product of an adjoint global mode with a resonant third order forcing term, arising from the second order base flow modification and harmonics generation. We show that all nonlinear interactions between modes take place in the recirculation bubble, as the contribution to the scalar product of regions located outside the recirculation bubble is zero. The normal form accurately predicts the sequence of bifurcations, the associated thresholds and symmetry properties observed in the DNS calculations.

1. Introduction

When a steady flow loses its stability owing to the variation of a control parameter, it bifurcates towards a new state, that may be either steady or unsteady. If the bifurcation is supercritical and a single eigenmode is responsible for the instability, the dynamics close to the threshold will occur in the one-dimensional slow manifold spanned by the destabilizing eigenmode. The only degree of freedom is then the amplitude along the unstable eigenmode direction, which is ruled by a first order differential equation of polynomial form, the normal form. When several eigenmodes are concomitantly responsible for the destabilization of the steady state, the same reasoning holds, the dimension

of the slow manifold being then equal to the number of bifurcating modes, and the normal form involves one degree of freedom per bifurcating mode. Such cases are known as multiple codimension bifurcations, and usually require several independent parameters to be tuned for the different modes to be simultaneously neutral. The normal form then describes the nonlinear interactions between each bifurcating mode and reduces the dynamics of the whole system to a low dimensional model. For codimension larger than one, the normal form may successfully predict complex behaviors (Crawford & Knobloch 1991). The analysis requires the following steps to be achieved:

(*i*) resolution of the linear stability problem to identify the marginally stable modes,

(*ii*) computation of the nonlinear terms governing the time-asymptotic evolution of these modes,

(*iii*) truncation of the system at some given order and analysis of the resulting dynamics.

In many physical problems, the structure of the normal form may be directly deduced from phase and symmetry considerations, and multiple codimension bifurcation theory has been successfully used to unravel complex bifurcation structures (Golubitsky & Stewart 1985; Cross 1986; Iooss 1987; Crawford *et al.* 1988; Golubitsky & Langford 1988). However, these problems were involving a base state inhomogeneous only in a single direction, making the expansion procedure tractable. Wakes, and more generally open flows are more complex since the base flow is usually strongly non-parallel. Analyzing their stability thus requires to consider modes that are inhomogeneous in both the cross-stream and the streamwise directions, called global modes in reference to their specific streamwise structure, first introduced by Jackson (1987) and Zebib (1987) (see Chomaz 2005, for a review).

The flow past a circular cylinder is a simple example of codimension one bifurcation, where the steady flow is destabilized by an oscillating global mode at the Reynolds number $Re = 47$ (Ding & Kawahara 1999; Barkley 2006). The flow undergoes a Hopf bifurcation, and the normal form reduces to the Stuart-Landau amplitude equation that reads

$$\dot{A} = \lambda A - \mu A|A|^2 \,, \tag{1.1}$$

where A is the amplitude of the bifurcating mode and λ its linear complex growth rate. In this case, the complex Landau coefficient μ has been computed by fitting methods from experimental measurements (Provansal *et al.* 1987) or from direct numerical simulations (Dušek *et al.* 1994). In this context, the Landau coefficient is relative to the particular point in space where the experimental or numerical signal is extracted, and to the particular variable that is indeed measured. Recently, the Landau coefficient has been obtained by a standard weakly nonlinear stability analysis based on the bifurcating global mode (Sipp & Lebedev 2007), which showed that the nonlinear self-interaction was mainly acting through base flow modification and not through harmonics generation.

We here consider the wake past a flat circular disk of diameter D, placed orthogonally with respect to a uniform flow of velocity U_∞, at low Reynolds numbers $Re < 150$, where $Re = DU_\infty/\nu$ and ν is the kinematic viscosity of the fluid. This problem has been recently addressed using DNS calculations by Fabre *et al.* (2008). When the Reynolds number is increased from sufficiently low values, the flow undergoes several successive bifurcations. A first steady bifurcation occurs for $Re \simeq 115$: it breaks the axisymmetry but preserves the time invariance, leading to a 3D steady state with a reflectional symmetry. A Hopf bifurcation then occurs for $Re \simeq 121$: it breaks the remaining reflectional symmetry and the time invariance, leading to a fully 3D periodic state. A third bifurcation finally oc-

curs for $Re \simeq 140$, where the flow remains unsteady, but restores a reflectional symmetry normal to that preserved by the first bifurcation. Natarajan & Acrivos (1993) have carried out a global stability analysis of the axisymmetric disk flow in the same range of Reynolds number. These authors have shown that the axisymmetric state is successively destabilized by a stationary mode of azimuthal wavenumber $m = 1$ at $Re = 116.5$ and by an oscillating mode of same azimuthal wavenumber at $Re = 126.5$. One should note that the DNS calculations and from the stability analysis provide consistent results concerning the first steady bifurcation, but that the critical Reynolds numbers corresponding to the onset of unsteadiness predicted by both approaches do not match. This could have been expected, though, as the analysis of Natarajan & Acrivos (1993) considered only small disturbances superimposed on the axisymmetric base flow, and not on the three-dimensional state issuing from the first $m = 1$ bifurcation.

In this study, since the two critical Reynolds numbers associated to the destabilization of the axisymmetric base flow are close to one another, we analytically compute the dynamics in the three-dimensional slow manifold supported by the stationary $m = 1$ mode and the two oscillating $m = \pm 1$ modes identified by Natarajan & Acrivos (1993). Owing to the specific symmetries of the flow, i.e. invariance under time translation and $O(2)$ symmetry, if we retain only the lowest-order nonlinear terms, the normal form describing this interaction should read

$$\dot{A} = \lambda_A A - \mu_A A|A|^2 - \nu_A A|B^+|^2 - \nu_A{}^* A|B^-|^2 - \chi_A B^+ B^{-*} A^* \,, \tag{1.2a}$$

$$\dot{B}^+ = \lambda_B B^+ - \mu_B B^+|B^+|^2 - \nu_B B^+|B^-|^2 - \eta_B B^+|A|^2 - \chi_B B^- A^2 \,, \tag{1.2b}$$

$$\dot{B}^- = \lambda_B B^- - \mu_B B^-|B^-|^2 - \nu_B B^-|B^+|^2 - \eta_B B^-|A|^2 - \chi_B B^+ A^{*2} \,, \tag{1.2c}$$

where A is the complex amplitude of the stationary mode, $B^\pm$ are the amplitudes of the two counter-rotating oscillating modes and the superscript $*$ stands for the complex conjugate. The normal form (1.2) is therefore generic as being the leading-order system of polynomial differential equations that remains invariant under a translation of t_0 in time ($t \to t + t_0$), a rotation of angle θ_0 ($\theta \to \theta + \theta_0$), and reflection ($\theta \to -\theta$). This imposes invariance of equations (1.2) under phase transformations

$$(A, B^+, B^-) \longrightarrow (A, B^+ e^{\mathrm{i}\psi}, B^- e^{\mathrm{i}\psi}) \qquad (t \to t + t_0) \,, \tag{1.3a}$$

$$(A, B^+, B^-) \longrightarrow (A e^{\mathrm{i}\varphi}, B^+ e^{\mathrm{i}\varphi}, B^- e^{-\mathrm{i}\varphi}) \qquad (\theta \to \theta + \theta_0) \,, \tag{1.3b}$$

$$(A, B^+, B^-) \longrightarrow (A^*, B^-, B^+) \qquad (\theta \to -\theta) \,, \tag{1.3c}$$

that may be easily verified (see Golubitsky *et al.* 1988, for details). It may also be verified that the normal form (1.2) is exhaustive, i.e. no other term of same polynomial order can be added to any of equations (1.2) without breaking the phase invariance.

In their study, Fabre *et al.* (2008) have deduced, from symmetry breaking considerations, a normal form of structure similar to (1.2) upon estimating all coefficients by a best fit procedure based on their DNS calculations. It turns out that even if this approach indeed leads to a successful model of the bifurcation sequence undergone by the real flow, it can be shown that the actual analytical normal form is slightly different. This is not too surprising since in the context of multiple codimension bifurcations, the number of coefficients to be found by fitting is particularly large (here, 15 real coefficients), so that agreement may be fortuitous. In the present study, we follow the line of thought introduced in Sipp & Lebedev (2007) and carry out a thoroughly analytical asymptotic expansion of the flow field based on the global modes destabilizing the axisymmetric wake. The normal form (1.2) is then rigorously derived at the third order of a standard weakly nonlinear analysis as the result of a Fredholm alternative applied to resonant

terms. All coefficients of the normal form are analytically computed as the scalar product between an adjoint global mode and a resonant forcing terms determined by the first and second order solutions. These coefficients, which describe the nonlinear interactions between modes, are of particular interest since they determine the effective bifurcation sequence. Besides, we would like to emphasize here that performing the analytical derivation of this normal form provides additional insight into the flow physics. In particular, the use of an asymptotic expansion makes it possible to investigate each nonlinear interaction independently. It completes the study of Fabre *et al.* (2008) by shedding new light on the physical origin of the coupling terms between modes, as we show here that all interactions take place only in the recirculating bubble, which can therefore be viewed as the *effective wavemaker*. We also compute the analytical solution up to the second order where base flow modification and harmonics forcing occur. As will be shown in § 4, this is essential to discuss some realistic features of the bifurcated flow. The resulting dynamics is then analyzed and compared to that observed in the DNS computations. It turns out that our analytical study predicts with a remarkable precision the bifurcation diagram observed in Fabre *et al.* (2008).

The paper is organized as follows. The problem formulation is presented in § 2. The global linear stability analysis is presented in § 3, where we compute the leading modes and their associated adjoint modes that are required to compute the coefficients of the normal form. In § 4, we carry out the standard weakly nonlinear analysis: the values of all coefficients of the normal form (1.3) are given and the associated sequence of bifurcations is discussed and compared to that observed in the DNS calculations of Fabre *et al.* (2008). The sensitivity of this sequence of bifurcations to experimental imperfections is discussed in § 5.

2. Flow configuration and methodology

In the following, all quantities are made nondimensional using D and U_∞. Standard cylindrical coordinates r, θ and z with origin taken at the center of the disk are used. The state vector $\boldsymbol{q}$ stands for the flow field $(\boldsymbol{u}, p)^T$, where ^{T} designates the transpose, $\boldsymbol{u} = (u, v, w)$ is the fluid velocity where u, v and w are the radial, azimuthal and axial components, and p is the pressure. The fluid motion is governed by the incompressible Navier-Stokes equations

$$\boldsymbol{\nabla} \cdot \boldsymbol{u} = 0\,, \qquad \partial_t \boldsymbol{u} + \boldsymbol{\nabla}\boldsymbol{u} \cdot \boldsymbol{u} + \boldsymbol{\nabla} p - \frac{1}{Re}\boldsymbol{\nabla}^2 \boldsymbol{u} = 0\,. \tag{2.1}$$

with $Re = U_\infty D/\nu$, as previously introduced. The computational domain is shown in Figure 1. The disk is located on the axis of an enclosing cylinder of radius $r = r_\infty$. The boundaries $\partial\Omega_a$ and $\partial\Omega_{ext}$ represent respectively the revolution axis of the disk and the boundary of the enclosing cylinder. The inlet $\partial\Omega_{in}$, outlet $\partial\Omega_{out}$ are located respectively at $z = z_{-\infty}$ and $z = z_\infty$ (see Table 1 for numerical values). We use the inlet conditions $\boldsymbol{u} = (0, 0, 1)$ on $\partial\Omega_{in}$, no-slip conditions $\boldsymbol{u} = \boldsymbol{0}$ on the body wall $\partial\Omega_b$ and no-stress conditions $(-p\boldsymbol{I} + Re^{-1}\boldsymbol{\nabla}\boldsymbol{u}) \cdot \boldsymbol{n} = \boldsymbol{0}$ on the outlet $\partial\Omega_{out}$. On the external boundary $\partial\Omega_{ext}$, we impose a free slip boundary condition $u = v = \partial_r w = 0$, so that the body surface $\partial\Omega_b$ is the only source of vorticity, as would be the case without this artificial boundary. Note that for computational reasons, the width of the disk L cannot be chosen strictly equal to zero, so that we use a very small width corresponding to an aspect ratio $L/D = 10^{-3}$.

The numerical approach is based on a finite element method. A given equation is first multiplied by r to avoid the singularity on the $r = 0$ axis. Its associated variational

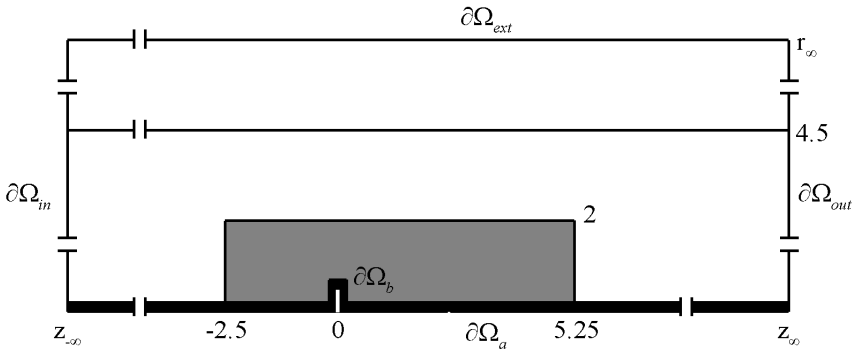

Figure 1: Schematic of the mesh structure: $z_{-\infty}$, z_{∞} and r_{∞} are, respectively, the location of the inlet, outlet and lateral boundaries. The inner solid lines delimit regions characterized by different vertex densities. The black shaded area corresponds to the region of highest vertex density and the grey shaded area is the near-wake region Ω_{in} used for the normalization of the global modes.

	$z_{-\infty}$	z_{∞}	r_{∞}	n_t	DoF_0	DoF_m
M_1	-100	200	25	397992	1802527	2603136
M_2	-100	150	25	362672	1642617	2372198
M_3	-70	200	25	394173	1784759	2577497
M_4	-100	200	20	379576	1720445	2484574
M_5	-100	200	25	290609	1316891	1901769

Table 1: Properties of the meshes as a function of parameters $z_{-\infty}$, z_{∞} and r_{∞}, corresponding to the inlet, outlet and lateral boundaries. n_t is the number of triangles, DoF_0 is the number of degrees of freedom for a state vector $(u, w, p)^T$ used in the base flow calculations, and DoF_m is the number of degrees of freedom for a state vector $(u, v, w, p)^T$ used in the stability analysis. Meshes M_1 and M_2 have the same vertex densities but with a different location of the outlet boundary. In the same way, M_1 and M_3 differ by the location of the inlet boundary, while M_1 and M_4 differ by the location of the lateral boundary. M_1 and M_5 have the same spatial extent but M_5 is built with lower vertex densities.

formulation is then derived, and spatially discretized using a mesh composed of triangular elements. The FreeFem++ software (*http://www.freefem.org*) is used to generate the triangulation with the Delaunay-Voronoi algorithm. The mesh refinement is controlled by the vertex densities on both external and internal boundaries. Regions where the mesh density varies are depicted in Figure 1. To avoid any computational difficulty, a zone of width 0.05 and high vertex density (250 vertex per unit length) is defined at the axis $r = 0$ and around the disk, corresponding to the black shaded area in Figure 1. The unknown velocity and pressure fields $(\boldsymbol{u}, p)^T$ are spatially discretized using a basis of Taylor-Hood elements ($P2$ elements of velocities and $P1$ elements for pressure). The sparse matrices resulting from the projection of the variational formulations onto the basis of finite elements are built with the FreeFem++ software. The matrix inverses are computed using the UMFPACK library, which consists in a sparse direct LU solver (Davis & Duff 1997; Davis 2004). Five different meshes, denoted M_1 to M_5 have been used to assess convergence in numerical results. These meshes exhibit various spatial extents and vertex densities, detailed in Table 1. The corresponding number of degrees

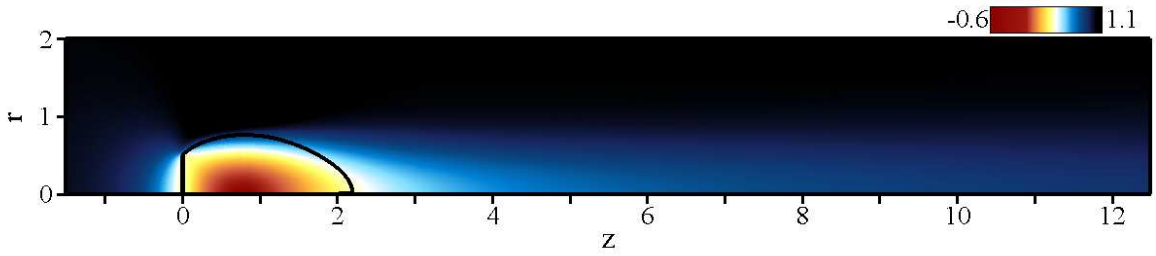

Figure 2: Steady axisymmetric base flow at the threshold of the first instability ($Re = 116.9$). The solid line in the flow indicates the separatrix of the recirculation zone.

of freedom for an axisymmetric and a three-dimensional state vector, such as those used in the base flow calculations and the stability analysis respectively, are also provided. In the following, we will focus on the finest mesh M_1 to present all results. A comparison of the results obtained with the meshes M_1 to M_5 is given in Appendix B.

3. Linear analysis

The aerodynamic flow field $\boldsymbol{q} = (\boldsymbol{u}, p)^T$ is decomposed into an axisymmetric steady base flow $\boldsymbol{q^0} = (u^0, 0, w^0, p^0)^T$ and a three-dimensional perturbation $\boldsymbol{q^1} = \epsilon(u^1, v^1, w^1, p^1)^T$ of amplitude ϵ assumed, in this section, infinitesimal.

3.1. *Base flow calculations*

The base flow $\boldsymbol{q^0}$ is sought as a steady axisymmetric solution of the Navier-Stokes equations:

$$\boldsymbol{\nabla} \cdot \boldsymbol{u^0} = 0\,, \qquad \boldsymbol{\nabla u^0} \cdot \boldsymbol{u^0} + \boldsymbol{\nabla} p^0 - \frac{1}{Re}\boldsymbol{\nabla}^2 \boldsymbol{u^0} = \boldsymbol{0}\,. \tag{3.1}$$

On the axis $\partial\Omega_a$, the condition given by mass and momentum conservation as $r \to 0$ for axisymmetric solutions is $u^0 = \partial_r w^0 = 0$. An approximate guess solution $\boldsymbol{q^0}$ satisfying the required boundary conditions is first obtained by time marching the axisymmetric equations (2.1). The solution $\boldsymbol{q^0}$ of the steady nonlinear equations (3.1) is then obtained using an iterative Newton method involving the resolution of simple linear problems, as described in Barkley *et al.* (2002); Sipp & Lebedev (2007). In the present study, the iterative process is carried out until the $\mathcal{L}^2$-norm of the residual of the governing equations for $\boldsymbol{q^0}$ becomes smaller than 10^{-12}. Figure 2 shows contours of axial velocity w^0 of the base flow for $Re = 116.9$. We observe a recirculation region of length $\simeq 2.1$ diameters, developing in the lee of the disk, with negative values of the axial velocity close to the axis reaching 60 % of the free-stream velocity.

3.2. *Global eigenmode analysis*

At leading-order in ϵ, $\boldsymbol{q^1} = (\boldsymbol{u^1}, p^1)^T$ is a solution of the unsteady equations linearized about $\boldsymbol{q^0}$ that read

$$\mathcal{B}\partial_t \boldsymbol{q^1} + \mathcal{A}\,\boldsymbol{q^1} = \boldsymbol{0}\,, \tag{3.2}$$

where $\mathcal{A}$ and $\mathcal{B}$ are the linear operators defined by

$$\mathcal{A} = \begin{pmatrix} \mathcal{C}(\cdot, \boldsymbol{u^0}) - \frac{1}{Re}\boldsymbol{\nabla}^2 & \boldsymbol{\nabla} \\ \boldsymbol{\nabla}^T & 0 \end{pmatrix}, \qquad \mathcal{B} = \begin{pmatrix} \mathcal{I} & 0 \\ 0 & 0 \end{pmatrix}, \tag{3.3}$$

and $\mathcal{C}(\boldsymbol{a}, \boldsymbol{b})$ is the advection operator $\boldsymbol{\nabla a} \cdot \boldsymbol{b} + \boldsymbol{\nabla b} \cdot \boldsymbol{a}$. Note that the operator $\mathcal{C}$ is symmetric, i.e. $\mathcal{C}(\boldsymbol{a}, \boldsymbol{b}) = \mathcal{C}(\boldsymbol{b}, \boldsymbol{a})$. Since the base flow is axisymmetric, eigenmodes take

the form of normal modes

$$\boldsymbol{q^1} = \hat{\boldsymbol{q}}^{\boldsymbol{1}}(r,z)e^{(\sigma+\mathrm{i}\omega)t+\mathrm{i}m\theta} + \text{ c.c.}\,, \tag{3.4}$$

where $\boldsymbol{q^1} = (\hat{u}^1, \hat{v}^1, \hat{w}^1, \hat{p}^1)$ is the so-called global mode for which both the cross-stream and streamwise directions are eigendirections. The azimuthal wavenumber of the global mode is m, its growth rate and pulsation are σ and ω respectively. Substitution of the development (3.4) in equations (3.2) leads to a generalized eigenvalue problem for $\sigma + \mathrm{i}\omega$ and $\hat{\boldsymbol{q}}^{\boldsymbol{1}}$ that reads

$$(\sigma + \mathrm{i}\omega)\mathcal{B}\hat{\boldsymbol{q}}^{\boldsymbol{1}} + \mathcal{A}_m\hat{\boldsymbol{q}}^{\boldsymbol{1}} = \boldsymbol{0}\,, \tag{3.5}$$

where $\mathcal{A}_m$ is the linear operator

$$\mathcal{A}_m = \begin{pmatrix} \mathcal{C}_{m,0}(\cdot,\boldsymbol{u^0}) - \frac{1}{Re}{\boldsymbol{\nabla_m}}^2 & \boldsymbol{\nabla_m} \\ {\boldsymbol{\nabla_m}}^T & 0 \end{pmatrix}. \tag{3.6}$$

In (3.6), $\boldsymbol{\nabla_m}$ is the gradient operator relative to the azimuthal wavenumber m, and $\mathcal{C}_{m,n}(\hat{\boldsymbol{a}},\hat{\boldsymbol{b}})$ is the symmetric advection operator for a pair of normal modes $\hat{\boldsymbol{a}}$ and $\hat{\boldsymbol{b}}$ of respective azimuthal wavenumbers m and n, i.e. $\mathcal{C}_{m,n}(\hat{\boldsymbol{a}},\hat{\boldsymbol{b}}) = \boldsymbol{\nabla_m}\hat{\boldsymbol{a}}\cdot\hat{\boldsymbol{b}} + \boldsymbol{\nabla_n}\hat{\boldsymbol{b}}\cdot\hat{\boldsymbol{a}}$. Owing to the normal mode expansion (3.4), these operators are complex, since θ derivatives introduce product by im, and a complete expansion of these operators can be found in Appendix D. The global mode satisfies the boundary conditions

$$\hat{\boldsymbol{u}}^{\boldsymbol{1}} = \boldsymbol{0} \text{ on } \partial\Omega_{in}\cup\partial\Omega_b \text{ (inlet and body)}\,, \tag{3.7a}$$

$$(-\hat{p}^1\boldsymbol{I} + Re^{-1}\boldsymbol{\nabla_m}\hat{\boldsymbol{u}}^{\boldsymbol{1}})\cdot\boldsymbol{n} = \boldsymbol{0} \text{ on } \partial\Omega_{out} \text{ (outlet)}\,, \tag{3.7b}$$

$$\hat{u}^1 = \partial_r\hat{v}^1 = \partial_r\hat{w}^1 = 0 \text{ on } \partial\Omega_{ext} \text{ (external boundary)}\,. \tag{3.7c}$$

The conditions at the axis $\partial\Omega_a$ depend on the azimuthal wavenumber m: $\hat{u}^1 = \partial_r\hat{w}^1 = \partial_r\hat{p}^1 = 0$ for $m = 0$, $\partial_r\hat{u}^1 = \partial_r\hat{v}^1 = \hat{w}^1 = \hat{p}^1 = 0$ for $|m| = 1$ and $\hat{\boldsymbol{q}}^{\boldsymbol{1}} = \boldsymbol{0}$ for $|m| \geqslant 2$. This eigenvalue problem is solved using an Arnoldi method based on a shift-invert strategy, as in Ehrenstein & Gallaire (2005). Owing to the symmetries of the problem, one should note that equations (3.5) are invariant under the $(\hat{u}^1, \hat{v}^1, \hat{w}^1, \hat{p}^1, m) \to (\hat{u}^1, -\hat{v}^1, \hat{w}^1, \hat{p}^1, -m)$ transformation, so that we investigate only the case $m \geqslant 0$ in this section. Moreover, if $(\hat{\boldsymbol{q}}^{\boldsymbol{1}}, \sigma + \mathrm{i}\omega)$ is solution of problem (3.5), then $({\hat{\boldsymbol{q}}^{\boldsymbol{1}}}^*, \sigma - \mathrm{i}\omega)$ is also a solution, i.e. eigenvalues are complex conjugates, so that all spectra in the (σ,ω)-plane are symmetric with respect to the real axis.

In the following, $\langle , \rangle$ is the inner product defined by $\langle\hat{\boldsymbol{a}},\hat{\boldsymbol{b}}\rangle = \int_\Omega \hat{\boldsymbol{a}}^*\cdot\hat{\boldsymbol{b}}\, r\mathrm{d}r\mathrm{d}z$ where $\hat{\boldsymbol{a}}$ and $\hat{\boldsymbol{b}}$ belong to $\mathbb{C}^n$ and $\cdot$ refers to the canonical hermitian scalar product in $\mathbb{C}^n$. To normalize the global modes, we define arbitrarily a near-wake domain Ω_{in} as $z \in [-2.5, 5.25]$ and $r < 2$, corresponding to the grey shaded area in Figure 1. All global modes are normalized by imposing first the phase of the radial velocity to be zero at a particular location, namely $\hat{u}^1(0,1)$ must be real positive for $m = \pm 1$. The eigenmode energy is then normalized to unity in Ω_{in} by imposing that $\left\langle\hat{\boldsymbol{q}}^{\boldsymbol{1}}, \delta_{in}\mathcal{B}\hat{\boldsymbol{q}}^{\boldsymbol{1}}\right\rangle = 1$, where δ_{in} is the function defined as $\delta_{in}(r,z) = 1$ if $(r,z) \in \Omega_{in}$ and 0 otherwise. These normalization choices have no effect on the dynamics but ease the comparison between results when the convergence tests are carried out.

For a given global mode $\hat{\boldsymbol{q}}^{\boldsymbol{1}}$, we also compute its adjoint global mode $\hat{\boldsymbol{q}}^{\boldsymbol{1\dagger}}$ that verifies the adjoint eigenvalue problem

$$(\sigma - \mathrm{i}\omega)\mathcal{B}\hat{\boldsymbol{q}}^{\boldsymbol{1\dagger}} + \mathcal{A}_m^\dagger\hat{\boldsymbol{q}}^{\boldsymbol{1\dagger}} = \boldsymbol{0}\,, \tag{3.8}$$

where $\mathcal{A}_m^\dagger$ is the adjoint of operator $\mathcal{A}_m$, obtained by integrating by parts system (3.5)

(see Schmid & Henningson 2001, for details)

$$\mathcal{A}_m^\dagger = \begin{pmatrix} \mathcal{C}_{m,0}^\dagger(\cdot, \boldsymbol{u^0}) - \frac{1}{Re}\boldsymbol{\nabla_m}^2 & -\boldsymbol{\nabla_m} \\ \boldsymbol{\nabla_m}^T & 0 \end{pmatrix}. \tag{3.9}$$

$\mathcal{C}_{m,n}^\dagger(\hat{\boldsymbol{a}}, \hat{\boldsymbol{b}}) = \boldsymbol{\nabla_n}\hat{\boldsymbol{b}}^T \cdot \hat{\boldsymbol{a}} - \boldsymbol{\nabla_m}\hat{\boldsymbol{a}} \cdot \hat{\boldsymbol{b}}$ is the adjoint advection operator. It is worthwhile noting that $\mathcal{C}_{m,n}^\dagger$ is not symmetric. We would like to emphasize that the terms describing the convection of disturbances by the base flow, namely $\boldsymbol{\nabla_m}\hat{\boldsymbol{u}}^{\boldsymbol{1}} \cdot \boldsymbol{u^0}$ and $-\boldsymbol{\nabla_m}\hat{\boldsymbol{u}}^{\boldsymbol{1\dagger}} \cdot \boldsymbol{u^0}$ have opposite signs between the direct and adjoint advection operators. As a result, disturbances are convected downstream for $\mathcal{A}_m$ and upstream for $\mathcal{A}_m^\dagger$, inducing a spatial separation of direct and adjoint modes (Chomaz *et al.* 1990). This *convective* nonnormality is specific to open flows (Chomaz 2005).

The adjoint boundary conditions are defined so that all boundary terms arising from the integration by parts are nil. We obtain:

$$\hat{\boldsymbol{u}}^{\boldsymbol{1\dagger}} = \boldsymbol{0} \quad \text{on} \quad \partial\Omega_{in} \cup \partial\Omega_b\,, \tag{3.10a}$$

$$(\boldsymbol{u^0}.\boldsymbol{n})\hat{\boldsymbol{u}}^{\boldsymbol{1\dagger}} + (\hat{p}^{1\dagger}\boldsymbol{I} + Re^{-1}\boldsymbol{\nabla_m}\hat{\boldsymbol{u}}^{\boldsymbol{1\dagger}}) \cdot \boldsymbol{n} = \boldsymbol{0} \quad \text{on} \quad \partial\Omega_{out}\,, \tag{3.10b}$$

$$\hat{u}^{1\dagger} = \partial_r\hat{v}^{1\dagger} = \partial_r\hat{w}^{1\dagger} = 0 \quad \text{on} \quad \partial\Omega_{ext}\,. \tag{3.10c}$$

The condition on the axis $\partial\Omega_a$ is identical to that applied to the direct global mode. This eigenproblem is solved via the same Arnoldi method, and adjoint global modes are normalized so that $\langle \hat{\boldsymbol{q}}^{\boldsymbol{1\dagger}}, \mathcal{B}\hat{\boldsymbol{q}}^{\boldsymbol{1}} \rangle = 1$. Since the adjoint problem (3.8) has been formulated for continuous operators with associated adjoint boundary conditions, the spatial discretizations of problems (3.5) and (3.8) are not hermitian to one another, because operator $\mathcal{B}$ does not correspond to the scalar product in cylindrical coordinates. Consequently, we check a posteriori that both problems have identical spectra, and that the bi-orthogonality relation is satisfied for the 10 leading global modes, so that our numerical procedure accurately estimates the direct and adjoint global modes.

In the linear framework, we compute the leading global modes and their adjoint global modes, that will be used in section 4 to compute the coefficients of the normal form (1.2). The threshold Reynolds numbers and characteristics of the destabilizing global modes agree with the results of Natarajan & Acrivos (1993): the first instability is steady (i.e. $\omega_A = 0$) and occurs at $Re_c^A = 116.9$ for $m = 1$ and the second instability occurs at $Re_c^B = 125.3$ for an $m = 1$ oscillating mode of frequency $\omega_B = 0.760$, corresponding to a Strouhal number $St_B = \omega_B D/(2\pi U_\infty)$ of 0.121. Figure 3(a) shows the eigenvalue spectra at the first critical Reynolds number Re_c^A. $m = 1$ modes are shown as diamonds in the upper half-plane whereas $m = 0$ and $m = 2$ modes are shown respectively as $+$ and o symbols in the lower half-plane. The marginally unstable eigenvalue labelled A vanishes at threshold and corresponds to the large closed diamond. In the following, the eigenvector associated to this steady global mode is denoted $\hat{\boldsymbol{q}}_{\boldsymbol{A}}^{\boldsymbol{1}}$. Figure 4($a$) shows the spatial structure of the axial velocity $\hat{w}_A^1$: one observes a low speed region extending far downstream. Since the azimuthal wavenumber of this global mode is $m = 1$, the axial velocity perturbation is opposite on the other side of the revolution axis, which induces an increase of the streamwise velocity of the total flow. The stationary global mode therefore mainly induces an off-axis displacement of the wake. The associated adjoint global mode $\hat{\boldsymbol{q}}_{\boldsymbol{A}}^{\boldsymbol{1\dagger}}$ is presented in Figure 4(b). It is dominated by high magnitudes of adjoint axial velocity $\hat{w}_A^{1\dagger}$ within the recirculating area, the maximum value being reached close to the separating streamline, but it is also intense far upstream of the disk. As mentioned previously, the downstream localization of the global mode, and the upstream localization

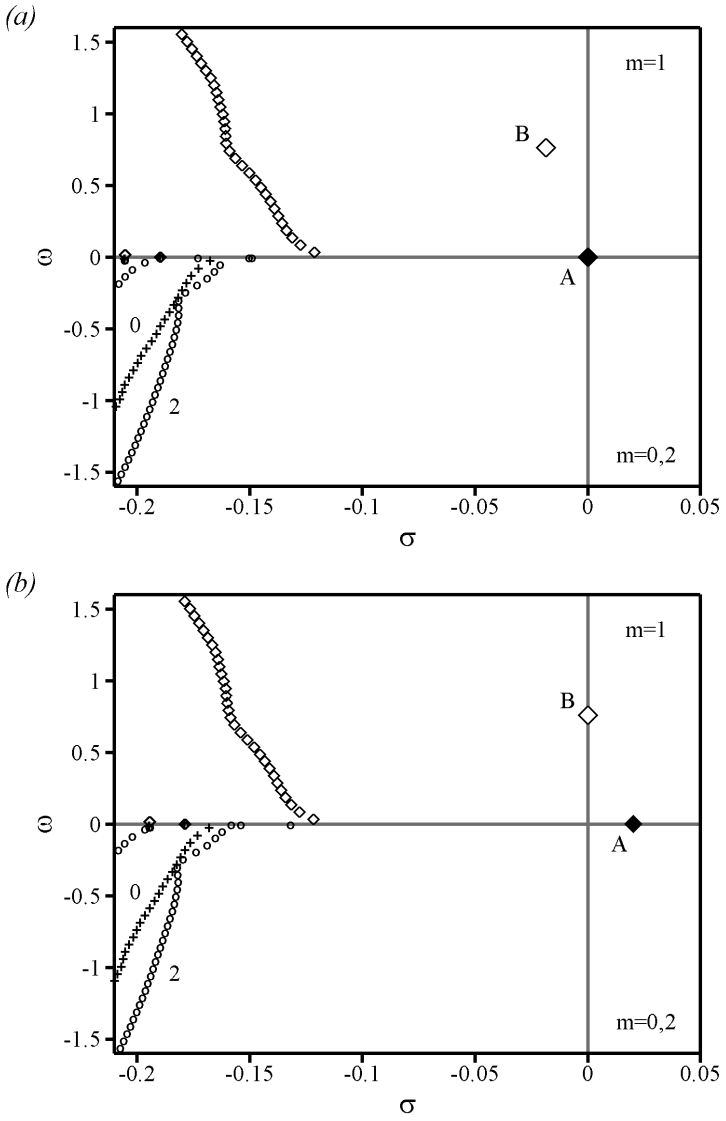

Figure 3: $m = 0, 1, 2$ eigenvalue spectra in the (σ, ω)-plane for the wake of a disk. (a) Threshold of the first instability at $Re_c^A = 116.9$. (b) Threshold of the second instability at $Re_c^B = 125.3$. All spectra are symmetric with respect to the real axis. The upper half-plane shows $m = 1$ disturbances as diamonds, and the lower half-plane shows $m = 0, 2$ disturbances as $+$ and o symbols, respectively. The large diamonds labelled A and B correspond respectively to the steady and oscillating destabilizing $m = 1$ modes.

of the adjoint global mode result from the convective nonnormality of the linearized Navier-Stokes operator (see Chomaz 2005). Figure 3(b) shows the eigenvalue spectra at the second instability threshold $Re_c^B = 125.3$. The eigenvalue corresponding to the first destabilizing eigenmode $\hat{\boldsymbol{q}}_{\boldsymbol{A}}^{\boldsymbol{1}}$ has moved to the unstable ($\sigma > 0$) half-plane. Moreover, the oscillating eigenvalue labelled B, corresponding to the large open diamond, which was in the stable domain ($\sigma < 0$) in Figure 3(a), is now crossing the $\sigma = 0$ axis. The marginally unstable eigenvalue $\mathrm{i}\omega_B$ is associated to the eigenvector denoted $\hat{\boldsymbol{q}}_{\boldsymbol{B^+}}^{\boldsymbol{1}}$, and $\hat{\boldsymbol{q}}_{\boldsymbol{B^-}}^{\boldsymbol{1}}$ stands for the symmetric eigenmode associated to the azimuthal wavenumber $m = -1$ for the same eigenvalue $\mathrm{i}\omega_B$. Since these modes are oscillating, their eigenvectors are complex, and Figure 5(a) shows the spatial structure of the real part of $\hat{w}_{B^+}^{1\dagger}$. One observes positive and negative velocity perturbations alternating downstream of the disk, in a regular, periodic

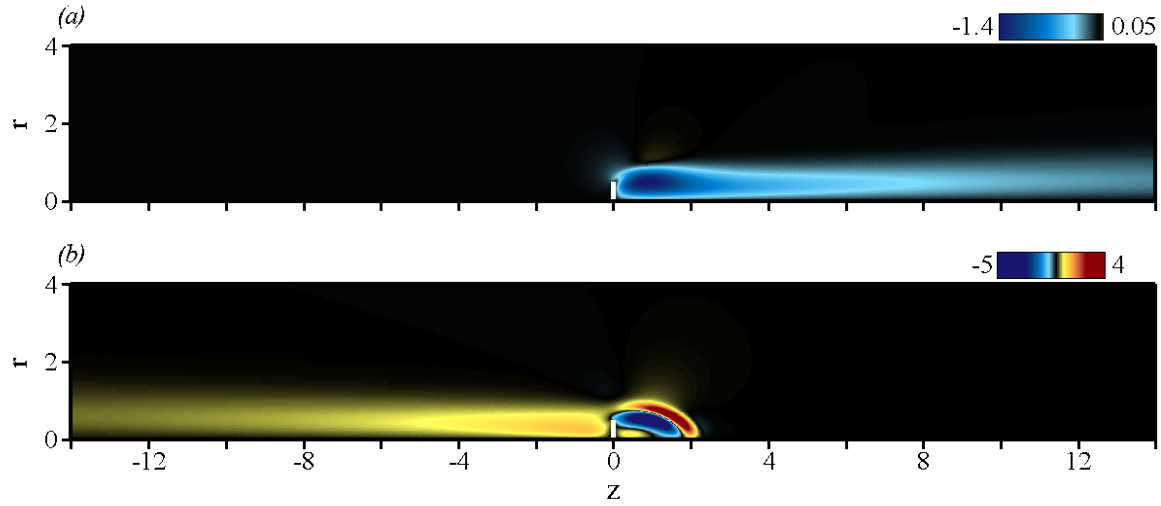

Figure 4: Steady global mode and adjoint global mode at the threshold of the first instability, $Re_c^A = 116.9$. (a) Spatial distribution of axial velocity $\hat{w}_A^1$ for the global mode. (b) Spatial distribution of axial velocity $\hat{w}_A^{1\dagger}$ for the adjoint global mode. The black hue corresponds to vanishing perturbations.

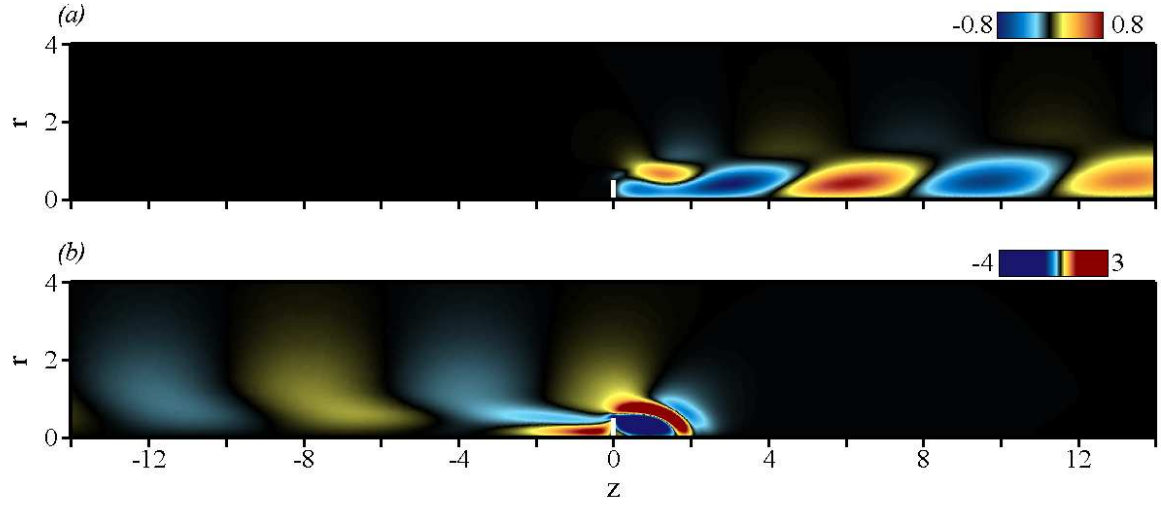

Figure 5: Same as Figure (4) for the oscillating global mode at threshold. Only the real part is shown here.

way that allows to define a local spatial wavelength of about 7 diameters. The imaginary part of $\hat{w}_{B^+}^{1\dagger}$ (not shown here) displays a similar structure, but is approximately in spatial quadrature since its extrema are located where the real part vanishes. This global mode corresponds therefore to a spiral perturbation in the lee of the disk, which rotates in time at the frequency ω_B. One should note that the eigenmode for the $m = -1$ perturbation is similar, but has the opposite pitch and rotates in time in the opposite direction at the same frequency ω_B. As for the stationary mode, the adjoint global mode $\hat{\boldsymbol{q}}_{\boldsymbol{B}^+}^{\boldsymbol{1\dagger}}$ shown in Figure 5(b) is intense only in the recirculating area and a few diameters upstream of the disk, where it presents a weak oscillation, and it vanishes downstream of the disk.

4. Weakly nonlinear analysis

4.1. *Presentation*

Since the critical Reynolds numbers for both destabilizing modes are close to one another, we implement here an asymptotic expansion where these three modes have the same order of magnitude. The Reynolds number Re is assumed to vary in a range close to the mean critical Reynolds number $Re_c = (Re_c^A + Re_c^B)/2 = 121.1$. The departure from criticality is assumed to be of order ϵ^2. Therefore, we introduce the order unity parameter δ, such that

$$\frac{1}{Re} = \frac{1}{Re_c} - \epsilon^2 \delta \,. \tag{4.1}$$

The threshold Reynolds numbers Re_c^A and Re_c^B are then rescaled into the criticality parameters δ^A and δ^B, so that

$$\frac{1}{Re_c^A} = \frac{1}{Re_c} - \epsilon^2 \delta^A \,, \qquad \frac{1}{Re_c^B} = \frac{1}{Re_c} - \epsilon^2 \delta^B \,. \tag{4.2}$$

In practice, ϵ is chosen equal to 10^{-1}, so that $\delta^A = -2.97 \times 10^{-2}$ and $\delta^B = 2.77 \times 10^{-2}$. However, the results, and in particular the final bifurcation diagram, are mainly insensitive to the precise choice of Re_c and of ϵ, as shown in Appendix C. As mentioned in the introduction, the weakly nonlinear analysis requires the introduction of multiple time scales with a *fast* time scale t and a *slow* time scale $t_1 = \epsilon^2 t$. The ∂_t term in equations (2.1) is transformed into $\partial_t + \epsilon^2 \partial_{t_1}$. Note that the growth rates σ_A and σ_B are non zero at Re_c, since the stationary mode $\hat{\boldsymbol{q}}^{\mathbf{1}}_{\boldsymbol{A}}$ is slightly unstable and the oscillating modes $\hat{\boldsymbol{q}}^{\mathbf{1}}_{\boldsymbol{B}^{\pm}}$ are slightly stable. However, with the present scaling assumption, the growth rates σ_A, σ_B of these modes differ from zero only at order ϵ^2. We define ω_0 as the frequency of modes $\hat{\boldsymbol{q}}^{\mathbf{1}}_{\boldsymbol{B}^{\pm}}$ at the mean critical Reynolds number Re_c, i.e. $\omega_0 = \omega_B(Re_c) = 0.764$, so that at Re_c:

$$\sigma_A = \epsilon^2 \tilde{\sigma}_A \,, \tag{4.3a}$$

$$\sigma_B + \mathrm{i}\omega_B = \mathrm{i}\omega_0 + \epsilon^2 \tilde{\sigma}_B \,, \tag{4.3b}$$

where the second order growth rates $\tilde{\sigma}_A$, $\tilde{\sigma}_B$ are assumed to be of order unity. This second order departure from neutrality is taken into account by replacing the leading-order operator $\mathcal{A}_m^c = \mathcal{A}_m(Re_c)$ defined in (3.6), for which $\hat{\boldsymbol{q}}^{\mathbf{1}}_{\boldsymbol{A}}$ and $\hat{\boldsymbol{q}}^{\mathbf{1}}_{\boldsymbol{B}^{\pm}}$ are not neutral, by the *shifted* operator $\widetilde{\mathcal{A}}_m^c = \mathcal{A}_m^c - \epsilon^2 \mathcal{S}_m$, where $\mathcal{S}_m$ is the shift operator defined by

$$\mathcal{S}_1 \hat{\boldsymbol{q}}^{\mathbf{1}}_{\boldsymbol{A}} = \tilde{\sigma}_A \hat{\boldsymbol{q}}^{\mathbf{1}}_{\boldsymbol{A}} \,, \tag{4.4a}$$

$$\mathcal{S}_1 \hat{\boldsymbol{q}}^{\mathbf{1}}_{\boldsymbol{B}^{+}} = \tilde{\sigma}_B \hat{\boldsymbol{q}}^{\mathbf{1}}_{\boldsymbol{B}^{+}} \,, \tag{4.4b}$$

$$\mathcal{S}_{-1} \hat{\boldsymbol{q}}^{\mathbf{1}}_{\boldsymbol{B}^{-}} = \tilde{\sigma}_B \hat{\boldsymbol{q}}^{\mathbf{1}}_{\boldsymbol{B}^{-}} \,, \tag{4.4c}$$

$$\mathcal{S}_{\pm 1} \hat{\boldsymbol{q}} = \mathbf{0} \ \text{ for the remaining } m = \pm 1 \text{ modes} \,, \tag{4.4d}$$

$$\mathcal{S}_m \hat{\boldsymbol{q}} = \mathbf{0} \ \text{ for all other } m \,. \tag{4.4e}$$

It is worthwhile emphasizing that $\widetilde{\mathcal{A}}_m^c$ has precisely the same spectra than $\mathcal{A}_m^c$ at the critical Reynolds number Re_c, excepted that $\hat{\boldsymbol{q}}^{\mathbf{1}}_{\boldsymbol{A}}$ and $\hat{\boldsymbol{q}}^{\mathbf{1}}_{\boldsymbol{B}^{\pm}}$ are now neutral.

The flow field $\boldsymbol{q}$ is expanded as

$$\boldsymbol{q} = \boldsymbol{q}^{\mathbf{0}} + \epsilon \boldsymbol{q}^{\mathbf{1}} + \epsilon^2 \boldsymbol{q}^{\mathbf{2}} + \epsilon^3 \boldsymbol{q}^{\mathbf{3}} + ... \tag{4.5}$$

and the governing equations (2.1) then give rise to a series of equations at successive order of ϵ.

4.2. *Orders 0 and 1*

At order ϵ^0, the equations are the nonlinear equations (2.1) for the Reynolds number Re_c, i.e. $\boldsymbol{q^0}$ is the steady axisymmetric solution computed, as in section 3.1, for Re_c. The equations at order ϵ^1 are the linearized equations given by (3.2) at Re_c:

$$\mathcal{B}\partial_t \boldsymbol{q^1} + \widetilde{\mathcal{A}}^c \, \boldsymbol{q^1} = \boldsymbol{0}\,, \tag{4.6}$$

where $\widetilde{\mathcal{A}}^c$ is the shifted evolution operator acting in the real space, at the critical Reynolds number Re_c, obtained from $\widetilde{\mathcal{A}}^c_m$ by inverse Fourier transform in time and in the azimuthal direction. Equations (4.6) specify that $\boldsymbol{q^1}$ is a superposition of eigenmodes destabilizing the steady state $\boldsymbol{q^0}$:

$$\boldsymbol{q^1} = A\hat{\boldsymbol{q}}^{\boldsymbol{1}}_{\boldsymbol{A}} e^{\mathrm{i}\theta} + B^+\hat{\boldsymbol{q}}^{\boldsymbol{1}}_{\boldsymbol{B^+}} e^{\mathrm{i}\theta+\mathrm{i}\omega_0 t} + B^-\hat{\boldsymbol{q}}^{\boldsymbol{1}}_{\boldsymbol{B^-}} e^{-\mathrm{i}\theta+\mathrm{i}\omega_0 t} + \text{ c.c.}\,, \tag{4.7}$$

where A is the complex amplitude of the steady mode $\hat{\boldsymbol{q}}^{\boldsymbol{1}}_{\boldsymbol{A}}$, and B^+ and B^- are the complex amplitudes of the oscillating mode $\hat{\boldsymbol{q}}^{\boldsymbol{1}}_{\boldsymbol{B^+}}$ and $\hat{\boldsymbol{q}}^{\boldsymbol{1}}_{\boldsymbol{B^-}}$ respectively, (A, B^+, B^-) being, at this stage, unknown functions of the slow time t_1.

4.3. *Order 2*

At order ϵ^2 we obtain the linearized Navier-Stokes equations applied to $\boldsymbol{q^2}$

$$\mathcal{B}\partial_t \boldsymbol{q^2} + \widetilde{\mathcal{A}}^c \, \boldsymbol{q^2} = \boldsymbol{F^2}\,, \tag{4.8}$$

forced by a term $\boldsymbol{F^2}$ depending only on zero and first order solutions

$$\boldsymbol{F^2} = -\left(\delta\boldsymbol{\nabla}^2\boldsymbol{u^0} + \mathcal{C}(\boldsymbol{u^1},\boldsymbol{u^1})\,,\, 0\right)^T\,. \tag{4.9}$$

The first term $-\delta\boldsymbol{\nabla}^2\boldsymbol{u^0}$ in (4.9) is linear and arises from the Reynolds number variation, quantified by δ and acting here on the base flow. The other contribution $-\mathcal{C}(\boldsymbol{u^1},\boldsymbol{u^1})$ is nonlinear and is due to the transport of the first order solution $\boldsymbol{q^1}$ by itself. Since the first order solution is made of six different contributions of respective amplitudes A, A^*, B^+, B^{+*}, B^- and B^{-*}, its self-transport generates 21 different nonlinear terms. Each of these terms, denoted $\hat{\boldsymbol{F}}^{\boldsymbol{2}}_{\boldsymbol{ij}} e^{(\mathrm{i}m\theta+\mathrm{i}\omega t)}$ (the subscripts i, j standing for one of the six first order amplitudes) exhibits a specific spatial periodicity m and frequency ω, gathered in Table 2. These forcing terms are non-resonant, since associated to azimuthal wavenumbers different from $m = \pm 1$, so that the forced equations (4.8) can be inverted. The second order solution $\boldsymbol{q^2}$ is thus sought as the superposition of the response $\boldsymbol{q^2_\delta}$ to the viscous forcing term $-\delta\boldsymbol{\nabla}^2\boldsymbol{u^0}$ of (4.9), which describes the axisymmetric base flow modification when the Reynolds number is varied, and of the 21 responses $\hat{\boldsymbol{q}}^{\boldsymbol{2}}_{\boldsymbol{ij}}$ to each individual forcing terms $\hat{\boldsymbol{F}}^{\boldsymbol{2}}_{\boldsymbol{ij}}$, i.e.

$$\begin{aligned}
\mathbf{q^2} = {} & \delta\hat{\boldsymbol{q}}^{\boldsymbol{2}}_{\boldsymbol{\delta}} + |A|^2\hat{\boldsymbol{q}}^{\boldsymbol{2}}_{\boldsymbol{AA^*}} + |B^+|^2\hat{\boldsymbol{q}}^{\boldsymbol{2}}_{\boldsymbol{B^+B^{+*}}} + |B^-|^2\hat{\boldsymbol{q}}^{\boldsymbol{2}}_{\boldsymbol{B^-B^{-*}}} && (4.10a)\\
& + A^2\hat{\boldsymbol{q}}^{\boldsymbol{2}}_{\boldsymbol{AA}} e^{2\mathrm{i}\theta} + B^+B^{-*}\hat{\boldsymbol{q}}^{\boldsymbol{2}}_{\boldsymbol{B^+B^{-*}}} e^{2\mathrm{i}\theta} + \text{c.c.} && (4.10b)\\
& + B^+A^*\hat{\boldsymbol{q}}^{\boldsymbol{2}}_{\boldsymbol{B^+A^*}} e^{\mathrm{i}\omega_0 t} + B^-A\hat{\boldsymbol{q}}^{\boldsymbol{2}}_{\boldsymbol{B^-A}} e^{\mathrm{i}\omega_0 t} + B^+B^-\hat{\boldsymbol{q}}^{\boldsymbol{2}}_{\boldsymbol{B^+B^-}} e^{2\mathrm{i}\omega_0 t} + \text{c.c.} && (4.10c)\\
& + {B^+}^2\hat{\boldsymbol{q}}^{\boldsymbol{2}}_{\boldsymbol{B^+B^+}} e^{2\mathrm{i}\theta+2\mathrm{i}\omega_0 t} + {B^-}^2\hat{\boldsymbol{q}}^{\boldsymbol{2}}_{\boldsymbol{B^-B^-}} + \text{c.c.} && (4.10d)\\
& + B^+A\hat{\boldsymbol{q}}^{\boldsymbol{2}}_{\boldsymbol{B^+A}} e^{2\mathrm{i}\theta+\mathrm{i}\omega_0 t} + B^-A^*\hat{\boldsymbol{q}}^{\boldsymbol{2}}_{\boldsymbol{B^-A^*}} e^{-2\mathrm{i}\theta+\mathrm{i}\omega_0 t} + \text{c.c.}\,. && (4.10e)
\end{aligned}$$

Each response $\hat{\boldsymbol{q}}^{\boldsymbol{2}}_{\boldsymbol{ij}}$ is solution of a linear problem

$$\left(\mathrm{i}\omega\mathcal{B} + \widetilde{\mathcal{A}}^c\right)\hat{\boldsymbol{q}}^{\boldsymbol{2}}_{\boldsymbol{ij}} = \hat{\boldsymbol{F}}^{\boldsymbol{2}}_{\boldsymbol{ij}}\,, \tag{4.11}$$

	AA^*	B^+B^{+*}	B^-B^{-*}	AA	B^+B^+	B^-B^-	B^+A	B^+A^*	B^+B^-	B^+B^{-*}	B^-A	B^-A^*
m	0	0	0	2	2	-2	2	0	0	2	0	-2
ω	0	0	0	0	$2\omega_0$	$2\omega_0$	ω_0	ω_0	$2\omega_0$	0	ω_0	ω_0

Table 2: Order 2 nonlinear forcing terms gathered by their amplitude dependency, and corresponding azimuthal and temporal periodicity (m, ω). Nine terms have been omitted as they are complex conjugated of the ones presented here.

with m and ω for each couple (i, j) being collected from Table (2). As already mentioned, none of the combinations (m, ω) gathered in Table (2) is an eigenvalue in Figure 3 since none of them is $m = \pm 1$, so that $\mathrm{i}\omega\mathcal{B} + \widetilde{\mathcal{A}}^c$ are always non-degenerate linear operators. The axial velocity components of some of the 21 forcing terms and of their associated responses are shown in Figure 6. The transport of the stationary mode of amplitude A by itself generates the forcing term $\hat{\boldsymbol{F}}^{\boldsymbol{2}}_{\boldsymbol{AA}}$ of azimuthal wavenumber $m = 2$ and zero frequency, shown in Figure 6(a), whose associated response $\hat{\boldsymbol{q}}^{\boldsymbol{2}}_{\boldsymbol{AA}}$ is shown in Figure 6(b). The advection of the spiralling mode of amplitude B^+ by the stationary mode of amplitude A^* (and vice versa) results in an axisymmetric forcing term beating at the frequency ω_0. As seen in Figures 6(c) and 6(d), the forcing term $\hat{\boldsymbol{F}}^{\boldsymbol{2}}_{\boldsymbol{B^+A^*}}$ and its associated response $\hat{\boldsymbol{q}}^{\boldsymbol{2}}_{\boldsymbol{B^+A^*}}$ are nearly periodic in space with a local wavelength close to that of the eigenmode $\hat{\boldsymbol{q}}^{\boldsymbol{1}}_{\boldsymbol{B^+}}$. Finally, the advection of the spiralling mode of amplitude B^+ by the co-rotating spiralling mode of amplitude B^- (and vice versa) generates a second order forcing term $\hat{\boldsymbol{F}}^{\boldsymbol{2}}_{\boldsymbol{B^+B^-}}$ of azimuthal wavenumber $m = 2$ and zero frequency presented in Figures 6(e) and 6(f).

4.4. *Order 3*

The problem at order ϵ^3 is similar to that obtained at order ϵ^2, as the third order solution $\boldsymbol{q^3}$ obeys the forced linear Navier-Stokes equations

$$\mathcal{B}\partial_t \boldsymbol{q^3} + \widetilde{\mathcal{A}}^c \boldsymbol{q^3} = \boldsymbol{F^3}\,. \tag{4.12}$$

The forcing term $\boldsymbol{F^3}$ depends only on lower order solutions and reads

$$\boldsymbol{F^3} = -\left(\partial_{t_1}\boldsymbol{q^1} - \mathcal{S}\boldsymbol{q^1} + \delta\boldsymbol{\nabla}^2\boldsymbol{u^1} + \mathcal{C}(\boldsymbol{u^1}, \boldsymbol{u^2})\,,\, 0\right)^T\,, \tag{4.13}$$

where $\mathcal{S}$ is the shift operator acting in the real space obtained from the operator $\mathcal{S}_m$ introduced in (4.4) by inverse Fourier transform in time and in the azimuthal direction. The first term $-\partial_{t_1}\boldsymbol{q^1}$ in (4.13) corresponds to the slow time evolution of the unknown amplitudes A, B^+, B^-, and will be referred to as the slow variation term. The second term $\mathcal{S}\boldsymbol{q^1}$ comes from the fact that, at the critical Reynolds number Re_c, the growth rates of the eigenmodes are zero at leading-order, but depart from criticality at order ϵ^2. To ease the discussion, this term will therefore be referred to as the off-criticality term. The third term $-\delta\boldsymbol{\nabla}^2\boldsymbol{u^1}$ arises from the Reynolds number variation acting here on the order ϵ^1 solution. The last term $-\mathcal{C}(\boldsymbol{u^1}, \boldsymbol{u^2})$ is due to the advection of the first order solution $\boldsymbol{q^1}$ by the second order solution $\boldsymbol{q^2}$ and vice versa.

The first three forcing terms are linear and therefore resonate. The term $-\mathcal{C}(\boldsymbol{u^1}, \boldsymbol{u^2})$ splits into two contributions: the linear term $-\mathcal{C}(\boldsymbol{u^1}, \boldsymbol{u^2_\delta})$ takes into account the action of the Reynolds number variation through modifications of the axisymmetric base flow, and the nonlinear terms of various space and time periodicity generated through the

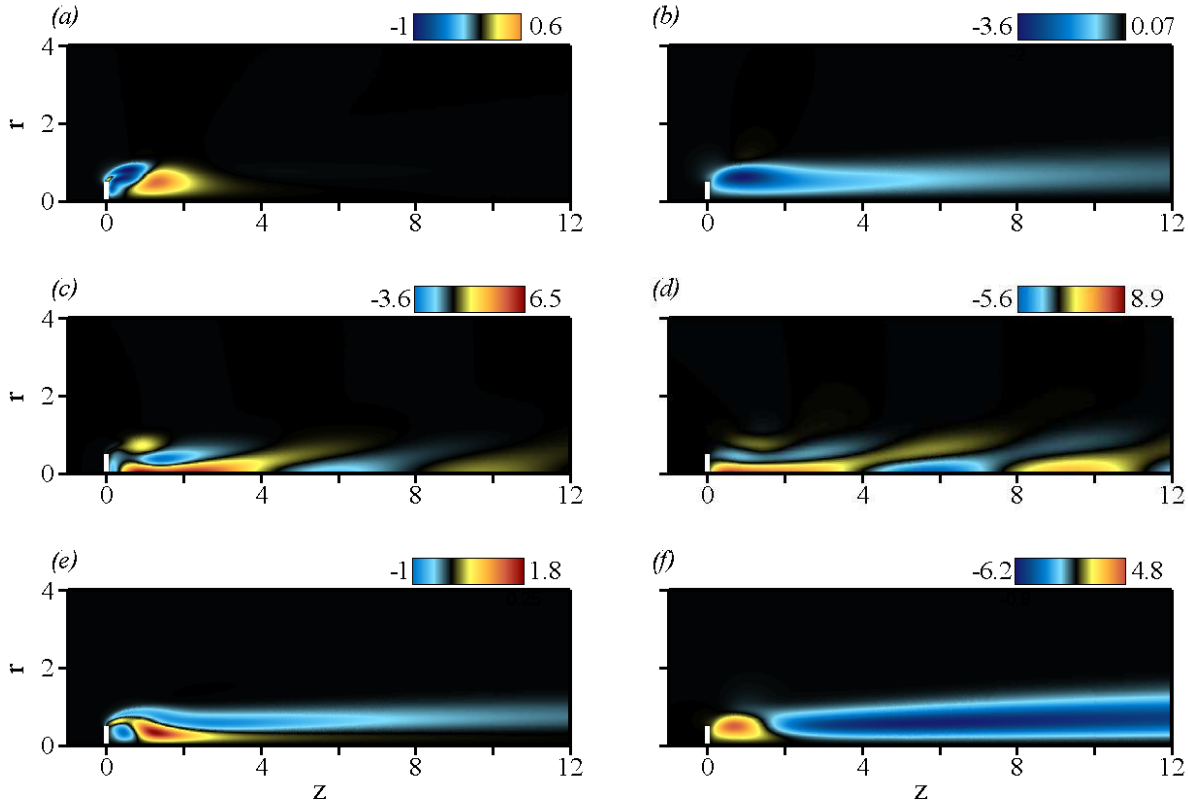

Figure 6: Second order forcing terms and associated responses: representation of various flow fields appearing at order ϵ^2 in the weakly nonlinear analysis. Figures on the left show the real part of the axial component of the forcing terms $\hat{\boldsymbol{F}}^{\mathbf{2}}_{\boldsymbol{ij}}$, and figures on the right show the real part of the associated response $\hat{w}^2_{ij}$. $(a)-(b)$ Flow field of amplitude A^2 $(m=2,\,\omega=0)$. $(c)-(d)$ Flow field of amplitude B^+A^* $(m=0,\,\omega=\omega_0)$. $(e)-(f)$ Flow field of amplitude B^+B^{-*} $(m=2,\,\omega=0)$.

combinations of the 6 contributions of the first order solution together with the 21 other contributions of the second order solution. Each of these terms is denoted $\hat{\boldsymbol{F}}^{\mathbf{3}}_{\boldsymbol{ij}}e^{(\mathrm{i}m\theta+\mathrm{i}\omega t)}$, the subscripts i (resp. j) standing for the amplitude of the first order (resp. second order) solution. Among these nonlinear forcing terms, many are resonant. This is for instance the case of the terms corresponding to the advection of the stationary mode $\hat{\boldsymbol{q}}^{\mathbf{1}}_{\boldsymbol{A}}$ $(m=1,$ $\omega=0)$, by second order contributions satisfying $(m=0,\,\omega=0)$ (see table 2). To avoid secular terms, or in other words, to be able to solve the expansion procedure at the third order, compatibility conditions have to be enforced using the Fredholm alternative (Friedrichs 1973). Specifically, the resonant forcing terms must be orthogonal to the kernel of the adjoint linearized Navier-Stokes operator. The compatibility conditions impose A, B^+, B^- to obey the relation

$$\dot{A} = \epsilon^2\left(\tilde{\lambda}_A A - \tilde{\mu}_A A|A|^2 - \tilde{\nu}_A A|B^+|^2 - \tilde{\nu}^*_A A|B^-|^2 - \tilde{\chi}_A B^+B^{-*}A^*\right), \qquad (4.14a)$$

$$\dot{B}^+ = \epsilon^2\left(\tilde{\lambda}_B B^+ - \tilde{\mu}_B B^+|B^+|^2 - \tilde{\nu}_B B^+|B^-|^2 - \tilde{\eta}_B B^+|A|^2 - \tilde{\chi}_B B^- A^2\right), \qquad (4.14b)$$

$$\dot{B}^- = \epsilon^2\left(\tilde{\lambda}_B B^- - \tilde{\mu}_B B^-|B^-|^2 - \tilde{\nu}_B B^-|B^+|^2 - \tilde{\eta}_B B^-|A|^2 - \tilde{\chi}_B B^+ A^{*2}\right), \qquad (4.14c)$$

which turns out to be identical to the normal form (1.2) if all coefficients in (1.2) are

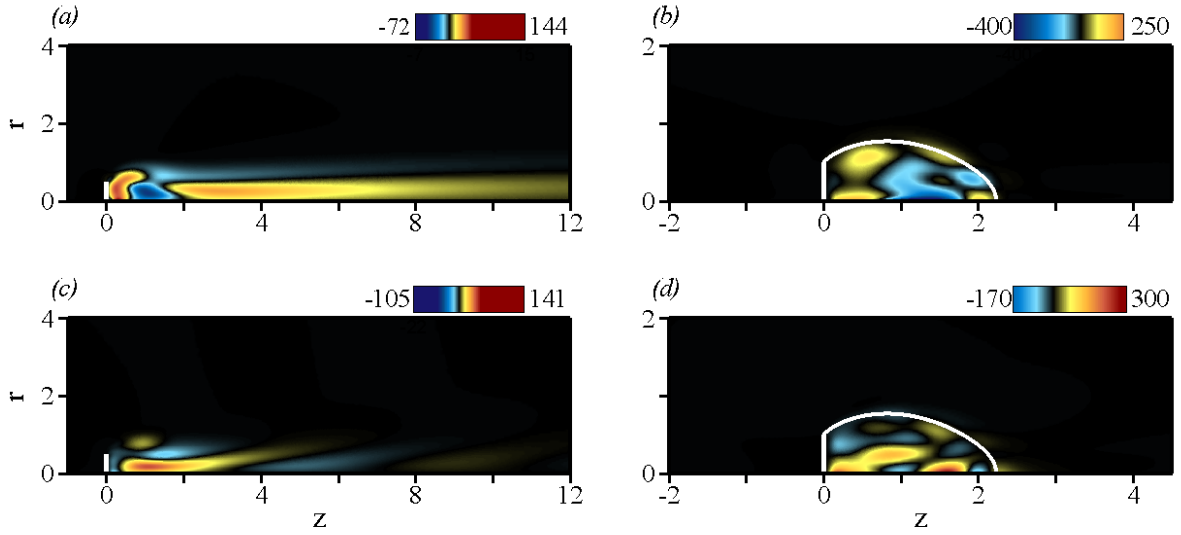

Figure 7: Representation of various resonant forcing fields appearing at order ϵ^3 in the weakly nonlinear analysis. (a) Axial component of the forcing term of amplitude $B^+B^{-*}A^*$ responsible for coefficient $\tilde{\chi}_A$ in equation (4.14a). (b) Coupling density field $\tilde{\chi}_A(r,z)$, defined as the scalar product between this forcing term and the adjoint global mode $\hat{\boldsymbol{q}}^{\mathbf{1}\dagger}_{\boldsymbol{A}}$. ($c$) Real part of the axial component of the forcing term of amplitude B^-A^2 responsible for coefficient $\tilde{\chi}_B$ in equations (4.14b) and (4.14c). (d) Real part of the coupling density field $\tilde{\chi}_B(r,z)$, defined as the scalar product between this forcing term and the adjoint global mode $\hat{\boldsymbol{q}}^{\mathbf{1}\dagger}_{\boldsymbol{B^+}}$.

rescaled into their second-order counterparts defined as

$$(\lambda_A,\, \mu_A, \cdots,\, \chi_B) = \epsilon^2(\tilde{\lambda}_A,\, \tilde{\mu}_A, \cdots,\, \tilde{\chi}_B)\,. \tag{4.15a}$$

The values of all complex coefficients of system (4.14) are computed as scalar products between the adjoint global modes $\hat{\boldsymbol{q}}^{\mathbf{1}\dagger}$ and the resonant forcing terms $\hat{\boldsymbol{F}}^{\mathbf{3}}$. For instance the $\tilde{\chi}_A$ coefficient arises from a forcing term of amplitude $B^+B^{-*}A^*$, generated by three different $\boldsymbol{q^1}$-$\boldsymbol{q^2}$ interactions:

$$\hat{\boldsymbol{F}}^{\mathbf{3}}_{\boldsymbol{B^+B^{-*}A^*}} = -\mathcal{C}_{1,0}\left(\hat{\boldsymbol{u}}^{\mathbf{1}}_{\boldsymbol{B^+}}, \hat{\boldsymbol{u}}^{\mathbf{2^*}}_{\boldsymbol{B^-A}}\right) - \mathcal{C}_{1,0}\left(\hat{\boldsymbol{u}}^{\mathbf{1^*}}_{\boldsymbol{B^-}}, \hat{\boldsymbol{u}}^{\mathbf{2}}_{\boldsymbol{B^+A^*}}\right) - \mathcal{C}_{-1,2}\left(\hat{\boldsymbol{u}}^{\mathbf{1^*}}_{\boldsymbol{A}}, \hat{\boldsymbol{u}}^{\mathbf{2}}_{\boldsymbol{B^+B^{-*}}}\right)\,. \tag{4.16}$$

It can be easily checked that, for instance, the interaction between the spiralling mode $\hat{\mathbf{q}}^{\mathbf{1}}_{\mathbf{B^+}}$ ($m=1$, $\omega=\omega_0$), and the axisymmetric response $\hat{\boldsymbol{u}}^{\mathbf{2^*}}_{\boldsymbol{B^-A}}$ ($m=0$, $\omega=-\omega_0$) is indeed resonant with the stationary mode $\hat{\boldsymbol{u}}^{\mathbf{1}}_{\boldsymbol{A}}$. The axial velocity component of $\hat{\boldsymbol{F}}^{\mathbf{3}}_{\boldsymbol{B^+B^{-*}A^*}}$ is presented in Figure 7(a). This forcing is extended downstream but reaches a maximum in the recirculating bubble. Since $\langle \hat{\boldsymbol{q}}^{\mathbf{1}\dagger}_{\boldsymbol{A}}, \mathcal{B}\hat{\boldsymbol{q}}^{\mathbf{1}}_{\boldsymbol{A}}\rangle = 1$ with the present normalization, $\tilde{\chi}_A$ is given by

$$\tilde{\chi}_A = \left\langle \hat{\boldsymbol{q}}^{\mathbf{1}\dagger}_{\boldsymbol{A}}\ ,\ \hat{\boldsymbol{F}}^{\mathbf{3}}_{\boldsymbol{B^+B^{-*}A^*}} \right\rangle\,. \tag{4.17}$$

It can be seen from (4.17) that the value of the second-order coefficient $\tilde{\chi}_A$ is intrinsic, i.e. it does not depend on the choice of ϵ, the same result pertaining to all coefficients of the normal form (4.14). In particular, it is worthwhile noting that choosing a different value for ϵ would only result into a rescaling of the coefficients. Consequently, all results will be hereinafter presented in terms of the second-order coefficients. Figure 7(b) shows the coupling density $\tilde{\chi}_A(r,z) = \hat{\boldsymbol{q}}^{\mathbf{1}\dagger}_{\boldsymbol{A}}(r,z)\cdot\hat{\boldsymbol{F}}^{\mathbf{3}}_{\boldsymbol{B^+B^{-*}A^*}}(r,z)$, such that the coupling coefficient $\tilde{\chi}_A$ reads $\tilde{\chi}_A = \int_\Omega \tilde{\chi}_A(r,z) r\mathrm{d}r\mathrm{d}z$. One observes that the coupling

density $\tilde{\chi}_A(r,z)$ vanishes outside the recirculation bubble, since the adjoint global mode is localized within the recirculation bubble and upstream of the disk (Figure 4b), and the nonlinear forcing $\hat{\boldsymbol{F}}^{\boldsymbol{3}}_{\boldsymbol{B^+B^-{}^*A^*}}$ is localized downstream (Figure 7a). This indicates that the resonant forcing of mode $\hat{\boldsymbol{q}}^{\boldsymbol{1}}_{\boldsymbol{A}}$ owing to the $B^+B^{-*}A^*$ interaction is efficient only in the recirculation bubble. It is worthwhile emphasizing that this result can be generalized to all nonlinear coefficients of the normal form (4.14), that are computed as the scalar product of a forcing term localized downstream of the disk, with an adjoint global mode localized upstream of the disk and in the recirculation bubble. They are therefore only determined by a coupling that occurs within the recirculation bubble. The recirculation region may therefore be viewed as the *effective wavemaker* since all nonlinear interactions between the instability modes take place in this region. Even though nonlinear forcing terms and nonlinear responses are all spatially extended downstream, the region outside the recirculation bubble may be viewed as passive since values of the flow field there do not influence the dynamics of the leading modes.

Similarly, $\tilde{\chi}_B$ results from a forcing term of amplitude B^-AA, whose real part of the axial velocity component is shown in Figure 7(c). It arises from different contributions

$$\hat{\boldsymbol{F}}^{\boldsymbol{3}}_{\boldsymbol{B^-AA}} = -\mathcal{C}_{1,0}\left(\hat{\boldsymbol{u}}^{\boldsymbol{1}}_{\boldsymbol{A}}, \hat{\boldsymbol{u}}^{\boldsymbol{2}}_{\boldsymbol{B^-A}}\right) - \mathcal{C}_{-1,2}\left(\hat{\boldsymbol{u}}^{\boldsymbol{1}}_{\boldsymbol{B^-}}, \hat{\boldsymbol{u}}^{\boldsymbol{2}}_{\boldsymbol{AA}}\right), \tag{4.18a}$$

$$\tilde{\chi}_B = \left\langle \hat{\boldsymbol{q}}^{\boldsymbol{1\dagger}}_{\boldsymbol{B^+}} \;,\; \hat{\boldsymbol{F}}^{\boldsymbol{3}}_{\boldsymbol{B^-AA}} \right\rangle. \tag{4.18b}$$

This means that the spiralling mode $\hat{\boldsymbol{q}}^{\boldsymbol{1}}_{\boldsymbol{B^-}}$ can force the production of the counter-rotating spiralling mode $\hat{\boldsymbol{q}}^{\boldsymbol{1}}_{\boldsymbol{B^+}}$ by its nonlinear interaction with the $m=2$ stationary solution $\hat{\boldsymbol{q}}^{\boldsymbol{2}}_{\boldsymbol{AA}}$ shown in Figure 6(b), or by interacting first with the stationary mode $\hat{\boldsymbol{q}}^{\boldsymbol{1}}_{\boldsymbol{A}}$ to produce the second order solution $\hat{\boldsymbol{q}}^{\boldsymbol{2}}_{\boldsymbol{B^-A}}$ ($m=0$, $\omega=\omega_0$), which eventually interacts with $\hat{\boldsymbol{q}}^{\boldsymbol{1}}_{\boldsymbol{A}}$ again. The real part of the associated coupling density field $\tilde{\chi}_B(r,z) = \hat{\boldsymbol{q}}^{\boldsymbol{1}}_{\boldsymbol{B^+}}(r,z)\cdot\hat{\boldsymbol{F}}^{\boldsymbol{3}}_{\boldsymbol{B^-AA}}(r,z)$, shown in Figure 7($d$), is also localized in the recirculation region, meaning that the spiralling mode $\hat{\boldsymbol{q}}^{\boldsymbol{1}}_{\boldsymbol{B^+}}$ is receptive to the forcing owing to the B^-AA interaction only close to the disk and in the recirculating bubble.

We obtain:

$\tilde{\lambda}_A = 2.01 + 71.4\delta$	$\tilde{\lambda}_B = -1.85 + 76.4\mathrm{i} + (66.7 + 9.35\mathrm{i})\delta$
$\tilde{\mu}_A = 3.11$	$\tilde{\mu}_B = 2.42 + 0.0321\mathrm{i}$
$\tilde{\nu}_A = 6.88 - 1.11\ \mathrm{i}$	$\tilde{\nu}_B = 3.13 - 0.816\mathrm{i}$
	$\tilde{\eta}_B = 0.955 - 3.47\mathrm{i}$
$\tilde{\chi}_A = 4.57$	$\tilde{\chi}_B = 1.62 - 1.36\mathrm{i}\,.$

4.5. *Bifurcation diagram*

We set now $A = |A|e^{\mathrm{i}\phi_\mathrm{A}}$, $B^+ = |B^+|e^{\mathrm{i}\phi^+_\mathrm{B}}$ and $B^- = |B^-|e^{\mathrm{i}\phi^-_\mathrm{B}}$. An exhaustive description of the solutions of system (4.14), up to ternary bifurcations, can be found in Golubitsky *et al.* (1988). In this section, we comment only the solutions relevant to our problem. The bifurcation diagram is shown in Figure 8, where the quantity $\Theta = |A| + |B^+| + |B^-|$ is plotted as a function of the Reynolds number. Note that Θ has no particular physical meaning but yields a convenient visualization of the bifurcation sequence. The solid thick lines (resp. thin dashed lines) correspond to stable (resp. unstable) solutions that are of three different kinds, as will now be explained.

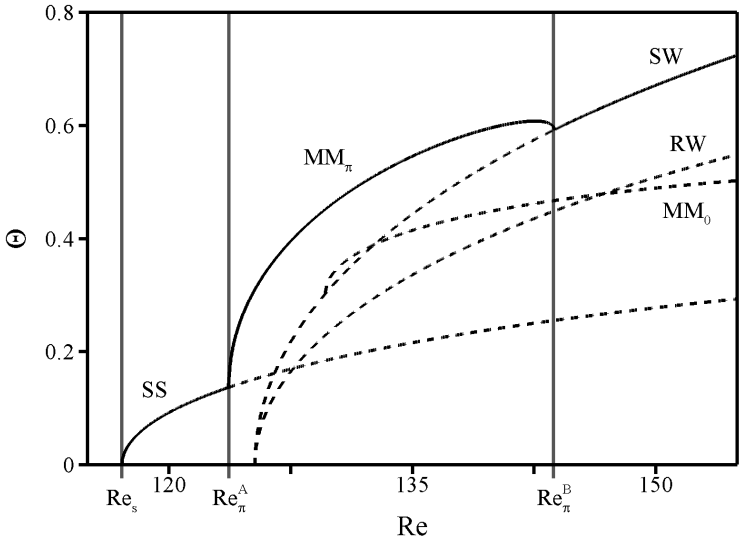

Figure 8: Theoretical bifurcation diagram associated to the normal form (4.14). Solid (resp. dashed) lines denote stable (resp. unstable) branches.

4.5.1. *Pure modes*

In addition to the trivial steady axisymmetric solution $(A, B^+, B^-) = (0, 0, 0)$, equations (4.14) have three types of solutions involving a single mode. The pure steady state SS $(A, 0, 0)$ is ruled by the real Landau equation for A

$$\dot{A} = \epsilon^2 \left(\tilde{\lambda}_A - \tilde{\mu}_A A |A|^2 \right) , \tag{4.19}$$

so that $A^2 = |A|^2 = \tilde{\lambda}_A / \tilde{\mu}_A$ and $\dot{\phi}_{\rm A} = 0$, and we can impose $\phi_{\rm A} = 0$ by choosing the phase of the initial disturbance to be zero. The pure Hopf states RW $(0, B^+, 0)$ and $(0, 0, B^-)$ are associated with spiralling modes, whose amplitude is governed by the complex Landau equation for $B^\pm$

$$\dot{B}^\pm = \epsilon^2 \left(\tilde{\lambda}_B B^\pm - \tilde{\mu}_B B^\pm |B^\pm|^2 \right) , \tag{4.20}$$

so that

$$|B^\pm|^2 = \frac{\tilde{\lambda}_{Br}}{\tilde{\mu}_{Br}} , \tag{4.21a}$$

$$\phi_{\rm B}^\pm = \epsilon^2 \left(\tilde{\lambda}_{Bi} - \tilde{\mu}_{Bi} |B^\pm|^2 \right) t + \phi_{\rm B}^{\pm 0} . \tag{4.21b}$$

4.5.2. *Standing waves*

The standing wave SW $(0, B^+, B^-)$ corresponds to the superimposition of two counter-rotating spiralling modes of same amplitude $|B^\pm|^2$ governed by the amplitude equation

$$\dot{B}^\pm = \epsilon^2 \left(\tilde{\lambda}_B B^\pm - \left(\tilde{\mu}_B + \tilde{\nu}_B \right) B^\pm |B^\pm|^2 \right) , \tag{4.22}$$

of solutions

$$|B^\pm|^2 = \frac{\tilde{\lambda}_{Br}}{\tilde{\mu}_{Br} + \tilde{\nu}_{Br}} , \tag{4.23a}$$

$$\phi_{\rm B}^\pm(t) = \epsilon^2 \left(\tilde{\lambda}_{Bi} - \left(\tilde{\mu}_{Bi} + \tilde{\nu}_{Bi} \right) |B^\pm|^2 \right) t + \phi_{\rm B}^{\pm 0} . \tag{4.23b}$$

4.5.3. *Mixed modes*

Mixed modes MM (A, B^+, B^-) correspond to a superposition of the three global modes, i.e. one stationary mode and two counter-rotating spiral modes of same amplitude $|B^\pm|$. Introducing the phase $\phi = \phi_{\rm B}^+ - \phi_{\rm B}^- - 2\phi_{\rm A}$ allows to reduce system (4.14) to a three-dimensional polar system for $|A|$, $|B^\pm|$ and ϕ that reads:

$$|\dot{A}| = \epsilon^2 \left(\tilde{\lambda}_A |A| - \tilde{\mu}_A |A|^3 - (2\tilde{\nu}_{Ar} + \tilde{\chi}_A \cos\phi)\, |A||B^\pm|^2 \right) , \tag{4.24a}$$

$$|\dot{B^\pm}| = \epsilon^2 \left(\tilde{\lambda}_{Br} |B^\pm| - (\tilde{\mu}_{Br} + \tilde{\nu}_{Br})\, |B^\pm|^3 - (\tilde{\eta}_{Br} + \tilde{\chi}_{Br} \cos\phi \pm \tilde{\chi}_{Bi} \sin\phi)\, |B^\pm||A|^2 \right) , \tag{4.24b}$$

$$\dot{\phi} = 2\epsilon^2 \left(\tilde{\chi}_{Br} |A|^2 + \tilde{\chi}_A |B^\pm|^2 \right) \sin\phi \, . \tag{4.24c}$$

The phase ϕ is thus solution of $\sin\phi = 0$, so that it comes from (4.24*c*) that ϕ is invariant. The solutions of system (4.24) are such that

$$\cos\phi = \pm 1 \, , \tag{4.25a}$$

$$|A|^2 = \frac{\tilde{\lambda}_A(\tilde{\mu}_{Br} + \tilde{\nu}_{Br}) - (2\tilde{\nu}_{Ar} + \cos\phi\tilde{\chi}_A)\tilde{\lambda}_{Br}}{\tilde{\mu}_A(\tilde{\mu}_{Br} + \tilde{\nu}_{Br}) - (2\tilde{\nu}_{Ar} + \cos\phi\tilde{\chi}_A)(\tilde{\eta}_{Br} + \cos\phi\tilde{\chi}_{Br})} \, , \tag{4.25b}$$

$$|B^\pm|^2 = \frac{-\tilde{\lambda}_A(\tilde{\eta}_{Br} + \cos\phi\tilde{\chi}_{Br}) + \tilde{\mu}_A\tilde{\lambda}_{Br}}{\tilde{\mu}_A(\tilde{\mu}_{Br} + \tilde{\nu}_{Br}) - (2\tilde{\nu}_{Ar} + \cos\phi\tilde{\chi}_A)(\tilde{\eta}_{Br} + \cos\phi\tilde{\chi}_{Br})} \, , \tag{4.25c}$$

$$\phi_{\rm B}^\pm(t) = \epsilon^2 \left(\tilde{\lambda}_{Bi} - (\tilde{\mu}_{Bi} + \tilde{\nu}_{Bi})|B^\pm|^2 - (\tilde{\eta}_{Bi} + \tilde{\chi}_{Bi}\cos\phi)|A|^2 \right) t \pm (\phi + 2\phi_{\rm A})/2 \, , \tag{4.25d}$$

so that the mixed modes come in two different states, referred to as MM_0 ($\cos\phi = 1$) and MM_π ($\cos\phi = -1$) respectively. Note that since coefficient $\tilde{\chi}_A$ is real, equation (4.14*a*) leads to $\dot{\phi}_{\rm A} = 0$, so that we can again impose $\phi_{\rm A} = 0$ without particularizing the solution of the system.

4.6. *Bifurcating modes*

Unless otherwise specified, all flow fields presented in this section refer to the second order nonlinear solution $\boldsymbol{q} = \boldsymbol{q^0} + \epsilon\boldsymbol{q^1} + \epsilon^2\boldsymbol{q^2}$, the term of order ϵ^2 being essential to discuss some realistic features. For the present coefficient values, the domains of existence and the stability of the different modes are shown in Figure 8.

(*a*) For low Reynolds numbers $Re < 117.1$, the trivial steady axisymmetric solution $\Theta = 0$ is stable. It exhibits an infinite number of symmetry planes.

(*b*) The first bifurcation occurs at $Re_s = 117.1$, where the trivial state bifurcates to the pure steady state SS. The threshold of this bifurcation, for which $\tilde{\lambda}_A = 0$, departs slightly from the critical Reynolds number issuing from the direct stability analysis Re_c^A, as it is obtained by considering the linear approximation of the growth rate. As discussed previously, the stationary mode that bifurcates corresponds to a shift of the wake in one direction, associated with the appearance of a pair of longitudinal vortices. If one only looks at the first order solution, the longitudinal vortex dipole is centered, but the asymptotic second order solution allows to describe the off-axis displacement of the dipole under its self-induction (Figures 9*a* and 9*b*). Figure 9(*a*) shows cross-sectional contour plots of the streamwise vorticity at a Reynolds number $Re = 118.5$ above threshold, the section being taken 20 diameters downstream of the disk. We observe a counter-rotating vortex dipole which is reminiscent of that observed experimentally in axisymmetric wakes in this regime (Thompson *et al.* 2001), and usually designated as 'vortex threads'. Note

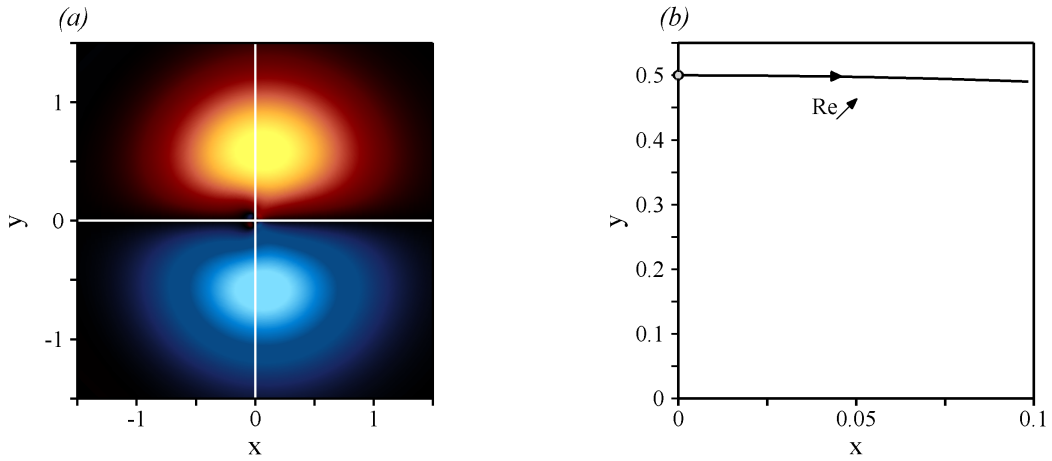

Figure 9: Streamwise vorticity of the SS-mode. (a) Cross-sectional contours of streamwise vorticity, computed at the bifurcation threshold Re_c^A, at the axial position $z = 20$. (b) For the same axial position, trajectory of the vortex core in the (x, y)-plane as the Reynolds number is increased in the range $117.1 < Re < 123$, for the solution computed up to the second order. This lateral shift of the longitudinal vortex dipole is due to the self-induction of the perturbation, accounted for by the second harmonic term $\hat{\boldsymbol{q}}_{\boldsymbol{AA}}^{\boldsymbol{2}}$ in the asymptotic expansion (4.10).

that the cores of the vortex dipole, defined as the points of extremal streamwise vorticity of $\boldsymbol{q}$, are located off the centreplane $x = 0$ at threshold, as each vortex induces a velocity at the centreline of the other, hence causing them to be convected away from the centreplane. This nonlinear effect is shown in Figure 9(b), where the position of the vortex core in the (x, y) plane is plotted as a function of the Reynolds number. The vertical position of the core barely changes, whereas the maximum horizontal deviation is zero at threshold and increases when the Reynolds number is increased, i.e. when the amplitude of the perturbation is increased. It finally reaches approximately 0.1 disk diameter for $Re = 123$. In the present asymptotic expansion procedure, this effect is taken into account through the second order term $\mathcal{C}_{1,1}(\hat{\boldsymbol{q}}_{\boldsymbol{A}}^{\boldsymbol{1}}, \hat{\boldsymbol{q}}_{\boldsymbol{A}}^{\boldsymbol{1}})$ corresponding to the generation of the $m = 2$ harmonic $\hat{\boldsymbol{q}}_{\boldsymbol{AA}}^{\boldsymbol{2}}$. Indeed, when the nonlinear contribution of this harmonic is removed, the vortex dipole remains on the y-axis (grey circular symbol in Figure 9b). When considering the flow field, these vortex threads break the reflectional symmetry with respect to the (y, z)-plane but preserve that with respect to the (x, z)-plane, as evidenced by the axial velocity fields of the saturated flow field shown in Figure 10: one thus observes that Figures 10(a) and 10(c), showing the (x, z)-plane, are not symmetric with respect to the (y, z)-plane, whereas Figure 10(b) and 10(d), showing the (y, z)-plane, are symmetric with respect to the (x, z)-plane. The breaking of the rotational symmetry is also evidenced in Figure 11, which simulates an experimental dye visualization and shows numerically computed dye lines emitted from the disk surface and transported by the second order analytic solution. Note that the symmetry plane can be arbitrarily rotated as the phase ϕ_{A} has been here arbitrarily selected.

(c) A second bifurcation occurs at $Re_\pi^A = 123.7$, where the SS-state bifurcates to the MM_π-branch where $\cos\phi = -1$ ($\phi = \pi$). At threshold, the SS-branch loses its stability to disturbances of small amplitudes $|B^+| = |B^-| = |B^\pm|$, their second-order growth rate being given by

$$\tilde{\sigma}_\pi^A = \tilde{\lambda}_{Br} - (\tilde{\eta}_{Br} - \tilde{\chi}_{Br})\frac{\tilde{\lambda}_A}{\tilde{\mu}_A}. \tag{4.26}$$

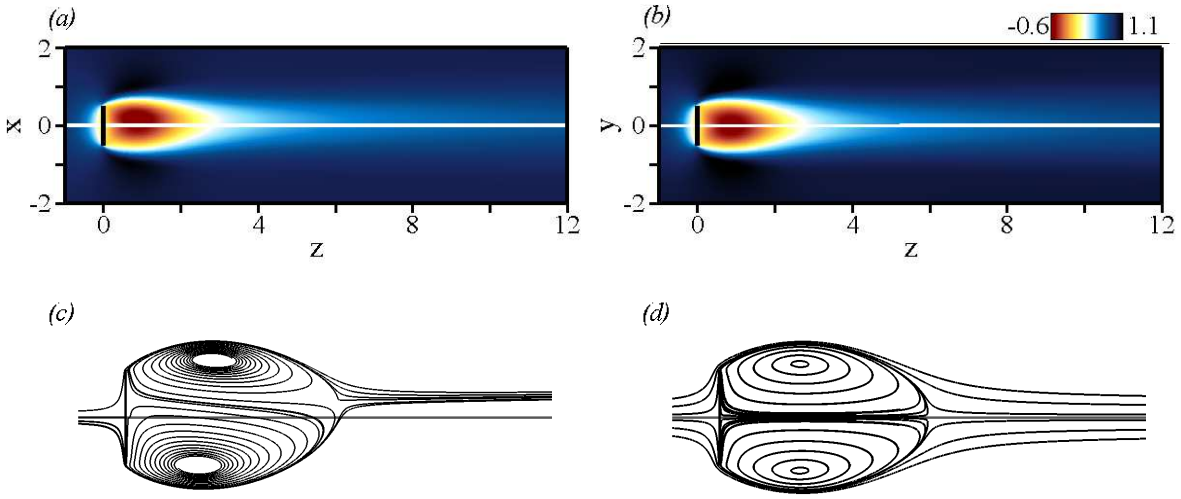

Figure 10: $(a)-(b)$ Streamwise velocity $\hat{w}$ and $(c)-(d)$ streamlines of the SS solution, expanded up to the second order (i.e. $\boldsymbol{q} = \boldsymbol{q^0} + \epsilon \boldsymbol{q^1} + \epsilon^2 \boldsymbol{q^2}$) at $Re = 123$. $(a)-(c)$ x,z)-plane. $(b)-(d)$ (y,z)-plane.

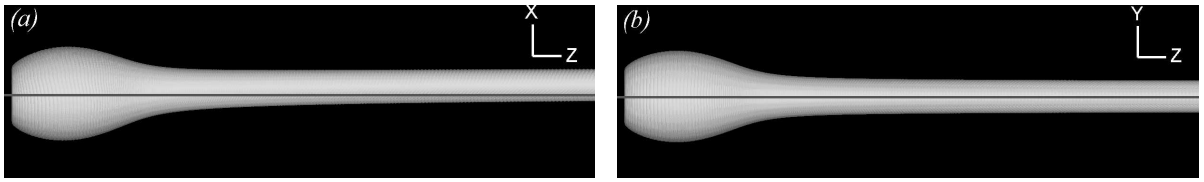

Figure 11: Numerically computed dye lines corresponding to the second order SS solution shown in Figure 10. The dark grey line represents the revolution axis and the wake has moved off-axis only in the (x,z) side view.

In the present case, the mode of invariant phase $\phi = \pi$ destabilizes first the SS-branch since $\tilde{\chi}_{Br}$ is positive (see Golubitsky *et al.* 1988, for more details) and the Hopf bifurcation from the SS branch occurs in favor of the MM_π mode. The resulting pattern breaks the reflectional symmetry of the SS-mode with a periodic flapping of the wake in the (y,z)-plane, associated with a shedding of vortices, as seen in Figure 12, showing the axial velocity component in the (x,z) and (y,z)-planes for the Reynolds number $Re = 136$. The dye lines computed using the periodic flow given by the second order asymptotic expansion are shown in Figure 12, and illustrate the loss of all symmetries of the flow. Moreover, Figure 12 demonstrates the ability of such asymptotic expansion to represent complex flows with dye lines exhibiting realistic knitted hairpin structures. Were $\tilde{\chi}_{Br}$ negative, then the SS mode would have bifurcated to the MM_0-branch. In the present case, this branch is not selected and is unstable. Still, the corresponding numerical dye lines are shown in Figure 16 for comparison at the same Reynolds number $Re = 136$, although one should keep in mind that the resulting flow is unstable and should not be observed.

(d) A third bifurcation occurs at $Re_\pi^B = 143.7$, where the MM_π-branch bifurcates to the SW-branch, where $A = 0$. The critical Reynolds number is found by considering the backward bifurcation from the SW to the MM_π states, i.e. by studying how the SW-branch loses its stability to disturbances of small amplitude $|A|$, whose second-order

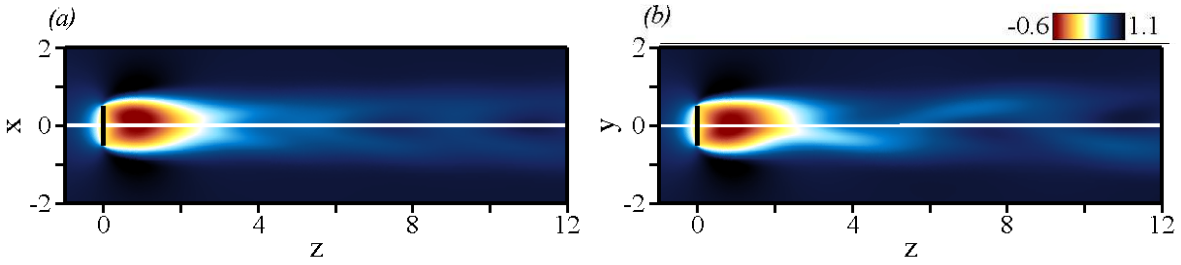

Figure 12: Flow after the second bifurcation: axial velocity w of the MM_π solution, expanded up up to the second order - $Re = 136$. (a) (x, z)-plane. (b) (y, z)-plane.

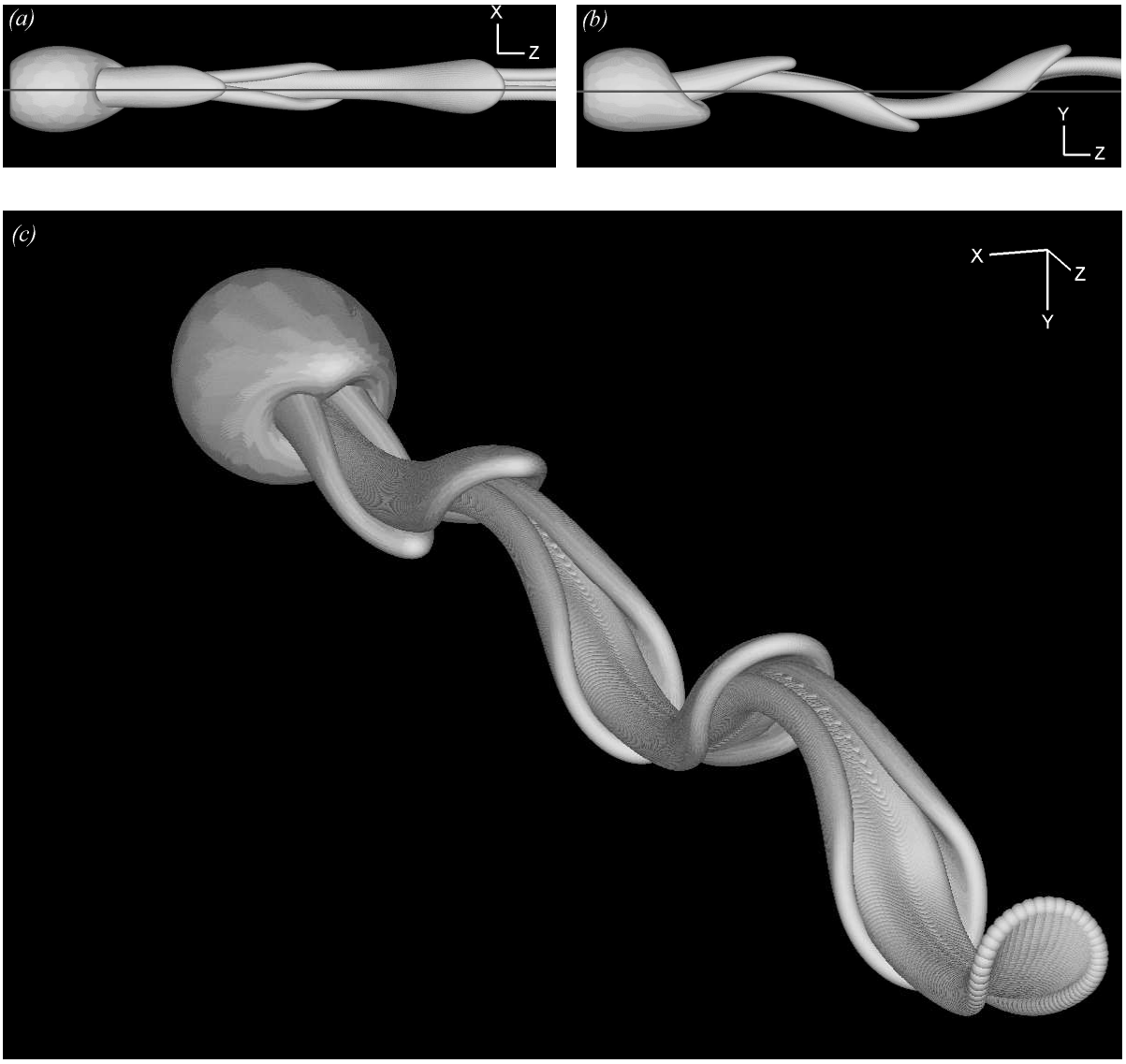

Figure 13: Numerically computed dye lines based on the asymptotic expansion up to the second order, corresponding to the MM_π solution shown in Figure 12. (a) (x, z)-plane: the $x \longrightarrow -x$ symmetry is broken by a drift of the wake towards positive values of x downstream of the disk. (b) (y, z)-plane. (c) 3D representation.

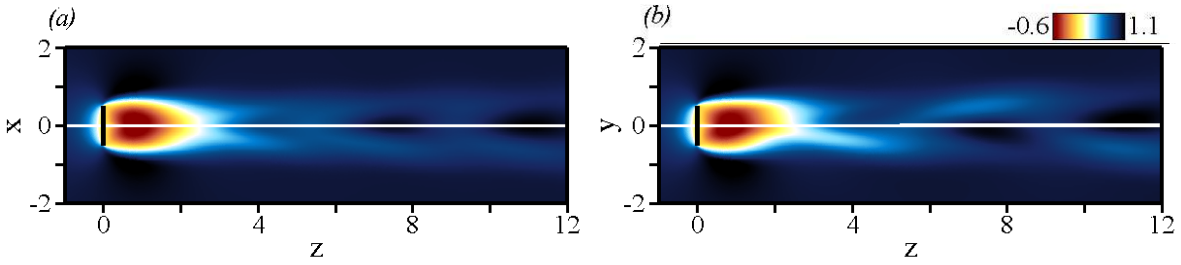

Figure 14: Flow after the third bifurcation: axial velocity w of the SW solution, expanded up to the second order - $Re = 144$. (a) (x, z)-plane. (b) (y, z)-plane.

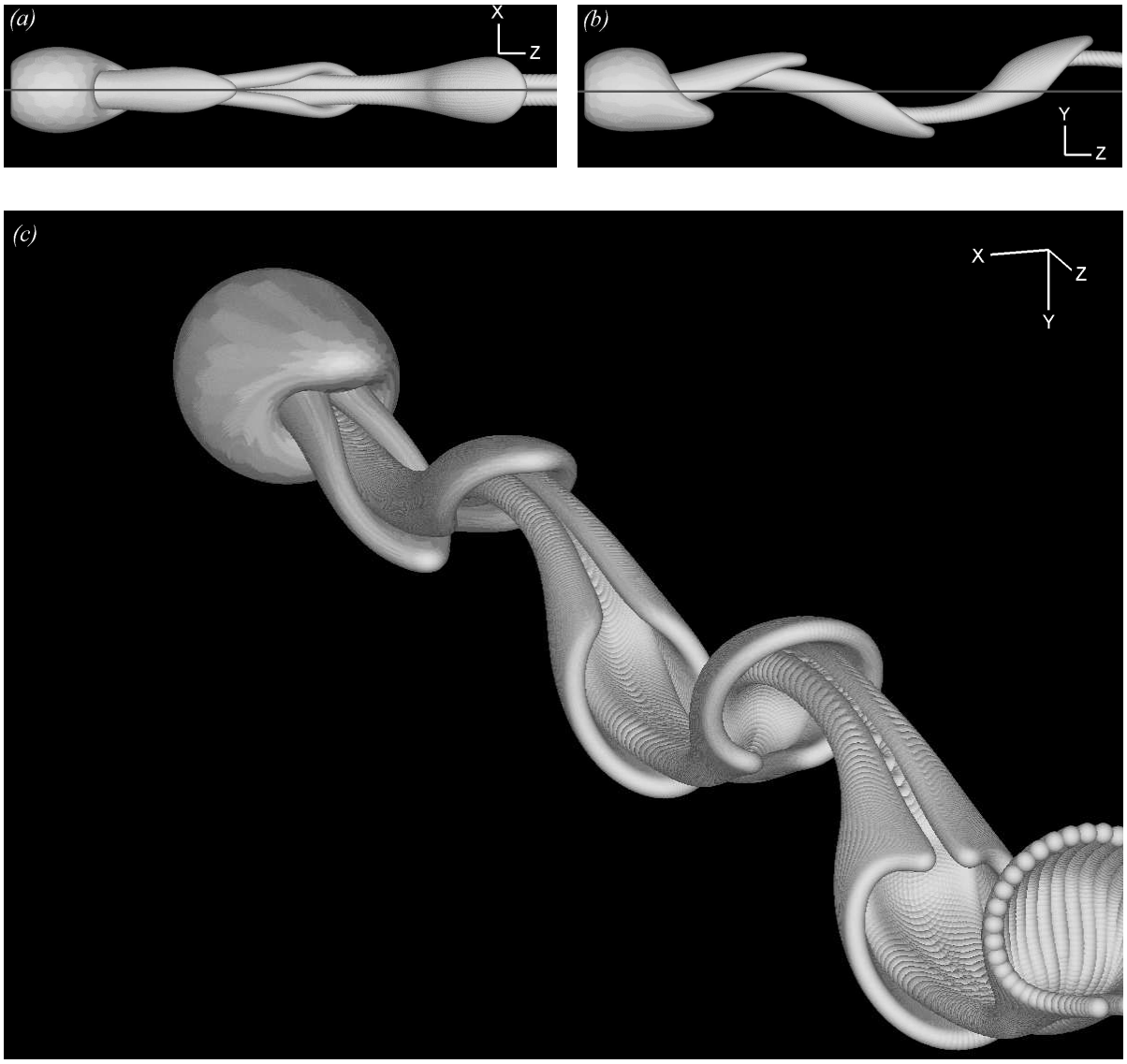

Figure 15: Numerical dye lines corresponding to the SW solution shown in Figure 14. (a) (x, z)-plane: the $x \longrightarrow -x$ symmetry is recovered. (b) (y, z)-plane. (c) 3D representation.

growth rate is given by

$$\tilde{\sigma}_{\pi}^{B} = \tilde{\lambda}_{A} - (2\tilde{\nu}_{Ar} - \tilde{\chi}_{A})\frac{\tilde{\lambda}_{Br}}{\tilde{\mu}_{Br} + \tilde{\nu}_{Br}}. \tag{4.27}$$

As reported in Golubitsky *et al.* (1988), the SW-branch, rather than the RW-branch, is

selected here, since $\tilde{\nu}_{Br} > \tilde{\mu}_{Br}$. The condition for this bifurcation to occur is $\tilde{\chi}_A > 0$, i.e. the development of the standing wave must restabilize the stationary eigenmode $\hat{\boldsymbol{q}}^{\mathbf{1}}_{\boldsymbol{A}}$, which is the case here (more details on the branch selection point can be found in Appendix A). Views of the axial velocity component at the Reynolds number $Re = 144$ are shown in Figure 14, and the associated numerical dye lines at this Reynolds number are shown in Figure 15. Comparing to the analogous representation of the MM_π-branch shown in Figures 12 and 13, the difference may appear subtle, but the symmetry with respect to the (y, z)-plane is recovered, as shown in Figures 14(a) and 15(a), whereas the wake was shifted up in Figures 12(a) and 13(a).

4.7. *Comparison with the DNS calculations*

Direct numerical simulations of the wake of a circular disk placed normal to a uniform flow have been performed by Fabre *et al.* (2008). In this study, it has been observed that, as the Reynolds number is increased, the flow undergoes a sequence of successive bifurcations, each state being characterized by specific time and space symmetry breaking or recovering. These authors report a first bifurcation at the Reynolds number $Re_s \simeq 115$, leading to a steady state with a reflectional symmetry, corresponding to the present SS-branch. Then, a Hopf bifurcation is found for $Re_\pi^A \simeq 121$, leading to a so-called *reflectional symmetry breaking* state, characterized by the periodic shedding of vortices twisted around the symmetry axis, with no symmetry plane. The bifurcation threshold and symmetry properties therefore agree with that of the present MM_π-branch. Finally, a third bifurcation is observed for $Re_\pi^B \simeq 140$ and allows the flow to recover a planar symmetry, the recovered symmetry plane being found to be orthogonal to that initially selected in the steady state. This bifurcation threshold and symmetry properties agree with that of the present SW-branch.

The whole bifurcation sequence, including the third bifurcation, predicted by the present asymptotic expansion matches qualitatively and quantitatively for threshold values with that found in the DNS calculations. Note that as mentioned in Section 1, there exist other techniques to compute the coefficients of the normal form (4.14). For instance, one could investigate experimentally or numerically the transient dynamics at various Reynolds numbers. In the case of the cylinder wake, such procedure has allowed Provansal *et al.* (1987) to compute with accuracy the Landau coefficient associated with the Hopf bifurcation. Though, such methods can be expected to also yield results in good agreement with that presented here, since we show in Appendix C that the sensitivity of the bifurcation diagram to small variations in the different coefficients is remarkably small.

4.8. *Recirculation length and Strouhal number evolution*

We investigate now the impact of the bifurcation sequence on the recirculation length and frequency of the bifurcated flow. Figure 17(a) shows the evolution of the recirculation length as a function of the Reynolds number. The vertical grey lines stand for the different bifurcation thresholds. The solid line corresponds to that of the mean flow obtained by time and azimuthal average, given in the present formalism by the axisymmetric stationary solution up to the second order

$$\boldsymbol{q} = \boldsymbol{q^0} + \epsilon^2 \left(\delta \hat{\boldsymbol{q}}^{\mathbf{2}}_{\boldsymbol{\delta}} + |A|^2 \hat{\boldsymbol{q}}^{\mathbf{2}}_{\boldsymbol{AA^*}} + |B^+|^2 \hat{\boldsymbol{q}}^{\mathbf{2}}_{\boldsymbol{B^+B^{+*}}} + |B^-|^2 \hat{\boldsymbol{q}}^{\mathbf{2}}_{\boldsymbol{B^-B^{-*}}} \right) , \tag{4.28}$$

and the dashed line corresponds to that of the axisymmetric base flow obtained as $\boldsymbol{q^0} + \epsilon^2 \delta \hat{\boldsymbol{q}}^{\mathbf{2}}_{\boldsymbol{\delta}}$. The results sketched in this Figure show that increasing the Reynolds number yields an increase in the recirculation length of the base flow. Figure 18 shows the

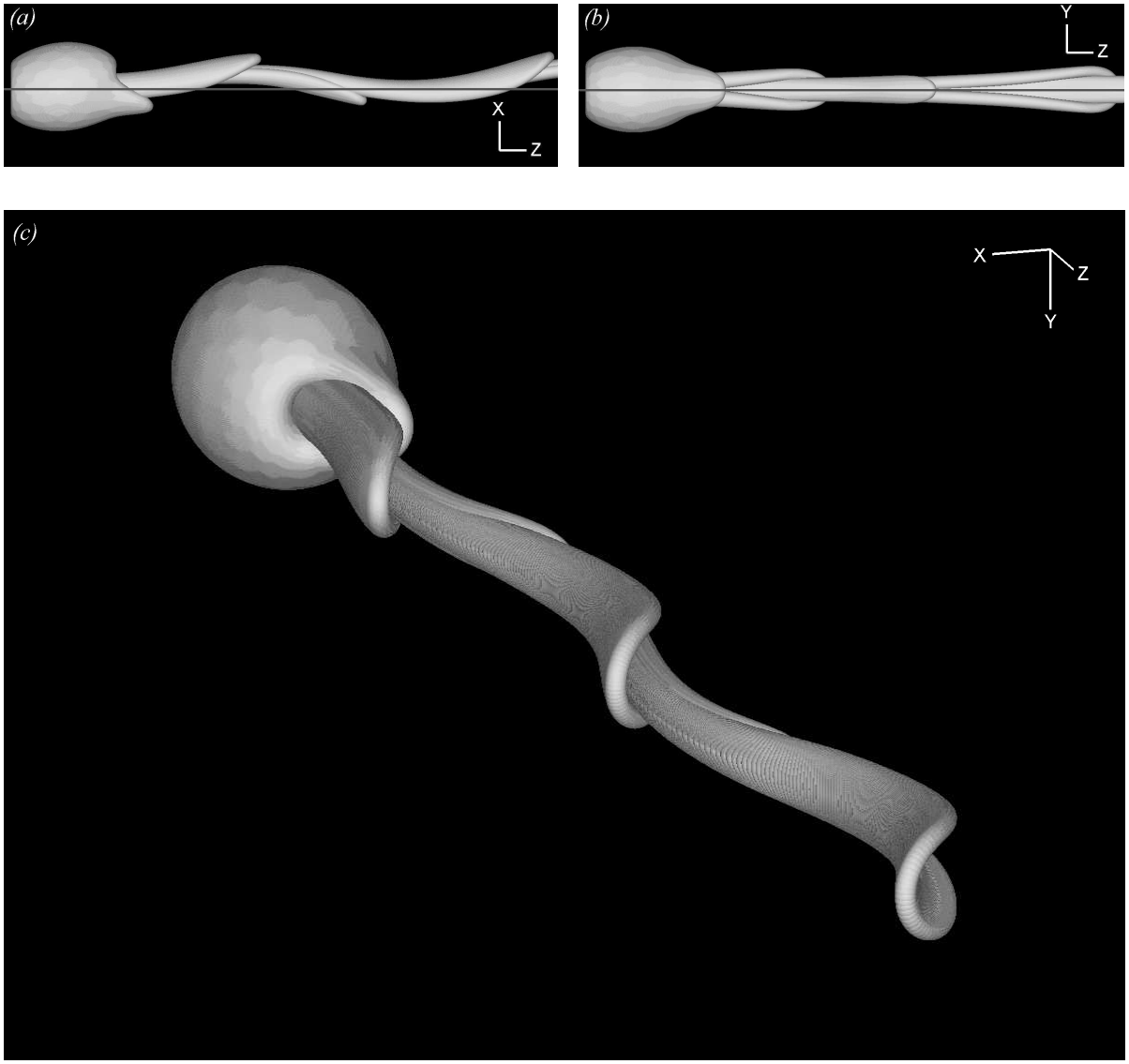

Figure 16: Numerical dye lines corresponding to the unstable MM_0 solution expanded up to the second order - $Re = 136$. (a) (x, z)-plane. (b) (y, z)-plane. (c) 3D representation.

axial velocity component $\hat{w}_\delta^2$ of the base flow modification owing to the variation of the Reynolds number. It can be seen that the increase in the recirculation length is due to $\hat{w}_\delta^2$ being negative in the wake. It is possible to note that on the SS-branch, this effect is exactly counterbalanced by the positive values of $\hat{w}_{AA^*}^2$, so that the overall recirculation length remains almost constant between Re_s and Re_π^A. For Reynolds larger than Re_π^A, the positive values of $\hat{w}_{AA^*}^2$ and $\hat{w}_{B^\pm B^{\pm *}}^2$ in the wake (not shown here) become dominant and the overall recirculation length continuously decreases down to 1.8 disk diameters. Note that in the case of the wake past a circular cylinder, a similar decrease of the recirculation length as the Reynolds numbers is increased above the critical value $Re = 47$ has been shown to arise due to the strong mean flow correction induced by the existence of an unstable mode (Zielinska *et al.* 1997).

Another consequence of this successive bifurcation scenario is the prediction of the frequency at the onset of unsteadiness. The frequency of the bifurcated flow is given by $\omega = \omega_0 + \epsilon^2 \tilde{\omega}_{nl}$ where $\tilde{\omega}_{nl}$ is the second-order nonlinear correction obtained from equations (4.23b) and (4.25d) as $\dot{\phi}_{\mathrm{B}}^{\pm} = \epsilon^2 \tilde{\omega}_{nl}$. Figure 17($b$) shows the evolution of the Strouhal

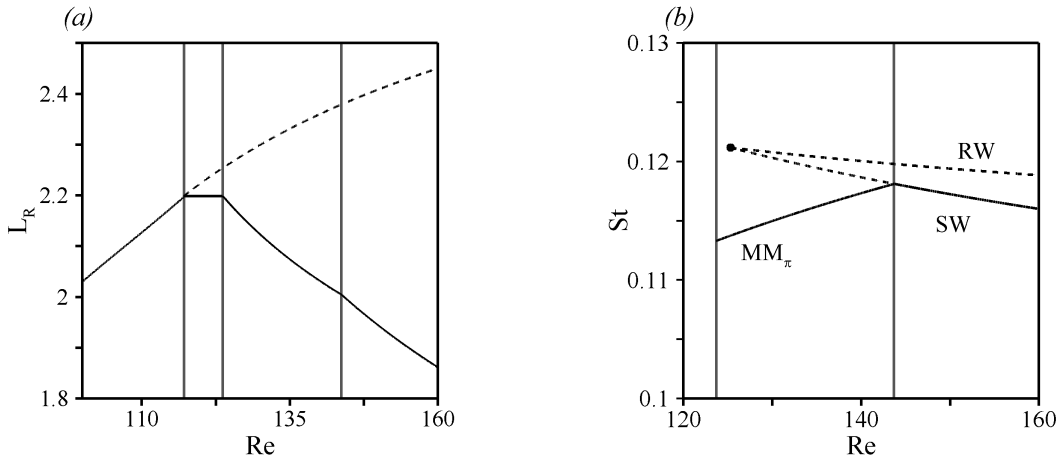

Figure 17: (a) Recirculation length L_r for the mean flow as a function of the Reynolds number. (b) Strouhal number St of the unsteady flow as a function of the Reynolds number.

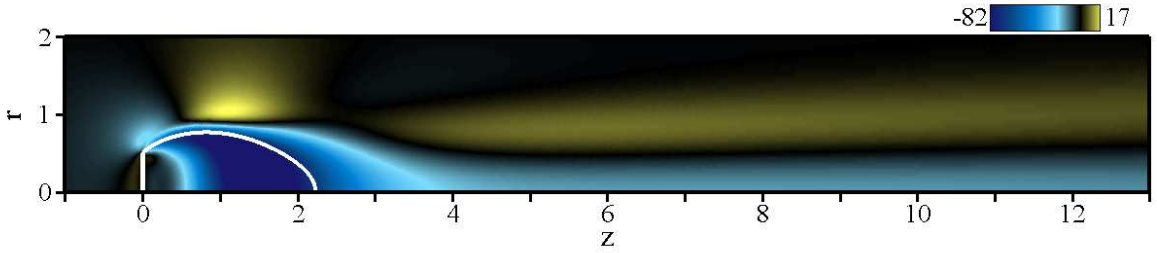

Figure 18: Axial velocity component $\hat{w}_\delta^2$ of the base flow modification owing to the variation of the Reynolds number. The solid line in the flow indicates the separatrix of the recirculation zone.

number $St = D\omega/(2\pi U_\infty)$ as a function of the Reynolds number. The continuous line represents the frequency of the selected MM_π and SW modes, and the dashed lines represent the frequency of the unstable SW and RW modes. As already commented, the bifurcation from the nonlinear SS-branch to the MM_π solution occurs earlier than that from the axisymmetric state to the oscillating modes. The remarkable feature is that the Strouhal number at the bifurcation is lower than that predicted solely by the stability analysis of the axisymmetric state by approximately 10 % (0.11 at Re_π^A on the MM_π-branch and 0.12 at Re_c^B on the SW-branch). This provides a simple explanation for the discrepancy between the shedding frequency predicted by the linear stability theory and by the full Navier-Stokes computations, as mentioned in Fabre *et al.* (2008).

5. Influence of external noise on the sequence of bifurcations

In experimental set-ups, the geometry of the apparatus, and in particular supporting devices, induce steady perturbations that may affect the bifurcation properties. In this section, we investigate the sensitivity of the theoretical bifurcation diagram shown in Figure 8 to such perturbations. We consider that the imperfections act as a small-amplitude steady forcing term in the Navier-Stokes equations, that now read

$$\boldsymbol{\nabla}\cdot\boldsymbol{u}=0\,,\qquad \partial_t\boldsymbol{u}+\boldsymbol{\nabla}\boldsymbol{u}\cdot\boldsymbol{u}+\boldsymbol{\nabla}p-\frac{1}{Re}\boldsymbol{\nabla}^2\boldsymbol{u}=\boldsymbol{f}_s\,, \tag{5.1}$$

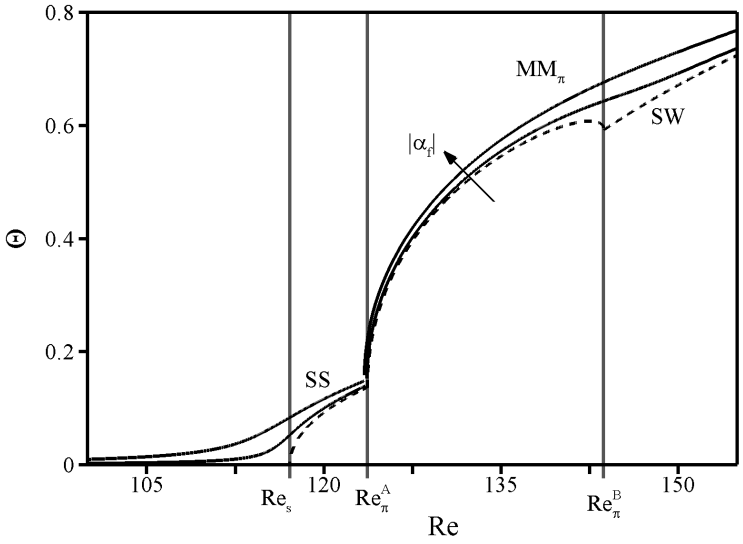

Figure 19: Bifurcation diagram for various forcing amplitudes $|\alpha_f|$.

where $\boldsymbol{f}_s$ is the steady forcing term, which, anticipating on the dominant balance, may be taken of order ϵ^3. The associated disturbance $\boldsymbol{f}_s$ can then be decomposed into the superposition of perturbations of various azimuthal wavenumbers:

$$\boldsymbol{f}_s = \epsilon^3 \sum_{m=0}^{\infty} \hat{\boldsymbol{f}}_{\boldsymbol{s}}^{\boldsymbol{m}}(r,z) e^{\mathrm{i}m\theta} \,. \tag{5.2}$$

Being assumed of order three in ϵ, this steady external forcing directly adds on to the third order forcing term in expansion (4.13). Among all contributions arising from $\boldsymbol{f}_s$, only $\hat{\boldsymbol{f}}_{\boldsymbol{s}}^{\boldsymbol{1}}$ is resonant and adds the new term

$$\alpha_f = \left\langle \hat{\boldsymbol{q}}_{\boldsymbol{A}}^{\boldsymbol{1}\dagger} \;,\; \hat{\boldsymbol{f}}_{\boldsymbol{s}}^{\boldsymbol{1}} \right\rangle \tag{5.3}$$

to the amplitude equation (4.14a) for the stationary mode $\hat{\boldsymbol{q}}_{\boldsymbol{A}}^{\boldsymbol{1}}$, so that the perturbed system reads

$$\dot{A} = \epsilon^2 \left(\alpha_f + \tilde{\lambda}_A A - \tilde{\mu}_A A|A|^2 - \tilde{\nu}_A A|B^+|^2 - \tilde{\nu}_A^* A|B^-|^2 - \tilde{\chi}_A B^+ B^{-*} A^* \right) , \tag{5.4a}$$

$$\dot{B}^+ = \epsilon^2 \left(\tilde{\lambda}_B - \tilde{\mu}_B B^+|B^+|^2 - \tilde{\nu}_B B^+|B^-|^2 - \tilde{\eta}_B B^+|A|^2 - \tilde{\chi}_B B^- A^2 \right) , \tag{5.4b}$$

$$\dot{B}^- = \epsilon^2 \left(\tilde{\lambda}_B - \tilde{\mu}_B B^-|B^-|^2 - \tilde{\nu}_B B^-|B^+|^2 - \tilde{\eta}_B B^-|A|^2 - \tilde{\chi}_B B^+ A^{*2} \right) . \tag{5.4c}$$

Interestingly, for $|B^{\pm}| = 0$, the imaginary part of equation (5.4a) reduces to

$$\dot{\phi}_{\mathrm{A}} = \frac{|\alpha_f|}{|A|} \sin(\phi_f - \phi_{\mathrm{A}}) \,, \tag{5.5}$$

where $\phi_f = \arg(\alpha_f)$, so that a steady solution requires that $\phi_{\mathrm{A}} = \phi_f \pm \pi$. The plane corresponding to the symmetry lost at the first bifurcation threshold is no more arbitrary, but is selected by the forcing term, even if of very small amplitude (order ϵ^3). Figure 19 shows the perturbed bifurcation diagrams for $|\alpha_f| = 2.5\times10^{-2}$ and 10^{-1}. The first steady bifurcation degenerates into an imperfect bifurcation, so that the amplitude A of the steady mode $\hat{\boldsymbol{q}}_{\boldsymbol{A}}^{\boldsymbol{1}}$ is non-zero even at Reynolds numbers lower than the first threshold. The Hopf bifurcation from the SS to the MM$_\pi$-branch is preserved and occurs at a Reynolds

number very close to the threshold $Re_\pi^A = 123.7$ found in the unperturbed case: we obtain $Re_\pi^{A*} = 123.6$ for $|\alpha_f| = 2.5 \times 10^{-2}$ and 123.4 for $|\alpha_f| = 10^{-1}$. The bifurcation from the MM_π to the SW-branch also degenerates into an imperfect bifurcation, so that the flow ultimately remains three-dimensional without recovering its lost reflectional symmetry, even for very low forcing amplitudes.

6. Conclusion

In this study, we have considered the nonlinear dynamics of the wake of a circular disk placed normal to a uniform flow. The performed linear stability analysis agrees with the results of Natarajan & Acrivos (1993). The first destabilization of the axisymmetric steady flow occurs for a stationary global mode of azimuthal wavenumber $m = 1$ and the second destabilization occurs for two oscillating global modes of azimuthal wavenumbers $m = \pm 1$. Since the critical Reynolds numbers for these three bifurcating modes are close to one another, we have assumed that the nonlinear dynamics close to these threshold Reynolds numbers could be described by the slow manifold spanned by the three destabilizing eigenmodes. To derive rigorously the normal form governing the dynamics in the slow manifold, a multiple time scale expansion has been carried out. In this procedure, the first order solution is made of the three modes with unknown amplitudes. The second order is decomposed into the base flow modification owing to the variation in the Reynolds number and harmonics generated by the nonlinear self-interaction of the first order solution. At third order, resonant terms are generated and the resulting solvability conditions impose the nonlinear equations that must be satisfied by the unknown amplitudes, the so-called normal form. Coefficients of the normal form have been systematically computed. They are given by the scalar product between a resonant forcing term arising at the third order and the adjoint of the forced mode. Owing to the convective nonnormality of the linearized Navier-Stokes operator, we have shown that strikingly, the region where all nonlinear interactions take place is located within the recirculating bubble. Analyzing the dynamics resulting from the normal form, we find that the wake undergoes a first bifurcation for Re=117.1, where the axisymmetry is lost but the time invariance is preserved, leading to a 3D steady state with a reflectional symmetry. A Hopf bifurcation then occurs for Re=123.7, where both the remaining reflectional symmetry and the time invariance are broken, leading to a fully 3D periodic state. A third bifurcation then occurs for Re=143.7, where the flow remains unsteady, but recovers the reflectional symmetry lost at the first bifurcation threshold. The nontrivial bifurcation sequence involving nonlinear interactions between unstable modes of the axisymmetric base flow agrees remarkably with the recent observations made by Fabre *et al.* (2008) using direct numerical simulations. These authors have reported three successive bifurcations at Reynolds numbers $Re \simeq 115$, 121 and 140, giving rise to bifurcated states with symmetry features identical to the ones found in this study. Furthermore, the frequency they have observed for the mixed state is lower than the frequency of the oscillating mode at threshold, an effect that results from the existence of the MM_π mixed mode in the present study. This suggests that the 3D dynamics of the whole system is efficiently captured using a reduced order model based on the destabilization of the axisymmetric steady state.

$\boldsymbol{u^1}$ - $\boldsymbol{u^2}$	$\boldsymbol{\nabla u^1 \cdot u^2}$	$\boldsymbol{\nabla u^2 \cdot u^1}$	$\mathcal{C}(\hat{\boldsymbol{u}}^1, \boldsymbol{u^2})$
A - $B^- A$	1.88	-0.747	1.14
B^- - A^2	0.495	-0.0105	0.485
$\tilde{\chi}_{Br}$	2.38	-0.758	1.62

Table 3: Detail of the different nonlinear interactions involved in the $\tilde{\chi}_{Br}$ coefficient of normal form (4.14).

$\boldsymbol{u^1}$ - $\boldsymbol{u^2}$	$\boldsymbol{\nabla u^1 \cdot u^2}$	$\boldsymbol{\nabla u^2 \cdot u^1}$	$\mathcal{C}(\boldsymbol{u^1}, \boldsymbol{u^2})$
A^* - $B^+ B^{-*}$	1.80	0.281	2.08
B^{-*} - $B^+ A^*$	1.72	-0.474	1.25
B^+ - $B^{-*} A^*$	1.72	-0.474	1.25
$\tilde{\chi}_A$	5.24	-0.667	4.57

Table 4: Detail of the different nonlinear interactions involved in the $\tilde{\chi}_A$ coefficient of normal form (4.14).

Appendix A. Analysis of the interactions selecting the bifurcation scenario

In this appendix, we try to provide more details on the branch selection point introduced in section 4.6. As previously mentioned, the Hopf bifurcation occurring on the SS-branch selects either the MM_0 or the MM_π-branch, depending only on the sign of the coefficient $\tilde{\chi}_{Br}$. From (4.18), $\tilde{\chi}_B$ can be decomposed into

$$\tilde{\chi}_B = \underbrace{-\left\langle \hat{\boldsymbol{q}}^{\boldsymbol{1}}_{\boldsymbol{B^-}} \ , \ \mathcal{C}_{1,0}\left(\hat{\boldsymbol{u}}^{\boldsymbol{1}}_{\boldsymbol{A}}, \hat{\boldsymbol{u}}^{\boldsymbol{2}}_{\boldsymbol{B^- A}}\right)\right\rangle}_{A\text{-}B^- A} \underbrace{-\left\langle \hat{\boldsymbol{q}}^{\boldsymbol{1}}_{\boldsymbol{B^-}} \ , \ \mathcal{C}_{-1,2}\left(\hat{\boldsymbol{u}}^{\boldsymbol{1}}_{\boldsymbol{B^-}}, \hat{\boldsymbol{u}}^{\boldsymbol{2}}_{\boldsymbol{AA}}\right)\right\rangle}_{B^-\text{-}A^2}, \tag{A 1}$$

$\tilde{\chi}_{Br}$ being determined by the real parts of these two scalar products. In the first two lines of Table 3, we detail these specific interactions by computing separately the contribution in the scalar product arising from the transport of $\boldsymbol{q^1}$ by $\boldsymbol{q^2}$, namely referred to as column $\boldsymbol{\nabla u^1 \cdot u^2}$ and that arising from the transport of $\boldsymbol{q^2}$ by $\boldsymbol{q^1}$, referred to as column $\boldsymbol{\nabla u^2 \cdot u^1}$. For each line, the sum of these contributions, corresponding to the real part of the associated scalar product in $(A\,1)$ is given in the last column $\mathcal{C}(\boldsymbol{u^1}, \boldsymbol{u^2})$. For each column, the sum of all contributions has also been computed and the result is given in the last line, where one ultimately retrieves the value of $\tilde{\chi}_{Br}$ already given in Section 4.4. Interestingly, it can be seen that both interactions select the MM_π-branch through the $\boldsymbol{\nabla u^1 \cdot u^2}$ term, i.e. the transport of the first order modes by the second order modes, whereas the $\boldsymbol{\nabla u^2 \cdot u^1}$ contributions are negative and would tend to select the unstable MM_0-branch.

Similarly, the coefficient $\tilde{\chi}_A$, whose sign determines the bifurcation from the MM_π to

	σ_A	σ_B	ω_B
M_1	5.3×10^{-6}	4.7×10^{-6}	0.7604
M_2	-9.9×10^{-5}	-9.0×10^{-5}	0.7605
M_3	-5.5×10^{-5}	-4.0×10^{-5}	0.7604
M_4	1.3×10^{-5}	1.6×10^{-5}	0.7605
M_5	8.9×10^{-5}	6.6×10^{-5}	0.7604

Table 5: Dependence of the eigenvalues on the different meshes characterized in Table 1. The real eigenvalue σ_A is computed at $Re_c^A = 116.9$ and the complex eigenvalue $\sigma_B + \mathrm{i}\omega_B$ is computed at $Re_c^B = 125.3$.

	$\tilde{\mu}_A$	$\tilde{\nu}_{Ar}$	$\tilde{\nu}_{Ai}$	$\tilde{\chi}_A$	$\tilde{\mu}_{Br}$	$\tilde{\mu}_{Bi}$	$\tilde{\nu}_{Br}$	$\tilde{\nu}_{Bi}$	$\tilde{\eta}_{Br}$	$\tilde{\eta}_{Bi}$	$\tilde{\chi}_{Br}$	$\tilde{\chi}_{Bi}$
M_1	3.11	6.88	−1.11	4.57	2.42	0.0321	3.13	−0.816	0.955	−3.47	1.62	−1.36
M_2	3.11	6.88	−1.11	4.57	2.42	0.0332	3.13	−0.814	0.955	−3.47	1.62	−1.36
M_3	3.11	6.88	−1.11	4.57	2.42	0.0329	3.13	−0.815	0.955	−3.47	1.62	−1.36
M_4	3.11	6.88	−1.11	4.57	2.42	0.0320	3.13	−0.817	0.955	−3.47	1.62	−1.36
M_5	3.11	6.88	−1.11	4.56	2.42	0.0310	3.13	−0.807	0.962	−3.47	1.62	−1.36

Table 6: Coefficient values of normal form (4.14) obtained for the different meshes characterized in Table 1.

the SW-branch, is decomposed into the sum of three scalar products reading

$$\begin{aligned}\tilde{\chi}_A = & \underbrace{-\left\langle \hat{\boldsymbol{q}}_{\boldsymbol{A}}^{\boldsymbol{1}} \,,\, \mathcal{C}_{1,0}\left(\hat{\boldsymbol{u}}_{\boldsymbol{B^+}}^{\boldsymbol{1}}, \hat{\boldsymbol{u}}_{\boldsymbol{B^-A}}^{\boldsymbol{2^*}}\right)\right\rangle}_{A^*\text{-}B^+B^{-*}} \\ & \underbrace{-\left\langle \hat{\boldsymbol{q}}_{\boldsymbol{A}}^{\boldsymbol{1}} \,,\, \mathcal{C}_{1,0}\left(\hat{\boldsymbol{u}}_{\boldsymbol{B^-}}^{\boldsymbol{1^*}}, \hat{\boldsymbol{u}}_{\boldsymbol{B^+A^*}}^{\boldsymbol{2}}\right)\right\rangle}_{B^{-*}\text{-}B^+A^*} \underbrace{-\left\langle \hat{\boldsymbol{q}}_{\boldsymbol{A}}^{\boldsymbol{1}} \,,\, \mathcal{C}_{-1,2}\left(\hat{\boldsymbol{u}}_{\boldsymbol{A}}^{\boldsymbol{1^*}}, \hat{\boldsymbol{u}}_{\boldsymbol{B^+B^{-*}}}^{\boldsymbol{2}}\right)\right\rangle}_{B^+\text{-}B^{-*}A^*} .\end{aligned} \tag{A 2}$$

These specific interactions are detailed in Table 4, where we have separated the contribution arising from the transport of $\boldsymbol{q^2}$ by $\boldsymbol{q^1}$ from that arising from the transport of $\boldsymbol{q^1}$ by $\boldsymbol{q^2}$. Again, the sign of $\tilde{\chi}_A$ is fully determined by the nonlinear term $\boldsymbol{\nabla u^1 \cdot u^2}$, i.e. by the transport of the first order modes by the second order modes.

Appendix B. Sensitivity of the results to mesh spacing

The eigenvalues, as well as the nonlinear coefficients of normal form (4.14) have been calculated for the five meshes M_1 to M_5, differing by the location of the external boundaries and by the vertex densities. Results are given in table 5 for the values of the linear growth rate σ and frequency ω at threshold, for both eigenmodes $\hat{\boldsymbol{q}}_{\boldsymbol{A}}^{\boldsymbol{1}}$ and $\hat{\boldsymbol{q}}_{\boldsymbol{B^\pm}}^{\boldsymbol{1}}$. Even for the coarser mesh M_5, the growth rate is zero down to the fourth digit, and the frequency of the oscillating mode is converged down to the third digit. On table 6, the coupling coefficients of normal form (4.14) are compared for the different meshes. Even for this very involved computations, coefficients are converged down to the third digit. Therefore, we can conclude that the present work is precise down to better than 1 %. Note that this is the numerical precision but not the convergence of the asymptotic expansion, whose precision increases as $|Re - Re_c|$ decreases.

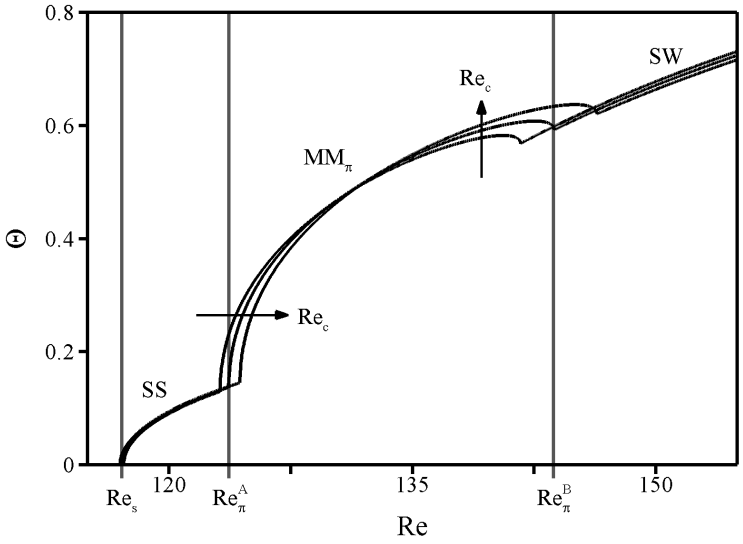

Figure 20: Bifurcation diagram obtained for different choices of the reference Reynolds number $Re_c = 116.9$, 121.1 and 125.3.

Appendix C. Comparison of bifurcation diagrams obtained with various choices of the reference Reynolds number

Figure 20 presents the bifurcation diagram obtained for different choices of the reference Reynolds number Re_c. Computations for $Re_c = 116.9$ and $Re_c = 125.3$ yield slightly different nonlinear coefficients, resulting in diagrams in good agreement with each other (see Figure 20). It can be seen that the choice of Re_c has no significant impact on the dynamics, both in terms of mode selection and symmetry breaking. We find a small effect on the bifurcation thresholds related to the MM_π-branch: the second threshold Re_π^A varies by less that 0.5 %, from 123.3 to 124.4, and the third threshold Re_π^B varies by approximately 3 %, from 140.9 to 146.7. This sensitivity is remarkably small since the expansion procedure is meant for small departures from threshold, which is no more the case at the third bifurcation threshold Re_π^B.

Appendix D. Expression of the complex differential operators

For a normal mode $\hat{\boldsymbol{a}}$ of azimuthal wavenumber m, the gradient operator and the velocity gradient tensor respectively read

$$\boldsymbol{\nabla}_{\boldsymbol{m}} = \begin{pmatrix} \partial_r \\ \frac{\mathrm{i}m}{r} \\ \partial_z \end{pmatrix}, \qquad \boldsymbol{\nabla}_{\boldsymbol{m}}\hat{\boldsymbol{a}} = \begin{pmatrix} \partial_r\hat{u} & \frac{\mathrm{i}m}{r}\hat{u} - \frac{1}{r}\hat{v} & \partial_z\hat{u} \\ \partial_r\hat{v} & \frac{\mathrm{i}m}{r}\hat{v} + \frac{1}{r}\hat{u} & \partial_z\hat{v} \\ \partial_r\hat{w} & \frac{\mathrm{i}m}{r}\hat{w} & \partial_z\hat{w} \end{pmatrix}. \tag{D 1}$$

For a couple of normal modes $\hat{\boldsymbol{a}}$ and $\hat{\boldsymbol{b}}$ of respective azimuthal wavenumbers m and n, the general form of the linearized advection operator $\mathcal{C}_{m,\,n}(\hat{\boldsymbol{a}}, \hat{\boldsymbol{b}})$ therefore reads

$$\mathcal{C}_{m,\,n}(\hat{\boldsymbol{a}}, \hat{\boldsymbol{b}}) = \begin{pmatrix} \hat{u}_b\partial_r\hat{u}_a + \hat{u}_a\partial_r\hat{u}_b + \frac{\mathrm{i}}{r}(m\hat{v}_b\hat{u}_a + n\hat{v}_a\hat{u}_b) - \frac{2}{r}\hat{v}_b\hat{v}_a + \hat{w}_b\partial_z\hat{u}_a + \hat{w}_a\partial_z\hat{u}_b) \\ \hat{u}_b\partial_r\hat{v}_a + \hat{u}_a\partial_r\hat{v}_b + \frac{\mathrm{i}}{r}(m+n)\hat{v}_b\hat{v}_a + \frac{1}{r}(\hat{v}_b\hat{u}_a + \hat{v}_a\hat{u}_b) + \hat{w}_b\partial_z\hat{v}_a + \hat{w}_a\partial_z\hat{v}_b \\ \hat{u}_b\partial_r\hat{w}_a + \hat{u}_a\partial_r\hat{w}_b + \frac{\mathrm{i}}{r}(m\hat{v}_b\hat{w}_a + n\hat{v}_a\hat{w}_b) + \hat{w}_b\partial_z\hat{w}_a + \hat{w}_a\partial_z\hat{w}_b \end{pmatrix}. \tag{D 2}$$

The linearized advection operator used in the order one problem (3.6) now reads

$$\mathcal{C}_{m,0}(\hat{\boldsymbol{u}}^{\mathbf{1}}, \boldsymbol{u}^{\mathbf{0}}) = \begin{pmatrix} \hat{u}^0\partial_r\hat{u}^1 + \hat{u}^1\partial_r\hat{u}^0 + \frac{\mathrm{i}}{r}m\hat{v}^1\hat{u}^0 + \hat{w}^0\partial_z\hat{u}^1 + \hat{w}^1\partial_z\hat{u}^0) \\ \hat{u}^0\partial_r\hat{v}^1 + \frac{1}{r}\hat{v}^1\hat{u}^0 + \hat{w}^0\partial_z\hat{v}^1 \\ \hat{u}^0\partial_r\hat{w}^1 + \hat{u}^1\partial_r\hat{w}^0 + \frac{\mathrm{i}}{r}m\hat{v}^1\hat{w}^0 + \hat{w}^0\partial_z\hat{w}^1 + \hat{w}^1\partial_z\hat{w}^0 \end{pmatrix}. \qquad (\mathrm{D}\,3)$$

Finally, the adjoint linearized advection operator used in the adjoint problem (3.8) reads

$$\mathcal{C}^{\dagger}_{m,0}(\hat{\boldsymbol{u}}^{\mathbf{1}}, \boldsymbol{u}^{\mathbf{0}}) = \begin{pmatrix} -u^0\partial_r\hat{u}^1 + \hat{u}^1\partial_r u^0 - w^0\partial_z\hat{u}^1 + \hat{w}^1\partial_r w^0 \\ -u^0\partial_r\hat{v}^1 + \frac{1}{r}\hat{v}^1 u^0 - w^0\partial_z\hat{v}^1 \\ -u^0\partial_r\hat{w}^1 + \hat{u}^1\partial_z u^0 - w^0\partial_z\hat{w}^1 + \hat{w}^1\partial_z w^0 \end{pmatrix}. \qquad (\mathrm{D}\,4)$$

REFERENCES

Barkley, D. 2006 Linear analysis of the cylinder wake mean flow. *Europhys. Lett.* **75**, 750756.

Barkley, D., Gomes, M.G.M. & Henderson, R.D. 2002 Three-dimensional instability in flow over a backward-facing step. *J. Fluid Mech.* **473**, 167–190.

Chomaz, J.-M. 2005 Global instabilities in spatially developing flows: Non-normality and nonlinearity. *Annu. Rev. Fluid. Mech.* **37**, 357–392.

Chomaz, J.-M., Huerre, P. & Redekopp, L.G. 1990 The effect of nonlinearity and forcing on global modes. In *Proc. Conf. on new trends in nonlinear dynamcs and pattern-forming phenomena: The geometry of nonequilibrium*, , vol. 237, pp. 259–274. NATO ASI Series B, Plenum, edited by P. Coulet & P. Huerre.

Crawford, J.D., Golubitsky, M. & Langford, W.F. 1988 Modulated rotating waves in $o(2)$ mode interactions. *Dyn. Stab. Syst.* **3**, 159–175.

Crawford, J.D. & Knobloch, E. 1991 Symmetry, symmetry-breaking bifurcations in fluid dynamics. *Annu. Rev. Fluid. Mech.* **23**, 341–387.

Cross, M.C. 1986 Traveling and standing waves in binary-fluid convection in finite geometries. *Phys. Rev. Lett.* **57**, 2935–2938.

Davis, T. A. 2004 A column pre-ordering strategy for the unsymmetric-pattern multifrontal method. *ACM Transactions on Mathematical Software* **30** (2), 165–195.

Davis, T. A. & Duff, I.S. 1997 An unsymmetric-pattern multifrontal method for sparse lu factorization. *SIAM Journal on Matrix Analysis and Applications* **18** (1), 140–158.

Ding, Y. & Kawahara, M. 1999 Three-dimensional linear stability analysis of incompressible viscous flows using finite element method. *Int. J. Num. Meth. Fluids* **31**, 451479.

Dušek, J., Le Gal, P. & Fraunie, P. 1994 A numerical and theoretical study of the first hopf bifurcation in a cylinder wake. *J. Fluid Mech.* **264**, 59–80.

Ehrenstein, U. & Gallaire, F. 2005 On two-dimensional temporal modes in spatially evolving open flows: the flat-plate boundary layer. *J. Fluid Mech.* **536**, 209–218.

Fabre, D., Auguste, F. & Magnaudet, J. 2008 Bifurcations and symmetry breaking in the wake of axisymmetric bodies. *Phys. Fluids* **20** (5), 051702 1–4.

Friedrichs, K.O. 1973 *Spectral theory of operators in Hilbert space*. Springer Verlag.

Golubitsky, M. & Langford, W. 1988 Pattern formation and bistability in flow between counterrotating cylinders. *Physica D* **32**, 362–392.

Golubitsky, M. & Stewart, I. 1985 Hopf bifurcation in the presence of symmetry. *Arch. Ratio. Mech. Anal.* **87**, 107–165.

Golubitsky, M., Stewart, I. & Schaeffer, D. 1988 *Singularities and groups in bifurcation theory Vol. II - Applied mathematical sciences*. Springer.

Iooss, G. 1987 Reduction of the dynamics of a bifurcation problem using normal forms and symmetries. In *Instabilities and Nonequilibrium Structures*, pp. 3–40. D. Reidel, Dordrecht, edited by E.Tirapegui and D. Villarroel.

Jackson, C.P. 1987 A finite-element study of the onset of vortex shedding in flow past variously shaped bodies. *J. Fluid Mech.* **182**, 2345.

Natarajan, R. & Acrivos, A. 1993 The instability of the steady flow past spheres and disks. *J. Fluid Mech.* **254**, 323–344.

Provansal, M., Mathis, C. & L., Boyer 1987 Bénard von-Kármán instability: Transient and forced regimes. *J. Fluid Mech.* **182**, 1–22.

Schmid, P.J. & Henningson, D.S 2001 *Stability and transition in shear flows*. Springer Verlag.

Sipp, D. & Lebedev, A. 2007 Global stability of base and mean flows: a general approach and its applications to cylinder and open cavity flows. *J. Fluid Mech.* **593**, 333–358.

Thompson, M.C., Leweke, T. & Provansal, M. 2001 Kinematics and dynamics of sphere wake transition. *J. Fluid Struct.* **15**, 575–585.

Zebib, A. 1987 Stability of a viscous flow past a circular cylindar. *J. Engng Math.* **21**, 155165.

Zielinska, B.J.A., Goujon-Durand, S., Dušek, J. & Wesfreid, J.E. 1997 Strongly nonlinear effect in unstable wakes. *Phys. Rev. Lett.* **79**, 3893–3896.

CHAPTER
FIVE

GLOBAL MODES IN A COMPRESSIBLE AFTERBODY FLOW

This chapter takes the form of an article in preparation. It presents a consistent theoretical formalism for the study of global modes up to the high subsonic regime. The latter formalism is applied to a compressible afterbody flow, for which the global modes of largest growth rates are identified and compared to that introduced in chapter 3 for incompressible flows. The effect of compressibility is investigated, and a physical interpretation is proposed. Results suggest that the underlying mechanisms are nonparallel in essence, thus outlining the importance of investigating wake flows in the global approach of stability.

keywords: compressible flows, global stability, adjoint-methods, nonnormality, sensitivity analysis.

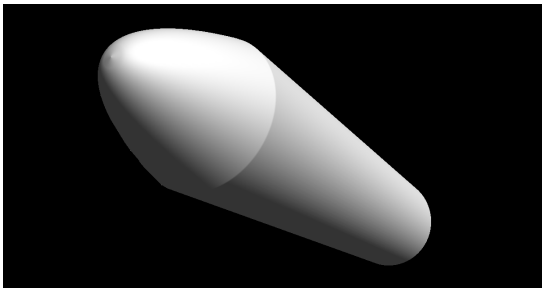

Manuscript in preparation

Global stability and adjoint-based sensitivity analyses for compressible flows - Part I: dynamics of a subsonic afterbody flow

PHILIPPE MELIGA[1], **DENIS SIPP**[1] AND **JEAN-MARC CHOMAZ**[1,2]

[1]ONERA/DAFE, 8 rue des Vertugadins, 92190 Meudon, France
[2]LadHyX, CNRS-Ecole Polytechnique, 91128 Palaiseau, France

A general theoretical formalism is developed in this paper for the study of global eigenmodes in complex compressible flows, up to the high subsonic regime. It is based on the sensitivity analysis to base flow modifications, that aims at predicting the variations of a given eigenvalue owing to a modification of the base flow, and relies on the evaluation of gradients using adjoint methods.

We present first a unified formalism, valid for incompressible and compressible flows, that generalizes sensitivity concepts originally formulated by Bottaro *et al.* (2003) and Marquet *et al.* (2008*b*). This theoretical framework is then applied to a compressible afterbody flow. We find that increasing the Mach number induces an increase of the recirculation length of the steady base flow as the result of a purely inviscid mechanism, triggered by the variation of the pressure gradient along the separation line. A global stability analysis is carried out, and we find that whatever the value of the Mach number up to $M = 0.7$, a first instability occurs for a stationary global mode of azimuthal wavenumber $m = 1$, and a subsequent instability occurs for an oscillating global mode of azimuthal wavenumber $m = 1$. This bifurcation sequence is reminiscent of that documented by Natarajan & Acrivos (1993) in the incompressible wake past a sphere and a disk. For both global modes, the adjoint global modes and sensitivity functions to base flow modifications are computed. Owing to the convective nonnormality of the evolution operator, the active zones are found to be located within the recirculating bubble which thus may be identified as the 'wavemaker' region, where the characteristics of the flow determines the properties of the instability.

The boundary separating the unstable and stable domains in the (M, Re)-plane have been determined. We show that an increase of the Mach number induces a stabilization of both eigenmodes, owing to a modification of the base flow. This effect is then investigated in the light of the sensitivity analysis, and a physical interpretation is proposed, based on the competition between production and downstream advection of disturbances. We show that increasing the Mach number mainly enhances the downstream advection of the disturbances. It turns out that this mechanism is strongly non-parallel, as it involves both the cross-stream and streamwise momentum components. We also find that the same mechanism induces an additional stabilization by weakening the production of disturbances.

1. Introduction

Predicting the bifurcation from a steady to an unsteady state is a problem of crucial importance in many engineering flows. The transonic flow past a launcher afterbody is characterized by a massive separated area that induces large-scale unsteadiness resulting in high fluctuating dynamic loads. These oscillations can trigger a response of the structural modes termed buffet, that can be detrimental to the engineering application. The prediction for the occurrence of these undesirable flow conditions is thus needed to guide future designs, in order to improve the aerodynamic performances and reliability of launch vehicles. To alleviate or control such unsteadiness, a physical understanding of the underlying mechanisms is also required.

Large-scale structures in axisymmetric wakes have been studied experimentally and numerically for different geometries of revolution, including spheres, disks or bullet-shaped bodies (Achenbach 1974; Fuchs *et al.* 1979; Berger *et al.* 1990; Siegel & Fasel 2001; Sevilla & Martínez-Bazàn 2004). It has been generally acknowledged that this class of flow is dominated by an instability of the helical mode, resulting in the low-frequency shedding of large-scale coherent structures in the form of either one or two counter-rotating modes of azimuthal wavenumbers $m = \pm 1$, corresponding to a flapping of the wake in a fixed plane. Low Strouhal numbers based on the body diameter of order $0.1 - 0.2$ have been reported. Though, these studies have not considered the transition to unsteadiness, and have rather focused on the properties of the unsteady flow. Indeed, finding the boundary between steady and unsteady flow conditions is not easily accessible using experimental set-ups or numerical simulations, as this would require either precise experimental measurements or direct numerical simulations to be carried out over a wide range of control parameters (Reynolds and Mach number, angle of attack...). Moreover, close to the bifurcation threshold, disturbances grow or decay over large time scales, thus further increasing the complexity of the task.

An alternative is to predict the onset of large-scale flow unsteadiness using the stability theory, that rely on the existence of a steady base flow solution about which perturbations are superimposed. The stable or unstable nature of these perturbations is then determined by resolving a classical eigenvalue problem. In the past, numerous studies have been conducted on the stability of parallel base states, i.e. base flows that are inhomogeneous only in the cross-stream direction, thus defining the so-called local stability. Though, wakes, and more generally open flows, are more complex since the base flow is usually strongly non-parallel. Analyzing their stability thus requires to consider eigenmodes that are inhomogeneous in both the cross-stream and the streamwise directions, called global modes in contrast to the local analysis of parallel flows. Global stability has been extensively used to study the problem of vortex-shedding in the incompressible flow past a circular cylinder, starting with Zebib (1987) and Jackson (1987) (see also Ding & Kawahara 1999; Barkley 2006; Sipp & Lebedev 2007). Since then, it has been used to study a large variety of open flows (see Theofilis 2003, for a review), though, the global stability of axisymmetric open flows has received less attention than its two-dimensional counterparts. Natarajan & Acrivos (1993) have investigated the incompressible axisymmetric wake past a disk and a sphere, and have shown that both dynamics bear similarities: at low Reynolds numbers, the steady separated flow field is axisymmetric and consists of a toroidal recirculation eddy past the body. A first instability is stationary and involves a global eigenmode of azimuthal wavenumber $m = 1$. The associated bifurcation, breaking the axisymmetry but preserving the time invariance, leads to a three-dimensional steady state. A second instability then occurs at a larger Reynolds number, for $m = \pm 1$ oscillating global eigenmodes that breaks the time

invariance. From Direct Numerical Simulations (DNS) and experimental observations, it turns out that this second instability mode dominates the dynamics of the fully three-dimensional flow at large Reynolds numbers, hence explaining the occurrence of a fully three-dimensional periodic state (see Ormières & Provansal 1998). Such a domination of the periodic instability mode over the stationary mode, despite the fact that the latter is the first to destabilize the axisymmetric base flow has recently been explained using slow manifold theory and normal forms (Fabre *et al.* 2008; Meliga *et al.* 2008*a*). Nevertheless, all these analyses have so far been applied almost exclusively to incompressible flows, whereas its application to the transonic afterbody-buffet requires to consider the effect of compressibility, which requires high computational capacities and introduces a number of computational issues associated with the numerical resolution of the steady flow and of the eigenvalue problem for the unsteady disturbances. A first compressible global stability analysis is that of Crouch *et al.* (2002) on the shock-induced buffet over a two-dimensional airfoil. Since then, only a very limited number of studies have been carried out in the compressible regime, including that of Theofilis & Colonius (2004) who considered the flow *within* a cavity as a crude approximation for the complex problem of open cavity flows, Crouch *et al.* (2007) on the shock-induced buffet and Robinet (2007) on a shock wave/boundary-layer interaction.

In this study, we investigate unsteadiness in an afterbody flow at zero angle of attack and high subsonic Mach numbers using a fully compressible global stability analysis. We aim at understanding the physical mechanisms responsible for the growth of perturbations, and particular attention is paid to the effect of the Mach number on the stability properties of the flow. Though, as pointed out in Giannetti & Luchini (2006), the instability mechanism cannot be identified from the study of the disturbance eigenfunctions only. Still, the *wavemaker* region, i.e. the flow region where the instability mechanisms are active (Chomaz 2005), can be straightforwardly identified as the region where the sensitivity of the eigenvalue with respect to generic structural modifications of the stability problem is the highest. Such modifications may arise for several reasons, including changes in the base flow, in the body geometry or even in the numerical boundary conditions imposed to solve the stability problem. We choose here to put particular emphasis on the role of the base flow in the perturbation dynamics, as we show in § 4.5 that varying the Mach number acts on the leading eigenmodes through a modification of the base flow. Variations of the eigenvalue are thus investigated with respect to small variations of the base flow, thus defining the so-called *sensitivity analysis to base flow modifications*, as formulated originally by Bottaro *et al.* (2003) and further discussed by Marquet *et al.* (2008*b*). By investigating how the growth rate and frequency of the unstable modes are affected by changes in the shape of the base flow profiles, this analysis is appropriate to to investigate theoretically where and which mechanisms are responsible for the instability. It should be noted that such analysis, where one identifies the flow region where small modifications in the flow conditions are susceptible to affect dramatically the flow dynamics, is intimately linked to the perspective of flow control. Indeed, most open-loop control strategies rely on the introduction of some fixed modification in the flow conditions. For instance, Strykowski & Sreenivasan (1990) have succeeded in suppressing the vortex-shedding phenomenon in the cylinder wake by placing a small control cylinder at appropriate locations in the lee of the main cylinder.

Sensitivity analyses rely on the evaluation of a gradient with respect to some control variable, and may be performed by forward calculations: in the case of the sensitivity analysis to base flow modifications, the stability problem has to be solved once to identify the global modes of the unmodified base flow, and once more for each base flow modification under consideration. Though, such procedure is not easily tractable

for complex stability problems such as those solved in the present case, as it turns out to be very computationally intensive. The main tool developed here is therefore based on adjoint methods, where the gradient is obtained by solving only once the state and adjoint problems, with a relatively 'low' computational cost. Adjoint equations have recently attracted the increased attention of fluid dynamicists, for a number of applications ranging from oceanography and atmospheric sciences (Hall 1986) to flow control (Collis *et al.* 2002). In the context of shape optimization (Pironneau 1984), the optimal design of transonic wings at realistic cruise conditions has been widely investigated (Jameson 1998; Jameson *et al.* 1998). Such studies now allow to optimize entire airplanes for a criterion such as drag under geometric and aerodynamic constraints such as volume and lift (see Mohammadi & Pironneau 2004, for a review). Similar methods are also used to estimate the sensitivity of the position of a shock with respect to the flow parameters, which is of practical interest for the fluttering of wings (Di Cesare & Pironneau 2000; Bardos & Pironneau 2003).

It should be noted that in these studies, adjoint methods are used in conjunction with computational flow simulations and that no particular attention has been paid to the particular knowledge of the adjoint state. On the contrary, in the context of hydrodynamic stability, where one aims at understanding the mechanisms responsible for the growth of disturbances, adjoint methods have proven fruitful to provide additional insight into the flow physics. For instance, they naturally introduce the concept of nonnormality of the flow, which is responsible for the energy of a perturbation to experience possibly large transient growth even though the flow is stable (Trefethen *et al.* 1993; Schmid 2007), or to lead to extreme sensitivity to forcing (see Chomaz 2005, for a detailed review on global modes and nonnormality). As a consequence, adjoint-based sensitivity analyses have naturally arisen in receptivity studies (Hill 1995; Tumin 1996). In the context of boundary-layer flows, an adjoint-based sensitivity formalism has been developed to investigate the ability of wall forcing to delay the transition to turbulence both in the incompressible and compressible regimes, assuming that both the base flow and the disturbances develop slowly in the direction parallel to the wall so that parabolic equations can be established to govern their evolution (Pralits *et al.* 2000, 2002; Airiau *et al.* 2003). The aim of this work is to develop a consistent adjoint-based formalism for the study of generic compressible spatially developing flows, in particular, departure from the slow variation assumption can be arbitrary. To this end, we derive the global stability and adjoint stability equations, as well as the sensitivity functions to a modification of the base flow. To the best of the authors knowledge, this is the first attempt to apply adjoint-based methods to global stability problems governed by the compressible Navier-Stokes equations. Physical interpretations for the observed compressible effects are given in terms of sensitivity of the leading eigenmodes. Following the line of thought introduced in Marquet *et al.* (2008*b*), we show that the base flow affects the flow stability by modifying the *advection* and *production* of the disturbances, the latter production terms being related to the advection of the base flow by the perturbation and to the source terms existing in the governing equations. One should note, though, that such competition between mechanisms of advection and production of perturbations are not specific to the global stability framework, since it has been introduced in local stability analyses through the concepts of convective and absolute instability (Briggs 1964; Bers 1975). In that case, if an arbitrary perturbation grows in time at any fixed location, or in other words if the production of the perturbation dominates its advection by the base flow, then the flow is said to be absolutely unstable. The existence of a global instability is then conditioned to the existence of an absolutely unstable region of 'sufficient' spatial extent (see Chomaz *et al.* 1988).

The paper is organized as follows. The theoretical formulation is presented in § 2. It provides with a formal derivation of the perturbation equations in a global framework and includes the presentation of the adjoint-based sensitivity analysis to generic base flow modifications. It is worthwhile emphasizing here that these concepts are not restricted to afterbody flows, but may be used for any open flow with two inhomogeneous directions. In § 2, the analysis is derived in a general framework, and thus pertains indifferently either to incompressible or to compressible flows. In § 3, we focus on an afterbody flow in the high subsonic regime, and the explicit, analytical expression for the base flow, perturbation, adjoint perturbation and sensitivity functions are detailed. In particular, we discuss the physical origin of the nonnormality of the compressible evolution operator. The numerical methods used throughout the study are presented in § 4. The steady axisymmetric flow past the afterbody is described in § 4.3. The global stability analysis is carried out in § 4.4, where we identify two unstable modes whose frequency and azimuthal wavenumber selection are identical to that documented by Natarajan & Acrivos (1993) in the wake of a disk and a sphere. The adjoint global modes necessary to the computation of the sensitivity functions are also computed in § 4.4, and we discuss nonnormal effects in the present application. In § 4.5, we investigate the impact of compressibility on both bifurcations, and appraise how the critical control parameters are affected by a modification of the Mach number. As will be shown, compressibility influences the stability of the leading eigenmodes mainly through the base flow. For both instabilities, the wavemaker regions are identified by performing the analysis of sensitivity to base flow modifications. The outcome of the sensitivity functions is first described in a general sense, i.e. we discuss the effect of generic modifications of the base flow on the growth rate and frequency of the instabilities. A physical interpretation of the stabilizing compressible effect is then proposed by applying the sensitivity analysis to the specific base flow modification induced by a small change in the Mach number. Note that the problem of flow control is out of the scope of this paper and will be treated in the second part of this study, where we present a systematic formalism for the open-loop control of compressible open flows, accounting for volumetric and wall forcing.

2. Theoretical formulation

This section is devoted to a description of the theoretical concepts used in the present study. We investigate the general configuration of an open flow in a closed domain for which we assume that suitable inlet, outlet, lateral boundaries and solid wall conditions have been defined. The concept of sensitivity of an eigenvalue to base flow modifications has been developed in Bottaro *et al.* (2003) and Marquet *et al.* (2008*b*) in the case of incompressible flows. In this study, we extend this concept to compressible flows, and propose a more general formalism that encompasses small modifications of the Mach number (§ 2.2). We insist that the present formalism is *unified*, as it pertains to incompressible and compressible flows indifferently. The problem of boundary conditions, that may be particularly involved, is voluntarily omitted so as to keep a general point of view. Therefore, we assume that all quantities fulfill 'appropriate' boundary conditions, that will be specified in § 3, where the concrete application is considered. The total flow field is described by a state vector $\boldsymbol{q}$ solution of a set of nonlinear governing equations, which is conveniently written as

$$\mathcal{B}(\boldsymbol{q})\partial_t \boldsymbol{q} + \mathcal{M}(\boldsymbol{q}, \mathcal{G}) = \boldsymbol{0}\,, \tag{2.1}$$

where $\mathcal{M}$ and $\mathcal{B}$ are differential operators and $\mathcal{G}$ is a set of relevant control parameters (Reynolds and Mach numbers, angle of attack...).

A stability analysis relies on the existence of a steady base flow solution about which perturbations are superimposed. In the present study, $\boldsymbol{q}$ is decomposed into a steady axisymmetric base flow $\boldsymbol{q^0}$ and a three-dimensional perturbation $\boldsymbol{q^1}$ of infinitesimal amplitude ϵ. $\boldsymbol{q^0}$ is solution of the steady, axisymmetric form of the nonlinear system (2.1)

$$\mathcal{M}_{_0}(\boldsymbol{q^0}, \mathcal{G}) = \boldsymbol{0}\,. \tag{2.2}$$

Substituting $\boldsymbol{q} = \boldsymbol{q^0} + \epsilon \boldsymbol{q^1}$ into equations (2.1), and retaining only terms of order ϵ leads to the linearized equations

$$\mathcal{B}(\boldsymbol{q^0})\partial_t \boldsymbol{q^1} + \mathcal{A}(\boldsymbol{q^0}, \mathcal{G})\boldsymbol{q^1} = \boldsymbol{0}\,, \tag{2.3}$$

where $\mathcal{A} = \partial\mathcal{M}/\partial\boldsymbol{q}$ is a linear differential operator. Since the base flow is axisymmetric, the perturbation is sought under the form of normal modes

$$\boldsymbol{q^1} = \hat{\boldsymbol{q}}^{\boldsymbol{1}}(r,z)e^{(\sigma+\mathrm{i}\omega)t+\mathrm{i}m\theta} + \text{ c.c.}\,, \tag{2.4}$$

where $\hat{\boldsymbol{q}}^{\boldsymbol{1}}$ is the so-called global mode for which both the cross-stream and streamwise directions are eigendirections. The azimuthal wavenumber of the global mode is m, its growth rate and pulsation are σ and ω respectively. Note that the same formalism holds for two-dimensional configurations if one chooses the appropriate normal mode expansion with a spanwise wavenumber k. Substituting (2.4) into (2.3) yields a system of equations governing the normal mode under the form of a generalized eigenvalue problem for $\lambda = \sigma + \mathrm{i}\omega$ and $\hat{\boldsymbol{q}}^{\boldsymbol{1}}$:

$$\lambda\mathcal{B}(\boldsymbol{q^0})\hat{\boldsymbol{q}}^{\boldsymbol{1}} + \mathcal{A}_{_m}(\boldsymbol{q^0}, \mathcal{G})\hat{\boldsymbol{q}}^{\boldsymbol{1}} = \boldsymbol{0}\,, \tag{2.5}$$

with $\mathcal{A}_{_m}$ the normal complex operator obtained from $\mathcal{A}$ by replacing the θ derivatives by im.

Let us now consider a particular eigenpair $\{\hat{\boldsymbol{q}}^{\boldsymbol{1}}, \lambda = \sigma + \mathrm{i}\omega\}$ solution of the eigenproblem (2.5). It is explicitly a function of the base flow variables $\boldsymbol{q^0}$ and of the set of control parameters $\mathcal{G}$. In the following, we investigate the effect of compressibility on the chosen eigenpair, so that we assume the Mach number to be the only varying control parameter. In particular, the Reynolds number is kept constant, though, we insist that the present approach is general and can thus be extended to investigate the effect of any other parameter. The eigenvalue λ can be written as $\lambda = \lambda(\boldsymbol{q^0}, M)$, and the variation of a given eigenvalue $\delta\lambda$ reads formally

$$\delta\lambda = \underbrace{\left.\frac{\partial\lambda}{\partial\boldsymbol{q^0}}\right|_{M} \boldsymbol{\delta q^0}}_{\delta\lambda|_{M}} + \underbrace{\left.\frac{\partial\lambda}{\partial M}\right|_{\boldsymbol{q^0}} \delta M}_{\delta\lambda|_{\boldsymbol{q^0}}}\,. \tag{2.6}$$

where $\delta\lambda|_{_M}$ (resp. $\delta\lambda|_{_{\boldsymbol{q^0}}}$) is the variation of λ arising from a small modification of the base flow $\boldsymbol{\delta q^0}$, the Mach number being kept constant (resp. a small modification of the Mach number, the base flow being kept constant). The expression of each specific variation is now derived in the framework of sensitivity analyses.

2.1. *Sensitivity to base flow modifications*

In this section, the Mach number is kept constant, and $\delta\lambda$ refers to the specific variation $\delta\lambda|_{_M}$ to ease the notation. $\delta\lambda$ is investigated with respect to a generic, small-amplitude, steady axisymmetric modification of the base flow $\boldsymbol{\delta q^0}$, thus defining the *sensitivity analysis to base flow modifications*. We emphasize on the fact that such a modification is arbitrary, i.e. we do not require $\boldsymbol{q^0} + \boldsymbol{\delta q^0}$ to be solution of equations (2.2). From a physical point of view, the sensitivity function defined in (2.7) allows to determine the

region of the flow where a small modification of the base flow is able to produce the greatest drift of the eigenvalue. Therefore, it allows to identify which region of the flow matters most to establish the dynamics of the global mode, i.e. the wavemaker region. The variations $\delta\lambda$ and $\boldsymbol{\delta q^0}$ are such that

$$\delta\lambda = \delta\sigma + \mathrm{i}\delta\omega = \left\langle \boldsymbol{\nabla}_{\boldsymbol{q^0}}\lambda \,,\, \boldsymbol{\delta q^0} \right\rangle \,, \tag{2.7}$$

where $\langle \,,\, \rangle$ is an inner product to be specified and $\boldsymbol{\nabla}_{\boldsymbol{q^0}}\lambda$ is a complex vector defining the so-called sensitivity to base flow modifications. The sensitivity of the growth rate σ and that of the frequency ω, denoted as $\boldsymbol{\nabla}_{\boldsymbol{q^0}}\sigma$ and $\boldsymbol{\nabla}_{\boldsymbol{q^0}}\omega$ respectively, can be similarly written as

$$\delta\sigma = \left\langle \boldsymbol{\nabla}_{\boldsymbol{q^0}}\sigma \,,\, \boldsymbol{\delta q^0} \right\rangle \,, \qquad \delta\omega = \left\langle \boldsymbol{\nabla}_{\boldsymbol{q^0}}\omega \,,\, \boldsymbol{\delta q^0} \right\rangle \,, \tag{2.8}$$

with $\boldsymbol{\nabla}_{\boldsymbol{q^0}}\sigma = \mathrm{Re}(\boldsymbol{\nabla}_{\boldsymbol{q^0}}\lambda)$ and $\boldsymbol{\nabla}_{\boldsymbol{q^0}}\omega = -\mathrm{Im}(\boldsymbol{\nabla}_{\boldsymbol{q^0}}\lambda)$ being now real vectors. In order to derive the analytical expression of these sensitivity functions, we use an approach based on Lagrange multipliers or adjoint equations. For a given operator $\mathcal{H}$ and inner product $\langle\,\rangle$, the adjoint operator $\mathcal{H}^\dagger$ is defined so that for any complex vectors $\hat{\boldsymbol{a}}$ and $\hat{\boldsymbol{b}}$ fulfilling 'appropriate' boundary conditions,

$$\left\langle \hat{\boldsymbol{a}}, \mathcal{H}\hat{\boldsymbol{b}} \right\rangle = \left\langle \mathcal{H}^\dagger \hat{\boldsymbol{a}}, \hat{\boldsymbol{b}} \right\rangle \,. \tag{2.9}$$

The derivation of an adjoint operator is always an exercise in part integration, and hence depends on the inner product considered (this point will be discussed in § 4). Note that the question of the boundary terms arising during the part integration process is not considered in this section, as it is intrinsically connected to that of boundary conditions. All details about the integration process are provided in Appendix D and E.

In the present formalism, the eigenpair $\{\hat{\boldsymbol{q}}^{\boldsymbol{1}}, \lambda\}$ is the *state variable*, the base flow $\boldsymbol{q^0}$ is the *control variable* and the eigenproblem (2.5) is the *state equation*, i.e. the constraint to be satisfied. We introduce the Lagrange multiplier $\hat{\boldsymbol{q}}^{\boldsymbol{1\dagger}}$ (also known as the *adjoint* or *co-state* variable) for the state equation, that is herein referred to as the adjoint perturbation. We consider now the functional

$$\mathcal{L}(\boldsymbol{q^0}, \hat{\boldsymbol{q}}^{\boldsymbol{1\dagger}}, \hat{\boldsymbol{q}}^{\boldsymbol{1}}, \lambda) = \lambda - \left\langle \hat{\boldsymbol{q}}^{\boldsymbol{1\dagger}} \,,\, \lambda\mathcal{B}(\boldsymbol{q^0})\hat{\boldsymbol{q}}^{\boldsymbol{1}} + \mathcal{A}_m(\boldsymbol{q^0})\hat{\boldsymbol{q}}^{\boldsymbol{1}} \right\rangle \,, \tag{2.10}$$

whose gradient with respect to any variable s is defined as

$$\frac{\partial\mathcal{L}}{\partial s}\delta s = \lim_{\epsilon\to 0} \frac{\mathcal{L}(s+\epsilon\delta s) - \mathcal{L}(s)}{\epsilon} \,. \tag{2.11}$$

In the following, we assume that the state equation (2.5) is satisfied for any arbitrary base flow modification. The eigenvalue variation $\delta\lambda$ resulting from a modification of the base flow $\boldsymbol{\delta q^0}$ can thus be expressed formally as

$$\delta\lambda = \left(\frac{\partial\mathcal{L}}{\partial\boldsymbol{q^0}} + \frac{\partial\mathcal{L}}{\partial\hat{\boldsymbol{q}}^{\boldsymbol{1\dagger}}}\frac{\partial\hat{\boldsymbol{q}}^{\boldsymbol{1\dagger}}}{\partial\boldsymbol{q^0}} + \frac{\partial\mathcal{L}}{\partial\{\hat{\boldsymbol{q}}^{\boldsymbol{1}}, \lambda\}}\frac{\partial\{\hat{\boldsymbol{q}}^{\boldsymbol{1}}, \lambda\}}{\partial\boldsymbol{q^0}} \right) \boldsymbol{\delta q^0} \tag{2.12}$$

The gradient of the functional with respect to $\hat{\boldsymbol{q}}^{\boldsymbol{1\dagger}}$ reads

$$\frac{\partial\mathcal{L}}{\partial\hat{\boldsymbol{q}}^{\boldsymbol{1\dagger}}}\boldsymbol{\delta}\hat{\boldsymbol{q}}^{\boldsymbol{1\dagger}} = -\left\langle \boldsymbol{\delta}\hat{\boldsymbol{q}}^{\boldsymbol{1\dagger}} \,,\, \lambda\mathcal{B}(\boldsymbol{q^0})\hat{\boldsymbol{q}}^{\boldsymbol{1}} + \mathcal{A}_m(\boldsymbol{q^0})\hat{\boldsymbol{q}}^{\boldsymbol{1}} \right\rangle \,. \tag{2.13}$$

Consequently, since $\{\hat{\boldsymbol{q}}^{\boldsymbol{1}}, \lambda\}$ is solution of the state equation (2.5), this gradient is nil. The gradient of the functional with respect to $\{\hat{\boldsymbol{q}}^{\boldsymbol{1}}, \lambda\}$ can be formally expressed as the

sum of two terms

$$\begin{aligned}\frac{\partial \mathcal{L}}{\partial\{\hat{\boldsymbol{q}}^{\mathbf{1}},\lambda\}}\delta\{\hat{\boldsymbol{q}}^{\mathbf{1}},\lambda\} =& \delta\lambda - \left\langle \hat{\boldsymbol{q}}^{\mathbf{1}\dagger}\,,\, \delta\lambda\mathcal{B}(\boldsymbol{q}^{\mathbf{0}})\hat{\boldsymbol{q}}^{\mathbf{1}}\right\rangle - \left\langle \hat{\boldsymbol{q}}^{\mathbf{1}\dagger}\,,\, \lambda\mathcal{B}(\boldsymbol{q}^{\mathbf{0}})\boldsymbol{\delta}\hat{\boldsymbol{q}}^{\mathbf{1}} + \mathcal{A}_{_m}(\boldsymbol{q}^{\mathbf{0}})\boldsymbol{\delta}\hat{\boldsymbol{q}}^{\mathbf{1}}\right\rangle \\ =& \underbrace{\delta\lambda - \left\langle \hat{\boldsymbol{q}}^{\mathbf{1}\dagger}\,,\, \delta\lambda\mathcal{B}(\boldsymbol{q}^{\mathbf{0}})\hat{\boldsymbol{q}}^{\mathbf{1}}\right\rangle}_{(i)} \underbrace{- \left\langle \lambda^*\mathcal{B}^\dagger(\boldsymbol{q}^{\mathbf{0}})\hat{\boldsymbol{q}}^{\mathbf{1}\dagger} + \mathcal{A}_{_m}^\dagger(\boldsymbol{q}^{\mathbf{0}})\hat{\boldsymbol{q}}^{\mathbf{1}\dagger}\,,\, \boldsymbol{\delta}\hat{\boldsymbol{q}}^{\mathbf{1}}\right\rangle}_{(ii)} .\end{aligned} \tag{2.14}$$

Defining the adjoint perturbation $\hat{\boldsymbol{q}}^{\mathbf{1}\dagger}$ as the solution of the new generalized eigenvalue problem

$$\lambda^*\mathcal{B}^\dagger(\boldsymbol{q}^{\mathbf{0}})\hat{\boldsymbol{q}}^{\mathbf{1}\dagger} + \mathcal{A}_{_m}^\dagger(\boldsymbol{q}^{\mathbf{0}})\hat{\boldsymbol{q}}^{\mathbf{1}\dagger} = \mathbf{0}\,, \tag{2.15}$$

along with the normalization condition

$$\left\langle \hat{\boldsymbol{q}}^{\mathbf{1}\dagger}\,,\, \mathcal{B}(\boldsymbol{q}^{\mathbf{0}})\hat{\boldsymbol{q}}^{\mathbf{1}}\right\rangle = 1\,. \tag{2.16}$$

yields that both terms (i) and (ii) are nil in (2.14). Consequently, (2.22) can be rewritten as

$$\delta\lambda = \frac{\partial \mathcal{L}}{\partial \boldsymbol{q}^{\mathbf{0}}}\boldsymbol{\delta q}^{\mathbf{0}}\,. \tag{2.17}$$

The gradient with respect to the control variable $\boldsymbol{q}^{\mathbf{0}}$ is now given by

$$\frac{\partial \mathcal{L}}{\partial \boldsymbol{q}^{\mathbf{0}}}\boldsymbol{\delta q}^{\mathbf{0}} = -\left\langle \hat{\boldsymbol{q}}^{\mathbf{1}\dagger}\,,\, \lambda\mathcal{R}(\boldsymbol{q}^{\mathbf{0}},\hat{\boldsymbol{q}}^{\mathbf{1}})\boldsymbol{\delta q}^{\mathbf{0}} + \mathcal{S}_{_m}(\boldsymbol{q}^{\mathbf{0}},\hat{\boldsymbol{q}}^{\mathbf{1}})\boldsymbol{\delta q}^{\mathbf{0}}\right\rangle \tag{2.18a}$$

$$= -\left\langle \lambda^*\mathcal{R}^\dagger(\boldsymbol{q}^{\mathbf{0}},\hat{\boldsymbol{q}}^{\mathbf{1}})\hat{\boldsymbol{q}}^{\mathbf{1}\dagger} + \mathcal{S}_{_m}^\dagger(\boldsymbol{q}^{\mathbf{0}},\hat{\boldsymbol{q}}^{\mathbf{1}})\hat{\boldsymbol{q}}^{\mathbf{1}\dagger}\,,\, \boldsymbol{\delta q}^{\mathbf{0}}\right\rangle\,, \tag{2.18b}$$

where $\mathcal{R}$ and $\mathcal{S}_{_m}$ are the linear differential operators defined by

$$\mathcal{R}(\boldsymbol{q}^{\mathbf{0}},\hat{\boldsymbol{q}}^{\mathbf{1}}) = \frac{\partial}{\partial \boldsymbol{q}^{\mathbf{0}}}\left(\mathcal{B}(\boldsymbol{q}^{\mathbf{0}})\hat{\boldsymbol{q}}^{\mathbf{1}}\right)\,, \qquad \mathcal{S}_{_m}(\boldsymbol{q}^{\mathbf{0}},\hat{\boldsymbol{q}}^{\mathbf{1}}) = \frac{\partial}{\partial \boldsymbol{q}^{\mathbf{0}}}\left(\mathcal{A}_{_m}(\boldsymbol{q}^{\mathbf{0}})\hat{\boldsymbol{q}}^{\mathbf{1}}\right)\,. \tag{2.19}$$

Comparing (2.7) and (2.18), it turns out that the complex sensitivity function $\boldsymbol{\nabla}_{\boldsymbol{q}^{\mathbf{0}}}\lambda$ is given by the knowledge of the adjoint operator $\mathcal{R}^\dagger$ and $\mathcal{S}_{_m}^\dagger$, according to

$$\boldsymbol{\nabla}_{\boldsymbol{q}^{\mathbf{0}}}\lambda = -\lambda^*\mathcal{R}^\dagger(\boldsymbol{q}^{\mathbf{0}},\hat{\boldsymbol{q}}^{\mathbf{1}})\hat{\boldsymbol{q}}^{\mathbf{1}\dagger} - \mathcal{S}_{_m}^\dagger(\boldsymbol{q}^{\mathbf{0}},\hat{\boldsymbol{q}}^{\mathbf{1}})\hat{\boldsymbol{q}}^{\mathbf{1}\dagger}\,. \tag{2.20}$$

The present approach is very similar to the Lagrangian technique classically used in optimization problems, where one aims at enforcing the stationary of a Lagrangian in order to minimize a given functional under specific constraints (Gunzburger 1997, 1999; Airiau *et al.* 2003). Though, it should be noted that no such stationarity is enforced here, and that the functional is only used as a mean to compute the gradient $\boldsymbol{\nabla}_{\boldsymbol{q}^{\mathbf{0}}}\lambda$. It is also worthwhile noting that expression (2.20) can be retrieved by an alternative technique based on a perturbation approach of the linear operators $\mathcal{B}$ and $\mathcal{A}_{_m}$.

For a given base flow $\boldsymbol{q}^{\mathbf{0}}$, the procedure to compute the variation of an eigenvalue resulting from a modification of the base flow is the following:

–resolution of the base flow equations (2.2),

–resolution of the stability problem (2.5) and selection of an eigenpair $\{\sigma + \mathrm{i}\omega, \hat{\boldsymbol{q}}^{\mathbf{1}}\}$,

–resolution of the adjoint stability problem (2.15) and normalization of the adjoint global mode using (2.16),

–derivation of operators $\{\mathcal{R}, \mathcal{S}_{_m}\}$ and of the adjoint operators $\{\mathcal{R}^\dagger, \mathcal{S}_{_m}^\dagger\}$,

–computation of the sensitivity to base flow modifications using (2.20) and computation of the scalar product (2.7).

2.2. *Sensitivity to a modification of the Mach number in the perturbation equations*

In this section, the Mach number varies but the base flow is kept constant. The variation $\delta\lambda$, which refers to the specific variation $\delta\lambda|_{\boldsymbol{q^0}}$ for simplicity, is thus investigated with respect to a small modification of the Mach number. A new problem can be defined for which the Mach number is the new control variable, the associated functional reading

$$\mathcal{L}(M, \hat{\boldsymbol{q}}^{\boldsymbol{1\dagger}}, \hat{\boldsymbol{q}}^{\boldsymbol{1}}, \lambda) = \lambda - \left\langle \hat{\boldsymbol{q}}^{\boldsymbol{1\dagger}} \, , \, \lambda \mathcal{B} \hat{\boldsymbol{q}}^{\boldsymbol{1}} + \mathcal{A}_{_m}(M) \hat{\boldsymbol{q}}^{\boldsymbol{1}} \right\rangle \, , \tag{2.21}$$

for which M is the new control variable. In the following, we assume that problem (2.5) is satisfied for any modification of the Mach number. The eigenvalue variation $\delta\lambda$ can thus be expressed as

$$\delta\lambda = \left(\frac{\partial \mathcal{L}}{\partial M} + \frac{\partial \mathcal{L}}{\partial \hat{\boldsymbol{q}}^{\boldsymbol{1\dagger}}} \frac{\partial \hat{\boldsymbol{q}}^{\boldsymbol{1\dagger}}}{\partial M} + \frac{\partial \mathcal{L}}{\partial \{\hat{\boldsymbol{q}}^{\boldsymbol{1}}, \lambda\}} \frac{\partial \{\hat{\boldsymbol{q}}^{\boldsymbol{1}}, \lambda\}}{\partial M} \right) \delta M \tag{2.22}$$

As previously, the gradients of the functional with respect to the state and adjoint variable is nil provided $\{\hat{\boldsymbol{q}}^{\boldsymbol{1}}, \lambda\}$ and $\hat{\boldsymbol{q}}^{\boldsymbol{1\dagger}}$ are again solutions of eigenproblems (2.5) and (2.15), along with the normalization condition (2.16). We obtain now that

$$\delta\lambda = \frac{\partial \mathcal{L}}{\partial M} \delta M = - \left\langle \hat{\boldsymbol{q}}^{\boldsymbol{1\dagger}} \, , \, \frac{\partial}{\partial M} \left(\mathcal{A}_{_m}(M) \hat{\boldsymbol{q}}^{\boldsymbol{1}} \right) \right\rangle \delta M \, . \tag{2.23}$$

For a given base flow $\boldsymbol{q^0}$, the procedure to compute the variation of an eigenvalue resulting from a small change in the Mach number can be summarized as follows:

–resolution of base flow equations (2.2),

–resolution of the stability problem (2.5) and selection of an eigenpair $\{\sigma + \mathrm{i}\omega, \hat{\boldsymbol{q}}^{\boldsymbol{1}}\}$

–resolution of the adjoint stability problem (2.15) and computation of the scalar product (2.23).

2.3. *Sensitivity to a modification of the Mach number*

We return now to the general case where both the base flow and Mach number can be varied. The eigenvalue λ has been previously written as $\lambda = \lambda(\boldsymbol{q^0}, M)$. From (2.6), we can now express the full variation $\delta\lambda$ as

$$\delta\lambda = \delta\lambda|_{_M} + \delta\lambda|_{\boldsymbol{q^0}} = \left\langle \boldsymbol{\nabla}_{\boldsymbol{q^0}} \lambda \, , \, \boldsymbol{\delta q^0} \right\rangle - \left\langle \hat{\boldsymbol{q}}^{\boldsymbol{1\dagger}} \, , \, \frac{\partial}{\partial M} \left(\mathcal{A}_{_m}(M) \hat{\boldsymbol{q}}^{\boldsymbol{1}} \right) \right\rangle \delta M \, . \tag{2.24}$$

The variation $\delta\lambda|_{_M}$ representing the variation of the eigenvalue owing to a base flow modification, the Mach number being kept constant, is computed in the framework of the sensitivity analysis to base flow modifications, which pertains to generic variation $\boldsymbol{\delta q^0}$. Though, for the whole analysis to be physically relevant, one must take into account that, when the Mach number is varied, the stability problem is altered owing to the specific base flow modification $\boldsymbol{\delta q^0_{_M}}$ arising from the explicit modification of the Mach number in the base flow equations. Provided operator $\mathcal{A}_{_0}$ is non-degenerate, $\boldsymbol{\delta q^0_{_M}}$ is solution of the linear problem

$$\mathcal{A}_{_0}(\boldsymbol{q^0}, M) \boldsymbol{\delta q^0_{_M}} = - \frac{\partial}{\partial M} \left(\mathcal{M}_{_0}(\boldsymbol{q^0}, M) \right) \delta M \, , \tag{2.25}$$

so that the relevant expression for the variation $\delta\lambda$ is finally obtained by substituting $\boldsymbol{\delta q^0}$ by $\boldsymbol{\delta q^0_{_M}}$ into (2.6).

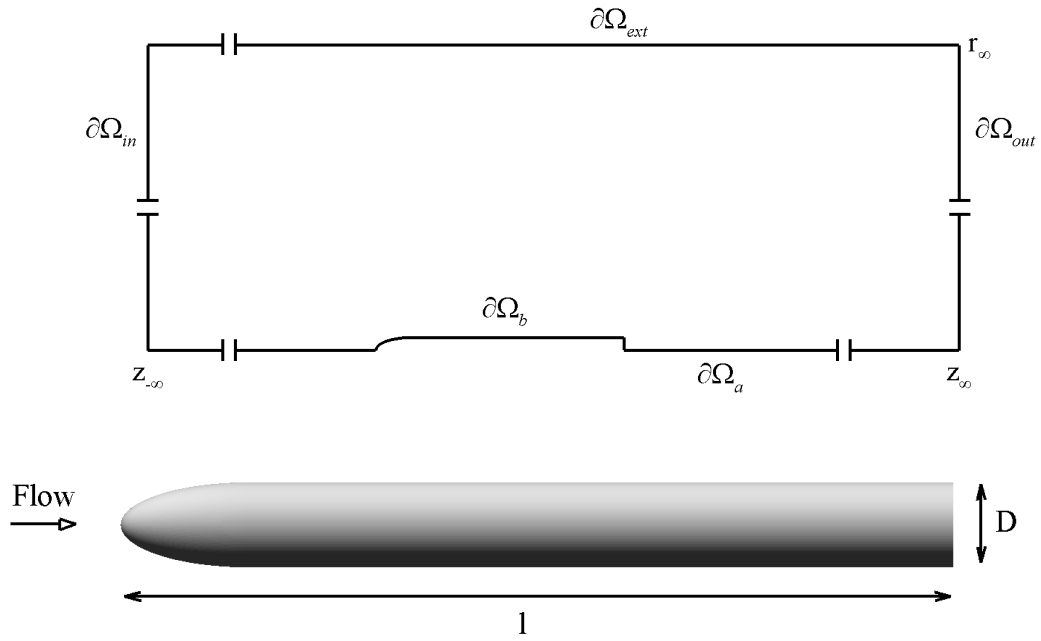

Figure 1: Schematic of the configuration under study: the slender body of revolution has a diameter D and a total length $l = 9.8D$. $z_{-\infty}$, z_∞ and r_∞ are, respectively, the location of the inlet, outlet and lateral boundaries.

3. Application to compressible flows

We aim at applying the general formalism presented in the previous section to the case of an afterbody flow. The body under study is shown in Figure 1: it models an ideal rocket shape, made of an axisymmetric body of revolution with a blunt trailing edge of diameter D placed into a uniform flow at zero angle of attack (Mair 1965; Weickgenannt & Monkewitz 2000). The body used in this study is identical to that used by Sevilla & Martínez-Bazàn (2004), with a total length $l = 9.8D$ and an ellipsoidal nose of aspect ratio 3 : 1. From the results of Weickgenannt & Monkewitz (2000), the estimated Reynolds number for transition to turbulence in the boundary-layer developing on the present body is $Re \simeq 12000$. The Reynolds number prevailing in the present work being such that $Re < 1500$, we can therefore assume that the boundary-layer remains laminar til the trailing edge.

Such afterbody flows require to consider the effect of compressibility, as in the experimental studies of Flodrops & Desse (1985) and Deprés *et al.* (2004). The fluid is thus taken as a non-homogeneous compressible perfect gas with constant specific heat c_p, thermal conductivity κ, and dynamic viscosity μ, related by a unit Prandtl number. To our knowledge, no global stability results are available in the literature on this configuration. Consequently, we have first revisited the low Mach number flow past a sphere as a test case to validate this fully compressible global formalism on a more academic configuration. All details are provided in Appendix A, including quantitative comparison with the results of Natarajan & Acrivos (1993) and numerical convergence tests. All equations are formulated in cylindrical coordinates (r, θ, z) with origin taken at the center of the body base. The fluid motion is governed by the unsteady compressible Navier-Stokes equations, which leads to a set of six nonlinear equations (continuity, radial, orthoradial and streamwise momentum, internal energy and perfect gas) formulated in non-conservative

variables as

$$\partial_t \rho + \rho \boldsymbol{\nabla} \cdot \boldsymbol{u} + \boldsymbol{u} \cdot \boldsymbol{\nabla} \rho = 0\,, \tag{3.1a}$$

$$\rho \partial_t \boldsymbol{u} + \rho \boldsymbol{\nabla} \boldsymbol{u} \cdot \boldsymbol{u} + \frac{1}{\gamma M^2} \boldsymbol{\nabla} p - \frac{1}{Re} \boldsymbol{\nabla} \cdot \boldsymbol{\tau}(\boldsymbol{u}) = \boldsymbol{0}\,, \tag{3.1b}$$

$$\rho \partial_t T + \rho \boldsymbol{u} \cdot \boldsymbol{\nabla} T + p \boldsymbol{\nabla} \cdot \boldsymbol{u} - \gamma(\gamma - 1) \frac{M^2}{Re}\, \boldsymbol{\tau}(\boldsymbol{u}) : \boldsymbol{d}(\boldsymbol{u}) - \frac{\gamma}{PrRe} \boldsymbol{\nabla}^2 T = 0\,, \tag{3.1c}$$

$$p - \rho T = 0\,. \tag{3.1d}$$

Note that a different set of equations can be obtained, as the internal energy equation may be replaced by its total energy or entropy counterpart. Here, ρ is the density, p the pressure, T the temperature, and $\boldsymbol{u} = (u, v, w)^T$ the three-dimensional velocity field with u, v and w its radial, azimuthal and streamwise components, so that the state vector is $\boldsymbol{q} = (\rho, \boldsymbol{u}, T, p)^T$. $\boldsymbol{d}(\boldsymbol{u})$ and $\boldsymbol{\tau}(\boldsymbol{u})$ are the strain and viscous stress tensors defined as

$$\boldsymbol{d}(\boldsymbol{u}) = \frac{1}{2} \left(\boldsymbol{\nabla} \boldsymbol{u} + \boldsymbol{\nabla} \boldsymbol{u}^T \right), \qquad \boldsymbol{\tau}(\boldsymbol{u}) = -\frac{2}{3} \left(\boldsymbol{\nabla} \cdot \boldsymbol{u} \right) \boldsymbol{I} + \boldsymbol{\nabla} \boldsymbol{u} + \boldsymbol{\nabla} \boldsymbol{u}^T. \tag{3.2}$$

In the following, a particular attention will be payed to the advection terms, that are gathered into the operator $\mathcal{N}$ defined by

$$\mathcal{N}(\boldsymbol{q}) = \begin{pmatrix} \rho \boldsymbol{\nabla} \cdot \boldsymbol{u} + \boldsymbol{u} \cdot \boldsymbol{\nabla} \rho \\ \rho \boldsymbol{\nabla} \boldsymbol{u} \cdot \boldsymbol{u} \\ \rho \boldsymbol{u} \cdot \boldsymbol{\nabla} T \\ 0 \end{pmatrix}. \tag{3.3}$$

Equations (3.1) have been made nondimensional using the body diameter D and the upstream quantities W_∞, ρ_∞, T_∞ and p_∞ as respective velocity, density, temperature and pressure scales. The Reynolds, Mach and Prandtl numbers are therefore defined as

$$Re = \frac{\rho_\infty D W_\infty}{\mu}, \qquad M = \frac{W_\infty}{\sqrt{\gamma R_g T_\infty}}, \qquad Pr = \frac{\mu c_p}{\kappa}\,, \tag{3.4}$$

with R_g and γ the ideal gas constant and the ratio of specific heats.

A schematic of the physical configuration is sketched in Figure 1: the body is located on the axis of a numerical enclosing cylinder of radius $r = r_\infty$. The inlet $\partial\Omega_{in}$ and outlet $\partial\Omega_{out}$ boundaries are located respectively at $z = z_{-\infty}$ and $z = z_\infty$ and boundaries $\partial\Omega_a$ and $\partial\Omega_{ext}$ represent respectively the revolution axis of the body and the boundary of the enclosing cylinder. We shall use the following conditions

$$\boldsymbol{u} = (0, 0, 1)^T,\ \rho, T = 1 \ \text{ on } \ \partial\Omega_{in} \text{ (inlet)}, \tag{3.5a}$$

$$\boldsymbol{u} = \boldsymbol{0},\ \partial_n T = 0 \text{ (adiabatic rigid wall) } \text{ on } \ \partial\Omega_b \text{ (body)}, \tag{3.5b}$$

along with appropriate far-field radiation conditions whose implementation in the compressible case requires particular attention. As a consequence, we postpone the question of the boundary conditions to § 4 where we present details of the numerical method.

3.1. *Base flow*

For the base flow $\boldsymbol{q^0} = \left(\rho^0, \boldsymbol{u^0}, T^0, p^0\right)^T$, the axisymmetric steady base flow equations (2.2) read

$$\mathcal{M}_0(\boldsymbol{q^0}, M) = \begin{pmatrix} \rho^0 \boldsymbol{\nabla}\cdot\boldsymbol{u^0} + \boldsymbol{u^0}\cdot\boldsymbol{\nabla}\rho^0\,, \\ \rho^0 \boldsymbol{\nabla}\boldsymbol{u^0}\cdot\boldsymbol{u^0} + \frac{1}{\gamma M^2}\boldsymbol{\nabla}p^0 - \frac{1}{Re}\boldsymbol{\nabla}\cdot\boldsymbol{\tau}(\boldsymbol{u^0})\,, \\ \rho^0 \boldsymbol{u^0}\cdot\boldsymbol{\nabla}T^0 + p^0\boldsymbol{\nabla}\cdot\boldsymbol{u^0} - \gamma(\gamma-1)\frac{M^2}{Re}\,\boldsymbol{\tau}(\boldsymbol{u^0}):\boldsymbol{d}(\boldsymbol{u^0}) - \frac{\gamma}{PrRe}\boldsymbol{\nabla}^2 T^0\,, \\ p^0 - \rho^0 T^0 \end{pmatrix} = \boldsymbol{0}\,. \tag{3.6}$$

3.2. *Perturbation equations*

The perturbation $\hat{\boldsymbol{q}}^{\boldsymbol{1}} = (\hat{\rho}^1, \hat{\boldsymbol{u}}^{\boldsymbol{1}}, \hat{T}^1, \hat{p}^1)^T$ is solution of the generalized eigenvalue problem

$$\lambda\mathcal{B}(\boldsymbol{q^0})\hat{\boldsymbol{q}}^{\boldsymbol{1}} + \mathcal{A}_m(\boldsymbol{q^0}, M)\hat{\boldsymbol{q}}^{\boldsymbol{1}} = \boldsymbol{0}\,. \tag{3.7}$$

Operator $\mathcal{B}$ is defined by

$$\mathcal{B}\left(\boldsymbol{q^0}\right) = \begin{pmatrix} 1 & \boldsymbol{0} & 0 & 0 \\ 0 & \rho^0\mathcal{I} & 0 & 0 \\ 0 & \boldsymbol{0} & \rho^0 & 0 \\ 0 & \boldsymbol{0} & 0 & 0 \end{pmatrix}, \tag{3.8}$$

where $\mathcal{I}$ is the identity operator. Operator $\mathcal{A}_m$ is split into $\mathcal{A}_m\left(\boldsymbol{q^0}, M\right) = \mathcal{C}_m\left(\boldsymbol{q^0}\right) + \mathcal{P}_m\left(\boldsymbol{q^0}, M\right)$ with $\mathcal{C}_m$ the linearized advection operator and $\mathcal{P}_m$ the source/sink operator encompassing the effect of the source terms of the governing equations, reading respectively

$$\mathcal{C}_m\left(\boldsymbol{q^0}\right) = \frac{\partial\mathcal{N}}{\partial\boldsymbol{q^0}}\left(\boldsymbol{q^0}\right) = \begin{pmatrix} \boldsymbol{u^0}\cdot\boldsymbol{\nabla} + \boldsymbol{\nabla}\cdot\boldsymbol{u^0} & \boldsymbol{\nabla}\rho^0\cdot + \rho^0\boldsymbol{\nabla}\cdot & 0 & 0 \\ \boldsymbol{\nabla}\boldsymbol{u^0}\cdot\boldsymbol{u^0} & \rho^0\boldsymbol{\nabla}[\,\bullet\,]\cdot\boldsymbol{u^0} + \rho^0\boldsymbol{\nabla}\boldsymbol{u^0}\cdot & 0 & 0 \\ \boldsymbol{u^0}\cdot\boldsymbol{\nabla}T^0 & \rho^0\boldsymbol{\nabla}T^0\cdot & \rho^0\boldsymbol{u^0}\cdot\boldsymbol{\nabla} & 0 \\ 0 & \boldsymbol{0} & 0 & 0 \end{pmatrix}, \tag{3.9}$$

and

$$\mathcal{P}_{m}\left(\boldsymbol{q^0}, M\right) = \begin{pmatrix} 0 & \boldsymbol{0} & 0 & 0 \\ 0 & -\frac{1}{Re}\boldsymbol{\nabla}\cdot\boldsymbol{\tau}[\,\bullet\,] & 0 & \frac{1}{\gamma M^2}\boldsymbol{\nabla} \\ 0 & -\gamma(\gamma-1)\frac{M^2}{Re}\left(\boldsymbol{\tau}(\boldsymbol{u^0}):\boldsymbol{d}\,[\,\bullet\,]+\boldsymbol{\tau}[\,\bullet\,]:\boldsymbol{d}(\boldsymbol{u^0})\right) & -\frac{\gamma}{PrRe}\boldsymbol{\nabla}^2 & \boldsymbol{\nabla}\cdot\boldsymbol{u^0} \\ -T^0 & \boldsymbol{0} & -\rho^0 & 1 \end{pmatrix}. \tag{3.10}$$

Of course, these analytical expressions rely on the choice of non-conservative variables, and alternative forms of the same operators could be derived using conservative variables. For incompressible flows, it turns out that the source/sink operator is independent of the base flow quantities. The base flow thus influences the perturbation dynamics via the advection operator only. One can then make the difference between terms associated with the *advection* of the perturbation by the base flow, and terms of *production* coming from the advection of the base flow by the perturbation (Marquet *et al.* 2008*b*). This is no more true in the case of compressible flows, as one can see from (3.10) that the base flow influences the disturbance dynamics via the source terms of the governing equations. For instance, Soteriou & Ghoniem (1995) have shown that the different instability characteristics of homogeneous and non-homogeneous shear-layers may be ascribed to the action of a baroclinic torque arising from base flow density gradients and from the pressure perturbations.

To identify terms related to *advection* and *production* in the perturbation equations, the latter set of equations is first recast in conservative variables and integral formulation. This yields

$$\delta_{t,\boldsymbol{u^0}}\left(\int_V \hat{\rho}^1 \mathrm{d}V\right) + \delta_{t,\boldsymbol{u^1}}\left(\int_V \rho^0 \mathrm{d}V\right) + \cdots = 0\,, \tag{3.11a}$$

$$\delta_{t,\boldsymbol{u^0}}\left(\int_V (\hat{\rho}^1\boldsymbol{u^0} + \rho^0\hat{\boldsymbol{u}}^{\boldsymbol{1}})\mathrm{d}V\right) + \delta_{t,\boldsymbol{u^1}}\left(\int_V \rho^0\boldsymbol{u^0}\mathrm{d}V\right) + \cdots = \boldsymbol{0}\,, \tag{3.11b}$$

$$\delta_{t,\boldsymbol{u^0}}\left(\int_V (\hat{\rho}^1 T^0 + \rho^0\hat{T}^1)\mathrm{d}V\right) + \delta_{t,\boldsymbol{u^1}}\left(\int_V \rho^0 T^0\mathrm{d}V\right) + \cdots = 0\,. \tag{3.11c}$$

In (3.11), we consider only the advection terms originating from operator $\mathcal{C}_m$, and the source terms are omitted to ease the notation. $\delta_{t,\boldsymbol{u}}$ is then the time derivative for a volumetric domain V whose bounding surface ∂V is advected with the specific velocity $\boldsymbol{u}$. The leftmost terms $\delta_{t,\boldsymbol{u^0}}$ in (3.11) therefore account for the perturbation advection mechanism, i.e. the advection of the perturbation quantities by the base flow, and the rightmost terms $\delta_{t,\boldsymbol{u^1}}$ account for the perturbation production mechanism through the reciprocal advection of the base flow quantities by the perturbation. When turning back equations (3.11) into non-conservative variables using the base flow and perturbation continuity equations, it is then possible to discriminate between terms accounting for advection or production of the perturbation. We thus split the operator $\mathcal{C}_m$ into $\mathcal{C}_m = \mathcal{C}_m^{(A)} + \mathcal{C}_m^{(P)}$, operator $\mathcal{C}_m^{(A)}$ being then the perturbation advection operator originating from

the terms $\delta_{t,\boldsymbol{u^0}}$ defined by

$$\mathcal{C}_m^{(A)}(\boldsymbol{q^0}) = \begin{pmatrix} \boxed{\boldsymbol{u^0}\cdot\boldsymbol{\nabla}+\boldsymbol{\nabla}\cdot\boldsymbol{u^0}} & \mathbf{0} & 0 & 0 \\ \boldsymbol{\nabla}\boldsymbol{u^0}\cdot\boldsymbol{u^0} & \boxed{\rho^0\boldsymbol{\nabla}[\bullet]\cdot\boldsymbol{u^0}} & 0 & 0 \\ \boldsymbol{u^0}\cdot\boldsymbol{\nabla}T^0 & \mathbf{0} & \boxed{\rho^0\boldsymbol{u^0}\cdot\boldsymbol{\nabla}} & 0 \\ 0 & \mathbf{0} & 0 & 0 \end{pmatrix}, \tag{3.12}$$

and operator $\mathcal{C}_m^{(P)}$ being a perturbation production operator originating from the terms $\delta_{t,\boldsymbol{u^1}}$ reading

$$\mathcal{C}_m^{(P)}(\boldsymbol{q^0}) = \begin{pmatrix} 0 & \boldsymbol{\nabla}\rho^0\cdot+\rho^0\boldsymbol{\nabla}\cdot & 0 & 0 \\ 0 & \rho^0\boldsymbol{\nabla}\boldsymbol{u^0}. & 0 & 0 \\ 0 & \rho^0\boldsymbol{\nabla}T^0\cdot & 0 & 0 \\ 0 & \mathbf{0} & 0 & 0 \end{pmatrix}. \tag{3.13}$$

Boxed terms refer to operators that have only diagonal terms. For conciseness, operators $\mathcal{C}_m^{(A)}$ and $\mathcal{C}_m^{(P)}$ are hereinafter referred to as the advection and production operators. Though, we insist that in the present compressible case, an exhaustive analysis of the perturbation production mechanisms should not be restricted to the production operator $\mathcal{C}_m^{(P)}$ but should point at the operator $\mathcal{C}_m^{(P)}+\mathcal{P}_m$ that encompasses the additional effect of the source terms of the governing equations.

3.3. *Adjoint perturbation equations*

We consider now the adjoint perturbation $\hat{\boldsymbol{q}}^{\boldsymbol{1\dagger}} = (\hat{\rho}^{1\dagger}, \hat{\boldsymbol{u}}^{\boldsymbol{1\dagger}}, \hat{T}^{1\dagger}, \hat{p}^{1\dagger})^T$. Since we use here only nondimensional variables, $\hat{\rho}^{1\dagger}$, $\hat{\boldsymbol{u}}^{\boldsymbol{1\dagger}}$, $\hat{T}^{1\dagger}$ and $\hat{p}^{1\dagger}$ can be referred to for simplicity as the adjoint density, velocity, temperature and pressure disturbances. As mentioned earlier, in order to derive adjoint operators, we must first define an inner product. In the following, we use the standard inner product

$$\left\langle \hat{\boldsymbol{a}}, \hat{\boldsymbol{b}} \right\rangle = \int_\Omega \hat{\boldsymbol{a}}\cdot\hat{\boldsymbol{b}}\, r\mathrm{d}r\mathrm{d}z\,, \tag{3.14}$$

where $\hat{\boldsymbol{a}}$ and $\hat{\boldsymbol{b}}$ are complex vectors and $\cdot$ refers to the canonic hermitian scalar product on $\mathbb{C}^n$. It should be noted here that this inner product is not physically motivated, as will be discussed in § 4. For a complete discussion on the relevance of inner products in compressible flows, the reader may refer to the study of Rowley *et al.* (2004). Though, we emphasize here on the fact that if the definition of adjoint operators is inner product dependent, the variations $\delta\lambda$ computed in the sensitivity analysis are intrinsical.

We recall that the adjoint perturbation $\hat{\boldsymbol{q}}^{\boldsymbol{1\dagger}}$ is solution of the generalized eigenvalue problem

$$\lambda^*\mathcal{B}^\dagger\left(\boldsymbol{q^0}\right)\hat{\boldsymbol{q}}^{\boldsymbol{1\dagger}} + \mathcal{A}_m^\dagger\left(\boldsymbol{q^0}, M\right)\hat{\boldsymbol{q}}^{\boldsymbol{1\dagger}} = \mathbf{0}\,, \tag{3.15}$$

where the subscript $*$ stands for the complex conjugate. Operators $\mathcal{B}$ being diagonal, we obtain simply that $\mathcal{B}^\dagger = \mathcal{B}$. The derivation of the adjoint operator $\mathcal{A}_m^\dagger$ detailed in

Appendix D yields $\mathcal{A}_m^\dagger\left(\boldsymbol{q^0}, M\right) = \mathcal{C}_m^\dagger\left(\boldsymbol{q^0}\right) + \mathcal{P}_m^\dagger\left(\boldsymbol{q^0}, M\right)$ with

$$\mathcal{C}_m^\dagger(\boldsymbol{q^0}) = \begin{pmatrix} -\boldsymbol{u^0}\cdot\boldsymbol{\nabla} & (\boldsymbol{\nabla u^0}\cdot\boldsymbol{u^0})\cdot & \boldsymbol{u^0}\cdot\boldsymbol{\nabla}T^0 & 0 \\ -\rho^0\boldsymbol{\nabla} & -\rho^0\boldsymbol{\nabla}[\bullet]\cdot\boldsymbol{u^0} + \rho^0\boldsymbol{\nabla u^0}^T\cdot & \rho^0\boldsymbol{\nabla}T^0 & 0 \\ 0 & \boldsymbol{0} & -\rho^0\boldsymbol{u^0}\cdot\boldsymbol{\nabla} & 0 \\ 0 & \boldsymbol{0} & 0 & 0 \end{pmatrix}. \tag{3.16}$$

and

$$\mathcal{P}_m^\dagger\left(\boldsymbol{q^0}, M\right) = \begin{pmatrix} 0 & \boldsymbol{0} & 0 & -T^0 \\ 0 & -\frac{1}{Re}\boldsymbol{\nabla}\cdot\boldsymbol{\tau}[\bullet] & -\boldsymbol{\nabla}(p^0[\bullet]) + 2\gamma(\gamma-1)\frac{M^2}{Re}\boldsymbol{\nabla}\cdot\left([\bullet]\boldsymbol{\tau}(\boldsymbol{u^0})\right) & 0 \\ 0 & \boldsymbol{0} & -\frac{\gamma}{PrRe}\boldsymbol{\nabla}^2 & -\rho^0 \\ 0 & -\frac{1}{\gamma M^2}\boldsymbol{\nabla}\cdot & \boldsymbol{\nabla}\cdot\boldsymbol{u^0} & 1 \end{pmatrix}, \tag{3.17}$$

$\mathcal{C}_m^\dagger$ and $\mathcal{P}_m^\dagger$ being the compressible adjoint operators obtained from the integration by parts of the operators $\mathcal{C}_m$ and $\mathcal{P}_m$.

As detailed in Appendix D, these equations have been derived for axisymmetric configurations, along with the inner product (3.14). Though, it is striking to find out that repeating the procedure for two-dimensional cartesian configurations leads to the exact same set of equations, provided the natural inner product in cartesian coordinates is used, namely $\langle\hat{\boldsymbol{a}}, \hat{\boldsymbol{b}}\rangle = \int_\Omega \hat{\boldsymbol{a}}\cdot\hat{\boldsymbol{b}}\,\mathrm{d}x\mathrm{d}y$. This justifies the privileged use of this inner product in adjoint related studies.

Operator $\mathcal{C}_m^\dagger$ can also been split into $\mathcal{C}_m^\dagger = \mathcal{C}_m^{(A)\dagger} + \mathcal{C}_m^{(P)\dagger}$, with an adjoint advection operator $\mathcal{C}_m^{(A)\dagger}$ and an adjoint production operator $\mathcal{C}_m^{(P)\dagger}$ obtained from the separate integration of operators $\mathcal{C}_m^{(A)}$ and $\mathcal{C}_m^{(P)}$. These operators read

$$\mathcal{C}_m^{(A)\dagger}(\boldsymbol{q^0}) = \begin{pmatrix} \boxed{-\boldsymbol{u^0}\cdot\boldsymbol{\nabla}} & (\boldsymbol{\nabla u^0}\cdot\boldsymbol{u^0})\cdot & \boldsymbol{u^0}\cdot\boldsymbol{\nabla}T^0 & 0 \\ 0 & \boxed{-\rho^0\boldsymbol{\nabla}[\bullet]\cdot\boldsymbol{u^0}} & 0 & 0 \\ 0 & \boldsymbol{0} & \boxed{-\rho^0\boldsymbol{u^0}\cdot\boldsymbol{\nabla}} & 0 \\ 0 & \boldsymbol{0} & 0 & 0 \end{pmatrix}, \tag{3.18}$$

and

$$\mathcal{C}_m^{(P)\dagger}(\boldsymbol{q^0}) = \begin{pmatrix} 0 & \mathbf{0} & 0 & 0 \\ -\rho^0\boldsymbol{\nabla} & \rho^0\boldsymbol{\nabla}\boldsymbol{u^0}^T\cdot & \rho^0\boldsymbol{\nabla}T^0 & 0 \\ 0 & \mathbf{0} & 0 & 0 \\ 0 & \mathbf{0} & 0 & 0 \end{pmatrix}, \tag{3.19}$$

where boxed terms designate again operators displaying only diagonal terms.

3.4. *Nonnormality of the compressible evolution operator*

In this section, we discuss the nonnormal effects originating from the advection and production operators. Though, it should be kept in mind that in compressible flows, the source terms of the perturbation and adjoint perturbation equations may trigger additional nonnormality which is out of the scope of the present study. Note that this discussion is only qualitative, as it mainly aims at pointing at the complex effects that may be possibly encountered in compressible flows.

3.4.1. *Convective nonnormality*

As suggested by Chomaz *et al.* (1990) (see Chomaz 2005, for a discussion), a specific type of nonnormality arises, owing to the advection of the perturbation by the base flow. This nonnormal effect affects similarly all components of the state vector, and thus arises due to diagonal terms of the advection operators. For incompressible flows, it is associated with the change of sign in the advection terms

$$\rho^0\boldsymbol{\nabla}\hat{\boldsymbol{u}}^{\mathbf{1}}\cdot\boldsymbol{u^0}\,, \qquad -\rho^0\boldsymbol{\nabla}\hat{\boldsymbol{u}}^{\mathbf{1}\dagger}\cdot\boldsymbol{u^0}\,, \tag{3.20}$$

in the momentum equations for the direct and adjoint advection operators $\mathcal{C}_m^{(A)}$ and $\mathcal{C}_m^{(A)\dagger}$, respectively (Marquet *et al.* 2008*a*). As a result, disturbances are convected downstream by $\boldsymbol{u^0}$ for the direct evolution operator, and upstream by $-\boldsymbol{u^0}$ for its adjoint counterpart, inducing a spatial separation of direct and adjoint modes. This *convective nonnormality* (also termed *convective modoki*) is therefore associated to direct and adjoint global modes that tend to be orthogonal one to the other because localized in different regions of the flow (Chomaz *et al.* 1990). The concept of convective nonnormality can be generalized to the case of compressible open flows by including similar diagonal terms existing in the advection operators $\mathcal{C}_m^{(A)}$ and $\mathcal{C}_m^{(A)\dagger}$ for the continuity and energy equations. One observes from (3.12) and (3.18) that each of this term changes signs, thus inducing a spatial separation between the direct and adjoint perturbations on all components of the state vector.

3.4.2. *Lift-up nonnormality*

In incompressible flows, a second type of nonnormality complements the *convective nonnormality*, and is classically associated to the perturbation production owing to the advection of the base flow by the perturbation. This nonnormal effect affects differentially the components of the state vector, and thus arises due to off-diagonal terms of the production operators. For incompressible flows, it is encompassed by the terms

$$\rho^0\boldsymbol{\nabla}\boldsymbol{u^0}\cdot\hat{\boldsymbol{u}}^{\mathbf{1}}\,, \qquad \rho^0\boldsymbol{\nabla}\boldsymbol{u^0}^T\cdot\hat{\boldsymbol{u}}^{\mathbf{1}\dagger}\,, \tag{3.21}$$

arising in the momentum equations for the production and adjoint production operators, respectively Marquet *et al.* (2008*a*). To ease the understanding of the physical mechanism

associated to this nonnormal effect, let us consider the example of an incompressible parallel shear flow, defined by $\boldsymbol{u^0} = w^0(r)\boldsymbol{e_z}$, in which a small radial velocity $\hat{u}^1$ is applied along the direction of the base flow gradient. Retaining only the contribution of terms 3.21 yields

$$\lambda(\hat{u}^1, \hat{v}^1, \hat{w}^1)^T = \cdots - (0, 0, \hat{u}^1 \partial_r w^0)^T \ldots \tag{3.22a}$$

$$\lambda^*(\hat{u}^{1\dagger}, \hat{v}^{1\dagger}, \hat{w}^{1\dagger})^T = \ldots, -(\hat{w}^{1\dagger} \partial_r w^0, 0, 0)^T \ldots . \tag{3.22b}$$

It can be seen that the small displacement $\hat{u}^1$ produces strong streamwise velocity perturbations, thus giving rise to the so-called *lift-up* effect (Landahl 1980) and strong adjoint velocity perturbations in the direction of the base flow gradient. This nonnormality is therefore associated to direct and adjoint global modes that tend to be orthogonal one to the other because concentrated on different components of the velocity vector.

This nonnormal effect can be generalized to the case of compressible flows by considering the additional off-diagonal terms arising in the production operators. If we consider now a compressible parallel shear flow, with $\rho^0 = \rho^0(r)$, $\boldsymbol{u^0} = w^0(r)\boldsymbol{e_z}$ and $T^0 = T^0(r)$, a small displacement $\hat{u}^1$ tends to concentrate the direct perturbation on the density, streamwise velocity and temperature components. In return, since off-diagonal terms in the adjoint production operator $\mathcal{C}_m^{(P)\dagger}$ exist only in the adjoint momentum equations, the adjoint perturbation tends to be concentrated along the velocity vector only, so that direct and adjoint global modes are concentrated on different components of the state vector. In the following, this effect is referred to as the *kinematics lift-up nonnormality*, as it is due to small displacement of fluid particles along the direction of the base flow gradients.

Moreover, in the case of real non-parallel axisymmetric flows, such as those considered here, one can easily verify that the nondiagonal terms of the advection operators $\mathcal{C}_m^{(A)}$ and $\mathcal{C}_m^{(A)\dagger}$ are nonzero. It can be seen from equations (3.12) – (3.18) that a small density perturbation $\hat{\rho}^1$ induces strong velocity and temperature perturbation through the off-diagonal terms $\hat{\rho}^1 \boldsymbol{\nabla} \boldsymbol{u^0} \cdot \boldsymbol{u^0}$ and $\hat{\rho}^1 \boldsymbol{u^0} \cdot \boldsymbol{\nabla} T^0$ respectively. For the adjoint perturbations, since all off-diagonal terms in $\mathcal{C}_m^{(A)\dagger}$ are located in the adjoint continuity equation (3.15a), one obtains in return strong adjoint density perturbations, so that direct and adjoint global modes are concentrated on different components of the state vector, an effect similar to the kinematics lift-up nonnormality. Since this additional nonnormality is due to small density perturbations, it can thus be referred to as the *thermodynamics lift-up nornormality.*

To summarize the various nonnormal effects existing for compressible flows, one can distinguish between

(i) the convective nonnormality, owing to the diagonal terms of the advection operators,

(ii) the kinematics lift-up nonnormality, owing to the production operators,

(iii) the thermodynamics lift-up nonnormality, owing to the off-diagonal terms of the advection operators.

3.5. *Sensitivity to base flow modifications*

We recall here that the sensitivity function $\boldsymbol{\nabla}_{\boldsymbol{q^0}} \lambda$ is related to the adjoint operators $\mathcal{R}^\dagger$ and $\mathcal{S}_m^\dagger$ defined in (2.19) by

$$\boldsymbol{\nabla}_{\boldsymbol{q^0}} \lambda = -\lambda^* \mathcal{R}^\dagger(\boldsymbol{q^0}, \hat{\boldsymbol{q}}^{\boldsymbol{1}}) \hat{\boldsymbol{q}}^{\boldsymbol{1}\dagger} - \mathcal{S}_m^\dagger(\boldsymbol{q^0}, \hat{\boldsymbol{q}}^{\boldsymbol{1}}) \hat{\boldsymbol{q}}^{\boldsymbol{1}\dagger} . \tag{3.23}$$

Following the Lagrangian technique detailed in § 2, we obtain a sensitivity function $\boldsymbol{\nabla}_{\boldsymbol{q^0}}\lambda = (\boldsymbol{\nabla}_{\rho^0}\lambda, \boldsymbol{\nabla}_{\boldsymbol{u^0}}\lambda, \boldsymbol{\nabla}_{T^0}\lambda, , \boldsymbol{\nabla}_{p^0}\lambda)^T$, with

$$\begin{aligned}\boldsymbol{\nabla}_{\rho^0}\lambda = &-\lambda^*\left(\hat{\boldsymbol{u}}^{\boldsymbol{1\dagger}}\cdot\hat{\boldsymbol{u}}^{\boldsymbol{1}\,*}+\hat{T}^{1\dagger}\hat{T}^{1\,*}\right)-\hat{\boldsymbol{u}}^{\boldsymbol{1\dagger}\,T}\cdot\left(\boldsymbol{\nabla}\boldsymbol{u^0}\cdot\hat{\boldsymbol{u}}^{\boldsymbol{1}\,*}+\boldsymbol{\nabla}\hat{\boldsymbol{u}}^{\boldsymbol{1*}}\cdot\boldsymbol{u^0}\right)+\boldsymbol{\nabla}\hat{\rho}^{1\dagger}\cdot\hat{\boldsymbol{u}}^{\boldsymbol{1}\,*}\\ &-\hat{T}^{1\dagger}\left(\hat{\boldsymbol{u}}^{\boldsymbol{1}\,*}\cdot\boldsymbol{\nabla}T^0+\boldsymbol{u^0}\cdot\boldsymbol{\nabla}\hat{T}^{1\,*}\right)+\hat{p}^{1\dagger}\hat{T}^{1\,*}, \qquad (3.24a)\end{aligned}$$

$$\begin{aligned}\boldsymbol{\nabla}_{\boldsymbol{u^0}}\lambda = &\quad\rho^0\left(-\boldsymbol{\nabla}\hat{\boldsymbol{u}}^{\boldsymbol{1*}\,T}\cdot\hat{\boldsymbol{u}}^{\boldsymbol{1\dagger}}+\boldsymbol{\nabla}\hat{\boldsymbol{u}}^{\boldsymbol{1\dagger}}\cdot\hat{\boldsymbol{u}}^{\boldsymbol{1}\,*}\right)+\hat{\rho}^{1\,*}\left(-\boldsymbol{\nabla}\boldsymbol{u^0}^{\,T}\cdot\hat{\boldsymbol{u}}^{\boldsymbol{1\dagger}}+\boldsymbol{\nabla}\hat{\boldsymbol{u}}^{\boldsymbol{1\dagger}}\cdot\boldsymbol{u^0}\right)\\ &-\lambda^*\hat{\rho}^{1\,*}\hat{\boldsymbol{u}}^{\boldsymbol{1\dagger}}+\hat{\rho}^{1\,*}\boldsymbol{\nabla}\hat{\rho}^{1\dagger}-\hat{T}^{1\dagger}(\hat{\rho}^{1\,*}\boldsymbol{\nabla}T^0+\rho^0\boldsymbol{\nabla}\hat{T}^{1\,*})+\boldsymbol{\nabla}(\hat{T}^{1\dagger}\hat{p}^{1\,*})\\ &-2\gamma(\gamma-1)\frac{M^2}{Re}\boldsymbol{\nabla}\cdot\left(\hat{T}^{1\dagger}\boldsymbol{\tau}(\hat{\boldsymbol{u}}^{\boldsymbol{1}})^*\right), \qquad (3.24b)\end{aligned}$$

$$\boldsymbol{\nabla}_{T^0}\lambda = \quad\boldsymbol{\nabla}\cdot\left(\hat{T}^{1\dagger}(\hat{\rho}^{1\,*}\boldsymbol{u^0}+\rho^0\hat{\boldsymbol{u}}^{\boldsymbol{1}\,*})\right)+\hat{p}^{1\dagger}\hat{\rho}^{1\,*}, \qquad (3.24c)$$

$$\boldsymbol{\nabla}_{p^0}\lambda = \quad-\hat{T}^{1\dagger}\boldsymbol{\nabla}\cdot\hat{\boldsymbol{u}}^{\boldsymbol{1}\,*}. \qquad (3.24d)$$

Note that in the limit of incompressible flows, this expression reduces to

$$\boldsymbol{\nabla}_{\boldsymbol{u^0}}\lambda = -\boldsymbol{\nabla}\hat{\boldsymbol{u}}^{\boldsymbol{1*}\,T}\cdot\hat{\boldsymbol{u}}^{\boldsymbol{1\dagger}}+\boldsymbol{\nabla}\hat{\boldsymbol{u}}^{\boldsymbol{1\dagger}}\cdot\hat{\boldsymbol{u}}^{\boldsymbol{1}\,*}, \qquad (3.25)$$

which is precisely the expression of the sensitivity function found a posteriori by Marquet *et al.* (2008*b*) using a fully incompressible framework. In this incompressible context, these authors argued that the simple expression of the sensitivity function allowed to distinguish between a sensitivity of the eigenvalue $\boldsymbol{\nabla}^{(A)}_{\boldsymbol{u^0}}\lambda$ to a modification of the advection of perturbations by the base flow, and a sensitivity $\boldsymbol{\nabla}^{(P)}_{\boldsymbol{u^0}}\lambda$ to a modification of the production of perturbations by the base flow. To ease the reading, these specific sensitivity functions will be referred to as the advection and production sensitivity functions. In the present case, obviously no simple distinction can be made from the complex expressions (3.24). We thus use operators $\mathcal{C}^{(A)}_m$ and $\mathcal{C}^{(P)}_m$ defined in (3.12) and (3.13) to generalize these concepts to the fully compressible case and propose a systematic method allowing the computation of complex sensitivity functions to a modification of the advection and production operators. Using the same Lagrangian technique than that detailed in § 2, it can be seen that $\mathcal{C}^{(A)}_m$ contributes in the gradient (2.18) through the quantity

$$-\left\langle\hat{\boldsymbol{q}}^{\boldsymbol{1\dagger}}\,,\,\mathcal{S}^{(A)}_m(\boldsymbol{q^0},\hat{\boldsymbol{q}}^{\boldsymbol{1}})\boldsymbol{\delta q^0}\right\rangle=-\left\langle\mathcal{S}^{(A)\dagger}_m(\boldsymbol{q^0},\hat{\boldsymbol{q}}^{\boldsymbol{1}})\hat{\boldsymbol{q}}^{\boldsymbol{1\dagger}}\,,\,\boldsymbol{\delta q^0}\right\rangle, \qquad (3.26)$$

where

$$\mathcal{S}^{(A)}_m(\boldsymbol{q^0},\hat{\boldsymbol{q}}^{\boldsymbol{1}})=\frac{\partial}{\partial\boldsymbol{q^0}}\left(\mathcal{C}^{(A)}_m(\boldsymbol{q^0})\hat{\boldsymbol{q}}^{\boldsymbol{1}}\right). \qquad (3.27)$$

It is therefore immediate to define the sensitivity to a modification of the advection operator $\boldsymbol{\nabla}^{(A)}_{\boldsymbol{q^0}}\lambda$ as

$$\boldsymbol{\nabla}^{(A)}_{\boldsymbol{q^0}}\lambda=-\mathcal{S}^{(A)\dagger}_m(\boldsymbol{q^0},\hat{\boldsymbol{q}}^{\boldsymbol{1}})\hat{\boldsymbol{q}}^{\boldsymbol{1\dagger}}. \qquad (3.28)$$

We obtain the following expressions:

$$\boldsymbol{\nabla}^{(A)}_{\rho^0}\lambda = -\left(\boldsymbol{\nabla}\hat{\boldsymbol{u}}^{\mathbf{1*}}\cdot\boldsymbol{u}^{\mathbf{0}}\right)\cdot\hat{\boldsymbol{u}}^{\mathbf{1\dagger}} - \hat{T}^{1\dagger}\boldsymbol{u}^{\mathbf{0}}\cdot\boldsymbol{\nabla}\hat{T}^{1\,*}\,, \tag{3.29a}$$

$$\begin{aligned}\boldsymbol{\nabla}^{(A)}_{\boldsymbol{u}^{\mathbf{0}}}\lambda = \quad & \rho^0\left(-\boldsymbol{\nabla}\hat{\boldsymbol{u}}^{\mathbf{1*}\,T}\cdot\hat{\boldsymbol{u}}^{\mathbf{1\dagger}}\right) + \hat{\rho}^{1\,*}\left(-\boldsymbol{\nabla}\boldsymbol{u}^{\mathbf{0}\,T}\cdot\hat{\boldsymbol{u}}^{\mathbf{1\dagger}} + \boldsymbol{\nabla}\hat{\boldsymbol{u}}^{\mathbf{1\dagger}}\cdot\boldsymbol{u}^{\mathbf{0}}\right)\\ & + \hat{\rho}^{1\,*}\boldsymbol{\nabla}\hat{\rho}^{1\dagger} - \rho^0\hat{T}^{1\dagger}\boldsymbol{\nabla}\hat{T}^{1\,*} - \hat{\rho}^{1\,*}\hat{T}^{1\dagger}\boldsymbol{\nabla}T^0\,,\end{aligned} \tag{3.29b}$$

$$\boldsymbol{\nabla}^{(A)}_{T^0}\lambda = \quad \boldsymbol{\nabla}\cdot\left(\hat{\rho}^{1\,*}\hat{T}^{1\dagger\,*}\boldsymbol{u}^{\mathbf{0}}\right)\,, \tag{3.29c}$$

$$\boldsymbol{\nabla}^{(A)}_{p^0}\lambda = \quad 0\,. \tag{3.29d}$$

The sensitivity to the modification of the overall production operator $\boldsymbol{\nabla}^{(P)}_{\boldsymbol{q}^{\mathbf{0}}}\lambda$, including source terms of the governing equations, is then defined as

$$\boldsymbol{\nabla}^{(P)}_{\boldsymbol{q}^{\mathbf{0}}}\lambda = \boldsymbol{\nabla}_{\boldsymbol{q}^{\mathbf{0}}}\lambda - \boldsymbol{\nabla}^{(A)}_{\boldsymbol{q}^{\mathbf{0}}}\lambda\,. \tag{3.30}$$

In the incompressible limit, theses analytical expressions reduce to

$$\boldsymbol{\nabla}^{(A)}_{\boldsymbol{u}^{\mathbf{0}}}\lambda = -\boldsymbol{\nabla}\hat{\boldsymbol{u}}^{\mathbf{1*}\,T}\cdot\hat{\boldsymbol{u}}^{\mathbf{1\dagger}}\,, \qquad \boldsymbol{\nabla}^{(P)}_{\boldsymbol{u}^{\mathbf{0}}}\lambda = \boldsymbol{\nabla}\hat{\boldsymbol{u}}^{\mathbf{1\dagger}}\cdot\hat{\boldsymbol{u}}^{\mathbf{1}\,*}\,, \tag{3.31}$$

which are precisely that introduced in the study of Marquet *et al.* (2008*b*).

At this point, it may be objected that the choice of using non-conservative variables is not physically relevant to the case of a compressible flow, since the base flow density modification $\delta\rho^0$ also integrates effects of the modification of the momentum $\rho^0\boldsymbol{u}^{\mathbf{0}}$ and of the internal energy ρ^0T^0. We insist here on the fact that, since

$$\delta\lambda = \left\langle\boldsymbol{\nabla}_{\boldsymbol{q}^{\mathbf{0}}}\lambda\,,\,\boldsymbol{\delta q}^{\mathbf{0}}\right\rangle = \int_\Omega\left(\boldsymbol{\nabla}_{\rho^0}\lambda\cdot\delta\rho^0 + \boldsymbol{\nabla}_{\boldsymbol{u}^{\mathbf{0}}}\lambda\cdot\boldsymbol{\delta u}^{\mathbf{0}} + \boldsymbol{\nabla}_{T^0}\lambda\cdot\delta T^0 + \boldsymbol{\nabla}_{p^0}\lambda\cdot\delta p^0\right)\,r\mathrm{d}r\mathrm{d}z\,, \tag{3.32}$$

a set of *conservative sensitivity functions* $\boldsymbol{\nabla}_{\rho^0}\lambda$, $\boldsymbol{\nabla}_{\rho^0\boldsymbol{u}^{\mathbf{0}}}\lambda$, $\boldsymbol{\nabla}_{\rho^0T^0}\lambda$ and $\boldsymbol{\nabla}_{p^0}\lambda$ can be elegantly deduced from the *non-conservative sensitivity functions* $\boldsymbol{\nabla}_{\rho^0}\lambda$, $\boldsymbol{\nabla}_{\boldsymbol{u}^{\mathbf{0}}}\lambda$, $\boldsymbol{\nabla}_{T^0}\lambda$ and $\boldsymbol{\nabla}_{p^0}\lambda$ through

$$\boldsymbol{\nabla}_{\rho^0}\lambda = \boldsymbol{\nabla}_{\rho^0}\lambda - \frac{\boldsymbol{u}^{\mathbf{0}}}{\rho^0}\cdot\boldsymbol{\nabla}_{\boldsymbol{u}^{\mathbf{0}}}\lambda - \frac{T^0}{\rho^0}\boldsymbol{\nabla}_{T^0}\lambda\,, \tag{3.33a}$$

$$\boldsymbol{\nabla}_{\rho^0\boldsymbol{u}^{\mathbf{0}}}\lambda = \frac{1}{\rho^0}\boldsymbol{\nabla}_{\boldsymbol{u}^{\mathbf{0}}}\lambda\,, \tag{3.33b}$$

$$\boldsymbol{\nabla}_{\rho^0T^0}\lambda = \frac{1}{\rho^0}\boldsymbol{\nabla}_{T^0}\lambda\,, \tag{3.33c}$$

the sensitivity function $\boldsymbol{\nabla}_{p^0}\lambda$ being unchanged. The same transformation can finally be used to derive the conservative advection and production sensitivity functions.

4. Numerical method

4.1. *Spatial discretization*

The numerical approach is based on a finite element method. Equations are first multiplied by r to avoid the singularity on the $r = 0$ axis. The associated variational formulation is then derived and spatially discretized using a mesh composed of triangular elements. The FreeFem++ software (*http://www.freefem.org*) is used to generate the triangulation with the Delaunay-Voronoi algorithm. The mesh refinement is controlled by the vertex densities on both external and internal boundaries. Regions where the mesh

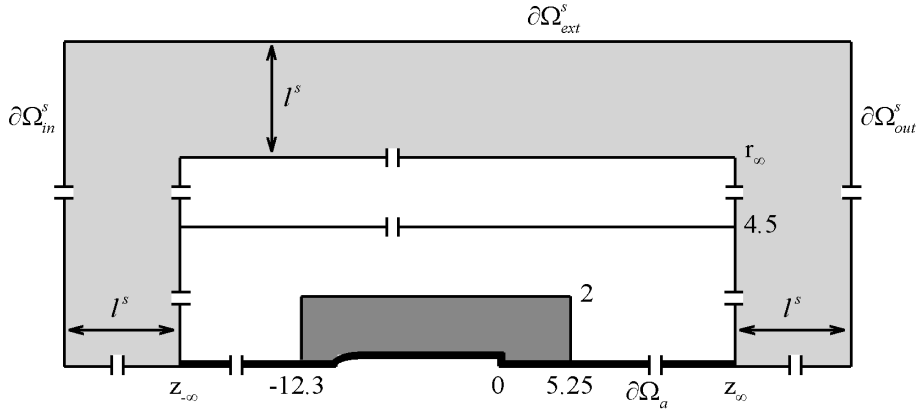

Figure 2: Schematic of the computational mesh: $z_{-\infty}$, z_∞ and r_∞ are, respectively, the location of the physical inlet, outlet and lateral boundaries shown in Figure 1. This physical domain is padded into a two-dimensional sponge zone of width l^s, shown as the light grey shaded area. The inner solid lines delimit regions characterized by different vertex densities. The black shaded area corresponds to the region of highest density and the dark grey shaded area corresponds to the near wake domain used to normalize the perturbation eigenmodes.

density varies are depicted in Figure 2. To avoid any computational difficulty, a zone of width 0.05 and high vertex density (250 vertex per unit length) is defined at the axis $r = 0$ and around the body, corresponding to the black shaded area shown in Figure 2. All pressure quantities are eliminated from the governing equations using the perfect gas state equation so that the state vector is from now on $\boldsymbol{q} = (\rho, \boldsymbol{u}, T)^T$. The unknown velocity, density and temperature fields are spatially discretized using a basis of Arnold-Brezzi-Fortin MINI-elements (Matsumoto & Kawahara 2000), with 4-node $P1b$ elements for the velocity components and 3-node $P1$ elements for the density and the temperature. The sparse matrices resulting from the projection of the variational formulations onto the basis of finite elements are built with the FreeFem++ software. The matrix inverses are computed using the UMFPACK library, which consists in a sparse direct LU solver (Davis & Duff 1997; Davis 2004).

4.2. *Numerical implementation of the boundary conditions*

As mentioned previously, the question of boundary conditions may be particularly involved in compressible flows. In the present study, the treatment of the inlet, lateral and outflow boundaries does not involve any physical modeling: the physical domain is padded with sponge regions, where all fluctuations are progressively damped to negligible levels through artificial dissipation (see Colonius 2004). The purpose of these sponge regions is to minimize numerical box size effects by gradually attenuating all vortical and acoustic fluctuations before they reach the boundary of the computational domain. The resulting domain Ω, corresponding to the azimuthal plane $\theta = 0$, is shown in Figure 2: the computational inlet $\partial\Omega^s_{in}$, outlet $\partial\Omega^s_{out}$ and external $\partial\Omega^s_{ext}$ boundaries are located at $z = z_\infty + l^s$, $z = z_{-\infty} - l^s$ and $r = r_\infty + l^s$. Considering the function defined by

$$f(x_1, x_2) = 1 + \tanh\left(4 \tan\left\{-\frac{\pi}{2}\left(1 - 2\frac{|x_1 - x_2|}{l^s}\right)\right\}\right), \tag{4.1}$$

the viscosity is smoothly increased from the fluid viscosity $\mu = 1$ in the inner domain to a large value $\mu^s = 10/Re$ on $\partial\Omega^s$ according to

$$\widetilde{\mu}(r,z) = 1 \quad \text{if} \quad r \leqslant r_\infty \quad \text{and} \quad |z| \leqslant |z_{\pm\infty}|\,, \tag{4.2a}$$

$$\widetilde{\mu}(r,z) = 1 + \frac{1}{2}\left(\mu^s - 1\right) f(z, z_{\pm\infty}) \quad \text{if} \quad r \leqslant r_\infty \quad \text{and} \quad |z| > |z_{\pm\infty}|\,, \tag{4.2b}$$

$$\widetilde{\mu}(r,z) = \widetilde{\mu}(r_\infty, z) + \frac{1}{2}\left(\mu^s - \widetilde{\mu}(r_\infty, z)\right) f(z, z_{\pm\infty}) \quad \text{if} \quad r > r_\infty\,. \tag{4.2c}$$

As a consequence, all viscous tensors $\boldsymbol{d}(\boldsymbol{u})$ and $\boldsymbol{\tau}(\boldsymbol{u})$ introduced in (3.2) should be replaced by the effective tensors reading

$$\widetilde{\boldsymbol{d}}(\boldsymbol{u}) = \widetilde{\mu}\,\boldsymbol{d}(\boldsymbol{u})\,, \qquad \widetilde{\boldsymbol{\tau}}(\boldsymbol{u}) = \widetilde{\mu}\,\boldsymbol{\tau}(\boldsymbol{u})\,. \tag{4.3}$$

In addition to this artificial damping, numerical dissipation in the sponge zones is increased by significant progressive grid stretching. The mesh used for this study is build using $z_\infty = -100$ $z_\infty = 300$, $r_\infty = 25$ and $l^s = 200$, resulting in 662816 triangles. In particular, all vertex densities used to build this mesh are identical to that of the mesh M_1, which is shown in Appendix A to provide with the most accurate results in the case of the sphere flow. Finally, the governing equations are solved using the following boundary conditions:

$$\boldsymbol{u} = (0,0,1)^T,\ \rho, T = 1 \ \text{ on } \ \partial\Omega^s_{in} \cup \partial\Omega^s_{ext} \cup \partial\Omega^s_{out} \ \text{(inlet, external \& outlet)}, \tag{4.4a}$$

$$\boldsymbol{u} = \boldsymbol{0},\ \partial_n T = 0 \quad \text{on} \ \ \partial\Omega_b \ \text{(body)}\,. \tag{4.4b}$$

The base flow satisfies identical boundary conditions, along with the additional condition $u^0 = 0$, $\partial_r(w^0, \rho^0, T^0) = 0$ on $\partial\Omega_a$ obtained from mass, momentum and internal energy conservation as $r \to 0$ for axisymmetric solutions. The perturbation satisfies the following boundary conditions

$$\hat{\boldsymbol{u}}^{\boldsymbol{1}} = \boldsymbol{0},\ \hat{\rho}^1, \hat{T}^1 = 0 \ \text{ on } \ \partial\Omega^s_{in} \cup \partial\Omega^s_{ext} \cup \partial\Omega^s_{out}, \tag{4.5a}$$

$$\hat{\boldsymbol{u}}^{\boldsymbol{1}} = \boldsymbol{0},\ \partial_n \hat{T}^1 = 0 \quad \text{on} \ \ \partial\Omega_b\,, \tag{4.5b}$$

$$\hat{w}^1, \hat{\rho}^1, \hat{T}^1 = 0,\ \partial_r(\hat{u}^1, \hat{v}^1) = 0 \quad \text{on} \ \ \partial\Omega_a\,, \tag{4.5c}$$

the condition at the axis being specific to $m = 1$ disturbances. All global modes are normalized by imposing the phase of the radial velocity to be zero at a particular location, namely $\hat{u}^1(0,1)$ must be real positive for $m = \pm 1$. The eigenmode energy is then normalized to unity in the near-wake domain defined arbitrarily as $z \in [-12.3,\ 5.25]$ and $r < 2$ and corresponding to the dark grey shaded area in Figure 2:

$$\left\langle \hat{\boldsymbol{q}}^{\boldsymbol{1}}, \delta_{in} \mathcal{B} \hat{\boldsymbol{q}}^{\boldsymbol{1}} \right\rangle = 1\,, \tag{4.6}$$

with δ_{in} the function defined as $\delta_{in}(r,z) = 1$ if $(r,z) \in \Omega_{in}$ and 0 otherwise. This normalization choice has no effect on the sensitivity analysis but eases the comparison between results when convergence tests are carried out. Note that for incompressible flows, this choice has a simple physical interpretation, since

$$\left\langle \hat{\boldsymbol{q}}^{\boldsymbol{1}}\,,\, \mathcal{B} \hat{\boldsymbol{q}}^{\boldsymbol{1}} \right\rangle = \int_\Omega |\hat{\boldsymbol{u}}^{\boldsymbol{1}}|^2 r \mathrm{d}r\mathrm{d}z\,, \tag{4.7}$$

owing to the specific form of operator $\mathcal{B}$ (Marquet *et al.* 2008*a*; Meliga *et al.* 2008*b*) i.e. the condition (4.6) imposes a unity kinematic energy in Ω_{in}. For compressible flows, we have already mentioned that the choice of the inner product was not physically motivated.

Indeed, using (3.8), we obtain now

$$\left\langle \hat{\boldsymbol{q}}^{\mathbf{1}} \, , \, \mathcal{B}\hat{\boldsymbol{q}}^{\mathbf{1}} \right\rangle = \int_{\Omega} \left(|\hat{\rho}^1|^2 + \rho^0 |\hat{\boldsymbol{u}}^{\mathbf{1}}|^2 + \rho^0 |\hat{T}^1|^2 \right) r \mathrm{d}r\mathrm{d}z \, , \tag{4.8}$$

so that the 'energy' defined by the induced norm is not a meaningful physical quantity, neither the total energy, nor the total enthalpy of the perturbation. In the following, the associated instantaneous 'energy density' of the perturbation will be referred to as the $\mathcal{B}$-norm, denoted $\| \ \|_{\mathcal{B}}$, thus defined by

$$\left\langle \hat{\boldsymbol{q}}^{\mathbf{1}} \, , \, \mathcal{B}\hat{\boldsymbol{q}}^{\mathbf{1}} \right\rangle = \int_{\Omega} \|\hat{\boldsymbol{q}}^{\mathbf{1}}\|^2_{\mathcal{B}}(r,z) r \mathrm{d}r\mathrm{d}z \, . \tag{4.9}$$

The conditions for the adjoint perturbation arising from the integration by parts of the perturbation equations are identical to that of the perturbation (see Appendix D for the details). Adjoint global modes are then normalized using condition (2.16).

4.3. *Base flow calculations*

The Reynolds and Mach numbers being fixed, we assume first that it is possible to find an approximate guess $\bar{\boldsymbol{q}}^0$ of the base flow $\boldsymbol{q}^{\mathbf{0}}$, solution of the steady nonlinear equations (3.6). $\boldsymbol{q}^{\mathbf{0}}$ is then obtained using an iterative Newton method, i.e. it is searched as a perturbation of this guess value $\bar{\boldsymbol{q}}^0 + \delta\bar{\boldsymbol{q}}^0$, as in Barkley *et al.* (2002). Such an approach involves the resolution of simple linear problems reading

$$\mathcal{A}_0(\bar{\boldsymbol{q}}^0)\delta\bar{\boldsymbol{q}}^0 = -\mathcal{M}_0(\bar{\boldsymbol{q}}^0) \, . \tag{4.10}$$

At each step, a matrix inversion is performed by use of the UMFPACK library. The iterative process is carried out until the $\mathcal{L}^2$-norm of $\mathcal{M}_0(\bar{\boldsymbol{q}}^{\mathbf{0}})$ becomes smaller than 10^{-12}. Two strategies are used to find the guess $\bar{\boldsymbol{q}}^{\mathbf{0}}$:

–in the limit of low Mach numbers, we represent the solution of the base flow equations (3.6) as power series in $\epsilon = \gamma M^2$ expanded about the steady condition of zero Mach number

$$\boldsymbol{u}^{\mathbf{0}}(\boldsymbol{r}) = \boldsymbol{u}_0(\boldsymbol{r}) + \epsilon \boldsymbol{u}_1(\boldsymbol{r},t) + \cdots \, , \tag{4.11a}$$
$$\rho^0(\boldsymbol{r}) = 1 + \epsilon\rho_1(\boldsymbol{r},t) + \cdots \, , \tag{4.11b}$$
$$T^0(\boldsymbol{r}) = T_0(r) + \epsilon T_1(\boldsymbol{r},t) + \cdots \, , \tag{4.11c}$$
$$p^0(\boldsymbol{r}) = p_0(r) + \epsilon p_1(\boldsymbol{r},t) + \cdots \, . \tag{4.11d}$$

Substituting the power series (4.11) into the governing equations, and equating the coefficients of powers of ϵ to zero yields the following lowest-order equations:

$$\boldsymbol{\nabla} p_0 = 0 \, , \tag{4.12a}$$
$$p_0 = T_0 \, , \tag{4.12b}$$
$$p_1 = \rho_1 T_0 + T_1 \, , \tag{4.12c}$$
$$\boldsymbol{\nabla} \cdot \boldsymbol{u}_0 = 0 \, , \tag{4.12d}$$
$$\boldsymbol{\nabla}\boldsymbol{u}_0 \cdot \boldsymbol{u}_0 + \boldsymbol{\nabla} p_1 - \frac{1}{Re}\boldsymbol{\nabla}^2 \boldsymbol{u}_0 = \mathbf{0} \, . \tag{4.12e}$$

Equations $(4.12a) - (4.12b)$ mean that p_0 and consequently T_0 are uniform in space. We can thus set $p_0 = T_0 = 1$. Moreover, it can be seen from equations $(4.12d) - (4.12e)$ that $\boldsymbol{u}_0$ and p_1 satisfy the incompressible steady axisymmetric Navier-Stokes equations and can therefore be computed by time marching the incompressible equations.

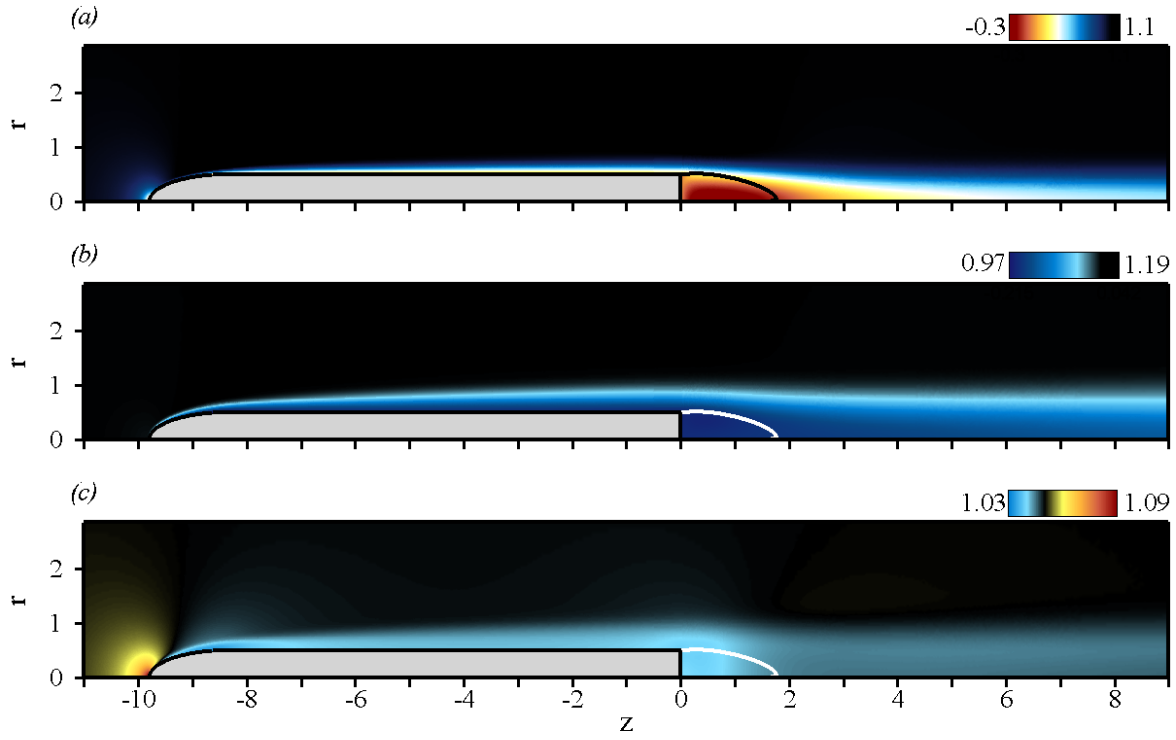

Figure 3: Steady axisymmetric base flow for $Re = 400$ and $M = 0.5$. The solid line in the flow indicates the separatrix of the recirculation zone. (a) Spatial distribution of axial velocity w^0. (b) Spatial distribution of total pressure p_i^0. The black hue corresponds to the free-stream value $p_{i\infty}^0 = 1.19$. (c) Spatial distribution of total temperature T_i^0. The black hue corresponds to the free-stream value $T_{i\infty}^0 = 1.05$.

The guess solution $\bar{\boldsymbol{q}}^{\mathbf{0}}$ of the compressible equations may then be chosen as

$$\overline{\boldsymbol{u}}^{\mathbf{0}} = \boldsymbol{u}_0, \tag{4.13a}$$
$$\overline{\rho}^0 = 1 + \gamma M^2 p_1, \tag{4.13b}$$
$$\overline{T}^0 = 1. \tag{4.13c}$$

–for values of the Mach number $M > 0.3$, the guess value $\bar{\boldsymbol{q}}^{\mathbf{0}}$ is simply chosen as a steady axisymmetric solution of the compressible equations, computed for a lower value of the Mach number.

Since we do not use the governing equations under their conservative form, the method presented here is unable to account for the presence of shock waves in the computational domain. Therefore, base flow computations can be carried out legitimately while the local Mach number $M_l = M\|\boldsymbol{u}^{\mathbf{0}}\|/\sqrt{T^0}$ remains smaller than unity at each point of the grid mesh. Practically, the free-stream Mach number can be increased up to $M = 0.7$. Figure 3(a), shows contours of axial velocity w^0 of the base flow for $Re = 400$ and $M = 0.5$. The solid line is the streamline linking the separation point to the stagnation point on the $r = 0$ axis, and defines the separatrix delimiting the recirculation bubble behind the base. The classical topology of wake flows is retrieved, with a recirculation region of length ~ 1.8 diameters developing in the wake of the afterbody, and negative values of streamwise velocity reaching 30 % of the free-stream velocity.

Figure 3(b) shows contours of total pressure p_i^0, computed as

$$p_i^0 = p^0 \left(1 + \frac{\gamma - 1}{2} M_l^2\right)^{\frac{\gamma}{\gamma - 1}} . \tag{4.14}$$

The total pressure at some given point is the pressure that would be measured if the local velocity was set to zero through an isentropic process. In the case of low Mach numbers, relation (4.14) allows to recover the usual incompressible expression $p^0 + \rho^0 \|\boldsymbol{u}^{\mathbf{0}}\|^2/2$. In the present compressible case, the total pressure remains constant only on isentropic lines of the flow. In Figure 3(b), p_i^0 is approximately equal to its free-stream value $p_{i\infty}^0 = 1.19$ except in the depression zone located in the recirculating bubble, and in the boundary-layer where irreversible processes (mainly viscous friction at the body wall) trigger an increase of entropy. Similarly, Figure 3(c) shows contours of the total temperature T_i^0, which is a nondimensional measure of the total enthalpy of the base flow H^0, according to

$$T_i^0 = \frac{H^0}{\rho^0} = T^0 \left(1 + \frac{\gamma - 1}{2} M_l^2\right) , \tag{4.15}$$

and which is a conserved quantity throughout the computational domain, owing to the adiabatic rigid wall condition imposed on $\partial\Omega_b$. One observes that the total temperature increases with respect to its free-stream value $T_{i\infty}^0 = 1.05$ at the front stagnation point, but decreases in the boundary-layer, despite the viscous friction that tends to act as a local heat source, and in the wake of the afterbody.

The recirculation length L_r has been computed as a function of the Mach number, for the same value of the Reynolds number $Re = 400$. Results are presented in Figure 4(a) where we also provide the value obtained for $M = 0$ by the resolution of the incompressible base flow equations on the same mesh than that used for the compressible calculations, as described in Meliga *et al.* (2008*a*,*b*). The low Mach number regime exhibits an excellent asymptotic behaviour with respect to the incompressible value. It can be seen that increasing the Mach number yields an increase in the recirculation length of the base flow. A similar effect has been observed by Bouhadji & Braza (2003) studying the effect of an increasing Mach number on the wake developing past a NACA 0012 at zero angle of attack by means of DNS calculations. Such an increase of the recirculation length is similar to that observed when increasing the Reynolds number in incompressible flows, where the mechanism is purely viscous, as it results from the thinning of the developing shear-layers. In the present study, it is further investigated by considering the effect on the base flow of a small increase in the Mach number $0 < \delta M/M \ll 1$, the Reynolds number being kept constant. As will be shown in the incoming sections, the azimuthal wavenumber of the leading eigenmodes is $m = 1$, so that operator $\mathcal{A}_0$ is non-degenerate for parameter settings (M, Re) considered throughout this study. As a consequence, and as mentioned in (2.25), such an increase in M induces a base flow modification $\boldsymbol{\delta q}_{M}^{\mathbf{0}}$ solution of the linear problem

$$\mathcal{A}_0 \boldsymbol{\delta q}_{M}^{\mathbf{0}} = \delta M (0, \boldsymbol{\delta F}_{\rho \boldsymbol{u}}, \boldsymbol{\delta F}_{\rho T})^T , \tag{4.16}$$

with

$$\boldsymbol{\delta F}_{\rho \boldsymbol{u}} = \frac{-2}{\gamma M^3} \boldsymbol{\nabla} p^0 , \tag{4.17a}$$

$$\boldsymbol{\delta F}_{\rho T} = \frac{-2\gamma(\gamma - 1)M}{Re} \, \boldsymbol{\tau}(\boldsymbol{u}^{\mathbf{0}}) : \boldsymbol{d}(\boldsymbol{u}^{\mathbf{0}}) . \tag{4.17b}$$

The streamwise velocity gradient $\delta w_{M}^0/\delta M$ is shown in Figure 4(b): it can be seen that

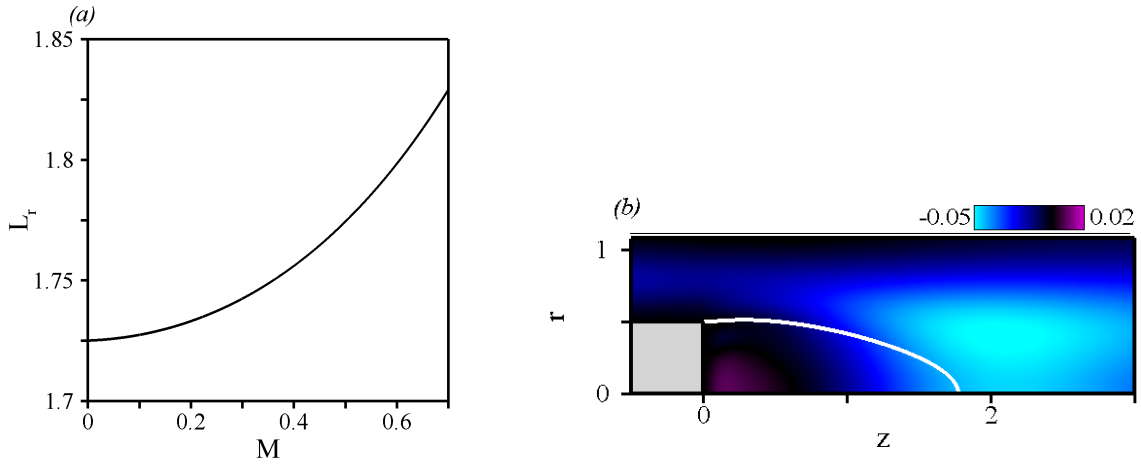

Figure 4: (a) Recirculation length L_r for the base flow as a function of the Mach number - $Re = 400$. (b) Streamwise velocity component of the base flow modification $\boldsymbol{\delta q}^{\mathbf{0}}_{M}$ resulting from a small increase of the Mach number. The solid line in the flow indicates the separatrix of the recirculation zone - $Re = 400$, $M = 0.5$. These values correspond to the arbitrary choice $\delta M = 10^{-1}$.

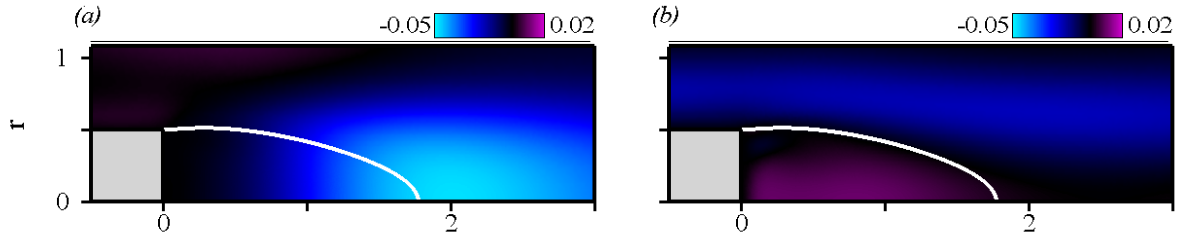

Figure 5: (a) Streamwise velocity gradient of the base flow modification induced by the modification of the pressure gradient, $\boldsymbol{\delta F}_{\rho T}$ being forced to zero - $Re400$, $M = 0.5$. (b) Same as (a) for the base flow modification induced by the modification of the power of the viscous forces, $\boldsymbol{\delta F}_{\rho \boldsymbol{u}}$ being forced to zero.

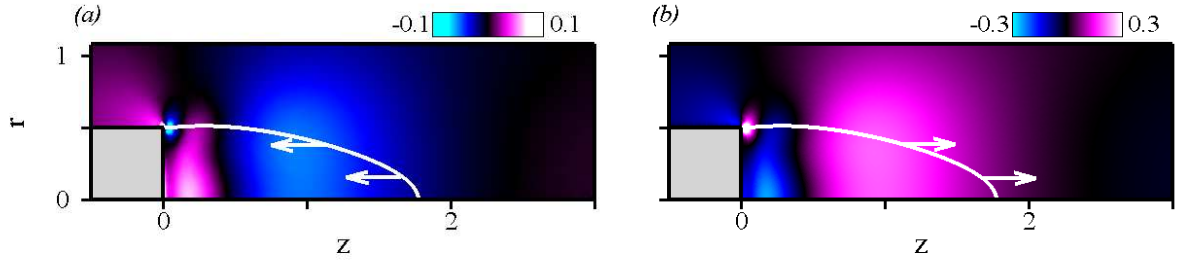

Figure 6: (a) Streamwise pressure force of the base flow $-\partial_z p^0/\gamma M^2$ - $Re400$, $M = 0.5$. (b) Additional streamwise component of the force $\boldsymbol{\delta F}_{\rho \boldsymbol{u}}$ resulting from the increase in the Mach number.

$\delta w^0_M/\delta M$ is negative in the recirculation, so that an increase in M ($\delta M > 0$) induces a negative additional streamwise velocity δw^0_M in this zone, thus explaining the observed behavior of the recirculation length L_r. Though, it turns out from (4.16) – (4.17) that $\boldsymbol{\delta q}^{\mathbf{0}}_{M}$ arises from two distinct effects, that are simultaneously at work: the first one is the modification of the pressure gradient in the momentum equations, related to the term $\boldsymbol{\delta F}_{\rho \boldsymbol{u}}$, and the second one is the modification of the power of the viscous forces

in the energy equation, related to the term $\boldsymbol{\delta F}_{\rho T}$. Since (4.16) is a linear problem, it is thus possible to compute separately the base flow modification induced by each effect by forcing alternatively $\boldsymbol{\delta F}_{\rho \boldsymbol{u}}$ and $\boldsymbol{\delta F}_{\rho T}$ to zero in (4.16). The resulting streamwise velocity gradients are depicted in Figures 5. One sees in Figure 5(b) that the streamwise velocity gradient induced by the viscous forcing term of the energy equation $\boldsymbol{\delta F}_{\rho T}$ is almost nil along the separatrix. Consequently, it can be claimed that the total additional streamwise velocity responsible for the increase of the recirculation length is related to pressure effects. We propose to interpret this result as follows. Consider the base flow at given Reynolds and Mach numbers. The recirculating area is a depression zone that induces a suction and thus tends to limit the spatial extension of the recirculating bubble. This is shown in Figure 6(a) presenting the streamwise force induced by the pressure gradient $-\partial_z p^0/(\gamma M^2)$. We obtain negative values, i.e. the pressure force points in the direction opposite to that of the flow, as shown by the arrows displayed along the separation line. When increasing the Mach number, this effect is relaxed, as $1/\gamma M^2$ decreases. This can also be seen through the forcing term $\boldsymbol{\delta F}_{\rho \boldsymbol{u}}$ whose streamwise component is shown in Figure 6(b): we obtain positive values along the separation line, resulting in an additional force that opposes the initial one, and thus allows the streamwise development of the recirculating area. It is worth insisting here that the increase in the recirculating length with the Mach number results from a pure inviscid mechanism, as this interpretation is opposite to that prevailing in incompressible flows when the Reynolds number is increased.

4.4. *Eigenvalue calculations*

The spatial discretization of the problems (3.7) − (3.15) results in large-scale generalized eigenvalue problems, solved using the "Implicitly Restarted Arnoldi method" of the ARPACK library (*http://www.caam.rice.edu/software/ARPACK*) based upon a shift and invert strategy (Ehrenstein & Gallaire 2005). Since the adjoint problem (3.15) has been formulated for continuous operators with associated adjoint boundary conditions, the spatial discretization of operators $\mathcal{A}_m$ and $\mathcal{A}_m^\dagger$ leads to discrete operators that are not hermitian one to the other because the operator $\mathcal{B}$ defined in (3.8) does not correspond to the scalar product in cylindrical coordinates. We check a posteriori that the adjoint eigenvalues are complex conjugate with the direct eigenvalues and that a bi-orthogonality relation (Chomaz 2005), is satisfied for the 10 leading global modes (i.e. that the scalar product of one of the 10 leading adjoint modes with any of the 10 leading direct global modes associated to a different eigenvalue is less that 10^{-8}) , and conclude that our numerical procedure accurately estimates the compressible direct and adjoint global modes.

In the range of Mach numbers under investigation ($M < 0.7$), the axisymmetric wake undergoes an intrinsical sequence of bifurcations identical to that previously documented in the incompressible regime for other shape of bodies (Natarajan & Acrivos 1993). When the Reynolds number is increased from small values, a first stationary mode ($\omega = 0$) destabilizes the axisymmetric base flow at Re_A, for all values of the Mach number. In the following, this mode is named mode A and the corresponding eigenvector is referred to $\hat{\boldsymbol{q}}_{\boldsymbol{A}}^{\boldsymbol{1}}$. For $M = 0.5$, we find a critical Reynolds number $Re_A = 483.5$. Figure 7 shows the spatial structure of the global mode A at the threshold of instability, which is dominated by axially extended streamwise velocity $\hat{w}_A^1$, density $\hat{\rho}_A^1$ and temperature $\hat{T}_A^1$ disturbances located downstream of the body. However, the thermodynamic effects are moderate, since the levels of density and of temperature perturbations remain significantly less important than that found for the streamwise velocity. Since the azimuthal wavenumber of this global mode is $m = 1$, the streamwise velocity perturbation is opposite on the other

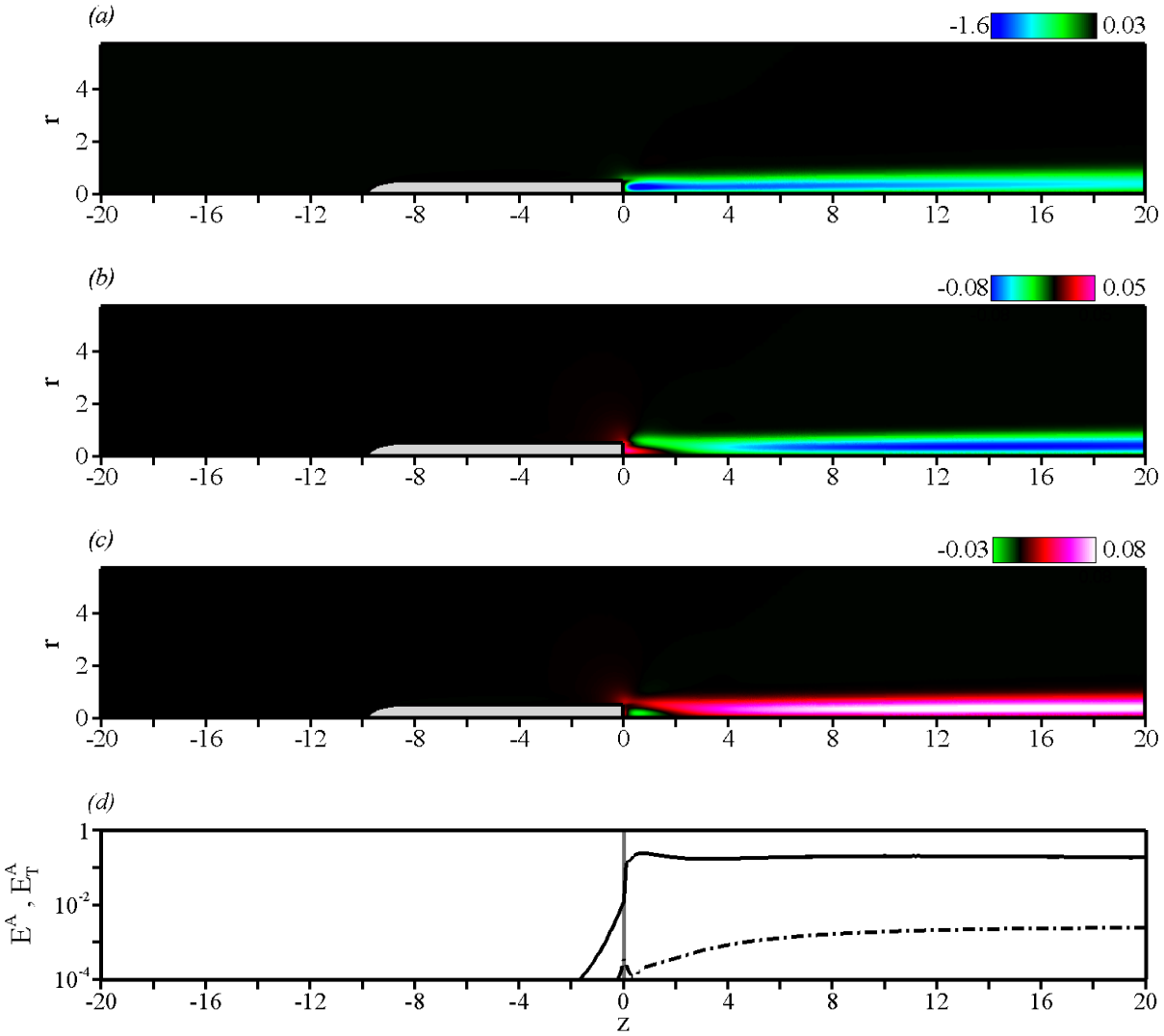

Figure 7: Stationary global mode at the threshold of the first instability, $Re_A = 483.5$ - $M = 0.5$. (a) Spatial distribution of axial velocity $\hat{w}_A^1$ for the global mode. (b) Spatial distribution of density $\hat{\rho}_A^1$. (c) Spatial distribution of temperature $\hat{T}_A^1$. The black hue corresponds to vanishing perturbations. (d) Streamwise distribution of energy density $E^A(z)$ for the direct global mode. The dashed line shows the contribution $E_T^A(z)$ of the thermodynamic components to the energy $E_A(z)$. The vertical grey line marks the position of the separation point.

side of the revolution axis, which induces an increase of the streamwise velocity of the total flow. Similarly, the temperature and density perturbation are opposite on the other side of the revolution axis, where they induce a decrease of the temperature (or equivalently an increase of the density) of the total flow. The stationary global mode therefore mainly induces an off-axis displacement of the wake, as in the case of a sphere at zero Mach number (Johnson & Patel 1999). Owing to the compressible effects, one observes an additional heating of the flow in this direction of displacement. The downstream localization of the global mode is evidenced in Figure 7(d), where we present the streamwise evolution of the amplitude of the global mode, computed as the 'density energy' of the

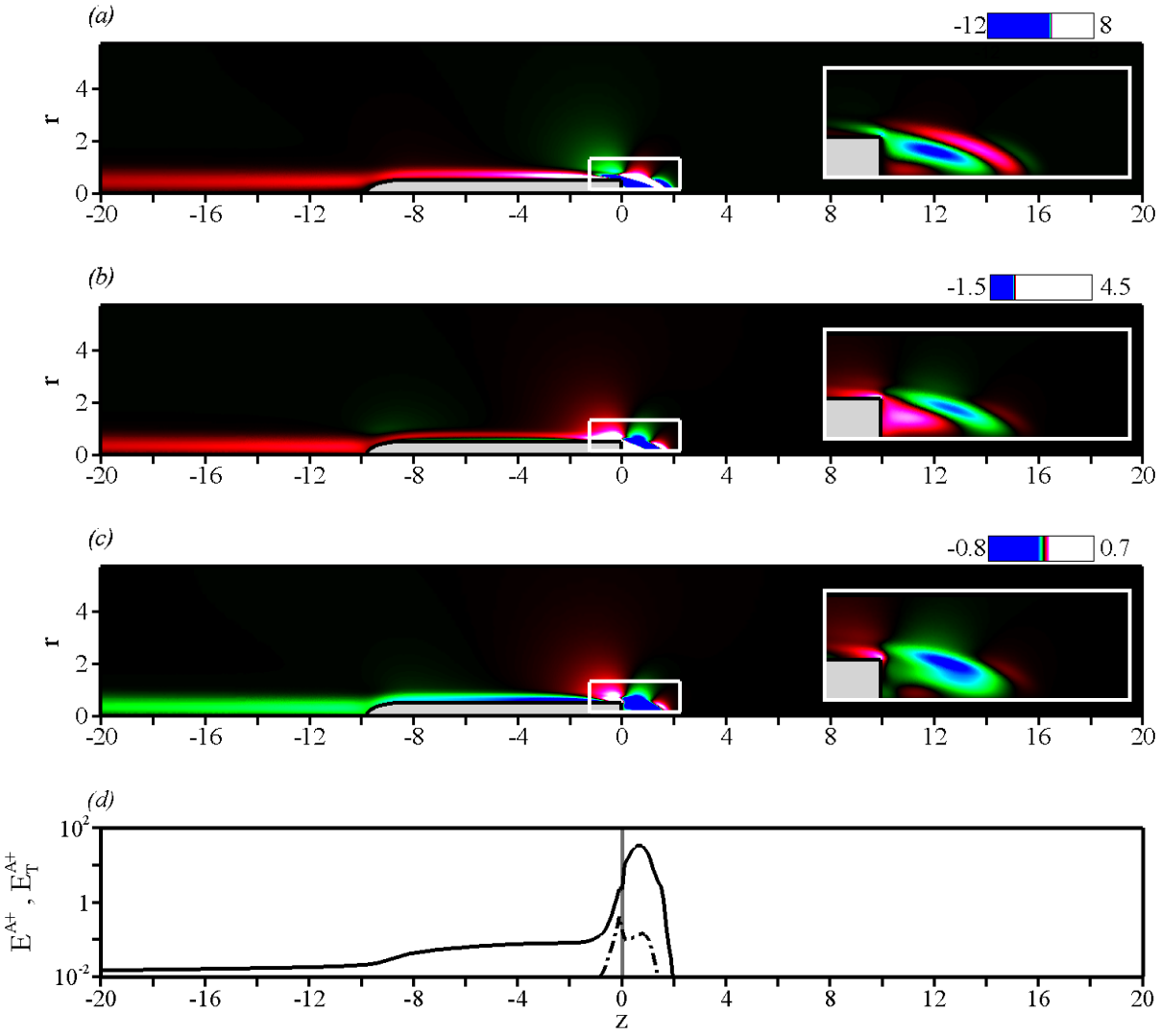

Figure 8: Same as Figure 7 for the stationary adjoint global mode at threshold. The low amplitude upstream distribution is enhanced by an appropriate choice of the color look-up. A close-up on the recirculating area is shown in the right frame.

perturbation, integrated over a vertical cross-section for each streamwise position, i.e.

$$E^A(z) = \int_0^{r_\infty} \left(|\hat{\rho}_A^1|^2 + \rho^0 |\hat{\boldsymbol{u}}_{\boldsymbol{A}}^{\boldsymbol{1}}|^2 + \rho^0 |\hat{T}_A^1|^2 \right) r \mathrm{d}r = \int_0^{r_\infty} \|\hat{\boldsymbol{q}}_{\boldsymbol{A}}^{\boldsymbol{1}}\|_{\mathcal{B}}^2 r \mathrm{d}r \,, \tag{4.18}$$

as well as the contribution of the thermodynamic variables to this amplitude, i.e.

$$E_T^A(z) = \int_0^{r_\infty} \left(|\hat{\rho}_A^1|^2 + \rho^0 |\hat{T}_A^1|^2 \right) r \mathrm{d}r \,. \tag{4.19}$$

The vertical grey lines mark the positions of the front and rear stagnation points. One can observe that the direct mode is nil upstream of the body, reaches a maximum in the recirculating bubble, and maintains a significant level even far downstream of the body. The contribution of the momentum to this amplitude dominates the entire field, as the thermodynamic contribution is two orders of magnitude smaller.

The associated adjoint global mode $\hat{\boldsymbol{q}}_{\boldsymbol{A}}^{\boldsymbol{1\dagger}}$ is presented in Figure 8. It presents high magnitudes of adjoint streamwise velocity $\hat{w}_A^{1\dagger}$, density $\hat{\rho}_A^{1\dagger}$ and temperature $\hat{T}_A^{1\dagger}$ within the recirculating bubble and close to the body, and low magnitude disturbances upstream

of the body. The upstream localization of the adjoint global mode, resulting from the convective nonnormality of the evolution operator, is further evidenced in Figure 8(d), showing the streamwise distribution of energy density $E^{A\dagger}(z)$ for the adjoint global mode and the contribution of the thermodynamic variables $E_T^{A\dagger}(z)$ to this amplitude. The adjoint global mode vanishes downstream of the body and reaches a maximum in the recirculating area. Upstream of the body, its energy density is two orders of magnitude smaller than in the recirculation bubble and decreases exponentially. It should be noted that the contribution of the thermodynamic variables to the total density energy is weak in the whole domain, since it is seen to be two to three orders of magnitude smaller than the total energy density.

Furthermore, the direct and adjoint global modes are mainly localized in the recirculation, with respectively downstream and upstream tails showing the influence of the convective nonnormality. This point can be further investigated by quantifying the nonnormality as the angle θ defined as

$$\cos\left(\frac{\pi}{2}-\theta_{_A}\right)=\frac{\langle\hat{\boldsymbol{q}}_{\boldsymbol{A}}^{\boldsymbol{1\dagger}},\mathcal{B}\hat{\boldsymbol{q}}_{\boldsymbol{A}}^{\boldsymbol{1}}\rangle}{\langle\hat{\boldsymbol{q}}_{\boldsymbol{A}}^{\boldsymbol{1\dagger}},\mathcal{B}\hat{\boldsymbol{q}}_{\boldsymbol{A}}^{\boldsymbol{1\dagger}}\rangle\times\langle\hat{\boldsymbol{q}}_{\boldsymbol{A}}^{\boldsymbol{1}},\mathcal{B}\hat{\boldsymbol{q}}_{\boldsymbol{A}}^{\boldsymbol{1}}\rangle},\tag{4.20}$$

with $\langle\hat{\boldsymbol{q}}_{\boldsymbol{A}}^{\boldsymbol{1\dagger}},\mathcal{B}\hat{\boldsymbol{q}}_{\boldsymbol{A}}^{\boldsymbol{1}}\rangle=1$ by convention here. The nonnormality is thus measured by the departure $\theta_{_A}$ to $\pi/2$ of the angle between the direct and adjoint global modes, i.e. the larger the nonnormality, the smaller $\theta_{_A}$. It is possible to quantify the contribution of the convective nonnormality to the overall nonnormality by considering the parameter γ_A defined by

$$\gamma_A=1-\frac{\int_\Omega\|\hat{\boldsymbol{q}}_{\boldsymbol{A}}^{\boldsymbol{1}}\|_{\mathcal{B}}\times\|\hat{\boldsymbol{q}}_{\boldsymbol{A}}^{\boldsymbol{1\dagger}}\|_{\mathcal{B}}r\mathrm{d}r\mathrm{d}z}{\underbrace{\left(\int_\Omega\|\hat{\boldsymbol{q}}_{\boldsymbol{A}}^{\boldsymbol{1}}\|_{\mathcal{B}}^2r\mathrm{d}r\mathrm{d}z\right)^{1/2}}_{\langle\hat{\boldsymbol{q}}_{\boldsymbol{A}}^{\boldsymbol{1}},\mathcal{B}\hat{\boldsymbol{q}}_{\boldsymbol{A}}^{\boldsymbol{1}}\rangle}\times\underbrace{\left(\int_\Omega\|\hat{\boldsymbol{q}}_{\boldsymbol{A}}^{\boldsymbol{1\dagger}}\|_{\mathcal{B}}^2r\mathrm{d}r\mathrm{d}z\right)^{1/2}}_{\langle\hat{\boldsymbol{q}}_{\boldsymbol{A}}^{\boldsymbol{1\dagger}},\mathcal{B}\hat{\boldsymbol{q}}_{\boldsymbol{A}}^{\boldsymbol{1\dagger}}\rangle}}.\tag{4.21}$$

Using a standard Cauchy-Schwartz inequality, it can be shown that $0\leqslant\gamma_A\leqslant1$. A value of γ_A close to 0 is reached if $\|\hat{\boldsymbol{q}}_{\boldsymbol{A}}^{\boldsymbol{1}}\|_{\mathcal{B}}=\alpha\|\hat{\boldsymbol{q}}_{\boldsymbol{A}}^{\boldsymbol{1\dagger}}\|_{\mathcal{B}}$ in the whole spatial domain, meaning that the direct and adjoint global modes have the same spatial distribution of energy. In that case, the convective nonnormality is not active since it would imply a dissymmetry in the distribution of the direct and adjoint modes. On the contrary, a value of γ_A close to 1 means that the direct and adjoint global modes are spatially separated. The results obtained at criticality show that the nonnormality is insensitive to the increase in the Mach number. For the stationary eigenmode A, we find that $\theta_{_A}$ barely decreases from 0.041 (2.35°) at $M=0$ to 0.040 (2.32°) at $M=0.7$, with a constant parameter $\gamma_A=0.888$, meaning that the nonnormality of mode A is significant and due to the convective nonnormality at approximately 90 %. Though, since the parameter γ_A remains constant, the slight increase in the nonnormality with the Mach number is probably due to a slight increase in the lift-up nonnormality discussed in § 3.4.

When the Reynolds number is increased above the threshold value $Re_{_A}$, a second oscillating mode of frequency $\omega=\omega_0$ destabilizes the axisymmetric base flow at $Re_{_B}$. This mode is named mode B and is thus associated to a complex eigenvector denoted $\hat{\boldsymbol{q}}_{\boldsymbol{B}}^{\boldsymbol{1}}$. For $M=0.5$, we find a critical Reynolds number $Re_{_B}=981.0$ and a frequency $\omega_0=0.399$ corresponding to a Strouhal number $St=\omega_0D/(2\pi U_\infty)=0.063$. Figure 9($a$) shows the spatial structure of the real part of the streamwise velocity component $\hat{w}_{_B}^1$. One observes positive and negative velocity perturbations alternating downstream of the body, in a regular, periodic way that defines a local spatial wavelength of about 12

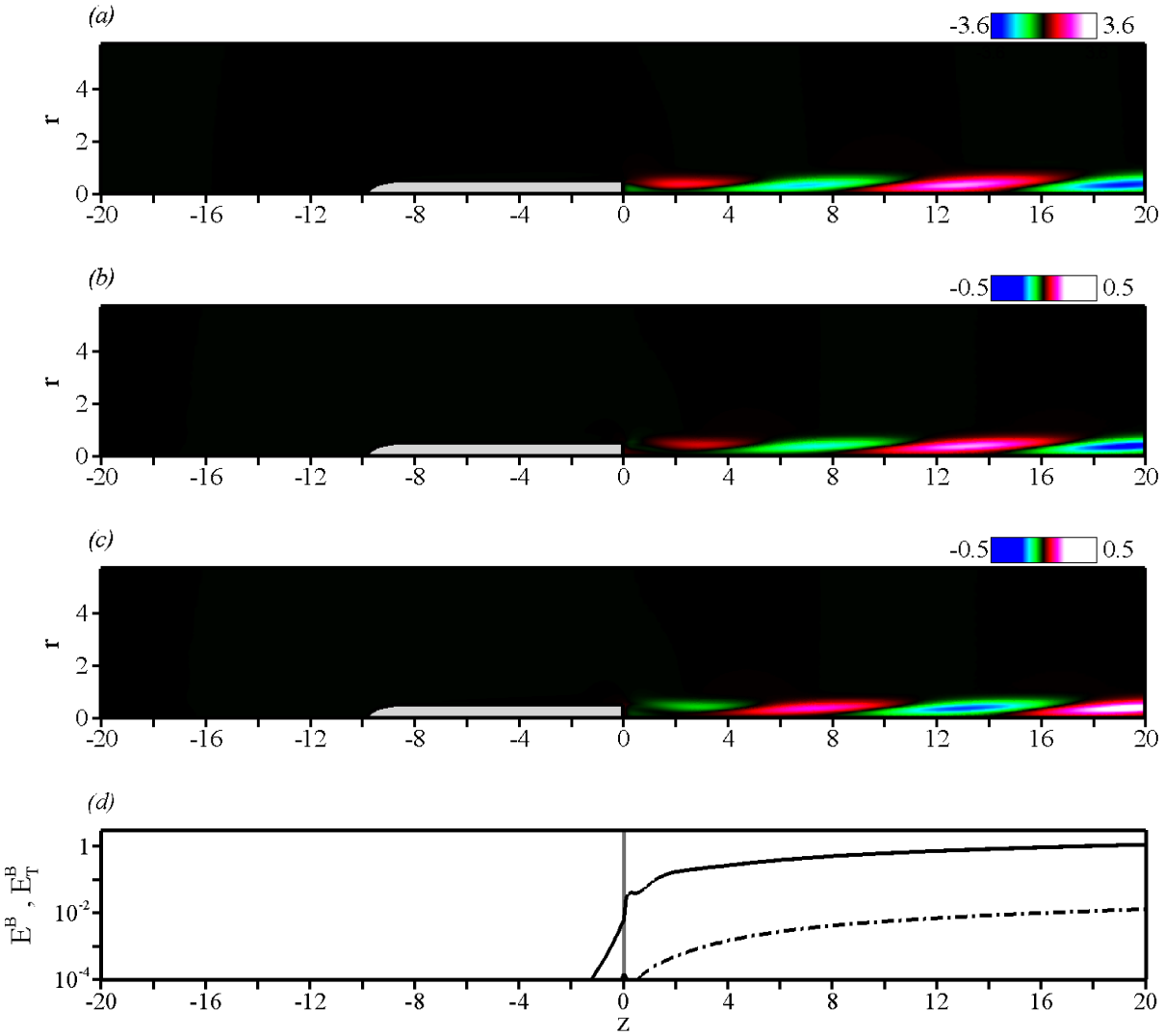

Figure 9: Same as Figure 7 for the oscillating global mode at the threshold of the second instability, $Re_B = 981.0$ - $M = 0.5$. Only the real parts are shown.

diameters, i.e. significantly larger than that found for the sphere in Appendix A. The imaginary part of $\hat{w}_B^1$ (not shown here) displays a similar structure, but is approximately in spatial quadrature since its extrema are located where the real part vanishes. This global mode corresponds therefore to a spiral perturbation in the lee of the body, which rotates in time at the frequency ω_0. Note that the density $\hat{\rho}_B^1$ and temperature $\hat{T}_B^1$ perturbations shown in Figures 9(b) and 9(c) are one order of magnitude smaller than that found for the streamwise velocity $\hat{w}_B^1$ shown in Figure 9(a). The adjoint global mode $\hat{\boldsymbol{q}}_{\boldsymbol{B}}^{\boldsymbol{1\dagger}}$ is shown in Figure 10: it is dominated by the adjoint velocity field, and is intense only in the recirculating area and a few diameters upstream of the body, where it presents a weak oscillation, and it vanishes downstream of the body. This downstream and upstream localizations of the direct and adjoint global modes are further evidenced on Figure 9(d) and 10(d). We find that the thermodynamic energy densities $E_T^B(z)$ and $E_T^{B\dagger}(z)$ are weak in the whole domain, the total energy densities $E^B(z)$ and $E^{B\dagger}(z)$ being thus dominated by the contribution of momentum. One observes that the direct mode is evanescent upstream of the body, reaches a local maximum at the separation point, but keeps increasing downstream of the recirculating area. The adjoint global mode vanishes

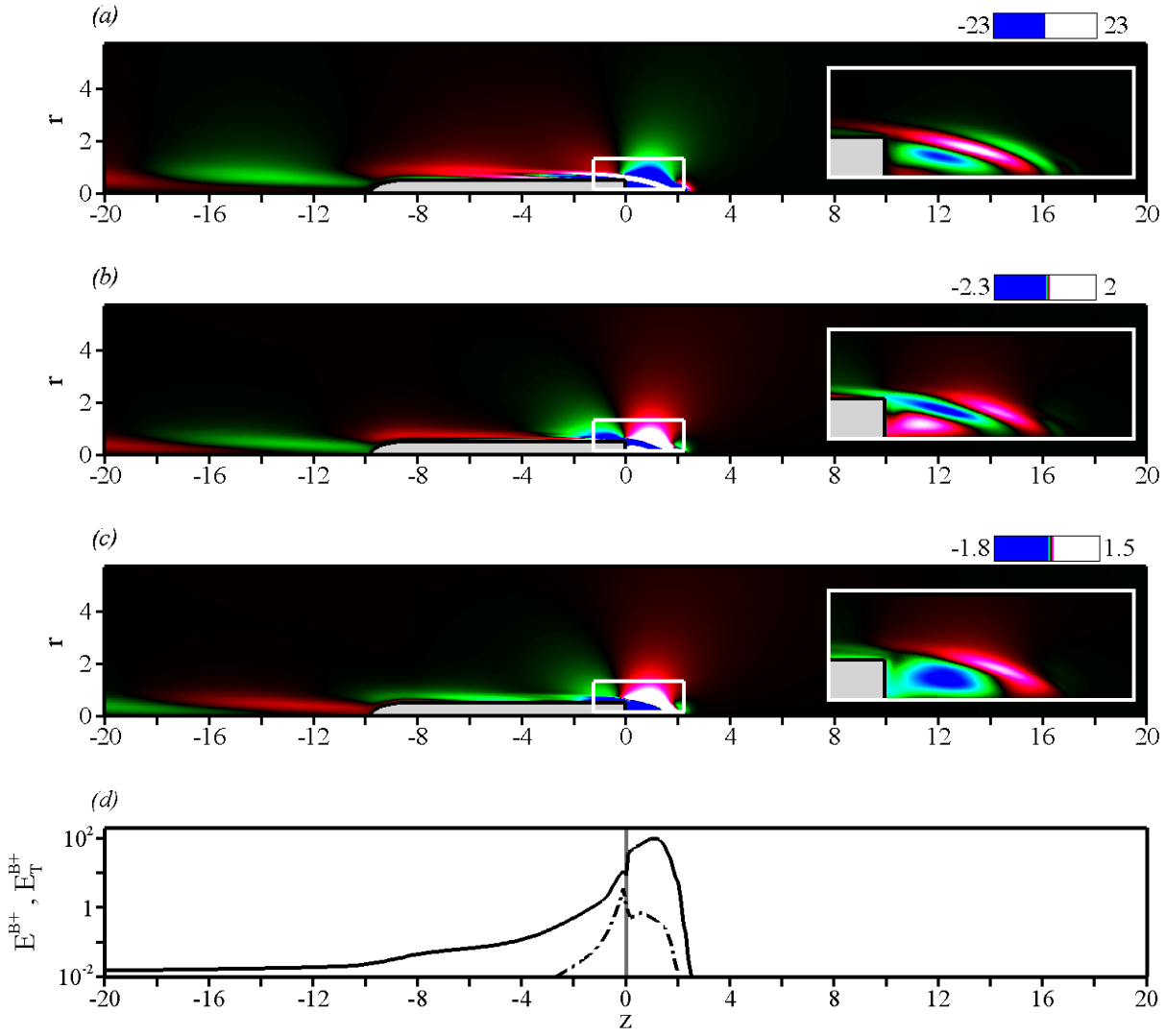

Figure 10: Same as Figure 8 for the oscillating adjoint global mode at threshold. Only the real part is shown.

downstream of the body, reaches a maximum in the recirculating area and decreases steadily upstream of the body. The nonnormality of this oscillating mode is large, as we find low values of θ_B barely increasing from 0.0021 (0.12°) at $M = 0$ to 0.0022 (0.13°) at $M = 0.7$. We also find a constant parameter $\gamma_B = 0.992$ indicating that the nonnormality is entirely triggered by the convective nonnormality mechanism.

It turns out that in the present case, we deal with momentum modes, i.e. the density and temperature components contribute weakly to the overall energy. In particular, the nonnormal effects are entirely dominated by the contribution of convective nonnormality, and the typical compressible effects introduced in § 3.4 are not active here. This can be explained by considering that these modes do not originate from compressible effects, as they already exist at $M = 0$. In particular, it may be inferred from this that the control of these instabilities by thermodynamics means, i.e. heating or cooling for example, will be quite difficult. It should be kept in mind, though, that all tools presented here, including the nonnormal effects discussed in § 3.4, are general and that different results may be obtained by considering configurations sustaining important thermal effects, such as the self-sustained oscillations in hot jets, for instance (Monkewitz *et al.* 1990).

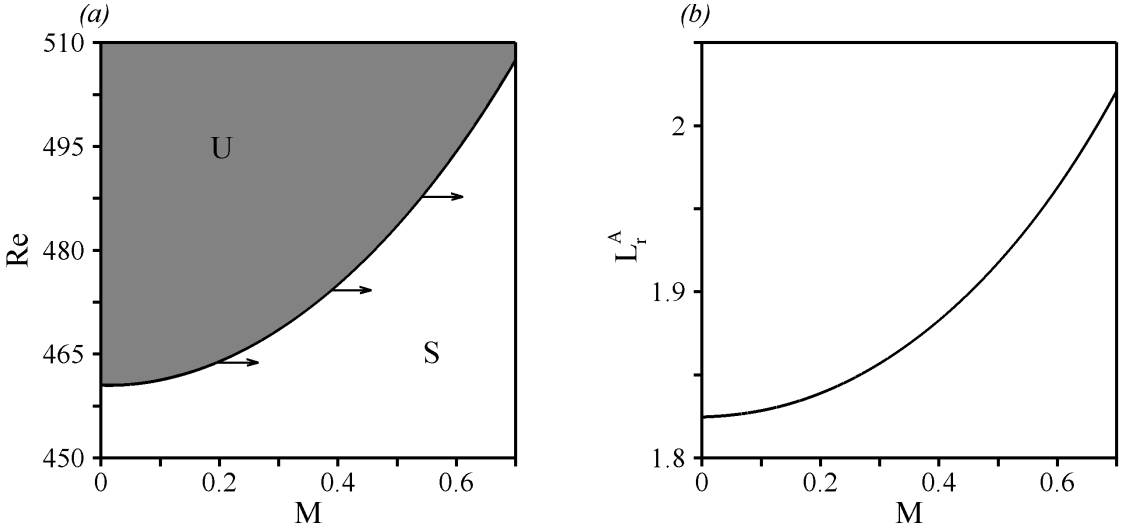

Figure 11: Stationary global mode. (a) Boundary separating the unstable domain (U-labeled shaded area) from the stable domain (S-labeled area) in the (M, Re)-plane . (b) Recirculation length L_r^A of the base flow at the threshold of the first instability, i.e. for Reynolds and Mach numbers (M, Re) varying along the neutral curve shown in (a).

4.5. *Impact of compressibility*

We investigate now the effect of the free-stream Mach number on the stability properties of the flow. We show in Figure 11(a) the boundary of the stability domain in the (M, Re)-plane for the stationary mode A, the flow being unstable for combinations of parameters located in the shaded region, labeled U, and stable for all other combinations of parameters (S-labeled region). The values for $M = 0$ issue from the resolution of the incompressible stability problem on the same mesh than that used for the compressible calculations, as described in Meliga *et al.* (2008a,b). Owing to the choice of the reference scales, we obtain an excellent asymptotic behaviour at low Mach numbers without supplementary rescaling of the compressible values. It can be seen that increasing the Mach number yields a significant increase of the critical Reynolds number Re_A, which varies significantly by approximately 10 % from $Re_A = 460.5$ to 507.5 when the Mach number is varied from $M = 0$ to the maximum value $M = 0.7$. We thus find a stabilizing effect of the Mach number. In the framework of local stability, similar stabilizing effects have been documented, for instance in plane mixing layers (Pavithran & Redekopp 1989), and interpreted in the light of the convective/absolute dichotomy: the generally admitted idea is that an increase of the compressibility promotes convective instability by reducing the pressure disturbances wave speed, which prevents their upstream propagation. The extension of this argument to the present global framework will be further discussed in § 5.2. Figure 11(b) shows the evolution of the recirculation length L_r^A at the threshold of the first instability, i.e. for parameter couples (M, Re) varying along the neutral curve shown in Figure 11(a). It can be seen that the recirculation length of the base flow increases by 11 %, from 1.82 at $M = 0$ to 2.02 at $M = 0.7$. This could have been expected, though, as both the increase of the Reynolds and the Mach number individually induce an increase of the recirculation length. Similarly, Figure 12(a) shows the boundary of the stability domain in the (M, Re)-plane for the oscillating mode. Again, the asymptotic behavior at low Mach numbers is excellent, and we find that increasing the Mach number results in a stabilization of the instability, as the value of Re_B increases significantly by approximately 17 % as the Mach number is varied from $M = 0$ ($Re_B = 909.1$) to

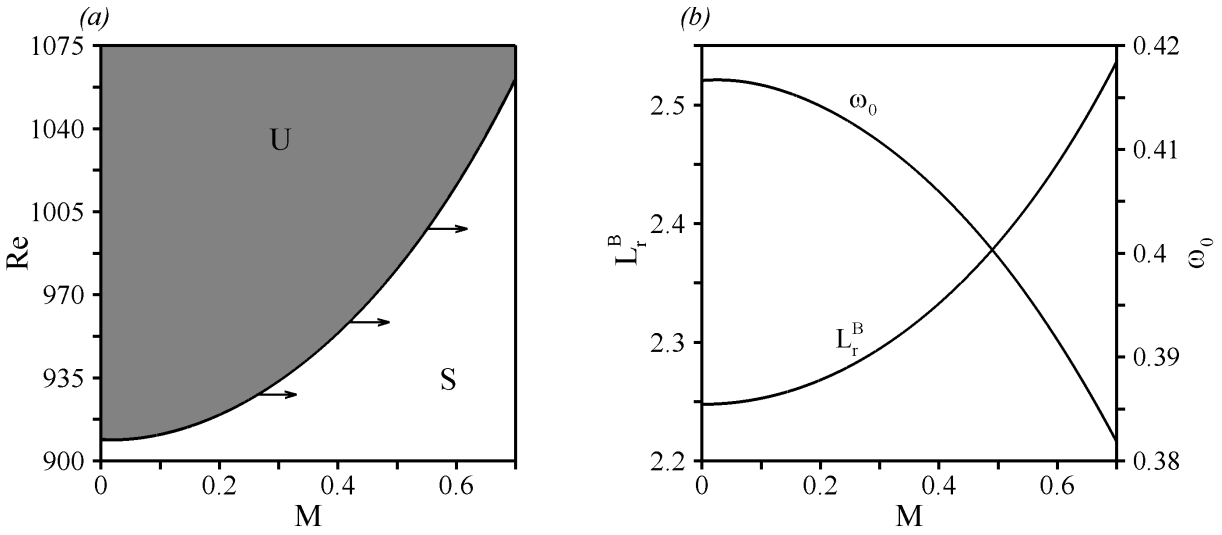

Figure 12: Oscillating global mode. (a) Boundary separating the unstable domain (U-labeled shaded area) from the stable domain (S-labeled area) in the (M, Re)-plane . (b) Recirculation length L_r^B of the base flow and frequency ω_0 of the eigenmode at the threshold of the second instability, i.e. for Reynolds and Mach numbers (M, Re) varying along the neutral curve shown in (a).

$M = 0.7$ ($Re_B = 1061.1$). Figure 11(b) shows the evolution of the recirculation length L_r^B and of the frequency ω_0 at the threshold of this second instability. We find that L_r^B increases by 13 %, from 2.25 at $M = 0$ to 2.54 at $M = 0.7$, owing to both the effect of the Reynolds and Mach numbers. The frequency ω_0 of the eigenmode decreases by 9 %, from 0.416 at $M = 0$ to 0.381 at $M = 0.7$.

This stabilizing effect of the Mach number on both eigenmodes is particularly interesting. In their study on the wake of a NACA 0012, Bouhadji & Braza (2003) have thus found that for a Reynolds number of 10000, the incompressible flow was steady, but that increasing solely the Mach number was responsible for the onset of vortex-shedding. These authors have then concluded that the Mach number mainly enhances the instability mechanisms by increasing the recirculation length, as the Reynolds number would do in a classical incompressible recirculating flow. Our results show a completely opposed case where increasing the Mach number restabilizes the unstable modes, despite the fact that it simultaneously triggers an increase of the recirculating length. It can be concluded that one cannot understand these complex compressible effects by considering only the variation of the recirculation length.

To further investigate the stabilizing effect of compressibility, we assume from now on that the Reynolds number remains constant, so that eigenvalues are function of the base flow quantities and the Mach number. At threshold of instability, we then investigate the variation $\delta\lambda$ resulting from a small increase of the Mach number $0 < \delta M/M \ll 1$ in the framework of the sensitivity analyses developed in § 2.2. In other terms, considering the (M, Re)-plane, we stand initially on the neutral curve and induce a slight displacement to the right along an horizontal imaginary line, as depicted by the horizontal arrows in Figures 11(a) and 12(a). We then try to interpret the reason why such displacement systematically points to the stable domain. To this end, performing the decomposition of $\delta\lambda$ into the contributions $\delta\lambda|_M$ and $\delta\lambda|_{\mathbf{q_0}}$ introduced in § 2.2 will be shown to be particularly fruitful.

In the following, $\delta\lambda$, $\delta\lambda|_M$ and $\delta\lambda|_{\mathbf{q_0}}$ are computed exclusively by use of the adjoint-

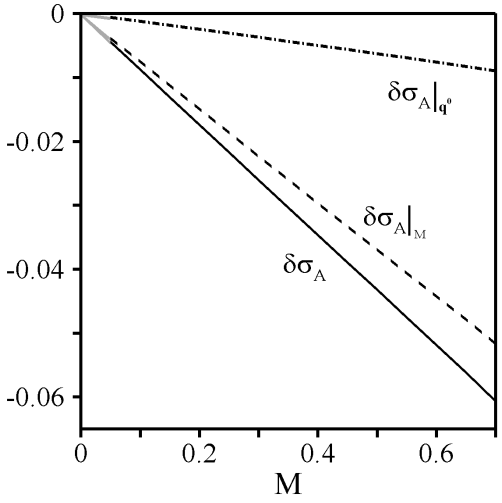

Figure 13: Stationary global mode: variation of the growth σ_A owing to a small modification of the Mach number computed as a function of the Mach number along the neutral curve shown in Figure 11(a). The solid curve stands for the overall variation $\delta\sigma_A$. The dashed and dash-dotted curves represent the variations $\delta\sigma_A|_M$ and $\delta\sigma_A|_{\boldsymbol{q}^0}$ denoting respectively the variations of σ_A owing to the base flow modification $\boldsymbol{\delta q}^{\mathbf{0}}_M$ induced by the modification of the Mach number, and that resulting from the modification of the Mach number in the linearized Navier-Stokes operator. All values presented here have been obtained for $\delta M = 10^{-1}$, and the curves have been prolonged from $M = 0.05$ down to 0 by linear regression.

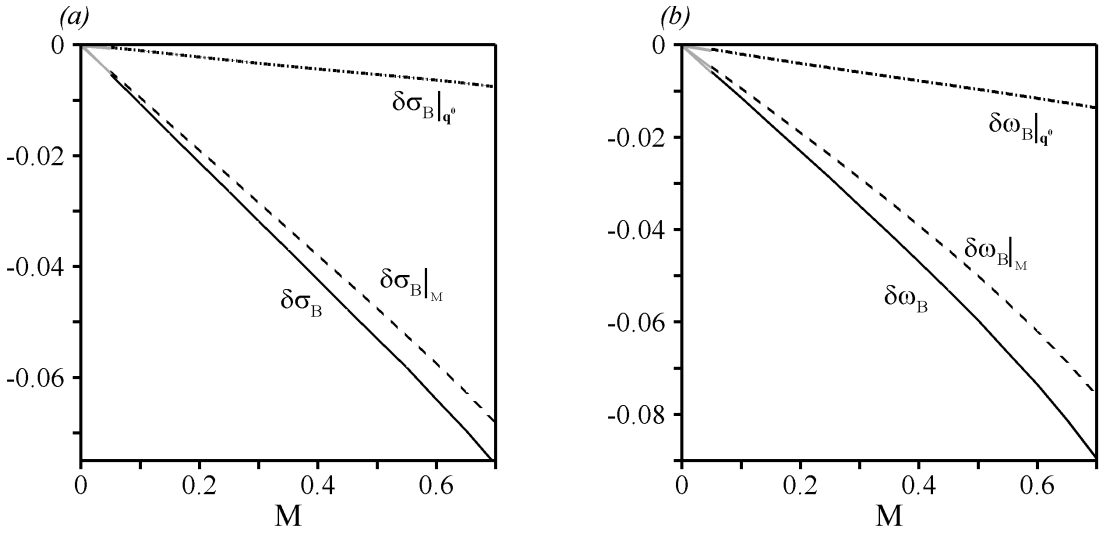

Figure 14: Same as Figure 13 for the oscillating global mode. (a) Variation of the growth rate σ_B. (b) Variation of the frequency ω_B.

based expressions (2.24), so that we implicitely set δM to unity. The sensitivity formalism being linear in essence since based on the evaluation of gradients, we compute first the gradient $\delta\lambda/\delta M$ and eventually obtain $\delta\lambda$ as $(\delta\lambda/\delta M)\delta M$, so that this choice has no physical effect. The correctness and accuracy of the adjoint method is discussed in Appendix B, where we present a comparison between the values issuing from the adjoint formalism and forward calculations.

The variation of the growth rate $\delta\sigma_A$ induced by a small modification of the Mach number has been computed along the neutral curve of the stationary mode shown in Figure 11(a). Results are presented in Figure 13. In the range $0 < M < 0.05$, values represented by the grey solid lines have been obtained by linear regression. We find negative values of $\delta\sigma_A$, thus confirming that increasing the Mach number ($\delta M > 0$) tends to stabilize the flow. Moreover, this effect is seen to increase with the Mach number, as $\delta\sigma_A$ reaches its largest magnitude for $M = 0.7$. Figure 13 also shows the respective contributions to $\delta\sigma_A$ of the variations $\delta\sigma_A|_M$ and $\delta\sigma_A|_{\boldsymbol{q}^0}$. For all values of the Mach number, we find that the contribution $\delta\lambda|_{\boldsymbol{q}^0\sigma_A}$ arising from the modification of the Mach number in the perturbation equations is negligible, and that the overall variation $\delta\sigma_A$ is due at 90 % to the modification of the base flow. Similarly, Figure 14 presents the values of $\delta\sigma_B$ and $\delta\omega_B$ computed along the neutral curve of the oscillating mode shown in Figure 12(a). We find negative values of $\delta\sigma_B$ and $\delta\omega_B$, meaning that an increase of the Mach number induces a slight decrease of both the growth rate and the frequency of the eigenmode. These effects are seen to increase with the Mach number, as $\delta\sigma_B$ and $\delta\omega_B$ are maximum for $M = 0.7$.

Figure 14 also details the respective contributions to $\delta\sigma_B$ (resp. $\delta\omega_B$) of the sensitivities $\delta\sigma_B|_M$ and $\delta\sigma_B|_{\boldsymbol{q}^0}$ (resp. $\delta\omega_B|_M$ and $\delta\omega_B|_{\boldsymbol{q}^0}$). We find that the variation $\delta\sigma_B|_M$ and $\delta\omega_B|_M$ induced by the base flow modification dominate in the whole range of Mach numbers considered here, where it represents 90 % of the overall variation, a result reminiscent of that already discussed for the stationary mode. It is thus worthwhile emphasizing here on the fact that sensitivity to base flow modification is of primary importance to understand the dynamics of the unstable global modes, and in particular the underlying compressible effects at work in the present case.

5. Sensitivity to base flow modification

The previous section has enlightened the importance of the base flow on the dynamics of the unstable modes through the variation $\delta\lambda|_M$ induced by the base flow modification $\boldsymbol{\delta q}^{\mathbf{0}}_M$. The role of the base flow is now further investigated by performing the so-called sensitivity analysis to base flow modifications. In the following, we discuss first the different sensitivity functions, and particular attention is paid to their spatial distributions, which lead to a straightforward identification of the wavemaker regions. To this end, we use the conservative set of sensitivity functions defined by (3.33). A more physical interpretation of the results given in § 4.5 is then proposed by applying the sensitivity analysis to the specific base flow modification $\boldsymbol{\delta q}^{\mathbf{0}}_M$ induced by the small change in the Mach number.

5.1. *Identification of the wavemaker regions*

In this section, results are presented in terms of the magnitude of the various sensitivity functions at the threshold of instability. The color look-up table has been cautiously set-up so as to enhance the active zones where the growth rate σ_A is sensitive to base flow modifications. Note that we do not consider the sign of the sensitivity, as its effect on the eigenvalue variation also depends on a relevant base flow modification. For instance, to consider an extreme case, the variation resulting from a momentum modification set orthogonal to the orientation of the sensitivity field is zero, even if the magnitude of the sensitivity function is high at this particular location.

Figure 15(a) presents the spatial distribution of magnitude of the momentum sensitivity function $\|\boldsymbol{\nabla}_{\rho^0\boldsymbol{u}^0}\sigma_A\|^2(r,z)$ for the stationary mode at $Re_c^A = 483.5$ and $M = 0.5$. The sensitivity is almost nil everywhere in the flow, except in the recirculating bubble,

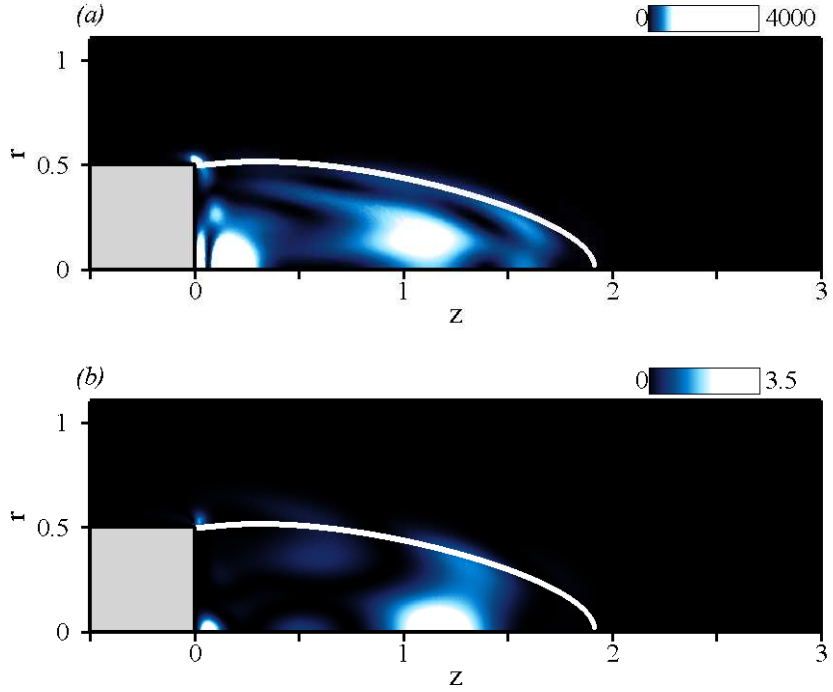

Figure 15: Stationary global mode at the threshold of the first instability, $Re_A = 483.5$ - $M = 0.5$: sensitivity to base flow modifications of the growth rate σ_A. Spatial distribution of the magnitude of the (a) momentum sensitivity function $\|\boldsymbol{\nabla}_{\rho^0 \boldsymbol{u}^0} \sigma_A\|^2$ and the (b) energy sensitivity function $|\boldsymbol{\nabla}_{\rho^0 T^0} \sigma_A|^2$. The black hue corresponds to vanishing magnitudes of sensitivity.

which acts as the wavemaker region. Since the sensitivity functions defined in (3.24) depend both from the perturbation and adjoint perturbation quantities, this specific spatial distribution results from the convective nonnormality of the linearized evolution operator, which induces direct global modes (resp. adjoint global modes) located downstream (resp. upstream) of the body and in the recirculating bubble. High sensitivity is obtained around the separation point, in the center of the recirculation bubble, and close to the base, where the largest values are reached. Similarly, Figure 15(b) presents the spatial distribution of magnitude of the energy sensitivity function $|\boldsymbol{\nabla}_{\rho^0 T^0} \sigma_A|^2(r, z)$, for which we find similar active zones. Though, strikingly, it can be seen that the sensitivity of σ_A to a modification of energy $\delta(\rho^0 T^0)$ is three orders of magnitude smaller than that to a modification of momentum $\delta(\rho^0 \boldsymbol{u}^0)$, identical results being found for the density and pressure sensitivity functions (not shown here).

The distribution of magnitude of the momentum sensitivity functions $\|\boldsymbol{\nabla}_{\rho^0 \boldsymbol{u}^0} \sigma_B\|^2(r, z)$ and $\|\boldsymbol{\nabla}_{\rho^0 \boldsymbol{u}^0} \omega_B\|^2(r, z)$are plotted in Figures 16(a) and 16(b) for the oscillating mode at $Re_c^B = 981.0$ and $M = 0.5$. Concerning the growth rate σ_B, results are reminiscent of that discussed for the first stationary instability of mode A, with a sensitivity almost nil everywhere in the flow, except within the recirculation which acts as the wavemaker. The localization of the active zones is somehow slightly different, with large magnitude of sensitivity found at the separation point and in the tail of the recirculating bubble, whereas the region close to the base, which was the most sensitive for the stationary mode, now exhibits low magnitudes of sensitivity. Interestingly, the active zones also differ between the growth rate σ_B and the frequency ω_B of the oscillating mode, since it can be seen from Figure 16(b) that the largest magnitudes of sensitivity of ω_B are reached

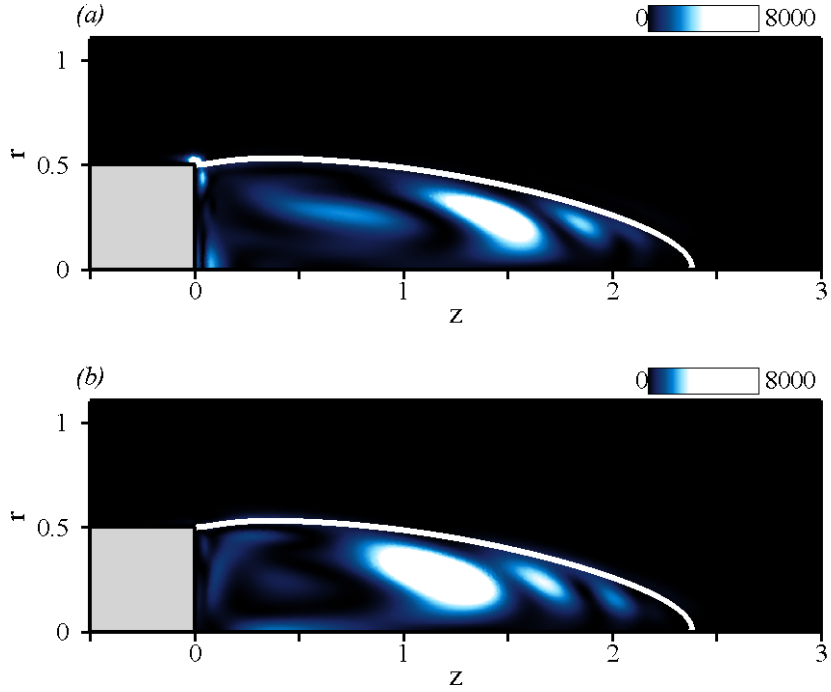

Figure 16: Oscillating global mode at the threshold of the second instability, $Re_B = 981.0$ - $M = 0.5$: sensitivity to base flow modifications of the eigenvalue $\sigma_B + \mathrm{i}\omega_B$. Spatial distribution of the magnitude of the momentum sensitivity functions (a) $\|\boldsymbol{\nabla}_{\rho^0 \boldsymbol{u}^0} \sigma_B\|^2$ and (b) $\|\boldsymbol{\nabla}_{\rho^0 \boldsymbol{u}^0} \omega_B\|^2$. The black hue corresponds to vanishing magnitudes of sensitivity.

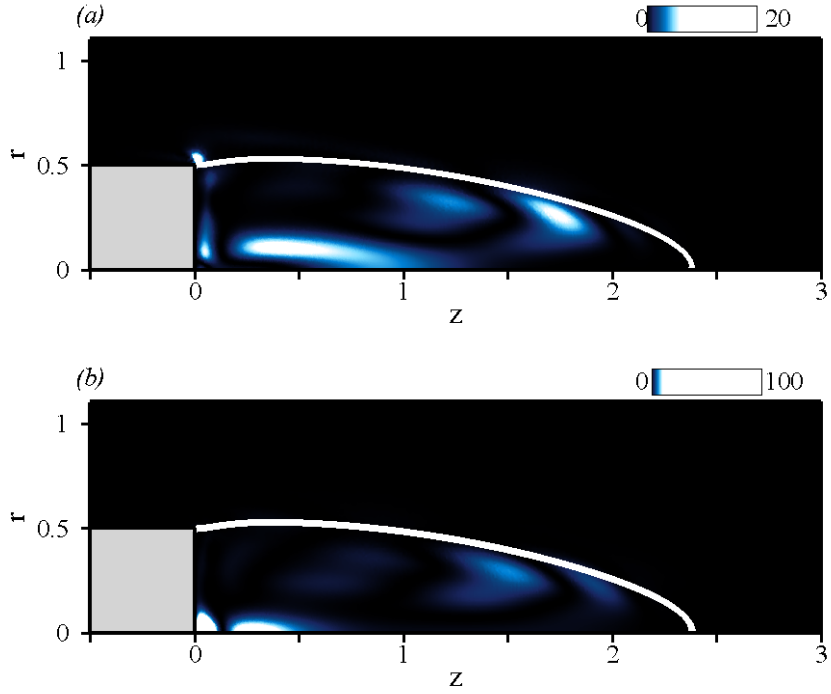

Figure 17: Same as 16 for spatial distribution of the magnitude of the temperature sensitivity functions (a) $|\boldsymbol{\nabla}_{\rho^0 T^0} \sigma_B|^2$ and (b) $|\boldsymbol{\nabla}_{\rho^0 T^0} \omega_B|^2$.

in the center of the recirculation, whereas the separation point is not active. Finally, it can be seen from Figure 17 presenting the spatial distribution of the energy sensitivity functions $|\boldsymbol{\nabla}_{\rho^0 T^0}\sigma_{_B}|^2(r,z)$ and $|\boldsymbol{\nabla}_{\rho^0 T^0}\omega_{_B}|^2(r,z)$ that the magnitudes of these sensitivities is two to three orders of magnitude smaller than their momentum counterparts. Since such results have also been obtained for the stationary mode, this point has an important physical interpretation in terms of base flow calculations, as it indicates that small errors in the computation of ρ^0 and T^0 have almost no effect on the stability calculations.

5.2. *Physical interpretation for the stabilizing effect of compressibility in terms of advection and production mechanisms*

It has been shown in § 4.5 that increasing the free-stream Mach number has a stabilizing effect on the stationary and oscillating eigenmodes. This point is now discussed in the light of sensitivity analyses. We consider a small modification of the Mach number δM. Since we have already said that such a modification alters the stability problem by acting at the base flow level, we further investigate the specific variation $\delta\lambda|_{_M}$, which is from now on abusively denoted $\delta\lambda$ to ease the notation.

Since $\delta\lambda$ is obtained by integration over space of the integrand $\boldsymbol{\nabla}_{\boldsymbol{q^0}}\lambda\cdot\boldsymbol{\delta q}^{\boldsymbol{0}}_{_M}(r,z)$, it is possible to integrate separately the four integrands

$$\delta_{\rho^0}\lambda=\int_\Omega\boldsymbol{\nabla}_{\rho^0}\lambda\cdot\delta\rho^{\boldsymbol{0}}_{_M}\,r\mathrm{d}r\mathrm{d}z\,,\tag{5.1a}$$

$$\delta_{\rho^0\boldsymbol{u^0}}\lambda=\int_\Omega\boldsymbol{\nabla}_{\rho^0\boldsymbol{u^0}}\lambda\cdot\delta(\rho^0\boldsymbol{u}^{\boldsymbol{0}})_{_M}\,r\mathrm{d}r\mathrm{d}z\,,\tag{5.1b}$$

$$\delta_{\rho^0 T^0}\lambda=\int_\Omega\boldsymbol{\nabla}_{\rho^0 T^0}\lambda\cdot\delta(\rho^0 T^0)_{_M}\,r\mathrm{d}r\mathrm{d}z\,,\tag{5.1c}$$

$$\delta_{p^0}\lambda=\int_\Omega\boldsymbol{\nabla}_{p^0}\lambda\cdot\delta p^{\boldsymbol{0}}_{_M}\,r\mathrm{d}r\mathrm{d}z\,,\tag{5.1d}$$

so that

$$\delta\lambda=\delta_{\rho^0}\lambda+\delta_{\rho^0\boldsymbol{u^0}}\lambda+\delta_{\rho^0 T^0}\lambda+\delta_{p^0}\lambda\,.\tag{5.2}$$

This allows to distinguish between the contributions to the overall variation $\delta\lambda$ issuing from the modification of density, momentum, internal energy and pressure.

Moreover, the origin of the stabilizing effect is discussed in terms of the competition between advection and production of disturbances, by use of the specific advection and production sensitivity functions defined in § 2. $\delta\lambda$ is thus decomposed into

$$\delta\lambda=\delta^{(A)}\lambda+\delta^{(P)}\lambda\,,\tag{5.3}$$

where $\delta^{(A)}\lambda$ and $\delta^{(P)}\lambda$ measure the variation of the eigenvalue owing to the modification of the advection operator $\mathcal{C}^{(A)}_{_m}$ and of the total production operator $\mathcal{C}^{(P)}_{_m}+\mathcal{P}_{_m}$ induced by the base flow modification $\boldsymbol{\delta q}^{\boldsymbol{0}}_{_M}$. Similar dichotomy has proven fruitful to discuss the effect of compressibility on the stability of axisymmetric wakes in the framework of the local theory (Meliga *et al.* 2008*c*). Physically, a positive (resp. negative) value of $\delta^{(A)}\lambda$ indicates a destabilization (resp. a stabilization) of the eigenmode owing to a weakening (resp. a strengthening) of the disturbances advection. Similarly, a positive (resp. negative) value of $\delta^{(P)}\lambda$ indicates a destabilization (resp. a stabilization) owing to an increase (resp. a decrease) of the disturbances production. These terms are computed respectively as the projection of $\boldsymbol{\delta q}^{\boldsymbol{0}}_{_M}$ onto the advection and production sensitivity functions, i.e.

$$\delta^{(A)}\lambda=\left\langle\boldsymbol{\nabla}^{(A)}_{\boldsymbol{q^0}}\lambda\,,\,\boldsymbol{\delta q}^{\boldsymbol{0}}_{_M}\right\rangle\,,\qquad\delta^{(P)}\lambda=\left\langle\boldsymbol{\nabla}^{(P)}_{\boldsymbol{q^0}}\lambda\,,\,\boldsymbol{\delta q}^{\boldsymbol{0}}_{_M}\right\rangle\,.\tag{5.4}$$

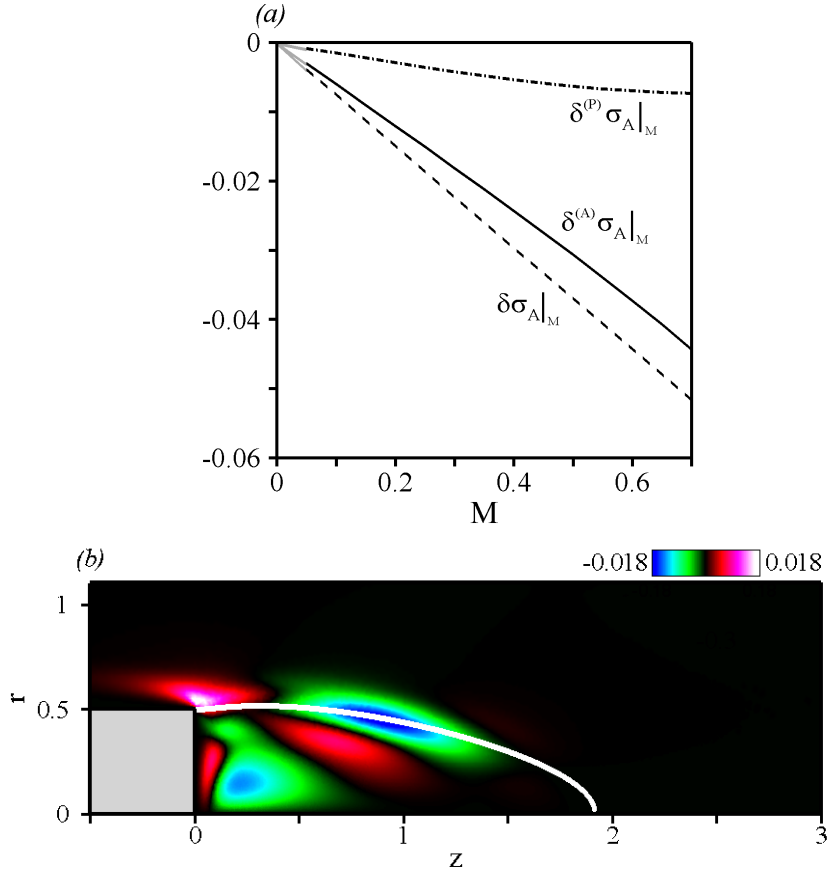

Figure 18: Stationary global mode at the threshold of the first instability, $Re_A = 483.5$ - $M = 0.5$. (a) Variation of the growth rate induced by the base flow modification $\boldsymbol{\delta q}^{\mathbf{0}}_M$ computed as a funtion of the Mach number. The dashed line represents the overall variation $\delta\sigma_A|_M$. The solid line (resp. dash-dotted line) represents the contribution to $\delta\sigma_A|_M$ of the variation $\delta^{(A)}\sigma_A|_M$ owing to the modification of the advection operator (resp. the variation $\delta^{(P)}\sigma_A|_M$ owing to the modification of the production operator). $\delta\sigma_A|_M$ is thus the sum of these two contributions. (b) Spatial distribution of the momentum integrand $\boldsymbol{\nabla}^{(A)}_{\rho^0\boldsymbol{u}^0}\sigma_A \cdot \delta(\rho^0\boldsymbol{u}^{\mathbf{0}})_M(r,z)$. The integration over space of this quantity yields the variation $\delta\sigma_A|^A_M$ that dominates the growth rate variation. The black hue corresponds to vanishing magnitudes of the integrand.

The magnitude of these two sensitivity functions, as well as a discussion on the localization of their respective active zones can be found in Appendix C.

5.2.1. *Stationary eigenmode A*

Figure 18(a) presents the adjoint-based values of $\delta^{(A)}\sigma_A$ (solid line) and $\delta^{(P)}\sigma_A$ (dash-dotted line) computed as functions of the Mach number at threshold of instability. The overall variation $\delta\sigma_A$, which appears as the dashed line in Figure 13 is also reported. One observes that all variations are negative, suggesting that both the modifications of the advection and production mechanism are stabilizing. Though, it can be seen that $\delta^{(P)}\sigma_A$ contributes little to the overall variation which is dominated by the $\delta^{(A)}\sigma_A$. For $M = 0.5$ and $Re^A_c = 483.5$, we have carried out both decompositions (5.2) and (5.3). Results are given in Table 1 and confirm that the variation $\delta^{(A)}\sigma_A$ arising from the modification of the advection operator is larger by one order of magnitude than its production counterpart. The production mechanism is equally dominated by momentum and energy modifications

	$\delta_{\rho^0}\sigma_A\vert_M$	$\delta_{\rho^0\boldsymbol{u}^0}\sigma_A\vert_M$	$\delta_{\rho^0 T^0}\sigma_A\vert_M$	$\delta_{p^0}\sigma_A\vert_M$	$\delta\sigma_A\vert_M$
$\boldsymbol{\nabla}$	-5.4×10^{-4}	-3.3×10^{-2}	-3.3×10^{-3}	-9.3×10^{-5}	-3.7×10^{-2}
$\boldsymbol{\nabla}^{(A)}$	6.7×10^{-5}	-3.1×10^{-2}	-1.1×10^{-5}	0	-3.1×10^{-2}
$\boldsymbol{\nabla}^{(P)}$	-6.1×10^{-4}	-2.3×10^{-3}	-3.3×10^{-3}	-9.3×10^{-5}	-6.3×10^{-3}

Table 1: Stationary global mode at the threshold of the first instability, $Re_A = 483.5$ - $M = 0.5$: variation of the growth rate σ_A induced by the base flow modification $\boldsymbol{\delta q}^{\boldsymbol{0}}_M$. $\delta_{\rho^0}\sigma_A\vert_M$, $\delta_{\rho^0\boldsymbol{u}^0}\sigma_A\vert_M$, $\delta_{\rho^0 T^0}\sigma_A\vert_M$ and $\delta_{p^0}\sigma_A\vert_M$ are the variations obtained by evaluating individually the specific variation arising from the modification of density, momentum, internal energy and pressure, so that the overall variation $\delta\sigma_A\vert_M$ is the sum of these four contributions. Results obtained using the overall sensitivity functions are provided on the first line. Results obtained using the advection/production decomposition (5.3) are provided on the second and third lines respectively.

while the advection mechanism is entirely triggered by momentum, as the density, energy and pressure modifications are seen to contribute for nothing in the overall variations. This is consistent with the results discussed in § 5.1, where we have shown that the magnitude of the sensitivity functions $\boldsymbol{\nabla}_{\rho^0}\lambda$, $\boldsymbol{\nabla}_{\rho^0 T^0}\lambda$ and $\boldsymbol{\nabla}_{p^0}\lambda$ are very small compared to that of their momentum counterpart. It can thus be claimed that the stabilizing effect of compressibility comes from a strong strengthening of the advection of perturbations, triggered by the variation of the base flow momentum. Interestingly, it turns out that the additional slight weakening of the production mechanism arises both from the momentum and energy contributions, i.e. specific compressible mechanisms are at work in this second order stabilizing effect.

One also sees that $\delta^{(P)}\sigma_A$ becomes asymptotic to the value 0.007 as M is increased above $M \simeq 0.5$. In this range of Mach numbers, the magnitude of the production weakening mechanism thus becomes independent of the Mach number. On the contrary, $\delta^{(A)}\sigma_A$ is approximatively linear in M, so that the magnitude of the downstream advection strengthening effect is larger at high subsonic Mach numbers, hence explaining the large overall stabilizing effect previously documented in this specific parameter range.

To identify the regions in space which are responsible for the stabilization of the global mode, we present in Figure 18(b) the spatial distribution of the advection momentum integrand $\boldsymbol{\nabla}^{(A)}_{\rho^0\boldsymbol{u}^0}\sigma_A \cdot \delta(\rho^0\boldsymbol{u}^{\boldsymbol{0}})_M(r,z)$. At a given station, a positive (resp. negative) value indicates that the base flow modifications $\boldsymbol{\delta q}^{\boldsymbol{0}}_M$ contributes to the destabilization (resp. stabilization) of the global mode. Several regions contributing either to a stabilization or to a destabilization are visible in Figure 18(b), thus outlining the complex effect of varying the Mach number on the variation of the growth rate. One sees for instance that the vicinity of the separation line (in the region $0.5 < z < 1.5$) contributes to a a strong stabilization of the global mode, whereas the vicinity of the separation point contributes to its destabilization. The dominating contribution being stabilizing, we can though identify the front part of the recirculating bubble and the separation line as responsible for the stabilizing effect of the modification of the advection operator.

5.2.2. *Oscillating eigenmode B*

Figure 19(a) presents the adjoint-based values of $\delta^{(A)}\sigma_B$ (solid line) and $\delta^{(P)}\sigma_B$ (dash-dotted line) at threshold of instability, as functions of the Mach number. The overall variation $\delta\sigma_B$ already shown as the dashed line in Figure 14 is also reported. The curve trends are similar to that presented in Figure 18(a) for the stationary mode, with neg-

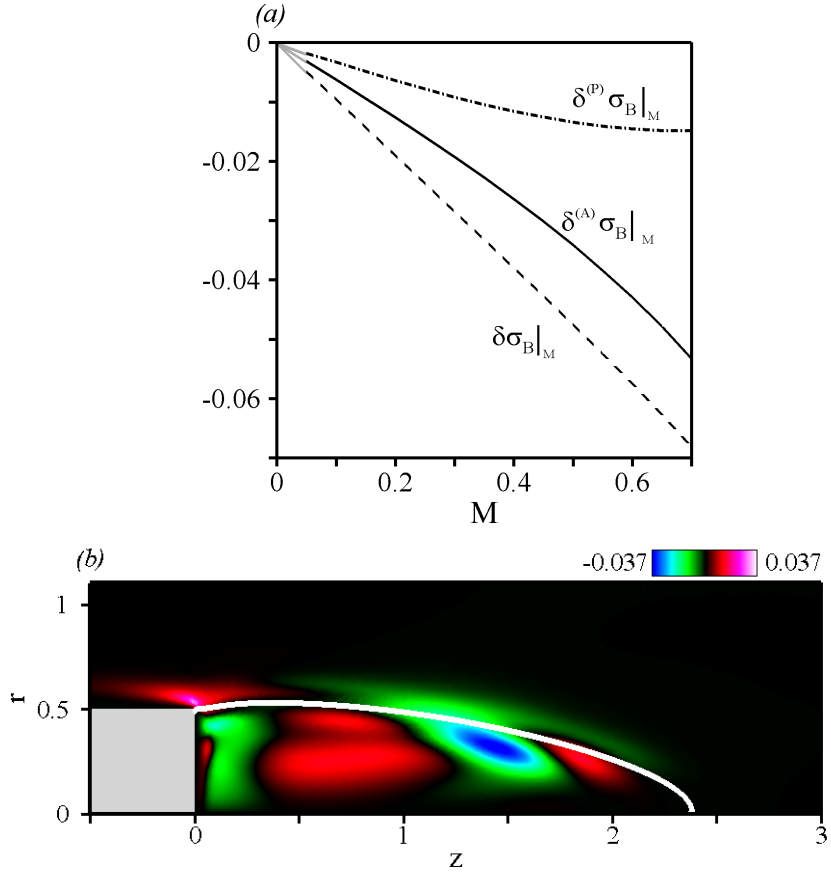

Figure 19: Same as Figure 18 for the growth rate of the oscillating global mode at the threshold of the second instability, $Re_B = 981.0$ - $M = 0.5$.

ative variations indicating that both the modifications of the advection and production mechanism are stabilizing. In particular, it can be seen that advection still dominates over production, but the contribution of $\delta^{(P)}\sigma_B$ is larger than that found for the stationary mode A, for instance it represent almost 35 % of the overall sensitivity $\delta\sigma_B$ at $M = 0.5$. The results of decompositions (5.2) and (5.3) at $M = 0.5$ and $Re_c^B = 981.0$ are given in Table 2, and show that both the advection and production mechanisms are dominated by the contribution of momentum, so that it can be claimed that the stabilization arising from an increase in the Mach number arises from a weakening of the production and a strong strengthening of the advection of perturbations, both being triggered by the variation of the base flow momentum.

Figure 19(b) shows the spatial distribution of the momentum advection integrand $\boldsymbol{\nabla}^{(A)}_{\rho^0\boldsymbol{u}^0}\sigma_B \cdot \delta(\rho^0\boldsymbol{u}^0)_M(r,z)$. Again, the effect of varying the Mach number on the growth rate is complex, as several regions contribute either to a stabilization or to a destabilization of the flow. As discussed previously for the stationary mode, one notes that the separation line (in the range $1 < z < 1.7$) contributes to a a strong stabilization of the global mode, whereas the very vicinity of the separation point and the core region (in the range $0.4 < z < 1.1$) both trigger a strong destabilizing effect.

Note that the compressibility effect on the frequency ω_B can be investigated similarly. For instance, Figure 20 presents the adjoint-based values of $\delta^{(A)}\omega_B$ (solid line) and $\delta^{(P)}\omega_B$ (dash-dotted line) and $\delta\omega_B$ (dashed line) at threshold of instability. Interestingly, we now observe that the advection and production mechanisms contribute both significantly to

	$\delta_{\rho^0}\sigma_B\vert_M$	$\delta_{\rho^0\boldsymbol{u}^0}\sigma_B\vert_M$	$\delta_{\rho^0 T^0}\sigma_B\vert_M$	$\delta_{p^0}\sigma_B\vert_M$	$\delta\sigma_B\vert_M$
$\boldsymbol{\nabla}$	8.0×10^{-3}	-5.3×10^{-2}	-2.6×10^{-3}	-4.9×10^{-5}	-4.8×10^{-2}
$\boldsymbol{\nabla}^{(A)}$	2.4×10^{-4}	-3.4×10^{-2}	-8.7×10^{-6}	0	-3.4×10^{-2}
$\boldsymbol{\nabla}^{(P)}$	7.7×10^{-3}	-1.9×10^{-2}	-2.6×10^{-3}	-4.9×10^{-5}	-1.3×10^{-2}
	$\delta_{\rho^0}\omega_B\vert_M$	$\delta_{\rho^0\boldsymbol{u}^0}\omega_B\vert_M$	$\delta_{\rho^0 T^0}\omega_B\vert_M$	$\delta_{p^0}\omega_B\vert_M$	$\delta\omega_B\vert_M$
$\boldsymbol{\nabla}$	8.1×10^{-2}	-1.3×10^{-1}	-2.8×10^{-3}	1.1×10^{-4}	-5.0×10^{-2}
$\boldsymbol{\nabla}^{(A)}$	-2.7×10^{-4}	-1.1×10^{-1}	-5.6×10^{-5}	0	-1.1×10^{-1}
$\boldsymbol{\nabla}^{(P)}$	8.2×10^{-2}	-1.9×10^{-2}	-2.7×10^{-3}	1.1×10^{-4}	6.0×10^{-2}

Table 2: Same as Table 1 for the oscillating global mode at the threshold of the second instability, $Re_B = 981.0$ - $M = 0.5$.

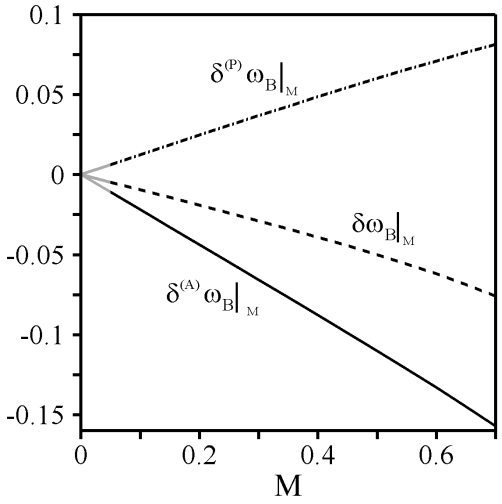

Figure 20: Same as Figure 18 for the frequency of the oscillating global mode at the threshold of the second instability, $Re_B = 981.0$ - $M = 0.5$.

the overall variation $\delta\omega_B$. Moreover, these mechanisms are competitive, since all values of $\delta^{(A)}\omega_B$ are negative and all values of $\delta^{(P)}\omega_B$ are positive. This means that when the Mach number is increased, the modification of the advection operator, that has been said to strongly strengthen the disturbances advection, also induce a decrease in the frequency ω_B. Simultaneously, the modification of the total production operator, that weakens the production of disturbances, also induces an increase of ω_B. As a consequence, the observed overall decrease of the frequency comes from the effect of advection being larger.

Table 2 also provides the results of decompositions (5.2) – (5.2) for ω_B. Interestingly, we find that the increase in the frequency by advection is entirely due to the modification of momentum. Though, it is interesting to note that production acts mainly through the modification of density. When considering the spatial distribution of the integrand $\boldsymbol{\nabla}^{(A)}_{\rho^0\boldsymbol{u}^0}\omega_B \cdot \delta(\rho^0\boldsymbol{u}^0)_M(r,z)$ (not shown here for conciseness), we find that the region responsible for the decrease in the frequency mechanism is located along the separation line, in the region $1 < z < 1.7$ already identified as responsible for the stabilizing effect, and visible in Figure 19(b). The study of the production integrand $\boldsymbol{\nabla}^{(A)}_{\rho^0}\omega_B \cdot \delta\rho^0_M(r,z)$ is less conclusive, as many different regions are found to induce either an increase or a decrease of the frequency, outlining the complexity of the underlying mechanism.

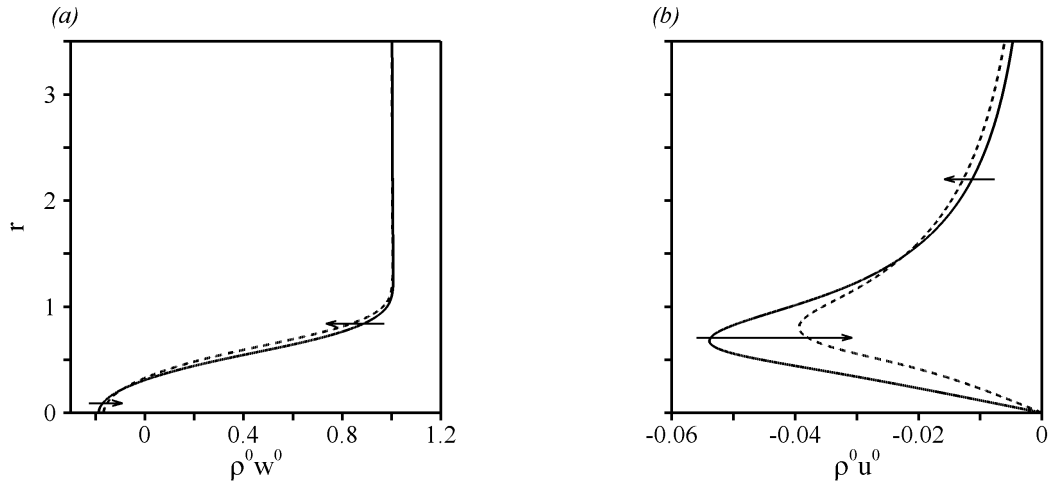

Figure 21: Specific base flow modification induced by a small increase in the Mach number, at the streamwise station $z = 1$ - $Re_c^A = 483.5$ and $M = 0.5$. (a) Spatial distribution of the streamwise momentum $\rho^0 w^0$. (b) Spatial distribution of the cross-stream momentum $\rho^0 u^0$. The base flow quantities are depicted by the solid lines and the modified quantities by the dashed lines.

5.3. *Discussion*

In the previous sections, the compressibility effect on the advection and production mechanisms have been shown to be stabilizing for both eigenmodes. Though, we would like to emphasize here that these are effects integrated over the whole recirculating bubble. Indeed, investigating the spatial distribution of the total integrands $\boldsymbol{\nabla}^{(A)}_{\boldsymbol{q^0}} \lambda \cdot \boldsymbol{\delta q}^{\boldsymbol{0}}_M(r,z)$ and $\boldsymbol{\nabla}^{(P)}_{\boldsymbol{q^0}} \lambda \cdot \boldsymbol{\delta q}^{\boldsymbol{0}}_M(r,z)$, we find that these quantities can be of opposite signs at the same location (not shown here). As a consequence, local effects can still be antagonist, with for instance a same flow region contributing both to stabilize and destabilize the global modes by locally increasing the advection of perturbations and strengthening their production. Therefore, it cannot be concluded from the present results that both mechanisms are cooperative.

It has also been mentioned that the localization of the zones responsible for the stabilization of both eigenmodes is strikingly similar. As an attempt to gain more physical insight at this mechanism, we now focus on the base flow modifications $\boldsymbol{\delta q}^{\boldsymbol{0}}_M$ itself, which has not yet been analyzed in terms of its impact on the stability problem. We consider here the case $Re_c^A = 486.5$, $M = 0.5$. Figure 21 shows the cross-stream and streamwise distributions of the momentum $\rho^0 \boldsymbol{u^0}(r)$ at the streamwise station $z = 1$, i.e. in the core of the region where the advection of disturbances induces the stabilizing effect. The solid and dashed lines refer to the base flows $\boldsymbol{q^0}$ and $\boldsymbol{q^0} + \boldsymbol{\delta q}^{\boldsymbol{0}}_M$ respectively, where δM has been set to unity. For the streamwise momentum, the effect of the Mach number is quite subtle, as seen from Figure 21(a). $\rho^0 w^0$ slightly decreases in the free shear part of the shear-layer and slightly increases in the reverse flow area, as outlined by the arrows. Figure 21(b) shows a similar reduction of the cross-stream gradients acting now on the cross-stream component, as one observes that the cross-stream momentum is significantly reduced within the shear-layer region, and increased in its free-shear part over a large cross-stream distance, presently larger than 3.5 body diameters. Though, the observed effect is much more significant for the cross-stream component, where the maximum relative variation reaches approximately 30 % of the momentum magnitude. As a consequence, it may thus be argued that increasing the Mach number has a stabilizing effect

	$\delta_{\rho^0 u^0}\sigma\vert_M$	$\delta_{\rho^0 w^0}\sigma\vert_M$	$\delta_{\rho^0 \boldsymbol{u^0}}\sigma\vert_M$
σ_A	-3.7×10^{-3}	-2.9×10^{-2}	-3.3×10^{-2}
σ_B	-6.5×10^{-2}	1.2×10^{-2}	-5.3×10^{-2}

Table 3: Variation of the growth rates σ_A and σ_B induced by the modification of the cross-stream and streamwise momentum components. The variation $\delta_{\rho^0 \boldsymbol{u^0}}\sigma\vert_M$ already provided in Tables 1 and 2 is therefore the sum of these two contributions.

because it tends to weaken the shear of the base flow by spreading out the momentum cross-stream gradients, and to simultaneously decrease the intensity of the counterflow, both effects being in favor of a stabilization. Identical effects are obtained at the threshold of the oscillating instability. Though, despite the important similarities born by both instabilities, important differences exist. For instance, the separate effect of cross-stream and streamwise momentum in the variations $\delta_{\rho^0 \boldsymbol{u^0}}\sigma_A$ and $\delta_{\boldsymbol{u^0}}\sigma_B$ is decomposed in Table 3. For conciseness, we do not carry out the advection/production decomposition, and present only the overall variations $\delta_{\rho^0 u^0}\sigma$ and $\delta_{\rho^0 w^0}\sigma$. It turns out that the stabilizing compressible effect observed for the stationary mode is triggered by the streamwise component, whereas that observed for the oscillating mode is triggered by the cross-stream component, the effect of the streamwise component being even destabilizing, which may seem rather counterintuitive. Though, it should be kept in mind that the effect on the growth rate is not only triggered by the base flow modification, but also by its orientation with respect to the sensitivity function. The latter point is probably responsible for the striking effects displayed in Table 3. As a result, this shows that a single base flow modification does not necessarily result in a a single stabilizing mechanism for both instabilities. Moreover, in the context of afterbody flow unsteadiness, this result shows that the effect of compressibility is non-parallel in essence, and may not be captured nor interpreted by performing only local stability analyses.

6. Conclusion

In the present paper, we have developed a theoretical framework for the study of global modes in compressible flows, up to the high subsonic regime. A sensitivity analysis to base flow modifications, aiming at predicting the variations of the eigenvalue of these global modes owing to a modification of the base flow, has been presented. It is based on the evaluation of gradients using adjoint methods. The sensitivity functions have been derived and depend on the base flow and perturbation quantities, as well as on the adjoint perturbation quantities, for which the adjoint stability equations have been derived in a consistent way. This has allowed us to discussed the physical origin of nonnormality of open compressible flows. Extending the discussion of Marquet *et al.* (2008*a*), we have shown that two types of nonnormality should be considered, namely the *convective* nonnormality, and the *lift-up* nonnormality that can arises from *kinematics* of *thermodynamics* mechanisms, the latter being specific to compressible flows. It has been seen that the sensitivity functions can be derived in terms of either non-conservative or conservative variables, which is an important point for the physical interpretation of results in the compressible regime. Moreover, when considering the variations of the eigenvalue resulting from a base flow modification, it is possible to distinguish between the variation owing to the respective modifications of the advection and production mechanisms. This

extends the concepts of convective and absolute instability that are classically used in the framework of parallel flows.

This framework has then been applied to gain insight at the dynamics of a subsonic afterbody flow. It has first been shown that the increase of the Mach number triggers that of the recirculating region, similar to what is commonly observed in incompressible recirculating flows when the Reynolds number is increased. Though, this effect has been shown to be purely inviscid, since it appears to be triggered by the variations of the pressure gradients close to the separatrix. A consistent bifurcation sequence has been found, whatever the value of the Mach number. A first instability occurs for a stationary global mode A of azimuthal wavenumber $m = 1$, and a second instability occurs for an oscillating global mode B of azimuthal wavenumber $m = 1$. The adjoint global modes and sensitivity functions to base flow modifications have been computed, and the wavemaker regions have been identified as being located within the recirculating bubble for both instabilities, a result owing to the convective nonnormality of the evolution operator which induces a spatial separation of the direct and adjoint global modes.

For both instabilities, the boundary separating the unstable and stable domains in the (M, Re)-plane have been determined, and it has been shown that increasing the Mach number has a stabilizing effect on both global modes. This effect has been investigated in the light of the sensitivity analysis, and a physical interpretation has been proposed. We have first shown that when the Mach number is increased, the stabilizing effect observed in return is triggered by the underlying modification of the base flow. Then, using the advection/production decomposition, we have shown that increasing the Mach number mainly enhances the downstream advection of the disturbances by spreading out the momentum cross-stream gradients. We also find that the same mechanism induces an additional stabilization by weakly weakening the production of disturbances.

This approach can be easily applied to other compressible flow configurations, as for instance cavity flows or hot jets that are known to sustain global instabilities. In particular, it would be of great interest to apply the present formalism to problems with significant thermodynamical effects, such as wakes developing past heated objects, for instance. Moreover, extending the present approach to the case of supersonic flows, in which one must also take into account the effect of shock waves, is an extremely challenging question to which we will devote future efforts.

Appendix A. The axisymmetric steady wake past a sphere

The global stability of the incompressible wake past a sphere is known to sustain a bifurcation sequence identical to that described here for an afterbody (Natarajan & Acrivos 1993, see), with a first stationary bifurcation involving a global eigenmode $\hat{\boldsymbol{q}}_{\boldsymbol{A}}^{\boldsymbol{1}}$ of azimuthal wavenumber $m = 1$ and a subsequent Hopf bifurcation occurring for a $m = 1$ oscillating global eigenmode $\hat{\boldsymbol{q}}_{\boldsymbol{B}}^{\boldsymbol{1}}$. We revisit here this problem at a low Mach number as a simple test case for the current compressible formulation. In the following, the Mach number is taken equal to $M = 0.1$. Contours of streamwise velocity for the steady, axisymmetric flow past a sphere are shown in Figure 22, for the Reynolds number $Re = 200$, where the flow is stable to small perturbations. The solid line is the streamline linking the separation point to the stagnation point on the $r = 0$ axis, it defines the separatrix delimiting the recirculation bubble behind the sphere. The negative values of the streamwise velocity close to the axis reaches 40 % of the free-stream velocity. The drag coefficient C_d and recirculation length L have been computed for this Reynolds numbers, so as to assess the accuracy of the base flow calculations. The values obtained ($L = 1.941$,

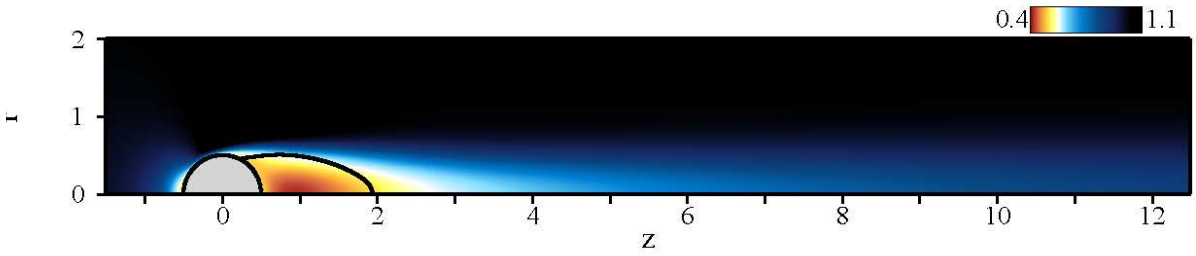

Figure 22: Steady axisymmetric base flow at $Re = 200$. The solid line in the flow indicates the separatrix of the recirculation zone.

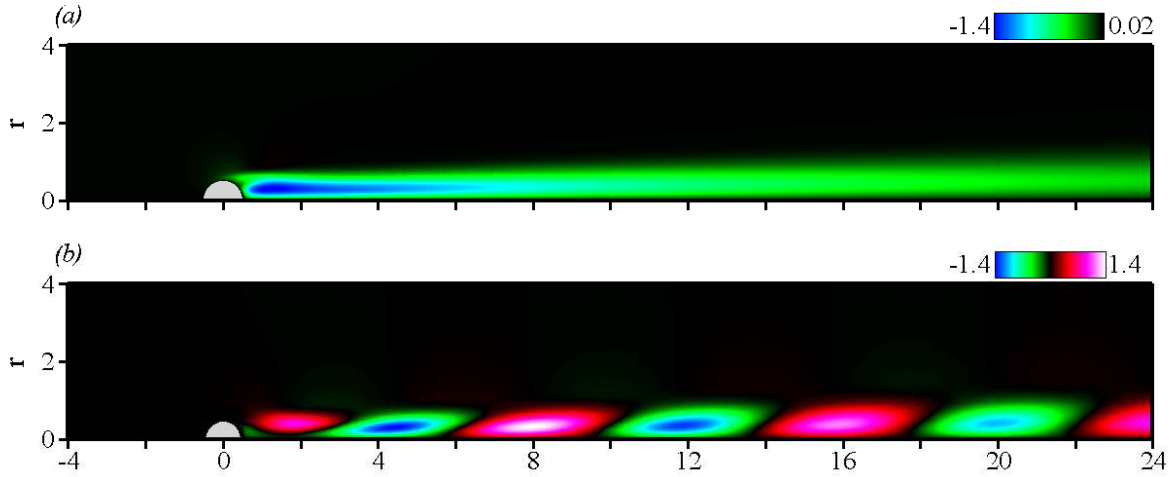

Figure 23: Spatial distribution of streamwise velocity $\hat{w}^1$ of the leading eigenmodes for the sphere, at their respective instability thresholds. (a) Stationary eigenmode, $Re_A = 212.6$, $M = 0.1$. (b) Oscillating eigenmode, $Re_B = 280.6$, $M = 0.1$.

$C_d = 0.769$) shows excellent agreement with the incompressible calculations of Fornberg (1988) ($L = 1.934$, $C_d = 0.768$), Natarajan & Acrivos (1993) ($L = 1.925$, $C_d = 0.79$) and Meliga *et al.* (2008*b*) ($L = 1.934$, $C_d = 0.770$). Note that in order to estimate the effect of the sponge zone on the numerical results, we have recomputed these compressible values with a constant viscosity μ within the sponge zones, which has resulted in identical results down to the sixth digit. We find both bifurcations to occur at $Re_A = 212.6$ and $Re_B = 280.6$, respectively, the frequency of the oscillating mode being $\omega = \omega_B = 0.698$ (corresponding to a Strouhal number of $St = \omega_B/2\pi = 0.111$). Again, these values are in good agreement with the incompressible calculations of Natarajan & Acrivos (1993) ($Re_A = 210$, $Re_B = 278$, $St = 0.113$) and Meliga *et al.* (2008*b*) ($Re_A = 212.6$, $Re_B = 280.7$, $St = 0.111$). Figure 23(a) shows the spatial structure of the streamwise velocity $\hat{w}^1_A$ at the first instability threshold. The result is reminiscent of that documented in the latter studies, with a global mode dominated by axially extended streamwise velocity disturbances located downstream of the sphere, that induce an off axis displacement of the wake (Johnson & Patel 1999). The real part $\hat{w}^1_{Br}$ of the streamwise velocity at the second instability threshold is shown in Figure 23(b), and exhibits a characteristic periodic positive and negative velocity perturbations downstream of the body, that allows to define a local spatial wavelength of about 4 diameters. Note that the imaginary part $\hat{w}^1_{Bi}$ displays a similar structure, but approximately in spatial quadrature, its maximum and minimum values occurring at the location of the zeros in $\hat{w}^1_{Br}$. Six different meshes,

	$z_{-\infty}$	z_{∞}	r_{∞}	l^s	n_t	DoF_0	DoF_m
M_1	-100	200	25	100	552513	2220938	3052429
M_2	-100	150	25	100	504703	2028922	2788504
M_3	-70	200	25	100	523038	2102572	2889734
M_4	-100	200	20	100	524337	2108222	2897446
M_5	-100	200	25	70	527048	2118780	2911999
M_6	-100	200	25	100	433351	1742706	2395058

Table 4: Properties of the meshes as a function of parameters $z_{-\infty}$, z_{∞}, r_{∞} and l^s, corresponding to the physical inlet, outlet and lateral boundaries, and to the size of the sponge zone. n_t is the number of triangles, DoF_0 is the number of degrees of freedom for an axisymmetric state vector used in the base flow calculations, and DoF_m is the number of degrees of freedom for a three-dimensional state vector used in the perturbation and adjoint perturbation calculations. Meshes M_1 and M_2 have the same vertex densities but with a different location of the outlet boundary. In the same way, M_1 and M_3 differ by the location of the inlet boundary, while M_1 and M_4 differ by the location of the lateral boundary and M_1 and M_5 differ by the size of the sponge zone. M_1 and M_6 have the same spatial extent but M_6 is built with lower vertex densities.

	σ_A	σ_B	ω_B
M_1	-9.7×10^{-7}	-4.3×10^{-7}	0.6983
M_2	-5.2×10^{-7}	-1.6×10^{-5}	0.6983
M_3	1.2×10^{-6}	-9.3×10^{-6}	0.6983
M_4	-2.0×10^{-6}	-1.7×10^{-5}	0.6983
M_5	7.9×10^{-6}	-2.0×10^{-6}	0.6983
M_6	7.6×10^{-5}	4.1×10^{-5}	0.6984

Table 5: Dependence of the eigenvalues on the different meshes characterized in Table 4. The stationary eigenvalue σ_A is computed at the first instability threshold $Re_A = 212.6$ and $M = 0.1$, and the oscillating eigenvalue $\sigma_B + \mathrm{i}\omega_B$ at the second instability threshold $Re_A = 280.6$ and $M = 0.1$.

denoted M_1 to M_6 have been used to assess convergence in the numerical results. These meshes exhibit various spatial extents and vertex densities, as well as various sizes for the sponge zones, and are detailed in Table 4. All results presented in this appendix correspond to the finest mesh M_1. A comparison of the results obtained with the meshes M_1 to M_6 is provided in Table 5 and shows that even for the coarser mesh M_6, all results converge to the same result within 3 significant digits.

Appendix B. Validation of the adjoint-based gradients

This appendix aims at assessing the correctness and accuracy of the adjoint method presented in this study. We recall that the variation of a given eigenvalue $\delta\lambda$ can be expressed as $\delta\lambda = \delta\lambda|_M + \delta\lambda|_{\boldsymbol{q}^0}$ where $\delta\lambda|_M$ (resp. $\delta\lambda|_{\boldsymbol{q}^0}$) is the variation of λ arising from the small modification of the base flow $\boldsymbol{\delta q}^0_M$, the Mach number being kept constant (resp. a small modification of the Mach number δM, the base flow being kept constant).

As mentioned previously, the sensitivity analysis is fundamentally linear since based on the evaluation of a gradient. Therefore, the variation of the eigenvalue computed thanks to the sensitivity analysis is exact in the limit of a modification of small amplitude, i.e.

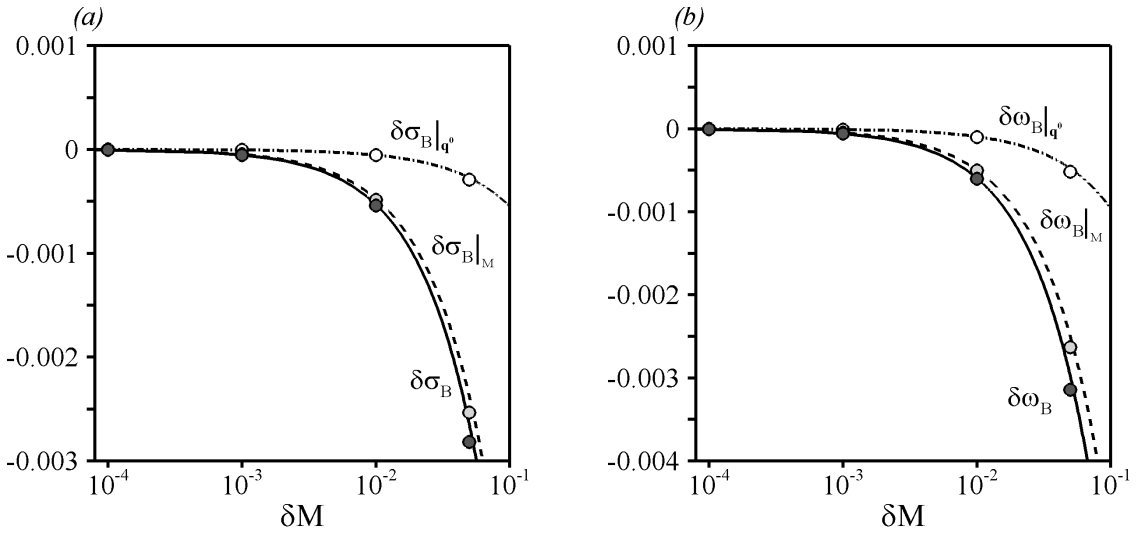

Figure 24: . Variation of the (a) growth rate σ_B and (b) frequency ω_B as a function of δM. Comparison of the linear results obtained from the sensitivity analysis (solid, dashed and dash-dotted lines) with the nonlinear results obtained from forward calculations (dark grey, light grey and white circle symbols) - $Re_B = 981.0$ and $M = 0.5$.

such that $\delta M/M \ll 1$. In the present appendix, we increase progressively the amplitude of δM. Considering the oscillating global mode at the threshold of the second instability, for $Re_B = 981.0$ and $M = 0.5$, we compute, for each value of δM, the linear estimation of the growth rate and frequency variations thanks to the adjoint-based expressions (2.24). These variations are then computed exactly by carrying out the following forward calculations: Assuming $\boldsymbol{q}^{\mathbf{0}}_M$ is the base flow solution at the Mach number M, we compute first for each value of δM the base flow $\boldsymbol{q}^{\mathbf{0}}_{M+\delta M}$ which is solution of the nonlinear base flow equations (3.6) for the Mach number $M + \delta M$. According to the quantity to estimate, we solve then the three stability problems

$$\delta\lambda \longrightarrow (\lambda+\delta\lambda)\mathcal{B}_m(\boldsymbol{q}^{\mathbf{0}}_{M+\delta M})\hat{\boldsymbol{q}}^{\mathbf{1}} + \mathcal{A}_m(\boldsymbol{q}^{\mathbf{0}}_{M+\delta M}, M+\delta M)\boldsymbol{q}^{\mathbf{1}} = \mathbf{0}\,, \qquad (\mathrm{B}\,1a)$$

$$\delta\lambda|_M \longrightarrow (\lambda+\delta\lambda|_M)\mathcal{B}_m(\boldsymbol{q}^{\mathbf{0}}_{M+\delta M})\hat{\boldsymbol{q}}^{\mathbf{1}} + \mathcal{A}_m(\boldsymbol{q}^{\mathbf{0}}_{M+\delta M}, M)\boldsymbol{q}^{\mathbf{1}} = \mathbf{0}\,, \qquad (\mathrm{B}\,1b)$$

$$\delta\lambda|_{\boldsymbol{q}^{\mathbf{0}}} \longrightarrow (\lambda+\delta\lambda|_{\boldsymbol{q}^{\mathbf{0}}})\mathcal{B}_m(\boldsymbol{q}^{\mathbf{0}})\hat{\boldsymbol{q}}^{\mathbf{1}} + \mathcal{A}_m(\boldsymbol{q}^{\mathbf{0}}, M+\delta M)\boldsymbol{q}^{\mathbf{1}} = \mathbf{0}\,. \qquad (\mathrm{B}\,1c)$$

Figure 24(a) depicts the growth rate variations computed as functions of the amplitude δM. The dark grey (resp. light grey and white circle symbols) stand for the exact nonlinear variation $\delta\sigma_B$ (resp. $\delta\sigma_B|_M$ and $\delta\sigma_B|_{\boldsymbol{q}^{\mathbf{0}}}$) obtained by forward calculations. The corresponding linear estimations issuing from the sensitivity analysis are presented as the solid, dashed and dash-dotted curves respectively. Results for the frequency variations are similarly presented in Figure 24(b). For small amplitudes $\delta M < 10^{-4}$, the relative difference is not measurable and results are superposed, indicating that the linear assumption holds, and in particular that the base flow modification $\boldsymbol{\delta q}^{\mathbf{0}}_M$ owing to the increase in M is linear in this range. These results validate the sensitivity analysis and in particular the accuracy of the sensitivity functions computed in the present study. For larger amplitudes, we observe small discrepancies for the variation $\delta\lambda_B|_M$ and for the overall variation $\delta\lambda_B$, as the decrease in the growth rate and the frequency are slightly larger if computed by forward calculations. This means that the true nonlinear stabilizing effect of the Mach number is slightly larger than the one estimated by the sensitivity analysis. Though, it should be noted that the variations obtained up to $\delta M = 0.05$ are very

well approximated by the linear estimation, as the maximum relative difference being approximately 6 % for $\sigma_{_B}$ and 5 % for $\omega_{_B}$.

Appendix C. Advection and production sensitivity functions

In this section, we discuss the magnitude of the advection sensitivity function $\boldsymbol{\nabla}^{(A)}_{\boldsymbol{q^0}}\lambda$ and of its production counterpart $\boldsymbol{\nabla}^{(A)}_{\boldsymbol{q^0}}\lambda$ for the growth rates of both global modes investigated in this study. As previously, the color look-up is set-up so as to enhance the active zones where the growth rate σ is most sensitive to a modification of the base flow.

We consider first the sensitivity of the stationary growth rate $\sigma_{_A}$ at $Re_c^A = 483.5$ and $M = 0.5$. Figure 25(a) and 25(b) present the spatial distribution of magnitude for advection and production sensitivity to momentum modifications, i.e. $\|\boldsymbol{\nabla}^{(A)}_{\rho^0\boldsymbol{u^0}}\sigma_{_A}\|^2(r,z)$ and $\|\boldsymbol{\nabla}^{(P)}_{\rho^0\boldsymbol{u^0}}\sigma_{_A}\|^2(r,z)$. Similarly, Figures 25($c$) and 25($d$) present the spatial distribution of magnitude for advection and production sensitivity to energy modifications, i.e. $|\boldsymbol{\nabla}^{(A)}_{\rho^0T^0}\sigma_{_A}|^2(r,z)$ and $|\boldsymbol{\nabla}^{(P)}_{\rho^0T^0}\sigma_{_A}|^2(r,z)$. As discussed previously for the overall sensitivity functions, we find magnitudes of sensitivity almost nil everywhere in the flow, except in the recirculating bubble, which acts as the wavemaker regions for both the advection and production mechanisms. Concerning the momentum components, we find that interestingly, regions of highest sensitivities are clearly distinct for both mechanisms, as the momentum component of the advection sensitivity function reaches high magnitudes rather close to the base and in the front part of the recirculation, whereas the momentum component of the production sensitivity function is maximum in the rear part of the recirculation. Moreover, it should be noted that the magnitude of both the advection and production sensitivity functions are important, but that of the production sensitivity dominates if one compares Figures 15(a) and 25(a). Though, it has been said that the advection mechanism is dominant in the stabilizing effect of the Mach number. This shows that to be physically relevant, the sensitivity analysis must not only consider the magnitude of the sensitivity functions alone, but also the shape of the associated base flow modification $\boldsymbol{\delta q^0}$. Concerning the energy components $|\boldsymbol{\nabla}^{(A)}_{\rho^0T^0}\sigma_{_A}|^2$ and $|\boldsymbol{\nabla}^{(P)}_{\rho^0T^0}\sigma_{_A}|^2$ shown in Figures 25(b) and 25(d), it is striking to note that the magnitude of advection sensitivity function is almost nil even within the recirculation bubble, and that the overall sensitivity observed in Figure 15(b) is entirely due to the sensitivity to modifications of the production operator. This means that modifying the energy ρ^0T^0 alters only the disturbances production, but not their advection by the base flow. We consider now the sensitivity of the oscillating growth rate $\sigma_{_B}$ at $Re_c^B = 981.0$ and $M = 0.5$. Figure 26 displays the spatial distribution of magnitude for advection and production sensitivity to momentum and energy. Results are very similar to that discussed of the stationary mode, with magnitudes of sensitivity nil everywhere except within the recirculation. Though, significant discrepancies should be noted here. Concerning the momentum components, the different in the location of the highest sensitivity regions is less clear, as the advection sensitivity function now reaches high magnitudes in the core of the recirculation, whereas the momentum component of the production sensitivity function is maximum in the rear part of the recirculation. Moreover, the magnitude of the advection sensitivity functions is now larger than that of the production in the whole recirculation. Therefore, comparing Figures 16(a) and 26(a), it can be concluded that the overall magnitude of sensitivity to a modification of momentum is dominated by the modifications of the advection operator, a result opposite to that found for the stationary global mode. Comparing now the energy components $|\boldsymbol{\nabla}^{(A)}_{\rho^0T^0}\sigma_{_B}|^2$ and $|\boldsymbol{\nabla}^{(P)}_{\rho^0T^0}\sigma_{_B}|^2$, we find again that the magnitude of the advection sensitivity function is almost nil even within the recirculation

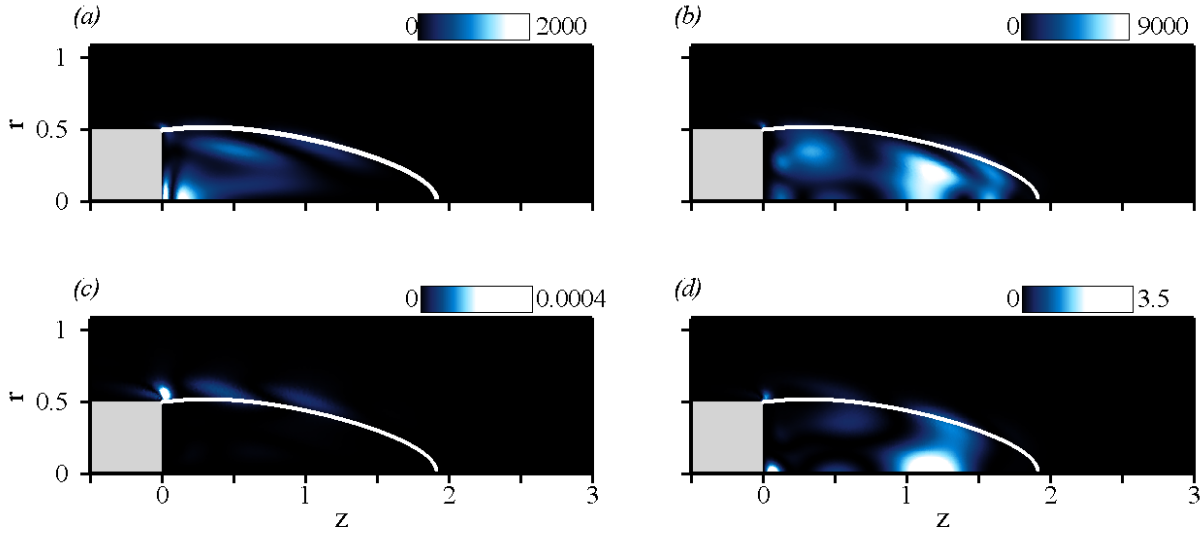

Figure 25: Sensitivity to base flow modifications of the stationary growth rate σ_A for the critical Reynolds number $Re_c^A = 483.5$ at $M = 0.5$. Spatial distribution of the magnitude of the (a) advection momentum sensitivity function $\|\boldsymbol{\nabla}^{(A)}_{\rho^0 \boldsymbol{u}^0}\sigma_A\|^2$, (b) production momentum sensitivity function $\|\boldsymbol{\nabla}^{(P)}_{\rho^0 \boldsymbol{u}^0}\sigma_A\|^2$, (c) advection energy sensitivity function $|\boldsymbol{\nabla}^{(A)}_{\rho^0 T^0}\sigma_A|^2$, (d) production energy sensitivity function $|\boldsymbol{\nabla}^{(P)}_{\rho^0 T^0}\sigma_A|^2$.

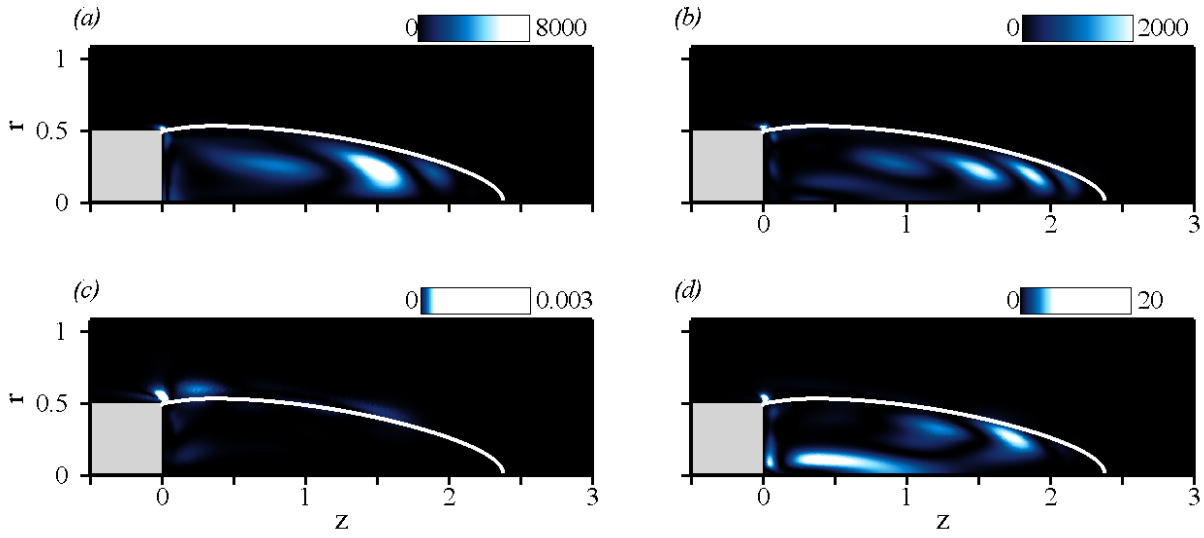

Figure 26: Same as Figure 25 for the oscillating global mode at the threshold of the second instability, $Re_B = 981.0$ - $M = 0.5$.

bubble, indicating that a modification of energy does not alter the downstream advection of disturbances. Although both global modes bear similarities, these results outline the complexity of the effects found in the present study.

Appendix D. Derivation of the adjoint perturbation equations

We define the r and z vector derivatives as $\partial_{r,z}\boldsymbol{q} = (\partial_{r,z}\rho, \partial_{r,z}u, \partial_{r,z}v, \partial_{r,z}w, \partial_{r,z}T)^T$. We recall that the adjoint operators $\mathcal{A}_m^\dagger$ and $\mathcal{B}^\dagger$ are such that

$$\left\langle \hat{\boldsymbol{q}}^{\mathbf{1}\dagger}\,,\, \lambda\mathcal{B}(\boldsymbol{q}^{\mathbf{0}})\boldsymbol{\delta}\hat{\boldsymbol{q}}^{\mathbf{1}} + \mathcal{A}_m(\boldsymbol{q}^{\mathbf{0}})\boldsymbol{\delta}\hat{\boldsymbol{q}}^{\mathbf{1}} \right\rangle = \left\langle \lambda^*\mathcal{B}^\dagger(\boldsymbol{q}^{\mathbf{0}})\hat{\boldsymbol{q}}^{\mathbf{1}\dagger} + \mathcal{A}_m^\dagger(\boldsymbol{q}^{\mathbf{0}})\hat{\boldsymbol{q}}^{\mathbf{1}\dagger}\,,\, \boldsymbol{\delta}\hat{\boldsymbol{q}}^{\mathbf{1}} \right\rangle , \qquad \text{(D 1)}$$

along with the inner product (3.14), where $\boldsymbol{\delta\hat{q}^1}$ is a small modification of the global mode. For convenience, the relevant terms are developed into a matrix form reading

$$\begin{aligned}\mathcal{A}_m(\boldsymbol{q^0})\boldsymbol{\delta\hat{q}^1} = {}& \boldsymbol{A}_1\boldsymbol{\delta\hat{q}^1} + \boldsymbol{A}_2\partial_r\boldsymbol{\delta\hat{q}^1} + \boldsymbol{A}_3\partial_z\boldsymbol{\delta\hat{q}^1} \\ & + \frac{1}{Re}\partial_r\left(\boldsymbol{V}_1\partial_r\boldsymbol{\delta\hat{q}^1} + \boldsymbol{V}_2\partial_z\boldsymbol{\delta\hat{q}^1} + \frac{1}{r}\boldsymbol{V}_3\boldsymbol{\delta\hat{q}^1}\right) \\ & + \frac{1}{Re}\partial_z\left(\boldsymbol{V}_2{}^T\partial_r\boldsymbol{\delta\hat{q}^1} + \boldsymbol{V}_4\partial_z\boldsymbol{\delta\hat{q}^1} + \frac{1}{r}\boldsymbol{V}_5\boldsymbol{\delta\hat{q}^1}\right) \\ & + \frac{1}{Re}\left(\frac{1}{r}\boldsymbol{V}_6\partial_r\boldsymbol{\delta\hat{q}^1} + \frac{1}{r}\boldsymbol{V}_7\partial_z\boldsymbol{\delta\hat{q}^1} + \frac{1}{r^2}\boldsymbol{V}_8\right), \qquad (\mathrm{D}\,2a)\end{aligned}$$

$$\mathcal{B}(\boldsymbol{q^0})\boldsymbol{\delta\hat{q}^1} = \boldsymbol{B}\boldsymbol{\delta\hat{q}^1}\,, \qquad (\mathrm{D}\,2b)$$

where $\boldsymbol{A}_{1\ldots3}$, $\boldsymbol{V}_{1\ldots8}$ and $\boldsymbol{B}$ are real 5×5 matrices whose coefficients depend on the base flow variables and are detailed at the end of this Appendix. Integrating by parts to remove the derivatives from the state variables yields

$$\begin{aligned}\mathcal{A}_m^\dagger\left(\boldsymbol{q^0}\right)\boldsymbol{\hat{q}^{1\dagger}} = {}& \boldsymbol{A}_1{}^T\boldsymbol{\hat{q}^{1\dagger}} - \frac{1}{r}\partial_r\left(r\boldsymbol{A}_2{}^T\boldsymbol{\hat{q}^{1\dagger}}\right) - \partial_z\left(\boldsymbol{A}_3{}^T\boldsymbol{\hat{q}^{1\dagger}}\right) \\ & + \frac{1}{Re}\frac{1}{r}\left(\partial_r\left(r\boldsymbol{V}_1{}^T\partial_r\boldsymbol{\hat{q}^{1\dagger}}\right) + \partial_r\left(\boldsymbol{V}_1{}^T\boldsymbol{\hat{q}^{1\dagger}}\right) + \partial_z\left(\boldsymbol{V}_2{}^T\partial_r(r\boldsymbol{\hat{q}^{1\dagger}})\right) - \frac{1}{r}\boldsymbol{V}_3{}^T\partial_r(r\boldsymbol{\hat{q}^{1\dagger}})\right) \\ & + \frac{1}{Re}\left(\frac{1}{r}\partial_r\left(r\boldsymbol{V}_2\partial_z\boldsymbol{\hat{q}^{1\dagger}}\right) + \partial_z\left(\boldsymbol{V}_4{}^T\partial_z\boldsymbol{\hat{q}^{1\dagger}}\right) - \frac{1}{r}\boldsymbol{V}_5{}^T\partial_z\boldsymbol{\hat{q}^{1\dagger}}\right) \\ & + \frac{1}{Re}\frac{1}{r}\left(-\partial_r\left(\boldsymbol{V}_6{}^T\boldsymbol{\hat{q}^{1\dagger}}\right) - \partial_z\left(\boldsymbol{V}_7{}^T\boldsymbol{\hat{q}^{1\dagger}}\right) + \frac{1}{r}\boldsymbol{V}_8{}^T\boldsymbol{\hat{q}^{1\dagger}}\right), \qquad (\mathrm{D}\,3a)\end{aligned}$$

$$\mathcal{B}^\dagger\boldsymbol{\hat{q}^{1\dagger}}\left(\boldsymbol{q^0}\right) = \boldsymbol{B}^T\boldsymbol{\hat{q}^{1\dagger}}\,. \qquad (\mathrm{D}\,3b)$$

This leads to the adjoint perturbation equations (3.15). $\boldsymbol{n} = (n_r, 0, n_z)^T$ being the vector normal to the boundary $\partial\Omega$, the boundary term then reads

$$\begin{aligned}BT = {}& \int_{\partial\Omega}\boldsymbol{\hat{q}^{1\dagger}}\cdot\boldsymbol{A}_2\boldsymbol{\delta\hat{q}^1}n_r r\mathrm{d}z + \int_{\partial\Omega}\boldsymbol{\hat{q}^{1\dagger}}\cdot\boldsymbol{A}_3\boldsymbol{\delta\hat{q}^1}n_z r\mathrm{d}r \\ & + \frac{1}{Re}\int_{\partial\Omega}\boldsymbol{\hat{q}^{1\dagger}}\cdot\left(\boldsymbol{V}_1\partial_r\boldsymbol{\delta\hat{q}^1} + \boldsymbol{V}_2\partial_z\boldsymbol{\delta\hat{q}^1} + \frac{1}{r}\boldsymbol{V}_6\boldsymbol{\delta\hat{q}^1}\right)n_r r\mathrm{d}z \\ & + \frac{1}{Re}\int_{\partial\Omega}\left(-\frac{1}{r}\boldsymbol{V}_1{}^T\partial_r\left(r\boldsymbol{\hat{q}^{1\dagger}}\right) + \boldsymbol{V}_2\partial_z\boldsymbol{\hat{q}^{1\dagger}} - \frac{1}{r}\boldsymbol{V}_3{}^T\boldsymbol{\hat{q}^{1\dagger}}\right)\cdot\boldsymbol{\delta\hat{q}^1}n_r r\mathrm{d}z \qquad (\mathrm{D}\,4) \\ & + \frac{1}{Re}\int_{\partial\Omega}\boldsymbol{\hat{q}^{1\dagger}}\cdot\left(\boldsymbol{V}_2{}^T\partial_r\boldsymbol{\delta\hat{q}^1} + \boldsymbol{V}_4\partial_z\boldsymbol{\delta\hat{q}^1} + \frac{1}{r}\boldsymbol{V}_7\boldsymbol{\delta\hat{q}^1}\right)n_z r\mathrm{d}r \\ & + \frac{1}{Re}\int_{\partial\Omega}\left(-\boldsymbol{V}_2{}^T\frac{1}{r}\partial_r\left(r\boldsymbol{\hat{q}^{1\dagger}}\right) + \boldsymbol{V}_4{}^T\partial_z\boldsymbol{\hat{q}^{1\dagger}} - \frac{1}{r}\boldsymbol{V}_5{}^T\boldsymbol{\hat{q}^{1\dagger}}\right)\cdot\boldsymbol{\delta\hat{q}^1}n_z r\mathrm{d}r\,.\end{aligned}$$

To determine the boundary conditions that must be satisfied by the adjoint based flow, it is necessary to take into account the boundary conditions of the problem itself. For instance on $\partial\Omega_b$, the boundary condition being $\boldsymbol{\hat{u}^1} = \boldsymbol{0}$ and $\hat{T}^1 = 0$, admissible conditions are such that $\boldsymbol{\delta\hat{u}^1} = \boldsymbol{0}$ and $\partial_n\delta\hat{T}^1 = 0$. Cancellation of this boundary term gives rise to the adjoint boundary conditions:

$$\boldsymbol{\hat{u}^{1\dagger}} = \boldsymbol{0},\ \hat{\rho}^{1\dagger}, \hat{T}^{1\dagger} = 0 \quad \text{on} \quad \partial\Omega^s_{in}\cup\partial\Omega^s_{ext}\cup\partial\Omega^s_{out}\,, \qquad (\mathrm{D}\,5a)$$

$$\boldsymbol{\hat{u}^{1\dagger}} = \boldsymbol{0},\ \partial_n\hat{T}^{1\dagger} = 0 \quad \text{on} \quad \partial\Omega_b\,, \qquad (\mathrm{D}\,5b)$$

$$\hat{w}^{1\dagger}, \hat{\rho}^{1\dagger}, \hat{T}^{1\dagger} = 0,\ \partial_r(\hat{u}^{1\dagger}, \hat{v}^{1\dagger}) = 0 \quad \text{on} \quad \partial\Omega_a\,. \qquad (\mathrm{D}\,5c)$$

Rearranging terms and using the continuity equation for $\boldsymbol{q^0}$ and $\hat{\boldsymbol{q}}^{\boldsymbol{1}}$ then yields expression (3.24). Finally, the various matrices used for the computation of the adjoint perturbation equations read:

$$
-\boldsymbol{A}_1 = \begin{pmatrix}
\boldsymbol{\nabla}\cdot\boldsymbol{u^0} & \frac{1}{r}\partial_r(r\rho^0) & \frac{m}{r}\rho^0 & \partial_z\rho^0 & 0 \\
\boldsymbol{u^0}\cdot\boldsymbol{\nabla}u^0 + \frac{1}{\gamma M^2}\partial_r T^0 & \rho^0\partial_r u^0 & 0 & \rho^0\partial_r w^0 & \frac{1}{\gamma M^2}\partial_r\rho^0 \\
-\frac{1}{\gamma M^2}\frac{m}{r}T^0 & 0 & \frac{1}{r}\rho^0 u^0 & 0 & -\frac{1}{\gamma M^2}\frac{m}{r}\rho^0 \\
\boldsymbol{u^0}\cdot\boldsymbol{\nabla}w^0 + \frac{1}{\gamma M^2}\partial_z T^0 & \rho^0\partial_r w^0 & 0 & \rho^0\partial_z w^0 & \frac{1}{\gamma M^2}\partial_z\rho^0 \\
\boldsymbol{u^0}\cdot\boldsymbol{\nabla}T^0 + T^0\boldsymbol{\nabla}\cdot\boldsymbol{u^0} & \rho^0\frac{1}{r}T^0 & \frac{m}{r}\rho^0 T^0 & \rho^0\partial_z T^0 & \rho^0\boldsymbol{\nabla}\cdot\boldsymbol{u^0}
\end{pmatrix}
$$

$$
-\ 2\gamma(\gamma-1)\frac{M^2}{Re}\begin{pmatrix}
0 & 0 & 0 & 0 & 0 \\
0 & 0 & 0 & 0 & 0 \\
0 & 0 & 0 & 0 & 0 \\
0 & 0 & 0 & 0 & 0 \\
0 & \frac{1}{r}\tau^0_{\theta\theta} & \frac{m}{r}\tau^0_{\theta\theta} & 0 & 0
\end{pmatrix},
$$

$$
-\boldsymbol{A}_2 = \begin{pmatrix}
u^0 & \rho^0 & 0 & 0 & 0 \\
\frac{1}{\gamma M^2}T^0 & \rho^0 u^0 & 0 & 0 & \frac{1}{\gamma M^2}\rho^0 \\
0 & 0 & \rho^0 u^0 & 0 & 0 \\
0 & 0 & 0 & \rho^0 u^0 & 0 \\
0 & \rho^0 T^0 & 0 & 0 & \rho^0 u^0
\end{pmatrix} - 2\gamma(\gamma-1)\frac{M^2}{Re}\begin{pmatrix}
0 & 0 & 0 & 0 & 0 \\
0 & 0 & 0 & 0 & 0 \\
0 & 0 & 0 & 0 & 0 \\
0 & 0 & 0 & 0 & 0 \\
0 & \tau^0_{rr} & 0 & \tau^0_{rz} & 0
\end{pmatrix},
$$

$$
-\boldsymbol{A}_3 = \begin{pmatrix}
w^0 & 0 & 0 & \rho^0 & 0 \\
0 & \rho^0 w^0 & 0 & 0 & 0 \\
0 & 0 & \rho^0 w^0 & 0 & 0 \\
\frac{1}{\gamma M^2}T^0 & 0 & 0 & \rho^0 w^0 & \frac{1}{\gamma M^2}\rho^0 \\
0 & 0 & 0 & \rho^0 T^0 & \rho^0 w^0
\end{pmatrix} - 2\gamma(\gamma-1)\frac{M^2}{Re}\begin{pmatrix}
0 & 0 & 0 & 0 & 0 \\
0 & 0 & 0 & 0 & 0 \\
0 & 0 & 0 & 0 & 0 \\
0 & 0 & 0 & 0 & 0 \\
0 & \tau^0_{rz} & 0 & \tau^0_{zz} & 0
\end{pmatrix},
$$

$$
\boldsymbol{V}_1 = \widetilde{\mu}\begin{pmatrix}
0 & 0 & 0 & 0 & 0 \\
0 & \frac{4}{3} & 0 & 0 & 0 \\
0 & 0 & 1 & 0 & 0 \\
0 & 0 & 0 & 1 & 0 \\
0 & 0 & 0 & 0 & \frac{\gamma}{Pr}
\end{pmatrix}, \qquad
\boldsymbol{V}_2 = \widetilde{\mu}\begin{pmatrix}
0 & 0 & 0 & 0 & 0 \\
0 & 0 & 0 & -\frac{2}{3} & 0 \\
0 & 0 & 0 & 0 & 0 \\
0 & 1 & 0 & 0 & 0 \\
0 & 0 & 0 & 0 & 0
\end{pmatrix},
$$

$$
\boldsymbol{V}_3 = -\widetilde{\mu}\begin{pmatrix}
0 & 0 & 0 & 0 & 0 \\
0 & \frac{2}{3} & \frac{2m}{3} & 0 & 0 \\
0 & m & 1 & 0 & 0 \\
0 & 0 & 0 & 0 & 0 \\
0 & 0 & 0 & 0 & 0
\end{pmatrix}, \qquad
\boldsymbol{V}_4 = \widetilde{\mu}\begin{pmatrix}
0 & 0 & 0 & 0 & 0 \\
0 & 1 & 0 & 0 & 0 \\
0 & 0 & 1 & 0 & 0 \\
0 & 0 & 0 & \frac{4}{3} & 0 \\
0 & 0 & 0 & 0 & \frac{\gamma}{Pr}
\end{pmatrix},
$$

$$
\boldsymbol{V}_5 = -\widetilde{\mu}\begin{pmatrix}
0 & 0 & 0 & 0 & 0 \\
0 & 0 & 0 & 0 & 0 \\
0 & 0 & 0 & m & 0 \\
0 & \frac{2}{3} & \frac{2m}{3} & 0 & 0 \\
0 & 0 & 0 & 0 & 0
\end{pmatrix}, \qquad
\boldsymbol{V}_6 = \widetilde{\mu}\begin{pmatrix}
0 & 0 & 0 & 0 & 0 \\
0 & 2 & m & 0 & 0 \\
0 & \frac{2m}{3} & 2 & 0 & 0 \\
0 & 0 & 0 & 1 & 0 \\
0 & 0 & 0 & 0 & \frac{\gamma}{Pr}
\end{pmatrix},
$$

$$
\boldsymbol{V}_7 = \widetilde{\mu}\begin{pmatrix}
0 & 0 & 0 & 0 & 0 \\
0 & 0 & 0 & 0 & 0 \\
0 & 0 & 0 & \frac{2m}{3} & 0 \\
0 & 1 & m & 0 & 0 \\
0 & 0 & 0 & 0 & 0
\end{pmatrix}, \qquad
\boldsymbol{V}_8 = \widetilde{\mu}\begin{pmatrix}
0 & 0 & 0 & 0 & 0 \\
0 & -m^2-2 & -3m & 0 & 0 \\
0 & -\frac{10m}{3} & -\frac{4m^2}{3}-2 & 0 & 0 \\
0 & 0 & 0 & -m^2 & 0 \\
0 & 0 & 0 & 0 & -\frac{\gamma}{Pr}m^2
\end{pmatrix},
$$

$$
\boldsymbol{B} = \begin{pmatrix}
1 & 0 & 0 & 0 & 0 \\
0 & \rho^0 & 0 & 0 & 0 \\
0 & 0 & \rho^0 & 0 & 0 \\
0 & 0 & 0 & \rho^0 & 0 \\
0 & 0 & 0 & 0 & \rho^0
\end{pmatrix}.
$$

Note that the change of variables $(\hat{v}^1, \hat{v}^{1\dagger}) \rightarrow (\mathrm{i}\hat{v}^1, \mathrm{i}\hat{v}^{1\dagger})$ has been used in order to deal with real matrices only.

Appendix E. Derivation of the sensitivity functions to base flow modifications

We recall that the adjoint operators $\mathcal{S}_m^\dagger$ and $\mathcal{R}^\dagger$ are such that

$$\left\langle \hat{\boldsymbol{q}}^{\boldsymbol{1}\dagger}\,,\, \lambda\mathcal{R}(\boldsymbol{q^0},\hat{\boldsymbol{q}}^{\boldsymbol{1}})\boldsymbol{\delta q^0} + \mathcal{S}_m(\boldsymbol{q^0},\hat{\boldsymbol{q}}^{\boldsymbol{1}})\boldsymbol{\delta q^0}\right\rangle = \left\langle \lambda^*\mathcal{R}^\dagger(\boldsymbol{q^0},\hat{\boldsymbol{q}}^{\boldsymbol{1}})\hat{\boldsymbol{q}}^{\boldsymbol{1}\dagger} + \mathcal{S}_m^\dagger(\boldsymbol{q^0},\hat{\boldsymbol{q}}^{\boldsymbol{1}})\hat{\boldsymbol{q}}^{\boldsymbol{1}\dagger}\,,\, \boldsymbol{\delta q^0}\right\rangle , \tag{E 1}$$

where $\boldsymbol{\delta q^0}$ is a small modification of the base flow. As previously, the relevant terms are written into the matrix form

$$\mathcal{S}_m\left(\boldsymbol{q^0},\hat{\boldsymbol{q}}^{\boldsymbol{1}}\right)\boldsymbol{\delta q^0} = \boldsymbol{A}_1'\boldsymbol{\delta q^0} + \boldsymbol{A}_2'\partial_r\boldsymbol{\delta q^0} + \boldsymbol{A}_3'\partial_z\boldsymbol{\delta q^0}\,, \tag{E 2a}$$

$$\mathcal{R}\left(\boldsymbol{q^0},\hat{\boldsymbol{q}}^{\boldsymbol{1}}\right)\boldsymbol{\delta q^0} = \boldsymbol{R}\boldsymbol{\delta q^0}\,, \tag{E 2b}$$

where $\boldsymbol{A}_{1\ldots3}'$ and $\boldsymbol{R}'$ are real 5×4 matrices whose coefficients depend on the state variables $(\boldsymbol{q^0},\hat{\boldsymbol{q}}^{\boldsymbol{1}})$. Derivative terms in the right side of equation E 2 are integrated by parts. We obtain

$$\mathcal{S}_m^\dagger\left(\boldsymbol{q^0}\right)\hat{\boldsymbol{q}}^{\boldsymbol{1}\dagger} = {\boldsymbol{A}_1'}^T\hat{\boldsymbol{q}}^{\boldsymbol{1}\dagger} - \frac{1}{r}\partial_r\left(r{\boldsymbol{A}_2'}^T\hat{\boldsymbol{q}}^{\boldsymbol{1}\dagger}\right) - \partial_z\left({\boldsymbol{A}_3'}^T\hat{\boldsymbol{q}}^{\boldsymbol{1}\dagger}\right)\,, \tag{E 3a}$$

$$\mathcal{R}^\dagger(\boldsymbol{q^0})\hat{\boldsymbol{q}}^{\boldsymbol{1}\dagger} = \boldsymbol{R}\hat{\boldsymbol{q}}^{\boldsymbol{1}\dagger}\,. \tag{E 3b}$$

Using boundary conditions (4.5) and (D 5), it turns out that the associated boundary term is zero. Assuming that the change of variables $(\hat{v}^1, \hat{v}^{1\dagger}) \rightarrow (\mathrm{i}\hat{v}^1, \mathrm{i}\hat{v}^{1\dagger})$ is used, the various matrices used for the computation of the sensitivity functions read:

$$\begin{aligned}
-\boldsymbol{A}_1' = &\begin{pmatrix} \boldsymbol{\nabla}\cdot\hat{\boldsymbol{u}}^{\boldsymbol{1}} & \frac{1}{r}\partial_r(r\hat{\rho}^1) & \partial_z\hat{\rho}^1 & 0 \\ \frac{1}{\gamma M^2}\partial_r\hat{T}^1 & 0 & 0 & \frac{1}{\gamma M^2}\partial_r\hat{\rho}^1 \\ -\frac{1}{\gamma M^2}\frac{m}{r}\hat{T}^1 & 0 & 0 & -\frac{1}{\gamma M^2}\frac{m}{r}\hat{\rho}^1 \\ \frac{1}{\gamma M^2}\partial_z\hat{T}^1 & 0 & 0 & \frac{1}{\gamma M^2}\partial_z\hat{\rho}^1 \\ 0 & 0 & 0 & 0 \end{pmatrix} - 2\gamma(\gamma-1)\frac{M^2}{Re}\begin{pmatrix} 0 & 0 & 0 & 0 \\ 0 & 0 & 0 & 0 \\ 0 & 0 & 0 & 0 \\ 0 & 0 & 0 & 0 \\ 0 & \frac{1}{r}\hat{\tau}^1_{\theta\theta} & 0 & 0 \end{pmatrix} \\
&+\begin{pmatrix} 0 & 0 & 0 & 0 \\ \boldsymbol{u^0}\cdot\boldsymbol{\nabla}\hat{u}^1 & \rho^0\partial_r\hat{u}^1 & \rho^0\partial_r\hat{w}^1 & 0 \\ \boldsymbol{u^0}\cdot\boldsymbol{\nabla}\hat{v}^1 & \rho^0\frac{1}{r}\partial_r(r\hat{v}^1) & \rho^0\partial_z\hat{v}^1 & 0 \\ \boldsymbol{u^0}\cdot\boldsymbol{\nabla}\hat{w}^1 & \rho^0\partial_r\hat{w}^1 & \rho^0\partial_z\hat{w}^1 & 0 \\ \boldsymbol{u^0}\cdot\boldsymbol{\nabla}\hat{T}^1 + T^0\boldsymbol{\nabla}\cdot\hat{\boldsymbol{u}}^{\boldsymbol{1}} & \rho^0\frac{1}{r}\partial_r(r\hat{T}^1) & \rho^0\partial_z\hat{T}^1 & \rho^0\boldsymbol{\nabla}\cdot\hat{\boldsymbol{u}}^{\boldsymbol{1}} \end{pmatrix} \\
&+\begin{pmatrix} 0 & 0 & 0 & 0 \\ \hat{\boldsymbol{u}}^{\boldsymbol{1}}\cdot\boldsymbol{\nabla}u^0 & \hat{\rho}^1\partial_r u^0 & \hat{\rho}^1\partial_r w^0 & 0 \\ 0 & 0 & 0 & 0 \\ \hat{\boldsymbol{u}}^{\boldsymbol{1}}\cdot\boldsymbol{\nabla}w^0 & \hat{\rho}^1\partial_r w^0 & \hat{\rho}^1\partial_z w^0 & 0 \\ \hat{\boldsymbol{u}}^{\boldsymbol{1}}\cdot\boldsymbol{\nabla}T^0 + \hat{T}^1\boldsymbol{\nabla}\cdot\boldsymbol{u^0} & \hat{\rho}^1\frac{1}{r}\partial_r(rT^0) & \hat{\rho}^1\partial_z T^0 & \hat{\rho}^1\boldsymbol{\nabla}\cdot\boldsymbol{u^0} \end{pmatrix},
\end{aligned}$$

$$-\boldsymbol{A}_2' = \begin{pmatrix} \hat{u}^1 & \hat{\rho}^1 & 0 & 0 \\ \frac{1}{\gamma M^2}\hat{T}^1 & 0 & 0 & \frac{1}{\gamma M^2}\hat{\rho}^1 \\ 0 & 0 & 0 & 0 \\ 0 & 0 & 0 & 0 \\ 0 & 0 & 0 & 0 \end{pmatrix} - 2\gamma(\gamma-1)\frac{M^2}{Re}\begin{pmatrix} 0 & 0 & 0 & 0 \\ 0 & 0 & 0 & 0 \\ 0 & 0 & 0 & 0 \\ 0 & 0 & 0 & 0 \\ 0 & \hat{\tau}^1_{rr} & \hat{\tau}^1_{rz} & 0 \end{pmatrix}$$
$$+\begin{pmatrix} 0 & 0 & 0 & 0 \\ 0 & \rho^0\hat{u}^1 & 0 & 0 \\ 0 & 0 & 0 & 0 \\ 0 & 0 & \rho^0\hat{u}^1 & 0 \\ 0 & \rho^0\hat{T}^1 & 0 & \rho^0\hat{u}^1 \end{pmatrix} + \begin{pmatrix} 0 & 0 & 0 & 0 \\ 0 & \hat{\rho}^1 u^0 & 0 & 0 \\ 0 & 0 & 0 & 0 \\ 0 & 0 & \hat{\rho}^1 u^0 & 0 \\ 0 & \hat{\rho}^1 T^0 & 0 & \hat{\rho}^1 u^0 \end{pmatrix},$$

$$-\boldsymbol{A}_3' = \begin{pmatrix} \hat{w}^1 & 0 & \hat{\rho}^1 & 0 \\ 0 & 0 & 0 & 0 \\ 0 & 0 & 0 & 0 \\ \frac{1}{\gamma M^2}\hat{T}^1 & 0 & 0 & \frac{1}{\gamma M^2}\hat{\rho}^1 \\ 0 & 0 & 0 & 0 \end{pmatrix} - 2\gamma(\gamma-1)\frac{M^2}{Re}\begin{pmatrix} 0 & 0 & 0 & 0 \\ 0 & 0 & 0 & 0 \\ 0 & 0 & 0 & 0 \\ 0 & 0 & 0 & 0 \\ 0 & \hat{\tau}^1_{rz} & \hat{\tau}^1_{zz} & 0 \end{pmatrix}$$
$$+\begin{pmatrix} 0 & 0 & 0 & 0 \\ 0 & \rho^0\hat{w}^1 & 0 & 0 \\ 0 & 0 & 0 & 0 \\ 0 & 0 & \rho^0\hat{w}^1 & 0 \\ 0 & 0 & \rho^0\hat{T}^1 & \rho^0\hat{w}^1 \end{pmatrix} + \begin{pmatrix} 0 & 0 & 0 & 0 \\ 0 & \hat{\rho}^1 w^0 & 0 & 0 \\ 0 & 0 & 0 & 0 \\ 0 & 0 & \hat{\rho}^1 w^0 & 0 \\ 0 & 0 & \hat{\rho}^1 T^0 & \hat{\rho}^1 w^0 \end{pmatrix},$$

$$\boldsymbol{R} = \begin{pmatrix} 0 & 0 & 0 & 0 \\ \hat{u}^1 & 0 & 0 & 0 \\ \hat{v}^1 & 0 & 0 & 0 \\ \hat{w}^1 & 0 & 0 & 0 \\ \hat{T}^1 & 0 & 0 & 0 \end{pmatrix}.$$

REFERENCES

Achenbach, E. 1974 Vortex shedding from spheres. *J. Fluid Mech.* **62**, 209–221.

Airiau, C., Bottaro, A., Walther, S. & Legendre, D. 2003 A methodology for optimal laminar flow control: Application to the damping of tollmien-schlichting waves in a boundary layer. *Phys. Fluids* **15** (5), 1131–1145.

Bardos, C. & Pironneau, O. 2003 Derivatives and control in the presence of shocks. *Comput. Fluid Dynam. J.* **11**, 383–392.

Barkley, D. 2006 Linear analysis of the cylinder wake mean flow. *Europhys. Lett.* **75**, 750–756.

Barkley, D., Gomes, M.G.M. & Henderson, R.D. 2002 Three-dimensional instability in flow over a backward-facing step. *J. Fluid Mech.* **473**, 167–190.

Berger, E., Scholz, D. & Schumm, M. 1990 Coherent vortex structures in the wake of a sphere and a circular disk at rest and under forced vibrations. *J. Fluids Struct.* **4**, 231–257.

Bers, A. 1975 *Plasma physics*, chap. Linear waves and instabilities, pp. 117–215. De Witt, C. and Peyraud, J.

Bottaro, A., Corbett, P. & Luchini, P. 2003 The effect of base flow variation on flow stability. *J. Fluid Mech.* **476**, 293–302.

Bouhadji, A. & Braza, M. 2003 Physical analysis by numerical simulation of organised modes and shock-vortex interaction in transonic flows around an aerofoil. part 1: mach number effect. *J. Comp. and Fluids* **32**, 1233–1260.

Briggs, R.J. 1964 *Electron stream interaction with plasmas*. M.I.T. Press.

Chomaz, J.-M. 2005 Global instabilities in spatially developing flows: Non-normality and nonlinearity. *Annu. Rev. Fluid. Mech.* **37**, 357–392.

Chomaz, J.-M., Huerre, P. & Redekopp, L.G. 1988 Bifurcations to local and global modes in spatially developing flows. *Phys. Rev. Lett.* **60**, 25–28.

Chomaz, J.-M., Huerre, P. & Redekopp, L.G. 1990 The effect of nonlinearity and forcing on global modes. In *Proc. Conf. on new trends in nonlinear dynamcs and pattern-forming phenomena: The geometry of nonequilibrium*, , vol. 237, pp. 259–274. NATO ASI Series B, Plenum, edited by P. Coulet & P. Huerre.

Collis, S.S., Ghayour, K., Heinkenschloss, M., Ulbrich, M. & Ulbrich, S. 2002 Optimal control of unsteady compressible viscous flows. *Int. J. Numer. Meth. Fluids* **40**, 1401–1429.

Colonius, T. 2004 Modeling artificial boundary conditions for compressible flow. *Annu. Rev. Fluid Mech.* **36**, 315–345.

Crouch, J.D., Garbaruk, A. & Magidov, D. 2007 Predicting the onset of flow unsteadiness based on global instability. *J. Comput. Phys.* **224**, 924–940.

Crouch, J.D., Garbaruk, A., Shur, M. & Strelets, M. 2002 Predicting buffet onset from the temporal instability of steady rans solutions. *Bull. Am. Phys. Soc.* **47**, 68.

Davis, T. A. 2004 A column pre-ordering strategy for the unsymmetric-pattern multifrontal method. *ACM Transactions on Mathematical Software* **30** (2), 165–195.

Davis, T. A. & Duff, I.S. 1997 An unsymmetric-pattern multifrontal method for sparse lu factorization. *SIAM Journal on Matrix Analysis and Applications* **18** (1), 140–158.

Deprés, D., Reijasse, P. & Dussauge, J.-P. 2004 Analysis of unsteadiness in afterbody transonic flows. *AIAA Journal* **42** (12), 2541–2550.

Di Cesare, N. & Pironneau, O. 2000 Shock sensitivity analysis. *Comput. Fluid Dynam. J.* **9**, 1–15.

Ding, Y. & Kawahara, M. 1999 Three-dimensional linear stability analysis of incompressible viscous flows using finite element method. *Int. J. Num. Meth. Fluids* **31**, 451–479.

Ehrenstein, U. & Gallaire, F. 2005 On two-dimensional temporal modes in spatially evolving open flows: the flat-plate boundary layer. *J. Fluid Mech.* **536**, 209–218.

Fabre, D., Auguste, F. & Magnaudet, J. 2008 Bifurcations and symmetry breaking in the wake of axisymmetric bodies. *Phys. Fluids* **20** (5), 051702 1–4.

Flodrops, J.-P. & Desse, J.-M. 1985 Sillage d'un culot axisymétrique. *Tech. Rep.* 85/19. Institut de Mécanique des Fluides de Lille, France.

Fornberg, B. 1988 Steady viscous flow past a sphere at high reynolds number. *J. Fluid Mech.* **190**, 471–489.

Fuchs, H.V., Mercker, E. & Michel, U. 1979 Large-scale coherent structures in the wake of axisymmetric bodies. *J. Fluid Mech.* **93**, 185–207.

Giannetti, F. & Luchini, P. 2006 Structural sensitivity of the first instability of the cylinder wake. *J. Fluid Mech.* **581**, 167–197.

Gunzburger, M.D. 1997 Introduction into mathematical aspects of flow control and optimization. In *Lecture series 1997-05 on inverse design and optimization methods*. Von Kármán Institute for Fluid Dynamics.

Gunzburger, M.D. 1999 Sensitivities, adjoints and flow optimization. *Int. J. Numer. Meth. Fluids* **31** (1), 53–78.

Hall, M.C.G. 1986 Application of adjoint sensitivity theory to an atmospheric general circulation model. *J. Atmospheric Sci.* **43**, 2644–2651.

Hill, D.C. 1995 Adjoint systems and their role in the receptivity problem for boundary layers. *J. Fluid Mech.* **292**, 183–204.

Jackson, C.P. 1987 A finite-element study of the onset of vortex shedding in flow past variously shaped bodies. *J. Fluid Mech.* **182**, 23–45.

Jameson, A. 1998 Aerodynamic design via control theory. *J. Sci. Comput.* **3**, 233–260.

Jameson, A., Martinelli, L. & Pierce, N.A. 1998 Fluid dynamics optimum aerodynamic design using the navier-stokes equations. *Theoret. Comput. Fluid Dynamics* **10**, 213–237.

Johnson, T.A. & Patel, V.C. 1999 Flow past a sphere up to a reynolds number of 300. *J. Fluid Mech.* **378**, 19–70.

Landahl, M.T. 1980 A note on an algebraic instability of inviscid parallel shear flows. *J. Fluid Mech.* **98**, 243–251.

Mair, W.A. 1965 The effect of a rear-mounted disc on the drag of a blunt-based body of revolution. *Aeronaut. Q.* **16**, 350–360.

Marquet, O., Lombardi, M., Chomaz, J.-M., Sipp, D. & Jacquin, L. 2008*a* Direct and

adjoint global modes of a recirculation bubble: lift-up and convective nonnormalities. *J. Fluid Mech. (in press)* .

Marquet, O., Sipp, D. & Jacquin, L. 2008*b* Sensitivity analysis and passive control of the cylinder flow. *J. Fluid Mech. (in press)* .

Matsumoto, J. & Kawahara, M. 2000 Stable shape identification for fluid-structure interaction problem using mini element. *J. Appl. Mech.* **3**, 263–274.

Meliga, P., Chomaz, J.-M. & Sipp, D. 2008*a* Global mode interaction and pattern selection in the wake of a disk: a weakly nonlinear expansion. *Submitted to the J. Fluid. Mech.* .

Meliga, P., Chomaz, J.-M. & Sipp, D. 2008*b* Unsteadiness in the wake of disks and spheres: instability, receptivity and control using direct and adjoint global stability analyses. *Submitted to the J. Fluid. Struc.* .

Meliga, P., Sipp, D. & Chomaz, J.-M. 2008*c* Absolute instability in axisymmetric wakes: compressible and density variation effects. *J. Fluid Mech.* **600**, 373–401.

Mohammadi, B. & Pironneau, O. 2004 Shape optimization in fluid mechanics. *Annu. Rev. Fluid Mech.* **36**, 255–279.

Monkewitz, P.A., Bechert, D., Barsikow, B. & Lehmann, B. 1990 Self-excited oscillations and mixing in a heated round jet. *J. Fluid Mech.* **213**, 611–639.

Natarajan, R. & Acrivos, A. 1993 The instability of the steady flow past spheres and disks. *J. Fluid Mech.* **254**, 323–344.

Ormières, D. & Provansal, M. 1998 Transition to turbulence in the wake of a sphere. *Phys. Rev. Lett.* **83**, 80–83.

Pavithran, S. & Redekopp, L.G. 1989 The absolute-convective transition in subsonic mixing layers. *Phys. Fluids A* **1** (10), 1736–1739.

Pironneau, O. 1984 *Optimal shape design for elliptic systems*. Springer Verlag.

Pralits, J.O., Airiau, C., Hanifi, A. & Henningson, D.S. 2000 Sensitivity analysis using adjoint parabolized stability equations for compressible flows. *Flow, Turb. Comb.* **65**, 321–346.

Pralits, J.O., Hanifi, A. & Henningson, D.S. 2002 Adjoint-based optimization of steady suction for disturbance control in incompressible flows. *J. Fluid. Mech.* **476**, 129–161.

Robinet, J.-C. 2007 Bifurcations in shock-wave/laminar-boundary layer interaction: global instability approach. *J. Fluid Mech.* **579**, 85–112.

Rowley, C.W., Colonius, T. & Murray, R.M. 2004 Model reduction for compressible flows using pod and galerkin projection. *Physica D* **189**, 115–129.

Schmid, P.J. 2007 Nonmodal stability theory. *Annu. Rev. Fluid. Mech.* **39**, 129–162.

Sevilla, A. & Martínez-Bazàn, C. 2004 Vortex shedding in high reynolds number axisymmetric bluff-body wakes: Local linear instability and global bleed control. *Phys. Fluids* **16** (9), 3460–3469.

Siegel, S.G. & Fasel, H.F. 2001 Effect of forcing on the wake drag of an axisymmetric bluff body. *AIAA Paper 2001-0736* .

Sipp, D. & Lebedev, A. 2007 Global stability of base and mean flows: a general approach and its applications to cylinder and open cavity flows. *J. Fluid Mech.* **593**, 333–358.

Soteriou, M.C. & Ghoniem, A.F. 1995 Effects of the free-stream density ratio on free and forced spatially developing shear layers. *Phys. Fluids* **7** (8), 2036–2051.

Strykowski, P. J. & Sreenivasan, K.R. 1990 On the formation and suppression of vortex shedding at 'low' reynolds numbers. *J. Fluid Mech.* **218**, 71–107.

Theofilis, V. 2003 Advances in global linear instability analysis of nonparallel and three-dimensional flows. *Prog. Aerospace Sci.* **39**, 249–315.

Theofilis, V. & Colonius, T. 2004 Three-dimensional instabilities of compressible flow over open cavities: direct solution of the biglobal eigenvalue problem. *AIAA Paper 2004-2544* .

Trefethen, L.N., Trefethen, A.E., Reddy, S.C. & Driscoll, T.A. 1993 Hydrodynamic stability without eigenvalues. *Science* **261**, 578–584.

Tumin, A. 1996 Receptivity of pipe poiseuille flow. *J. Fluid Mech.* **315**, 119–137.

Weickgenannt, A. & Monkewitz, P.A. 2000 Control of vortex shedding in an axisymmetric bluff body wake. *Eur. J. Mech. B/Fluids* **19**, 789–812.

Zebib, A. 1987 Stability of a viscous flow past a circular cylindar. *J. Engng Math.* **21**, 155–165.

CHAPTER
SIX

A STEP TOWARDS THE CONTROL OF AFTERBODY FLOW UNSTEADINESS

This last chapter is devoted to the control of a compressible afterbody configuration. It is presented under the form of a second article in preparation, closely connected to that provided in chapter 5. A theoretical framework is derived, that allows to predict beforehand the effect of a small-amplitude forcing on the growth rate of an unstable global mode. The application to various open-loop controls is discussed, including additional control devices acting as body forces, heat sources modeling gas discharges, and mass injection. A physical interpretation for the effect of base bleed is also proposed.

keywords: compressible flows, sensitivity analysis, control, base bleed.

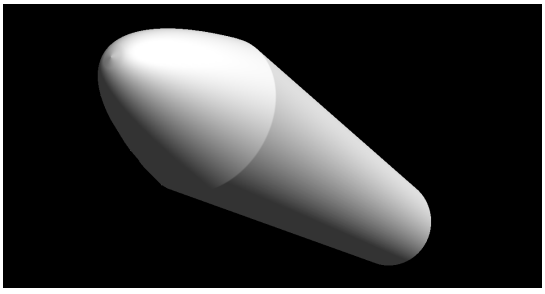

Manuscript in preparation

Global stability and adjoint-based sensitivity analyses for compressible flows - Part II: application to open-loop control.

PHILIPPE MELIGA[1], DENIS SIPP[1] AND JEAN-MARC CHOMAZ[1,2]

[1]ONERA/DAFE, 8 rue des Vertugadins, 92190 Meudon, France
[2]LadHyX, CNRS-Ecole Polytechnique, 91128 Palaiseau, France

A general formalism is developed for the open-loop control of unstable global modes in compressible flows, up to the high subsonic regime. It is based on the so-called sensitivity analysis to steady forcing, which relies on the evaluation of gradients using adjoint methods and aims at predicting beforehand the effect of a steady forcing on a given eigenvalue. Such a formalism has been originally formulated by Hill (1992) and Marquet *et al.* (2008), who studied the effect of momentum forcing on the global stability of the incompressible wake past a circular cylinder. In its present extension to the fully compressible regime, it encompasses new control methods including mass and heat sources and wall forcing, for instance base blowing or wall cooling.

This theoretical formalism is applied to a compressible afterbody flow. We show that the oscillating global mode which triggers the periodic state arising at higher Reynolds numbers can be stabilized if a small control ring is mounted past the main body along the separation line, or if axisymmetric heat sources modeling localized discharges are added within the recirculating bubble. The investigation of wall forcing at the base shows that a stabilizing effect can be obtained by blowing fluid through the whole base, a method also termed base bleed, or by cooling the inner region of the base. However, the sensitivity of the global mode to a pure thermal control is found to be limited.

The stabilizing effect of base bleed is further investigated in the light of the sensitivity analysis, and a physical interpretation is proposed, based on the competition between production and downstream advection of disturbances. We show that blowing through the base mainly enhances the advection of the perturbations by weakening the shear along the separation line. Strikingly, it turns out that this mechanism mainly acts through the cross-stream momentum component, whereas previous interpretations based on local stability analyses involved only the streamwise component. These results show the importance of studying such recirculating flows in a global framework.

1. Introduction

The transonic flow past an afterbody is dominated by an instability of helical modes of azimuthal wavenumbers $m = \pm 1$, resulting in the low-frequency shedding of large-scale coherent structures. This vortex-shedding may be detrimental to the engineering application, as it may increase drag or induce flow vibrations. The prediction for the occurrence

of these undesirable flow conditions is thus needed to guide future engineering designs, so as to improve the aerodynamic performances and reliability of launch vehicles. To alleviate or control such unsteadiness, a better understanding of the physical mechanisms is also required.

In the first part of this study, herein referred to as Part I, the flow past an axisymmetric afterbody at zero angle of attack and high subsonic Mach numbers has been investigated by means of a fully compressible global stability analysis. We have shown that the steady axisymmetric wake that develops at low Reynolds numbers is first destabilized by a stationary global mode of azimuthal wavenumber $m = 1$, leading to a 3D steady state, and that a second instability eventually occurred at a larger Reynolds number, for an oscillating $m = 1$ global eigenmode. From Direct Numerical Simulations (DNS) and experimental observations carried out on other configurations of axisymmetric wakes, it turns out that this latter instability mode dominates the dynamics of the fully 3D flow at large Reynolds numbers, hence explaining the occurrence of a fully 3D periodic state (Ormières & Provansal 1998). Such a domination of the periodic instability mode over the stationary mode, despite the fact that the latter is the first to destabilize the axisymmetric base flow has recently been explained using slow manifold theory and normal forms (Fabre *et al.* 2008; Meliga *et al.* 2008). We are now interested in the problem of open-loop control of the afterbody unsteadiness.

Control of vortex-shedding in the wake of bluff bodies has been a subject of great interest in the last decades (see Roshko 1954; Schumm *et al.* 1994; Roussopoulos & Monkewitz 1996, among others). A review on the various methods used for experimental and numerical control of the flow over bluff bodies can be found in Choi *et al.* (2008). In this study, we focus on open-loop methods, which rely on the simple idea that some fixed modification in the flow conditions is susceptible to affect the dynamics of the flow. In the context of wake flows, a simple open-loop strategy is based on the action of a small secondary body, referred to as the control device, generally placed past the main body whose unsteadiness has to be controlled. Strykowski & Sreenivasan (1990) have experimentally investigated how a small control cylinder placed in the wake of the main cylinder could alter the vortex-shedding phenomenon. These authors determined the regions of the flow where the placement of the control cylinder leads to a complete suppression of the phenomenon over a specific range of Reynolds numbers. Moreover, they provided evidence linking vortex-shedding to the onset of a global instability, and the effect of the suitably positioned control device to a damping of this instability. Similar studies have been conducted in the context of afterbody flows. For instance, Mair (1965) found that a significant drag reduction could be achieved by adding a control disk mounted at the rear of the main body and Weickgenannt & Monkewitz (2000) identified different regions of the flow where the control disk can trigger either a sharp increase or a reduction of the vortex-shedding activity.

Other methods can be used. Localized gas discharges acting as volumetric heat sources have been proven fruitful to significantly decrease the drag coefficient and to prevent flow separation for a number of configurations ranging from the cylinder wake to supersonic airflows (Fomin *et al.* 2004; Moreau 2007, among others). As an example, Elias *et al.* (2008) have studied the unsteady flow past a truncated conical body with a central spike, characterized by a pulsating shock wave, and have shown that the use of such discharges allows to completely inhibit the unsteadiness. Wall forcing strategies have also been widely investigated. One could imagine to add porosity or surface roughness. In the context of bluff bodies, it has been early recognized that a mass injection into the wake, also termed base bleed, allows to alleviate unsteadiness (Bearman 1967; Leal & Acrivos 1969, among others), whereas wall cooling strategies were proven fruitful to delay the

transition to turbulence in boundary-layer flows (Diaconis *et al.* 1957; Jack *et al.* 1957). There is no doubt that such approaches can help develop successful controls. Though, they are intrinsically empirical as they generally rely on a 'trial and error' process. Namely one has to estimate the influence of the different control parameters by separately varying each variable. If we take the example of base bleed, this means in practice to test different control domains, bleed flow rates, distributions and further more. For a small control device, it means to test different sizes and shapes of the device, and for each case, evaluate the effect on the disturbance growth by carrying out either experimental measurements or numerical simulations. Consequently, this can be an extremely time-consuming approach if the number of degrees of freedom is large.

This study provides a more systematic approach for the open-loop control of vortex-shedding, viewed as a global instability. We assume that the flow modifications resulting from a steady forcing acts directly at the base flow level. The base flow modification, if occurring in an appropriate region, is then expected to induce structural modifications of the stability problem that may result in a stabilization of the unstable modes. Such an approach is intimately connected with the *sensitivity analysis to base flow modifications* presented in Part I, whose aim is precisely to identify regions of the flow where the stability problem is most affected by small modifications of the base flow. This region can then be identified as the *wavemaker* (Chomaz 2005; Giannetti & Luchini 2006), i.e. the flow region where the instability mechanisms are active. Such an analysis allows to investigate theoretically where and which mechanisms are responsible for the global instability. Still, it fails to answer to the question "How to produce physically relevant base flow modifications susceptible to stabilize the unstable modes?" To this end, seminal studies have been carried out by Hill (1992) and Marquet *et al.* (2008), who investigated theoretically the effect of a momentum forcing on the incompressible flow past a cylinder. These authors modeled the presence of the control device by the steady force it exerts on the base flow, and developed a consistent framework to predict the effect of this force on the flow unsteadiness, thus defining the so-called *sensitivity to a steady force*. They succeeded in identifying specific flow regions where the control cylinder proved fruitful to suppress the vortex-shedding, these results exhibiting a striking agreement with that of Strykowski & Sreenivasan (1990).

In this paper, these sensitivity concepts are extended to the case of nonparallel compressible flows and applied to the control of an afterbody flow in the high subsonic regime. We focus on the stabilization of the oscillating global mode, by predicting beforehand the effect on this mode of a small-amplitude forcing. It should be noted that owing to the complex bifurcation sequence leading to vortex-shedding in axisymmetric wakes, the connection between a damping of this global instability and the suppression of vortex-shedding is not as straightforward as it is in the case of the cylinder flow. However, this investigation stands as a step in the perspective of the full control of afterbody flow unsteadiness. Moreover, it is worthwhile emphasizing that in its compressible extension, the present framework now encompasses the effect of additional mass and heat sources, and also integrates the effect of boundary forcing, which allows to obtain predictive results for wall blowing and wall heating or cooling. In order to account for these different aspects of forcing, the analysis is renamed *sensitivity to a steady forcing*. It should be noted that such sensitivity analyses do not restrict to steady forcing, for instance Pralits *et al.* (2000) characterized theoretically the sensitivity of disturbances to periodic wall conditions and source of momentum in a compressible boundary-layer, assuming that both the base flow and the disturbances develop slowly in the direction parallel to the wall so that parabolic equations can be established to govern their evolution.

Sensitivity analyses may be performed by forward calculations. A stability problem

must then be solved once to identify the global modes of the base flow, and once more for each forcing under consideration. Though, such a procedure is not easily tractable for complex stability problems such as those solved in the present case, as it turns out to be very computationally intensive. As in Part I, the main tool developed here is based on adjoint methods, whose advantage is that the sensitivity of a disturbance can be obtained by solving the state and adjoint equations once (Bewley *et al.* 2000). This formalism can thus be easily extended to provide optimal control strategies with a relatively low computational cost by means of gradient based optimization techniques. Note however that how to practically implement the theoretically predicted optimal controls remains a thorny and open question, that lies out of the scope of the present study.

The paper is organized as follows. The theoretical formulation is presented in § 2, where we recall first the main results issuing from Part I and pertaining to the derivation of the stability eigenproblem and to the sensitivity analysis to base flow modifications in a global compressible framework. We eventually introduce the sensitivity analysis to a steady forcing, based on the determination of gradients through adjoint methods. It is worthwhile emphasizing here that these concepts are not restricted to afterbody flows, and may be used for any open flow with two inhomogeneous directions. We then consider the case of an afterbody flow and its open-loop control, which stands as an application of these techniques. In § 3, we detail the retained configuration and the numerical methods. A description of the unforced steady axisymmetric flow is provided in § 4, where we also present the stationary and oscillating global modes which are reminiscent of that discussed in Part I. We then focus on the stability of the oscillating global mode, that has been said to trigger the vortex-shedding phenomenon at larger Reynolds numbers. Open-loop control by means of volumetric forcing is investigated in § 5.1 to 5.2, where we consider successively the case of momentum forcing and volumetric mass and heat sources. In the case of momentum forcing, the sensitivity analysis is particularized by considering the effect on the oscillating global mode of a small control ring placed at various positions in the wake, whose effect on the base flow is modeled as a pure resistance force. The case of wall forcing is considered in § 5.4. Finally, base bleed strategies are discussed in § 6, where we propose physical interpretations for the stabilizing effect in the light of the sensitivity analysis to base flow modifications.

2. Theoretical formulation

This section is devoted to a description of the theoretical concepts used in the present study. We generalize the framework of Hill (1992) and Marquet *et al.* (2008) to the case of a generic compressible wake flow with suitable inlet, outlet, lateral boundaries and solid walls. For a given eigenvalue, we revisit the concepts of sensitivity to base flow modifications and to steady volumetric and wall forcing. For simplicity, the problem is formulated in cylindrical coordinates (r, θ, z), but this approach can be generalized to other orthogonal curvilinear coordinate systems.

2.1. *Governing equations*

The fluid is taken as a non-homogeneous compressible perfect gas with constant specific heat c_p, thermal conductivity κ, and dynamic viscosity μ, related by a unit Prandtl number. The fluid motion is described by the state vector $\boldsymbol{q} = (\rho, \boldsymbol{u}, T, p)^T$, where ρ is the density, T the temperature, p the pressure and $\boldsymbol{u} = (u, v, w)^T$ the three-dimensional velocity field with u, v and w its radial, azimuthal and streamwise components. $\boldsymbol{q}$ obeys the unsteady compressible Navier-Stokes equations, thus leading to a set of six nonlinear

equations (continuity, momentum, internal energy and perfect gas) formulated in non-conservative variables as

$$\partial_t \rho + \rho \boldsymbol{\nabla} \cdot \boldsymbol{u} + \boldsymbol{u} \cdot \boldsymbol{\nabla} \rho = m \,, \tag{2.1a}$$

$$\rho \partial_t \boldsymbol{u} + \rho \boldsymbol{\nabla} \boldsymbol{u} \cdot \boldsymbol{u} + \frac{1}{\gamma M^2} \boldsymbol{\nabla} p - \frac{1}{Re} \boldsymbol{\nabla} \cdot \boldsymbol{\tau}(\boldsymbol{u}) = \boldsymbol{f} \,, \tag{2.1b}$$

$$\rho \partial_t T + \rho \boldsymbol{u} \cdot \boldsymbol{\nabla} T + p \boldsymbol{\nabla} \cdot \boldsymbol{u} - \gamma(\gamma - 1) \frac{M^2}{Re} \, \boldsymbol{\tau}(\boldsymbol{u}) : \boldsymbol{d}(\boldsymbol{u}) - \frac{\gamma}{PrRe} \boldsymbol{\nabla}^2 T = h \,, \tag{2.1c}$$

$$p - \rho T = 0 \,. \tag{2.1d}$$

that can also be written formally as

$$\mathcal{B}(\boldsymbol{q}) \partial_t \boldsymbol{q} + \mathcal{M}(\boldsymbol{q}, \mathcal{G}) = (\mathscr{s}, 0)^T \,, \tag{2.2}$$

where $\mathscr{s} = (m, \boldsymbol{f}, h)^T$. $\mathcal{B}$ and $\mathcal{M}$ are differential operators and $\mathcal{G}$ is a set of relevant control parameters (Reynolds and Mach numbers, angle of attack...) which is assumed to be constant in the present study, so that the dependence in $\mathcal{G}$ is from now on omitted to ease the notation. As mentioned previously, the present formalism accounts not only for momentum forcing ($\boldsymbol{f}$), but also for mass and heat sources (m, h). Physically, $\boldsymbol{f}$ (resp. m and h) corresponds the volumetric momentum rate per time-unit (resp. volumetric mass and internal energy rates per time-unit). Finally, $\boldsymbol{d}(\boldsymbol{u})$ and $\boldsymbol{\tau}(\boldsymbol{u})$ are the strain and viscous stress tensors defined as

$$\boldsymbol{d}(\boldsymbol{u}) = \frac{1}{2} \left(\boldsymbol{\nabla} \boldsymbol{u} + \boldsymbol{\nabla} \boldsymbol{u}^T \right) \,, \qquad \boldsymbol{\tau}(\boldsymbol{u}) = -\frac{2}{3} (\boldsymbol{\nabla} \cdot \boldsymbol{u}) \, \boldsymbol{I} + \boldsymbol{\nabla} \boldsymbol{u} + \boldsymbol{\nabla} \boldsymbol{u}^T \,. \tag{2.3}$$

Equations (2.1) have been made nondimensional using the body diameter D and the upstream quantities W_∞, ρ_∞, T_∞ and p_∞ as respective velocity, density, temperature and pressure scales. The Reynolds, Mach and Prandtl numbers are defined as

$$Re = \frac{\rho_\infty D W_\infty}{\mu}, \qquad M = \frac{W_\infty}{\sqrt{\gamma R_g T_\infty}}, \qquad Pr = \frac{\mu c_p}{\kappa} \,, \tag{2.4}$$

with R_g and γ the ideal gas constant and the ratio of specific heats. The additional effect of wall forcing is taken into account by defining a specific boundary Γ_c referred to as the control surface, chosen by now as an arbitrary part of the body wall. On Γ_c, the flow is required to satisfy the boundary condition

$$\boldsymbol{u} = \boldsymbol{u_w} \,, \qquad T = T_w \,, \tag{2.5}$$

i.e. we impose a velocity and temperature $\boldsymbol{u_w}$ and T_w corresponding to a subsonic wall injection. The other boundary conditions are for now voluntarily omitted for all other boundaries so as to keep a general point of view. We thus assume in particular that all quantities fulfill appropriate far-field radiation conditions. Note that the boundary condition (2.5) may not be relevant to the case of a subsonic suction, as the number of degrees of freedom corresponding to subsonic inlet and outlet conditions is not the same.

In the following, all governing equations are conveniently written as formal relations between differential operators, whose detailed expressions have been provided in Part I and are not be repeated here for conciseness. The state vector $\boldsymbol{q} = (\rho, \boldsymbol{u}, T, p)^T$ is decomposed into a steady axisymmetric base flow $\boldsymbol{q^0}$ and a three-dimensional perturbation $\boldsymbol{q^1}$ of infinitesimal amplitude ϵ. Furthermore the volumetric and wall forcing are assumed to be steady and axisymmetric, so that $\boldsymbol{q^0}$ is solution of the forced steady, axisymmetric equations, that are written as

$$\mathcal{M}_0(\boldsymbol{q^0}) = (\mathscr{s}, 0)^T \,. \tag{2.6}$$

along with the boundary conditions on Γ_c

$$\boldsymbol{u^0} = \boldsymbol{u_W}\,, \qquad T^0 = T_W\,. \tag{2.7}$$

In (2.6), $\mathcal{M}_0$ is the axisymmetric form of operator $\mathcal{M}$. Since the base flow is axisymmetric, the perturbation is sought under the form of normal modes

$$\boldsymbol{q^1} = \hat{\boldsymbol{q}}^{\boldsymbol{1}}(r,z)e^{(\sigma+\mathrm{i}\omega)t+\mathrm{i}m\theta} + \text{ c.c.}\,, \tag{2.8}$$

where $\hat{\boldsymbol{q}}^{\boldsymbol{1}}$ is the so-called global mode for which both the cross-stream and streamwise directions are eigendirections. The azimuthal wavenumber of the global mode is m, its growth rate and pulsation are σ and ω respectively.

Substituting $\boldsymbol{q} = \boldsymbol{q^0} + \epsilon\boldsymbol{q^1}$ into equations (2.1) yields a system of equations governing the normal mode under the form of a generalized eigenvalue problem for $\lambda = \sigma + \mathrm{i}\omega$ and $\hat{\boldsymbol{q}}^{\boldsymbol{1}} = (\hat{\rho}^1, \hat{\boldsymbol{u}}^{\boldsymbol{1}}, \hat{T}^1, \hat{p}^1)^T$, reading

$$\lambda\mathcal{B}(\boldsymbol{q^0})\hat{\boldsymbol{q}}^{\boldsymbol{1}} + \mathcal{A}_m(\boldsymbol{q^0})\hat{\boldsymbol{q}}^{\boldsymbol{1}} = \boldsymbol{0}\,. \tag{2.9}$$

along with the conditions on Γ_c

$$\hat{\boldsymbol{u}}^{\boldsymbol{1}} = \boldsymbol{0}\,, \qquad \hat{T}^1 = 0\,. \tag{2.10}$$

In (2.9), $\mathcal{A}_m$ is the complex operator obtained from $\mathcal{A} = \partial\mathcal{M}/\partial\boldsymbol{q}$ by replacing the θ derivatives by the product by $\mathrm{i}m$. It should be noted that since all forcing terms have been assumed to be steady, they act only at the base flow level, but do not alter explicitly the disturbance equations. $\mathcal{A}_m$ can be written as $\mathcal{A}_m = \mathcal{C}_m + \mathcal{P}_m$ where $\mathcal{C}_m$ is the advection operator arising from the linearization of the advection terms in (2.1), and $\mathcal{P}_m$ is the source/sink operator encompassing the effect of the source terms in (2.1). In part I, we have shown that operator $\mathcal{C}_m$ can be further split into $\mathcal{C}_m = \mathcal{C}_m^{(A)} + \mathcal{C}_m^{(P)}$, where operator $\mathcal{C}_m^{(A)}$ is the *advection operator* accounting for the advection of disturbances by the base flow, and operator $\mathcal{C}_m^{(P)}$ is the *production operator* accounting for the production of perturbation through the reciprocal advection of the base flow quantities by the perturbation. The total production operator can thus be defined as $\mathcal{C}_m^{(P)} + \mathcal{P}_m$.

Consider now a particular pair $\{\hat{\boldsymbol{q}}^{\boldsymbol{1}}, \lambda = \sigma + \mathrm{i}\omega\}$, associated to a base flow $\boldsymbol{q^0}$, solution of the eigenproblem (2.9). It is explicitly a function of the base flow variables $\lambda = \lambda(\boldsymbol{q^0})$. Though, as seen from equations $(2.6 - 2.7)$, the base flow $\boldsymbol{q^0}$ itself is a function of the volumetric and boundary sources $\mathscr{F}$, $\boldsymbol{u_W}$ and T_W. The eigenvalue is thus also a function of the steady forcing, i.e. $\lambda = \lambda(\boldsymbol{q^0}(\mathscr{F}, \boldsymbol{u_W}, T_W))$.

2.2. *Sensitivity to base flow modifications*

If λ is viewed as a function of $\boldsymbol{q^0}$, variations of a given eigenvalue $\delta\lambda$ can be investigated with respect to small variations of the base flow $\boldsymbol{\delta q^0}$, thus defining the sensitivity analysis to base flow modifications presented in Part I. We recall that $\boldsymbol{\delta q^0}$ is here generic, i.e. we do not require $\boldsymbol{q^0} + \boldsymbol{\delta q^0}$ to be solution of equations (2.6). $\delta\lambda$ and $\boldsymbol{\delta q^0}$ are such that

$$\delta\lambda = \int_\Omega (\boldsymbol{\nabla}_{\rho^0}\lambda \cdot \delta\rho^0 + \boldsymbol{\nabla}_{\boldsymbol{u^0}}\lambda \cdot \boldsymbol{\delta u^0} + \boldsymbol{\nabla}_{T^0}\lambda \cdot \delta T^0 + \boldsymbol{\nabla}_{p^0}\lambda \cdot \delta p^0)\, r\mathrm{d}r\mathrm{d}z\,, \tag{2.11}$$

where $\boldsymbol{\nabla}_{\rho^0}\lambda$, $\boldsymbol{\nabla}_{\boldsymbol{u^0}}\lambda$, $\boldsymbol{\nabla}_{T^0}\lambda$ and $\boldsymbol{\nabla}_{p^0}\lambda$ are complex quantities and define the sensitivities of the eigenvalue λ to a small modification of the base flow density, velocity, temperature and pressure, respectively, and $\cdot$ stands for the canonic hermitian scalar product in $\mathbb{C}^n$. The sensitivity to a small modification of the base flow $\boldsymbol{\delta q^0}$ is then defined as $\boldsymbol{\nabla}_{\boldsymbol{q^0}}\lambda = (\boldsymbol{\nabla}_{\rho^0}\lambda, , \boldsymbol{\nabla}_{\boldsymbol{u^0}}\lambda, \boldsymbol{\nabla}_{T^0}\lambda, \boldsymbol{\nabla}_{p^0}\lambda)^T$, so that

$$\delta\lambda = \int_\Omega \boldsymbol{\nabla}_{\boldsymbol{q^0}}\lambda \cdot \boldsymbol{\delta q^0}\, r\mathrm{d}r\mathrm{d}z\,. \tag{2.12}$$

The sensitivity of the growth rate σ and that of the frequency ω, denoted as $\boldsymbol{\nabla}_{\boldsymbol{q^0}}\sigma$ and $\boldsymbol{\nabla}_{\boldsymbol{q^0}}\omega$ respectively, can be similarly written as

$$\delta\sigma = \int_\Omega \boldsymbol{\nabla}_{\boldsymbol{q^0}}\sigma \cdot \boldsymbol{\delta q^0}\, r\mathrm{d}r\mathrm{d}z\,, \qquad \delta\omega = \int_\Omega \boldsymbol{\nabla}_{\boldsymbol{q^0}}\omega \cdot \boldsymbol{\delta q^0}\, r\mathrm{d}r\mathrm{d}z\,, \tag{2.13}$$

with $\boldsymbol{\nabla}_{\boldsymbol{q^0}}\sigma = \mathrm{Re}(\boldsymbol{\nabla}_{\boldsymbol{q^0}}\lambda)$ and $\boldsymbol{\nabla}_{\boldsymbol{q^0}}\omega = -\mathrm{Im}(\boldsymbol{\nabla}_{\boldsymbol{q^0}}\lambda)$ being now real vectors.

In Part I, the sensitivity functions have been derived using a Lagrangian technique that is classically used in flow control and optimization problems (Gunzburger 1997, 1999; Airiau *et al.* 2003). We have shown that these functions depend simultaneously on the perturbation $\hat{\boldsymbol{q}}^{\boldsymbol{1}}$ and on the adjoint perturbation $\hat{\boldsymbol{q}}^{\boldsymbol{1\dagger}} = (\hat{\rho}^{1\dagger}, \hat{\boldsymbol{u}}^{\boldsymbol{1\dagger}}, \hat{T}^{1\dagger}, \hat{p}^{1\dagger})^T$, solution of the generalized eigenproblem

$$\lambda^* \mathcal{B}(\boldsymbol{q^0})\hat{\boldsymbol{q}}^{\boldsymbol{1\dagger}} + \mathcal{A}_m^\dagger(\boldsymbol{q^0})\hat{\boldsymbol{q}}^{\boldsymbol{1\dagger}} = \boldsymbol{0}\,, \tag{2.14}$$

where the subscript $*$ stands for the complex conjugate, and operator $\mathcal{A}_m^\dagger$ is the adjoint operator of $\mathcal{A}_m$, so that

$$\int_\Omega \hat{\boldsymbol{a}} \cdot \left(\mathcal{A}_m \hat{\boldsymbol{b}}\right) r\mathrm{d}r\mathrm{d}z = \int_\Omega \left(\mathcal{A}_m^\dagger \hat{\boldsymbol{a}}\right) \cdot \hat{\boldsymbol{b}}\, r\mathrm{d}r\mathrm{d}z\,, \tag{2.15}$$

for any complex vectors $\hat{\boldsymbol{a}}$ and $\hat{\boldsymbol{b}}$ fulfilling the disturbance and adjoint disturbance boundary conditions. In particular on Γ_c, the boundary condition for the adjoint perturbation reads

$$\hat{\boldsymbol{u}}^{\boldsymbol{1\dagger}} = \boldsymbol{0}\,, \qquad \hat{T}^{1\dagger} = 0\,. \tag{2.16}$$

The adjoint perturbations are normalized with respect to the perturbation, so that

$$\int_\Omega (\hat{\rho}^{1\dagger\,*}\hat{\rho}^1 + \rho^0 \hat{\boldsymbol{u}}^{\boldsymbol{1\dagger}\,*} \cdot \hat{\boldsymbol{u}}^{\boldsymbol{1}} + \rho^0 \hat{T}^{1\dagger\,*}\hat{T}^1) r\mathrm{d}r\mathrm{d}z = 1\,. \tag{2.17}$$

All details concerning the specific derivation of the sensitivity functions are provided in Part I, and are briefly recalled in Appendix A. We give here only the resulting analytical expressions in terms of the sensitivity function $\boldsymbol{\nabla}_{\boldsymbol{q^0}}\lambda$:

$$\begin{aligned}\boldsymbol{\nabla}_{\rho^0}\lambda = &-\lambda^*\left(\hat{\boldsymbol{u}}^{\boldsymbol{1\dagger}} \cdot \hat{\boldsymbol{u}}^{\boldsymbol{1}\,*} + \hat{T}^{1\dagger}\hat{T}^{1\,*}\right) - \hat{\boldsymbol{u}}^{\boldsymbol{1\dagger}\,T} \cdot \left(\boldsymbol{\nabla}\boldsymbol{u^0} \cdot \hat{\boldsymbol{u}}^{\boldsymbol{1}\,*} + \boldsymbol{\nabla}\hat{\boldsymbol{u}}^{\boldsymbol{1*}} \cdot \boldsymbol{u^0}\right) + \boldsymbol{\nabla}\hat{\rho}^{1\dagger} \cdot \hat{\boldsymbol{u}}^{\boldsymbol{1}\,*} \\ &- \hat{T}^{1\dagger}\left(\hat{\boldsymbol{u}}^{\boldsymbol{1}\,*} \cdot \boldsymbol{\nabla}T^0 + \boldsymbol{u^0} \cdot \boldsymbol{\nabla}\hat{T}^{1\,*}\right) + \hat{p}^{1\dagger}\hat{T}^{1\,*}\,, \end{aligned} \tag{2.18a}$$

$$\begin{aligned}\boldsymbol{\nabla}_{\boldsymbol{u^0}}\lambda = \;& \rho^0\left(-\boldsymbol{\nabla}\hat{\boldsymbol{u}}^{\boldsymbol{1}\,*\,T} \cdot \hat{\boldsymbol{u}}^{\boldsymbol{1\dagger}} + \boldsymbol{\nabla}\hat{\boldsymbol{u}}^{\boldsymbol{1\dagger}} \cdot \hat{\boldsymbol{u}}^{\boldsymbol{1}\,*}\right) + \hat{\rho}^{1\,*}\left(-\boldsymbol{\nabla}\boldsymbol{u^0}^T \cdot \hat{\boldsymbol{u}}^{\boldsymbol{1\dagger}} + \boldsymbol{\nabla}\hat{\boldsymbol{u}}^{\boldsymbol{1\dagger}} \cdot \boldsymbol{u^0}\right) \\ &- \lambda^*\hat{\rho}^{1\,*}\hat{\boldsymbol{u}}^{\boldsymbol{1\dagger}} + \hat{\rho}^{1\,*}\boldsymbol{\nabla}\hat{\rho}^{1\dagger} - \hat{T}^{1\dagger}(\hat{\rho}^{1\,*}\boldsymbol{\nabla}T^0 + \rho^0\boldsymbol{\nabla}\hat{T}^{1\,*}) + \boldsymbol{\nabla}(\hat{T}^{1\dagger}\hat{p}^{1\,*}) \\ &- 2\gamma(\gamma-1)\frac{M^2}{Re}\boldsymbol{\nabla} \cdot \left(\hat{T}^{1\dagger}\boldsymbol{\tau}(\hat{\boldsymbol{u}}^{\boldsymbol{1}})^*\right)\,, \end{aligned} \tag{2.18b}$$

$$\boldsymbol{\nabla}_{T^0}\lambda = \quad \boldsymbol{\nabla} \cdot \left(\hat{T}^{1\dagger}(\hat{\rho}^{1\,*}\boldsymbol{u^0} + \rho^0\hat{\boldsymbol{u}}^{\boldsymbol{1}\,*})\right) + \hat{p}^{1\dagger}\hat{\rho}^{1\,*}\,, \tag{2.18c}$$

$$\boldsymbol{\nabla}_{p^0}\lambda = \quad -\hat{T}^{1\dagger}\boldsymbol{\nabla} \cdot \hat{\boldsymbol{u}}^{\boldsymbol{1}\,*}\,. \tag{2.18d}$$

Moreover, considering the specific modifications of the advection operator $\mathcal{C}_m^{(A)}$, it has been shown possible to define sensitivity functions to a modification of the advection operator $\boldsymbol{\nabla}_{\boldsymbol{q^0}}^{(A)}\lambda = (\boldsymbol{\nabla}_{\rho^0}^{(A)}\lambda, \boldsymbol{\nabla}_{\boldsymbol{u^0}}^{(A)}\lambda, \boldsymbol{\nabla}_{T^0}^{(A)}\lambda, \boldsymbol{\nabla}_{p^0}^{(A)}\lambda)^T$. The following expressions have been

obtained:

$$\boldsymbol{\nabla}^{(A)}_{\rho^0}\lambda = -\left(\boldsymbol{\nabla}\hat{\boldsymbol{u}}^{\mathbf{1*}}\cdot\boldsymbol{u}^{\mathbf{0}}\right)\cdot\hat{\boldsymbol{u}}^{\mathbf{1\dagger}} - \hat{T}^{1\dagger}\boldsymbol{u}^{\mathbf{0}}\cdot\boldsymbol{\nabla}\hat{T}^{1\,*}\,, \tag{2.19a}$$

$$\begin{aligned}\boldsymbol{\nabla}^{(A)}_{\boldsymbol{u}^{\mathbf{0}}}\lambda = \quad & \rho^0\left(-\boldsymbol{\nabla}\hat{\boldsymbol{u}}^{\mathbf{1*}\,T}\cdot\hat{\boldsymbol{u}}^{\mathbf{1\dagger}}\right) + \hat{\rho}^{1\,*}\left(-\boldsymbol{\nabla}\boldsymbol{u}^{\mathbf{0}\,T}\cdot\hat{\boldsymbol{u}}^{\mathbf{1\dagger}} + \boldsymbol{\nabla}\hat{\boldsymbol{u}}^{\mathbf{1\dagger}}\cdot\boldsymbol{u}^{\mathbf{0}}\right)\\ & + \hat{\rho}^{1\,*}\boldsymbol{\nabla}\hat{\rho}^{1\dagger} - \rho^0\hat{T}^{1\dagger}\boldsymbol{\nabla}\hat{T}^{1\,*} - \hat{\rho}^{1\,*}\hat{T}^{1\dagger}\boldsymbol{\nabla}T^0\,,\end{aligned} \tag{2.19b}$$

$$\boldsymbol{\nabla}^{(A)}_{T^0}\lambda = \quad \boldsymbol{\nabla}\cdot\left(\hat{\rho}^{1\,*}\hat{T}^{1\dagger\,*}\boldsymbol{u}^{\mathbf{0}}\right)\,, \tag{2.19c}$$

$$\boldsymbol{\nabla}^{(A)}_{p^0}\lambda = \quad 0\,. \tag{2.19d}$$

We have also defined sensitivity functions to a modification of the total production operator $\mathcal{C}^{(P)}_m + \mathcal{P}_m$ encompassing both the production mechanism arising from the advection of the base flow quantities by the perturbation and that owing to the source/sink terms of the governing equations. These sensitivity functions $\boldsymbol{\nabla}^{(P)}_{\boldsymbol{q}^{\mathbf{0}}}\lambda$, referred to as the production sensitivity functions, are such that

$$\boldsymbol{\nabla}^{(P)}_{\boldsymbol{q}^{\mathbf{0}}}\lambda = \boldsymbol{\nabla}_{\boldsymbol{q}^{\mathbf{0}}}\lambda - \boldsymbol{\nabla}^{(A)}_{\boldsymbol{q}^{\mathbf{0}}}\lambda\,. \tag{2.20}$$

An important point raised in Part I concerns the choice of primitive or conservative variables to carry out such a sensitivity analysis. We have shown in particular that a set of *conservative sensitivity functions* $\boldsymbol{\nabla}_{\rho^0}\lambda$, $\boldsymbol{\nabla}_{\rho^0\boldsymbol{u}^{\mathbf{0}}}\lambda$, $\boldsymbol{\nabla}_{\rho^0 T^0}\lambda$ and $\boldsymbol{\nabla}_{p^0}\lambda$ could be elegantly deduced from the *primitive sensitivity functions* $\boldsymbol{\nabla}_{\rho^0}\lambda$, $\boldsymbol{\nabla}_{\boldsymbol{u}^{\mathbf{0}}}\lambda$, $\boldsymbol{\nabla}_{T^0}\lambda$ and $\boldsymbol{\nabla}_{p^0}\lambda$ as

$$\boldsymbol{\nabla}_{\rho^0}\lambda = \boldsymbol{\nabla}_{\rho^0}\lambda - \frac{\boldsymbol{u}^{\mathbf{0}}}{\rho^0}\cdot\boldsymbol{\nabla}_{\boldsymbol{u}^{\mathbf{0}}}\lambda - \frac{T^0}{\rho^0}\boldsymbol{\nabla}_{T^0}\lambda\,, \tag{2.21a}$$

$$\boldsymbol{\nabla}_{\rho^0\boldsymbol{u}^{\mathbf{0}}}\lambda = \frac{1}{\rho^0}\boldsymbol{\nabla}_{\boldsymbol{u}^{\mathbf{0}}}\lambda\,, \tag{2.21b}$$

$$\boldsymbol{\nabla}_{\rho^0 T^0}\lambda = \frac{1}{\rho^0}\boldsymbol{\nabla}_{T^0}\lambda\,, \tag{2.21c}$$

the sensitivity function $\boldsymbol{\nabla}_{p^0}\lambda$ being unchanged. The same transformation can finally be used to derive the conservative advection and production sensitivity functions.

2.3. *Sensitivity to a steady forcing*

If λ is viewed as a function of the forcing terms $\mathscr{I}$, $\boldsymbol{u}_{\boldsymbol{W}}$ and T_W, the variation $\delta\lambda$ can similarly be investigated with respect to the small variations $\delta\mathscr{I}$, $\boldsymbol{\delta u}_{\boldsymbol{W}}$ and δT_W, thus defining the sensitivity analysis to a modification of the steady forcing, which is termed *sensitivity analysis to a steady forcing* for conciseness. The variations are now such that

$$\begin{aligned}\delta\lambda = & \int_\Omega \left(\boldsymbol{\nabla}_m\lambda\cdot\delta m + \boldsymbol{\nabla}_{\boldsymbol{f}}\lambda\cdot\boldsymbol{\delta f} + \boldsymbol{\nabla}_h\lambda\cdot\delta h\right) r\mathrm{d}r\mathrm{d}z\\ & + \int_{\Gamma_c}\left(\boldsymbol{\nabla}_{\boldsymbol{u}_{\boldsymbol{W}}}\lambda\cdot\boldsymbol{\delta u}_{\boldsymbol{W}} + \boldsymbol{\nabla}_{T_W}\lambda\cdot\delta T_W\right) r\mathrm{d}l\,,\end{aligned} \tag{2.22}$$

where $\boldsymbol{\nabla}_m\lambda$, $\boldsymbol{\nabla}_{\boldsymbol{f}}\lambda$ and $\boldsymbol{\nabla}_h\lambda$ now define the sensitivities of the eigenvalue λ to mass, momentum and heat sources, respectively. Similarly, $\boldsymbol{\nabla}_{\boldsymbol{u}_{\boldsymbol{W}}}\lambda$ and $\boldsymbol{\nabla}_{T_W}\lambda$ define the sensitivities of the eigenvalue λ to wall velocity and temperature forcing. In the following, we will also use the sensitivity to a volumetric forcing $\delta\mathscr{I}$ defined as $\boldsymbol{\nabla}_{\mathscr{I}}\lambda =$

$(\boldsymbol{\nabla}_m\lambda, , \boldsymbol{\nabla}_{\boldsymbol{f}}\lambda\,, \boldsymbol{\nabla}_h\lambda)^T$, so that

$$\delta\lambda = \int_\Omega \boldsymbol{\nabla}_{\mathscr{I}}\lambda \cdot \delta\mathscr{I}\, r\mathrm{d}r\mathrm{d}z + \int_{\Gamma_c} (\boldsymbol{\nabla}_{\boldsymbol{u_W}}\lambda \cdot \boldsymbol{\delta u_W} + \boldsymbol{\nabla}_{T_W}\lambda \cdot \delta T_W) r\mathrm{d}l\,. \tag{2.23}$$

As above, the corresponding sensitivities of the growth rate σ and frequency ω can be obtained by considering separately the real and imaginary parts of these complex fields. The derivation of the sensitivity functions $\boldsymbol{\nabla}_{\mathscr{I}}\lambda$, $\boldsymbol{\nabla}_{\boldsymbol{u_W}}\lambda$ and $\boldsymbol{\nabla}_{T_W}\lambda$ is detailed in Appendix B, and yields the following expression:

$$\boldsymbol{\nabla}_{\mathscr{I}}\lambda = (\rho^{0\dagger}, \boldsymbol{u}^{\mathbf{0}\dagger}, T^{0\dagger})^T\,, \tag{2.24a}$$

$$\boldsymbol{\nabla}_{\boldsymbol{u_W}}\lambda = \rho^0\rho^{0\dagger}\boldsymbol{n} + \frac{1}{Re}\boldsymbol{\tau}(\boldsymbol{u}^{\mathbf{0}\dagger})\cdot\boldsymbol{n}\,, \tag{2.24b}$$

$$\boldsymbol{\nabla}_{T_W}\lambda = \frac{\gamma}{PrRe}\boldsymbol{\nabla}T^{0\dagger}\cdot\boldsymbol{n}\,, \tag{2.24c}$$

where $\boldsymbol{n}$ is the normal to the control surface oriented from the body to the fluid, and $\boldsymbol{q}^{\mathbf{0}\dagger} = (\rho^{0\dagger}, \boldsymbol{u}^{\mathbf{0}\dagger}, T^{0\dagger}, p^{0\dagger})^T$ is the adjoint base flow, solution of the non-homogeneous, non-degenerate, linear problem

$$\mathcal{A}_0^\dagger\left(\boldsymbol{q}^{\mathbf{0}}\right)\boldsymbol{q}^{\mathbf{0}\dagger} = \boldsymbol{\nabla}_{\boldsymbol{q}^{\mathbf{0}}}\lambda\,, \tag{2.25}$$

along with the boundary condition on Γ_c:

$$\boldsymbol{u}^{\mathbf{0}\dagger} = \mathbf{0}\,, \qquad T^{0\dagger} = 0\,. \tag{2.26}$$

In (2.25), $\mathcal{A}_0^\dagger$ is the adjoint operator for the axisymmetric linearized operator $\mathcal{A}_0$. We insist that these equations have been derived for axisymmetric configurations, along with the specific inner product

$$\langle\hat{\boldsymbol{a}}, \hat{\boldsymbol{b}}\rangle = \int_\Omega \hat{\boldsymbol{a}}\cdot\hat{\boldsymbol{b}}\, r\mathrm{d}r\mathrm{d}z\,. \tag{2.27}$$

It can be shown, though, that repeating the procedure for two-dimensional cartesian configurations, for instance, leads to the exact same set of equations, provided the natural inner product in cartesian coordinates is used, namely $\langle\hat{\boldsymbol{a}}, \hat{\boldsymbol{b}}\rangle = \int_\Omega \hat{\boldsymbol{a}}\cdot\hat{\boldsymbol{b}}\, dxdy$. This consistency justifies the privileged use of this inner product in adjoint related studies. It should be noted that the sensitivity to base flow modifications acts as a source term in the adjoint base flow equations (2.25). The determination of $\boldsymbol{\nabla}_{\boldsymbol{q}^{\mathbf{0}}}\lambda$ is thus a prerequisite to the determination of the sensitivity to a steady volumetric forcing. The procedure to compute the sensitivity of an eigenvalue to a steady forcing is the following:

- resolution of the base flow equations (2.6),
- resolution of the stability problem (2.9) and selection of an eigenpair $\{\sigma + \mathrm{i}\omega, \hat{\boldsymbol{q}}^{\mathbf{1}}\}$,
- resolution of the adjoint stability problem (2.14) and normalization of the adjoint global mode using (2.17),
- computation of the sensitivity to base flow modifications (2.18),
- resolution of the adjoint base flow equations (2.25),
- computation of the adjoint wall quantities defined from the adjoint base flow by (2.24).

2.4. *Connection between both sensitivity analyses*

Both sensitivity analyses are closely connected, as seen from (2.25). Consider a small variation in the forcing $\delta\mathscr{I}$, $\boldsymbol{\delta u_W}$, δT_W: it induces a specific base flow modification $\boldsymbol{\delta q_F^0}$, solution of the linear problem

$$\mathcal{A}_0\boldsymbol{\delta q_F^0} = (\delta\mathscr{I}, 0)^T\,, \tag{2.28}$$

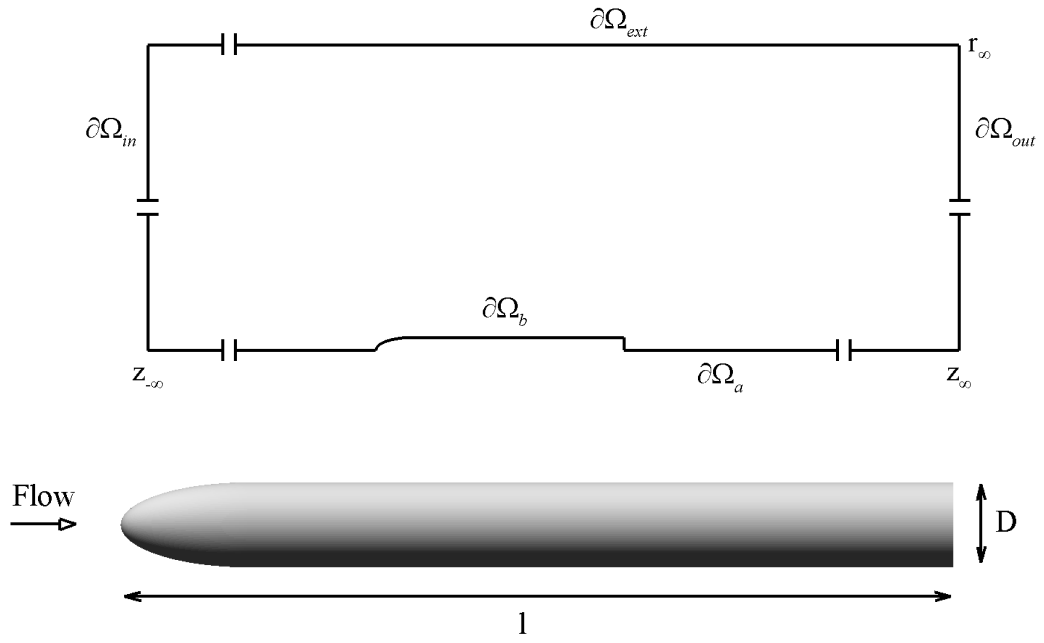

Figure 1: Schematic of the configuration under study: the slender body of revolution has a diameter D and a total length $l = 9.8D$. $z_{-\infty}$, z_∞ and r_∞ are, respectively, the location of the inlet, outlet and lateral boundaries.

along with the boundary condition on Γ_c:

$$\boldsymbol{\delta u^0} = \boldsymbol{\delta u_W}\,, \qquad \delta T^0 = \delta T_W\,. \tag{2.29}$$

The resulting modification of the eigenvalue $\delta\lambda$ can be calculated using both sensitivity analyses. In the framework of the sensitivity to base flow modifications, it reads

$$\delta\lambda = \int_\Omega \boldsymbol{\nabla}_{\boldsymbol{q^0}}\lambda \cdot \boldsymbol{\delta q^0_F}\, r\mathrm{d}r\mathrm{d}z\,. \tag{2.30}$$

In the framework of the sensitivity to a steady forcing, we obtain

$$\delta\lambda = \int_\Omega \boldsymbol{\nabla}_{\mathscr{J}}\lambda \cdot \delta\mathscr{J}\, r\mathrm{d}r\mathrm{d}z + \int_{\Gamma_c} (\boldsymbol{\nabla}_{\boldsymbol{u_W}}\lambda \cdot \boldsymbol{\delta u_W} + \boldsymbol{\nabla}_{\boldsymbol{u_W}}\lambda \cdot \delta T_W) r\mathrm{d}l. \tag{2.31}$$

The sensitivity analysis to a steady forcing can then be seen as particularizing the sensitivity analysis from generic base flow modifications $\boldsymbol{\delta q^0}$ to the specific base flow modifications $\boldsymbol{\delta q^0_F}$ induced by a small modification of the steady forcing. Though, the main interest of the sensitivity analysis to a steady forcing is that the variation $\delta\lambda$ can be directly determined from the knowledge of the sensitivity functions $\boldsymbol{\nabla}_{\mathscr{J}}\lambda$, $\boldsymbol{\nabla}_{\boldsymbol{u_W}}\lambda$ and $\boldsymbol{\nabla}_{T_W}\lambda$, without having to compute the specific base flow modification $\boldsymbol{\delta q^0_F}$.

3. Flow configuration and numerical approach

The body under study is shown in Figure 1: it models an ideal rocket shape, made of an axisymmetric body of revolution with a blunt trailing edge of diameter D placed into a uniform flow at zero angle of attack (Mair 1965; Weickgenannt & Monkewitz 2000). The body used in this study is identical to that used by Sevilla & Martínez-Bazàn (2004), with a total length $l = 9.8D$ and an ellipsoidal nose of aspect ratio $3:1$. A schematic of the physical configuration is sketched in Figure 1: the body is located on the axis of a

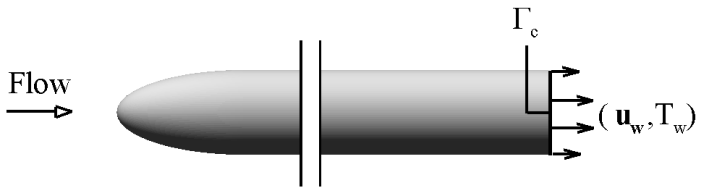

Figure 2: Schematic of the configuration for boundary forcing and localization of the control surface Γ_c at the base.

numerical enclosing cylinder of radius $r = r_\infty$. The origin of the cylindrical coordinates is taken at the center of the body base. The inlet $\partial\Omega_{in}$ and outlet $\partial\Omega_{out}$ boundaries are located respectively at $z = z_{-\infty}$ and $z = z_\infty$ and boundaries $\partial\Omega_a$ and $\partial\Omega_{ext}$ represent respectively the revolution axis of the body and the boundary of the enclosing cylinder.

The computational domain and mesh used for this study are identical to that presented in Part I, with $z_\infty = -100$ $z_\infty = 300$ and $r_\infty = 25$. Boundary conditions are enforced by use of a sponge zone of length $l^s = 200$ padding the physical domain (see Figure 2 of Part I). In the following, all pressure quantities are eliminated from the governing equations using the perfect gas state equation so that the state vector is $\boldsymbol{q} = (\rho, \boldsymbol{u}, T)^T$. The governing equations (2.1) are thus solved using the following boundary conditions:

$$\boldsymbol{u} = (0,0,1)^T,\ \rho, T = 1 \text{ on } \partial\Omega^s_{in} \cup \partial\Omega^s_{ext} \cup \partial\Omega^s_{out} \text{ (inlet, external \& outlet)}, \quad (3.1a)$$

$$\boldsymbol{u} = \boldsymbol{u_w},\ T = T_w \quad \text{on } \Gamma_c \text{ (subsonic injection)}\,, \quad (3.1b)$$

$$\boldsymbol{u} = \boldsymbol{0},\ \partial_n T = 0 \quad \text{on } \partial\Omega_b \backslash \Gamma_c \text{ (adiabatic body wall)}\,. \quad (3.1c)$$

The base flow satisfies identical boundary conditions, along with the additional condition $u^0 = 0$, $\partial_r(w^0, \rho^0, T^0) = 0$ on $\partial\Omega_a$ obtained from mass, momentum and internal energy conservation as $r \to 0$ for axisymmetric solutions. The perturbation satisfies the following boundary conditions

$$\hat{\boldsymbol{u}}^{\boldsymbol{1}} = \boldsymbol{0},\ \hat{\rho}^1, \hat{T}^1 = 0 \quad \text{on} \quad \partial\Omega^s_{in} \cup \partial\Omega^s_{ext} \cup \partial\Omega^s_{out}, \quad (3.2a)$$

$$\hat{\boldsymbol{u}}^{\boldsymbol{1}} = \boldsymbol{0},\ \partial_n \hat{T}^1 = 0 \quad \text{on} \quad \partial\Omega_b\,, \quad (3.2b)$$

$$\hat{w}^1, \hat{\rho}^1, \hat{T}^1 = 0,\ \partial_r(\hat{u}^1, \hat{v}^1) = 0 \quad \text{on} \quad \partial\Omega_a\,, \quad (3.2c)$$

the condition at the axis being specific to $m = 1$ disturbances, and the conditions for the adjoint perturbation arising from the integration by parts of the perturbation equations are identical. All details pertaining to the numerical method can be found in Part I, including space discretization, base flow computations and resolution of the eigenvalue problems. We recall that global modes are normalized by imposing the phase of the radial velocity to be zero at a particular location, namely $\hat{u}^1(0,1)$ must be real positive for $m = \pm 1$. The eigenmode energy is then normalized to unity in the near-wake domain defined arbitrarily as $z \in [-12.3,\ 5.25]$ and $r < 2$, and adjoint global modes are normalized using condition (2.17).

4. Global stability results

We intend to apply the sensitivity analyses presented in Section 2 to the afterbody flow configuration described in Section 3. From now on, all results pertain to the same

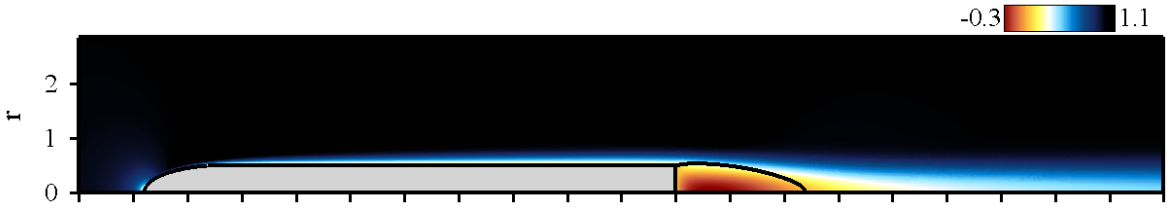

Figure 3: Spatial distribution of axial velocity w^0 of the steady axisymmetric base flow for $Re = 983.0$ and $M = 0.5$. The solid line in the flow indicates the separatrix of the recirculation zone.

configuration for which the base is chosen as the control surface, as depicted in Figure 2. The afterbody flow refers to as the *unforced* afterbody flow which is solution of the governing equations (2.1) with

$$\boldsymbol{f} = \boldsymbol{0}\,, \qquad m = h = 0\,, \tag{4.1a}$$

$$\boldsymbol{u_w} = \boldsymbol{0}\,, \qquad T = T_w\,, \tag{4.1b}$$

T_w being chosen equal to the free-stream total temperature

$$T_w = 1 + \frac{\gamma - 1}{2} M^2 \tag{4.2}$$

Similarly, the base flow refers to as the *unforced* base flow which is solution of the steady equations (2.6) along with conditions (4.1). Since we do not use the governing equations under their conservative form, the method presented here is unable to account for the presence of shock waves in the computational domain. Therefore, base flow computations can be carried out legitimately while the local Mach number $M_l = M\|\boldsymbol{u^0}\|/\sqrt{T^0}$ remains smaller than unity at each point of the grid mesh. Practically, the free stream Mach number can be increased up to $M = 0.7$. From now on, the Mach number is taken equal to $M = 0.5$, so that $T_w = 1.05$. Figure 3, shows contours of the base flow axial velocity w^0 for $Re = 983.0$ and $M = 0.5$. The solid line is the streamline linking the separation point to the stagnation point on the $r = 0$ axis, and defines the separatrix delimiting the recirculation bubble behind the base. The classical topology of wake flows is retrieved, with a recirculation region of length ~ 2.5 diameters developing in the wake of the afterbody, and negative values of streamwise velocity reaching 30 % of the free-stream velocity.

In Part I, we have investigated the global stability of this afterbody flow with no control surface. It has been mentioned for introductory purposes that in the range of Mach numbers under investigation ($M < 0.7$), the axisymmetric wake undergoes a consistent sequence of bifurcation identical to that previously documented in the incompressible regime for other geometries of revolution (Natarajan & Acrivos 1993). Namely, when the Reynolds number is increased from small values, the axisymmetric base flow is first destabilized at Re_A by a stationary mode ($\omega = 0$) whose eigenvector is referred to $\hat{\boldsymbol{q}}^{\boldsymbol{1}}_{\boldsymbol{A}}$ (not shown here). A subsequent destabilization occurs at $Re_B > Re_A$ for an oscillating mode of frequency $\omega = \omega_0$, whose complex eigenvector is denoted $\hat{\boldsymbol{q}}^{\boldsymbol{1}}_{\boldsymbol{B}}$. This sequence is not modified by the introduction of the control surface. For $M = 0.5$, the critical Reynolds number for the Hopf bifurcation is $Re_B = 983.0$ and the frequency of the oscillating global mode is $\omega_0 = 0.399$ corresponding to a Strouhal number $St = \omega_0 D/(2\pi U_\infty) = 0.063$. These values are almost identical to that found in Part I in the absence of control surface,

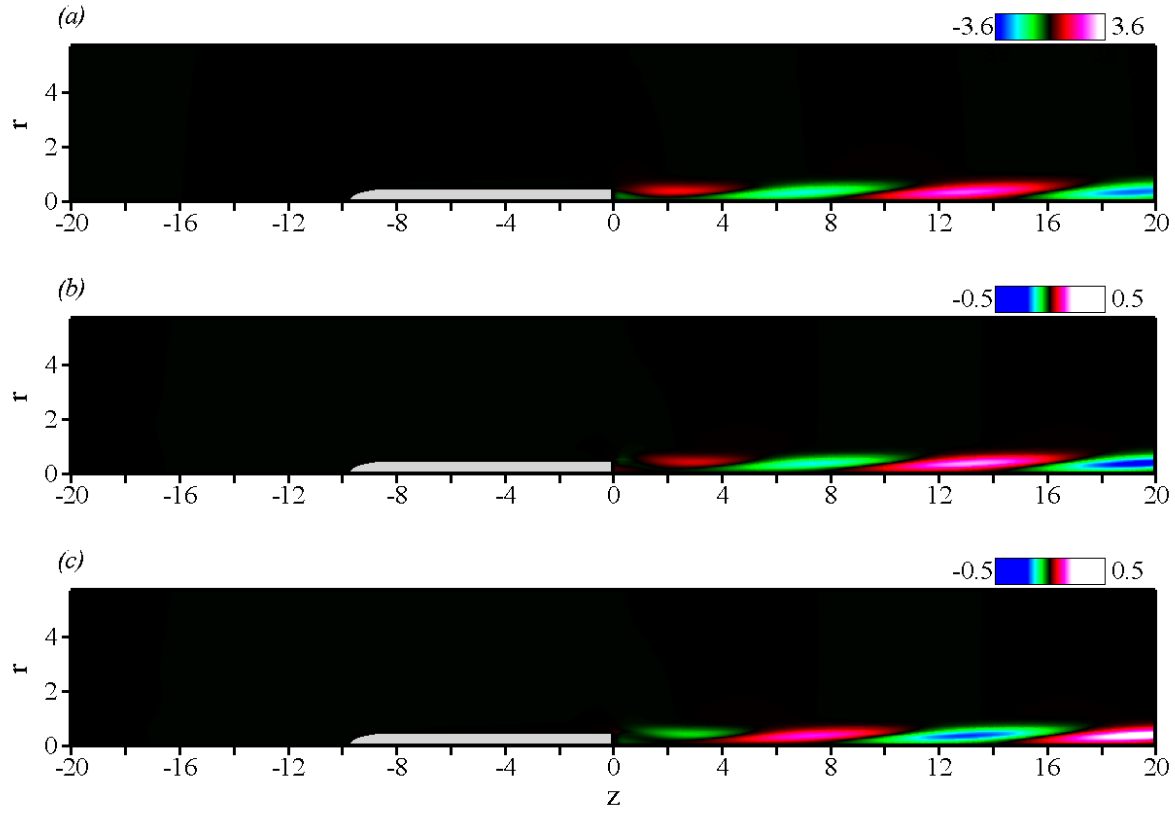

Figure 4: Oscillating global mode at the threshold of the first instability, $Re_B = 983.0$ - $M = 0.5$. (a) Spatial distribution of axial velocity $\hat{w}_B^1$ for the global mode. (b) Spatial distribution of density $\hat{\rho}_B^1$. (c) Spatial distribution of temperature $\hat{T}_B^1$. The black hue corresponds to vanishing perturbations. Only the real parts are shown.

the shift in the Reynolds number representing a variation of only 2 ‰, and show that the effect of the additional base temperature condition (4.1b) barely affects the results of the stability analysis. This is consistent with the results documented in Part I showing that small discrepancies in the base flow density, temperature and pressure do not alter significantly the stability problem, due to low magnitudes of the associated sensitivity functions. Figure 4 shows the spatial structure of the real part of the streamwise velocity component $\hat{w}_B^1$. One observes positive and negative velocity perturbations alternating downstream of the body, in a regular, periodic way that defines a local spatial wavelength of about 12 diameters. The imaginary part of $\hat{w}_B^1$ (not shown here) displays a similar structure, but is approximately in spatial quadrature since its extrema are located where the real part vanishes. This global mode corresponds therefore to a spiral perturbation in the lee of the body, which rotates in time at the frequency ω_0. Note that the density $\hat{\rho}_B^1$ and temperature $\hat{T}_B^1$ perturbations shown in Figures 4(b) and 4(c) are one order of magnitude smaller than that found for the streamwise velocity $\hat{w}_B^1$ shown in Figure 4(a). The adjoint global mode $\hat{\boldsymbol{q}}_{\boldsymbol{B}}^{\boldsymbol{1\dagger}}$ has been computed and is depicted in Figure 5: it is dominated by the adjoint velocity field, and is intense only in the recirculating area and a few diameters upstream of the body, where it presents a weak oscillation, whereas it vanishes downstream of the body. The specific downstream localization of the global mode, as well as the upstream localization of the adjoint global mode, results from the convective nonnormality of the evolution operator, which has been discussed in Part I and is out of the scope of the present study.

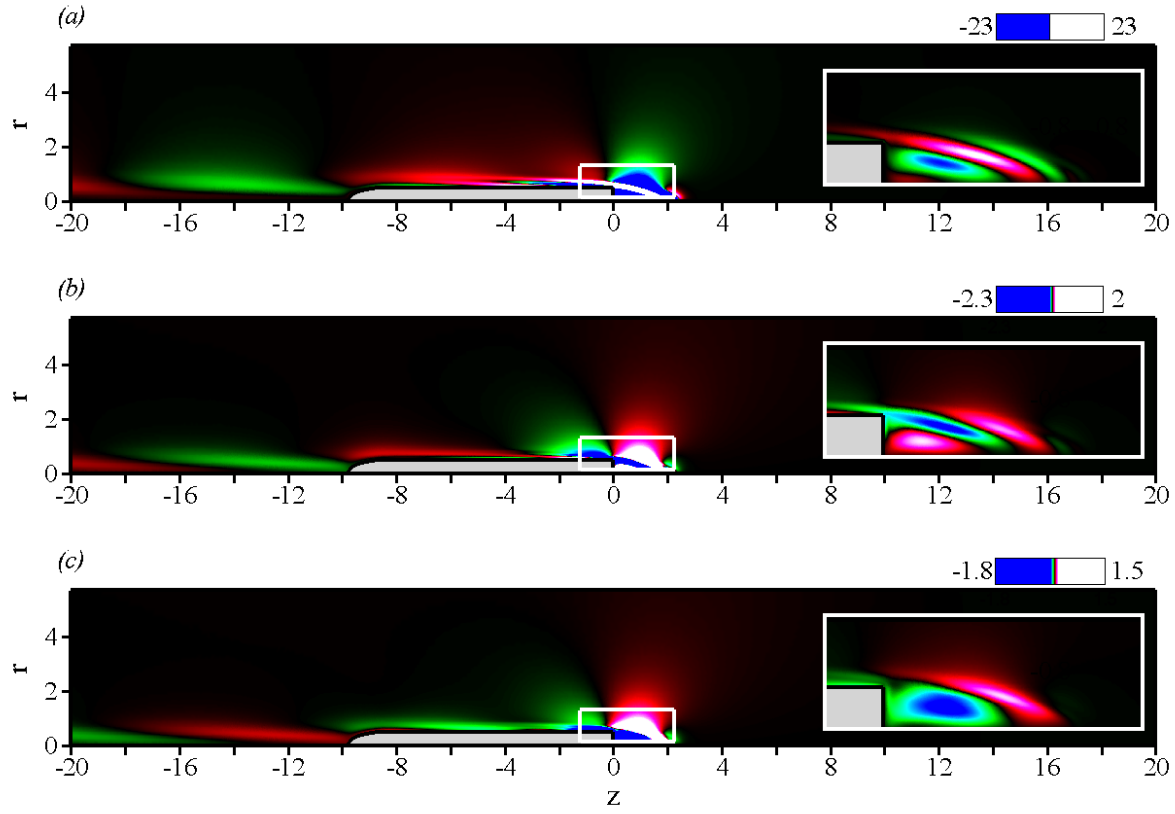

Figure 5: Same as Figure 4 for the oscillating adjoint global mode at threshold.

5. Sensitivity to steady forcing

In this section, the oscillating global mode is marginally unstable, i.e. $Re = 983.0$ and $M = 0.5$. In the perspective of control, we aim at appraising how the stability of the oscillating global mode $\hat{\boldsymbol{q}}_{\boldsymbol{B}}^{\boldsymbol{1}}$ can be affected by a small-amplitude forcing $(\delta\mathscr{I}, \boldsymbol{\delta u_W}, \delta T_W)$, assumed to act only at the base flow level. Such forcing induces a specific base flow modification $\boldsymbol{\delta q}_W^{\boldsymbol{0}}$ that results in a modification of the stability problem, and in particular in a modification of the growth rate $\delta\sigma_B$. In order to estimate this modification, we use here the sensitivity analysis to a steady forcing developed in § 2, in which the knowledge of the base flow modification $\boldsymbol{\delta q}_W^{\boldsymbol{0}}$ is not needed. § 5.1 to 5.3 deal with pure volumetric forcing, so that we impose $\boldsymbol{\delta u_W} = \mathbf{0}$ and $\delta T_W = 0$. On the contrary, § 5.4 considers the case of pure boundary forcing, along with $\delta\mathscr{I} = \mathbf{0}$.

5.1. *Sensitivity to momentum forcing*

We set for now $\delta m = \delta h = 0$, and investigate the effect of momentum forcing on the stability of the oscillating global mode. We consider first the growth rate variation $\delta\sigma_B$ resulting from an axisymmetric punctual momentum source localized at the station (r_c, z_c). Since the global mode is marginally stable, negative variations $\delta\sigma_B < 0$ (resp. positive variations $\delta\sigma_B > 0$) therefore correspond to a stabilization (resp. a destabilization) of the global mode. In order to achieve a maximum stabilizing effect, the orientation of the momentum source is chosen opposite to that of the sensitivity function $\boldsymbol{\nabla_f}\sigma_B$, so that $\boldsymbol{\delta f}$ can be modeled as

$$\boldsymbol{\delta f}(r,z) = -\frac{1}{2\pi r_c}\delta\hat{f}\frac{\boldsymbol{\nabla_f}\sigma_B(r,z)}{\|\boldsymbol{\nabla_f}\sigma_B(r,z)\|}\delta(r-r_c, z-z_c)\,, \tag{5.1}$$

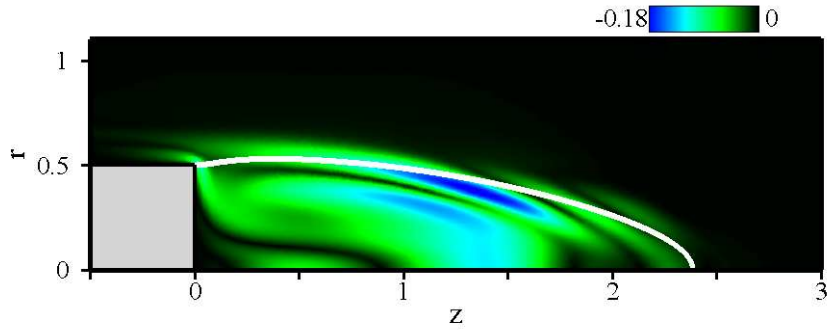

Figure 6: Oscillating global mode at the threshold of the second instability, $Re_{B} = 983.0$ - $M = 0.5$: spatial distribution of the growth rate variation $\delta\sigma_{B}(r_c, z_c)$ obtained with a momentum source modeled by (5.1). Negative variations $\delta\sigma_{B} < 0$ (resp. positive variations $\delta\sigma_{B} > 0$) therefore correspond to a stabilization (resp. a destabilization) of the global mode. The black hue corresponds to vanishing magnitudes of sensitivity.

where the constant $\delta\hat{f} > 0$ corresponds to the momentum rate per time-unit applied by the control device, since

$$\int \|\boldsymbol{\delta f}(r,z)\|\, r\mathrm{d}r\mathrm{d}\theta\mathrm{d}z = \delta\hat{f}\,. \tag{5.2}$$

To each position of the source (r_c, z_c) corresponds a variation of the oscillating growth rate $\delta\sigma_{B}(r_c, z_c)$, given by

$$\delta\sigma_{B}(r_c,z_c) = \int_{\Omega} \boldsymbol{\nabla_f}\sigma_{B}(r,z)\cdot\boldsymbol{\delta f}(r,z)\, r\mathrm{d}r\mathrm{d}z = -\frac{1}{2\pi}\|\boldsymbol{\nabla_f}\sigma_{B}(r_c,z_c)\|\delta\hat{f}\,, \tag{5.3}$$

so that $\delta\sigma_{B}$ is directly proportional to the momentum rate and to the magnitude of the sensitivity function. Figure 8 presents the spatial distribution of the growth rate variation for $\delta\hat{f} = 10^{-2}$, i.e. the control $\delta\hat{f}$ represents 1% of the free-stream momentum rate. The black hue corresponds to vanishing variations of the growth rate, so that one can observe that the magnitude of sensitivity is almost nil everywhere in the flow, except in the recirculating bubble. This is not too surprising, though, as we have shown in Part I that the recirculation acts as the wavemaker of the instability, a result that has been shown to result from the convective nonnormality of the linearized evolution operator, which induces a downstream localization (resp. upstream) of the direct global modes (resp. adjoint global modes) illustrated in Figures 4 and 5. It can be seen that the a maximum stabilizing effect is obtained by placing the momentum source in the vicinity of the separation line and in the core of the recirculating bubble, where the effect is however lower.

We consider now the action of a small control device, whose presence is modeled by the force it exerts on the flow. We assume that whatever its location, the wake of the control device remains steady. This means that the Reynolds number based on the typical size of the control device and the magnitude of the local base flow velocity must be low enough, i.e. that the control device must be small. For instance, in the studies of Strykowski & Sreenivasan (1990) and Marquet *et al.* (2008), the diameter of the control cylinder is ten times smaller than that of the main cylinder. Of course, disks such as those used in Mair (1965) and Weickgenannt & Monkewitz (2000) are not precisely small control devices, since the ratio between of their diameter to that of the main body is even close to unity. Therefore, we do not claim that our approach provides a full interpretation of the results

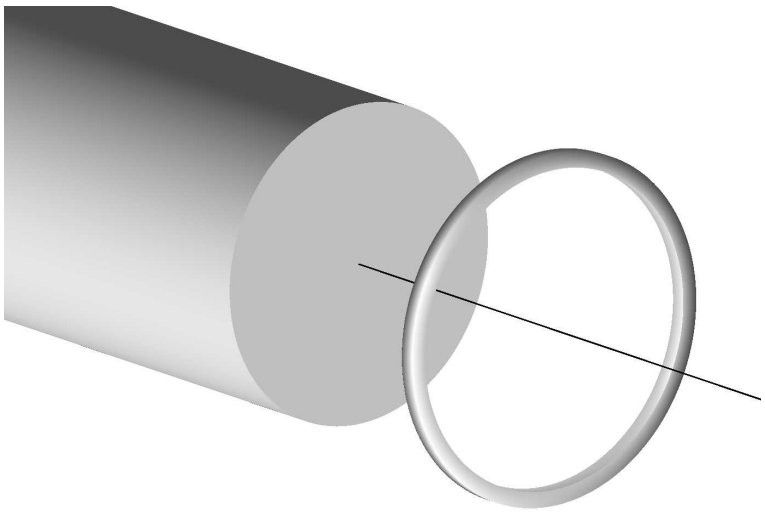

Figure 7: View of a control ring mounted at the rear of the main body, whose action on the base flow is modeled by (5.4).

documented by these authors. Though, it consists in a more systematic approach for the open-loop control of vortex-shedding by means of an additional control device.

The latter device is chosen as a small control ring of radius r_c and width $e = 0.1$, mounted at the rear of the main body, at a distance z_c from the base, as shown in Figure 7. We assume that such the width e is small enough for the force to be punctual, i.e. localized at the station (r_c, z_c). As in Hill (1992) and Marquet *et al.* (2008), we consider that the base flow exerts a steady drag force on the control ring, and that the ring exerts in return an opposite force, modeled as

$$\boldsymbol{\delta f}(r,z) = -\frac{1}{2} C e \rho^0(r,z) \|\boldsymbol{u^0}(r,z)\| \boldsymbol{u^0}(r,z) \delta(r-r_c, z-z_c)\,, \tag{5.4}$$

where C is a drag coefficient depending on the value of the Reynolds number Re_e based on the ring width. Typical values of the Reynolds number in the recirculating bubble are of order $Re_e \simeq 30$. Consequently, we set here $C = 1$, an empirical value determined from the drag coefficient for a cylinder at low Reynolds numbers. To each position of the ring (r_c, z_c) corresponds a variation of the oscillating growth rate $\delta\sigma_{_B}(r_c, z_c)$, given by

$$\delta\sigma_{_B}(r_c,z_c) = -\frac{1}{2} C e r_c \rho^0(r_c,z_c) \|\boldsymbol{u^0}(r_c,z_c)\| \boldsymbol{\nabla_f} \sigma_{_B}(r_c,z_c) \cdot \boldsymbol{u^0}(r_c,z_c)\,. \tag{5.5}$$

Figure 8 presents the spatial distribution of the resulting growth rate variations $\delta\sigma_{_B}$. It can be seen that the control ring has a significant stabilizing effect if it is placed along the separation line. However, these results also outline the complex effect of momentum forcing, as several regions contributing either to a weaker stabilization or destabilization of the global mode are visible around the main stabilizing region.

5.2. *Sensitivity to a heat source*

We set now $\delta m = 0$ and $\boldsymbol{\delta f} = \boldsymbol{0}$, and investigate the growth rate variation resulting from an axisymmetric punctual volumetric energy source, modeled as

$$\delta h(r,z) = \frac{1}{2\pi r_c} \delta\hat{h}\, \delta(r-r_c, z-z_c)\,, \tag{5.6}$$

where the constant $\delta\hat{h}$ corresponds to the energy rate per time-unit. Positive values of $\delta\hat{h}$ (resp. negative values) therefore correspond to a local heating (resp. a local cooling)

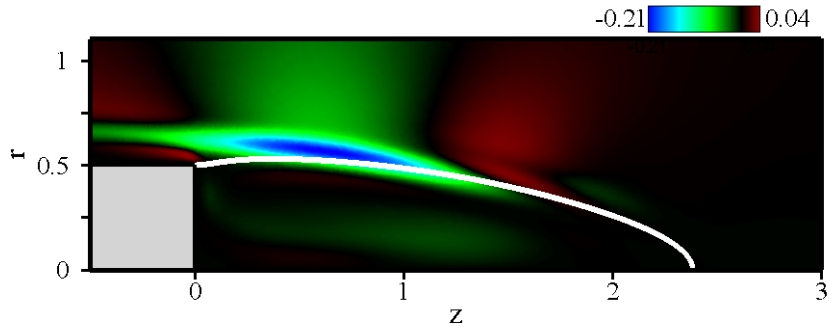

Figure 8: Same as Figure 6 for the growth rate variation $\delta\sigma_{_B}(r_c, z_c)$ obtained when the presence of a small control ring is modeled by (5.4).

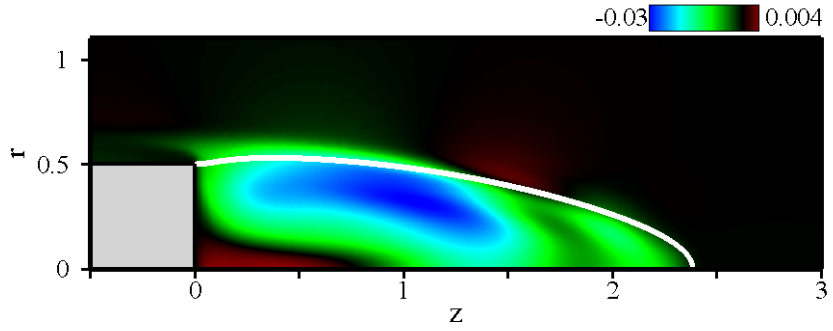

Figure 9: Same as Figure 6 for the growth rate variation $\delta\sigma_{_B}(r_c, z_c)$ obtained with a heat source modeled by (5.6).

of the flow. The variation of the growth rate is then given by

$$\delta\sigma_{_B}(r_c, z_c) = \int_\Omega \boldsymbol{\nabla}_h \sigma_{_B}(r, z) \cdot \delta h(r, z)\, r\mathrm{d}r\mathrm{d}z = \frac{1}{2\pi} \boldsymbol{\nabla}_h \sigma_{_B}(r_c, z_c) \cdot \delta\hat{h}\,. \tag{5.7}$$

We consider the case of heating in order to mimic the effect obtained using an axisymmetric gas discharge and set $\delta\hat{h} = 10^{-2}$, i.e. the control $\delta\hat{h}$ now represents 1% of the free-stream internal energy rate. Figure 9 presents the spatial distribution of the resulting variations of the oscillating growth rate $\delta\sigma_{_B}(r_c, z_c)$ as given by (5.7).

We find that forcing the base flow in the separation region has a stabilizing effect for almost all positions of the discharge ($\delta\sigma_{_B} < 0$) whereas forcing in the outer region has no effect. It should be noted that the opposite effect would have been obtained in the case of cooling, since the variation $\delta\sigma_{_B}$ is directly proportional to $\delta\hat{h}$. It is worthwhile noting that the maximum stabilization achieved by means of the heat source is $\delta\sigma_{_B} = -0.03$, i.e. lower to that documented in § 5.1 by means of a momentum source representing 1% of the free-stream momentum rate. Though, such effect is not negligible. Since it has been said that modifying the thermodynamic base flow within the recirculation has almost no effect on the oscillating growth rate $\sigma_{_B}$, it might thus be inferred that the effect of such energy source is non-thermal, i.e. it mainly acts by modifying the base flow momentum.

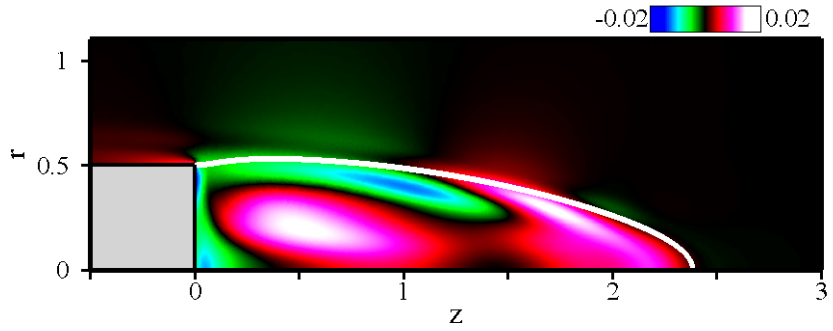

Figure 10: Same as Figure 6 for the growth rate variation $\delta\sigma_{_B}(r_c, z_c)$ obtained with a mass source modeled by (5.8).

5.3. *Sensitivity to mass injection*

Finally, we set $\boldsymbol{\delta f} = \mathbf{0}$ and $\delta h = 0$ and investigate the growth rate variation $\delta\sigma_{_B}$ resulting from an axisymmetric localized mass injection, modeled by

$$\delta m(r, z) = \frac{1}{2\pi r_c}\delta\hat{m}\,\delta(r - r_c, z - z_c)\,, \tag{5.8}$$

where the constant $\delta\hat{m}$ corresponds to the mass rate per time-unit. Positive values of $\delta\hat{m}$ (resp. negative values) correspond to a mass source (resp. a mass sink). The variation of the growth rate is thus given by

$$\delta\sigma_{_B}(r_c, z_c) = \int_\Omega \boldsymbol{\nabla}_m\sigma_{_B}(r, z)\cdot\delta m(r, z)\, r\mathrm{d}r\mathrm{d}z = \frac{1}{2\pi}\boldsymbol{\nabla}_m\sigma_{_B}(r_c, z_c)\cdot\delta\hat{m}\,. \tag{5.9}$$

In the following, we set $\delta\hat{m} = 10^{-2}$, i.e. the control $\delta\hat{m}$ represents 1% of the free-stream density rate. A map of the variation $\delta\sigma_{_B}(r_c, z_c)$ is depicted on Figure 10. It can be seen in particular that the region sensitive to mass injection are localized within the recirculation bubble only. Figure 10 also shows that a mass injection close to the base or along the front part of the separation line has a stabilizing effect ($\delta\sigma_{_B} < 0$), the most sensitive region being located close to the separation point. On the contrary, a mass injection in the core and in the rear part of the recirculating bubble has a destabilizing effect ($\delta\sigma_{_B} > 0$). Note that an additional destabilizing region of moderate sensitivity exists within the boundary-layer region, upstream from the blunt edge. Though, implementing an axisymmetric mass injection in the inner region of a flow is not very realistic, and practically, such injection is rather achieved through boundary forcing, as will be discussed in the following section.

5.4. *Sensitivity to steady wall forcing*

We aim now at characterizing the effect of wall forcing, by setting $\mathscr{I} = \mathbf{0}$. We recall that the variation of the eigenvalue resulting from the small-amplitude boundary forcing are such that

$$\delta\sigma_{_B} = \int_{\Gamma_c}\left(\rho^0\rho^{0\dagger}\boldsymbol{n} + \frac{1}{Re}\boldsymbol{\tau}(\boldsymbol{u}^{\mathbf{0}\dagger})\cdot\boldsymbol{n}\right)\cdot\boldsymbol{\delta u_w}\, r\mathrm{d}l + \int_{\Gamma_c}\frac{\gamma}{PrRe}(\boldsymbol{\nabla}T^{0\dagger}\cdot\boldsymbol{n})\cdot\delta T_{_W}\, r\mathrm{d}l \tag{5.10}$$

When a modification of the wall velocity occurs, the variation of the eigenvalue $\delta\sigma_{_B}$ is determined by the product of the wall density and adjoint densities $\rho^0\rho^{0\dagger}$ and by the viscous stress tensor $\boldsymbol{\tau}(\boldsymbol{u}^{\mathbf{0}\dagger})$ weighted by the inverse of the Reynolds number. The orientation of the forcing velocity with respect to the wall also influences the eigenvalue variation. Indeed, when the viscous term in (5.10) is neglected, for a given magnitude of

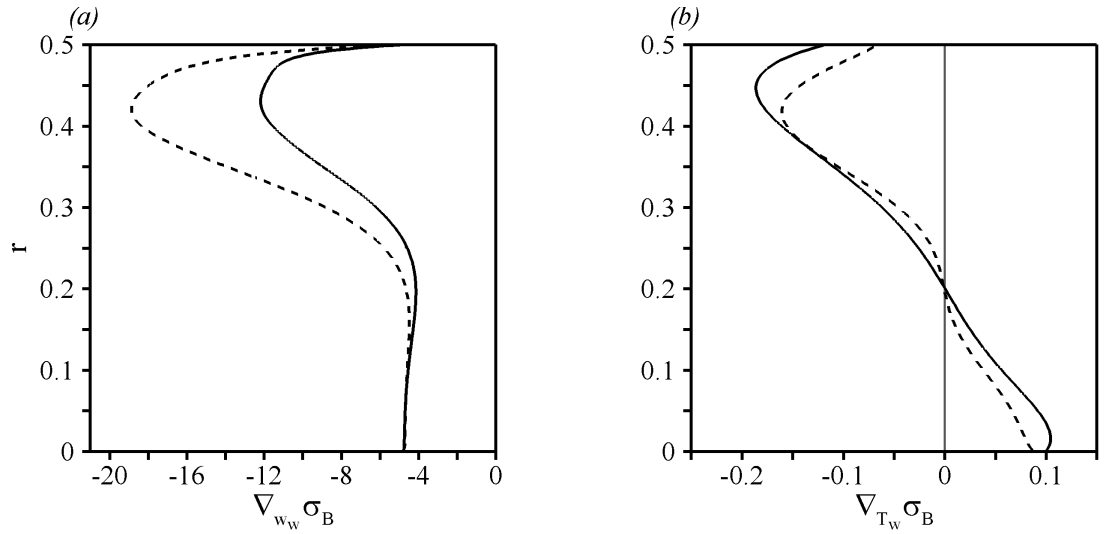

Figure 11: Oscillating global mode - $M = 0.5$: spatial distribution of (a) streamwise wall velocity $\boldsymbol{\nabla}_{w_W}\sigma_B$ and (b) wall temperature $\boldsymbol{\nabla}_{T_W}\sigma_B$ sensitivity functions. Solid lines (resp. dashed lines) stand for the functions at threshold of instability, i.e. $Re_B = 983.0$ (resp. at the supercritical Reynolds number $Re = 2000$).

the wall velocity, the closer the orientation to the normal vector to the wall, the larger the variation. In the following, we thus consider only the case of wall velocities oriented normal to the control surface. For the configuration under consideration, this corresponds to a steady streamwise blowing $\boldsymbol{\delta u_W} = \delta w_W \boldsymbol{e_z}$, for which the sensitivity functions read

$$\boldsymbol{\nabla}_{w_W}\sigma_B = \rho^0\rho^{0\dagger}\delta w_W + \frac{1}{Re}\left(-\frac{2}{3}\boldsymbol{\nabla}\cdot\boldsymbol{u}^{\mathbf{0}\dagger} + 2\partial_z w^{0\dagger}\right) \tag{5.11a}$$

$$\boldsymbol{\nabla}_{T_W}\sigma_B = \frac{\gamma}{PrRe}\partial_z T^{0\dagger}\delta T_W \tag{5.11b}$$

The distributions of the sensitivity functions as a function of the radial position r on the base are presented at threshold of instability as the solid lines in Figures 11(a) and 11(b). The vertical grey line on Figure 11(b) corresponds to the axis $\boldsymbol{\nabla}_{T_W}\sigma_B = 0$. It should be noted that the magnitude of these sensitivities is quite different, since the wall temperature sensitivity is one order of magnitude lower than its velocity counterpart. As a consequence, it may be inferred that a small-amplitude heating or cooling of the base will have only a limited effect on the eigenvalue. We find negative values of the wall velocity sensitivity whatever the location at the base. This means that for a steady blowing ($\delta w_W > 0$) we obtain a negative variation $\delta\sigma_B$, consistently with the stabilizing effect of base bleed strategies. The sensitivity is seen to be almost invariant at the center of the base, namely for $r < 0.3$. Then, its magnitude increases significantly close to the separation point, where the maximum value is reached. Therefore, an actuator imposing a steady blowing will achieve maximum efficiency if placed at the edge of the base. Concerning the wall temperature sensitivity, we find positive values at the center decreasing down to negative values at the edge, where the maximum magnitude is reached. To obtain a stabilizing effect, one should thus cool the base in its inner region ($r < 0.2$) and heat it in its external region.

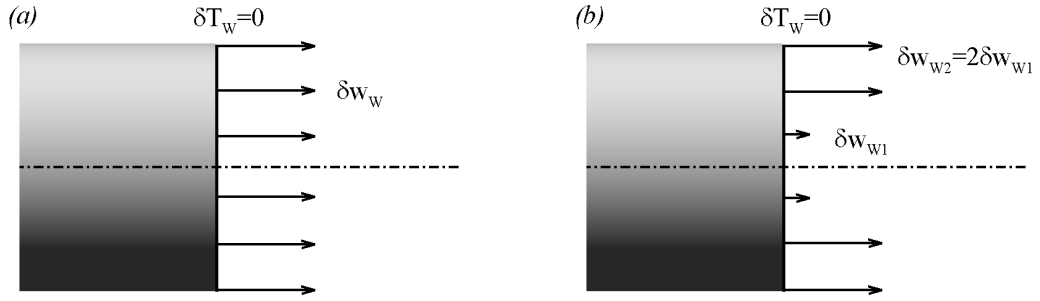

Figure 12: Spatial distribution of the bleed velocity $\boldsymbol{\delta u_W}$. (a) Uniform bleed. (b) Piecewise-constant distribution.

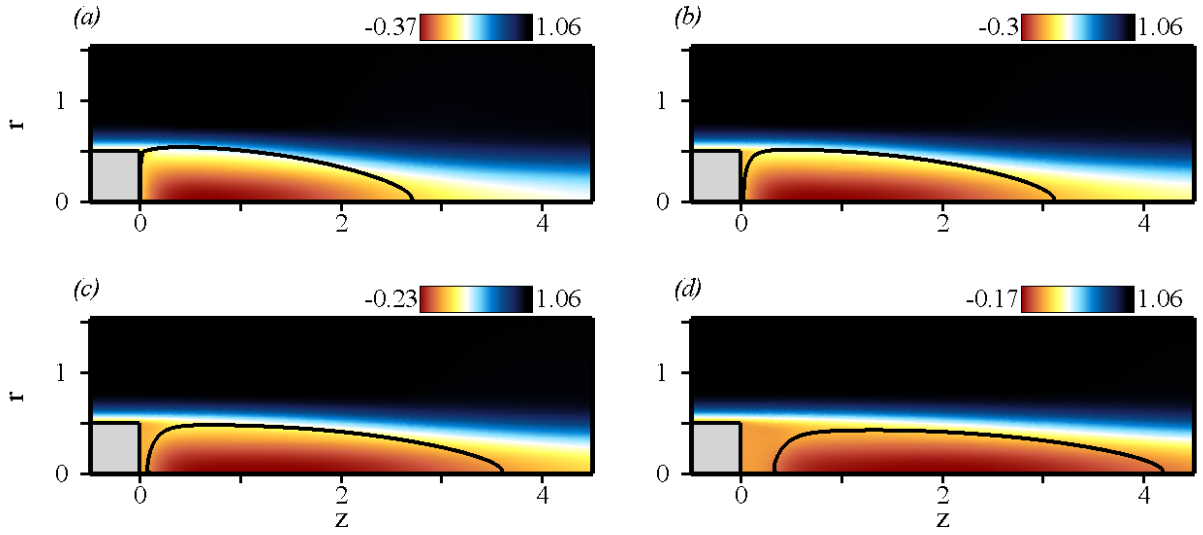

Figure 13: Spatial distribution of axial velocity w^0 of the base flow obtained for different values of wall velocities. (a) $\delta w_W = 0.001$, (b) $\delta w_W = 0.02$, (c) $\delta w_W = 0.04$, and (d) $\delta w_W = 0.06$. The solid line in the flow indicates the separatrix of the recirculation zone.

6. Application to wall blowing - Base bleed

Base blowing is a simple and well-known means of stabilizing various shapes of bluff-bodies at supercritical Reynolds numbers (Motallebi & Norbury 1981; Higuchi 2005). We consider in this section such an unstable configuration, with a Reynolds number $Re = 2000$, the Mach number still being $M = 0.5$. For this parameter setting, the growth rate of the unforced oscillating global mode is $\sigma_B \simeq 8.5 \times 10^{-2}$. For this value of the Reynolds number, the distributions of the sensitivity functions are represented as the dashed lines in Figures 11(a) and 11(b). It can be seen that the sensitivity to a streamwise wall velocity has significantly increased, which makes it possible to control unstable configurations. On the contrary, the sensitivity to wall temperature is only weakly modified. It can thus be inferred that controlling this specific instability by means of pure wall heating or cooling will be quite difficult. Such control has been investigated in the framework of the present study, and it turns out that the effect is indeed very limited. Consequently, in the following, the wall temperature is kept constant and only a uniform bleed velocity is applied at the base, as seen in Figure 12(a). For different values of the wall velocity $\delta w_W = 0.001$, 0.01, 0.03 and 0.06, we present on Figure 13 axial

velocity contours of the forced base flow $\boldsymbol{q}_{W}^{\mathbf{0}}$, obtained by solving the nonlinear base flow equations (2.6) for the corresponding wall velocity. It can be observed that increasing the blowing velocity affects the wake by progressively shifting downstream the recirculating bubble. For $\delta w_{W} = 0.001$, which is close to the natural unforced wake, we find a single stagnation point on the $r = 0$ axis, meaning that the recirculating bubble is still stuck against the base. It can thus be delimited by the streamline linking the separation point to the stagnation point, shown as the solid line in Figure 13(a). On the contrary, for $\delta w_{W} = 0.06$, we find two stagnation points, meaning that the recirculating bubble has been advected downstream under the effect of base bleed. It is thus delimited by the streamline linking both stagnation points, as shown by the solid line in Figure 13(d). This displacement of the separated area occurs along with a simultaneous increase in the recirculating length defined as the distance between both stagnation points, from 2.7 diameters at $\delta w_{W} = 0.001$ to 3.9 diameters at $\delta w_{W} = 0.06$. Another effect of base blowing can be noticed, as the magnitude of counterflow rate is seen to be severely weakened, from 37 % to only 17 % for $\delta w_{W} = 0.06$. Such results are not new, as similar ideas were already conveyed in the early study of Bearman (1967), for instance. Though, new insights in the physics of vortex-shedding have arisen from the stability theory, as numerous theoretical approaches have evidenced a strong connection between the synchronized oscillations observed in wakes and the existence of a region of local absolute instability in the near wake, where the small-amplitude wave packet generated by an arbitrary perturbation withstands advection and grows in time at any fixed location. This has given rise to renewed discussions about the mechanisms underlying this successful control strategy. Since it is well known that reverse flow promotes absolute instability (see Monkewitz 1988, among others), it is now generally acknowledged that base bleed stabilizes the flow by inhibiting absolute instability, as discussed in Sevilla & Martínez-Bazàn (2004). We propose now to characterize the effect of base blowing in the global framework. To this end, we use the advection/production dichotomy introduced in Part I, which stands as the global counterpart of the local concepts of convective/absolute instability.

6.1. *Analysis of the stabilization mechanism in terms of modifications of the advection and production mechanisms*

Consider first the case $\delta w_{W} = 0.01$. It has been said previously that such blowing is expected to have a stabilizing effect, owing to the negative values of $\boldsymbol{\nabla}_{w_{W}}\sigma_{B}$ at the base. From a theoretical point of view, $\delta\sigma_{B}$ can be indifferently estimated in the framework of the sensitivity analyses to steady forcing and base flow modifications, according to

$$\delta\sigma_{B} = \int_{\Gamma_{c}} \boldsymbol{\nabla}_{w_{W}}\sigma_{B} \cdot \delta w_{W} = \left\langle \boldsymbol{\nabla}_{\boldsymbol{q}^{\mathbf{0}}}\sigma_{B} \, , \, \boldsymbol{\delta q}_{W}^{\mathbf{0}} \right\rangle , \tag{6.1}$$

where $\boldsymbol{\delta q}_{W}^{\mathbf{0}}$ is the linear base flow modification obtained by resolution of equation (2.28) along with the following boundary condition on Γ_{c}:

$$\boldsymbol{\delta u}^{\mathbf{0}} = \delta w_{W} \boldsymbol{e_{z}} \, , \qquad \delta T^{0} = 0 \, . \tag{6.2}$$

In the present case, we obtain the expected stabilization, with $\delta\sigma_{B} = -3.02 \times 10^{-2}$ using the sensitivity function $\boldsymbol{\nabla}_{w_{W}}\sigma_{B}$ and $\delta\sigma_{B} = -3.10 \times 10^{-2}$ using the sensitivity function $\boldsymbol{\nabla}_{\boldsymbol{q}^{\mathbf{0}}}\sigma_{B}$. These results are consistent and validate the present computations since the relative error is less than 3 %. The relative error on the frequency is even smaller, of order 1 % (not shown here). It should be noted that if the estimation of $\delta\sigma_{B}$ requires integration over space in the case of the sensitivity to base flow modifications, it relies on wall integration in the case of the sensitivity to forcing. In such blunt configurations where integration up to the edge is carried out, this formalism is thus more demanding,

as sufficient precision in the numerical results must be enforced at this specific location, which may be quite involved. This certainly accounts for the small discrepancies between both sensitivity approaches.

It is worth recalling that the main interest of the sensitivity analysis to steady forcing is that $\delta\sigma_{_B}$ can be directly determined from the knowledge of the sensitivity functions $\boldsymbol{\nabla}_{w_{_W}}\sigma_{_B}$, without having to compute the specific base flow modifications $\boldsymbol{\delta q}^{\mathbf{0}}_{W}$. Though, the knowledge of $\boldsymbol{\delta q}^{\mathbf{0}}_{W}$ is of great interest if one aims at gaining insight into the underlying physical mechanisms. Since $\delta\sigma_{_B}$ is obtained by integration over space of the integrand $\boldsymbol{\nabla}_{\boldsymbol{q}^{\mathbf{0}}}\sigma_{_B}\cdot\boldsymbol{\delta q}^{\mathbf{0}}_{W}(r,z)$, it is possible to integrate separately the four integrands

$$\delta_{\rho^0}\sigma_{_B}=\int_\Omega \boldsymbol{\nabla}_{\rho^0}\sigma_{_B}\cdot\delta\rho^{\mathbf{0}}_{W}\,r\mathrm{d}r\mathrm{d}z\,, \tag{6.3a}$$

$$\delta_{\rho^0\boldsymbol{u}^{\mathbf{0}}}\sigma_{_B}=\int_\Omega \boldsymbol{\nabla}_{\rho^0\boldsymbol{u}^{\mathbf{0}}}\sigma_{_B}\cdot\delta(\rho^0\boldsymbol{u}^{\mathbf{0}})_{_W}\,r\mathrm{d}r\mathrm{d}z\,, \tag{6.3b}$$

$$\delta_{\rho^0T^0}\sigma_{_B}=\int_\Omega \boldsymbol{\nabla}_{\rho^0T^0}\sigma_{_B}\cdot\delta(\rho^0T^0)_{_W}\,r\mathrm{d}r\mathrm{d}z\,, \tag{6.3c}$$

$$\delta_{p^0}\sigma_{_B}=\int_\Omega \boldsymbol{\nabla}_{p^0}\sigma_{_B}\cdot\delta(p^0)_{_W}\,r\mathrm{d}r\mathrm{d}z\,, \tag{6.3d}$$

so that

$$\delta\sigma_{_B}=\delta_{\rho^0}\sigma_{_B}+\delta_{\rho^0\boldsymbol{u}^{\mathbf{0}}}\sigma_{_B}+\delta_{\rho^0T^0}\sigma_{_B}+\delta_{p^0}\sigma_{_B}\,. \tag{6.4}$$

This allows to distinguish between the contributions to the overall variation $\delta\sigma_{_B}$ issuing from the modification of density, momentum, internal energy and pressure. Moreover, the stabilizing effect of base bleed can be investigated in terms of the competition between advection and production of disturbances, using the specific advection and production sensitivity functions defined in § 2. $\delta\sigma_{_B}$ can then be decomposed into

$$\delta\sigma_{_B}=\delta^{(A)}\sigma_{_B}+\delta^{(P)}\sigma_{_B}\,, \tag{6.5}$$

where $\delta^{(A)}\sigma_{_B}$ and $\delta^{(P)}\sigma_{_B}$ measure the variation of the eigenvalue owing to the modification of the advection operator and of the total production operator induced by the base flow modification $\boldsymbol{\delta q}^{\mathbf{0}}_{W}$. Physically, a positive (resp. negative) value of $\delta^{(A)}\sigma_{_B}$ indicates a destabilization (resp. a stabilization) of the eigenmode owing to a weakening (resp. a strengthening) of the disturbances advection. Similarly, a positive (resp. negative) value of $\delta^{(P)}\sigma_{_B}$ indicates a destabilization (resp. a stabilization) owing to an increase (resp. a decrease) of the disturbances production. These terms are computed respectively as the projection of $\boldsymbol{\delta q}^{\mathbf{0}}_{W}$ onto the advection and production sensitivity functions, i.e.

$$\delta^{(A)}\sigma_{_B}=\left\langle \boldsymbol{\nabla}^{(A)}_{\boldsymbol{q}^{\mathbf{0}}}\sigma_{_B}\,,\,\boldsymbol{\delta q}^{\mathbf{0}}_{W}\right\rangle\,,\qquad \delta^{(P)}\sigma_{_B}=\left\langle \boldsymbol{\nabla}^{(P)}_{\boldsymbol{q}^{\mathbf{0}}}\sigma_{_B}\,,\,\boldsymbol{\delta q}^{\mathbf{0}}_{W}\right\rangle\,. \tag{6.6}$$

Results of the decompositions (6.4) and (6.5) are provided in Table 1. It can be seen first that both variations $\delta^{(A)}\sigma_{_B}$ and $\delta^{(P)}\sigma_{_B}$ are negative, meaning that the modifications of the advection and production mechanisms are both stabilizing, and that the main stabilization comes from the advection mechanism. Furthermore, both mechanisms are entirely triggered by the contribution of momentum, as the density, energy and pressure modifications are seen to contribute for nothing in the overall variation. As a result, it can be claimed that the stabilizing effect of base bleed arises simultaneously from a weakening of the production and a strong strengthening of the advection of perturbations, both being triggered by the variation of the base flow momentum. Note that at the high Reynolds numbers considered here, the contribution to these variations of the terms weighted by the inverse of the Reynolds number in (5.11) has been estimated, and accounts for

	$\delta_{\rho^0}\sigma_B$	$\delta_{\rho^0\boldsymbol{u}^0}\sigma_B$	$\delta_{\rho^0 T^0}\sigma_B$	$\delta_{p^0}\sigma_B$	$\delta\sigma_B$
$\boldsymbol{\nabla}$	7.0×10^{-4}	-3.2×10^{-2}	1.2×10^{-4}	-1.6×10^{-6}	-3.1×10^{-2}
$\boldsymbol{\nabla}^{(A)}$	4.1×10^{-6}	-2.1×10^{-2}	6.5×10^{-6}	0	-2.1×10^{-2}
$\boldsymbol{\nabla}^{(P)}$	7.0×10^{-4}	-1.1×10^{-2}	1.2×10^{-4}	-1.6×10^{-6}	-1.0×10^{-2}

Table 1: Evaluation of the oscillating growth rate variation $\delta_{\boldsymbol{q}^0}\sigma_B$ from the base flow modification $\boldsymbol{\delta q}^{\boldsymbol{0}}_W$ owing to the modification of the wall forcing velocity δw_W. $\delta_{\rho^0}\sigma_B$, $\delta_{\rho^0\boldsymbol{u}^0}\sigma_B$, $\delta_{\rho^0 T^0}\sigma_B$ and $\delta_{p^0}\sigma_B$ are the variations obtained by evaluating individually the specific variation arising from the modification of density, momentum, internal energy and pressure, so that the overall variation $\delta_{\boldsymbol{q}^0}\sigma_B$ is the sum of these four contributions. Results obtained using the overall sensitivity functions are provided on the first line. Results obtained using the advection/production decomposition (6.5) are provided on the second and third lines respectively - $Re = 2000$, $M = 0.5$, $\delta w_W = 0.01$.

	$\delta_{\rho^0 u^0}\sigma_B$	$\delta_{\rho^0 w^0}\sigma_B$	$\delta_{\rho^0\boldsymbol{u}^0}\sigma_B$
$\boldsymbol{\nabla}$	-2.7×10^{-2}	-4.6×10^{-3}	-3.2×10^{-2}
$\boldsymbol{\nabla}^{(A)}$	-2.5×10^{-2}	4.2×10^{-3}	-2.1×10^{-2}
$\boldsymbol{\nabla}^{(P)}$	-2.2×10^{-3}	-8.8×10^{-3}	-1.1×10^{-2}

Table 2: Decomposition of the momentum variation $\delta_{\rho^0\boldsymbol{u}^0}\sigma_B$ displayed in Table 1 in terms of the cross-stream and streamwise momentum components.

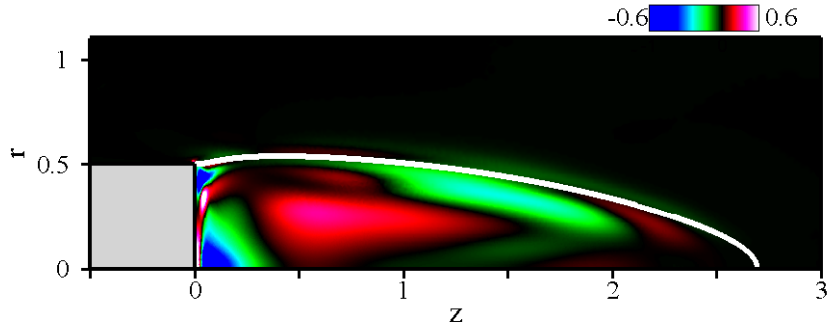

Figure 14: Spatial distribution of the momentum integrand $\boldsymbol{\nabla}^{(A)}_{\rho^0\boldsymbol{u}^0}\sigma_B \cdot \delta(\rho^0\boldsymbol{u}^{\boldsymbol{0}})_M(r,z)$ that dominates the overall growth rate variation. The integration over space of this field yields the variation $\delta^{(A)}\sigma_B$ and the black hue corresponds to vanishing magnitudes of the integrand - $Re = 2000$, $M = 0.5$, $\delta w_W = 0.01$.

approximatively 1 % of the overall variations documented in Table 1, despite the fact that the components of the symmetrical tensor $\boldsymbol{\tau}(\boldsymbol{u}^{\boldsymbol{0\dagger}})/Re$ may grow up to order-one quantities in the vicinity of the edge. As a consequence, it can be claimed that the wall sensitivity is triggered by the product of the wall density and adjoint densities $\rho^0\rho^{0\dagger}$.

To identify the regions in space which are responsible for the stabilization of the global mode, we present in Figure 14 the spatial distribution of the advection momentum integrand $\boldsymbol{\nabla}^{(A)}_{\rho^0\boldsymbol{u}^0}\sigma_B \cdot \delta(\rho^0\boldsymbol{u}^{\boldsymbol{0}})_W(r,z)$, whose integration over space yields the variation $\delta^{(A)}\sigma_B$ that dominates the overall variation $\delta\sigma_B$. At a given station, a positive (resp. negative) value indicates that the base flow modification $\boldsymbol{\delta q}^{\boldsymbol{0}}_W$ contributes to the destabilization

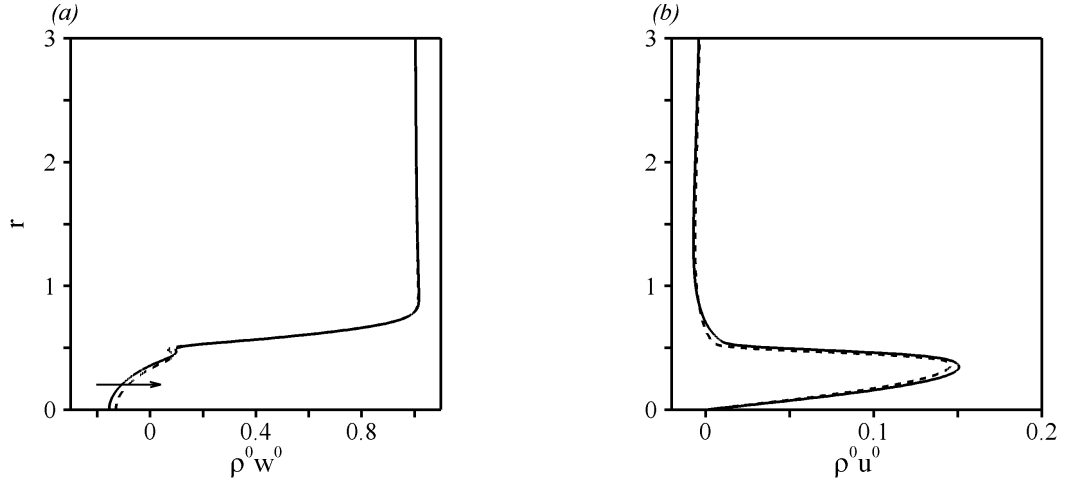

Figure 15: Effect of a base bleed at the streamwise station $z = 0.1$ - $Re = 2000$, $M = 0.5$, $\delta w_W = 0.01$. Spatial distribution of the (a) streamwise momentum $\rho^0 w^0$ and (b) cross-stream momentum $\rho^0 u^0$. The base flow quantities, i.e. $\boldsymbol{q^0}$, and the modified quantities, i.e. $\boldsymbol{q^0} + \boldsymbol{\delta q^0_W}$, are depicted by the solid and dashed lines respectively.

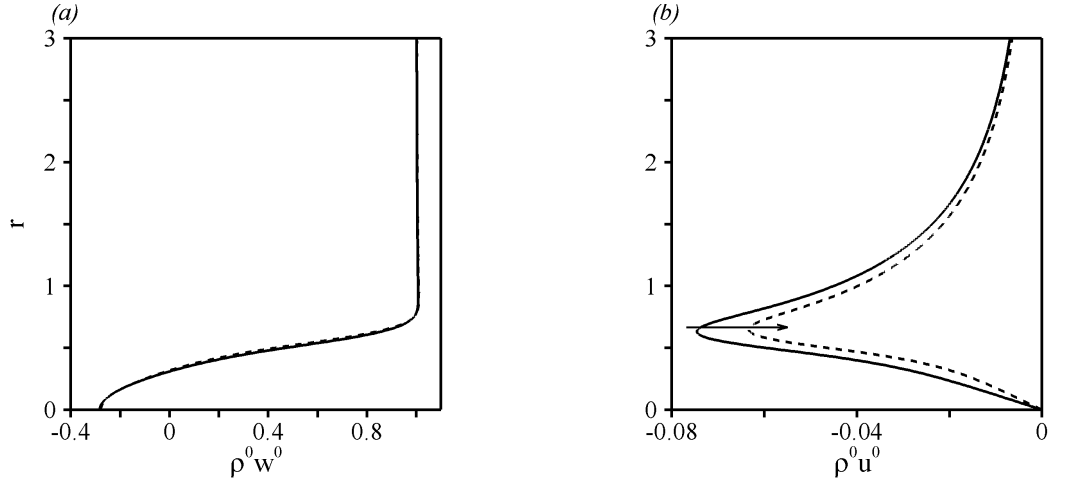

Figure 16: Same as Figure 15 for the streamwise station $z = 1.5$.

(resp. stabilization) of the global mode. Several regions contributing either to a stabilization or to a destabilization are visible in Figure 14, thus outlining the complex effect of base blowing on the variation of the growth rate. For instance the vicinity of the base, as well as the separation line contribute to a strong stabilization of the global mode, whereas the core of the recirculation contributes to its destabilization. Figure 15 shows the cross-stream and streamwise momentum distributions at the streamwise station $z = 0.1$, i.e. in the core of the stabilizing region located close to the base. The solid and dashed lines refer to the base flows $\boldsymbol{q^0}$ and $\boldsymbol{q^0} + \boldsymbol{\delta q^0_W}$ respectively. Blowing reduces the streamwise counterflow velocity by approximatively 16 %, whereas the effect on the cross-stream component is more subtle. It turns out that at this location, the effect of base bleed is due to the *streamwise* momentum variation. Figure 16 shows similar momentum distributions at the station $z = 1.5$, i.e. in the core of the second stabilizing region. It can be seen now that the effect of blowing on the streamwise component is now barely visible, whereas it significantly spreads out the cross-stream momentum gradients over a large cross-stream distance. It can be claimed as well that at this location,

the effect of base bleed is triggered by a weakening of the cross-stream gradients, that occurs through *cross-stream* momentum variations. Since variations of both momentum components are involved in the overall stabilizing effect, we have further investigated their specific contribution to the variation $\delta_{\rho^0 \boldsymbol{u}^0}\sigma_B$. Results are provided in Table 2. Strikingly, we find that base bleed acts mainly through the cross-stream component, the contribution of the streamwise component to the overall variation $\delta\sigma_B$ being smaller by one order of magnitude, and the contribution of the streamwise component relative to the advection variation $\delta^{(A)}\sigma_B$ being even slightly destabilizing. It is worth noting that the latter effect is opposite to that relative to the production variation $\delta^{(P)}\sigma_B$ which is stabilizing. These results are very interesting with regards to the interpretations usually made in the framework of the local theory. Although they might seem counterintuitive, we recall that the effect on the growth rate is not only triggered by the magnitude of the base flow modification but also by its orientation with respect to the sensitivity function. This strongly suggests that the action of base bleed is non-parallel in essence, and may not be fully captured nor interpreted by performing only local analyses, although there is no doubt that useful insight at the underlying physics can be gained from the local theory.

6.2. *Discussion*

It should be kept in mind that the sensitivity analysis is fundamentally linear since it is based on the evaluation of a gradient. In particular, it is assumed that the forced base flow $\boldsymbol{q}_W^{\mathbf{0}}$ can be sought for as a linear modification of the unforced base flow $\boldsymbol{q}^{\mathbf{0}}$. Though, it has been seen that for large wall velocities, the modification of the base flow is large as it results in a significant displacement of the recirculation and reduction of the counterflow rate. This means that the amplitude of forcing being not infinitesimal anymore, the induced base flow modification $\boldsymbol{\delta q}_W^{\mathbf{0}}$ may become large enough to invalidate the linear assumption. Consequently, the variation of the eigenvalue computed by means of the sensitivity analysis is exact only in the limit of small wall velocities. For wall velocities of larger magnitude, it consists in a linear estimation of a variation of unit order of magnitude.

As a way to investigate the effect of nonlinearities on the present problem, we consider now different magnitudes of wall velocities, still with uniform distribution at the base. The growth rate σ_B of the oscillating global mode is depicted in Figure 17(a) as a function of δw_W. Results are also presented in terms of the flow rate through the base δD, defined as

$$\delta D = 8 \int_{\Gamma_c} \rho^0 \delta w_W r \mathrm{d}r \,. \tag{6.7}$$

The solid line corresponds to the evaluation of σ_B issuing from the adjoint-based gradient (5.11a). Practically, the sensitivity analysis provides the linear estimation of the growth rate variation $\delta\sigma_B$ which, added to the unforced growth rate σ_B, yields the linear estimation of the growth rate of the forced base flow. For each wall velocity, the real growth rate can also be computed exactly by performing the standard global stability analysis on the base flow which satisfies the nonlinear equations (2.6) for the corresponding wall velocity, i.e. the base flow depicted in Figure 13. Results of these forward calculations are shown in Figure 17(a) as the grey circle symbols. We find that σ_B decreases as the wall velocity increases, thus illustrating the stabilizing effect of base blowing. The small-amplitude range $\delta w_W \leqslant 0.01$ is more clearly visible on the close-up in Figure 17(b). It can be seen that the relative difference between linear and nonlinear estimations of the growth rate is not measurable for $\delta w_W \leqslant 0.001$, a result indicating that the linear assumption holds

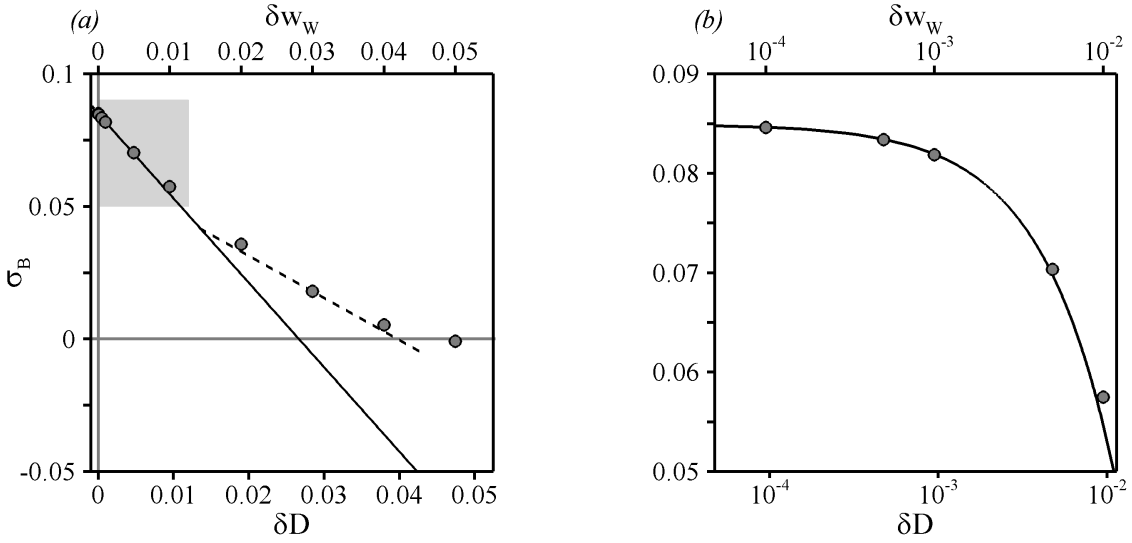

Figure 17: (a) Growth rate $\sigma_{_B}$ as a function of the wall velocity $\delta w_{_W}$/flow rate δD. Comparison of the linear results obtained from the sensitivity analysis (solid line) with the nonlinear results obtained from forward calculations on the real forced base flow (circle symbols). The dashed line stands for the linear results obtained by applying the sensitivity analysis to the forced base flow, along with $w_{_W} = 0.03$. (b) Enlargement of the small velocity shaded area of (a). - $Re_{_B} = 2000$ and $M = 0.5$.

and thus validating the correctness of the sensitivity functions computed in the present study. For larger wall velocities, we observe small discrepancies, as nonlinearities set in. We observe in particular that the decrease in the growth rate computed by the sensitivity analysis slightly overestimates the stabilizing effect of forcing, meaning that the linear and non-linear mechanisms are competitive. As a result, the critical wall velocity, for which the zero-growth rate is achieved, is shifted from $\delta w_{_W} \simeq 0.048$, which stands from the value predicted by forward calculations, to 0.028, as predicted by the sensitivity analysis.

In order to understand the origin of the discrepancies observed between the linear and nonlinear growth rate predictions, we present in Figure 18(a) the location of the front stagnation point z_r^u (resp. the rear stagnation point z_r^d) computed as a function of the wall velocity. The solid lines (resp. the dashed lines) correspond to the forced base flow $\boldsymbol{q}_{_W}^{\mathbf{0}}$ (resp. the linear approximation $\boldsymbol{q}^{\mathbf{0}} + \boldsymbol{\delta q}_{_W}^{\mathbf{0}}$). It can be seen that the position of the rear stagnation point is quite well estimated in the linear approach, the maximum difference being of 4 % for $\delta w_{_W} = 0.06$. However, the position of the front stagnation point is significantly underestimated in the linear approach, as soon as $\delta w_{_W} \geqslant 0.03$, which results in a large overestimation of the recirculating length. Figure 18(b) presents the evolution of the counterflow rate for different values of wall blowing. Again, the solid and dashed lines refer to the nonlinear and linearly approximated forced base flow. Strikingly, we find that the linear approach fails to reproduce the significant reduction of reverse flow velocity that has been previously illustrated. Even more surprising, we find that the linear and nonlinear effects are opposed when the wall velocity exceeds $\delta w_{_W} = 0.03$, a range where the linearly predicted counterflow rate is seen to increase. These arguments are not fully conclusive, though. In particular, in terms of local stability, it remains quite unclear why the linear approach finally slightly overestimates the stabilizing effect of base blowing, as an overestimation of the counterflow rate would be expected to favor the growth of the instability rather than its damping. This outlines the complexity of the mechanisms at

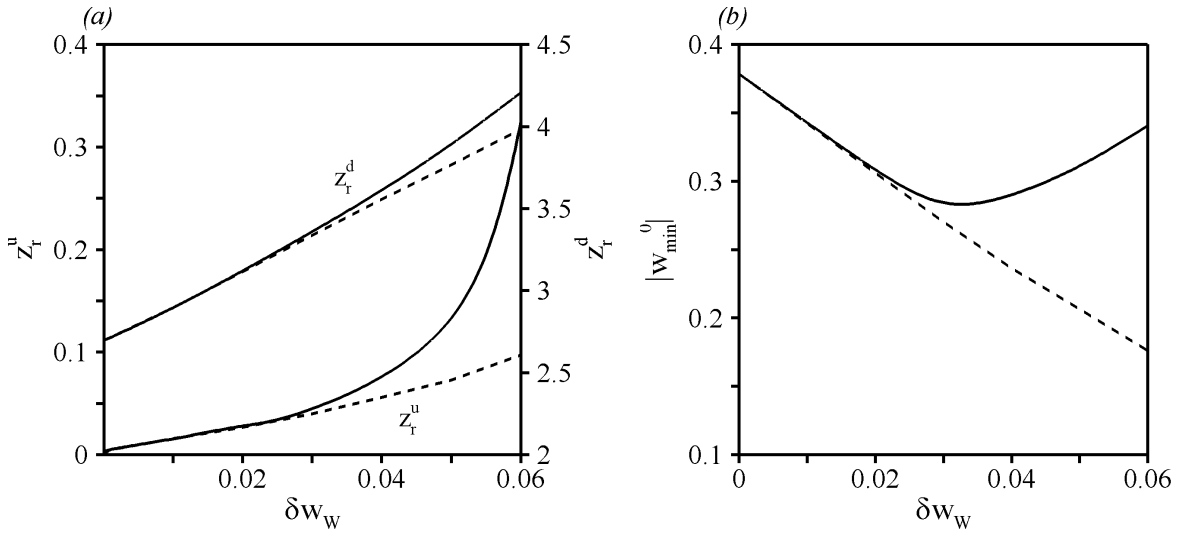

Figure 18: (a) Location of the front (resp. rear) stagnation point z_r^u (resp. z_r^d) on the $r = 0$ axis for the base flow in presence of base bleed. (b) Same as (a) for the magnitude of counterflow as a function of the wall velocity. The solid lines (resp. the dashed lines) correspond to the real base flow $\boldsymbol{q}_W^{\mathbf{0}}$ solution of the forced base flow equations (resp. the linear approximation of the forced base flow $\boldsymbol{q}^{\mathbf{0}} + \boldsymbol{\delta q}_W^{\mathbf{0}}$).

work and comes in support of the idea that the stability and control of this class of flows should be achieved in a global framework.

Moreover, it should be kept in mind that in the framework of optimal control, one does not necessarily have to violate the linear assumption. For instance, an optimal distribution of possibly large-amplitude base bleed can be found by departing progressively from the unforced case, following a naive steepest descent technique. To this end, one does not directly infer the effect of the ultimate distribution from the gradient of the unforced eigenvalue. Considering for simplicity the case of uniform bleed, one jumps from one circle symbol to another in Figure 17, and at each symbol, the present sensitivity analysis provides with an accurate estimation of the sensitivity with respect to a modification of the wall velocity. For instance the dashed line in Figure 17(a) corresponds to the values of $\sigma_{_B}$ issuing from the sensitivity analysis applied to the forced base flow along with $w_{_W} = 0.03$: it is seen to lead a good estimation of the real growth rate prevailing close to this specific value. This formalism therefore stands as a promising tool for the design of future control laws, even at realistic parameter settings were nonlinear effects may be non-negligible.

Finally, it has been said previously that the present sensitivity formalism can be extended and used to derive optimal control strategies. Such an extension is out of the scope of this study. Though, as very a simple illustration of this point, we propose to conclude this study by considering the effect on the growth rate $\sigma_{_B}$ of two alternative velocity distributions $\delta w_{_W}(r)$, the question of nonlinearities being now left aside. The first distribution is depicted in Figure 12(b): it consists in a piecewise-constant distribution, with low speed blowing in the center region ($r < 0.2$) where the sensitivity is the lowest, and high speed blowing close to the edge, and stands for a roughly optimized distribution. The second one is chosen so as to achieve the maximum stabilizing effect, namely we set

$$\delta w_{_W} = -\alpha \boldsymbol{\nabla}_{w_{_W}} \sigma_{_B} \,, \tag{6.8}$$

where α is a normalization coefficient. The variations $\delta\sigma_{_B}$ associated to these two dis-

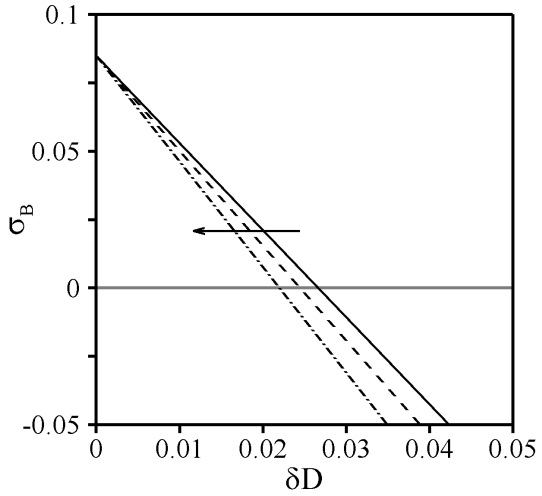

Figure 19: Growth rate $\sigma_{_B}$ as a function of the flow rate δD. Comparison of the linear results obtained from the sensitivity analysis with a uniform velocity distribution (solid line), the piecewise-constant velocity distribution pictured in Figure 12(b) (dashed line), and the gradient-based distribution (6.8) (dash-dotted line) - $Re_{_B} = 2000$ and $M = 0.5$.

tributions have been computed for the unforced base flow ($w_{_W} = 0$), and are shown in Figure 19 as the dashed and dash-dotted lines respectively. Results are presented in term of the flow rate δD only, so as to allow comparison with the case of uniform bleed described previously, also shown as the solid line in Figure 19. One notes that it is possible to achieve a stronger stabilization using the optimized blowing distribution, as the critical flow rate drops by approximately 8 % from $\delta D \simeq 0.027$ to 0.025 with the piecewise-constant distribution, and 0.022 using the gradient-based distribution (6.8), thus illustrating the importance of using physically motivated blowing distributions.

7. Conclusion

Following the line of thought of the seminal studies by Hill (1992) and Marquet *et al.* (2008), this paper develops sensitivity analyses whose aim is to predict variations of the eigenvalue of global modes in compressible flows, up to the high subsonic regime. This stands for a systematic approach of open-loop control, in which the eigenvalue variations are viewed as resulting from a specific modification of the base flow induced by a steady volumetric and/or wall forcing. The variation can then be investigated as a function of the base flow modification, defining the sensitivity analysis to base flow modifications, or directly as a function of forcing, thus defining the sensitivity analysis to steady forcing. Both analyses are based on the evaluation of gradients using adjoint methods.

The sensitivity functions to base flow modification depend on the base flow and perturbation quantities, as well as on the adjoint perturbation quantities, for which adjoint stability equations have been derived in a consistent way. Extending the study of Marquet *et al.* (2008), it has also been shown possible to distinguish between the variation owing to the respective modifications of the advection and production mechanisms, which extend to spatially developing flows the concepts of convective and absolute instability pertaining to parallel flows. The sensitivity functions to volumetric forcing are derived by introducing, on top of the sensitivity to base flow modifications, an adjoint base flow problem which is forced by a source term involving the sensitivity to base flow modifi-

cations. Finally, the sensitivity functions to wall forcing can then be deduced from the knowledge of the base flow and of their volumetric counterpart.

The sensitivity to steady forcing has been applied to a subsonic afterbody flow at $M = 0.5$. In Part I, it has been previously shown that the axisymmetric base flow that develops past such bodies is first destabilized by a stationary global mode of azimuthal wavenumber $m = 1$ and then, at a larger Reynolds, by an oscillating global mode, the latter being responsible for the occurrence of a fully 3D periodic state at large Reynolds numbers. In this study, we use the sensitivity functions to steady forcing to assess the efficiency of various open-loop control techniques, whose aim is to restabilize this oscillating global mode, as a possible way to alleviate afterbody unsteadiness. It has been shown that for all techniques, the global mode is most sensitive to forcing within the recirculating bubble. High sensitivity to an axisymmetric punctual momentum source has been found close to the separation line. In this particular flow region, a small control ring, whose presence has been modeled by the force it exerts on the base flow, has been shown to be stabilizing. Axisymmetric heat sources mimicking axisymmetric gas discharges are also stabilizing for almost all positions in the recirculation, as well as mass sources close to the base or along the separation line. The latter case being not very realistic, mass injection has been further investigated in the framework of wall control at the base. The sensitivity of the global mode has been shown to be fully dominated by the product of the base flow and adjoint base flow densities. The spatial distribution of the sensitivity functions shows that a stabilizing effect can be obtained if fluid is blown through the whole base, or if the base is cooled in its inner part and heated at its periphery. However, the latter technique has been found to produce only very limited results, owing to the sensitivity being weighted by the inverse of the Reynolds number.

Base bleed has finally been investigated in the framework of the sensitivity analysis to base flow modifications. We have shown that its stabilizing effect arises from a strengthening of the disturbances advection occurring through variations of the base flow momentum components. Further investigation has shown that this effect is simultaneously at work in two distinct flow regions, namely close to the base, where it is due to a reduction of the counterflow rate, and further downstream, where it is due to the cross-stream momentum gradients being spread out. Moreover, the contribution of the cross-stream momentum in the stabilizing effect of base bleed has been shown to be dominant, which outlines the importance of studying such spatially developing flows in a global framework.

This approach consisting in the open-loop control of a global instability can be easily applied to other compressible flow configurations, as for instance cavity flows or hot jets that are known to sustain global instabilities. Extending the present approach to the case of transonic and supersonic flows, where one must deal with the presence of shock waves in the flow, also deserves future efforts, as it may for instance open new ways to explore the problem of the shock-induced transonic-buffet onset on airplanes.

Appendix A. Derivation of the sensitivity functions to base flow modifications

We recall here that the base flow equations have been written as

$$\mathcal{M}_0(\boldsymbol{q^0}) = (\mathscr{I}, 0)^T . \tag{A 1}$$

Similarly, the direct stability problem has been written as

$$\lambda\mathcal{B}(\boldsymbol{q^0})\hat{\boldsymbol{q}}^{\boldsymbol{1}} + \mathcal{A}_m(\boldsymbol{q^0})\hat{\boldsymbol{q}}^{\boldsymbol{1}} = \boldsymbol{0}\,. \tag{A 2}$$

The eigenvalue variation $\delta\lambda$ and the base flow modification $\boldsymbol{\delta q^0}$ are such that

$$\delta\lambda = \delta\sigma + \mathrm{i}\delta\omega = \left\langle \boldsymbol{\nabla}_{\boldsymbol{q^0}}\lambda\,,\, \boldsymbol{\delta q^0}\right\rangle\,, \tag{A 3}$$

where we use $\langle \hat{\boldsymbol{a}}\,, \hat{\boldsymbol{b}}\rangle = \int_\Omega \hat{\boldsymbol{a}}\cdot\hat{\boldsymbol{b}}\, r\mathrm{d}r\mathrm{d}z$ for compact notation.

In the present formalism, the eigenpair $\{\hat{\boldsymbol{q}}^{\boldsymbol{1}}, \lambda\}$ is the *state variable*, the base flow $\boldsymbol{q^0}$ is the *control variable* and the eigenproblem ($A\,2$) is the *state equation*, i.e. the constraint to be satisfied. We introduce a Lagrange multiplier $\hat{\boldsymbol{q}}^{\boldsymbol{1\dagger}}$ (also known as *adjoint* or *co-state* variable) for the state variable, that are herein referred to as the adjoint perturbation, and define the functional

$$\mathcal{L}(\boldsymbol{q^0}, \hat{\boldsymbol{q}}^{\boldsymbol{1\dagger}}, \hat{\boldsymbol{q}}^{\boldsymbol{1}}, \lambda) = \lambda - \left\langle \hat{\boldsymbol{q}}^{\boldsymbol{1\dagger}}\,,\, \lambda\mathcal{B}(\boldsymbol{q^0})\hat{\boldsymbol{q}}^{\boldsymbol{1}} + \mathcal{A}_m(\boldsymbol{q^0})\hat{\boldsymbol{q}}^{\boldsymbol{1}}\right\rangle\,. \tag{A 4}$$

The gradient with respect to any variable s, is defined as

$$\frac{\partial\mathcal{L}}{\partial s}\delta s = \lim_{\epsilon\to 0}\frac{\mathcal{L}(s+\epsilon\delta s) - \mathcal{L}(s)}{\epsilon}\,. \tag{A 5}$$

In the following, we assume that the state equation is satisfied for any arbitrary base flow modification. Under this assumption, it has been shown in Part I that defining the adjoint perturbation as the solution of the adjoint eigenproblem (2.14), along with the normalization condition (2.17) yields

$$\delta\lambda = \frac{\partial\mathcal{L}}{\partial\boldsymbol{q^0}}\boldsymbol{\delta q^0}\,. \tag{A 6}$$

The gradient of the functional with respect to the base flow can be expressed as

$$\frac{\partial\mathcal{L}}{\partial\boldsymbol{q^0}}\boldsymbol{\delta q^0} = -\left\langle \hat{\boldsymbol{q}}^{\boldsymbol{1\dagger}}\,,\, \lambda\mathcal{R}(\boldsymbol{q^0}, \hat{\boldsymbol{q}}^{\boldsymbol{1}})\boldsymbol{\delta q^0} + \mathcal{S}_m(\boldsymbol{q^0}, \hat{\boldsymbol{q}}^{\boldsymbol{1}})\boldsymbol{\delta q^0}\right\rangle \tag{A 7a}$$

$$= -\left\langle \lambda^*\mathcal{R}^\dagger(\boldsymbol{q^0}, \hat{\boldsymbol{q}}^{\boldsymbol{1}})\hat{\boldsymbol{q}}^{\boldsymbol{1\dagger}} + \mathcal{S}_m^\dagger(\boldsymbol{q^0}, \hat{\boldsymbol{q}}^{\boldsymbol{1}})\hat{\boldsymbol{q}}^{\boldsymbol{1\dagger}}\,,\, \boldsymbol{\delta q^0}\right\rangle\,, \tag{A 7b}$$

so that the sensitivity function $\boldsymbol{\nabla}_{\boldsymbol{q^0}}\lambda$ is given by

$$\boldsymbol{\nabla}_{\boldsymbol{q^0}}\lambda = -\lambda^*\mathcal{R}^\dagger(\boldsymbol{q^0}, \hat{\boldsymbol{q}}^{\boldsymbol{1}})\hat{\boldsymbol{q}}^{\boldsymbol{1\dagger}} - \mathcal{S}_m^\dagger(\boldsymbol{q^0}, \hat{\boldsymbol{q}}^{\boldsymbol{1}})\hat{\boldsymbol{q}}^{\boldsymbol{1\dagger}}\,. \tag{A 8}$$

where $\mathcal{R}$ and $\mathcal{S}_m$ are the linear differential operators defined by

$$\mathcal{R}(\boldsymbol{q^0}, \hat{\boldsymbol{q}}^{\boldsymbol{1}}) = \frac{\partial}{\partial\boldsymbol{q^0}}\left(\mathcal{B}(\boldsymbol{q^0})\hat{\boldsymbol{q}}^{\boldsymbol{1}}\right)\,, \qquad \mathcal{S}_m(\boldsymbol{q^0}, \hat{\boldsymbol{q}}^{\boldsymbol{1}}) = \frac{\partial}{\partial\boldsymbol{q^0}}\left(\mathcal{A}_m(\boldsymbol{q^0})\hat{\boldsymbol{q}}^{\boldsymbol{1}}\right)\,. \tag{A 9}$$

This yields the expressions given in (2.18). Using the same Lagrangian technique, it can be seen that the advection operator $\mathcal{C}_m^{(A)}$ contributes in the gradient ($A\,7$) through the quantity

$$-\left\langle \hat{\boldsymbol{q}}^{\boldsymbol{1\dagger}}\,,\, \mathcal{S}_m^{(A)}(\boldsymbol{q^0}, \hat{\boldsymbol{q}}^{\boldsymbol{1}})\boldsymbol{\delta q^0}\right\rangle = -\left\langle \mathcal{S}_m^{(A)\dagger}(\boldsymbol{q^0}, \hat{\boldsymbol{q}}^{\boldsymbol{1}})\hat{\boldsymbol{q}}^{\boldsymbol{1\dagger}}\,,\, \boldsymbol{\delta q^0}\right\rangle\,, \tag{A 10}$$

where

$$\mathcal{S}_m^{(A)}(\boldsymbol{q^0}, \hat{\boldsymbol{q}}^{\boldsymbol{1}}) = \frac{\partial}{\partial\boldsymbol{q^0}}\left(\mathcal{C}_m^{(A)}(\boldsymbol{q^0})\hat{\boldsymbol{q}}^{\boldsymbol{1}}\right)\,. \tag{A 11}$$

It is therefore immediate to define the sensitivity to a modification of the advection operator $\boldsymbol{\nabla}_{\boldsymbol{q^0}}^{(A)}\lambda$

$$\boldsymbol{\nabla}_{\boldsymbol{q^0}}^{(A)}\lambda = -\mathcal{S}_m^{(A)\dagger}(\boldsymbol{q^0}, \hat{\boldsymbol{q}}^{\boldsymbol{1}})\hat{\boldsymbol{q}}^{\boldsymbol{1\dagger}}\,, \tag{A 12}$$

thus yielding expressions (2.19).

Appendix B. Derivation of the sensitivity functions to a steady forcing

For simplicity, we consider here that the volumetric term $\mathscr{I}$ forces all governing equations, including the perfect gas relation, although this has no real physical interpretation. The formalism used in this study can thus be viewed as a subset of this more general approach. The base flow $\boldsymbol{q^0}$ and the eigenpair $\{\hat{\boldsymbol{q}}^{\boldsymbol{1}}, \lambda\}$ are now the state variables, the forcing $\{\mathscr{I}, \boldsymbol{u_w}, T_W\}$ are the control variables, and the base flow equations ($A\,1$) and the eigenproblem ($A\,2$) are the state equations. In addition to the adjoint perturbation $\hat{\boldsymbol{q}}^{\boldsymbol{1\dagger}}$, we thus introduce a new Lagrange multiplier for the base flow $\boldsymbol{q^{0\dagger}}$, herein referred to as the adjoint base flow. A new functional is defined as

$$\mathcal{L}(\mathscr{I}, \boldsymbol{q^{0\dagger}}, \boldsymbol{q^0}, \hat{\boldsymbol{q}}^{\boldsymbol{1\dagger}}, \hat{\boldsymbol{q}}^{\boldsymbol{1}}, \lambda) = \lambda - \left\langle \hat{\boldsymbol{q}}^{\boldsymbol{1\dagger}} \,,\, \lambda\mathcal{B}(\boldsymbol{q^0})\hat{\boldsymbol{q}}^{\boldsymbol{1}} + \mathcal{A}_{_m}(\boldsymbol{q^0})\hat{\boldsymbol{q}}^{\boldsymbol{1}} \right\rangle - \left\langle \boldsymbol{q^{0\dagger}} \,,\, \mathcal{M}_{_0}(\boldsymbol{q^0}) - \mathscr{I} \right\rangle - \int_{\Gamma_c} (\boldsymbol{u}^{\dagger}_{\boldsymbol{w}} \cdot (\boldsymbol{u^0} - \boldsymbol{u_w}) + T^{\dagger}_{W}(T^0 - T_W) r \mathrm{d}l \,. \tag{B 1}$$

We consider the variation of the eigenvalue $\delta\lambda$ resulting from a modification of the forcing terms $\boldsymbol{\delta F} = \delta\{\mathscr{I}, \boldsymbol{u_w}, T_W\}$, assuming that the state equations remain satisfied . $\delta\lambda$ can then be expressed formally as

$$\delta\lambda = \left(\frac{\partial \mathcal{L}}{\partial \boldsymbol{F}} + \frac{\partial \mathcal{L}}{\partial \boldsymbol{q^{0\dagger}}} \frac{\partial \boldsymbol{q^{0\dagger}}}{\partial \boldsymbol{F}} + \frac{\partial \mathcal{L}}{\partial \boldsymbol{q^0}} \frac{\partial \boldsymbol{q^0}}{\partial \boldsymbol{F}} + \frac{\partial \mathcal{L}}{\partial \hat{\boldsymbol{q}}^{\boldsymbol{1\dagger}}} \frac{\partial \hat{\boldsymbol{q}}^{\boldsymbol{1\dagger}}}{\partial \boldsymbol{F}} + \frac{\partial \mathcal{L}}{\partial \{\hat{\boldsymbol{q}}^{\boldsymbol{1}}, \lambda\}} \frac{\partial \{\hat{\boldsymbol{q}}^{\boldsymbol{1}}, \lambda\}}{\partial \boldsymbol{F}} \right) \boldsymbol{\delta F} \tag{B 2}$$

The gradients of the functional with respect to the adjoint variables read

$$\frac{\partial \mathcal{L}}{\partial \boldsymbol{q^{0\dagger}}} \boldsymbol{\delta q^{0\dagger}} = - \left\langle \boldsymbol{\delta q^{0\dagger}} \,,\, \mathcal{M}_{_0}(\boldsymbol{q^0}) - \mathscr{I} \right\rangle \,, \tag{B 3a}$$

$$\frac{\partial \mathcal{L}}{\partial \hat{\boldsymbol{q}}^{\boldsymbol{1\dagger}}} \boldsymbol{\delta \hat{q}^{1\dagger}} = - \left\langle \boldsymbol{\delta \hat{q}^{1\dagger}} \,,\, \lambda\mathcal{B}(\boldsymbol{q^0})\hat{\boldsymbol{q}}^{\boldsymbol{1}} + \mathcal{A}_{_m}(\boldsymbol{q^0})\hat{\boldsymbol{q}}^{\boldsymbol{1}} \right\rangle \,. \tag{B 3b}$$

Since $\boldsymbol{q^0}$ and $\{\hat{\boldsymbol{q}}^{\boldsymbol{1}}, \lambda\}$ are solutions of the state equations, both gradients are nil. Moreover, it can be checked that the adjoint perturbation being solution of the adjoint eigenproblem (2.14) along with the normalization condition (2.17), the gradient of the functional with respect to the state variable $\{\hat{\boldsymbol{q}}^{\boldsymbol{1}}, \lambda\}$ is still zero. If we enforce that the gradient of the functional with respect to the base flow $\boldsymbol{q^0}$ is nil, as will be discussed in the following, ($B\,2$) can be rewritten as

$$\delta\lambda = \frac{\partial \mathcal{L}}{\partial \{\mathscr{I}, \boldsymbol{u_w}, T_W\}} \delta\{\mathscr{I}, \boldsymbol{u_w}, T_W\} = \underbrace{\frac{\partial \mathcal{L}}{\partial \mathscr{I}} \delta\mathscr{I}}_{(i)} + \underbrace{\frac{\partial \mathcal{L}}{\partial \boldsymbol{u_w}} \boldsymbol{\delta u_w} + \frac{\partial \mathcal{L}}{\partial T_W} \delta T_W}_{(ii)} \,, \tag{B 4}$$

so that the sensitivity functions can be expressed from the gradient of the functional with respect to the different forcing terms as

$$\frac{\partial \mathcal{L}}{\partial \mathscr{I}} \delta\mathscr{I} = \langle \boldsymbol{\nabla}_{\mathscr{I}} \lambda \,,\, \delta\mathscr{I} \rangle \,, \tag{B 5a}$$

$$\frac{\partial \mathcal{L}}{\partial \boldsymbol{u_w}} \boldsymbol{\delta u_w} = \int_{\Gamma_c} \boldsymbol{\nabla}_{\boldsymbol{u_w}} \lambda \cdot \boldsymbol{\delta u_w} d\Gamma \,, \tag{B 5b}$$

$$\frac{\partial \mathcal{L}}{\partial \boldsymbol{u_w}} \delta T_W = \int_{\Gamma_c} \boldsymbol{\nabla}_{T_W} \lambda \cdot \delta T_W d\Gamma \,. \tag{B 5c}$$

In ($B\,4$), term (i) and (ii) stand for the eigenvalue variations arising from volumetric forcing and wall forcing. These specific variations, respectively denoted $\delta\lambda|_{_W}$ and $\delta\lambda|_{_{\mathscr{I}}}$

are now derived in the framework of sensitivity analyses. As stated in Part I, such an approach is very similar to that used in optimization problems, where one enforces the stationary of a Lagrangian as a mean to minimize a given functional under specific constraint. Again, we would like to insist that no such stationarity is enforced here, and that the functional is only used as a mean to compute the different gradients of interest.

B.1. *Sensitivity to volumetric forcing*

We consider first the variation of the eigenvalue as a function of the volumetric forcing $\mathscr{I}$, the wall quantities $\boldsymbol{u_W}$ and T_W being kept constant. The gradient with respect to $\boldsymbol{q^0}$ reads

$$\frac{\partial \mathcal{L}}{\partial \boldsymbol{q^0}}\boldsymbol{\delta q^0} = -\left\langle \hat{\boldsymbol{q}}^{\boldsymbol{1\dagger}} \,,\, \lambda \mathcal{R}(\boldsymbol{q^0},\hat{\boldsymbol{q}}^{\boldsymbol{1}})\boldsymbol{\delta q^0} + \mathcal{S}_m(\boldsymbol{q^0},\hat{\boldsymbol{q}}^{\boldsymbol{1}})\boldsymbol{\delta q^0}\right\rangle - \left\langle \boldsymbol{q^{0\dagger}} \,,\, \mathcal{A}_0(\boldsymbol{q^0})\boldsymbol{\delta q^0}\right\rangle \quad (\mathrm{B}\,6a)$$

$$= -\left\langle \lambda^* \mathcal{R}(\boldsymbol{q^0},\hat{\boldsymbol{q}}^{\boldsymbol{1}})\hat{\boldsymbol{q}}^{\boldsymbol{1\dagger}} + \mathcal{S}_m^\dagger(\boldsymbol{q^0},\hat{\boldsymbol{q}}^{\boldsymbol{1}})\hat{\boldsymbol{q}}^{\boldsymbol{1\dagger}} \,,\, \boldsymbol{\delta q^0}\right\rangle - \left\langle \mathcal{A}_0^\dagger(\boldsymbol{q^0})\boldsymbol{q^{0\dagger}} \,,\, \boldsymbol{\delta q^0}\right\rangle \quad (\mathrm{B}\,6b)$$

Details on the integration by parts are given in Appendix C. Cancelling this gradient, we obtain that the adjoint base flow $\boldsymbol{q^{0\dagger}}$ is solution of the non-degenerate, linear, non-homogenous problem reading

$$\mathcal{A}_0^\dagger(\boldsymbol{q^0})\boldsymbol{q^{0\dagger}} = -\lambda^* \mathcal{R}(\boldsymbol{q^0},\hat{\boldsymbol{q}}^{\boldsymbol{1}})\hat{\boldsymbol{q}}^{\boldsymbol{1\dagger}} - \mathcal{S}_m^\dagger(\boldsymbol{q^0},\sigma,\hat{\boldsymbol{q}}^{\boldsymbol{1}})\hat{\boldsymbol{q}}^{\boldsymbol{1\dagger}} = \boldsymbol{\nabla}_{\boldsymbol{q^0}}\lambda \quad (\mathrm{B}\,7)$$

where one recognizes in the right-hand side the sensitivity to base flow modifications computed in the previous section. The boundary conditions to be fulfilled by the adjoint base flow are such that all boundary terms arising during the integration are zero. Since admissible variations $\boldsymbol{\delta u^0}$ and δT^0 are therefore such that $\boldsymbol{\delta u^0} = \boldsymbol{0}$ and $\delta T^0 = 0$ on Γ_c, we obtain after elimination of the pressure terms:

$$\boldsymbol{u^{0\dagger}} = \boldsymbol{0},\ \rho^{0\dagger}, T^{0\dagger} = 0 \quad \text{on} \quad \partial\Omega^s_{in} \cup \partial\Omega^s_{ext} \cup \partial\Omega^s_{out}\,, \quad (\mathrm{B}\,8a)$$

$$\boldsymbol{u^{0\dagger}} = \boldsymbol{0},\ \partial_n T^{0\dagger} = 0 \quad \text{on} \quad \partial\Omega_b \backslash \Gamma_c\,, \quad (\mathrm{B}\,8b)$$

$$u^0 = 0,\ \partial_r(w^0,\rho^0,T^0) = 0 \quad \text{on} \quad \partial\Omega_a\,. \quad (\mathrm{B}\,8c)$$

In the unforced case solved in the present study ($\boldsymbol{u_W} = \boldsymbol{0}$), the condition on the control surface Γ_c simply reads

$$\boldsymbol{u^{0\dagger}} = \boldsymbol{0},\ T^{0\dagger} = 0\,. \quad (\mathrm{B}\,9)$$

Since the gradient with respect to the control variable $\mathscr{I}$ is simply given by

$$\frac{\partial \mathcal{L}}{\partial \mathscr{I}}\delta\mathscr{I} = \left\langle \boldsymbol{q^{0\dagger}} \,,\, \delta\mathscr{I}\right\rangle\,, \quad (\mathrm{B}\,10)$$

it can be deduced from ($B\,5a$) and ($B\,10$) that $\boldsymbol{\nabla}_{\mathscr{I}}\lambda = \boldsymbol{q^{0\dagger}}$, i.e. the sensitivity function to a modification of the volumetric forcing $\boldsymbol{\nabla}_{\mathscr{I}}\lambda$ is precisely given by the adjoint base flow $\boldsymbol{q^{0\dagger}}$.

B.2. *Sensitivity to wall forcing*

We consider now that only the sensitivity to boundary forcing where the volumetric force is assumed to remain constant, i.e. $\boldsymbol{\delta f} = \mathbf{0}$. The gradient with respect to $\boldsymbol{q^0}$ now reads

$$\begin{aligned}\frac{\partial \mathcal{L}}{\partial \boldsymbol{q^0}}\boldsymbol{\delta q^0} = &- \left\langle \hat{\boldsymbol{q}}^{\boldsymbol{1}\dagger}\,,\, \lambda\mathcal{R}(\boldsymbol{q^0},\hat{\boldsymbol{q}}^{\boldsymbol{1}})\boldsymbol{\delta q^0} + \mathcal{S}_m(\boldsymbol{q^0},\hat{\boldsymbol{q}}^{\boldsymbol{1}})\boldsymbol{\delta q^0}\right\rangle - \left\langle \boldsymbol{q^{0\dagger}}\,,\, \mathcal{A}_0(\boldsymbol{q^0})\boldsymbol{\delta q^0}\right\rangle \\ &- \int_{\Gamma_c} \boldsymbol{u}_{\boldsymbol{W}}^{\dagger}\cdot\boldsymbol{\delta u^0} d\Gamma - \int_{\Gamma_c}(\boldsymbol{u}_{\boldsymbol{W}}^{\dagger}\cdot\boldsymbol{\delta u^0} + T_W^{\dagger}\delta T^0) r \mathrm{d}l \qquad (\mathrm{B}\,11a) \\ = &\underbrace{- \left\langle \lambda^*\mathcal{R}(\boldsymbol{q^0},\hat{\boldsymbol{q}}^{\boldsymbol{1}})\hat{\boldsymbol{q}}^{\boldsymbol{1}\dagger} + \mathcal{S}_m^{\dagger}(\boldsymbol{q^0},\hat{\boldsymbol{q}}^{\boldsymbol{1}})\hat{\boldsymbol{q}}^{\boldsymbol{1}\dagger}\,,\, \boldsymbol{\delta q^0}\right\rangle - \left\langle \mathcal{A}_0^{\dagger}(\boldsymbol{q^0})\boldsymbol{q^{0\dagger}}\,,\, \boldsymbol{\delta q^0}\right\rangle}_{(i)} \\ &\underbrace{- \int_{\Gamma_c}(\boldsymbol{u}_{\boldsymbol{W}}^{\dagger}\cdot\boldsymbol{\delta u^0} + T_W^{\dagger}\delta T^0) r \mathrm{d}l + \ \mathrm{BT}}_{(ii)} \qquad (\mathrm{B}\,11b)\end{aligned}$$

Since $\boldsymbol{q^{0\dagger}}$ is solution of (B 7), the volumetric term (i) in (B 11b) is zero. Though, on Γ_c, admissible variations $\boldsymbol{\delta u^0}$ and δT^0 are now such that $\boldsymbol{\delta u^0} = \boldsymbol{\delta u_W}$ and $\delta T^0 = \delta T_W$, so that the boundary term BT arising during the integration is not zero anymore. Cancellation of the gradient (B 11b) thus yielding the adjoint wall quantities $\boldsymbol{u}_{\boldsymbol{W}}^{\dagger}$ and $T_W^{\dagger}$ as functions of $\boldsymbol{q^0}$ and $\boldsymbol{q^{0\dagger}}$. Again, all details are provided in Appendix C. We find

$$\boldsymbol{u}_{\boldsymbol{W}}^{\dagger} = \rho^0\rho^{0\dagger}\boldsymbol{n} + \frac{1}{Re}\boldsymbol{\tau}(\boldsymbol{u^{0\dagger}})\cdot\boldsymbol{n}\,, \qquad (\mathrm{B}\,12a)$$

$$T_W^{\dagger} = \frac{\gamma}{PrRe}\boldsymbol{\nabla}T^{0\dagger}\cdot\boldsymbol{n}\,. \qquad (\mathrm{B}\,12b)$$

Since the gradients with respect to $\boldsymbol{u_W}$ and T_W are simply given by

$$\frac{\partial \mathcal{L}}{\partial \boldsymbol{u_W}}\boldsymbol{\delta u_W} = \int_{\Gamma_c}\boldsymbol{u}_{\boldsymbol{W}}^{\dagger}\cdot\boldsymbol{\delta u_W} r\mathrm{d}l\,, \qquad \frac{\partial \mathcal{L}}{\partial T_W}\delta T_W = \int_{\Gamma_c} T_W^{\dagger}\delta T_W r\mathrm{d}l\,, \qquad (\mathrm{B}\,13)$$

it can be deduced from B 5 and (B 13) that $\boldsymbol{\nabla}_{\boldsymbol{u_W}}\lambda = \boldsymbol{u}_{\boldsymbol{W}}^{\dagger}$ and $\boldsymbol{\nabla}_{T^0}\lambda = T_W^{\dagger}$, i.e. the sensitivity function to a modification of the boundary forcing $\boldsymbol{\nabla}_{\boldsymbol{u_W}}\lambda$ and $\boldsymbol{\nabla}_{T_W}\lambda$ are precisely the adjoint wall velocity $\boldsymbol{u}_{\boldsymbol{W}}^{\dagger}$ and temperature $T_W^{\dagger}$.

B.3. *Link between both approaches*

It has been said previously that both approaches are connected through the base flow modification $\boldsymbol{\delta q_F^0}$ induced by a small variation of the steady forcing $\delta\mathscr{I}$, $\boldsymbol{\delta u_W}$, δT_W, $\boldsymbol{\delta q_F^0}$ being solution of the linear problem

$$\mathcal{A}_0\boldsymbol{\delta q_F^0} = \delta\mathscr{I} \qquad (\mathrm{B}\,14)$$

along with the boundary condition on Γ_c:

$$\boldsymbol{\delta u^0} = \boldsymbol{\delta u_W}\,, \qquad \delta T^0 = \delta T_W\,. \qquad (\mathrm{B}\,15)$$

The modification of the eigenvalue $\delta\lambda$ can be expressed in the framework of the sensitivity to base flow modifications as

$$\delta\lambda = \left\langle \boldsymbol{\nabla}_{\boldsymbol{q^0}}\lambda\,,\, \boldsymbol{\delta q_F^0}\right\rangle \qquad (\mathrm{B}\,16)$$

Using (B 7), and since $\boldsymbol{\nabla}_{\mathscr{I}}\lambda = \boldsymbol{q^{0\dagger}}$, this relation can be rewritten as

$$\delta\lambda = \left\langle \mathcal{A}_0^{\dagger}\boldsymbol{\nabla}_{\mathscr{I}}\lambda\,,\, \boldsymbol{\delta q_F^0}\right\rangle = \left\langle \boldsymbol{\nabla}_{\mathscr{I}}\lambda\,,\, \mathcal{A}_0\boldsymbol{\delta q_F^0}\right\rangle + \mathrm{BT} = \langle \boldsymbol{\nabla}_{\mathscr{I}}\lambda\,,\, \delta\mathscr{I}\rangle + \mathrm{BT}\,, \qquad (\mathrm{B}\,17)$$

according to (*B* 11) and (*B* 14). The boundary term (*ii*) in (*B* 11) being zero, we thus have

$$\delta\lambda = \langle \boldsymbol{\nabla}_{\mathscr{J}}\lambda\,, \delta\mathscr{J}\rangle + \int_{\Gamma_c} (\boldsymbol{\nabla}_{\boldsymbol{u_W}}\lambda\cdot\boldsymbol{\delta u_W} + \boldsymbol{\nabla}_{\boldsymbol{u_W}}\lambda\cdot\delta T_W) r\mathrm{d}l\,, \tag{B 18}$$

and retrieve the variation (2.23) defined formally in the framework of the sensitivity to steady forcing.

Appendix C. Derivation of the adjoint base flow equations

The complete derivation of the adjoint perturbation equations (2.14) is provided in Part I. We focus here on the derivation of the adjoint base flow equations (2.25) and recall that the adjoint operator $\mathcal{A}_0^\dagger$ is such that

$$\left\langle \boldsymbol{q^{0\dagger}}\,,\, \mathcal{A}_0(\boldsymbol{q^0})\boldsymbol{\delta q^0}\right\rangle = \left\langle \mathcal{A}_0^\dagger(\boldsymbol{q^0})\boldsymbol{q^{0\dagger}}\,,\, \boldsymbol{\delta q^0}\right\rangle \tag{C 1a}$$

where $\boldsymbol{\delta q^0}$ is a small modification of the base flow. We define the r and z vector derivatives as $\partial_{r,z}\boldsymbol{q} = (\partial_{r,z}\rho, \partial_{r,z}u, \partial_{r,z}v, \partial_{r,z}w, \partial_{r,z}T)^T$. For convenience, the relevant terms are developed into a matrix form reading

$$\begin{aligned}
\mathcal{A}_0(\boldsymbol{q^0})\boldsymbol{\delta q^0} =& \boldsymbol{A}_1''\boldsymbol{\delta q^0} + \boldsymbol{A}_2''\partial_r\boldsymbol{\delta q^0} + \boldsymbol{A}_3''\partial_z\boldsymbol{\delta q^0} \\
&+ \frac{1}{Re}\partial_r\left(\boldsymbol{V}_1''\partial_r\boldsymbol{\delta q^0} + \boldsymbol{V}_2''\partial_z\boldsymbol{\delta q^0} + \frac{1}{r}\boldsymbol{V}_3''\boldsymbol{\delta q^0}\right) \\
&+ \frac{1}{Re}\partial_z\left(\boldsymbol{V}_2''^T\partial_r\boldsymbol{\delta q^0} + \boldsymbol{V}_4''\partial_z\boldsymbol{\delta q^0} + \frac{1}{r}\boldsymbol{V}_5''\boldsymbol{\delta q^0}\right) \\
&+ \frac{1}{Re}\left(\frac{1}{r}\boldsymbol{V}_6''\partial_r\boldsymbol{\delta q^0} + \frac{1}{r}\boldsymbol{V}_7''\partial_z\boldsymbol{\delta q^0} + \frac{1}{r^2}\boldsymbol{V}_8''\right),
\end{aligned} \tag{C 2}$$

where $\boldsymbol{A}''_{1\ldots3}$ and $\boldsymbol{V}''_{1\ldots8}$ are real 4×4 matrices whose coefficients depend on the base flow variables and are detailed at the end of this Appendix. Integrating by parts leads to

$$\begin{aligned}
\mathcal{A}_0^\dagger\left(\boldsymbol{q^0}\right)\boldsymbol{q^{0\dagger}} =& \boldsymbol{A}_1''^T\boldsymbol{q^{0\dagger}} - \frac{1}{r}\partial_r\left(r\boldsymbol{A}_2''^T\boldsymbol{q^{0\dagger}}\right) - \partial_z\left(\boldsymbol{A}_3''^T\boldsymbol{q^{0\dagger}}\right) \\
&+ \frac{1}{Re}\frac{1}{r}\left(\partial_r\left(r\boldsymbol{V}_1''^T\partial_r\boldsymbol{q^{0\dagger}}\right) + \partial_r\left(\boldsymbol{V}_1''^T\boldsymbol{q^{0\dagger}}\right) + \partial_z\left(\boldsymbol{V}_2''^T\partial_r(r\boldsymbol{q^{0\dagger}})\right) - \frac{1}{r}\boldsymbol{V}_3''^T\partial_r(r\boldsymbol{q^{0\dagger}})\right) \\
&+ \frac{1}{Re}\left(\frac{1}{r}\partial_r\left(r\boldsymbol{V}_2''\partial_z\boldsymbol{q^{0\dagger}}\right) + \partial_z\left(\boldsymbol{V}_4''^T\partial_z\boldsymbol{q^{0\dagger}}\right) - \frac{1}{r}\boldsymbol{V}_5''^T\partial_z\boldsymbol{q^{0\dagger}}\right) \\
&+ \frac{1}{Re}\frac{1}{r}\left(-\partial_r\left(\boldsymbol{V}_6''^T\boldsymbol{q^{0\dagger}}\right) - \partial_z\left(\boldsymbol{V}_7''^T\boldsymbol{q^{0\dagger}}\right) + \frac{1}{r}\boldsymbol{V}_8''^T\boldsymbol{q^{0\dagger}}\right).
\end{aligned} \tag{C 3}$$

Rearranging terms and using the continuity equation for $\boldsymbol{q^0}$ and $\boldsymbol{\hat{q}^1}$ then leads to

$$\mathcal{A}_0^\dagger\left(\boldsymbol{q^0}\right)\boldsymbol{q^{0\dagger}} = \begin{pmatrix} -\boldsymbol{u^0}\cdot\boldsymbol{\nabla}\rho^{0\dagger} + (\boldsymbol{\nabla u^0}\cdot\boldsymbol{u^0})\cdot\boldsymbol{u^{0\dagger}} + (\boldsymbol{u^0}T^{0\dagger})\cdot\boldsymbol{\nabla}T^0 - T^0p^{0\dagger} \\ -\rho^0\boldsymbol{\nabla}\rho^{0\dagger} - \rho^0\boldsymbol{\nabla u^{0\dagger}}\cdot\boldsymbol{u^0} + \rho^0\boldsymbol{\nabla u^0}^T\cdot\boldsymbol{u^{0\dagger}} + \rho^0T^{0\dagger}\boldsymbol{\nabla}T^0 \\ -\frac{1}{Re}\boldsymbol{\nabla}\cdot\boldsymbol{\tau(u^{0\dagger})} - \boldsymbol{\nabla}(p^0T^{0\dagger}) + 2\gamma(\gamma-1)\frac{M^2}{Re}\boldsymbol{\nabla}\cdot\left(T^{0\dagger}\boldsymbol{\tau}(\boldsymbol{u^0})\right) \\ -\rho^0\boldsymbol{u^0}\cdot\boldsymbol{\nabla}T^{0\dagger} - \frac{\gamma}{Pr}\frac{1}{Re}\boldsymbol{\nabla}^2T^{0\dagger} - \rho^0p^{0\dagger} \\ -\frac{1}{\gamma M^2}\boldsymbol{\nabla}\cdot\boldsymbol{u^{0\dagger}} + T^{0\dagger}\boldsymbol{\nabla}\cdot\boldsymbol{u^0} + p^{0\dagger} \end{pmatrix}, \tag{C 4}$$

which yields equation (2.25).

$\boldsymbol{n} = (n_r, 0, n_z)^T$ being the vector normal to the boundary $\partial\Omega$, the boundary term then reads

$$\begin{aligned} BT = &\int_{\partial\Omega}''' \boldsymbol{q^{0\dagger}}\cdot\boldsymbol{A_2''}\boldsymbol{\delta q^0}n_r''r\mathrm{d}z + \int_{\partial\Omega}''' \boldsymbol{q^{0\dagger}}\cdot\boldsymbol{A_3''}\boldsymbol{\delta q^0}n_z''r\mathrm{d}r \\ &+ \frac{1}{Re}\int_{\partial\Omega}''' \boldsymbol{q^{0\dagger}}\cdot\left(\boldsymbol{V_1''}\partial_r\boldsymbol{\delta q^0} + \boldsymbol{V_2''}\partial_z\boldsymbol{\delta q^0} + \frac{1}{r}\boldsymbol{V_6''}\boldsymbol{\delta q^0}\right)n_r r\mathrm{d}z \\ &+ \frac{1}{Re}\int_{\partial\Omega}\left(-\frac{1}{r}\boldsymbol{V_1''}^T\partial_r\left(r\boldsymbol{q^{0\dagger}}\right) + \boldsymbol{V_2''}\partial_z\boldsymbol{q^{0\dagger}} - \frac{1}{r}\boldsymbol{V_3''}^T\boldsymbol{q^{0\dagger}}\right)\cdot\boldsymbol{\delta q^0}n_r r\mathrm{d}z \\ &+ \frac{1}{Re}\int_{\partial\Omega}\boldsymbol{q^{0\dagger}}\cdot\left(\boldsymbol{V_2''}^T\partial_r\boldsymbol{\delta q^0} + \boldsymbol{V_4''}\partial_z\boldsymbol{\delta q^0} + \frac{1}{r}\boldsymbol{V_7''}\boldsymbol{\delta q^0}\right)n_z r\mathrm{d}r \\ &+ \frac{1}{Re}\int_{\partial\Omega}\left(-\boldsymbol{V_2''}^T\frac{1}{r}\partial_r\left(r\boldsymbol{q^{0\dagger}}\right) + \boldsymbol{V_4''}^T\partial_z\boldsymbol{q^{0\dagger}} - \frac{1}{r}\boldsymbol{V_5''}^T\boldsymbol{q^{0\dagger}}\right)\cdot\boldsymbol{\delta q^0}n_z r\mathrm{d}r\,. \end{aligned} \tag{C 5}$$

To determine the boundary conditions that must be satisfied by the adjoint based flow, it is necessary to take into account the boundary conditions of the problem itself. Indeed, on the control surface Γ_c, the boundary condition being $\boldsymbol{u^0} = \boldsymbol{u_W}$ and $T^0 = T_W$, admissible conditions are such that $\boldsymbol{\delta u^0} = \boldsymbol{0}$ and $\delta T_W = 0$ in case one considers only volumetric forcing. Cancellation of this boundary term gives rise to the adjoint boundary conditions $(B\,8) - (B\,9)$. and to the determination of the adjoint base flow quantities.

Finally, the various matrices used for the computation of the sensitivity functions read:

$$-\boldsymbol{A}_1'' = \begin{pmatrix} \boldsymbol{\nabla}\cdot\boldsymbol{u^0} & \frac{1}{r}\partial_r(r\rho^0) & \partial_z\rho^0 & 0 \\ \boldsymbol{u^0}\cdot\boldsymbol{\nabla}u^0 + \frac{1}{\gamma M^2}\partial_r T^0 & \rho^0\partial_r u^0 & \rho^0\partial_r w^0 & \frac{1}{\gamma M^2}\partial_r\rho^0 \\ \boldsymbol{u^0}\cdot\boldsymbol{\nabla}w^0 + \frac{1}{\gamma M^2}\partial_z T^0 & \rho^0\partial_r w^0 & \rho^0\partial_z w^0 & \frac{1}{\gamma M^2}\partial_z\rho^0 \\ \boldsymbol{u^0}\cdot\boldsymbol{\nabla}T^0 + T^0\boldsymbol{\nabla}\cdot\boldsymbol{u^0} & \rho^0\frac{1}{r}T^0 & \rho^0\partial_z T^0 & \rho^0\boldsymbol{\nabla}\cdot\boldsymbol{u^0} \end{pmatrix}$$

$$-2\gamma(\gamma-1)\frac{M^2}{Re}\begin{pmatrix} 0 & 0 & 0 & 0 \\ 0 & 0 & 0 & 0 \\ 0 & 0 & 0 & 0 \\ 0 & \frac{1}{r}\tau^0_{\theta\theta} & 0 & 0 \end{pmatrix}$$

$$-\boldsymbol{A}_2'' = \begin{pmatrix} u^0 & \rho^0 & 0 & 0 \\ \frac{1}{\gamma M^2}T^0 & \rho^0 u^0 & 0 & \frac{1}{\gamma M^2}\rho^0 \\ 0 & 0 & \rho^0 u^0 & 0 \\ 0 & \rho^0 T^0 & 0 & \rho^0 u^0 \end{pmatrix} - 2\gamma(\gamma-1)\frac{M^2}{Re}\begin{pmatrix} 0 & 0 & 0 & 0 \\ 0 & 0 & 0 & 0 \\ 0 & 0 & 0 & 0 \\ 0 & \tau^0_{rr} & \tau^0_{rz} & 0 \end{pmatrix}$$

$$-\boldsymbol{A}_3'' = \begin{pmatrix} w^0 & 0 & \rho^0 & 0 \\ 0 & \rho^0 w^0 & 0 & 0 \\ \frac{1}{\gamma M^2}T^0 & 0 & \rho^0 w^0 & \frac{1}{\gamma M^2}\rho^0 \\ 0 & 0 & \rho^0 T^0 & \rho^0 w^0 \end{pmatrix} - 2\gamma(\gamma-1)\frac{M^2}{Re}\begin{pmatrix} 0 & 0 & 0 & 0 \\ 0 & 0 & 0 & 0 \\ 0 & 0 & 0 & 0 \\ 0 & \tau^0_{rz} & \tau^0_{zz} & 0 \end{pmatrix}$$

$$\boldsymbol{V}_1'' = \widetilde{\mu}\begin{pmatrix} 0 & 0 & 0 & 0 \\ 0 & \frac{4}{3} & 0 & 0 \\ 0 & 0 & 1 & 0 \\ 0 & 0 & 0 & \frac{\gamma}{Pr} \end{pmatrix} \qquad \boldsymbol{V}_2'' = \widetilde{\mu}\begin{pmatrix} 0 & 0 & 0 & 0 \\ 0 & 0 & -\frac{2}{3} & 0 \\ 0 & 1 & 0 & 0 \\ 0 & 0 & 0 & 0 \end{pmatrix}$$

$$\boldsymbol{V}_3'' = \widetilde{\mu}\begin{pmatrix} 0 & 0 & 0 & 0 \\ 0 & -\frac{2}{3} & 0 & 0 \\ 0 & 0 & 0 & 0 \\ 0 & 0 & 0 & 0 \end{pmatrix} \qquad \boldsymbol{V}_4'' = \widetilde{\mu}\begin{pmatrix} 0 & 0 & 0 & 0 \\ 0 & 1 & 0 & 0 \\ 0 & 0 & \frac{4}{3} & 0 \\ 0 & 0 & 0 & \frac{\gamma}{Pr} \end{pmatrix}$$

$$\boldsymbol{V}_5'' = \widetilde{\mu}\begin{pmatrix} 0 & 0 & 0 & 0 \\ 0 & 0 & 0 & 0 \\ 0 & -\frac{2}{3} & 0 & 0 \\ 0 & 0 & 0 & 0 \end{pmatrix} \qquad \boldsymbol{V}_6'' = \widetilde{\mu}\begin{pmatrix} 0 & 0 & 0 & 0 \\ 0 & 2 & 0 & 0 \\ 0 & 0 & 1 & 0 \\ 0 & 0 & 0 & \frac{\gamma}{Pr} \end{pmatrix}$$

$$\boldsymbol{V}_7'' = \widetilde{\mu}\begin{pmatrix} 0 & 0 & 0 & 0 \\ 0 & 0 & 0 & 0 \\ 0 & 1 & 0 & 0 \\ 0 & 0 & 0 & 0 \end{pmatrix} \qquad \boldsymbol{V}_8'' = \widetilde{\mu}\begin{pmatrix} 0 & 0 & 0 & 0 \\ 0 & -2 & 0 & 0 \\ 0 & 0 & 0 & 0 \\ 0 & 0 & 0 & 0 \end{pmatrix}$$

REFERENCES

Airiau, C., Bottaro, A., Walther, S. & Legendre, D. 2003 A methodology for optimal laminar flow control: Application to the damping of tollmien-schlichting waves in a boundary layer. *Phys. Fluids* **15** (5), 1131–1145.

Bearman, W. 1967 The effect of base bleed on the flow behind a twodimensional model with a blunt trailing edge. *Aeronaut. Q.* **18**, 207–224.

Bewley, T.R., Temam, R. & Ziane, M. 2000 A general framework for robust control in fluid mechanics. *Physica D* **138**, 363–392.

Choi, H., Jeon, W.-P. & Kim, J. 2008 Control of flow over a bluff body. *Annu. Rev. Fluid Mech.* **40**, 113–139.

Chomaz, J.-M. 2005 Global instabilities in spatially developing flows: Non-normality and nonlinearity. *Annu. Rev. Fluid. Mech.* **37**, 357–392.

Diaconis, N.S., Jack, J.R. & Wisniewski, R.J. 1957 Boundary-layer transition at mach 3.12 as affected by cooling and nose blunting. *Tech. Rep.* 3928. NASA.

Elias, P.-Q., Chanetz, B., Larigaldie, S., Packan, D. & Laux, C.O. 2008 Mach 3 shock wave unsteadiness alleviation using a negative corona discharge. *AIAA Journal* **46** (8), 2042–2049.

Fabre, D., Auguste, F. & Magnaudet, J. 2008 Bifurcations and symmetry breaking in the wake of axisymmetric bodies. *Phys. Fluids* **20** (5), 051702 1–4.

Fomin, V., Tretyakov, P. & Taran, J.-P. 2004 Flow control using various plasma and aerodynamic approaches (short review). *Aero. Sci. Tech.* **8**, 411–421.

Giannetti, F. & Luchini, P. 2006 Structural sensitivity of the first instability of the cylinder wake. *J. Fluid Mech.* **581**, 167–197.

Gunzburger, M.D. 1997 Introduction into mathematical aspects of flow control and optimization. In *Lecture series 1997-05 on inverse design and optimization methods*. Von Kármán Institute for Fluid Dynamics.

Gunzburger, M.D. 1999 Sensitivities, adjoints and flow optimization. *Int. J. Numer. Meth. Fluids* **31** (1), 53–78.

Higuchi, H. 2005 Passive and active controls of three-dimensional wake of bluff-body. *JSME Int. J. Ser. B* **48** (2), 322–327.

Hill, D.C. 1992 A theoretical approach for analyzing the restabilization of wakes. *Tech. Rep.* 103858. NASA.

Jack, J.R., Wisniewski, R.J. & Diaconis, N.S. 1957 Effects of extreme surface cooling on boundary-layer transition. *Tech. Rep.* 4094. NASA.

Leal, G. & Acrivos, A. 1969 The effect of base bleed on the steady separated flow past bluff objects. *J. Fluid Mech.* **39**, 735–752.

Mair, W.A. 1965 The effect of a rear-mounted disc on the drag of a blunt-based body of revolution. *Aeronaut. Q.* **16**, 350–360.

Marquet, O., Sipp, D. & Jacquin, L. 2008 Sensitivity analysis and passive control of the cylinder flow. *J. Fluid Mech. (in press)* .

Meliga, P., Chomaz, J.-M. & Sipp, D. 2008 Global mode interaction and pattern selection in the wake of a disk: a weakly nonlinear expansion. *Submitted to the J. Fluid. Mech.* .

Monkewitz, P.A. 1988 A note on vortex shedding from axisymmetric bluff bodies. *J. Fluid Mech.* **192**, 561–575.

Moreau, E. 2007 Airflow control by non-thermal plasma actuators. *Jour. Phys. D* **40**, 605–636.

Motallebi, F. & Norbury, J.F. 1981 The effect of base bleed on vortex shedding and base pressure in compressible flow. *J. Fluid Mech.* **110**, 273–292.

Natarajan, R. & Acrivos, A. 1993 The instability of the steady flow past spheres and disks. *J. Fluid Mech.* **254**, 323–344.

Ormières, D. & Provansal, M. 1998 Transition to turbulence in the wake of a sphere. *Phys. Rev. Lett.* **83**, 80–83.

Pralits, J.O., Airiau, C., Hanifi, A. & Henningson, D.S. 2000 Sensitivity analysis using adjoint parabolized stability equations for compressible flows. *Flow, Turb. Comb.* **65**, 321–346.

Roshko, A. 1954 On the drag and shedding frequency of two-dimensional bluff bodies. *Tech. Rep.* 3169. NACA.

Roussopoulos, K. & Monkewitz, P.A. 1996 Nonlinear modelling of vortex shedding control in cylinder wakes. *Physica D* **97**, 264Ũ273.

Schumm, M., Berger, E. & Monkewitz, P.A. 1994 Self-excited oscillations in the wake of two-dimensional bluff bodies and their control. *J. Fluid Mech.* **271**, 17Ũ53.

Sevilla, A. & Martínez-Bazàn, C. 2004 Vortex shedding in high reynolds number axisymmetric bluff-body wakes: Local linear instability and global bleed control. *Phys. Fluids* **16** (9), 3460–3469.

Strykowski, P. J. & Sreenivasan, K.R. 1990 On the formation and suppression of vortex shedding at 'low' reynolds numbers. *J. Fluid Mech.* **218**, 71–107.

Weickgenannt, A. & Monkewitz, P.A. 2000 Control of vortex shedding in an axisymmetric bluff body wake. *Eur. J. Mech. B/Fluids* **19**, 789–812.

ÉPILOGUE

Conclusions

The main objective of this dissertation has been to establish whether the intrinsic synchronized oscillations observed in high-Reynolds number compressible axisymmetric wakes may be ascribed to a hydrodynamic instability occurring at low Reynolds numbers. Different approaches of the stability theory have been used: parallel wakes have first been investigated in the framework of the WKBJ theory (chapter 2), and realistic spatially developing wakes have then been considered (chapters 3 to 6). Results have been presented for both incompressible and compressible flows. Although some questions remain open, as will be discussed in the following, the stability theory has provided converging lines of evidence for the onset of a periodic regime exhibiting large-scale oscillations at sufficiently high Reynolds numbers.

Linear and nonlinear local instability

A numerical method for the linear local stability analysis of ideal parallel axisymmetric wakes has been implemented. A parametric study carried out at low Reynolds numbers has shown that the transition to absolute instability is essentially led by a large-scale mode of axisymmetric wavenumber $m = 1$, whose frequency and azimuthal wavenumber are in qualitative agreement with experimental observations. Various regimes of compressibility effects have been interpreted in terms of a competition between an advection mechanism, that tends to favor convective instability by decreasing the pressure disturbances wave speed, and a production mechanism triggered by the baroclinic torque. The stability of realistic velocity profiles, computed at ONERA via a high resolution LES simulation in the fully turbulent and compressible regimes, has also been considered. Results show that the axisymmetric mean flow sustains a pocket of absolute instability, detached from the base. Even at these highly supercritical parameter settings, the global frequency of the oscillations, as measured by a spectral analysis of time series of the numerical data, is predicted with striking accuracy by the absolute frequency at the upstream station of marginal absolute instability, in agreement with the theory of nonlinear global modes. This makes probable that a nonlinear global mode, the so-called elephant mode, develops in the lee of the afterbody and is responsible for the synchronized oscillations.

Linear and weakly nonlinear global stability

The global stability of the steady axisymmetric wake developing past model geometries of blunt and bluff bodies, namely the disk and the sphere, has first been considered in the incompressible limit (chapter 3). As already outlined in Natarajan & Acrivos [61], the dynamics are somehow similar, as both flows undergo the same sequence of bifurcations. Namely, the first bifurcation involves a stationary global mode of azimuthal wavenumber $m = 1$, and the second Hopf bifurcation, occurring at a higher Reynolds number, involves two oscillating modes of azimuthal wavenumbers $m \pm 1$. The stability analysis has been completed by an adjoint stability analysis, that allowed to discuss the nonnormality of this class of flows, and to identify the recirculating bubble as the intrinsical wavemaker for both global modes and both geometries. However, this analysis fails to consider the fully three-dimensional state prevailing after the first bifurcation, as it focuses on the steady axisymmetric state.

In order to assess the role of the oscillating global mode identified in chapter 3 in the onset of unsteadiness, the leading-order equations describing the nonlinear interaction of the bifurcating eigenmodes have been analytically computed for the disk flow, using the slow manifold and normal form theories (chapter 4). It has been demonstrated that the whole bifurcation sequence predicted by this approach matches qualitatively and quantitatively that found in Fabre *et al.* [28] by means of direct numerical simulations, both for threshold values and symmetries featured by the stable solutions. This indicates that the three-dimensional dynamics of the real flow, in particular the global frequency of the large-scale oscillations, is efficiently captured using a reduced order model based on the destabilization of the axisymmetric steady state. Another conclusion of this study is that unsteadiness arises due to the destabilization of the three-dimensional steady state by the oscillating global mode, the latter mode dominating the dynamics of the three-dimensional flow at larger Reynolds numbers, hence explaining the occurrence of a fully three-dimensional periodic state. However, whether a similar approach can be used to study bodies of any particular shape remains an open question. As an attempt to provide a small part of the answer, we have computed the normal form pertaining to the sphere flow. It was disappointing to find that the resulting sequence of bifurcation is identical to that of the disk, whereas the study of Fabre *et al.* [28] points at subtle differences existing between both flows in terms of the symmetry properties of the stable solutions. A possible explanation for this result lies in the amplitude of the saturated global modes, which have been found to depend strongly on the choice of the critical Reynolds number for the sphere, a result opposite to that discussed in chapter 4 for the disk. This may result from the nonnormality of the bifurcating modes being larger in the case of the sphere, as documented in chapter 3.

In the last two chapters of this dissertation, a consistent framework has been developed in order to extend the classical tools of global stability and adjoint methods to the fully compressible regime. This formalism has been applied to investigate the dynamics of a subsonic axisymmetric afterbody flow. For all Mach numbers up to $M = 0.7$, the bifurcation sequence is identical to that discussed in the incompressible disk and sphere flows (chapter 3). A parametric study has shown that when the Mach number is increased, the associated stationary and oscillating global modes are both stabilized. A sensitivity analysis has demonstrated that this effect is driven by the underlying modification of the base flow that occurs within the recirculating bubble.

A physical interpretation has been proposed in terms of an advection/production dichotomy that stands for the global counterpart of the discussion held in chapter 2 in the framework of the local approach. It turns out that increasing the Mach number mainly thickens the shear-layer region by spreading out the cross-stream gradients of the base flow momentum. In return, this mechanism, which acts on both the streamwise and cross-stream components, enhances the downstream advection of the disturbances. We also find that the same non-parallel mechanism induces an additional stabilization by slightly weakening the production of disturbances.

Flow control

Chapter 6 has put emphasis on the question of flow control, following the line of thought of Hill [38] and Marquet *et al.* [53]. A systematical approach for the open-loop control of unsteady flows has been presented, in case unsteadiness results from a global instability. The main result is that the use of adjoint methods makes it possible to predict beforehand the effect of forcing on the stability of a global mode. In the compressible regime, different forcing methods can be considered, including body forces, mass and heat sources, blowing at the body wall or wall heating and cooling. This formalism has been applied to the subsonic afterbody flow studied in chapter 5. The oscillating global mode has been shown to be most sensitive to forcing within the recirculating bubble. A small control ring mounted at the rear of the afterbody has been proven efficient to stabilize the latter global mode if placed in the vicinity of the separated shear-layer. Similar stabilization has been obtained using axisymmetric heat sources within the recirculation or by blowing fluid through the base, the latter case corresponding to the well-known base bleed strategy. The sensitivity analysis to base flow modifications presented in chapter 5 has evidenced that the stabilizing effect of base bleed is strongly non-parallel, and arises from the simultaneous strengthening of disturbances advection and weakening of disturbances production, involving both the streamwise and cross-stream momentum components.

Suggestions for future works

The insights gained from the investigation of the global dynamics of axisymmetric wakes immediately lead on to the question: *how do these analyses, presented for low Reynolds numbers, pertain to the engineering application?*

It should be kept in mind that all conclusions drawn at this point regarding the development of unsteadiness remain only partial, as they result from linear and weakly nonlinear analyses carried out at low Reynolds numbers, thus valid only close to the bifurcation threshold. At practically meaningful high Reynolds numbers, though, nonlinear effects may be important. For instance, it is obvious that owing to the low Reynolds numbers considered in the present dissertation, the frequencies predicted by the linear global stability analysis of afterbody flows, which are found to be of order $St \simeq 0.05$, do not match the Strouhal number $St \simeq 0.2$ found in experimental set-ups or numerical simulations. Such result is not too surprising, though, as an increase in the Reynolds number is known to yield a significant modification of the frequency of the saturated state. As a result, the Strouhal number measured in the

cylinder wake increases from $St = 0.12$ at the threshold of instability ($Re = 47$) to $St = 0.2$ at $Re = 180$ (Williamson [84]).

The taking into account of the high Reynolds numbers prevailing in the engineering application will certainly represent a main issue to be addressed in future works. The simplest idea would be to investigate the linear stability of global modes sought as perturbations to a high Reynolds number laminar base flow, and to compare the unsteady dynamics to that observed in the wind tunnel experiments. It has been mentioned in chapter 2 that pursuing the presently used Newton methods up to large Reynolds numbers may be particularly involved. Though, other numerical approaches exist to obtain steady solutions beyond the threshold of instability. An alternative has been proposed by Åkervik *et al.* [3] based on a simple time-marching method, along with an artificial damping of the most dangerous temporal frequencies. Such a strategy opens new ways to compute the base flow underlying all stability analyses, as it can be simply implemented into existing numerical codes, such as the elsA and FLU3M solvers developed by ONERA. For blunt geometries, where the separation point is imposed by the geometry of the body, it seems possible to compute a high-Reynolds number laminar steady state. Though, in the most general case, the existence of such a solution is not guaranteed. For instance, in the problem of the shock-induced transonic-buffet over an airfoil, the flow exhibits a shockwave on the upper surface of the airfoil. The boundary-layer interestingly separates from the upper surface downstream of the shock foot and upstream of the trailing edge. Though, a laminar incoming boundary-layer would tend to separate upstream of the shock foot, even close to the leading edge, so that a laminar base flow most likely does not exist for this configuration. The existence of a high-Reynolds number laminar steady state may therefore constitute a critical question.

A possible alternative is to investigate the stability of global modes sought as perturbations to a turbulent base flow. In this perspective, the analysis of the fully turbulent transonic LES simulation in chapter 2 stands as a first and promising step. Though, it has focused on the stability of the axisymmetric *mean* flow, obtained by time and azimuth average of the time-dependent three-dimensional solution. We recall that such mean flow may not be relevant to a stability analysis, as it departs from the *base* flow by encompassing nonlinear interactions under the form of base flow modifications and resonance with the harmonics. Still, it is possible to investigate the stability of a steady axisymmetric RANS solution, as performed by Crouch *et al.* [18], who successfully predicted the occurrence of the shock-induced buffet phenomenon over a NACA 0012 airfoil in high-Reynolds number turbulent compressible flows. Though, the implementation of such an approach requires a substantial modification of the present formalism, namely the addition of an eddy-viscosity equation.

Moreover, we recall here that the present study has considered only the case of Type I configurations, where no reattachment of the separated shear-layer occurs. In the perspective of dealing with more realistic afterbody configurations, there is no doubt that Type II separating-reattaching configurations are to be considered in the future. For introductory purpose, we have proposed to interpret the differences featured by these two classes of flows in terms of the oscillator/amplifier dichotomy. It has been said that Type I flows act as oscillators, whereas Type II flows are more complex: far from the reattachment area, their unsteady dynamics is typical of oscillators. Close to the reattachment point, their specific spectra make probable that they rather act as amplifiers excited by small-scale turbulent eddies developing in the incoming

boundary-layer, amplified while traveling downstream along the separated shear-layer, impinging on the downstream surface and ultimately decaying when leaving the recirculation bubble. Though, this remains unproved. Evidence may come from experimental measurements or numerical simulations of the response of such flows to harmonic forcing.

(a) *Schematic of a model Type II configuration. The main body is identical to that studied in chapters 5 and 6, i.e. the slender body of revolution has a diameter D and a total length $l = 9.8D$. The rear-body extension has a length $L = 1.2D$ and a diameter $d = 0.4D$, as in the S3Ch tests.*

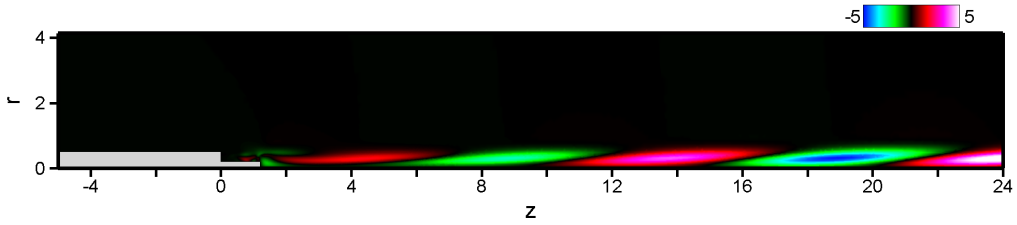

(b) *Spatial distribution of axial velocity for the oscillating global mode (only the real part is shown). The black hue corresponds to vanishing perturbations.*

Figure 7.1. *Global stability analysis of a Type II configuration, $Re = 1800$ - $M = 0.1$.*

Preliminary computations have been carried out during this PhD on the model Type II configuration pictured in Figure 7.1(a), based on the axisymmetric body of diameter D studied in chapters 5 and 6. A cylindrical extension of diameter $d = 0.4D$ and length $L = 1.2D$ is now mounted at the rear of the main body, so as to mimic the experimental configuration introduced in Figure 1.3(b). It turns out that even if the separated flow reattaches, the sequence of global instabilities undergone by the axisymmetric steady state is identical to that documented for the blunt base alone. Figure 7.1(b) shows the spatial structure of the oscillating global mode, namely the real part of the streamwise velocity component, computed for the slightly supercritical settings $Re = 1800$ and $M = 0.1$. One immediately recognizes the typical pattern evidenced for Type I flows, with a global mode exhibiting positive and negative velocity perturbations alternating downstream of the body. Such similarity indicates the existence of a single oscillator dynamics for by both kinds of separations.

To explain the differences featured by these classes of flows, future studies should be devoted to the amplifier dynamics of Type II configurations. This can be done by means of optimal growth analyses, as in the recent study by Ehrenstein & Gallaire [24]. These authors investigated the amplifier dynamics of boundary-layer flows and showed that the appropriate superposition of a moderate number of global modes gives rise to a spatially localized wave packet that experiences large transient energetic growth, characteristic of amplifiers. A possible line of research, that is certainly worth being pursued, lies in this application of such formalism to model axisymmetric separating-reattaching flows, for instance an axisymmetric backward-facing step. The idea is that the complex Type II dynamics may be interpreted as a

competition between the oscillator and the amplifier dynamics, as discussed by Marquet *et al.* [52] in the case of two-dimensional recirculating bubbles. Indeed, it has been said that realistic afterbody flows are inherently subject to noise, owing to the small-scale turbulent eddies that develop in the incoming boundary-layer and act as external sustained perturbations. The amplifier dynamics, which characterizes the transient behaviour of the flow, may thus become dominant if the time necessary to amplify the small-scale turbulence is sufficiently short compared to that needed by the leading global modes to achieve the same energy growth. If so, it would be of great interest to consider developing sensitivity analyses able to encompass transient behaviours, for instance by predicting beforehand the variation of the transient energy gain due to small modifications of the flow conditions.

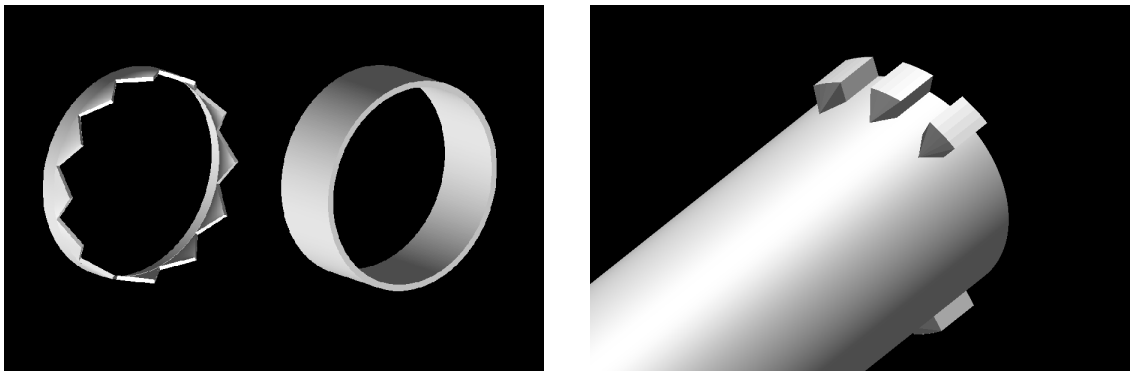

(a) *Serrated and plain cylindrical skirts.* (b) *So-called LBS protuberances.*

Figure 7.2. *A selection of devices used for afterbody flow control.*

A last but very exciting point concerns the ability of the present sensitivity analyses to design efficient open-loop control laws at practically meaningful parameter settings. Figure 7.2 presents a selection of devices, whose ability to reduce the levels of wall-pressure fluctuations has been evaluated in the S3Ch wind tunnel, in the framework of the ATAC program. Two classes of devices were investigated, namely plain/serrated cylindrical skirts and small protuberances mounted at the base, both approaches relying on the introduction of some fixed modification in the flow conditions. Though, it has been said previously that the experimental implementation of such open-loop control is often empirical. In the case of the LBS protuberances, for instance, it means in practice to choose the number of protuberances (even or odd), their shape and orientation with respect to the incoming flow.

In the following, we focus on the effect of the serrated skirt shown in Figure 7.2(a). This skirt, made of 12 teeth for a total length of $0.33D$, has been tested in 2004 on the Type II configuration introduced in Figure 1.3(b). Details, including experimental set-up, wall-pressure distributions and spectral analysis, can be found in Meliga *et al.* [55]. The spectra of the wall-pressure fluctuations measured 0.72 diameter downstream of the base are shown in Figure 7.3, for the nominal configuration (black line) and in the presence of the skirt (grey line). As a matter of fact, if the question of the reattachment phenomenon is left aside, the effect of the skirt on the vortex-shedding activity is disappointing. As an attempt to interpret such results, we have further investigated the model Type II configuration pictured in Figure 7.1(a) by appraising how the addition of a cylindrical skirt of same length than that used in the S3Ch experiment, would

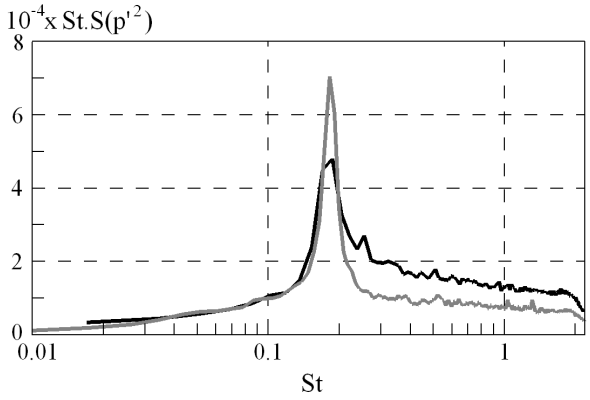

Figure 7.3. *Wall-fluctuations spectra of the Type II configuration shown in Figure 1.3(b) in the absence and in the presence of a short serrated skirt. The black line corresponds to the spectrum obtained for the nominal configuration, 0.72 diameter downstream of the base, which is therefore identical to that already shown in Figure 1.3(d). The grey line corresponds to the spectrum obtained at the same location with the additional skirt.*

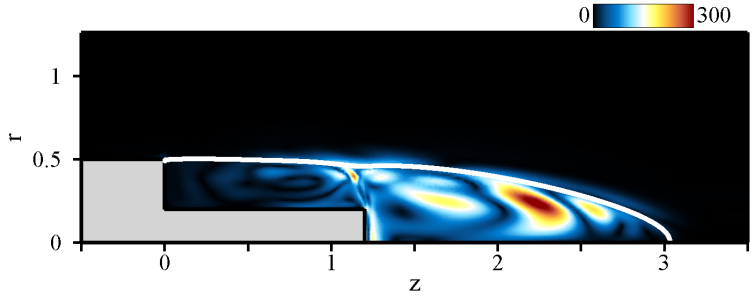

(a) *Magnitude of sensitivity to modifications of the base flow momentum for the oscillating global mode shown in Figure 7.1(b).*

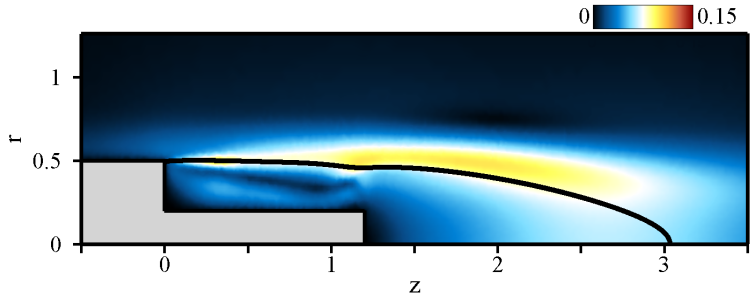

(b) *Base flow momentum modification resulting from the addition of a plain cylindrical skirt of length* $0.33D$.

Figure 7.4. *Sensitivity analysis of the afterbody shown in Figure 7.1(a),* $Re = 1800$ - $M = 0.1$.

affect the growth rate σ_B of the oscillating global mode. The underlying assumption is that the effect of such a skirt is to induce a modification of the base flow, as does the small control cylinder in the studies of Strykowski & Sreenivasan [76] and Marquet *et al.* [53]. Figure 7.4(a) shows the magnitude of the sensitivity function to base flow modifications of the growth rate σ_B, at $Re = 1800$ and $M = 0.1$. This spatial distribution is reminiscent of that discussed in chapter 5 for the blunt base, with large magnitudes of sensitivity found at the separation point and in the tail of the recirculating bubble, but low magnitudes of sensitivity close to the base. Figure 7.4(b) presents the base flow modification resulting from the addition of a cylindrical skirt of length $0.33D$, that has been roughly estimated as the difference between the base flow computed with and without the skirt. It can be seen that interestingly, the magnitude of the base flow modification in the shear-layer region lies at the external periphery of the recirculating bubble, but that the modification of the base flow within the bubble is actually weak. Consequently, it can be predicted beforehand that the effect of the skirt on the oscillating global mode will be somehow limited. Of course, several points remain questionable, for instance, is the base flow modification induced by such a skirt small enough for the linear assumption underlying the sensitivity analysis to hold? At the high Reynolds numbers prevailing in the wind-tunnel tests, the forcing acts both at the level of the steady axisymmetric state and at the perturbation level, as it also modifies the unsteady dynamics of the small-scale turbulence. In this context, is the effect of forcing stationary at leading-order? However, it should be kept in mind that these are only qualitative results, aiming at illustrating the possible fields of application of the sensitivity analysis.

A last possible line of investigation concerns the extension of the compressible adjoint formalism presented in this dissertation to the field of shape optimization. This approach would be particularly well adapted to afterbody flows, as it can be seen that most control strategies consist in a modification of the base geometry. It would thus be of great interest to try implementing adjoint-based sensitivity algorithms into existing solvers. Such procedure may not be easily tractable, though, it may open promising ways to design entirely optimized afterbodies.

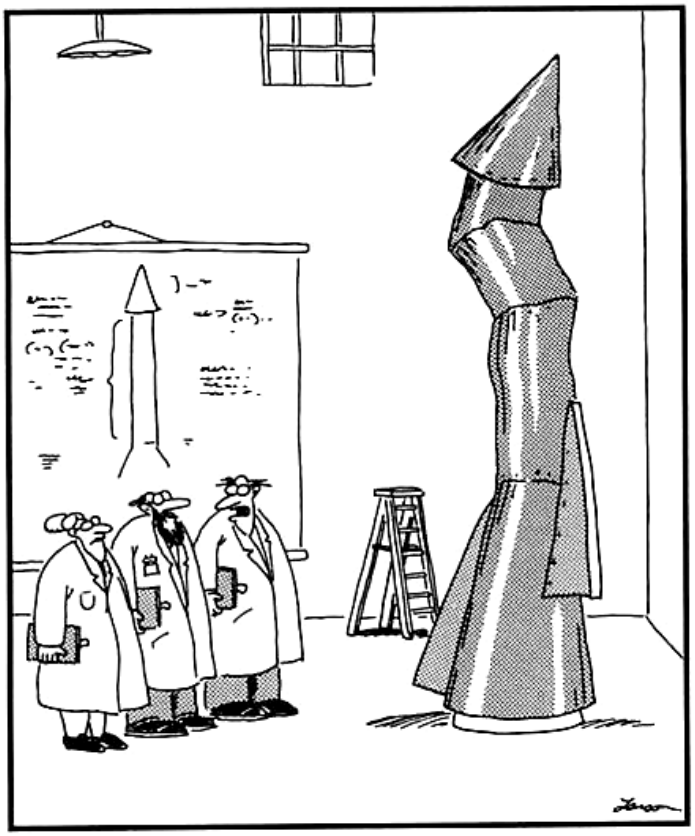

"It's time we face reality, my friends. ...
We're not exactly rocket scientists."

POSTLUDE

Nice, juillet 2008 (et aussi août 2008, septembre 2008)

Carla : Tonton, tonton, tu viens à la plage avec nous?
Moi : Ah euh... non, là, tu sais, je dois finir de rédiger ma thèse... *(lire avec des trémolos dans la voix)*
Carla : Alors tu vas pas à la plage, il fallait finir ta thèse avant de venir!
Moi : ...

BIBLIOGRAPHY

[1] E. Achenbach. Experiments on the flow past spheres at very high Reynolds numbers. *J. Fluid Mech.*, 54:565–575, 1972.

[2] E. Achenbach. Vortex shedding from spheres. *J. Fluid Mech.*, 62:209–221, 1974.

[3] E. Åkervik, L. Brandt, D.S. Henningson, J. Hoepffner, O. Marxen, and P. Schlatter. Steady solutions of the Navier-Stokes equations by selective frequency damping. *Phys. Fluids*, 18(6):068102 1–4, 2006.

[4] D. Barkley, M.G.M. Gomes, and R.D. Henderson. Three-dimensional instability in flow over a backward-facing step. *J. Fluid Mech.*, 473:167–190, 2002.

[5] W. Bearman. The effect of base bleed on the flow behind a twodimensional model with a blunt trailing edge. *Aeronaut. Q.*, 18:207–224, 1967.

[6] H. Bénard. Formation de centres de giration à l'arrière d'un obstacle en mouvement. *Comptes rendus hebdomadaires des séances de l'Académie des sciences*, 147:839–842, 1908.

[7] E. Berger, D. Scholz, and M. Schumm. Coherent vortex structures in the wake of a sphere and a circular disk at rest and under forced vibrations. *J. Fluids Struct.*, 4:231–257, 1990.

[8] A. Bers. *Plasma physics*, chapter Linear waves and instabilities, pages 117–215. Gordon & Breach, published by C. De Witt and J. Peyraud, 1975.

[9] A. Bottaro, P. Corbett, and P. Luchini. The effect of base flow variation on flow stability. *J. Fluid Mech.*, 476:293–302, 2003.

[10] R.J. Briggs. *Electron stream interaction with plasmas*. M.I.T. Press, 1964.

[11] K.M. Butler and B.F. Farrell. Three-dimensional optimal perturbations in viscous shear flow. *Phys. Fluids A*, 4(8):1637–1650, 1992.

[12] J.-M. Chomaz. Absolute and convective instability in non linear systems. *Phys. Rev. Lett.*, 69:1931–1934, 1992.

[13] J.-M. Chomaz. Global instabilities in spatially developing flows: Non-normality and nonlinearity. *Annu. Rev. Fluid. Mech.*, 37:357–392, 2005.

[14] J.-M. Chomaz, P. Huerre, and L.G. Redekopp. A frequency selection criterion in spatially developing flows. *Stud. App. Maths*, 84:119–144, 1991.

[15] S.S. Collis, K. Ghayour, M. Heinkenschloss, M. Ulbrich, and S. Ulbrich. Optimal control of unsteady compressible viscous flows. *Int. J. Numer. Meth. Fluids*, 40:1401–1429, 2002.

[16] A. Couairon and J.-M. Chomaz. Absolute and convective instabilities, front velocities and global modes in nonlinear systems. *Physica D*, 108:236–276, 1997.

[17] J.D. Crouch. Localized receptivity of boundary layers. *Phys. Fluids A*, 4(7):1408–1414, 1992.

[18] J.D. Crouch, A. Garbaruk, and D. Magidov. Predicting the onset of flow unsteadiness based on global instability. *J. Comput. Phys.*, 224:924–940, 2007.

[19] M. Délery J. & Sirieix. Base flows behind missiles. Technical Report LS-98, AGARD, 1979.

[20] D. Deprés. *Analyse physique et modélisation des instationnarités dans les écoulements d'arrière-corps transsoniques*. PhD thesis, Université de la Méditerranée - Aix-Marseille II, 2003.

[21] D. Deprés, P. Reijasse, and J.-P. Dussauge. Analysis of unsteadiness in afterbody transonic flows. *AIAA Journal*, 42(12):2541–2550, 2004.

[22] N. Di Cesare and O. Pironneau. Shock sensitivity analysis. *Comput. Fluid Dynam. J.*, 9:1–15, 2000.

[23] Y. Ding and M. Kawahara. Three-dimensional linear stability analysis of incompressible viscous flows using finite element method. *Int. J. Num. Meth. Fluids*, 31:451–479, 1999.

[24] U. Ehrenstein and F. Gallaire. On two-dimensional temporal modes in spatially evolving open flows: the flat-plate boundary layer. *J. Fluid Mech.*, 536:209–218, 2005.

[25] K.M. Eldred. Base pressure fluctuations. *J. Acoust. Soc. America*, 33(1):59–63, 1961.

[26] P.-Q. Elias. *Effet de plasmas sur une onde de choc dans un écoulement supersonique à Mach 3*. PhD thesis, École Centrale de Paris, 2007.

[27] P.-Q. Elias, B. Chanetz, S. Larigaldie, D. Packan, and C.O. Laux. Mach 3 shock wave unsteadiness alleviation using a negative corona discharge. *AIAA Journal*, 46(8):2042–2049, 2008.

[28] D. Fabre, F. Auguste, and J. Magnaudet. Bifurcations and symmetry breaking in the wake of axisymmetric bodies. *Phys. Fluids*, 20(5):051702 1–4, 2008.

[29] J.-P. Flodrops and J-M. Desse. Sillage d'un culot axisymétrique. Rapport technique 85/19, Institut de Mécanique des Fluides de Lille, France, 1985.

[30] V. Fomin, P. Tretyakov, and J.-P. Taran. Flow control using various plasma and aerodynamic approaches (short review). *Aero. Sci. Tech.*, 8:411–421, 2004.

[31] H.V. Fuchs, E. Mercker, and U. Michel. Large-scale coherent structures in the wake of axisymmetric bodies. *J. Fluid Mech.*, 93:185–207, 1979.

[32] S. L. Gai and S. R. Patil. Subsonic axisymmetric base flow experiments with base modifications. *J. Spacecr. Rockets*, 17:42–46, 1980.

[33] F. Gallaire and J.-M. Chomaz. Mode selection in swirling jet experiments: a linear stability analysis. *J. Fluid Mech.*, 494:223–253, 2003.

[34] F. Gallaire, M. Ruith, E. Meiburg, J.-M. Chomaz, and P. Huerre. Spiral vortex breakdown as a global mode. *J. Fluid Mech.*, 549:71–80, 2006.

[35] F. Giannetti and P. Luchini. Structural sensitivity of the first instability of the cylinder wake. *J. Fluid Mech.*, 581:167–197, 2006.

[36] K. Gumowski, J. Miedzik, S. Goujon-Durand, P. Jenffer, and J.E. Wesfreid. Transition to a time-dependent state of fluid flow in the wake of a sphere. *Phys. Rev. E*, 77:055308 1–4, 2008.

[37] M.C.G. Hall. Application of adjoint sensitivity theory to an atmospheric general circulation model. *J. Atmospheric Sci.*, 43:2644–2651, 1986.

[38] D.C. Hill. A theoretical approach for analyzing the restabilization of wakes. Technical Report TR-103858, NASA, 1992.

[39] D.C. Hill. Adjoint systems and their role in the receptivity problem for boundary layers. *J. Fluid Mech.*, 292:183–204, 1995.

[40] P. Huerre and P.A. Monkewitz. Local and global instabilities in spatially developing flows. *Annu. Rev. Fluid. Mech.*, 22:473–537, 1990.

[41] H. Illy. *Contrôle de l'écoulement au-dessus d'une cavité en régime transsonique*. PhD thesis, Université de Lyon, 2005.

[42] C.P. Jackson. A finite-element study of the onset of vortex shedding in flow past variously shaped bodies. *J. Fluid Mech.*, 182:23–45, 1987.

[43] A. Jameson. Aerodynamic design via control theory. *J. Sci. Comput.*, 3:233–260, 1998.

[44] A. Jameson, L. Martinelli, and N.A. Pierce. Fluid dynamics optimum aerodynamic design using the Navier-Stokes equations. *Theoret. Comput. Fluid Dynamics*, 10:213–237, 1998.

[45] T.A. Johnson and V.C. Patel. Flow past a sphere up to a Reynolds number of 300. *J. Fluid Mech.*, 378:19–70, 1999.

[46] H.J. Kim and P.A. Durbin. Observations of the frequencies in a sphere wake and of drag increase by acoustic excitation. *Phys. Fluids*, 31(11):3260–3265, 1988.

[47] S. Le Dizès, P. Huerre, J.-M. Chomaz, and P.A. Monkewitz. Linear global modes in spatially developing media. *Phil. Trans. R. Soc. Lond.*, 354:169–212, 1996.

[48] G. Leal and A. Acrivos. The effect of base bleed on the steady separated flow past bluff objects. *J. Fluid Mech.*, 39:735–752, 1969.

[49] L. Lesshafft, P. Huerre, P. Sagaut, and M. Terracol. Nonlinear global modes in hot jets. *J. Fluid Mech.*, 554:393–409, 2006.

[50] W.A. Mair. The effect of a rear-mounted disc on the drag of a blunt-based body of revolution. *Aeronaut. Q.*, 16:350–360, 1965.

[51] O. Marquet, M. Lombardi, J.-M. Chomaz, D. Sipp, and L. Jacquin. Direct and adjoint global modes of a recirculation bubble: lift-up and convective nonnormalities. *J. Fluid Mech. (in press)*, 2008.

[52] O. Marquet, D. Sipp, and L. Jacquin. Amplifier and resonator dynamics of a low-Reynolds-number recirculation bubble in a global framework. *J. Fluid Mech.*, 605:429–443, 2008.

[53] O. Marquet, D. Sipp, and L. Jacquin. Sensitivity analysis and passive control of the cylinder flow. *J. Fluid Mech. (in press)*, 2008.

[54] P. Meliga and P. Reijasse. Analyse des mesures instationnaires sur des configurations d'arrière-corps de type Ariane 5 dans la soufflerie transsonique S3ch. Rapport technique RT 3/08645, ONERA, 2007.

[55] P. Meliga, P. Reijasse, and J.-M. Chomaz. Effect of a serrated skirt on the buffeting phenomenon in transonic afterbody flows. In *Proc. of the IUTAM symposium on unsteady separated flows and their control*, 2007.

[56] R.A. Merz. Subsonic base pressure fluctuations. *AIAA Journal*, 17(4):436–438, 1979.

[57] B. Mohammadi and O. Pironneau. Shape optimization in fluid mechanics. *Annu. Rev. Fluid Mech.*, 36:255–279, 2004.

[58] P. A. Monkewitz, P. Huerre, and J.-M. Chomaz. Global linear stability analysis of weakly non-parallel shear flows. *J. Fluid Mech.*, 251:1–20, 1993.

[59] P.A. Monkewitz. A note on vortex shedding from axisymmetric bluff bodies. *J. Fluid Mech.*, 192:561–575, 1988.

[60] F. Motallebi and J.F. Norbury. The effect of base bleed on vortex shedding and base pressure in compressible flow. *J. Fluid Mech.*, 110:273–292, 1981.

[61] R. Natarajan and A. Acrivos. The instability of the steady flow past spheres and disks. *J. Fluid Mech.*, 254:323–344, 1993.

[62] D. Ormières and M. Provansal. Transition to turbulence in the wake of a sphere. *Phys. Rev. Lett.*, 83:80–83, 1998.

[63] B. Pier. On the frequency selection of finite-amplitude vortex shedding in the cylinder wake. *J. Fluid Mech.*, 458:407–417, 2002.

[64] B. Pier and P. Huerre. Nonlinear self-sustained structures and fronts in spatially developing wake flows. *J. Fluid Mech.*, 435:145–174, 2001.

[65] O. Pironneau. *Optimal shape design for elliptic systems*. Springer Verlag, 1984.

[66] J.O. Pralits, C. Airiau, A. Hanifi, and D.S. Henningson. Sensitivity analysis using adjoint parabolized stability equations for compressible flows. *Flow, Turb. Comb.*, 65:321–346, 2000.

[67] J.-C. Robinet. Bifurcations in shock-wave/laminar-boundary layer interaction: global instability approach. *J. Fluid Mech.*, 579:85–112, 2007.

[68] A. Roshko. On the drag and shedding frequency of two-dimensional bluff bodies. Technical Report TN-3169, NACA, 1954.

[69] K. Roussopoulos and P.A. Monkewitz. Nonlinear modelling of vortex shedding control in cylinder wakes. *Physica D*, 97:264–273, 1996.

[70] P.J. Schmid. Nonmodal stability theory. *Annu. Rev. Fluid. Mech.*, 39:129–162, 2007.

[71] M. Schumm, E. Berger, and P.A. Monkewitz. Self-excited oscillations in the wake of two-dimensional bluff bodies and their control. *J. Fluid Mech.*, 271:17–53, 1994.

[72] V. Schwarz and H. Bestek. Numerical simulation of nonlinear waves in the wake of an axisymmetric bluff body. *AIAA Paper 1994-2285*, 1994.

[73] S. Siegel, J. Seidel, K. Cohen, S. Aradag, and T. McLaughlin. Open loop transient forcing of an axisymmetric bluff body wake. *AIAA Paper 2008-595*, 2008.

[74] S.G. Siegel and H.F. Fasel. Effect of forcing on the wake drag of an axisymmetric bluff body. *AIAA Paper 2001-0736*, 2001.

[75] D. Sipp and A. Lebedev. Global stability of base and mean flows: a general approach and its applications to cylinder and open cavity flows. *J. Fluid Mech.*, 593:333–358, 2007.

[76] P. J. Strykowski and K.R. Sreenivasan. On the formation and suppression of vortex shedding at 'low' Reynolds numbers. *J. Fluid Mech.*, 218:71–107, 1990.

[77] S. Taneda. Visual observations of the flow past a sphere at Reynolds numbers between 10^4 and 10^6. *J. Fluid Mech.*, 85:187–192, 1978.

[78] V. Theofilis. Advances in global linear instability analysis of nonparallel and three-dimensional flows. *Prog. Aerospace Sci.*, 39:249–315, 2003.

[79] V. Theofilis and T. Colonius. Three-dimensional instabilities of compressible flow over open cavities: direct solution of the biglobal eigenvalue problem. *AIAA Paper 2004-2544*, 2004.

[80] M.C. Thompson, T. Leweke, and M. Provansal. Kinematics and dynamics of sphere wake transition. *J. Fluid Struct.*, 15:575–585, 2001.

[81] L.N. Trefethen, A.E. Trefethen, S.C. Reddy, and T.A. Driscoll. Hydrodynamic stability without eigenvalues. *Science*, 261:578–584, 1993.

[82] B. Viaud, E. Serre, and J.-M. Chomaz. The elephant mode between two rotating disks. *J. Fluid Mech.*, 598:451–464, 2008.

[83] A. Weickgenannt and P.A. Monkewitz. Control of vortex shedding in an axisymmetric bluff body wake. *Eur. J. Mech. B/Fluids*, 19:789–812, 2000.

[84] C. H. K. Williamson. Defining a universal and continuous Strouhal-Reynolds number relationship for the laminar vortex shedding of a circular cylinder. *Phys. Fluids*, 31(10):2742–2744, 1988.

[85] A. Zebib. Stability of a viscous flow past a circular cylindar. *J. Engng Math.*, 21:155–165, 1987.